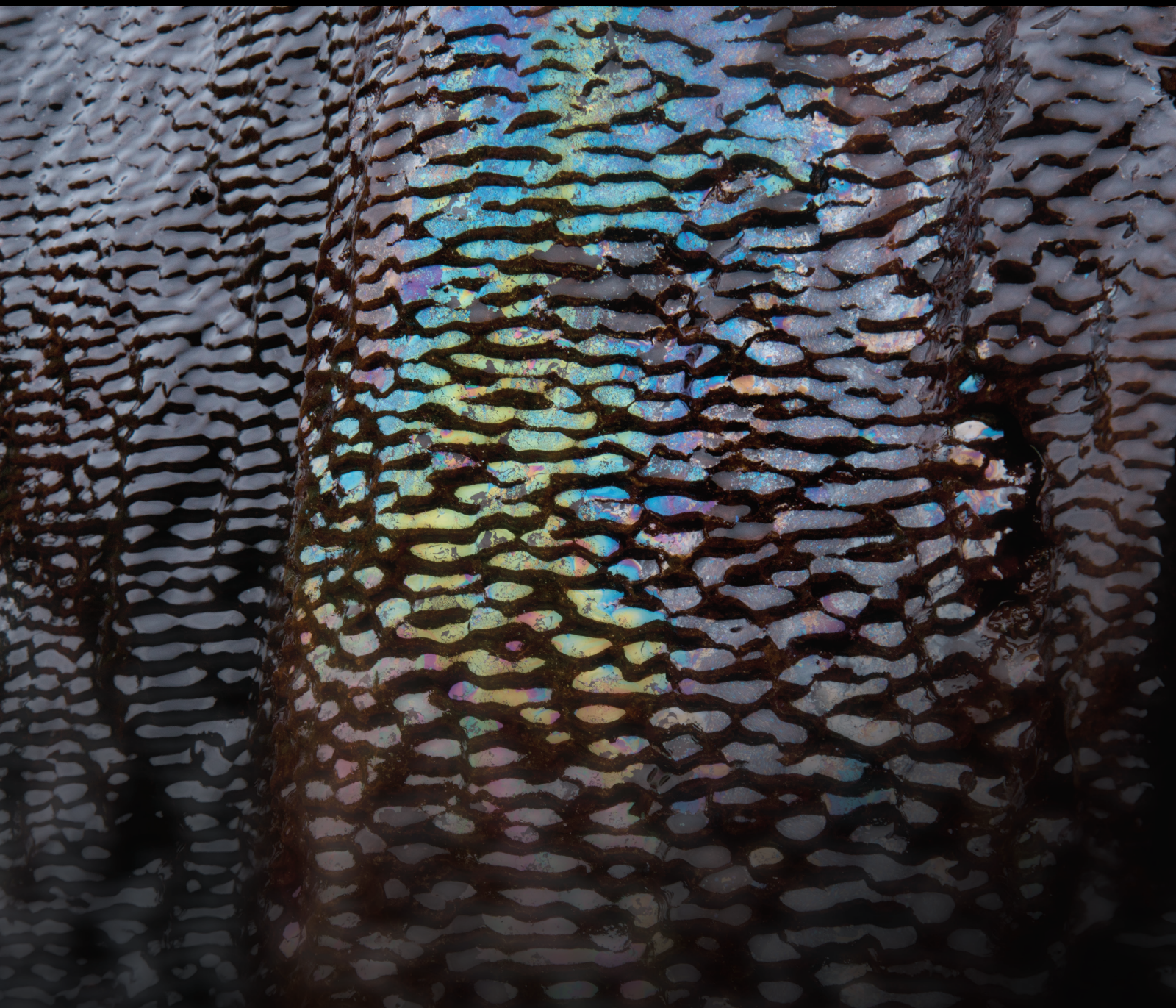


Geofluids Flow in Rock Strata Movement Induced by Coal Mining

Lead Guest Editor: Guozhong Hu

Guest Editors: Qingdong Qu, Yingchun Li, and Jingmin Xu





Geofluids Flow in Rock Strata Movement Induced by Coal Mining

Geofluids

**Geofluids Flow in Rock Strata
Movement Induced by Coal Mining**

Lead Guest Editor: Guozhong Hu

Guest Editors: Qingdong Qu, Yingchun Li, and
Jingmin Xu







Copyright © 2021 Hindawi Limited. All rights reserved.

This is a special issue published in "Geofluids." All articles are open access articles distributed under the Creative Commons Attribution License, which permits unrestricted use, distribution, and reproduction in any medium, provided the original work is properly cited.



























Chief Editor

































Umberta Tinivella, Italy

Associate Editors

Paolo Fulignati , Italy
Huazhou Li , Canada
Stefano Lo Russo , Italy
Julie K. Pearce , Australia

Academic Editors




Basim Abu-Jdayil , United Arab Emirates
Hasan Alsaedi , USA
Carmine Apollaro , Italy
Baojun Bai, USA
Marino Domenico Barberio , Italy
Andrea Brogi , Italy
Shengnan Nancy Chen , Canada
Tao Chen , Germany
Jianwei Cheng , China
Paola Cianfarra , Italy
Daniele Cinti , Italy
Timothy S. Collett , USA
Nicoló Colombani , Italy
Mercè Corbella , Spain
David Cruset, Spain
Jun Dong , China
Henrik Drake , Sweden
Farhad Ehya , Iran
Lionel Esteban , Australia
Zhiqiang Fan , China
Francesco Frondini, Italy
Ilaria Fuoco, Italy
Paola Gattinoni , Italy
Amin Gholami , Iran
Michela Giustiniani, Italy
Naser Golsanami, China
Fausto Grassa , Italy
Jianyong Han , China
Chris Harris , South Africa
Liang He , China
Sampath Hewage , Sri Lanka
Jian Hou, China
Guozhong Hu , China
Lanxiao Hu , China
Francesco Italiano , Italy
Azizollah Khormali , Iran
Hailing Kong, China

Karsten Kroeger, New Zealand
Cornelius Langenbruch, USA
Peter Leary , USA
Guangquan Li , China
Qingchao Li , China
Qibin Lin , China
Marcello Liotta , Italy
Shuyang Liu , China
Yong Liu, China
Yueliang Liu , China
Constantinos Loupasakis , Greece
Shouqing Lu, China
Tian-Shou Ma, China
Judit Mádl-Szonyi, Hungary
Paolo Madonna , Italy
Fabien Magri , Germany
Micòl Mastroicco , Italy
Agnes Mazot , New Zealand
Yuan Mei , Australia
Evgeniy M. Myshakin , USA
Muhammad Tayyab Naseer, Pakistan
Michele Paternoster , Italy
Mandadige S. A. Perera, Australia
Marco Petitta , Italy
Chao-Zhong Qin, China
Qingdong Qu, Australia
Reza Rezaee , Australia
Eliahu Rosenthal , Israel
Gernot Rother, USA
Edgar Santoyo , Mexico
Mohammad Sarmadivaleh, Australia
Venkatramanan Senapathi , India
Amin Shokrollahi, Australia
Rosa Sinisi , Italy
Zhao-Jie Song , China
Ondra Sracek , Czech Republic
Andri Stefansson , Iceland
Bailu Teng , China
Tivadar M. Tóth , Hungary
Orlando Vaselli , Italy
Benfeng Wang , China
Hetang Wang , China
Wensong Wang , China
Zhiyuan Wang , China
Ruud Weijermars , Saudi Arabia

Bisheng Wu , China
Da-yang Xuan , China
Yi Xue , China
HE YONGLIANG, China
Fan Yang , China
Zhenyuan Yin , China
Sohrab Zendeboudi, Canada
Zhixiong Zeng , Hong Kong
Yuanyuan Zha , China
Keni Zhang, China
Mingjie Zhang , China
Rongqing Zhang, China
Xianwei Zhang , China
Ye Zhang , USA
Zetian Zhang , China
Ling-Li Zhou , Ireland
Yingfang Zhou , United Kingdom
Daoyi Zhu , China
Quanle Zou, China
Martina Zucchi, Italy

Contents

Development of Modified Grouting Material and Its Application in Roadway Repair Engineering

Yang Yu , Zhengyuan Qin , Xiangyu Wang, Lianying Zhang, Dingchao Chen , and Siyu Zhu
Research Article (15 pages), Article ID 8873542, Volume 2021 (2021)

Evolution Law of Floor Fracture Zone above a Confined Aquifer Using Backfill Replacement Mining Technology

Shan Ning , Weibing Zhu , Xiaoyong Yi, and Laolao Wang
Research Article (14 pages), Article ID 8842021, Volume 2021 (2021)


Experimental Study on the Flow Behavior of Grout Used in Horizontal Directional Drilling Borehole Grouting to Seal Mining-Induced Overburden Fractures

Jinfeng Ju, Jialin Xu , and Jing Yang
Research Article (12 pages), Article ID 8823902, Volume 2021 (2021)



Influence of Three-Dimensional Stress Field Variation on Fracture Evolution Characteristics of a Roof

Xuyang Shi , Zhaolin Li , Qingxiang Cai , Wei Zhou , and Wenshuai Li 
Research Article (15 pages), Article ID 8810619, Volume 2020 (2020)

Effect of Strain-Dependent Hydraulic Conductivity of Coal Rock on Groundwater Inrush in Mining

Haifeng Lu , Nan Shan, You-Kuan Zhang, and Xiuyu Liang 
Research Article (15 pages), Article ID 8887392, Volume 2020 (2020)



Experimental Investigation into the Influences of Weathering on the Mechanical Properties of Sedimentary Rocks

Xiaoshuang Li, Yingchun Li , and Saisai Wu 
Research Article (12 pages), Article ID 8893299, Volume 2020 (2020)

Evolution Mechanism of Interconnected Vertical Fractures in the Overburden of Longwall Coal Mining

He Changchun , Lu Weiyong , and Zha Wenhua
Research Article (12 pages), Article ID 8862517, Volume 2020 (2020)


Investigation on the Ground Pressure Induced by Hard Roof Fracturing at Different Layers during Extra Thick Coal Seam Mining

Rui Gao , Jingxuan Yang , Tiejun Kuang, and Hongjie Liu
Research Article (15 pages), Article ID 8834235, Volume 2020 (2020)


Analysis and Modeling of Particle Velocities in Premixed Abrasive Water Jets

Wei Qin Zuo , Cheng Huang, Yanwei Liu, Hongkai Han , Fuchang Hao, Fajun Zhao, and Fei Huang
Research Article (9 pages), Article ID 8822502, Volume 2020 (2020)


Model of Heat and Mass Exchange between a Downcast Shaft and the Air Flow to the Mine

WenJing Li, ShengHua Zou , WanXin Yang, and Qi Hu
Research Article (10 pages), Article ID 8853839, Volume 2020 (2020)

Preliminary Study on High-Energy and Low-Energy Microfracture Event Evolution Characteristics in the Development Process of Rock Failure

Guofeng Yu, Guanwen Cheng , Lianchong Li, Chunan Tang, Bo Ren, and Yunchun Han
Research Article (17 pages), Article ID 8880107, Volume 2020 (2020)

Research on the Influence of Slurry Filling on the Stability of Floor Coal Pillars during Mining above the Room-and-Pillar Goaf: A Case Study

Zhu Li, Guorui Feng , and Jiaqing Cui
Research Article (21 pages), Article ID 8861348, Volume 2020 (2020)


Influence of Key Strata on the Gas Downward Leakage Law in Dual-System of Coal Seam

Feng Du, Kun Jiao, and Zhanyuan Ma 
Research Article (10 pages), Article ID 8897260, Volume 2020 (2020)

Effect of Stress and Moisture Content on Permeability of Gas-Saturated Raw Coal

Junhui Wang, Zhijun Wan , Yi Wang , Zhixiang Liu, Sifei Liu, Hongwei Zhang , and Qiuyan Pei
Research Article (13 pages), Article ID 8837758, Volume 2020 (2020)


Experimental Study of Slurry Flow in Mining-Induced Fractures during Longwall Overburden Grout Injection

Dayang Xuan, Jian Li , Kaidan Zheng, and Jialin Xu
Research Article (10 pages), Article ID 8877616, Volume 2020 (2020)


Failure Behavior of Thin Disc Sandstone under Coupled Bending-Seepage Condition

Luzhen Wang and Hailing Kong 
Research Article (15 pages), Article ID 8830358, Volume 2020 (2020)

A Discussion of Reinforcement Timing Optimization for Main Inclined Shaft Roadway with Water Seepage

Minglei Zhang , Chaoyu Chang, and Wen Cao
Research Article (8 pages), Article ID 8850911, Volume 2020 (2020)

Experimental Study on the Gas Flow Characteristics and Pressure Relief Gas Drainage Effect under Different Unloading Stress Paths

Chaolin Zhang , Jiang Xu, Enyuan Wang, and Shoujian Peng
Research Article (10 pages), Article ID 8837962, Volume 2020 (2020)

Numerical Simulation of the Influence of Natural Fractures on Hydraulic Fracture Propagation


Song Yaobin, Lu Weiyong , He Changchun, and Bai Erhu
Research Article (12 pages), Article ID 8878548, Volume 2020 (2020)

Development and Application of Fluid-Solid Coupling Similar Materials in Discharge Test of Old Goaf Water

Zhenhua Li, Mingxiao Ma, and Yongsheng Bao 
Research Article (12 pages), Article ID 8834885, Volume 2020 (2020)

Contents

The Influence of Hydrogeology to Generation of Hydrogen Sulfide of Low-Rank Coal in the Southeast Margin of Junggar Basin, China

Qigen Deng , Tao Zhang, Fajun Zhao, Hao Wang, and Jingping Yin
Research Article (10 pages), Article ID 8859100, Volume 2020 (2020)

Research Article

Development of Modified Grouting Material and Its Application in Roadway Repair Engineering

Yang Yu ¹, Zhengyuan Qin ², Xiangyu Wang,³ Lianying Zhang,¹ Dingchao Chen ¹, and Siyu Zhu¹

¹College of Civil Engineering, Xuzhou University of Technology, Xuzhou, Jiangsu 221111, China

²Nottingham Geospatial Institute, Jubilee Campus, University of Nottingham, Nottingham NG7 2TU, UK

³School of Mines, China University of Mining & Technology, Xuzhou, Jiangsu 221116, China

Correspondence should be addressed to Zhengyuan Qin; originxzit@126.com

Received 30 July 2020; Revised 8 September 2020; Accepted 23 February 2021; Published 4 March 2021

Academic Editor: Qingdong Qu

Copyright © 2021 Yang Yu et al. This is an open access article distributed under the Creative Commons Attribution License, which permits unrestricted use, distribution, and reproduction in any medium, provided the original work is properly cited.

It is very extraordinary for the success of coal mine roadway grouting with the following factors of high early strength, good fluidity, and convenient pumping, but the existing grouting materials make it difficult to achieve the above characteristics at the same time. Therefore, a modified grouting material is developed, which is composed of two kinds of dry materials A and B, which are mixed with water and in equal amounts. The physical and mechanical properties of modified grouting materials under different ratios were tested by laboratory orthogonal test, and the optimal ratio of grouting materials and additives was obtained: (1) the water-cement ratio is 0.8 : 1; (2) base material: the mass ratio of cement, fly ash, bentonite, and water is 1 : 0.3 : 0.1 : 1.44; (3) admixture: the mass ratio of water reducer C, accelerator D, and retarder E is 1.5% : 0.05% : 0.3%. The basic properties of the modified grouting materials were studied from the aspects of slurry flow state, diffusion range, and grouting parameters by using the numerical simulation method, and the reinforcement mechanism of slurry to the broken surrounding rock properties of the roadway was revealed: (1) the grouting pressure is the main factor affecting the slurry diffusion radius; (2) the mechanical properties of the roadway surrounding rock are improved, the plastic zone and deformation of surrounding rock are reduced, and the active support function of the anchor and cable is enhanced through grouting reinforcement; (3) the control effect of the roadway is improved, and the balanced bearing with anchorage structure of the roadway surrounding rock is realized through grouting reinforcement. On this basis, the modified grouting material is applied to roadway repair and reinforcement engineering practice. The field monitoring data show that the production practices were guided by roadway repair and reinforcement technology with the modified grouting material, as the core of the roadway surrounding rock control effect is good, and the modified grouting material has a wide range of application prospects.

1. Introduction

Coal is the main energy and important industrial raw material in China. With the increase of coal mining depth and intensity, there are a large number of complex and difficult roadways in the mine, including soft rock roadway, high stress roadway, strong dynamic pressure roadway, and broken surrounding rock roadway. Among them, the control of broken surrounding rock roadway has been one of the major problems perplexing coal mine safety production [1–6]. Under the influence of tectonic

stress, mining stress, folding fault zone, and other factors, the surrounding rock of the roadway is seriously broken, the deformation is large, the failure rate of the support structure is high, and the control is difficult. According to statistics, 60%–80% of broken surrounding rock roadways need to be repaired many times to maintain their normal use, which leads to heavy maintenance workload, high cost, and poor safety [7–15].

In recent years, various grouting materials are used to reinforce the surrounding rock of roadway, fill cracks, cement broken surrounding rock, increase the integrity and

strength of surrounding rock, improve the self-supporting capacity of broken surrounding rock, improve the anchoring performance of supporting components, control the deformation of surrounding rock, and enhance the stability of roadway. The support and nursing concept and method are gradually applied to mine roadway repair engineering [16–20]. As the key and core factor, the comprehensive performance of grouting material will significantly affect the flow and diffusion range of slurry and ultimately determine the grouting reinforcement effect of the roadway. At present, many scholars have carried out effective research on grouting materials and developed grouting materials with different types and properties [21–34]. It can be divided into inorganic cement slurry and organic chemical slurry: (1) Inorganic cement slurry has the advantages of wide source, high strength of stone body, good impermeability, low price, convenient preparation, simple operation, nontoxic, and harmless. It is the most widely used and the largest amount of grouting material. However, it also has the disadvantages of large size, poor injectivity, long solidification time, and difficulty to control. In grouting engineering, cement admixture is usually added to the cement slurry to improve the water conductivity, stability, fluidity, and solidification properties of slurry, so that the slurry performance can meet the needs of field work. At present, cement slurry is developed in the direction of ultrafine cement, high water quick setting material, silica fume cement slurry material, and nanocement material. (2) Organic chemical grout has the advantages of low viscosity, good injectivity, strong impermeability, good solidification time control, good stability, small grouting pressure, and large slurry diffusion radius, but it also has the characteristics of high price, toxicity, fever, consolidation, low strength, strict construction technology requirements, and other defects and can easily cause coal washing difficulties, pollution of groundwater, and harm to human health, so its application scope is greatly limited.

At present, engineering materials research is focused on a wide range of sources, local conditions, environmental friendliness, and low price. In view of this, according to the characteristics of grouting reinforcement in broken surrounding rock stratum of roadway, a modified grouting material is developed by the author's team. Based on the different mineral composition and hydration mechanism of Portland cement and sulphoaluminate cement, full use was made of industrial solid waste fly ash to turn waste into treasure and reduce the cost of the modified grouting material, which not only has the advantages of adjustable solidification time and high strength, but also overcomes the shortcomings, such as easy pulverization, unstable chemical structure, and ease of corrosion by water. Through the experimental study, the best ratio of grouting materials under specific conditions is determined, and the flow diffusion laws and grouting reinforcement are revealed by numerical simulation. On this basis, the developed modified grouting material is applied to the repair project of broken surrounding rock roadway, which achieves the purpose of fast and stable solidification of broken coal and rock stratum and good control effect of roadway surrounding rock and effectively ensures the safe and efficient mining of coal resources.

2. Preparation of Modified Grouting Material

2.1. Determination of Composition

2.1.1. Grouting Mode. At present, the grouting mode is mainly divided into single liquid and double liquid. The single liquid is composed of one kind of slurry, the most common being cement slurry; the double liquid consists of two kinds of slurry, which are prepared and stored independently, and then injected into the matrix rapidly after the two are fully mixed. From the characteristics of mine roadway repair engineering, it is necessary to adjust the gelation time and early strength according to the broken degree of surrounding rock. Therefore, the modified grouting material adopts double liquid grouting mode.

2.1.2. Composition. The selection of grouting material composition is based on the wide sources of materials, low cost, strong comprehensive performance, and environmental friendliness. The grouting material is composed of two groups of dry materials A and B, which are mixed with water and in equal amounts. Material A is made of Portland cement, and material B is made of sulphoaluminate cement. Two kinds of dry materials with highly complementary chemical properties are composed of fly ash, bentonite, and additives. Before grouting, A material and B material are added into water, to make slurry. Both of them can maintain good fluidity within 2 hours. When grouting, the two slurries are fully mixed. By adjusting the proportion of the two materials, the condensation time can be achieved from a few minutes to several hours, and strength is produced by rapid hardening after condensation.

- (1) *Cementitious materials.* The cementitious material of material A is Portland cement, which has the characteristics of stable strength development, high long-term strength, and large hydration heat due to its high content of silicate minerals. The cementing material of material B is sulphoaluminate cement, which has the characteristics of early strength, high strength, impermeability, and corrosion resistance. When the two kinds of cement are mixed in the proper proportion, the effect of quick setting and early strength can be achieved.
- (2) *Active materials.* Fly ash is a kind of pozzolanic material with certain activity. It has fine particles, many spherical vitreous bodies, and smooth surface. It is distributed between cement particles and increases the compactness of the grouting body. Adding fly ash into cementitious materials can not only increase the fluidity of the paste but also recover industrial waste residue, reduce the amount of cement, and reduce the cost.
- (3) *Bentonite.* Bentonite is a kind of clay mineral with montmorillonite as the main component. It has strong water absorption and is in suspension and gel state in aqueous solution. Using bentonite as the suspending agent can improve the dispersion and

suspension of solid particles of materials A and B in the slurry, avoid the phenomenon of sedimentation and bleeding, and make the material uniformly and stably hydrated to form a homogeneous hydration hardening body.

- (4) *Admixtures*. It includes accelerator, water reducer in material A, and retarder and water reducer in material B. The main function of the admixture is to improve the pumping performance of material A and material B.

2.1.3. Mechanism of Hydration Reaction. The strength of double liquid grouting materials can be rapidly solidified, which is mainly due to the accelerated hydration reaction of Portland cement and sulphoaluminate cement. With Portland cement as the matrix and adding a certain amount of sulphoaluminate cement, the hydration of cement is promoted, the amount of ettringite in the hydration product increases, the setting time of composite cement is shortened, the early strength is increased, and the microexpansion is also observed. When sulphoaluminate cement is used as the matrix and a certain amount of Portland cement is added, the 24-hour strength of the composite system cement is increased, and the dry shrinkage rate of the cement is reduced. At the same time, the production cost of cement can be reduced without reducing the strength. Therefore, the addition of a small amount of other cement clinker has a great influence on the early hydration rate of the matrix cement, which is the same as the hydration mechanism of the matrix cement in the later stage, but it changes the relative proportion and microstructure of the hydration products of the system, thus improving its comprehensive performance.

2.2. The Optimum Ratio Test of Modified Grouting Material

2.2.1. Orthogonal Experimental Design. There are two characteristics of orthogonal experimental design method: balanced dispersion and uniformity. Compared with the uniform test method, the number of tests can be reduced regularly and only representative tests can be done. The correct estimation of test error and intuitive results can be obtained by range analysis. The orthogonal experiment design includes three aspects: (1) select factors and levels according to the experimental requirements, (2) select the orthogonal test table and develop a test plan according to the number of factors and levels, and (3) carry out experiments and analyze the test results.

In the design of slurry proportioning, the additive content is not considered at first, which involves three factors: water cement ratio, fly ash content, and bentonite content. The water cement ratio is the total mass ratio of water to cement, fly ash, and bentonite. The number of levels is determined according to the influence degree of each factor.

(1) Influence of Water-Cement Ratio on Compressive Strength of Slurry Stone. According to the previous test results [35–38], the setting time of Portland cement and sulphoaluminate cement is the shortest after mixing with the same amount. To make the slurry achieve the performance of rapid setting and

early strength, the two are mixed according to the volume ratio of 1:1. The uniaxial compressive strength of mixed slurry stone under five different water-cement ratios is shown in Figure 1.

It can be seen from Figure 1 that with the increase of the water-cement ratio, the compressive strength of the slurry stone specimen gradually decreases, and the reduction range is obvious. When the water-cement ratio is 0.5:1, the compressive strength of the specimen is the highest, which reaches 5.6 MPa in 2 h and 22.8 MPa in 28 d; when the water-cement ratio is 1.5:1, the 28 d compressive strength of the specimen is 10.4 MPa, which is 12.4 MPa lower than that of the water cement ratio of 0.5:1; when the water cement ratio is 2.0:1, its compressive strength is the lowest, which is only 3.4 MPa at 28 d, which is 19.4 MPa lower than that of the 0.5:1 water cement ratio. Therefore, when the water-cement ratio is greater than 1.5:1, the strength of the slurry stone decreases significantly, which cannot meet the requirements of roadway engineering. Therefore, the water-cement ratio should not be greater than 1.5:1.

(2) Influence of Fly Ash on Compressive Strength of Slurry Stone. When the water-cement ratio is 1.0:1, the compressive strength of the slurry stone with different fly ash content is shown in Figure 2. It can be seen from Figure 2 that the cement concentration in the solution decreases because of addition of fly ash, the effective water-cement ratio for controlling the hydration rate of cement increases, and the calcium ion concentration decreases, which weakens the connection between particles and reduces the early compressive strength of the slurry stone.

With the increase of fly ash content, the latter strength of the slurry stone increases first and then decreases. When the content of fly ash is 20%, the compressive strength reaches the maximum, and the 28 d strength reaches 17.68 MPa, which is 16.32% higher than that of the specimen without fly ash. It is mainly due to the remarkable pozzolanic property of fly ash in the later hardening stage. When the content of fly ash is more than 30%, the strength at 2 h is 0 MPa and the strength at 28 d is only 14.8 MPa, which is lower than that of the specimen without fly ash. Therefore, the content of fly ash must be controlled in a certain range, preferably not more than 30%.

(3) Influence of Bentonite on Compressive Strength of Slurry Stone. When materials A and B are mixed with water to form slurry, the phenomenon of water separation will occur, which will affect the performance of the slurry. The addition of bentonite can improve the performance of slurry. When the bentonite is added into the slurry, the smaller montmorillonite particles will be attached to the surface of the larger cement particles due to the larger cement particles and the positive charge on the surface of the cement particles. Due to the good water retention, lubrication, and fluidity of the bentonite slurry, the cement particles will be suspended in the farther and finer rock cracks, thus preventing the cement slurry from solidification due to premature water loss. When the water-

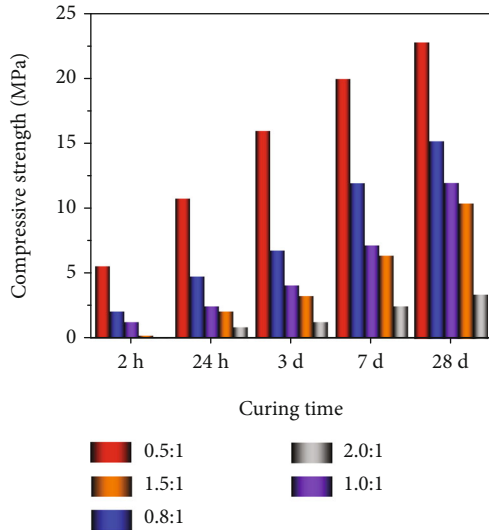


FIGURE 1: Relationship between water-cement ratio and compressive strength of slurry stone.

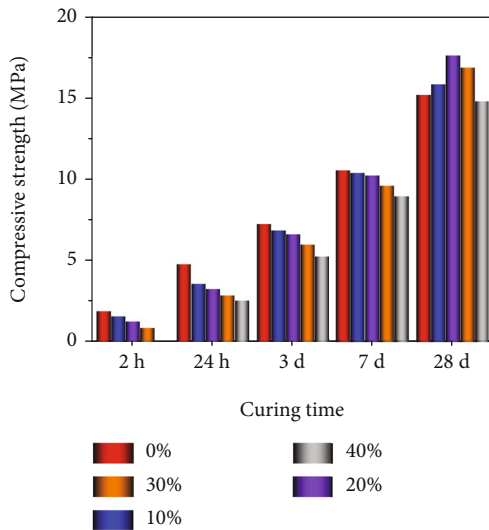


FIGURE 2: Relationship between slurry stone compressive strength and fly ash content.

cement ratio is 1.0:1, the water separation rate of single slurry A and B under different bentonite contents is shown in Figure 3(a). It can be seen from Figure 3(a) that with the increase of bentonite content, the slurry water separation rate gradually decreases. When the bentonite content exceeds 10%, the slurry suspension effect is better, and the water separation rate meets the general requirements. When the bentonite content is 20%, the slurry suspension effect is the best, the water separation rate of liquid A is 4.1%, and that of liquid B is 0%. Therefore, the bentonite content should be more than 10%.

When the water-cement ratio is 1.0:1, the compressive strength of bentonite slurry stone with different content is shown in Figure 3(b). It can be seen from Figure 3(b) that

with the increase of bentonite content, the compressive strength of slurry stone gradually decreases, which is due to the fact that bentonite has almost no cementitious property. When the bentonite content is less than 15%, with the increase of bentonite content, the slurry stone strength decreases slightly, but the strength increases in 2 h. This is because a small amount of bentonite provides an alkaline environment, which speeds up the reaction time and shortens the condensation time.

In conclusion, three factors were selected in the orthogonal test, and three levels were selected for each factor. The levels and factors of orthogonal test are shown in Table 1. Using the L_9 (3^4) orthogonal test table, only 9 tests are needed.

The materials A and B are prepared into slurry. Firstly, Portland cement, sulphoaluminate cement, and fly ash are ground, and the fineness is controlled at the specific surface area of $400 \text{ m}^2/\text{kg}$. Then, the ground materials are mixed with water for 10 min according to the scheme. Finally, A and B solutions are mixed according to the volume ratio of 1:1. The ratio of the orthogonal test is shown in Table 2.

2.2.2. Comprehensive Performance Test Results and Mix Proportion Optimization

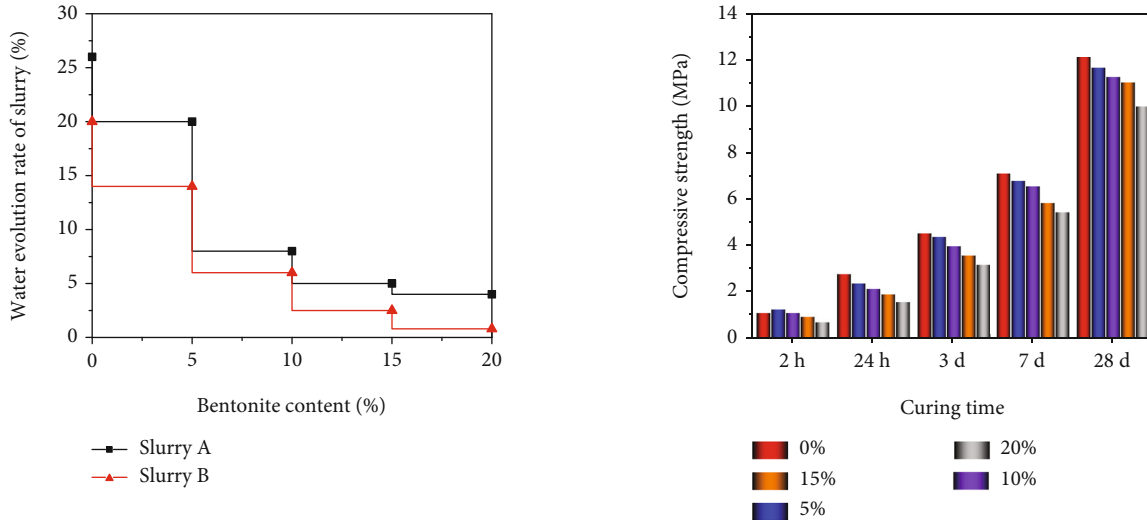
(1) *Analysis of Physical Property Test Results.* The test results of physical properties of A and B slurry are shown in Table 3.

According to the above test results, the range analysis method is used to determine the primary and secondary factors and determine the optimal level and combination. The range analysis method is simple and intuitive. The range analysis results of slurry viscosity, water separation rate, and condensation time are shown in Table 4.

According to the analysis results of slurry viscosity range, the water-cement ratio is the most important factor affecting the slurry viscosity, followed by the bentonite content, and finally the fly ash content. The optimal combination is $A_3C_1B_1$. The slurry viscosity decreases with the increase of water-cement ratio and increases with the increase of bentonite and fly ash content.

According to the range of analysis results of slurry water separation rate, the water-cement ratio is the most important factor affecting the water separation rate of single slurry A and B, followed by the content of bentonite, and finally the content of fly ash. The optimal combination is $A_1C_3B_1$. The increase of fly ash content will lead to the increase of water separation rate, while the increase of bentonite content will lead to smaller water separation rate and better slurry stability.

According to the range of analysis results of condensation time of slurry, the degree of importance of the impact on the condensation time, from large to small, is the water-cement ratio, bentonite content, and fly ash content. For comprehensive initial condensation and final condensation time, the optimal combination is $A_1B_1C_1$. The condensation time of slurry increases with the increase of the water-cement ratio, fly ash, and bentonite content, which is due to the decrease of cement relative concentration in slurry,



(a) Relationship between bentonite content and water separation rate (b) Relationship between bentonite content and compressive strength of slurry

FIGURE 3: Influence of bentonite on compressive strength of slurry.

TABLE 1: Factor level table of orthogonal test.

Level	Water cement ratio	Mass percentage of fly ash	Mass percent of bentonite
	A	B	C
1	0.5 : 1	10%	10%
2	0.8 : 1	20%	15%
3	1.0 : 1	30%	20%

TABLE 2: Orthogonal test group distribution ratio table.

Test serial number	Water cement ratio	Mass ratio of various materials		
		Cement	Fly ash	Bentonite
1	0.5 : 1	1	0.10	0.10
2	0.5 : 1	1	0.20	0.15
3	0.5 : 1	1	0.30	0.20
4	0.8 : 1	1	0.10	0.15
5	0.8 : 1	1	0.20	0.20
6	0.8 : 1	1	0.30	0.10
7	1.0 : 1	1	0.10	0.20
8	1.0 : 1	1	0.20	0.10
9	1.0 : 1	1	0.30	0.15

resulting in slower hydration rate and longer condensation time.

It can be seen that the water-cement ratio is the most important factor affecting the physical properties of the slurry. When the water-cement ratio is 0.8 : 1, the physical properties of the slurry are the best. Under the condition of this ratio, the stability and fluidity of the slurry are good, the stone rate is 100%, and the condensation time is moderate; the slurry with the water-cement ratio of 1.0 : 1 has a

slightly poor stability and a slightly longer condensation time. Although the slurry with the water-cement ratio of 0.5 : 1 has good stability, it has a high viscosity and can only be used in special projects.

(2) Analysis of Mechanical Property Test Results. The test results of mechanical properties of slurry stone are shown in Table 5.

It can be seen from Table 5 that when the water-cement ratio is 0.5 : 1, the compressive strength of the slurry stone specimen is the highest, among which the mechanical properties of the first group of specimens are the best, the 2 h compressive strength is 5.09 MPa, and the 28 d compressive strength is 19.95 MPa; when the water cement ratio is 0.8 : 1, the mechanical properties of the sixth group of specimens are better, and the 28 d compressive strength is 15.48 MPa; when the water cement ratio is 1.0 : 1, the mechanical properties of the eighth group of specimens are better, and the 28 d compressive strength reaches 11.43 MPa.

According to the above test results, the range analysis method is used to determine the primary and secondary factors and determine the optimal level and combination. The range analysis method is simple and intuitive, and the range analysis results of compressive strength of slurry stone at different curing time are shown in Table 6.

The range analysis results show that the water-cement ratio has the greatest influence on the strength of the slurry stone, followed by the content of bentonite and fly ash. According to the requirements of general roadway grouting engineering, the early and late compressive strengths of materials are mainly investigated. The optimal combination of 2 h compressive strength is $A_1B_1C_1$, and that of 28 d compressive strength is $A_1C_1B_3$.

To sum up, when the water-cement ratio is 0.8 : 1, the physical properties of the slurry are the best, and when the water-cement solid ratio is 0.5 : 1, the mechanical properties

TABLE 3: Physical property test results.

Test serial number	Viscosity (s)	Water separation rate (%)		Coagulation (min)	
		Material A	Material B	Primary solidification	Final solidification
1	70.2	1.5	0.2	10	16
2	77.8	2.0	1.4	15	20
3	85.4	2.3	1.8	18	24
4	34.6	7.5	5.8	24	30
5	38.9	4.3	2.4	28	45
6	36.4	8.4	7.5	26	40
7	24.6	12.8	9.6	51	80
8	21.9	15.6	12.6	44	65
9	25.6	12.1	8.3	60	92

TABLE 4: Range analysis table of slurry physical performance.

Test items		Mean and range			Primary and secondary factors	Optimal combination
		A	B	C		
Viscosity	K_1	77.8	43.133	42.833	ACB	$A_3C_1B_1$
	K_2	36.633	46.2	46.267		
	K_3	24.033	49.133	47.3		
	R	53.767	6	6.8		
Water separation rate of material A	K_1	1.933	7.267	8.5	ACB	$A_1C_3B_1$
	K_2	6.733	7.3	7.2		
	K_3	13.5	7.6	6.467		
	R	11.567	0.333	2.033		
Water separation rate of material B	K_1	1.133	5.2	6.767	ACB	$A_1C_3B_1$
	K_2	5.233	5.467	5.167		
	K_3	10.167	5.867	4.6		
	R	9.034	0.667	2.167		
Primary solidification time	K_1	14.333	28.333	26.667	ABC	$A_1B_1C_1$
	K_2	26	29	33		
	K_3	51.667	34.667	32.33		
	R	37.334	6.334	6.333		
Final solidification time	K_1	20	42	40.333	ABC	$A_1B_1C_1$
	K_2	38.333	43.333	47.333		
	K_3	79	52	49.667		
	R	59	10	9.334		

of the slurry stone are the best, but the slurry viscosity under this ratio is large, the flow performance is poor, and it is difficult to pump. When the water-cement ratio is 0.8:1, the mechanical properties of the slurry stone can meet the engineering requirements. Therefore, considering that increasing the content of fly ash can effectively reduce the cost of slurry, the sixth group, namely, the mass ratio of cement, fly ash, bentonite, and water, is 1:0.3:0.1:1.44 as the optimal proportion of slurry.

2.3. Experimental Study on Slurry Admixture Ratio. The main performance requirements of modified grouting mate-

rials in mine roadway engineering include high early strength, good fluidity, and convenient pumping. The specific performance indexes of the modified grouting material are as follows.

- (1) The condensation speed is fast and the early strength is high. The compressive strength is more than 2.0 MPa and not less than 15.0 MPa after 28 days
- (2) The initial viscosity of the slurry is low, the fluidity is good, the slurry does not solidify within 2 hours, and the water separation rate is less than 5%

TABLE 5: Mechanical property test results.

Test serial number	Compressive strength (MPa)			
	2 h	24 h	3 d	28 d
1	5.09	10.03	14.11	19.95
2	3.11	6.94	11.32	18.77
3	1.66	5.02	8.28	17.25
4	1.31	4.01	6.05	13.01
5	0.82	2.99	5.10	11.09
6	1.05	3.43	5.88	15.48
7	0.49	2.41	4.12	9.51
8	0.59	3.01	5.03	11.43
9	0.3	1.88	3.92	10.98

- (3) The gel time can be adjusted from a few seconds to a few minutes

However, reasonable admixtures should be added in practical application to make its strength performance and working performance meet the engineering requirements. In this experiment, the sixth group of slurry with a water-cement ratio of 0.8:1 was selected. The orthogonal test design method was used to study the influence of the content of water reducer C, accelerator D, and retarder E on the compressive strength of slurry stone. The content of admixture was comprehensively determined by measuring the compressive strength of slurry stone at 2 h, 24 h, 2 d, and 7 d. The test process and method are similar to the above optimized proportion of the slurry, so we will not repeat it. We only state the test results: the content of water reducer C and accelerator D has the greatest impact on the 2 d and 7 d compressive strength of the slurry, and the content of retarder E has a greater impact on the 2 h compressive strength of the slurry. From the point of view of improving the compressive strength of the slurry stone, the optimal ratio of the admixture content is finally selected. The mass ratio of water reducer C: accelerator D: retarder E is 1.5%:0.05%:0.3%.

3. The Action Mechanism of Slurry on Broken Rock Mass

3.1. Numerical Simulation Model. The process of grouting reinforcement of roadway surrounding rock involves two physical field coupling problems: stress field and seepage field. Therefore, the fluid analysis module in UDEC numerical simulation software is selected to establish fluid-solid coupling model by setting Bingham fluid model to simulate of slurry flow along surrounding rock fracture of roadway. Taking the belt transportation roadway of Qipanjing coal mine in Inner Mongolia of China as the research background, a numerical calculation model is established. Considering the boundary conditions of roadway and grouting, leakage, and other factors, the size of the model is length \times height = 100 m \times 83.2 m. The upper boundary of the model is a stress boundary. The vertical load is about 11.3 MPa calculated by the buried depth of 450 m. The length \times height of the roadway is 5.2 m \times 3.6 m. The grouting slurry is designed as

cement slurry with the following main parameters: density 1500 kg/m³, viscosity 25 Pa·s, and yield strength 5.0 MPa. The grouting hole is located at the end of the bolt. The designed grouting depth is 3.0 m, and the sealing length is 1.0 m. The grouting reinforcement is carried out after the roadway excavation and the implementation of bolt support. The constitutive model is the Mohr-Coulomb model. The mechanical parameters of the rock stratum and structural plane are shown in Tables 7 and 8.

3.2. Influence of Grouting Parameters on Grout Diffusion Range. By changing the two key parameters of grouting pressure and water-cement ratio, the variation law of slurry diffusion range is studied. The statistical results are shown in Figure 4. It can be seen from Figure 4 that when the distribution of surrounding rock fissures is fixed, the grouting pressure has a greater influence on the slurry diffusion range, while the water-cement ratio has a small impact. However, with the increase of grouting pressure, the influence of grouting pressure on the diffusion range of slurry decreases, and the influence of the water-cement ratio gradually increases. Therefore, the grouting pressure should not exceed 2.0 MPa, the water cement ratio is about 0.8:1, and the slurry diffusion range can meet the requirements of general roadway engineering.

3.3. Distribution of Grouting Pressure in Surrounding Rock. When the water-cement ratio of slurry is 0.6 and 0.8, respectively, the distribution curve of slurry pressure along the axial direction of grouting hole is shown in Figure 5 under different grouting pressure conditions. It can be seen from Figure 5 that the slurry pressure reaches the peak value about 1.2 m away from the roadway surface, the slurry pressure diffuses to the roadway surface for a short distance, the pressure attenuation is fast, and the attenuation is 0 MPa when reaching the roadway surface; the slurry pressure diffuses to the deep part of the surrounding rock of the roadway, the attenuation speed is slow, and there is still a certain residual pressure after attenuation of 3.0 m. Therefore, while increasing the grouting pressure to increase the spreading range of the grout, it is necessary to seal the surface of the roadway. In addition, the grouting pressure distribution curve is similar under different grouting pressure conditions. With the decrease of water-cement ratio, the grouting pressure decreases continuously.

3.4. Influence of Grouting on Plastic Zone of Surrounding Rock of Roadway. Two kinds of working conditions of repairing and strengthening the deformed and damaged roadway are simulated, respectively: (1) bolt and cable support alone and (2) grouting in the roadway first and then supporting with bolt and cable. The distribution characteristics of the plastic zone of surrounding rock under two working conditions are shown in Figure 6. It can be seen from Figure 6 that the plastic zone of the roadway with bolt and cable support based on grouting is smaller than that of simple bolt and cable support, especially on the two sides of roadway with an average reduction of more than 40%. It shows that grouting reinforcement technology in broken surrounding rock can improve the mechanical properties of surrounding rock,

TABLE 6: Range analysis table of mechanical properties of slurry stone.

Test items		Mean and range			Primary and secondary factors	Optimal combination
		A	B	C		
Compressive strength of 1 h	K_1	3.287	2.297	2.243	ABC	$A_1B_1C_1$
	K_2	1.060	1.507	1.573		
	K_3	0.460	1.003	0.990		
	R	2.827	1.294	1.253		
Compressive strength of 24 h	K_1	7.330	5.483	5.490	ABC	$A_1B_1C_1$
	K_2	3.477	4.313	4.277		
	K_3	2.433	3.443	3.473		
	R	4.897	2.040	2.017		
Compressive strength of 3 d	K_1	11.237	8.093	8.340	ACB	$A_1C_1B_1$
	K_2	5.677	7.150	7.097		
	K_3	4.357	6.027	5.833		
	R	6.880	2.066	2.507		
Compressive strength of 28 d	K_1	18.675	14.157	15.620	ACB	$A_1C_1B_3$
	K_2	13.193	13.763	14.253		
	K_3	10.640	14.570	12.617		
	R	8.017	0.807	3.003		

TABLE 7: Rock mechanics parameters.

Rock stratum	Bulk modulus (GPa)	Shear modulus (GPa)	Internal friction angle ($^\circ$)	Cohesion (MPa)	Tensile strength (MPa)
Overlying strata	9.80	8.00	34	5.50	2.10
Main roof	6.40	5.30	28	3.30	1.90
Immediate roof	4.50	4.90	27	3.10	1.70
9# coal seam	2.60	2.50	20	1.20	1.30
Immediate floor	4.80	4.80	28	2.90	1.68
Main floor	5.40	5.30	28	3.35	1.89
Underlying strata	9.70	8.32	33	5.40	2.06

TABLE 8: Mechanical parameters of contact surface.

Rock stratum	Normal stiffness (GPa)	Tangential stiffness (GPa)	Internal friction angle ($^\circ$)	Cohesion (MPa)	Tensile strength (MPa)
Overlying strata	4.90	0.45	30	0.27	0.11
Main roof	3.20	0.26	24	0.16	0.08
Immediate roof	2.92	0.18	19	0.11	0.05
9# coal seam	1.11	0.10	16	0.06	0.03
Immediate floor	2.82	0.16	18	0.12	0.06
Main floor	3.31	0.24	23	0.15	0.09
Underlying strata	4.86	0.46	32	0.26	0.12

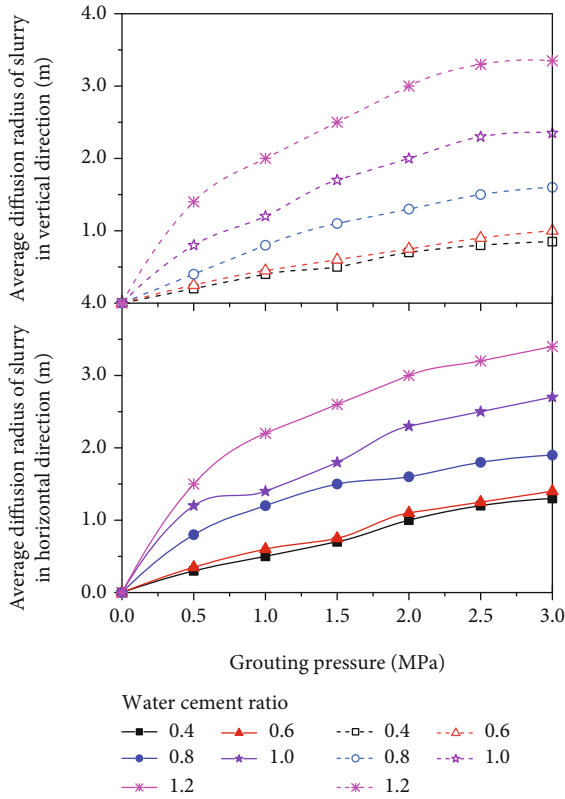


FIGURE 4: Variation law of slurry diffusion range.

increase the stability of the structure, enhance the active support effect of anchor cable, and improve the control effect of surrounding rock.

3.5. Influence of Grouting on Surrounding Rock Displacement of Roadway. After roadway deformation and failure, the deformation of roadway under two different working conditions is shown in Figure 7. After bolt and cable support, the roadway roof subsidence is 260 mm, the displacement of two sides is 675 mm, and the floor heave is 208 mm; after bolt and cable support based on grouting, the roadway roof subsidence is 165 mm, the displacement of two sides is 432 mm, and the floor heave is 138 mm. The decline rates were 36.5%, 36%, and 33.7%, respectively. It can be seen from Figure 7 that under the two different working conditions, the deformation of roadway is relatively large, but after grouting reinforcement, the bearing capacity of surrounding rock of the roadway has limited improvement. The deformation of the roadway can be effectively controlled by implementing the reasonable support mode and parameters of bolt and cable.

3.6. The Influence of Grouting on the Supporting Structure. After the deformation and failure of the roadway, two different working conditions are used to repair and reinforce the roadway, and the stress situation of the roadway support structure is shown in Figure 8. It can be seen from Figure 8 that the loose range of the roadway is effectively controlled by grouting reinforcement of the broken roadway, and the cracks of loose circle are filled with slurry, so that the original

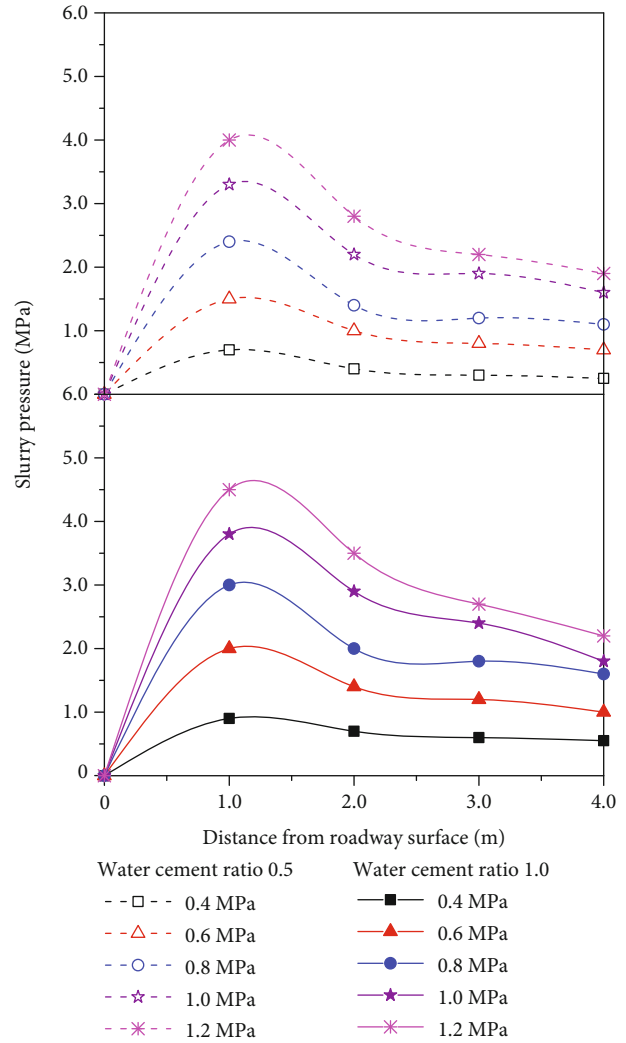


FIGURE 5: Grouting pressure distribution curve.

broken surrounding rock is reinforced, the shallow surrounding rock becomes relatively homogeneous, and the anchoring effect is improved. Compared with the simple bolt and cable support, the bolting structure with bolt and cable support based on grouting has better anchoring performance and more uniform stress. The anchorage structure of the roadway realizes balanced bearing, avoids the damage of support structure caused by local stress concentration, and increases the overall stability of the roadway.

4. Industrial Test

4.1. Engineering Background. The Qipanjing coal mine is located in Inner Mongolia, China, with a design production capacity of 0.3 Mt/a, a field area of 19.59 km², and a service life of 34.3 a. It adopts inclined shaft development, single level, and panel mining, and the main roadways are arranged along the 9# coal seam. The coal seam has a buried depth of 450 m, an average thickness of 2.91 m, and a complex structure with five layers of mudstone and gangue. The immediate roof is sandy mudstone (2.6 m), the main roof is coarse and fine sandstone (8.25 m), the immediate floor is sandy

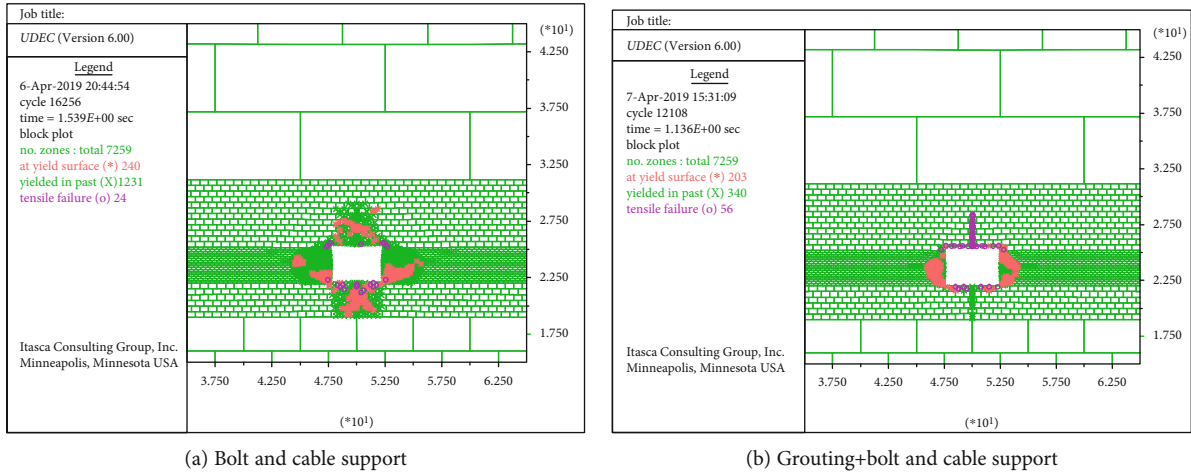


FIGURE 6: Distribution characteristics of plastic zone in surrounding rock of roadway.

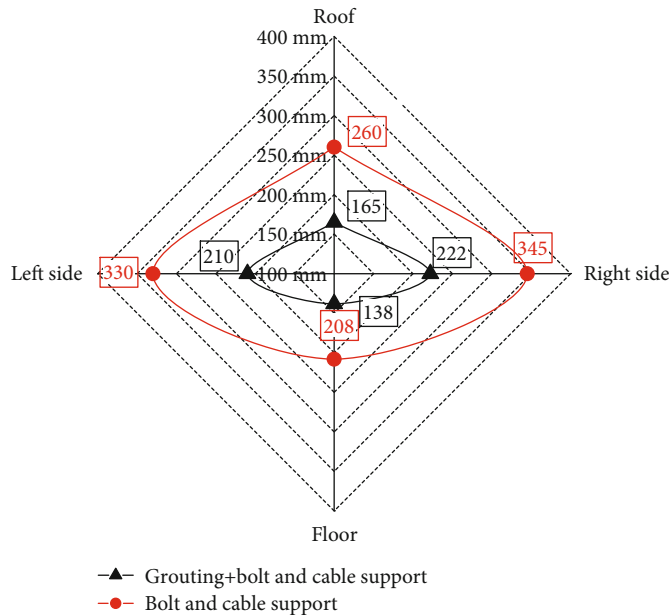


FIGURE 7: Deformation of surrounding rock of roadway.

mudstone (1.5 m), and the main floor is siltstone and sandy mudstone (5.05 m). Auxiliary transportation, belt transportation, and return air roadways (hereinafter referred to as roadway group) are arranged along the 9# coal seam roof. Due to the influence of mining on the two wings of the 020906 and 020907 working faces, the overall deformation is large and the damage occurs in different degrees. Among them, the auxiliary transportation roadway is the most serious, as shown in Figure 9.

4.2. Roadway Repair Principle. The roadway group has been disturbed by mining stress for many times. The loose circle of surrounding rock is large, the structure is loose and broken, the deformation of surrounding rock is large, and the local position is damaged and unstable. It is difficult to ensure

the stability of the roadway with original bolt shotcrete support. Therefore, in order to ensure the normal operation of the mine, it is necessary to repair and reinforce the roadway group, restore the original design section, reshape the structure of the surrounding rock, improve the mechanical properties of the surrounding rock, and form a long-term effective support structure.

The grouting technology can fill the surrounding rock cracks, block the water passage, reduce the weathering and hydration of the surrounding rock, consolidate the surrounding rock into a whole, reduce the stress concentration coefficient of the surrounding rock, and provide a reliable anchoring foundation for the bolt and cable support. Meanwhile, the bolt and cable support system can form a certain supporting pressure on the surrounding rock after grouting

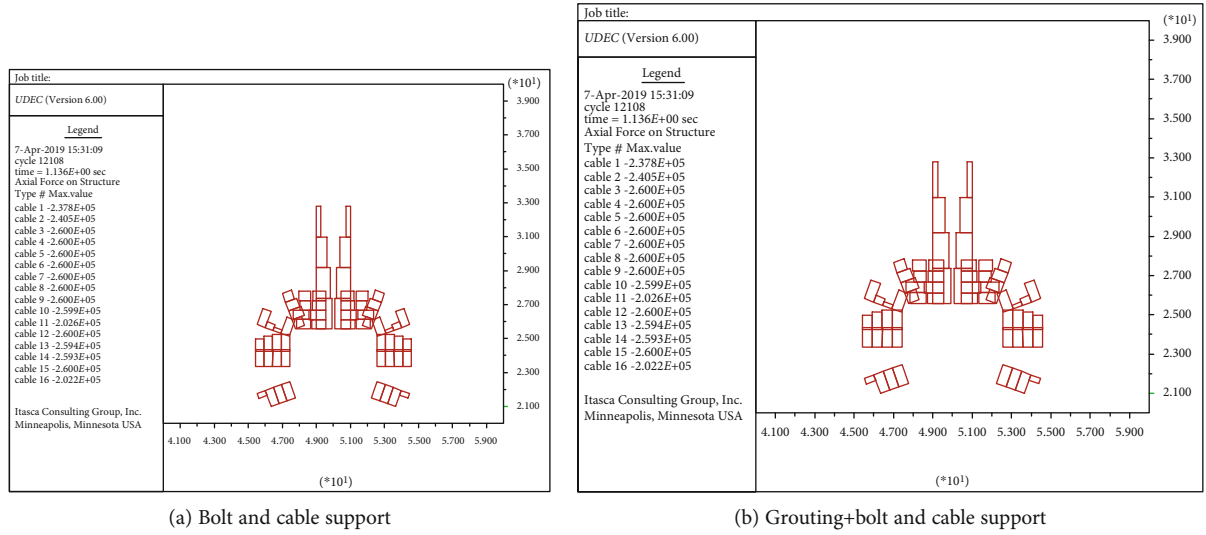


FIGURE 8: Stress state of roadway support structure.

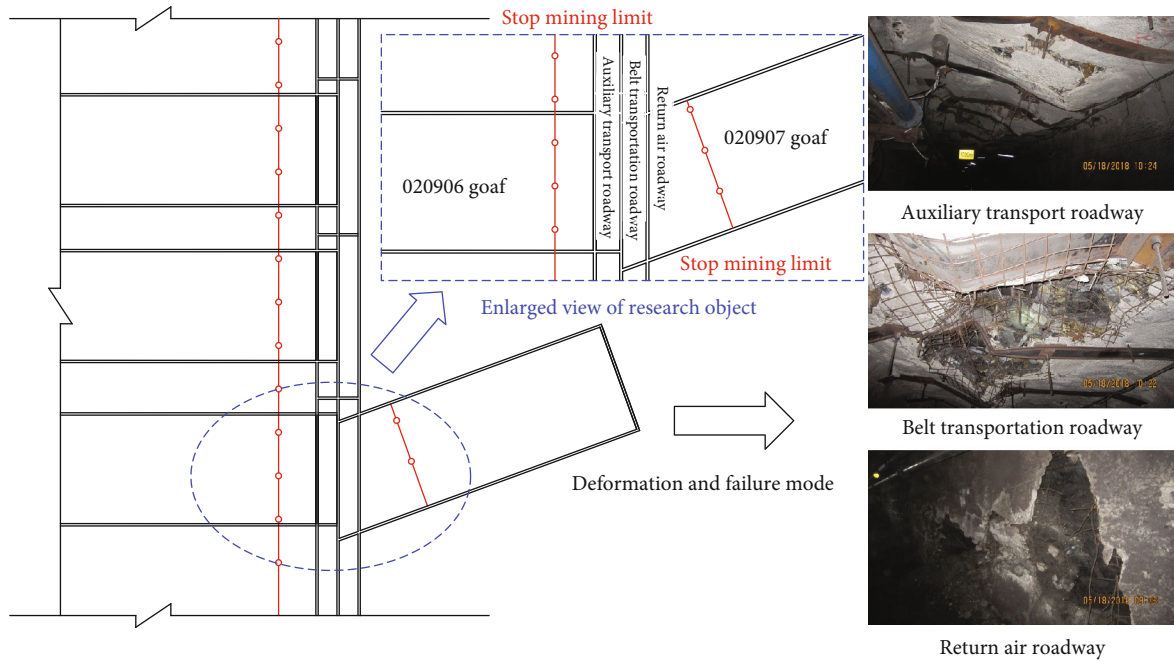


FIGURE 9: Roadway position and deformation and failure.

and improve the stress environment of the roadway. Therefore, the combination of the bolt, cable support, and grouting can help to form the reinforcement layer and reshape the structure of the surrounding rock.

4.3. Roadway Surrounding Rock Control Parameters

4.3.1. Grouting Parameters. The industrial test was carried out in the auxiliary transportation roadway. The grouting parameters of the roadway are shown in Table 9. The row spacing between grouting holes is mainly determined by the slurry diffusion radius, and the row spacing of the grouting holes is 0.6-0.8, twice the diffusion radius. Grouting is divided into two times: the first grouting hole is drilled according to the row spacing of 3.2 m, and the hole depth is

3.0 m; the second grouting hole is arranged in the middle of the first two rows of grouting holes, and the final row spacing is 1.6 m, as shown in Figure 10.

4.3.2. Bolt and Cable Support Parameters. According to the dynamic system design method, the roadway support parameters are obtained. Bolt parameters: HRB500, 20 mm in diameter, 2400 mm in length, and 80 mm in yield distance are used in the roof and sides, with the spacing of 800 mm \times 800 mm; the 10# wire mesh is laid and the diameter of 14 mm steel ladder beam is connected. Cable parameters: the roof is supported by high-strength prestressed yield cable with a diameter of 21.6 mm, length of 8300 mm, and yield distance of 120 mm, with spacing of 2000 mm \times 2400 mm;

TABLE 9: The grouting parameters.

Serial number	Project	Parameters
1	Grouting materials	Modified grouting material
2	Water cement ratio	1.5 : 1
3	Lag grouting time	3-5 days after shotcreting
4	Grouting pipe	R25N self-drilling grouting anchor with length of 2.5 m and yield strength of 150 kN
5	Grouting pressure	2.0-3.0 MPa
6	Grouting quantity	Stop grouting when the design grouting pressure is reached or a large amount of grout leakage occurs
7	Slurry diffusion radius	About 2.5 m
8	Depth of grouting hole	3.0 m

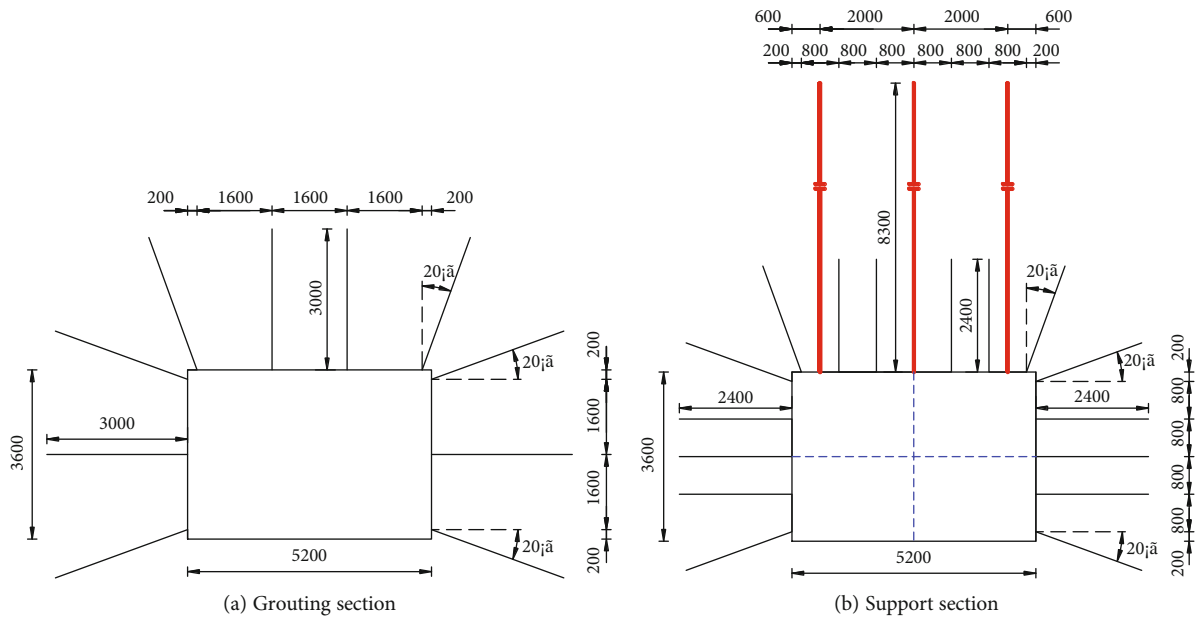
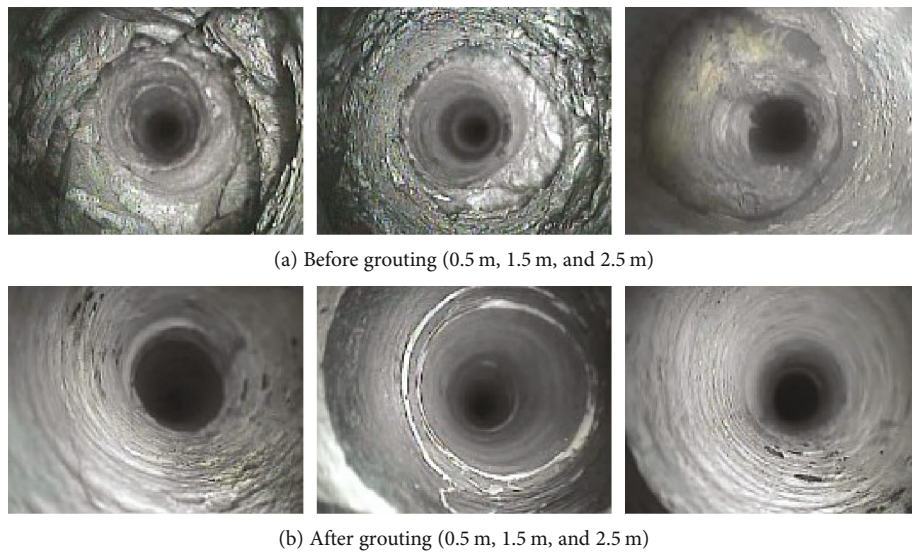


FIGURE 10: Roadway section with repair and reinforcement.



(a) Before grouting (0.5 m, 1.5 m, and 2.5 m)

(b) After grouting (0.5 m, 1.5 m, and 2.5 m)

FIGURE 11: Borehole peep.

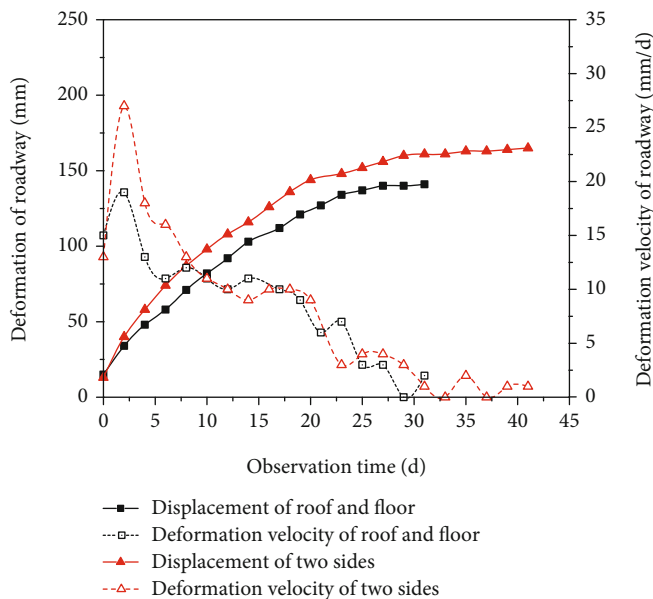


FIGURE 12: Surface displacement curve.

M-shaped steel strip with thickness of 3.5 mm is connected, as shown in Figure 10.

4.4. Mine Pressure Monitoring and Analysis. After the reinforcement and repair of auxiliary transportation roadway, two stations were set up at an interval of 20 m to monitor the grouting effect and surface displacement.

4.4.1. Borehole Peeping. YTJ20 rock detector is used to carry out borehole detection, as shown in Figure 11. Before grouting, the shallow part of the roof is completely broken, there are a lot of cracks, and the integrity is poor; after grouting, the broken coal and rock mass is fully cemented and evenly distributed, and the surrounding rock strength is strengthened. The grouting effect of the two sides is similar.

4.4.2. Surface Displacement. After the roadway is repaired and reinforced, the stability period of the surrounding rock is about 25 days. Due to grouting and high-strength yielding bolt and cable reinforcement support from the reinforcement layer, the bearing capacity of surrounding rock is significantly improved, the surrounding rock deformation is uniform, and the overall deformation is small, and the section meets the production requirements, as shown in Figure 12.

5. Conclusions

(1) Based on the defects of existing grouting materials and the characteristics of a coal mine roadway, a modified grouting material was developed by using the double liquid grouting mode. The material is composed of two groups of dry materials A and B, which are mixed with water and in equal amounts. The material A is made of Portland cement and material B is made of sulphoaluminate cement.

The influence of component content on the physical and mechanical properties of grouting materials was studied by orthogonal test, and the optimal ratio was obtained, in which the water-cement ratio was 0.8:1 and the mass ratio of cement, fly ash, bentonite, and water was 1:0.3:0.1:1.44. Considering from the perspective of improving the compressive strength of the slurry stone, the optimized ratio of admixture content is selected, and the mass ratio of water reducing agent C:accelerator D:retarder E is 1.5%:0.05%:0.3%

(2) By means of numerical simulation, the influence of grouting parameters and grouting pressure of modified grouting material on grouting flow properties is simulated. The reinforcement effect of modified grouting material on surrounding rock properties of the roadway is mainly studied, and the rules of modified grouting material on surrounding rock properties of roadway are revealed: grouting makes the surrounding rock stress transfer from deep to shallow, and the surrounding rock stress distribution is more uniform. Broken surrounding rock grouting can improve the mechanical properties of roadway surrounding rock, enhance the stability of roadway surrounding rock, control the deformation of roadway surrounding rock, and realize the balanced bearing of roadway surrounding rock anchorage structure. The feasibility of the application of modified grouting material in tunnel grouting engineering is verified

(3) The results obtained by theoretical analysis, laboratory test, and numerical simulation are applied to the practice of roadway repair and reinforcement of the north roadway group in the Qipanjing coal mine.

The field monitoring data show that the production practice was well guided with the repair and reinforcement technology with high-strength yielding bolt and shallow grouting reinforcement as the core, and the modified grouting material has good effect on grouting reinforcement of roadway surrounding rock

Data Availability

The data in the manuscript can be available on request through Dingchao Chen, whose email address is chendingchaoxizit@163.com.

Conflicts of Interest

The authors declare that they have no known competing financial interests or personal relationships that could have appeared to influence the work reported in this paper.

Acknowledgments

This work was supported by the National Natural Science Foundation of China (grant numbers 51904296, 52074240, and 51974296), the Outstanding Backbone Teachers of "Innovation Project" of the University in Jiangsu Province, China, in 2020, and Major Projects of Natural Science Foundation of Universities in Jiangsu Province, China (grant number 20KJA560001). The sources of this support are gratefully acknowledged.



References

- [1] H. P. Kang, G. Xu, B. M. Wang et al., "Forty years development and prospects of underground coal mining and strata control technologies in China," *Journal of Mining and Strata Control Engineering*, vol. 1, no. 1, article 013501, 2019.
- [2] G. Wang, F. Liu, Y. Pang, H. Ren, and Y. Ma, "Coal mine intellectualization: the core technology of high quality development," *Journal of China Coal Society*, vol. 44, no. 2, pp. 349–357, 2019.
- [3] M. He, Z. Ma, Z. Guo, and S. Chen, "Key parameters of the gob-side entry retaining formed by roof cutting and pressure release in deep medium-thickness coal seams," *Journal of China University of Mining and Technology*, vol. 47, no. 3, pp. 468–477, 2018.
- [4] M. Qian and J. Xu, "Behaviors of strata movement in coal mining," *Journal of China Coal Society*, vol. 44, no. 4, pp. 973–984, 2019.
- [5] C. Hou, "Key technologies for surrounding rock control in deep roadway," *Journal of China University of Mining and Technology*, vol. 46, no. 5, pp. 970–978, 2017.
- [6] J. X. Zhang, Q. Zhang, F. Ju, N. Zhou, M. Li, and Q. Sun, "Theory and technique of greening mining integrating mining, separating and backfilling in deep coal resources," *Journal of China Coal Society*, vol. 43, no. 2, pp. 377–389, 2018.
- [7] N. Zhang, X. Xue, and F. Han, "Technical challenges and countermeasures of the co-excavation of coal and gas with no-pillar retains in deep coalmine," *Journal of China Coal Society*, vol. 40, no. 10, pp. 2251–2259, 2015.
- [8] W. Wang, C. Yuan, W. J. Yu et al., "Stability control method of surrounding rock in deep roadway with large deformation," *Journal of China Coal Society*, vol. 41, no. 12, pp. 2921–2931, 2016.
- [9] X. Q. Qi, Y. S. Pan, H. T. Li et al., "Theoretical basis and key technology of prevention and control of coal-rock dynamic disasters in deep coal mining," *Journal of China Coal Society*, vol. 45, no. 5, pp. 1567–1584, 2016.
- [10] Y. Wu, D. Yun, P. Xie, Z. D. Fan, D. F. Wang, and Y. H. Zhang, "Progress, practice and scientific issues in steeply dipping coal seams fully-mechanized mining," *Journal of China Coal Society*, vol. 45, no. 1, pp. 24–34, 2020.
- [11] M. He, Y. Gao, J. Yang, and W. Gong, "An innovative approach for gob-side entry retaining in thick coal seam long-wall mining," *Energies*, vol. 10, no. 11, p. 1785, 2017.
- [12] Y. Wu, F. Gao, J. Chen, and J. He, "Experimental study on the performance of rock bolts in coal burst-prone mines," *Rock Mechanics & Rock Engineering*, vol. 52, no. 10, article 1794, pp. 3959–3970, 2019.
- [13] L. Yuan, "Research progress on risk identification, assessment, monitoring and early warning technologies of typical dynamic hazards in coal mines," *Journal of China Coal Society*, vol. 45, no. 5, pp. 1557–1566, 2019.
- [14] S. Q. Yang, M. Chen, H. W. Jing, K. F. Chen, and B. Meng, "A case study on large deformation failure mechanism of deep soft rock roadway in Xin'An coal mine, China," *Engineering Geology*, vol. 217, pp. 89–101, 2017.
- [15] H. Kang, X. Zhang, L. Si, F. Gao, and Y. Wu, "In-situ stress measurements and stress distribution characteristics in underground coal mines in China," *Engineering Geology*, vol. 116, no. 3–4, pp. 333–345, 2010.
- [16] J. Zhang and Y. Sun, "Experimental and mechanism study of a polymer foaming grouting material for reinforcing broken coal mass," *KSCE Journal of Civil Engineering*, vol. 23, no. 1, pp. 346–355, 2019.
- [17] X. Gao, X. Wang, and X. Liu, "New chemical grouting materials and rapid construction technology for inclined shaft penetrating drift-sand layer in coal mine," *Advances in Materials Science and Engineering*, vol. 2018, Article ID 2797419, 5 pages, 2018.
- [18] C. Liu, J. Yang, and F. Wu, "A proposed method of coal pillar design, goaf filling, and grouting of steeply inclined coal seams under water-filled strata," *Mine Water and the Environment*, vol. 34, no. 1, pp. 87–94, 2015.
- [19] R. Pan, Q. Wang, B. Jiang et al., "Failure of bolt support and experimental study on the parameters of bolt-grouting for supporting the roadways in deep coal seam," *Engineering Failure Analysis*, vol. 80, pp. 218–233, 2017.
- [20] D. Xuan, B. Wang, and J. Xu, "A shared borehole approach for coal-bed methane drainage and ground stabilization with grouting," *International Journal of Rock Mechanics & Mining Sciences*, vol. 86, pp. 235–244, 2016.
- [21] X. Ao, X. Wang, X. Zhu, Z. Zhou, and X. Zhang, "Grouting simulation and stability analysis of coal mine goaf considering hydromechanical coupling," *Journal of Computing in Civil Engineering*, vol. 31, no. 3, article 04016069, 2017.
- [22] Y. Sun, G. Li, J. Zhang, and D. Qian, "Stability control for the rheological roadway by a novel high-efficiency jet grouting technique in deep underground coal mines," *Sustainability*, vol. 11, no. 22, article 6494, 2019.
- [23] X. Sun, L. Wang, Y. Lu, B. Jiang, Z. Li, and J. Zhang, "A yielding bolt-grouting support design for a soft-rock roadway

- under high stress: a case study of the Yuandian no. 2 coal mine in China,” *Journal of the Southern African Institute of Mining and Metallurgy*, vol. 118, no. 1, pp. 71–82, 2018.
- [24] T. Zhao and C. Liu, “Roof instability characteristics and pre-grouting of the roof caving zone in residual coal mining,” *Journal of Geophysics and Engineering*, vol. 14, no. 6, pp. 1463–1474, 2017.
- [25] G. Lu, Y. Wang, Y. Zhang, and S. T. Ariaratnam, “Feasibility of using sodium silicate as grouting in loose coal bed sections for methane drainage,” *Tunnelling & Underground Space Technology*, vol. 72, pp. 107–113, 2018.
- [26] K. T. Crane and T. R. West, “Prioritizing grouting operations for abandoned underground coal mines, southwestern Indiana,” *Asian Journal of Chemistry*, vol. 26, no. 5, pp. 1509–1512, 2014.
- [27] J. Xia, Q. Su, and D. Liu, “Optimal gypsum-lime content of high water material,” *Materials Letters*, vol. 215, pp. 284–287, 2018.
- [28] X. Zhou, C. Liu, Y. Liu, C. Wang, and Y. J. Ma, “Effect of dry-wet cycling on the mechanical properties of high-water materials,” *Advances in Civil Engineering*, vol. 2020, Article ID 2605751, 11 pages, 2020.
- [29] L. Calvo and J. Casas, “Sterilization of biological weapons in technical clothing and sensitive material by high-pressure CO₂ and water,” *Industrial & Engineering Chemistry Research*, vol. 57, no. 13, pp. 4680–4687, 2018.
- [30] G. Hu, W. He, and C. Lan, “Sealing behavior and flow mechanism of expandable material slurry with high water content for sealing gas drainage boreholes,” *Geofluids*, vol. 2018, Article ID 2954306, 15 pages, 2018.
- [31] Y. Zhang, Y. Wang, T. Li, Y. Sun, and Z. Xiong, “Effects of lithium carbonate on performances of sulfoaluminate cement-based dual liquid high water material and its mechanisms,” *Construction & Building Materials*, vol. 161, pp. 374–380, 2018.
- [32] J. Lee and T. Lee, “Effects of high CaO fly ash and sulfate activator as a finer binder for cementless grouting material,” *Materials*, vol. 12, no. 22, 2019.
- [33] J. Lee, G. Kim, Y. Kim, K. Mun, and J. Nam, “Engineering properties and optimal conditions of cementless grouting materials,” *Materials*, vol. 12, no. 19, 2019.
- [34] H. Shimada, A. Hamanaka, T. Sasaoka, and K. Matsui, “Behaviour of grouting material used for floor reinforcement in underground mines,” *International Journal of Mining, Reclamation and Environment*, vol. 28, no. 2, pp. 133–148, 2014.
- [35] Y. Yu, J. Bai, X. Wang, and L. Zhang, “Control of the surrounding rock of a goaf-side entry driving heading mining face,” *Sustainability*, vol. 12, no. 7, article 2623, 2020.
- [36] H. Li, Y. Zhang, L. Xu, X. Jia, and X. Gu, “Examination of the treatment quality of filling mined-out voids using super-high-water material by the TEM technique,” *Environmental Earth Sciences*, vol. 76, no. 3, article 6431, 2017.
- [37] J. Kim, G. Yoon, H. Kim, K. Kang, and Y. U. Park, “Na₃V(PO₄)₂: a new layered-type cathode material with high water stability and power capability for Na-ion batteries,” *Chemistry of Materials*, vol. 30, no. 11, pp. 3683–3689, 2018.
- [38] Y. Yu, X. Wang, J. Bai, L. Zhang, and H. Xia, “Deformation mechanism and stability control of roadway surrounding rock with compound roof: research and applications,” *Energies*, vol. 13, no. 6, article 1350, 2020.

Research Article

Evolution Law of Floor Fracture Zone above a Confined Aquifer Using Backfill Replacement Mining Technology

Shan Ning ^{1,2} Weibing Zhu ^{1,2} Xiaoyong Yi^{1,2} and Laolao Wang^{1,2}

¹State Key Laboratory of Coal Resources and Safe Mining, China University of Mining and Technology, Xuzhou, China

²School of Mines, China University of Mining and Technology, Xuzhou, China

Correspondence should be addressed to Weibing Zhu; cumtzbw@cumt.edu.cn

Received 9 July 2020; Revised 9 September 2020; Accepted 15 February 2021; Published 3 March 2021

Academic Editor: Constantinos Loupasakis

Copyright © 2021 Shan Ning et al. This is an open access article distributed under the Creative Commons Attribution License, which permits unrestricted use, distribution, and reproduction in any medium, provided the original work is properly cited.

Disturbances owing to coal mining result in the movement and failure of floor strata. Mining-induced fractures within the floor may propagate to the confined aquifer, thereby causing water inrush disasters. In this study, we propose using strip mining and backfill replacement mining above the confined aquifer to investigate the failure depth of the floor. The problem is simplified as a distributed force model on a half-plane body. First, the stress disturbance of the floor during strip mining is calculated and the results are combined with the von Mises yield criterion. Then, the destruction of the floor after replacing the remaining coal pillars is explored. The results show that the widths of the strip mining face and coal pillars play an important role in affecting the failure depth of the floor: the greater the width, the larger the failure depth. Based on the parametric study results, the mining face and retention coal pillar width of 20 m is sufficient to prevent the occurrence of water inrush accidents. After the replacement of the remaining coal pillars, the failure area of the floor rock mass increases, but the maximum failure depth remains unchanged. Finally, we employed field measurement techniques at the Bucun coal mine to monitor the shear and vertical strains of the floor. The data collected was compared with the predicted results obtained from the proposed theoretical model. Good agreement was found between the monitoring and calculation results, which demonstrate the effectiveness of the proposed method.

1. Introduction

During the mining of a coal seam above a confined aquifer, there are many incidents of water inrush from the floor resulting in huge casualties and economic loss [1–3]. Excavation activities cause floor damage, and the formation of water channels is the main cause of water inrush [4]. To ensure safety during mining, the widely adopted method called strip mining is used [5]. Strip mining can effectively reduce the failure depth of floor strata and avoid the occurrence of such accidents. Given that strip mining needs a certain width of coal pillar to maintain the stability of mining space, the recovery rate of coal resources is lower than the traditional caving method. After strip mining, backfilling with high water content material helps to reduce the loss of coal resources and ensure the safety of the process [6].

In general, coal mining activities change the stress distribution characteristics of surrounding rock [7–9]. When the

stress of the floor strata exceeds the ultimate strength, cracks appear in its interior part [10, 11]. As the excavation intensity increases, the cracks develop gradually and eventually penetrate the strata between the working face and the confined aquifer [12–14]. Strip mining can effectively reduce the disturbance to the surrounding rock and the failure depth of the floor [15]. Previous studies have suggested the technology of grouting reinforcement of the floor, which can improve the strength of the floor rock mass and avoid the generation of permeable passages [16, 17].

After strip mining, the sustained strength of the stope surrounding rock decreases as time increases [6, 18, 19]. As the rock failure develops, it is possible to form a new permeable passage. Then, backfilling the goaf in time to improve the stress environment of surrounding rock can eliminate the continuous development of floor failure zone [20–22]. According to experiments and field observations, the stress concentration at the surrounding rock of the goaf decreases

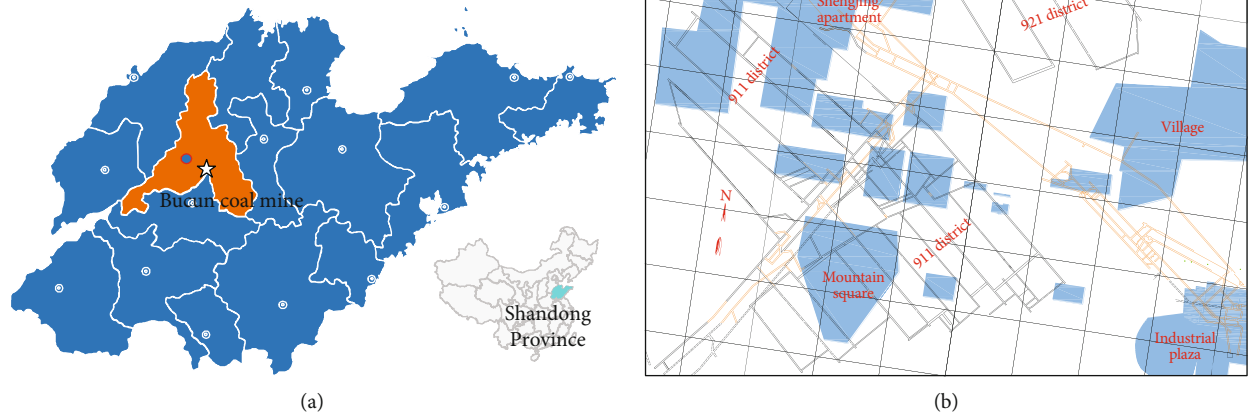


FIGURE 1: Bucun coal mine geographic information map: (a) location of Bucun coal mine; (b) location of the down hole working face and surface buildings.

after backfilling [23, 24]. Simultaneously, the failure of the floor rock mass is under control and the floor accident can be effectively prevented [25–27]. Moreover, the deformation and settlement of overlying strata decreased [28, 29].

Previous studies focused on the problem of water inrush and subsidence caused by coal mining. Additionally, significant research has been done on strip mining and goaf backfill to prevent water inrush. However, the recovery of the abandoned coal pillar and floor failure after the backfill replacement mining has not been considered. When backfilling material is used to recover the abandoned coal pillar, the coal seam floor will be affected by mining, and new deformations and destruction will occur at the floor strata. In particular, in the case of the coal seam above a confined aquifer, the floor is easy to form a water diversion channel under the influence of multiple mining, resulting in the problem of water inrush.

This study examines the stress distribution on the floor boundary during strip and backfill replacement mining above a confined aquifer. The two types of mining are simplified as mechanical problems under different boundary conditions. Using the elastic mechanics method, the stress distribution and floor failure evolution in the process of strip mining and backfill replacement mining are studied, respectively. As a result, the study provides theoretical guidance for safe mining of coal seams above a confined aquifer at the Bucun coal mine as well as overcoming shortcomings of the low extraction rate of strip mining and reducing the wastage of coal resources.

2. Backfill Replacement Mining Technology

2.1. Background. To begin with, the Bucun coal mine belongs to the Zibo Mining Group, located in the Jinan Shandong Province as presented in Figure 1. Its industrial square is in the town of Bucun, which is distributed in four townships: Bucun, Wenzu, Shengjing, and Xusheng. More than 80% of the mine resources are No. 9 and No. 10 coal seams, which are mostly under buildings and threatened by water inrush

from the floor. Therefore, the way to mine those coal seams safely and effectively is a major technical problem for Bucun coal mine.

From 2005 to 2009, strip mining was used to mine underground coal under confined water pressure in the 911 district of Bucun coal mine. The width of the excavated coal pillar was between 6 and 20 m, the width of the retained coal pillar was 10 to 25 m, and the recovery rate was only 34.2%. During the period of 2010–2011, 921 district used inclined strip mining to extract the coal above confined aquifer. The widths of the excavated and the retained pillars were 20 m and 25 m, respectively, and the recovery rate was 44.4%. The average recovery rate of the two mining areas was 39.3%, while many coal resources remained underground.

2.2. Floor Water Inrush. Since the 1970s, the Bucun coal mine has been mining No. 9-2 coal seam threatened by a confined aquifer. The mining area of these coal seams was approximately 5.42 km², and the lower level of mining was -372.8 m. Moreover, there have been two instances of floor water inrush reaching a maximum amount of 60 m³/h.

Further, the 9110 working face had been mined since July 15, 2004, and strip mining had been adopted (Figure 2). Initially, the designed mining width was 40 m. On July 31st, after mining 33 m in the 9110 working face, water inrush occurred at the back of the working face. The initial water volume was 150 m³/h, while the maximum reached 334.8 m³/h. After this incident, grouting was used to treat the water inrush, and the production was resumed in August 2005.

After this incident, the distribution of the aquifer on the floor of the area was investigated in detail. According to the geological exploration data, it consisted of, mainly, the Xushang sandstone, Xujiashuang limestone, and Ordovician limestone aquifers. The thickness of the Xushang sandstone aquifer was 0 to 14.07 m, the distance from the coal seam was 43.54 to 63.77 m, and the average distance was 54.40 m. It was, generally, attached to Xujiashuang limestone and had a thickness of approximately 0 to 1.29 m shale or clay shale with a maximum water pressure of 3 MPa. In addition,

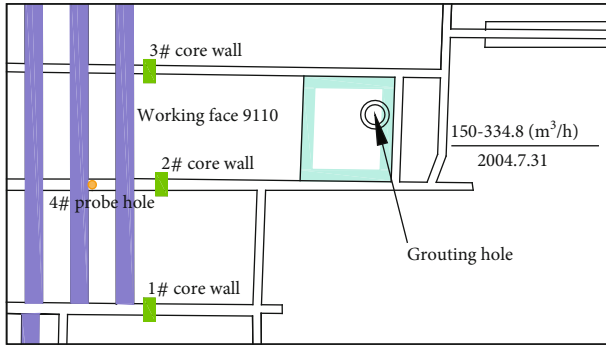


FIGURE 2: Water inrush position of 9110 working face.

the thickness of Xujiazhuang limestone aquifer was 8.45 to 12.19 m, with an average of 10.47 m. The distance from No. 9-1 coal seam was 52.17 to 71.50 m, and the average distance was 61.59 m. The distance from the lower part of the Ordovician limestone aquifer was 9.79 to 12.45 m, with an average of 10.81 m. This type of limestone was generally rich in water and had a certain regionalization. It was mainly recharged by the Ordovician limestone aquifer while recharging upwards the Xushang sandstone aquifer. The maximum water inrush coefficient and maximum water pressure were 0.132 MPa/m and 0.132 MPa/m, respectively, and the maximum water pressure was 6.3 MPa.

Moreover, the main aquifer in the coal seam floor was the Ordovician limestone, which was rich in water and had good recharge conditions that made it the main water supply source of every aquifer in the lower part of the coal seam. The average distance from the No. 9-1 coal seam was 82.87 m, and the average distance from the Xujiazhuang limestone was 10.81 m. The maximum water inrush coefficient of the Ordovician limestone was 0.082 MPa/m, and the maximum water pressure of the Ordovician limestone aquifer was 6.52 MPa.

Based on the characteristics of mining above the confined aquifer and under the buildings in the Bucun coal mine, strip mining method was adopted. The reason is that the width of the working face in strip mining is narrow, causing smaller damage to the floor, which can achieve safe mining above the confined aquifer [30]. Additionally, strip mining can effectively control surface subsidence, with a reduction rate between 80% and 90% [31].

2.3. Backfill Replacement Mining. Due to the low recovery ratio of strip mining, many pillars remain underground. To further improve the recovery rate of coal resources, high water content material is used to fill the goaf and replace the retained coal pillar [6, 31]. The mining plan is divided into three main steps, and Figure 3 illustrates the mining and backfilling process.

At first, the strip mining method is used to recover the coal seam (Figure 3(a)). The coal seam is mined according to the design plan, and the goaf and coal pillars are distributed at intervals after mining. In the second step, the goaf is filled with high water content material (Figure 3(b)). The fill-

ing body and the coal pillar form an integral unit to support the roof. After the filling body acquires certain strength, the remaining coal pillars are mined at intervals (Figure 3(c)). Then, in the third part, after the mining of the coal pillar, the newly formed goaf is filled. After the filling body has certain strength, all the remaining coal pillars are recovered individually (Figure 3(d)).

Throughout the process of replacing the remaining coal pillar with filling material, the floor is affected by multiple mining, which can easily lead to the increase of the floor fracture zone to form a new permeable passage. As shown in Figure 3, the shallow area of the floor affected by coal seam mining is damaged. Since the deep part of the floor is less affected by mining, the rock mass still maintains a good elastic state, which can block the inrush of confined water. Under the influence of multiple mining, the failure area of the floor and the risk of water inrush accidents in the working face will increase. To avoid that, the law of floor fracture, in the process of filling and replacement of coal pillars, must be examined.

3. Mechanical Model

3.1. Stress Analysis of Floor Rock Mass. Through the use of strip mining, the weight of the overburden is transferred to both sides of the coal pillars and the load on each pillar is elevated. At this point, the load is given by the following equation:

$$q = \frac{l+m}{l} \sum_{i=0}^n \gamma_i h_i, \quad (1)$$

where q is the load on the pillar (in MPa), l and m are the widths of the pillar and the mining width (in meters), respectively, γ_i is the bulk density of layer i' , and h_i is the thickness of layer i (in meters).

Due to the impact of coal seam excavation, the stress over the floor changes. The overburden stress passes through the coal pillars, which in turn causes redistribution of the stress on the floor of the coal bed. Many researchers use the half-plane body model to study the stress disturbance of the floor [7, 32]. According to these studies, the influence of the strip coal pillars on the floor is simplified as shown in Figure 4.

The stress concentration occurs beneath the coal pillar, and when the rock mass stress exceeds the strength limit, the rock mass enters the plastic state and it can be destroyed.

According to Saint Venant's principle, the surface force acting on the boundary will change significantly near the system of force while the influence at a distance can be ignored. Therefore, the force acting on any area on the floor boundary only affects the shallow area of the floor rock mass. The influence decreases significantly at a considerable distance from this area. Within the scope of influence, the risk of rock mass failure is higher. In particular, when the aquifer is significantly affected by mining, water inrush is very likely to occur.

3.2. Mechanical Model. As shown in Figure 5, strip mining is simplified to a model of distributed force on the semiplanar body boundary. The force on the floor boundary is mainly

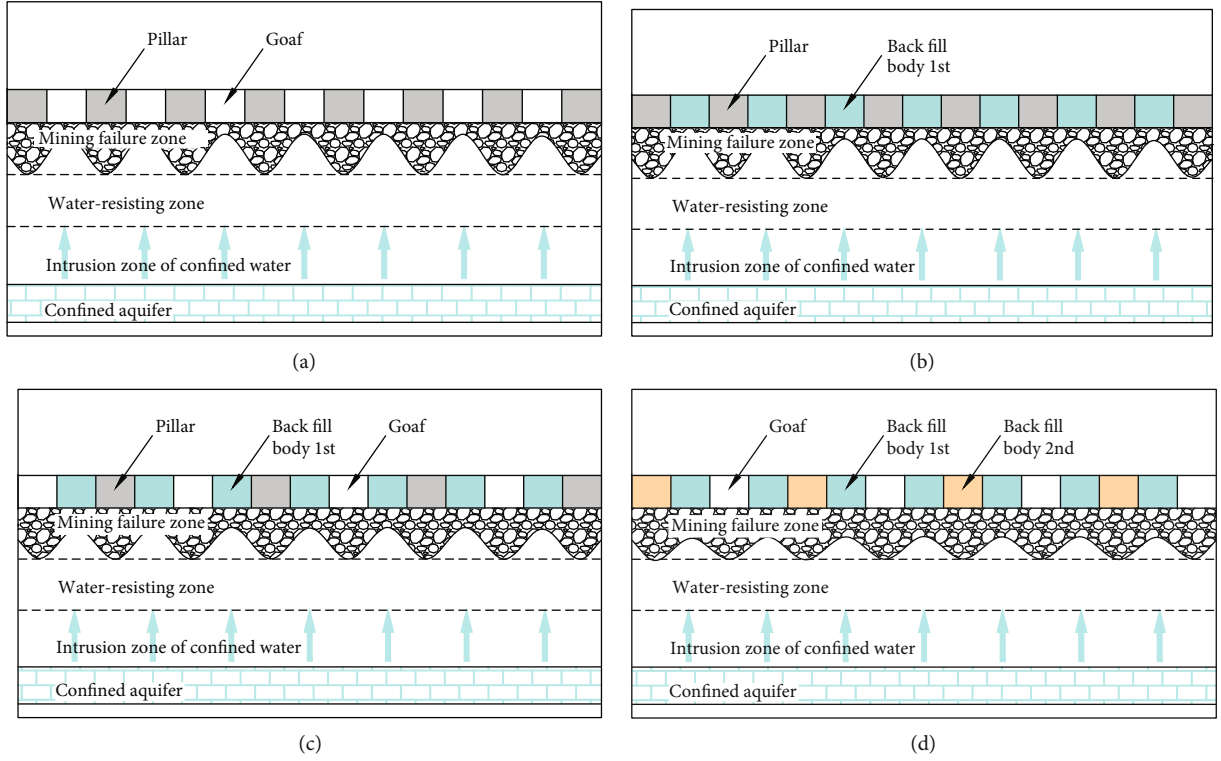


FIGURE 3: Schematic diagram of the backfill replacement mining above a confined aquifer: (a) strip mining, (b) goaf filling, (c) the first backfill replacement mining, and (d) the second backfill replacement mining.

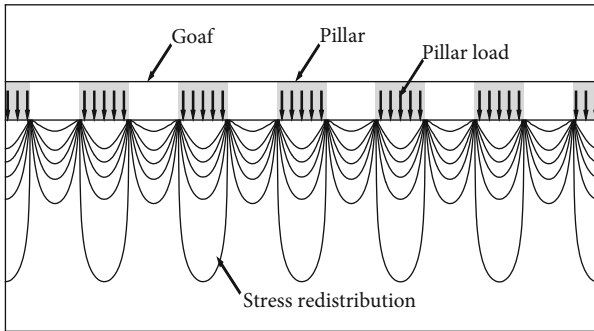


FIGURE 4: Simplified model diagram of the stress redistribution after strip mining.

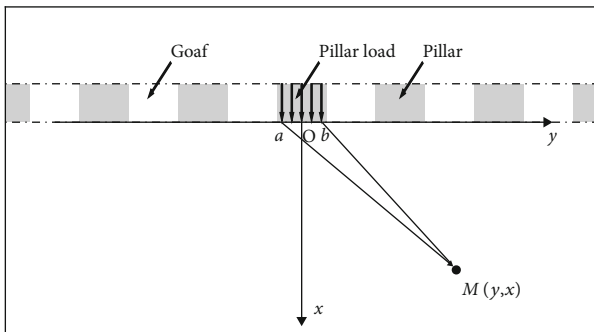


FIGURE 5: A model of half-plane body subjected to distributed force on the boundary.

transmitted by the overlying strata through the coal pillar. The floor is regarded as a half-plane body, and the load distributed on it is regarded as a force on the half-plane body.

First, the impact of one coal pillar on floor rock mass is calculated. According to elasticity theory, the stress caused by the uniformly distributed force on the boundary of the half plane at any point in the region is estimated using the following equations:

$$\begin{aligned}\sigma_x &= -\frac{2}{\pi} \int_a^b \frac{qx^3 d\xi}{[x^2 + (y - \xi)^2]^2}, \\ \sigma_y &= -\frac{2}{\pi} \int_a^b \frac{qx(y - \xi)^2 d\xi}{[x^2 + (y - \xi)^2]^2}, \\ \tau_{xy} &= -\frac{2}{\pi} \int_a^b \frac{qx^2(y - \xi) d\xi}{[x^2 + (y - \xi)^2]^2},\end{aligned}\quad (2)$$

where a and b are the lower and upper limits of the interval where the coal pillar is located.

For strip mining, the influence of other coal pillars should be considered when calculating the stress of any point on the floor. According to the principle of superposition, the effect of different loads on a body is equal to the accumulated influence of each group of loads alone. Therefore, the stress caused by every coal pillar in the mining area at point M

can be superimposed, and the calculation formula is as follows.

$$\left. \begin{aligned} \sigma_x &= -\sum_{i=0}^n \left(-\frac{2}{\pi} \int_{a_i}^{b_i} \frac{qx^3 d\xi}{[x^2 + (y-\xi)^2]^2} \right), \\ \sigma_y &= \sum_{i=0}^n \left(-\frac{2}{\pi} \int_{a_i}^{b_i} \frac{qx(y-\xi)^2 d\xi}{[x^2 + (y-\xi)^2]^2} \right), \\ \tau_{xy} &= \sum_{i=0}^n \left(-\frac{2}{\pi} \int_{a_i}^{b_i} \frac{qx^2(y-\xi) d\xi}{[x^2 + (y-\xi)^2]^2} \right), \end{aligned} \right\} \quad (3)$$

where a_i and b_i are the lower and upper limits of the interval where a coal pillar is located. The expansion form of equation (3) is presented in

$$\left. \begin{aligned} \sigma_x &= \sum_{i=0}^n -\frac{q}{\pi} \left(\frac{-\frac{x(a_i-y)}{x^2 + (a_i-y)^2} - \arctan \left[\frac{a_i-y}{x} \right]}{+\frac{x(b_i-y)}{x^2 + (b_i-y)^2} + \arctan \left[\frac{b_i-y}{x} \right]} \right), \\ \sigma_y &= \sum_{i=0}^n -\frac{q}{\pi} \left[\frac{\frac{x(a_i-y)}{x^2 + (a_i-y)^2} - \arctan \left[\frac{a_i-y}{x} \right]}{+\frac{x(y-b_i)}{x^2 + (b_i-y)^2} + \arctan \left[\frac{b_i-y}{x} \right]} \right], \\ \tau_{xy} &= \sum_{i=0}^n -\frac{q}{\pi} \left(-\frac{x^2}{(a_i-y)^2 + x^2} + \frac{x^2}{(b_i-y)^2 + x^2} \right). \end{aligned} \right\} \quad (4)$$

For the convenience of the calculations, the coal pillars are distributed symmetrically on the x -axis (Figure 6) so the action interval of a coal pillar is equal to

$$[a_i, b_i] = \left[\frac{m}{2} \pm (m+l), \left(\frac{m}{2} + l \right) \pm (m+l) \right], \quad (5)$$

where $i = 0, 1, 2, 3 \dots$.

The x -axis interval of the study area is $(x \in [-100, 100], y \in [0, 50])$, and the rock mass is studied within a 50 m depth. To ensure the boundaries of the study area are consistent with the stress and failure laws in the middle, the calculation interval should be much larger than the study interval. According to the experiment, when the interval of the calculation area is $(x \in [-300, 300], y \in [0, 50])$, the stress distribution law of the floor does not change.

Python is used to visualize the stress distribution of the floor. A script calculates the stress at each position and then employs Matplotlib to display the calculation results and generate contour and line maps. The calculations shown in this paper are all performed using Python 3.0. The stress values are generated in a 1 cm grid in the X and Y directions to ensure sufficient accuracy and resolution.

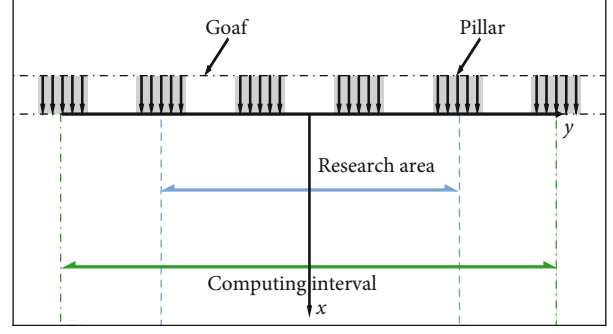


FIGURE 6: Calculation and study intervals.

3.3. Maximum Shear Stress. After the coal seam is mined, the stress is redistributed on the floor. The maximum shear stress has a significant effect on the deformation and failure of the rock mass and can also characterize the shear failure of the rock body to a certain extent. The distribution characteristics are typical when analyzing the deformation and failure of the floor. At the plastic stage, the plastic flow slip line failure is also related to maximum shear stress. Therefore, the maximum shear stress at different positions of the bottom plate is analyzed. Subsequently, this determines the disturbance range of the strip coal pillar to the floor stress.

The maximum and minimum principal stresses of rock mass at any point on the floor are given by

$$\left. \begin{aligned} \sigma_1 \\ \sigma_3 \end{aligned} \right\} = \frac{\sigma_x + \sigma_y}{2} \pm \sqrt{\left(\frac{\sigma_x + \sigma_y}{2} \right)^2 + \tau_{xy}^2}. \quad (6)$$

After the simplification to a plane problem and without considering the effect of intermediate stress σ_2 , the maximum shear stress is equal to

$$\tau_{\max} = \frac{\sigma_1 - \sigma_3}{2} = \frac{1}{2} \sqrt{(\sigma_x - \sigma_y)^2 + 4\tau_{xy}^2}. \quad (7)$$

Through combining equations (4)–(6), the formula for calculating the maximum shear stress is

$$\tau_{\max} = \sum_{i=0}^n \frac{qx}{\pi} \sqrt{\left(\frac{(a_i - b_i) + 4x^2}{[(a_i - y)^2 + x^2][(b_i - y)^2 + x^2]} \right)}. \quad (8)$$

3.4. Floor Yield Stress. Under the effect of the overburden load, in which the floor rock mass stress reaches the limit, the rock mass enters the plastic state. For rock materials, this means that cracks are generated inside. As the plastic failure continues to develop, the crack penetrates and eventually produces a slip failure surface.

According to plastic mechanics, an indication of plastic failure is the fact that the material enters the yield state. For the destruction of rock materials, the von Mises yield criterion is typically used to determine the state of the floor rock mass. Under certain deformation conditions, when the equivalent von Mises stress of a point in the loaded body reaches the yield stress, it is considered that the point has

plastic failure. The calculation formula for the equivalent von Mises stress is described using

$$(\sigma_1 - \sigma_2)^2 + (\sigma_2 - \sigma_3)^2 + (\sigma_3 - \sigma_1)^2 = 2\sigma_s^2. \quad (9)$$

The model was considered as a two-dimensional plane, and equation (9) was converted for the calculation of a two-dimensional problem, without considering the effect of intermediate stress σ_2 . The von Mises stresses were calculated using the following equation:

$$\sigma_1^2 + \sigma_3^2 - \sigma_1\sigma_3 = \sigma_s^2. \quad (10)$$

$$\sigma_s = \sum_{i=0}^n \frac{q}{\pi} \sqrt{\frac{3x^2[(a_i - b_i) + 4x^2]}{[(a_i - y)^2 + x^2][(b_i - y)^2 + x^2]}} + \left[\arctan\left(\frac{a_i - y}{x}\right) - \arctan\left(\frac{b_i - y}{x}\right) \right]^2. \quad (11)$$

3.5. Calculation Schemes. Under different widths of excavated and retained coal pillars, the floor is disturbed to different degrees. To determine the optimal mining plan based on the various widths of excavated and retained coal pillars, four schemes were designed for this study. By comparing and analyzing the stress and failure characteristics of the floor under different conditions, the optimal mining plan is determined. The parameters of each scheme are listed in Table 1.

According to the geological data of the Bucun coal mine [30], most parts of the floor are composed of sandstone and sandpaper shale. The physical properties of rocks are similar, and therefore, the floor rock is simplified to the same type of rock.

4. The Effect of Strip Mining

4.1. Shear Stress Effect. Figure 7 shows the contour of shear stress of floor rock mass under different schemes.

Figure 7 shows the shear stress contours of the floor under different mining schemes. As seen in the figure, the contours of the maximum shear stress regions appear in the shallow area of the floor in the shape of a bubble, which gradually transforms into a wave as the depth increases. When the shear stress is greater than 3.6 MPa, the shear stress isoline forms a more obvious bubble shape; when the shear stress is less than 3.6 MPa, the shear stress isoline forms a wave shape.

As the shear stress decreases, the disturbance to the bottom plate gradually decreases. By comparing the contour shapes under different conditions, the following can be concluded. When scheme 1 is adopted, the floor suffers the least disturbance, i.e., the disturbance range is mainly within the depth of 0 to 10 m; the area with a depth of more than 10 m is less affected by mining. In scheme 2, the disturbance range of the floor is further expanded, and the maximum shear stress is in the range 0–30 m while the maximum shear stress is less affected in the range 30–50 m. For schemes 3 and

TABLE 1: Parameters of each scheme.

Plan number	Width of excavated coal pillar (m)	Width of retained coal pillar (m)
1	10	10
2	20	20
3	30	30
4	40	40

With the combination of equations (4), (5), and (10), the von Mises stresses can be calculated as follows:

4, the maximum shear stress changes significantly within the range 0–50 m.

Additionally, it can be found that the central axis of the bubble is located below the edge of each coal pillar in the shallow area; the maximum likewise appears in this area. The bubble contour is pointed upward in the direction of the coal pillar, and this characteristic becomes more obvious as the mining width increases. Below the central area of the retained coal pillar and the middle of the goaf, the maximum shear stress of the floor rock mass is small.

4.2. Influence Range of Shear Stress. To obtain the variation law of shear stress at different depths, the shear stresses were calculated at depths of 10, 20, 30, 40, and 50 m. The distribution curves of shear stress are presented in Figure 8.

As the depth increases, the maximum shear stress of floor rock mass decreases until it stabilizes at approximately 0.5 MPa. Therefore, the average value of 0.5 MPa is considered as the boundary of mining influence. The influence depths of the shear stress in scheme 1 and scheme 2 are 20 m and 30 m, respectively. In scheme 1, the shear stress at 20 m is 0.253 MPa, which is less than 0.5 MPa. For scheme 2, the shear stress at 30 m is less than 0.5 MPa. When schemes 3 and 5 are adopted, the average shear stress values at 50 m are 0.634 MPa and 0.787 MPa, respectively, and the influence range of shear stress is more than 50 m.

Furthermore, the excavation and retention widths of a strip coal pillar are the main factors affecting the shear stress of floor rock mass. As they increase, the shear stress increases as well. Taking the shear stress at a depth of 20 m as an example, the average value in scheme 1 is 0.253 MPa, and the maximum values in schemes 2, 3, and 4 are 1.250 MPa, 2.418 MPa, and 3.014 MPa, respectively.

4.3. Von Mises Stress Distribution Law. Under the impact of coal pillars, the floor rock mass will gradually enter the yield state. The von Mises yield criterion is used to assess whether

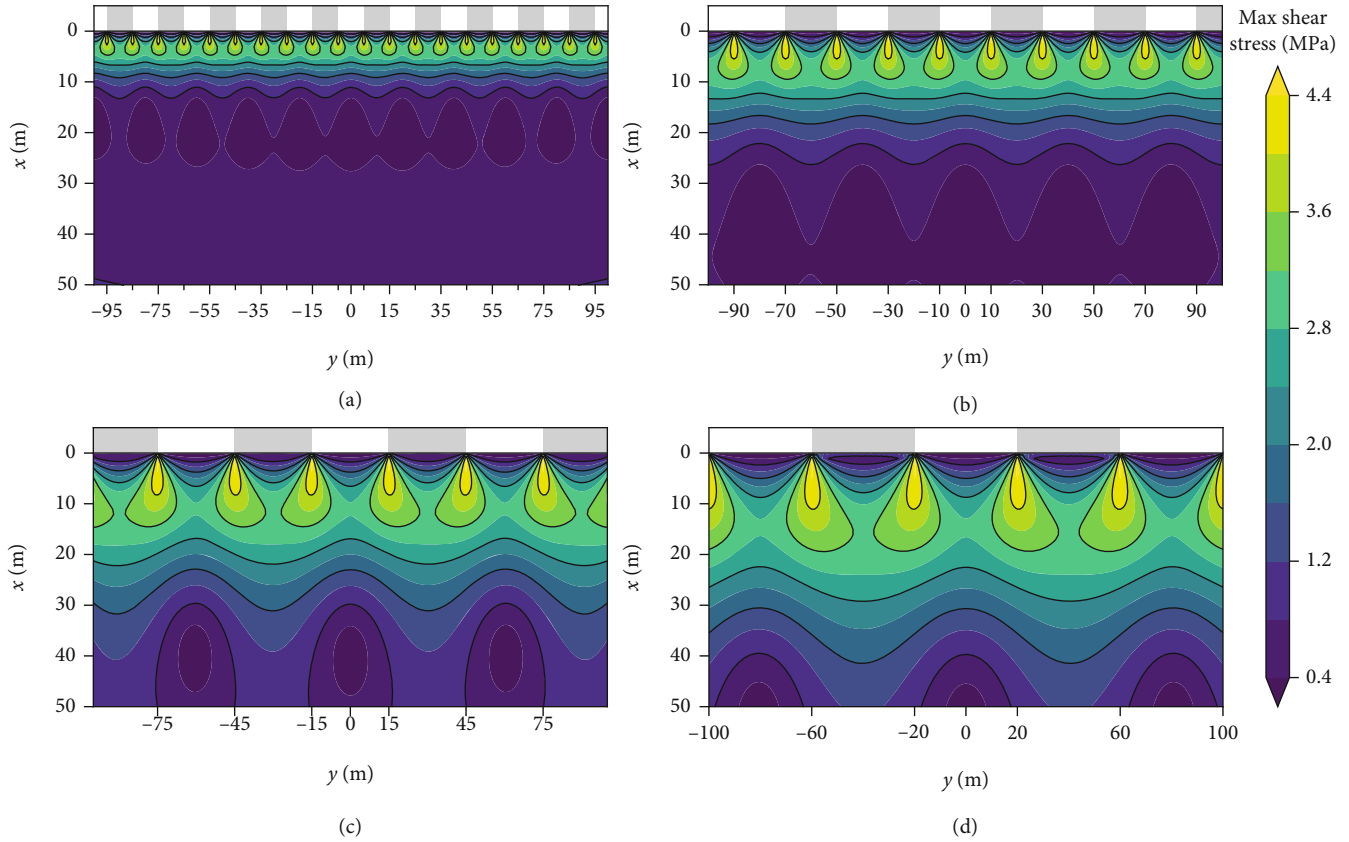


FIGURE 7: Cloud maps of maximum shear stress distributions when the width of the excavated coal pillar is (a) 10 m, (b) 20 m, (c) 30 m, and (d) 40 m.

the floor rock mass has entered the plastic state, and the equivalent stress value can be calculated using equation (6). Figure 9 is a contour of the von Mises equivalent stress distributions of the floor rock mass.

As shown in Figure 9, the von Mises stress at the lower part of the pillar is significantly higher than that at the lower part of the goaf. When x equals 0, the stress value at the lower part of the coal pillar is the highest, i.e., 15 MPa, while at the lower part of the goaf, it is the lowest, i.e., 0 MPa. As the depth increases, the von Mises stress in the pillar and the lower part of the goaf gradually decreases or increases and finally approaches the value of 6 MPa.

Below the coal pillar, the isoline of von Mises stress is uniformly distributed in the shape of a spindle. With the increase of the width of the coal pillar and goaf, the spindle-like area gradually increases. For scheme 1, the maximum depth of the spindle region is 10.8 m, while for schemes 2 and 3 they are 20.95 m and 31.4 m, respectively. When scheme 4 is adopted, the maximum depth is 41.8 m.

4.4. Depth of Floor Failure. To ensure that there is no water inrush in the mining process of the working face, it is necessary to ensure that the floor has a certain thickness of waterproof layer. If the average yield stress of the floor rock mass is $\sigma_s = 9.5$ MPa, the shape and depth of the floor failure area are shown in Figure 10.

As seen in Figure 10, the maximum failure depths of schemes 1, 2, 3, and 4 are 6.88 m, 13.72 m, 20.58 m, and 27.44 m, respectively.

According to the original data of Bucun coal mine, the height of the permeable passage is 10 m, and the minimum depth of the confined aquifer on the floor of the 911 working face is 42.5 m. The thickness of the isolation rock strata of schemes 1, 2, 3, and 4 is 25.62 m, 18.78 m, 11.92 m, and 5.06 m, respectively.

In scheme 4, the failure depth of the floor is large and the thickness of the isolated rock layer is small; therefore, it is difficult to meet the safety requirements. Although the failure depth of scheme 3 is relatively smaller, it is still significantly affected by shear stress at a depth of 20 m. To ensure mining safety, scheme 1 and scheme 2 should be selected.

After mining a face, it is necessary to move the mining equipment to the next face. When scheme 1 is adopted, the working face width is 10 m, and when scheme 2 is adopted, the working face width is 20 m. Scheme 2 has fewer working surfaces than scheme 1, which can effectively reduce the number of equipment moves. Therefore, from a financial point of view, it is more efficient to mine with scheme 2. In combination with the west wing of the 911 mining area, there are four tendencies in the lower working face of 9115 and the upper working face of 9115. When the width of the mining strip reaches 20 to 23 m, there is no water inrush. Thus, the recommended mining plan is scheme 2.

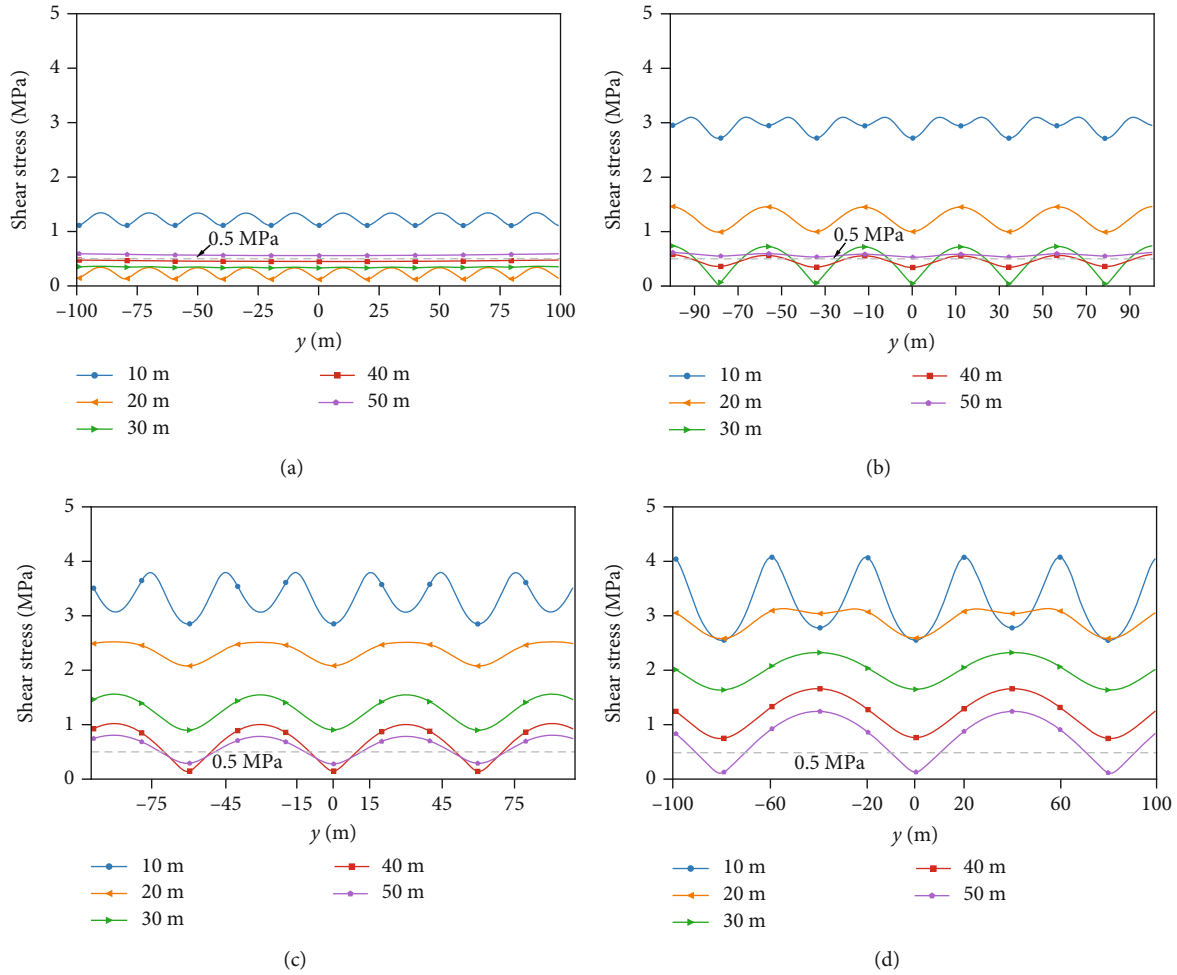


FIGURE 8: Shear stress distributions at various depths: (a) width of excavated coal pillar is 10 m, (b) width of excavated coal pillar is 20 m, (c) width of excavated coal pillar is 30 m, and (d) width of excavated coal pillar is 40 m.

5. Influence of Backfill Replacement Mining

First, the scheme of excavating 20 m and reserving 20 m was adopted in Bucun coal mine, and there was no water inrush in the process of mining. After strip mining, high water content material was backfilled to replace the coal pillar in this area. To avoid water inrush from the floor in the process of replacement mining, the failure depth of the floor, after replacement mining, must be studied.

As shown in Figures 3(c) and 3(d), the roof is supported by coal pillars and filling body together, and the load of coal pillar changes after backfill replacement mining. Therefore, goaf backfill and coal pillar mining are simulated through changing the range of load. Moreover, the load on the boundary is changed according to the width of the supporting material.

5.1. Influence of Multiple Mining on Shear Stress. Due to multiple mining, the maximum shear stress of the floor rock mass changed. Additionally, the maximum shear stresses of the floor during strip mining, first backfill replacement mining, and second backfill replacement mining were compared.

Figure 11 shows the distribution curves of shear stress at different depths.

The effect of the two backfill replacement mining processes on floor stress is the same. The maximum shear stress distribution curve is the same, but the position of the peak and valley changes. When the depth is 10 m, 20 m, 30 m, and 40 m, the average maximum shear stress is 1.173 MPa, 1.186 MPa, 0.911 MPa, and 0.858 MPa, respectively.

Moreover, the comparison with the shear stress of the floor after strip mining shows that the maximum shear stress in the shallow part of the floor decreases after backfill replacement mining and gradually approaches to the maximum shear stress in the deep part. When the depth is 10 m, the average maximum shear stress decreases by 1.902 MPa after backfill replacement mining, and when the depth is 20 m, 30 m, and 40 m, the von Mises stress values decrease to 0.194 MPa, 0.061 MPa, and 0.185 MPa, respectively. These results suggest that the degree of disturbance in the deep part does not obviously change after backfill replacement mining.

5.2. Effect of Replacement Mining on Floor Fracture. According to the previous analysis, the yield stress σ_s of the floor

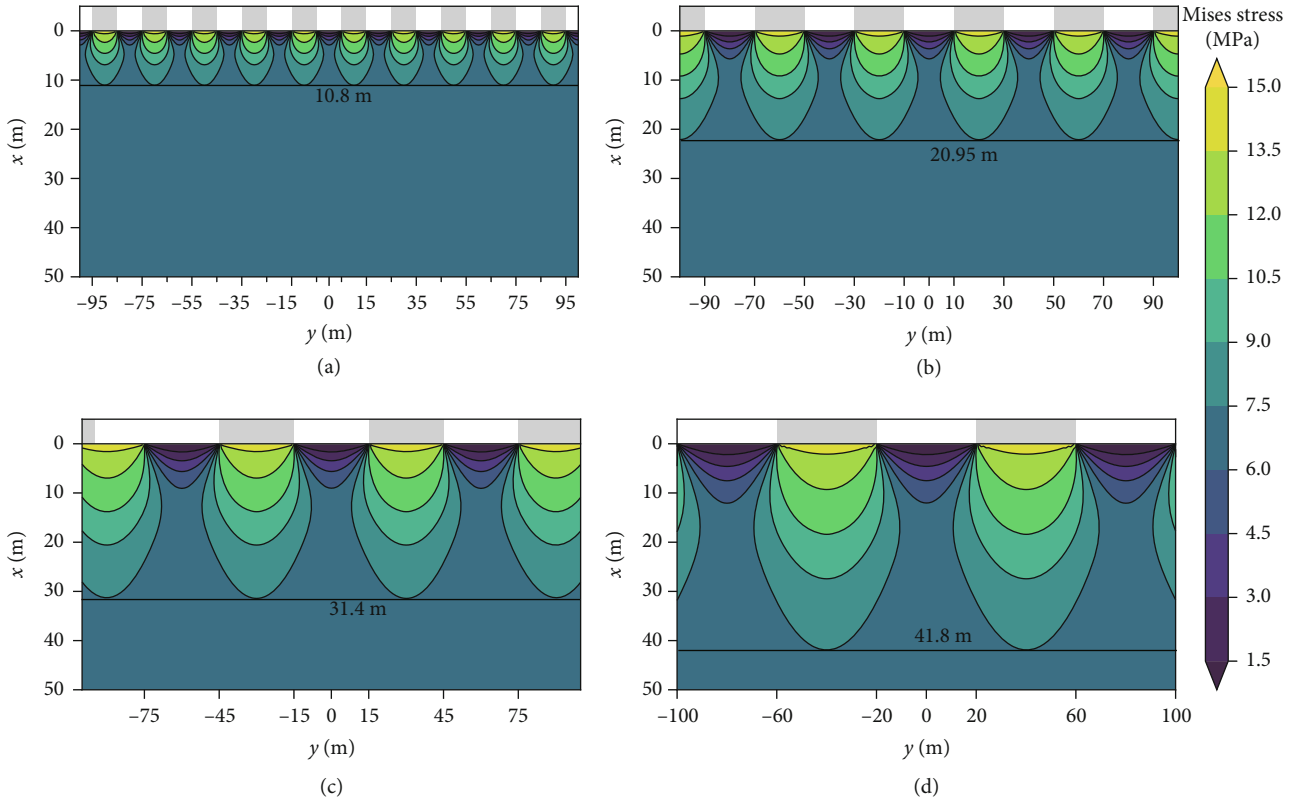


FIGURE 9: Cloud maps of von Mises stress distributions when the width of the excavated coal pillar is (a) 10 m, (b) 20 m, (c) 30 m, and (d) 40 m.

rock mass is 9.5 MPa, and the plastic zone formed is shown in Figures 12(a) and 12(b).

Figure 12(a) shows the shape of the plastic zone of the floor rock mass after the first replacement mining. After that, a new plastic zone is formed on the basis of the original plastic zone. The new zone appears in the lower part of the original goaf, but the maximum failure depth of the newly formed zone is 4.41 m, which does not exceed the depth of the original one.

Additionally, Figure 12(b) shows the plastic zone of the floor formed after the second backfill replacement mining, which is similar to the plastic zone formed in the first one, while a new plastic zone is formed in the lower part of the replacement material. Under the influence of multiple mining, the rock mass is destroyed in the range of 4.41 m floor depth.

6. Field Measurements

6.1. Monitoring Program. To further study the mechanical behavior of floor rock mass under the influence of mining, measuring stations were set up in the 9113 and 9111 working faces. The layout of the measuring station and working face is shown in Figure 13.

The measuring station 1# was set up at the 9113 working face, which mainly monitored the deformation and failure of the floor in the process of strip mining. The 9113 working

face was in the west wing of the 911 district, and the measuring station was located at the upper exit of the working face. Five angle transducers were arranged to monitor the inclination of the borehole to the 9113 working face, and they were installed at depths of 5 m, 12 m, 19 m, 25 m, and 30 m.

Furthermore, the measuring station arranged in the 9111 working face mainly monitored the floor deformation and failure before and after the replacement mining of coal pillar. This measuring station was located at the exit of the 9111 working face, and the strain sensor was embedded before the high water content material filled the original strip falling area. Five measuring points were arranged, and the vertical depths (vertical floor depths) were 7 m, 9 m, 11 m, 13 m, and 15 m, respectively.

6.2. Prediction of Rock Mass Mechanical Behavior. According to the previous analysis, the stress values of different positions of floor rock mass are calculated. When these are combined with the physical equation, the strain of rock mass can be calculated at any point and its mechanical behavior can be predicted. According to the rock mechanics parameter of the floor, the elastic modulus is 2.5 GPa, and Poisson's ratio is $\mu = 0.15$.

In addition, measuring station 1# used angle transducers for monitoring, which could monitor the shear strain of rock floor mass. Equation (8) gives the calculation method of the maximum shear stress at any point on the floor. The shear

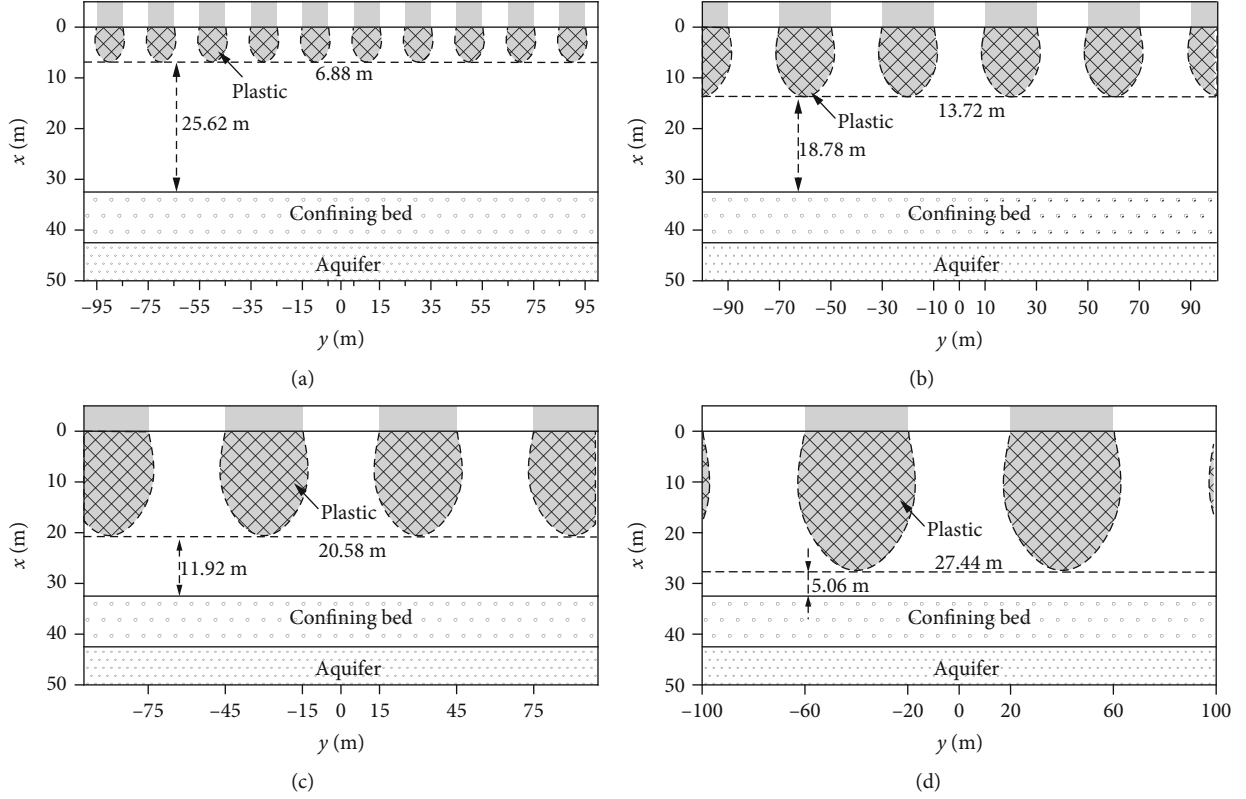


FIGURE 10: Floor failure area distribution patterns: (a) width of excavated coal pillar is 10 m, (b) width of excavated coal pillar is 20 m, (c) width of excavated coal pillar is 30 m, and (d) width of excavated coal pillar is 40 m.

strain of floor rock mass is calculated according to the physical equation of the plane strain problem given in

$$\begin{aligned} \gamma_{\max} &= \frac{2(1+\mu)}{E} \tau_{\max} \\ &= \sum_{i=0}^n \frac{2(1+\mu)qx}{E\pi} \sqrt{\frac{(a_i - b_i)^2 + 4x^2}{[(a_i - y)^2 + x^2][(b_i - y)^2 + x^2]}}. \end{aligned} \quad (12)$$

The strain value at any point on the floor can be calculated using equation (12). The angular displacement of the point can be obtained by transforming the angle from radians to degrees.

Moreover, measuring station 2# used strain transducers for monitoring, which could monitor the strain of the floor rock mass. Equation (4) gives the calculation method of vertical stress at any point at the bottom of the station. As previously, the shear strain of floor rock mass is calculated according to the physical equation of the plane strain problem as follows:

$$\begin{aligned} \varepsilon_x &= \sum_{i=0}^n \frac{q(1+\mu)}{E\pi} \left((1+2\mu) \left[\arctan\left(\frac{a_i - y}{x}\right) - \arctan\left(\frac{b_i - y}{x}\right) \right] \right. \\ &\quad \left. + x \frac{a_i^2(y - b_i) + b_i^2(a_i - y) + (a_i - b_i)(x^2 - y^2)}{[(a_i - y)^2 + x^2][(b_i - y)^2 + x^2]} \right). \end{aligned} \quad (13)$$

6.3. Observation Results. To prevent the deformation law of the floor being affected by mining, the research data after the mining in the area around each station were collected. The monitoring results and theoretical settlement results of floor deformation after mining are shown in Figure 14. Here, Figure 14(a) shows the theoretical calculation results and monitoring angle of the angle transducers. Figure 14(b) shows the strain value of the rock as measured by the strain sensor.

Figure 14(a) shows the results of field observation. When the depth is 5 m, the shear deformation of the floor rock mass reaches its maximum. The shear deformation decreases with the increase of depth and becomes stable when the depth is greater than 19 m. This result is in good agreement with the theoretical calculation. According to that, the shear deformation of the floor rock mass also reaches its maximum value at approximately 5 m, which will gradually decrease with the increase of the depth, while the depth of the significant influence area is 19 m.

Based on Figure 14(b), the vertical deformation of the floor rock mass reaches its maximum at around 5 m. The vertical strain decreases when the depth is greater than 5 m. The general tendency is a decreasing one, and when the depth is less than 9 m, the effect is more significant. From the theoretical calculation, the deformation of floor rock mass decreases with the increase of depth, which is consistent with the results of field monitoring.

According to the field monitoring results, the mechanical behavior of rock mass changes with the increase of depth. In

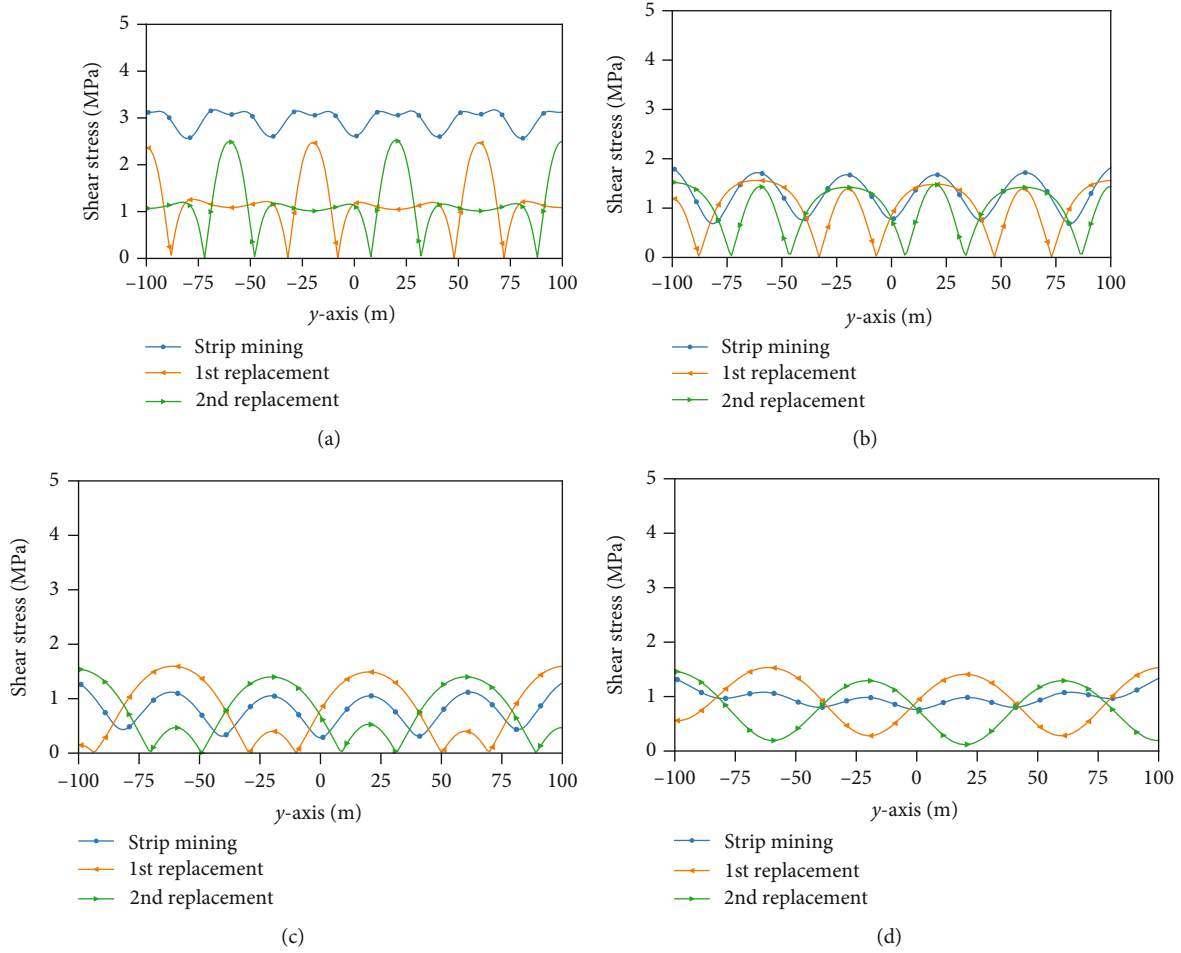


FIGURE 11: Characteristics of shear stress distribution at various depths: (a) depth of 10 m, (b) depth of 20 m, (c) depth of 30 m, and (d) depth of 40 m.

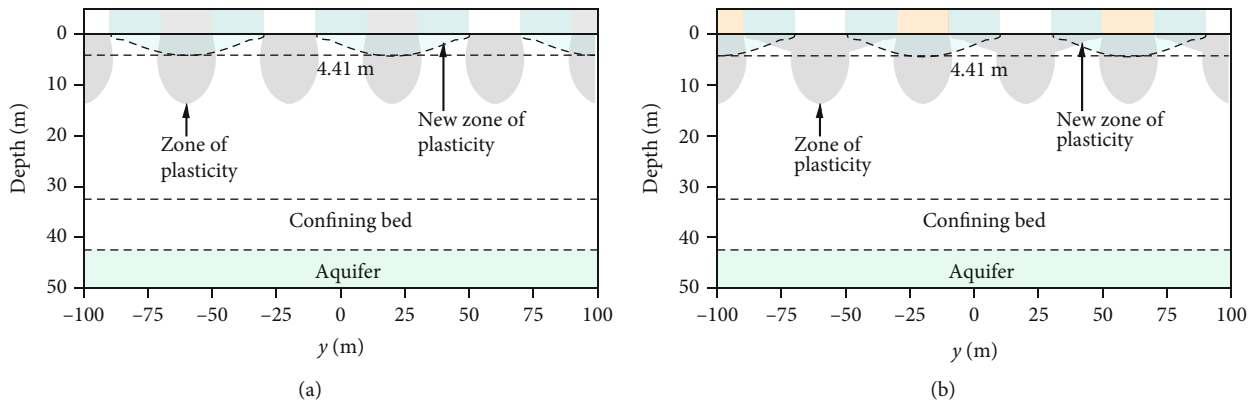


FIGURE 12: Plastic zone distributions of replacement mining floor: (a) first backfill replacement mining; (b) second backfill replacement mining.

Figure 14(a), it can be seen that the deformation of the floor rock mass is relatively continuous and tends to be stable when the depth is greater than 19 m. However, in Figure 14(b), it can be seen that a deformation discontinuity occurs at a depth of 9 m. The results show that when the depth is 9 m, the floor rock mass enters the plastic state, the rock mass is discontinuous, and the integrity is destroyed.

7. Discussion

In this study, we found that the widths of excavated and retained coal pillars are the key factors affecting the development of floor fracture. By adjusting the width of retained pillar and excavation width, the failure depth and mechanical behavior of floor rocks can be changed. When the coal seam

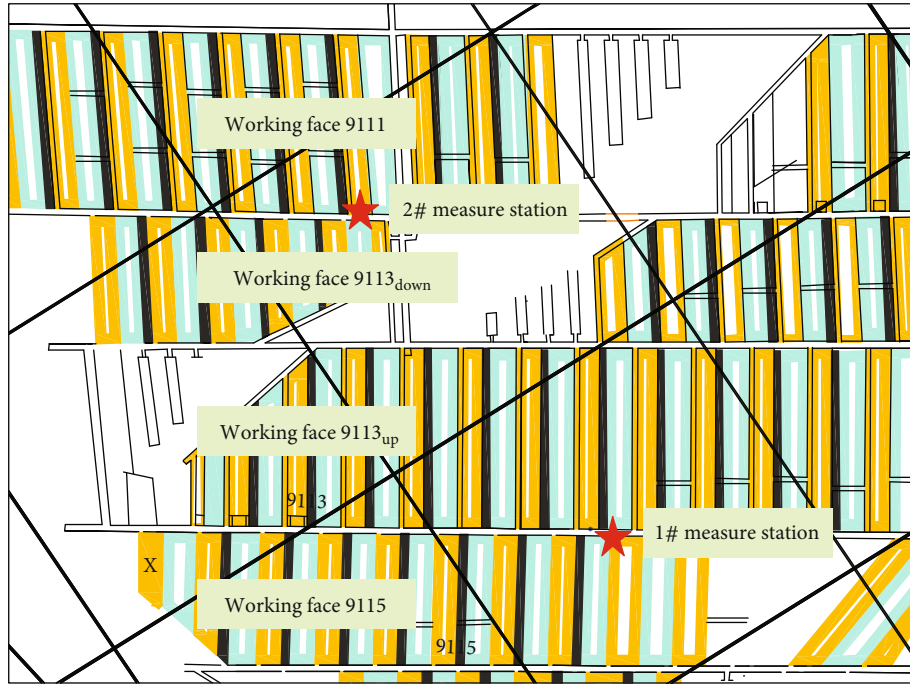


FIGURE 13: Station location.

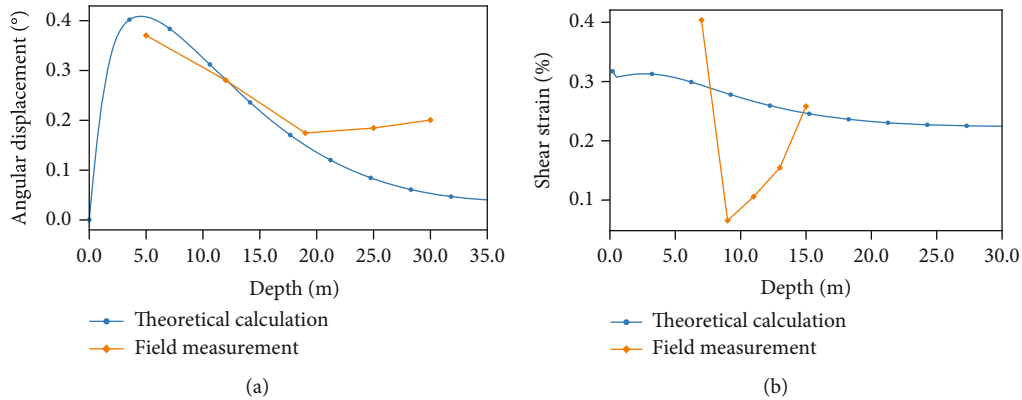


FIGURE 14: Deformation law of floor rock mass: (a) measuring station 1#; (b) measuring station 2#.

is not excavated, the force on the floor is uniformly distributed, and with the increase of the width of strip mining, the stress is concentrated leading to an increasing failure depth of the floor. According to the resistivity of strip coal pillar floor by Yu et al. [30], the failure depth is 50.7m when the width of the strip coal pillar is 15 m, and the failure depth increases gradually with the increase of mining width. According to previous research by Zha et al. [33], when the longwall face is used for normal mining, the maximum floor failure depth is 76.18m. Therefore, the use of strip coal pillar and the reduction of the excavation width are beneficial to reduce the failure depth of floor rock mass.

Additionally, a strong relationship between cracks and yield state of rock mass has been reported in the literature. The characteristics and density of microcracks can be ana-

lyzed by the yield state of the floor rock mass. The von Mises yield criterion reflects the spatial shape and the threatening degree of rock mass failure. With the increase of von Mises stress, the fracture density of rock mass increases and the failure direction is related to the specific stress state. With the depth increase of the floor rock mass, the crack density decreases gradually, and the possibility of forming a permeable passage decreases as well. At the plastic state, the direction of plastic flow is related to the maximum shear stress. In this study, we found that shear stress is concentrated at the lower part of the boundary on both sides of the coal pillar while it is small in the middle area of the bottom of the coal pillar. Based on these data, we can infer that there is a rock mass failure surface below the edge of the coal pillar. As a result, these findings can help us predict the location of water inrush.

In order to prevent the accident of water inrush in confined water and improve the safety of coal mining on it, attention should be paid into the following aspects: (a) an exhaustive exploration should be carried out for the floor aquifer to determine the distribution of confined water and the value of water pressure; (b) strip mining can effectively reduce the floor failure depth, and in combination with high water content material backfilling replacement, it does not only reduce the disturbance to the floor rock mass but also improves the coal resource recovery rate; and (c) reducing the size of strip mining can effectively reduce the degree of disturbance of the floor and reduce the failure depth of the floor by increasing the strength of the floor rock mass.

8. Conclusions

This study examines the safe mining of coal resources on a confined water aquifer. The influence of stress disturbance on rock mass at different depths is analyzed using a mechanical model, and the failure depth of floor before and after coal seam mining is determined.

Based on the elastic mechanics theory, a mechanical model of strip mining and filling material replacement of the remaining coal pillars is constructed, the expression of the floor stress distribution is given, and its evolution law is revealed. Results show that the mining and coal pillar widths are the main influencing factors of floor stress distribution. With an increase of their values (the widths of working faces and coal pillars), the floor stress influence area gradually increases as well.

Then, according to the von Mises yield criterion, the failure depth of the floor rock mass is studied, and the equivalent expressions of the stress at different depths are given. Under the influence of coal seam mining, the rock mass of the floor has a certain depth of damage, and its range gradually decreases as the depth increases. From the calculation results, the maximum depth of floor rock failure before and after replacement is 13.72 m, which can meet the requirements for water isolation.

Finally, the field measurement results indicate that as the depth increases, the deformation of the floor rock mass gradually decreases, and its mechanical behavior is consistent with the theoretical calculation results. The use of strip mining significantly affects the depth of the area to 19 m, and the use of filling materials to replace the coal pillars had a significant influence depth of 9 m.

Data Availability

In our manuscript, the experiment and test data used to support the findings of this study are available from the corresponding author upon request.

Conflicts of Interest

The authors declare that they have no conflicts of interest.

Acknowledgments

The research was supported by the independent research project of State Key Laboratory of Coal Resources and Safe Mining, CUMT (SKLRCRSM19X008), and National Natural Science Foundation of China (Grant no. 52074265).

References

- [1] Z. Meng, G. Li, and X. Xie, "A geological assessment method of floor water inrush risk and its application," *Engineering Geology*, vol. 143-144, pp. 51–60, 2012.
- [2] L. Meng, Q. Y. Feng, and Q. Li, "Coupled simulation-optimization model for draining confined aquifer via underground boreholes to prevent water inrush of coal mines," *Environmental Earth Sciences*, vol. 77, no. 17, pp. 1–20, 2018.
- [3] D. Donglin, S. Wenjie, and X. Sha, "Water-inrush assessment using a gis-based Bayesian network for the 12-2 coal seam of Kailuan Donghuantuo Coal Mine coal mine in China," *Mine Water and the Environment*, vol. 31, no. 2, pp. 138–146, 2012.
- [4] Y. L. Jiang, D. F. Zhang, K. Wang, and X. Q. Zhang, "Mining-induced damage characteristics of floors during fully mechanized caving mining: a case study," *Advances in Materials Science and Engineering*, vol. 2018, 11 pages, 2018.
- [5] J. A. Wang and H. D. Park, "Coal mining above a confined aquifer," *International Journal Of Rock Mechanics And Mining Sciences*, vol. 40, no. 4, pp. 537–551, 2003.
- [6] W. B. Zhu, S. C. Yu, D. Y. Xuan, Z. J. Shan, and J. L. Xu, "Experimental study on excavating strip coal pillars using caving zone backfill technology," *Arabian Journal of Geosciences*, vol. 11, no. 18, p. 554, 2018.
- [7] Y. Zhao, H. Zhou, J. Zhong, and D. Liu, "Study on the relation between damage and permeability of sandstone at depth under cyclic loading," *International Journal of Coal Science & Technology*, vol. 6, no. 4, pp. 479–492, 2019.
- [8] B. Guo, T. Cheng, L. Wang, T. Luo, and X. Yang, "Physical simulation of water inrush through the mine floor from a confined aquifer," *Mine Water and the Environment*, vol. 37, no. 3, pp. 577–585, 2018.
- [9] Z. Li, S. Yu, W. Zhu et al., "Dynamic loading induced by the instability of voussoir beam structure during mining below the slope," *International Journal of Rock Mechanics and Mining Sciences*, vol. 132, article 104343, 2020.
- [10] J. Sun, L. G. Wang, and G. M. Zhao, "Failure characteristics and confined permeability of an inclined coal seam floor in fluid-solid coupling," *Advances in Civil Engineering*, vol. 2018, 12 pages, 2018.
- [11] J. Sun, Y. Hu, and G. Zhao, "Relationship between water inrush from coal seam floors and main roof weighting," *International Journal of Mining Science and Technology*, vol. 27, no. 5, pp. 873–881, 2017.
- [12] A. Li, Y. Liu, L. Mou, and K. Li, "Numerical analysis and case study on the mitigation of mining damage to the floor of no. 5 coal seam of Taiyuan group by grouting," *Journal of the Southern African Institute of Mining and Metallurgy*, vol. 118, no. 5, pp. 461–470, 2018.
- [13] S. C. Zhang, W. J. Guo, and Y. Y. Li, "Experimental simulation of water-inrush disaster from the floor of mine and its mechanism investigation," *Arabian Journal of Geosciences*, vol. 10, no. 22, p. 503, 2017.

- [14] A. Li, Q. Ma, Y. Lian, L. Ma, Q. Mu, and J. Chen, "Numerical simulation and experimental study on floor failure mechanism of typical working face in thick coal seam in Chenghe mining area of Weibei, China," *Environmental Earth Sciences*, vol. 79, no. 5, p. 118, 2020.
- [15] D. Xu, S. Peng, S. Xiang, M. Liang, and W. Liu, "The effects of caving of a coal mine's immediate roof on floor strata failure and water inrush," *Mine Water and the Environment*, vol. 35, no. 3, pp. 337–349, 2016.
- [16] S. Q. Liu, Y. Fei, Y. C. Xu, L. Huang, and W. Y. Guo, "Full-floor grouting reinforcement for working faces with large mining heights and high water pressure: a case study in China," *Mine Water and the Environment*, vol. 39, no. 2, pp. 268–279, 2020.
- [17] C. H. Han, W. J. Zhang, W. W. Zhou et al., "Experimental investigation of the fracture grouting efficiency with consideration of the viscosity variation under dynamic pressure conditions," *Carbonates and Evaporites*, vol. 35, no. 2, p. 30, 2020.
- [18] W. B. Liu, J. M. Xu, W. B. Zhu, and S. H. Wang, "A novel short-wall caving zone backfilling technique for controlling mining subsidence," *Energy Science & Engineering*, vol. 7, no. 5, pp. 2124–2137, 2019.
- [19] B. Wang, F. Dang, W. Chao, Y. Miao, J. Li, and F. Chen, "Surrounding rock deformation and stress evolution in pre-driven longwall recovery rooms at the end of mining stage," *International Journal of Coal Science & Technology*, vol. 6, no. 4, pp. 536–546, 2019.
- [20] N. Jiang, C. Wang, H. Pan, D. Yin, and J. Ma, "Modeling study on the influence of the strip filling mining sequence on mining-induced failure," *Energy Science & Engineering*, vol. 8, no. 6, pp. 2239–2255, 2020.
- [21] Y. Yu, K. Z. Deng, Y. Luo, S. E. Chen, and H. F. Zhuang, "An improved method for long-term stability evaluation of strip mining and pillar design," *International Journal of Rock Mechanics and Mining Sciences*, vol. 107, pp. 25–30, 2018.
- [22] L. Li, F. Li, Y. Zhang, D. Yang, and X. Liu, "Formation mechanism and height calculation of the caved zone and water-conducting fracture zone in solid backfill mining," *International Journal of Coal Science & Technology*, vol. 7, no. 1, pp. 208–215, 2020.
- [23] C. X. Wang, Y. Lu, B. T. Shen, Y. Y. Li, and Y. B. Liang, "Design and monitoring of cpb replacement mining rscp: a case study in china," *Energy Sources, Part A: Recovery, Utilization, and Environmental Effects*, vol. 43, pp. 80–95, 2019.
- [24] D. R. Tesarik, J. B. Seymour, and T. R. Yanske, "Long-term stability of a backfilled room-and-pillar test section at the buick mine, Buick Mine, Missouri, USA," *International Journal of Rock Mechanics and Mining Sciences*, vol. 46, no. 7, pp. 1182–1196, 2009.
- [25] J. H. Zhai, D. L. Liu, G. Li, and F. T. Wang, "Floor failure evolution mechanism for a fully mechanized longwall mining face above a confined aquifer," *Advances in Civil Engineering*, vol. 2019, 11 pages, 2019.
- [26] H. Lu, X. Liang, N. Shan, and Y. Zhang, "Study on the stability of the coal seam floor above a confined aquifer using the structural system reliability method," *Geofluids*, vol. 2018, 15 pages, 2018.
- [27] J. Hao, Y. Shi, J. Lin, X. Wang, and H. Xia, "The effects of backfill mining on strata movement rule and water inrush: a case study," *Processes*, vol. 7, no. 2, p. 66, 2019.
- [28] W. Cai, Z. Chang, D. Zhang, X. Wang, W. Cao, and Y. Zhou, "Roof filling control technology and application to mine roadway damage in small pit goaf," *International Journal of Mining Science and Technology*, vol. 29, no. 3, pp. 477–482, 2019.
- [29] X. Zhu, G. Guo, H. Liu, X. Peng, and X. Yang, "Research on the stability evaluation model of composite support pillar in backfill-strip mining," *Mathematical Problems in Engineering*, vol. 2020, 11 pages, 2020.
- [30] S. C. Yu, J. M. Xu, W. B. Zhu, S. H. Wang, and W. B. Liu, "Development of a combined mining technique to protect the underground workspace above confined aquifer from water inrush disaster," *Bulletin of Engineering Geology and the Environment*, vol. 79, no. 7, pp. 3649–3666, 2020.
- [31] W. Zhu, J. Xu, J. Xu, D. Chen, and J. Shi, "Pier-column backfill mining technology for controlling surface subsidence," *International Journal of Rock Mechanics and Mining Sciences*, vol. 96, pp. 58–65, 2017.
- [32] X. Y. Hu, H. L. Zhang, and L. G. Wang, "Analysis on stress concentration factors of roadway surrounding rock affected by cross mining," *Chinese Journal of Underground Space and Engineering*, vol. 11, no. 3, pp. 658–664, 2015.
- [33] H. Zha, W. Liu, and Q. Liu, "Physical simulation of the water-conducting fracture zone of weak roofs in shallow seam mining based on a self-designed hydromechanical coupling experiment system," *Geofluids*, vol. 2020, 14 pages, 2020.

Research Article

Experimental Study on the Flow Behavior of Grout Used in Horizontal Directional Drilling Borehole Grouting to Seal Mining-Induced Overburden Fractures

Jinfeng Ju,^{1,2} Jialin Xu ,^{3,4} and Jing Yang⁵

¹The National and Local Joint Engineering Laboratory of Internet Application Technology on Mine, China University of Mining and Technology, Xuzhou, Jiangsu 221008, China

²IoT/Perception Mine Research Center, China University of Mining and Technology, Xuzhou, Jiangsu 221008, China

³State Key Laboratory of Coal Resources and Safe Mining, Xuzhou, Jiangsu 221116, China

⁴School of Mines, China University of Mining and Technology, Xuzhou, Jiangsu 221116, China

⁵Shendong Coal Group Co., Ltd., China Energy, Yulin, Shaanxi 719315, China

Correspondence should be addressed to Jialin Xu; xujlcmu@163.com

Received 21 July 2020; Revised 12 August 2020; Accepted 29 December 2020; Published 12 January 2021

Academic Editor: Eliahu Rosenthal

Copyright © 2021 Jinfeng Ju et al. This is an open access article distributed under the Creative Commons Attribution License, which permits unrestricted use, distribution, and reproduction in any medium, provided the original work is properly cited.

The development of water-conducting fractures from underground coal mining is a geological cause of groundwater loss. Sealing mining-induced rock fracture channels through borehole grouting is an effective way to protect groundwater resources. A ground-based engineering test was conducted at the Gaojiabao coal mine that utilized horizontal directional drilling (HDD) to grout and seal water-conducting overburden fractures. This study carried out a theoretical and experimental exploration using HDD to evaluate the development characteristics and grout hydraulic conductivity of these mining-induced fractures. The results showed that, as a result of varying fracture morphologies in different zones of the mining overburden, multiple fracture types were sequentially exposed as the HDD borehole advanced from the original rock mass outside the mining area towards the mining-induced fractured rock mass. The fracture types were exposed in the following order: compressive shear fractures, tensile failure fractures, and bed separation fractures. Moreover, the void characteristics of the exposed fractures in the borehole were significantly different at different drilling horizons, which affected the flow behavior and sealing performance of the injected grout. Lastly, three typical orders in which the different types of fractures were sequentially exposed by the borehole were summarized, and further analysis of the orders led to a scheme for determining drilling horizons favorable for efficient fracture sealing. The results of this study will enable efficient grout sealing of the fractures caused by mining and reduce groundwater loss.

1. Introduction

Underground coal mining produces movement and destruction of the overburden in the form of mining-induced fractures. Mining-induced fractures not only provide a pathway for groundwater loss but also constitute a geological source of the degradation of ground-surface ecosystems [1, 2]. Therefore, reasonable control of the water seepage capacity of fracture channels is crucial to the protection of groundwater in coal mining areas [3, 4]. Grout sealing is a well-developed water control method currently used in subsurface engineering applications [5–7]. Grout sealing works

by constructing grout holes in a fractured rock mass and injecting those holes with sealing materials, such as cement and clay, such that the fracture voids are effectively filled, and channel isolation and water blocking are achieved.

The Gaojiabao coal mine is located in the Binchang mining area in Shaanxi, China. As the mine's coal seam roof contains a very thick, water-rich aquifer (i.e., the Luohe aquifer), it has been subject to the risk of an influx of water from the roof for a long time. To reduce the underground drainage burden and maximize the conservation of groundwater resources, an engineering test was carried out to evaluate the practicability of using HDD to seal mining-induced

water-conducting fractures in the overburden [8]. It has been observed in practice that, although various sealing materials such as fly ash, cement, water glass, clay, walnut shells, and cottonseed hulls have been implemented on site, none have exhibited satisfactory water blocking performance. Owing to the diverse development patterns of mining-induced water-conducting fractures, strong fracture conductivity, and the varying flow behavior of grout in different fractures, one or more of the following phenomena was often observed to take place during grouting: (1) fractures could not be effectively sealed (i.e., the grouting materials leaked into the underground goaf), (2) grouting materials clogged the boreholes earlier than expected, and (3) additional water leakage was observed when drilling continued after successful sealing. Each of these phenomena greatly compromised the sealing performance of the mining-induced fracture channels. It was obvious that these phenomena were closely related to the development characteristics (e.g., fracture aperture) and grout hydraulic conductivity of the borehole-exposed water-conducting fractures. Accurate determination of a reasonable drilling trajectory based on the flow behavior of sealing grout in water-conducting fractures is the key to ensuring effective fracture sealing.

In coal mining, the theory and practice of grout sealing has focused on reinforcing the surrounding rock mass, water blocking in shaft and roadway construction [7, 9–14], and preventing water inrush when mining below a confined aquifer [15–17]. Relevant research has centered on the selection of water blocking materials, law of grout diffusion, optimization of the grouting procedure, and evaluation of the fracture sealing performance, which has laid an important foundation for the practice of grout sealing in mining-induced overburden fractures. However, the fractures to be sealed in the rocks surrounding roadways or coal seam floor rocks are significantly different from the mining-induced overburden fractures in terms of their development morphologies, as well as their abilities to conduct and confine grout (Figure 1). Therefore, it is difficult to directly apply the existing research results for the former fracture types to engineering practice with the latter types, leading to the aforementioned dilemma in the grout sealing of water-conducting fractures in the coal seam roof of the Gaojiabao coal mine. The fractures in the rocks surrounding the roadway or in coal seam floor rocks are mostly compressive shear fractures generated by the concentrated stress that results from mining disturbances or pre-existing fractures generated by the diagenetic process. These fractures are distributed in a relatively enclosed space and sufficiently confine the grout (except for the fractures at the grouting end, fractures in a rock mass are not connected to other free spaces), thereby enabling good sealing performance. In contrast, mining-induced overburden fractures tend to be tensile fractures generated during the breaking and rotation of strata, and the channel sizes of these fractures are obviously larger than the previously mentioned fractures [18]. As mining-induced overburden fractures have good connectivity to the underground mining space, the grout often gushes into the goaf under the action of gravity in a phenomenon known as grout escape. This results in significantly higher difficulty in grout sealing these fractures.

Therefore, the development of a grouting procedure or method favorable for efficient fracture sealing based on full consideration of the special development morphology and grout hydraulic conductivity of mining-induced overburden fractures is essential. Accordingly, this study carried out a theoretical and experimental exploration using HDD to evaluate the development morphology and grout hydraulic conductivity of fractures in light of the engineering test performed in the Gaojiabao coal mine, which utilized HDD borehole grouting to seal water-conducting overburden fractures and aimed to provide a basis and support for improving the sealing efficacy of mining-induced overburden fractures.

2. Case Study

2.1. Engineering Background. The Gaojiabao coal mine is located in Xianyang City, Shaanxi Province. The mine field is approximately 25.7 km long in the east-west direction, 16.6 km wide in the north-south direction, and has an area of approximately 219.1681 km². The designed production capacity of the mine is 5 million t/a, and it has a service life of 62.5 years. The No. 4 coal seam is currently the primary working coal seam of the mine. It has an average thickness of 9.8 m and is subjected to fully mechanized top coal cave mining. Owing to the special hydrogeological conditions in this region, an exceedingly thick, water-rich aquifer (i.e., the Luohe aquifer) stretches across much of the coal measure strata. The aquifer is 400–440 m thick and has a permeability coefficient of 0.05471–1.08265 m/d. The aquifer is located 30–110 m above the No. 4 coal seam and poses a serious water hazard to the on-going coal extraction at the underground working face. The mining-induced water-conducting fractures in the overburden directly connect to the aquifer, which has resulted in a large amount of water gushing into the underground goaf. In the No. 1 panel, for example, longwall faces 101, 102, and 103 still face a continuous increase in water inflow under limited-height mining (i.e., within a mining height of 5 m), and the maximum water inflow on one side has reached 720 m³/h, with a total of water inflow of 800 m³/h even after mining of the three faces was complete. This poses a significant threat to safe and efficient mine production and mine drainage. To reduce the underground drainage burden, reduce the roof water hazard, and protect groundwater resources as much as possible, a ground-based engineering test was carried out that evaluated the use of HDD to grout and seal the water-conducting overburden fractures (Figure 2). However, owing to an incomplete understanding of the development characteristics and grout hydraulic conductivity of the water-conducting overburden fractures exposed by the HDD, the grout sealing was difficult to implement, and no obvious sealing effectiveness was ultimately observed. Consequently, the test was suspended.

2.2. Overview of Grouting and Water Blocking. The HDD boreholes were designed to consist of identical vertical and build-up sections. After reaching the target horizons, the boreholes were advanced separately at each horizon in a “coordinated drilling-sealing” manner. That is, when the drilling fluid failed to return to the ground as the borehole

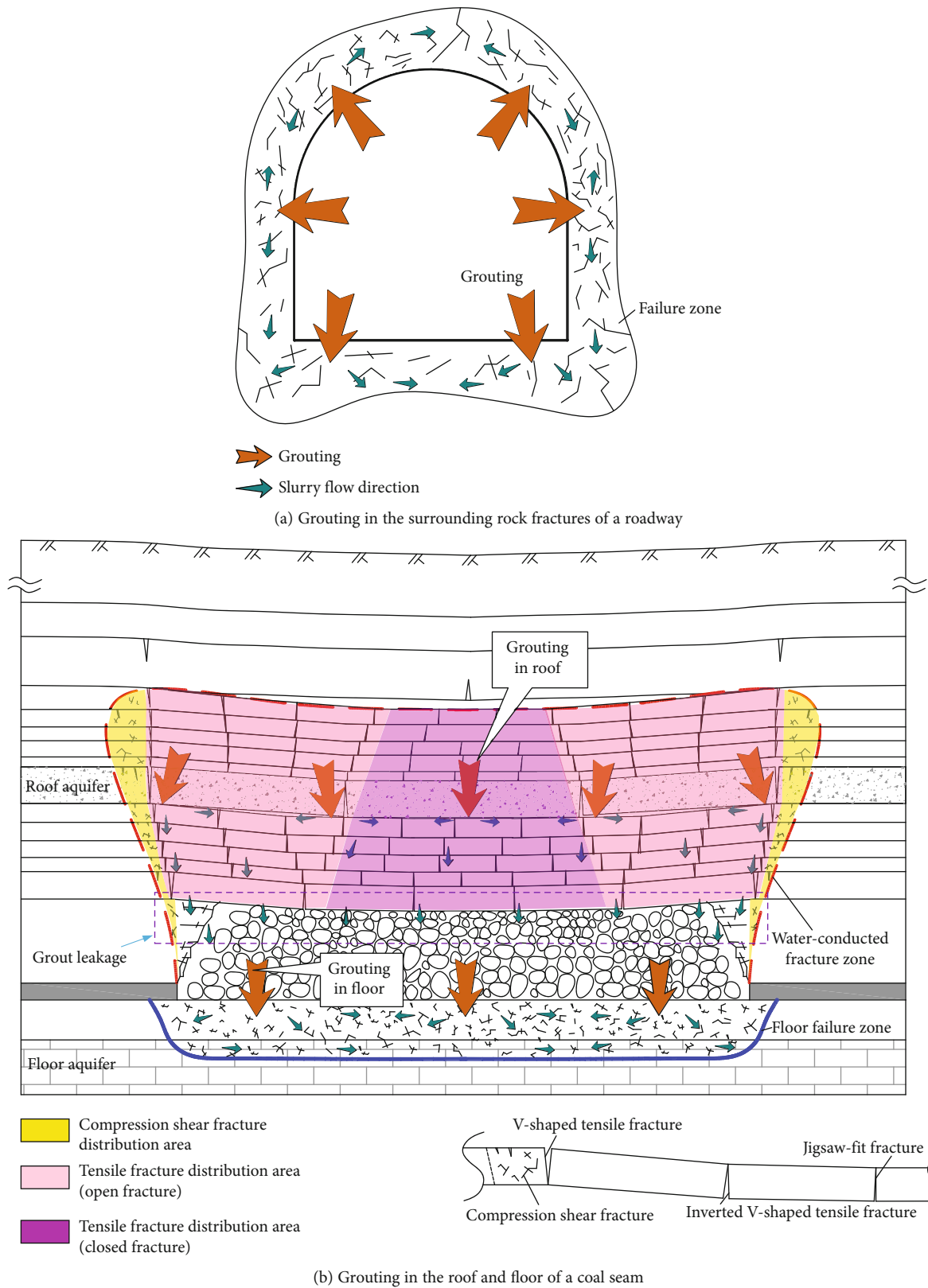


FIGURE 1: Schematic diagram of grouting in the surrounding rock fractures of a roadway and the mining-induced roof and floor fractures of a coal seam.

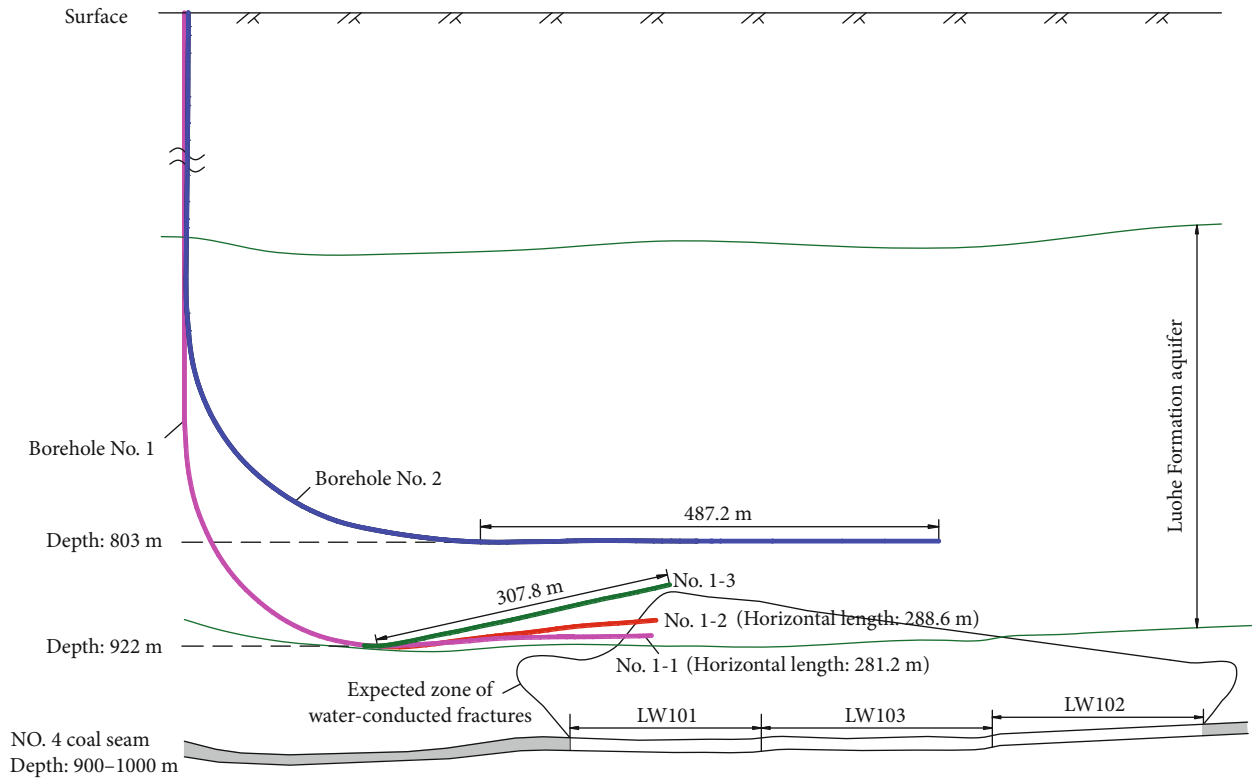


FIGURE 2: Trajectory of the HDD borehole in the Gaojiabao coal mine.

advanced (indicating that the borehole had exposed mining-induced fractures), drilling was immediately stopped, and grouting was implemented to seal the fractures. When the sealing proved effective, drilling was resumed. As mentioned in Introduction, when a borehole entered the predicted range of the water-conducting fracture zone (WCFZ) (Figure 2), drilling fluid was frequently lost, and grout sealing was required every 1.4–5.2 m of drilling distance. Various grouting materials were tested; however, the sealing performance was not satisfactory, and frequent leakage of those materials into the underground goaf or plugging of the borehole was observed. In particular, when cement, fly ash, clay, or other fine-grained materials were used for grouting, the grout did not remain in the fractures and directly leaked into the goaf. When using coarse-grained materials, such as walnut shells and cotton seeds, the boreholes were immediately plugged, and the grout was unable to be pumped into the fractures. As a result, the drilling horizons were adjusted on-site, and a total of four horizons were explored with two boreholes (Figure 2). For borehole 1, the vertical section was 630 m deep, and three horizontal sections, referred to as horizontal sections 1-1, 1-2, and 1-3, were explored. Horizontal section 1-1 was approximately 8 m above the bottom boundary of the Luohe Formation and 107 m above the top of the coal seam; horizontal section 1-2 was approximately 25 m above the bottom boundary of the Luohe Formation and 125 m above the top of the coal seam, and the highest point of horizontal section 1-3 was approximately 63 m above the bottom boundary of the Luohe Formation and 161.0 m above the top of the coal seam. Borehole 2 was a redrilled hole, spaced

6 m from borehole 1, that consisted of a 580 m deep vertical section and a horizontal section. The horizontal section was approximately 203 m above the top of the coal seam and 105 m above the bottom boundary of the Luohe Formation. An on-site test indicated that, although the intervals of grout sealing increased significantly after the adjustment of the drilling horizons (grout sealing was performed for every 7.9–44 m of drilling distance in borehole 2), it was still difficult to achieve sufficient fracture sealing, and there was no significant reduction in the inflow of water to the underground goaf.

As shown by the positions of the four horizontal sections relative to the range of the WCFZ in the overburden, grout sealing of the fractures tend to be difficult if the horizontal drilling was performed within the WCFZ or the curved subsidence zone above the WCFZ (i.e., the bed separation fracture distribution zone). It was evident that this difficulty was closely related to the development characteristics and grout hydraulic conductivity of the mining-induced overburden fractures exposed by the boreholes. Under current engineering conditions and with the given types of grouting materials, developing a method by which to determine a drilling trajectory and horizon favorable for the retention of grouting materials in mining-induced fractures is the key to solve this difficulty. To this end, the remainder of this study is focused on evaluating the grout hydraulic conductivity of the various types of water-conducting fractures exposed by HDD and exploring reasonable drilling horizons to provide a theoretical basis for improving the practical efficacy of using HDD borehole grouting to seal water-conducting overburden fractures.

3. Development Features of Mining-Induced Overburden Fractures Exposed by HDD

3.1. Types of Mining-Induced Overburden Fractures. The formation of mining-induced overburden fractures is accompanied by the failure and movement of strata and the redistribution of stress in the rock mass. The strata in different regions may be subject to various stress conditions with different free space configurations, which can lead to different morphologies and development degrees (or apertures) in the fractures that ultimately affect the fracture conductivity. As shown in Figures 1 and 3, mining-induced fractures can be classified into three main types according to how they are formed. Type 1 fractures are tensile-shear fractures (i.e., break failure fractures) that are generated during the periodic break and rotation of strata. They exhibit a relatively uniform distribution in the overburden, with the horizontal spacing of such fractures in the same stratum being approximately equal to the broken step of the stratum. Type 2 fractures are shear fractures that are generated by the advanced abutment pressure in the coal-rock masses outside the mining boundaries. They are distributed in a disorderly manner and typically have a higher density than Type 1 fractures. Type 3 fractures are bed separation fractures that are generated during the uncoordinated movement of adjacent strata.

Type 1 fractures are also classified into three subtypes according to the location of the failed stratum in the overburden (Figure 3):

- (a) V-shaped tensile fractures near the mining boundaries, which are generated when the stratum undergoes a single rotation with a clearly visible rotation angle
- (b) Jigsaw-fit fractures in the central compacted zone of the mining area, which are generated when broken blocks of the strata undergo two rotations, each in an opposite direction (so there is no clearly visible rotation angle), and the fracture surfaces of adjacent broken blocks are pressed against each other. Although the fractures appear closed, the fracture surfaces cannot be fully fitted to each other owing to the differences in surface morphology and roughness. That is, the fractures still have a certain degree of aperture and flow conductivity
- (c) Inverted V-shaped tensile fractures between the mining boundaries and central compacted zone, which are generated by two adjacent broken blocks with different rotation angles

Type 3 fractures have a similar distribution pattern to Type 1. That is, bed separation fractures are open near the mining boundaries where the fracture void volume is relatively large and are closed in the central compacted zone.

As shown above, fractures in different areas of the overburden will have different morphologies and development degrees (or apertures) when the overlying strata are in various stress states with different movement characteristics. When HDD is directed from the original rock mass outside

the mining area towards the fractured rock mass in the mining-affected area, the various fracture types will be successively exposed at different positions. Moreover, the distribution pattern of the exposed fractures will vary at different drilling horizons. All these factors will ultimately affect the diffusion and flow behavior of the grout and the sealing results of the fractures.

3.2. Simulation Experiment of HDD to Expose Mining-Induced Overburden Fractures

3.2.1. Experimental Scheme. A simplified experimental set-up was constructed using the 2.5 m long physical model frame shown in Figure 4(a) with consideration for the strata conditions of the No. 1 panel of the Gaojiabao coal mine. To simulate HDD and demonstrate the morphology of the borehole-exposed fractures in a straightforward manner, the model was installed in one half of the model frame, while the drilling process was simulated in the other half. A borehole observation instrument was deployed onsite to photograph the exposed fractures inside the borehole. The physical model had dimensions of 1.2 m (length) \times 1 m (height) \times 0.2 m (width). The geometric similarity ratio of the set-up was 1:100, the stress similarity ratio was 1:125, and the density similarity ratio was 1:1.25. The similar material proportions of the physical model for each stratum are listed in Table 1. Coal seam excavation advanced from the left side of the model towards the right side, and 5 cm wide protective coal pillars were reserved at each of the two mining boundaries of the model.

3.2.2. Experimental Results. As shown by the sketch in Figure 5 of the overburden failure and fracture development after the coal seam was completely excavated, a water-conducting fracture propagated to the bottom boundary of the third overlying stratum, which was a key stratum (KS). The corresponding WCFZ had a height of 43 m. An electric drill was used to simulate HDD from the left side of the model towards the mining-induced fracture area, while a drill TV was used to photograph the morphologies of the different types of fractures exposed by the borehole, as shown in Figure 3. As the physical model was unable to simulate compressive shear fractures outside the mining boundary, no corresponding photos were taken during the drilling simulation. The results showed that, when exposed by the borehole, the fractures manifested as voids of different scales as a result of their varying apertures. The aperture differences of the exposed fractures varied with the drilling horizons. These characteristics directly affected the flow behavior and sealing performance of the injected grout. Therefore, the types and apertures (or void size) of the borehole-exposed fractures at the different drilling horizons were statistically analyzed. A total of six survey lines were set as shown in Figure 5. In particular, survey lines L1 and L2 were outside the WCFZ but inside KS 3, while the other survey lines were all within the WCFZ and ran through different strata, resulting in a “multi-stratum run-through” phenomenon.

Figure 6 shows the distribution of the fracture types and apertures exposed at the different horizons. To facilitate

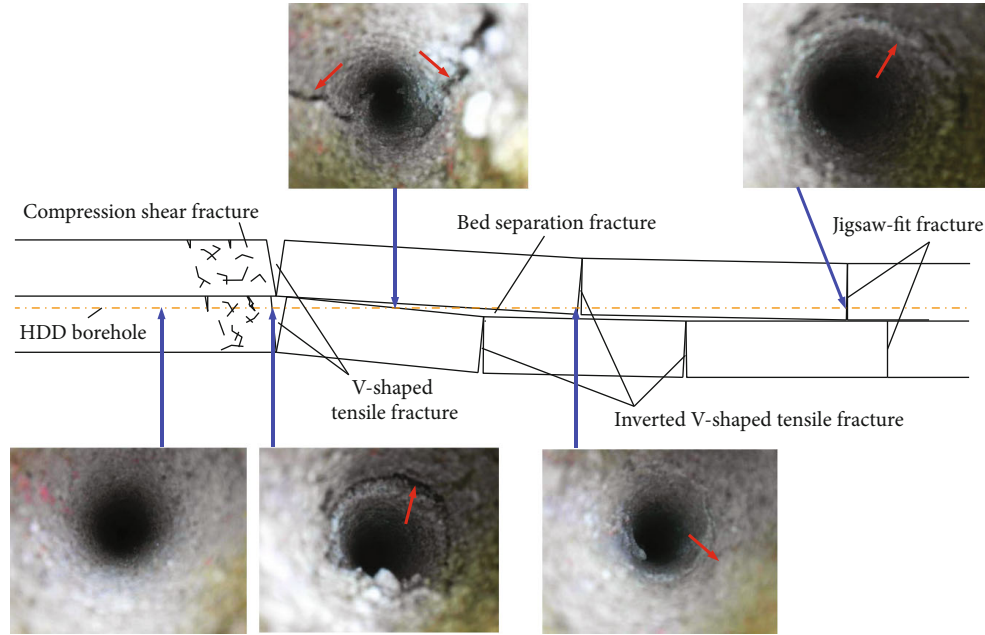


FIGURE 3: Types of mining-induced fractures exposed by HDD. Note: the photos are of the fractures exposed by the simulated borehole created in the physical simulation discussed in Section 3.2.

calibration and distinction, the different types of fractures in the stratum where a survey line was made, as well as in the adjacent (upper and lower) strata, were numbered. “A” represented the failure fractures in a given stratum and was divided into three subtypes: A-1, representing V-shaped tensile fractures in the stratum; A-2, representing inverted V-shaped tensile fractures in the stratum; and A-3, representing jigsaw-fit fractures in the stratum. “B” and “C” represented failure fractures in the adjacent strata above and below, respectively, and were each divided into three subtypes (namely, B-1, B-2, and B-3 and C-1, C-2, and C-3) to represent V-shaped tensile fractures, inverted V-shaped tensile fractures, and jigsaw-fit fractures, respectively. “D” represented the bed separation fractures between adjacent strata.

The six survey lines revealed that, as the drilling horizon was lowered, the number of exposed mining-induced fractures increased, and their apertures widened. Survey lines L1 and L2 were outside the WCFZ and only revealed three break failure fractures with small apertures in KS 3. In contrast, the other four survey lines below KS 3 ran through different strata, and each revealed bed separation fractures with unusually large fracture apertures (or void sizes) when in proximity to the bottom boundary of the KS. On survey line L3, for example, which was 3 cm below the bottom boundary of the KS, the voids in the bed separation fractures had a total length of 180.72 mm. Considering the geometric similarity ratio of the simulation model, this data suggested that, when drilling in this stratum, the borehole would advance 18 m into the delamination space before it entered the rock mass. In other words, such a void would need to be grouted and sealed to avoid the loss of drilling fluid and indicates a significant increase in the difficulty of using borehole grouting to seal fractures. Similarly, survey lines near the mining boundaries revealed significantly large voids in the V-shaped tensile

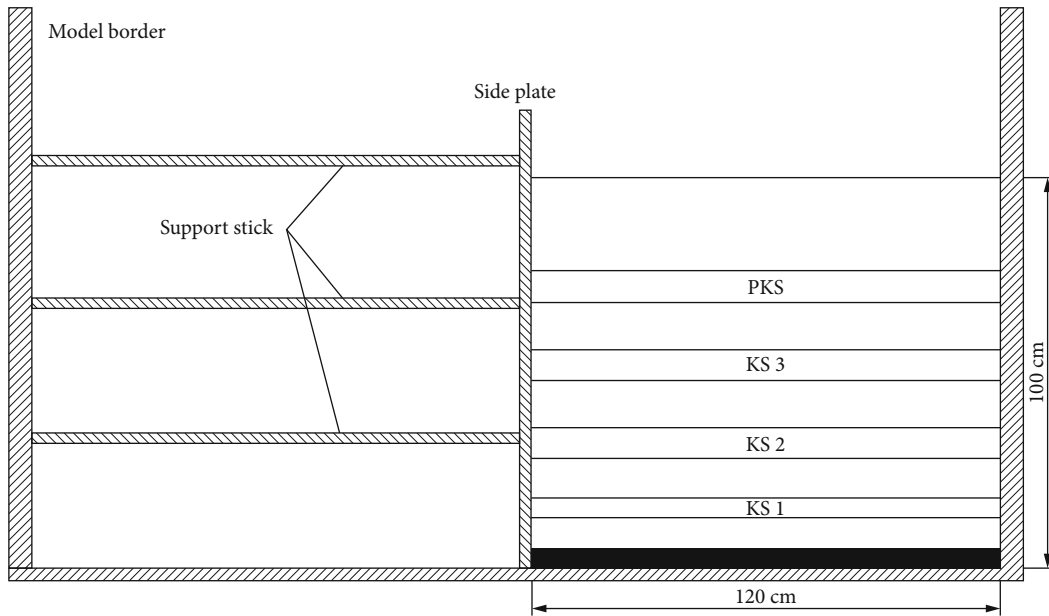
fractures or inverted V-shaped tensile fractures. For example, survey line L5 near the right mining boundary revealed that the aperture of the V-shaped tensile fractures was as wide as 6 mm, equating to an exposed void width of 0.6 m in practical drilling operations. A similar observation was made for survey line L6, which was about 50 cm from the left mining boundary and revealed an aperture of approximately 3.5 mm in the inverted V-shaped tensile fractures.

These observations explain the extreme difficulty associated with using HDD borehole grouting to seal water-conducting fractures that was experienced in the engineering test in the Gaojiabao coal mine. Essentially, owing to the large voids in the break tensile fractures and bed separation fractures that were frequently exposed by the boreholes, it was difficult to retain the injected grout, which was the main cause of the difficulty associated with grout sealing the fractures. Setting a proper drilling horizon and trajectory according to the grout hydraulic conductivity of the various types of fractures is the key to overcome this difficulty.

4. Types of Fractures Exposed by the HDD Boreholes and Their Grout Hydraulic Conductivity

4.1. Grout Hydraulic Conductivity. As indicated by the observed distribution pattern of the fracture apertures on the different survey lines in the simulation experiment, when HDD was performed from outside the mining area into the mining overburden, the different types of fractures were exposed in one of the following orders depending on the drilling horizon.

4.1.1. Order I. The borehole advanced in a single stratum within the WCFZ (Figure 7(a)). During drilling, the fractures



(a) Model layout



(b) Physical photos

FIGURE 4: Physical simulation model.

TABLE 1: Similar material proportion for each stratum.

Strata	Thickness/cm	Sand/kg	Calcium carbonate/kg	Gypsum/kg
Soft strata	24	69.2	12.10	5.20
Primary key stratum (PKS)	8	21.6	2.16	5.04
Soft strata	12	34.6	6.05	2.60
KS 3	8	23.04	1.73	4.03
Soft strata	12	34.6	2.60	6.05
KS 2	8	23.04	1.73	4.03
Soft strata	10	28.8	5.04	2.16
KS 1	5	14.4	1.08	2.52
Soft strata	8	23.04	4.02	1.73
Coal seam	5	15.8	1.58	0.675

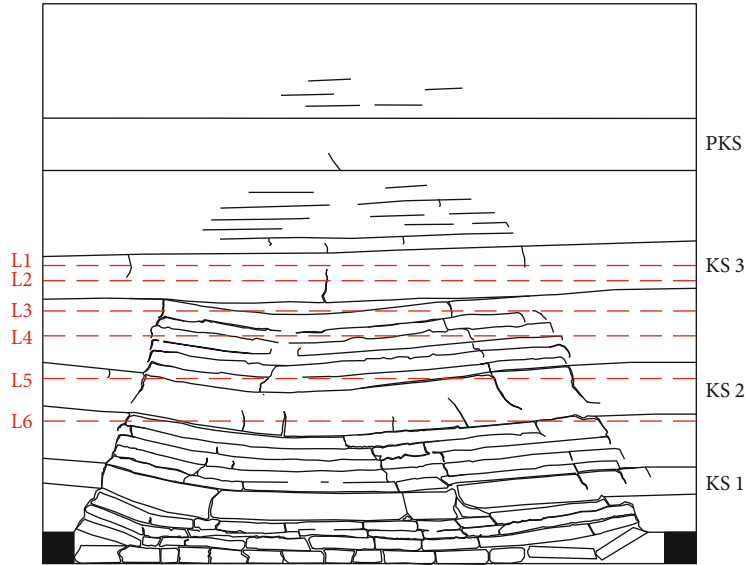


FIGURE 5: Sketched simulation results of the overburden failure.

were exposed in the following order: compressive shear fractures → V-shaped tensile fractures → inverted V-shaped tensile fractures → jigsaw-fit fractures. Then, as the borehole continued to advance toward another mining boundary, the fractures were exposed in the opposite order. This exposure order is often observed when drilling through a thick stratum, and the drilling distance between two consecutive rounds of drilling fluid loss and grout sealing was close to the broken step of the stratum.

When compressive shear fractures were exposed by the borehole, it was easy to conduct grout sealing with a low risk of grout escape owing to the small fracture apertures and poor fracture connectivity [19, 20]. In this scenario, fine-grained grouting materials, such as fly ash, cement, and water glass, are preferred. When V-shaped tensile fractures were exposed in a stratum, owing to their numerous voids and the fact that the fractures were often connected to other V-shaped tensile fractures in the lower adjacent stratum, it was advisable to first inject a coarse-grained grout until the channel connecting the lower V-shaped tensile fractures was sealed. Then, a large volume of fine-grained grout could be injected. The grout in an exposed fracture void will gradually accumulate upward only after it has flowed to its diffusion radius in the void, and the accumulation will continue until the grout reaches the drilling horizon and seals the fracture openings on the borehole wall [21]. Only after sealing is complete can drilling be resumed and continued smoothly (Figure 8). Therefore, horizontal drilling at various distances from the bottom boundary of a stratum leads to significantly different grouting volumes. The closer the drilling horizon is to the bottom boundary of the stratum, the smaller the exposed fracture opening and the lower the required volume of grout for sealing. Drilling is then resumed and continued until inverted V-shaped fractures are exposed. Inverted V-shaped fractures are connected to bed separation fractures and, thus, have a larger void volume which requires more grout than V-shaped fractures. Consequently, drilling can

only resume once the grout flows to its diffusion radius in the bed separation fractures and gradually accumulates at the drilling horizon. As the borehole advances, it will expose jigsaw-fit fractures. Although the exposed jigsaw-fit fractures are often connected to lower bed separation fractures or jigsaw-fit fractures in the adjacent stratum, they have small apertures and are easy to seal. This allows for the use of an easily solidifiable fine-grained grout to seal the fractures, which enables quick resumption of drilling. It should be noted that the size (i.e., diameter) of the borehole is significantly smaller than that of the V-shaped tensile apertures or delamination apertures, and coarse-sized grout is prone to plugging the boreholes. This results in a dilemma where although the grouting pressure is high, the fractures are not actually sealed. Therefore, when grouting and sealing fractures with large apertures or voids, it is necessary to increase the diameter of the borehole or reduce the grout injection flow rate to reduce the risk of borehole plugging.

4.1.2. Order II. Horizontal drilling proceeds through different strata within the WCFZ (Figure 7(b)) and exposes fractures in the following order: compressive shear fractures → V-shaped tensile fractures (in the same stratum) → bed separation fractures → inverted V-shaped tensile fractures (in the upper adjacent stratum) → jigsaw-fit fractures (in the upper adjacent stratum). The exposure order is reversed as the borehole continues to advance toward the other mining boundary. Drilling proceeded through different strata in Order II to allow the exposure of additional bed separation fractures near the mining boundaries, thereby making the drilling distance between two consecutive rounds of drilling fluid loss and grout sealing shorter than in the case of Order I. Due to the breaking and rotation of the strata, in practical drilling operations, HDD in the mining overburden inevitably leads to the “multi-stratum run-through” phenomenon. As a result, Order II is the most commonly adopted method in practice.

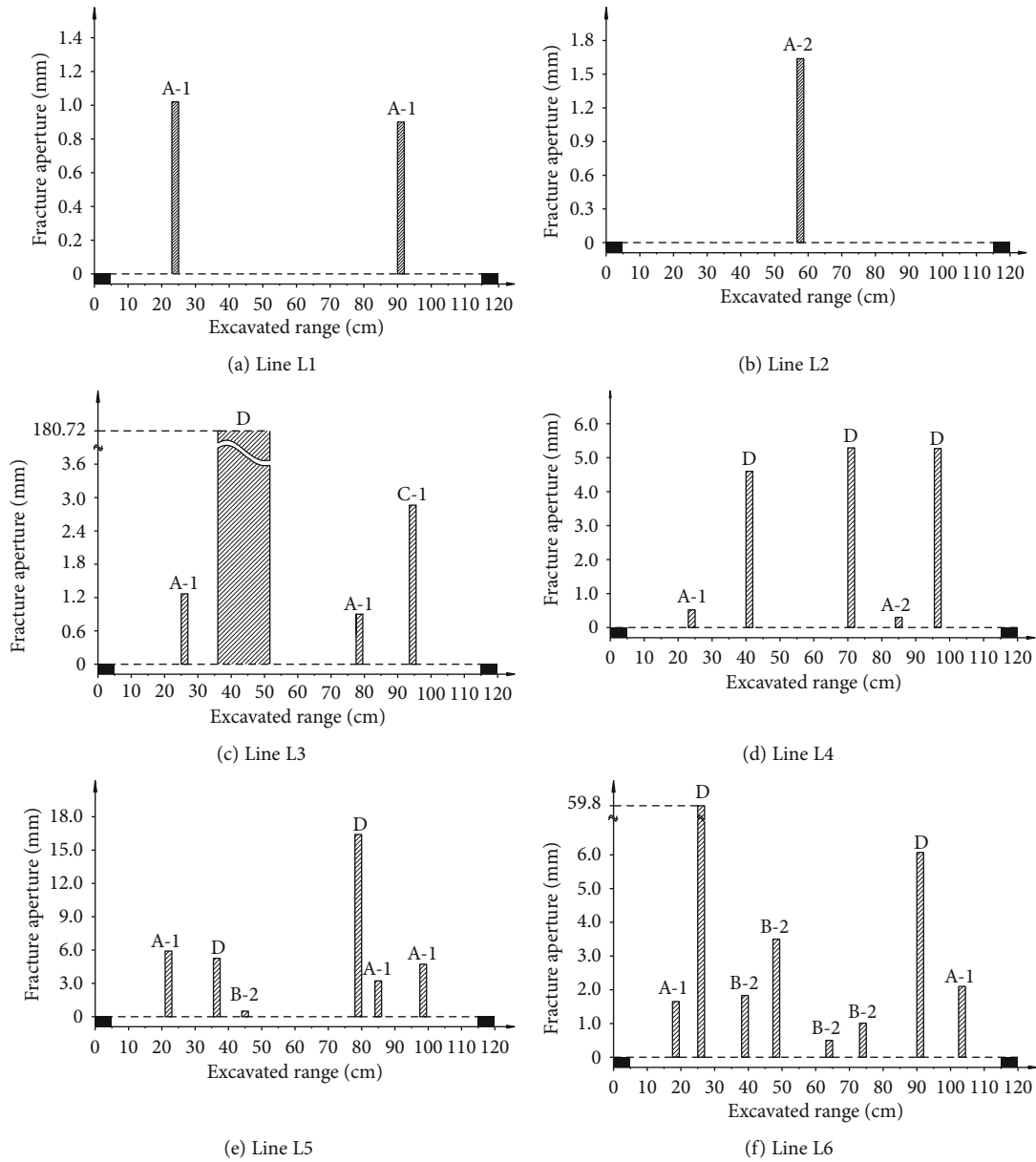


FIGURE 6: Distribution of the types and apertures of the mining-induced fractures at different horizons.

As the HDD borehole advances to expose bed separation fractures, the size of the voids in the drilling direction increases sharply. Thus, it is appropriate to use coarse-grained materials for grout sealing in this situation. Moreover, it is necessary to continuously grout the fractures while the grout flows to its horizontal diffusion radius and accumulates upward. When the grout reaches the drilling horizon, grouting could be stopped, and drilling could be resumed. As bed separation fractures are often connected to inverted V-shaped tensile fractures in the upper adjacent stratum (Figure 7(b)), the degree of grout sealing in the bed separation fractures (namely, the diffusion range and accumulation height of the grout) will affect the difficulty of sealing the inverted V-shaped tensile fractures next exposed by the drilling. The higher the degree of sealing in the bed separation fractures and the greater the diffusion range of the grout,

the smaller the required grouting volume will be to seal the inverted V-shaped fractures. As bed separation fractures are caused by the uncoordinated movement of two vertically adjacent strata, it is evident that bed separation fractures in the presence of a thicker and harder upper stratum (such as the KS) will exhibit a significantly higher void volume than those in the presence of a thinner and softer upper stratum. In addition, with a decrease in the rotation angles of the broken strata, the drilling distance in the delamination space will increase, leading to a larger grouting volume and higher sealing difficulty. Therefore, it is necessary to consider the conditions of the drilled strata in practical drilling operations in order to select proper grouting materials and volumes.

4.1.3. Order III. Drilling is performed in the curved subsidence zone outside the WCFZ (Figure 7(c)), and the borehole

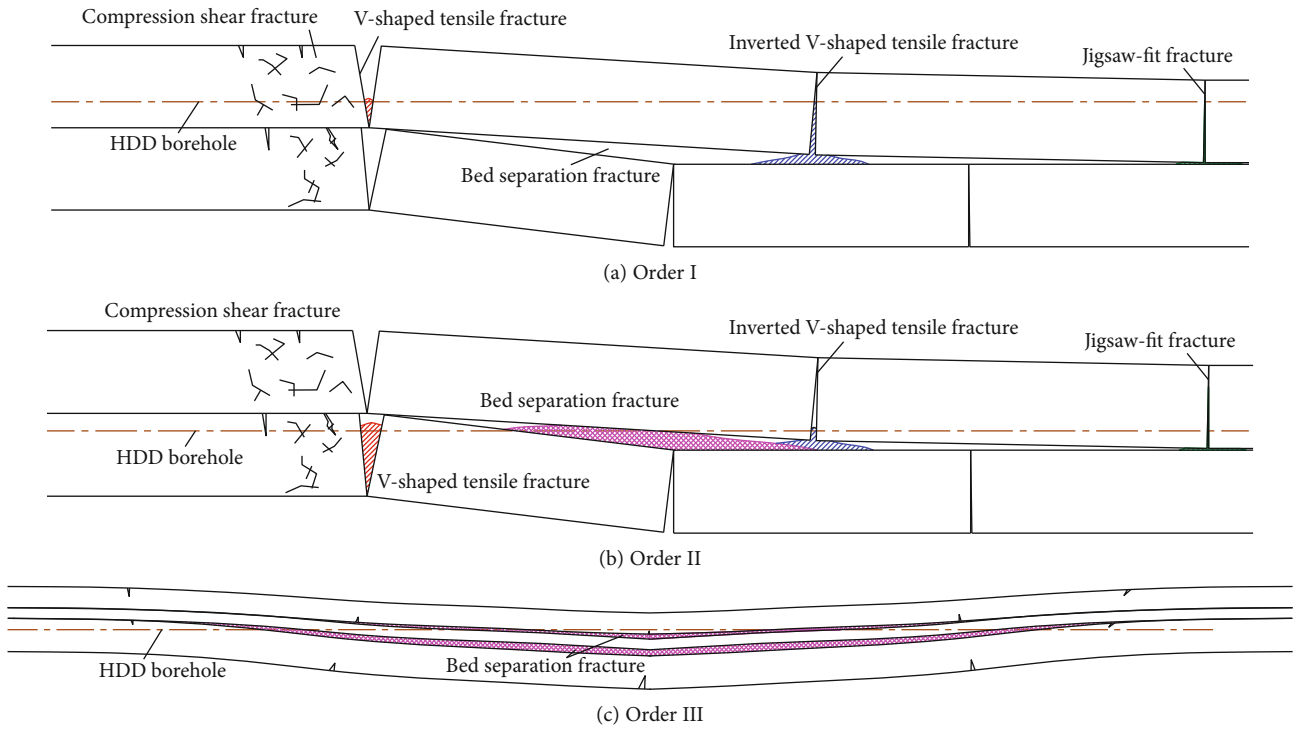


FIGURE 7: Types of fractures exposed by the HDD boreholes at different horizons.

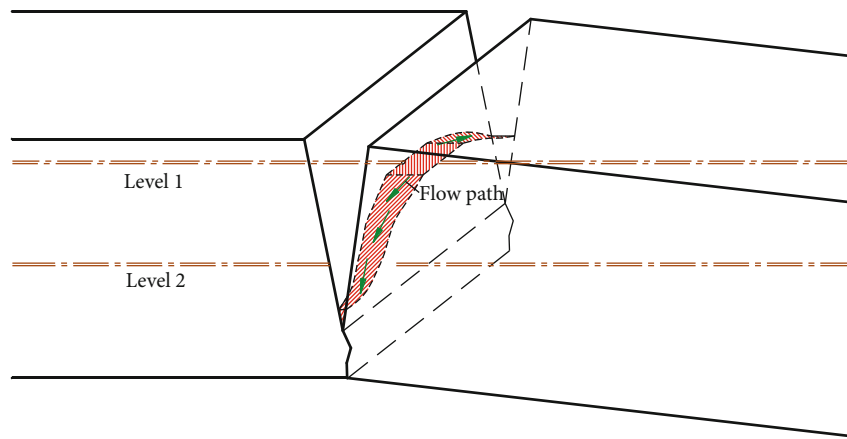


FIGURE 8: Schematic diagram of grouting the V-shaped tensile fractures exposed by HDD.

advances through different strata to expose bed separation fractures.

In contrast to the borehole-exposed bed separation fractures in the WCFZ in Order II, the bed separation fractures in the curved subsidence zone in Order III have a relatively closed space. Thus, they are suitable for grouting with a large volume of fine-grained materials and have a low risk of grout escape. As the rotation angles of the strata in the curved subsidence zone are relatively small, the borehole needs to advance a significant distance in the delamination fracture before entering the upper adjacent stratum. This results in high grouting volume and frequency in practice. Once the borehole enters the upper adjacent stratum, it needs to advance a significant distance before exposing another

delamination fracture where frequent grout sealing will again be required. Therefore, the frequency of grout sealing will alternate between high and low as the borehole advances, such as the case with the drilling of borehole 2 in the Gaojiabao coal mine. However, it should be noted that only the bed separation fractures in the curved subsidence zone are grouted and sealed in such a case, and it is impossible to achieve water blocking in practice. Ultimately, the bed separation fractures in the curved subsidence zone do not constitute a channel that leads to groundwater loss. This is in line with the observation that the influx of underground water into the Gaojiabao coal mine did not significantly decrease after the large-scale grouting of borehole 2 in the water blocking test.

4.2. Determination of Reasonable Drilling Horizons for Efficient Fracture Sealing. As previously shown, when using HDD borehole grouting to seal water-conducting overburden fractures while minimizing the grouting volume, it is exceedingly important to determine the reasonable drilling horizon in a scientific manner. Selection of the HDD horizons should be based on the following three principles.

- (1) Borehole grouting is intended to seal the water-conducting channels that lead to groundwater loss. Therefore, it is necessary to ensure that the drilling horizon is within the WCFZ of the mining overburden
- (2) The fractures exposed at the drilling horizon should have good capacity to retain the grout. In other words, the injected grout should remain within the fracture voids to seal the fractures without the risk of grout escape. Therefore, it is best to drill at horizons where the fracture apertures are small. It is also necessary to ensure that the vertical connectivity between the exposed fractures and the fractures in the lower stratum is as small as possible in order to avoid grout leakage to the underground goaf. In the meantime, it is necessary to increase the grout diffusion in the plane to increase the range of the grout sealing within a single borehole. Generally, the higher the borehole horizon, the smaller the aperture of the exposed mining-induced fractures. However, drilling may be performed under but near the bottom boundary of a thick, hard stratum (such as the KS) to expose large voids in the bed separation fractures, such as the voids shown on survey line L3 in Figures 5 and 6. On the one hand, proper selection of the drilling horizons would improve the planar diffusion range of the grout. On the other hand, since bed separation fractures are typically connected to multiple tensile fractures in the lower stratum, such selection would increase the risk of grout loss in the vertical direction. Therefore, full consideration should be given to the planar distribution characteristics of mining-induced fractures in order to comprehensively evaluate the planar diffusion of the grout in the fractures. This should then be compared to the risk of grout loss in the vertical direction in order to determine the most suitable horizon
- (3) The drilling horizon should be favorable for maintaining the stability of the drilled rock mass. An HDD borehole mainly consists of a vertical section, build-up section, and horizontal section. Both the vertical and build-up sections are lined and protected by a casing, while the horizontal section is unlined. If the horizontal section is drilled in a stratum with relatively weak lithology, there is a high risk of hole collapse due to mining-induced fractures. These types of accidents will affect the grouting procedure and water blocking performance. Therefore, it is necessary to set the drilling horizon in a stratum (e.g., sandstone) with stable lithology and high mechanical strength

according to the stratigraphic column of the overburden

According to these principles, it is possible to determine a reasonable borehole horizon for the HDD in the overburden with consideration for the overburden conditions presented by the physical simulation results and distribution of the water-conducting fractures (Figure 5). As the WCFZ extended vertically up to the bottom boundary of KS 3, the drilling horizon should be set below this stratum. Survey lines L3–L6 were all within the WCFZ; however, as shown in Figure 6, the fracture aperture on survey line L4 was the minimum (although survey line L3 was at a higher horizon, it ran through bed separation fractures; thus, revealing larger void volumes). Therefore, if a stable sandstone stratum was present near L4, it would serve as a suitable drilling horizon.

5. Conclusions

- (1) A ground-based engineering test was conducted in the Gaojiabao coal mine to evaluate the use of HDD to grout and seal water-conducting fractures; however, the water blocking performance was not satisfactory. The present study utilized HDD boreholes to expose the development characteristics and grout hydraulic conductivity of water-conducting fractures and determined reasonable drilling trajectories or horizons favorable for grout sealing of the fracture channels, which are the keys to solving these problems
- (2) As a horizontal directional borehole advances from the original rock mass outside the mining boundary towards the mining-induced fractured rock mass, the borehole will successively expose fractures with different development morphologies. The order of exposure was found to be dependent on the drilling horizon and whether the borehole runs through different strata. A simulation experiment was conducted and revealed three orders in which the various types of mining-induced fractures could be exposed by an HDD borehole. When using HDD boreholes to expose different types of mining-induced fractures and seal them with grout, each type of fracture will exhibit different grout hydraulic conductivity as a result of their varying void volumes and scales, which explains why the frequent grout sealing conducted in the engineering test resulted in such poor sealing performance
- (3) The capacity of the mining-induced fractures to retain grout was investigated, and further analysis of the results led to a scheme for determining reasonable horizons for HDD to facilitate efficient fracture sealing. The drilling horizon should be selected in such a way that the apertures of the borehole-exposed fractures are as small as possible, and the vertical connectivity of the borehole-exposed fractures to fractures in the lower stratum should also be as small as possible. This would reduce the risk

of grout escape in the vertical direction while enhancing the planar hydraulic conductivity of the grout. This scheme is intended to ultimately determine the achievable range of grout sealing for a single borehole while attaining the grout sealing of as many fractures as possible with as small a grouting volume as possible

- (4) Except for the fracture morphologies, the high flow-rate of water is also an important factor that prevented the grout from accumulating in and filling up the fractures, especially, for the readily hardenable grout such as cement. In addition, when sealing with different grout types, the influence degree of hydrodynamic erosion on the sealing effect may be different. Owing to limited space, the abovementioned factor was not discussed in the paper, and further research will be carried out in the future

Data Availability

The data used to support the finding of this study are available from the corresponding author upon request.

Conflicts of Interest

The authors declared that they have no conflicts of interest to this work.

Acknowledgments

Financial support from the Fundamental Research Funds for the Central Universities (2020ZDPYMS19) is greatly appreciated.

References

- [1] J. C. Zhang and B. H. Shen, "Coal mining under aquifers in China: a case study," *International Journal of Rock Mechanics and Mining Sciences*, vol. 41, no. 4, pp. 629–639, 2004.
- [2] X. X. Miao, X. M. Cui, J. A. Wang, and J. L. Xu, "The height of fractured water-conducting zone in undermined rock strata," *Engineering Geology*, vol. 120, no. 1–4, pp. 32–39, 2011.
- [3] J. L. Xu, *Green Mining in Coal Mines*, China University of Mining and Technology Press, Xuzhou, China, 2011.
- [4] J. F. Ju, J. L. Xu, Q. S. Li, W. B. Zhu, and X. Z. Wang, "Progress of water-preserved coal mining under water in China," *Coal Science and Technology*, vol. 46, no. 1, pp. 12–19, 2018.
- [5] H. Lisa, B. Christian, F. Asa, G. Gunnar, and F. Johan, "A hard rock tunnel case study: characterization of the water-bearing fracture system for tunnel grouting," *Tunnelling and Underground Space Technology*, vol. 30, pp. 132–144, 2012.
- [6] A. H. Høien and B. Nilsen, "Rock mass grouting in the Løren tunnel: case study with the main focus on the groutability and feasibility of drill parameter interpretation," *Rock Mechanics and Rock Engineering*, vol. 47, no. 3, pp. 967–983, 2014.
- [7] S. C. Li, R. T. Liu, Q. S. Zhang, and X. Zhang, "Protection against water or mud inrush in tunnels by grouting: a review," *Journal of Rock Mechanics and Geotechnical Engineering*, vol. 8, no. 5, pp. 753–766, 2016.
- [8] J. F. Ju and J. L. Xu, *Damage Mechanisms of Aquifers Induced by Underground Coal Mining and its Ecological Restoration*, China University of Mining and Technology Press, Xuzhou, China, 2019.
- [9] I. F. Oge, "Prediction of cementitious grout take for a mine shaft permeation by adaptive neuro-fuzzy inference system and multiple regression," *Engineering Geology*, vol. 228, pp. 238–248, 2017.
- [10] J. Chai, Q. Yuan, S. Wang et al., "Water inrush control and restoration of shaft construction in cretaceous aquifer," *Journal of China Coal Society*, vol. 41, no. 2, pp. 338–344, 2016.
- [11] H. Shimada, A. Hamanaka, T. Sasaoka, and K. Matsui, "Behaviour of grouting material used for floor reinforcement in underground mines," *International Journal of Mining, Reclamation and Environment*, vol. 28, no. 2, pp. 133–148, 2014.
- [12] B. T. Shen, "Coal mine roadway stability in soft rock: a case study," *Rock Mechanics and Rock Engineering*, vol. 47, no. 6, pp. 672225–672238, 2014.
- [13] F. Zhou, W. B. Sun, J. L. Shao, L. J. Kong, and X. Y. Geng, "Experimental study on nano silica modified cement base grouting reinforcement materials," *Geomechanics and Engineering*, vol. 20, no. 1, pp. 67–73, 2020.
- [14] Z. P. Xu, C. W. Liu, X. W. Zhou, G. R. Gao, and X. H. Feng, "Full-scale physical modelling of fissure grouting in deep underground rocks," *Tunnelling and Underground Space Technology*, vol. 89, pp. 249–261, 2019.
- [15] S. Q. Liu, Y. Fei, Y. C. Xu, L. Huang, and W. Y. Guo, "Full-floor grouting reinforcement for working faces with large mining heights and high water pressure: a case study in China," *Mine Water and the Environment*, vol. 39, no. 2, pp. 268–279, 2020.
- [16] W. Q. Zhu, X. X. Zhu, S. X. Xu, Z. Y. Wang, and W. Li, "Experimental study on properties of a new type of grouting material for the reinforcement of fractured seam floor," *Journal of Materials Research and Technology*, vol. 8, no. 6, pp. 5271–5282, 2019.
- [17] G. Y. Li and W. F. Zhou, "Impact of karst water on coal mining in North China," *Environmental Geology*, vol. 49, no. 3, pp. 449–457, 2006.
- [18] Z. G. Cao, J. F. Ju, and J. L. Xu, "Distribution model of water-conducted fracture main channel and its flow characteristics," *Journal of China Coal Society*, vol. 44, no. 12, pp. 3719–3728, 2019.
- [19] L. Sun, G. Grasselli, Q. S. Liu, and X. H. Tang, "Coupled hydro-mechanical analysis for grout penetration in fractured rocks using the finite-discrete element method," *International Journal of Rock Mechanics and Mining Sciences*, vol. 124, p. 104138, 2019.
- [20] H. M. Kim, J. W. Lee, M. Yazdani, E. Tohidi, H. R. Nejati, and E. S. Park, "Coupled viscous fluid flow and joint deformation analysis for grout injection in a rock joint," *Rock Mechanics and Rock Engineering*, vol. 51, no. 2, pp. 627–638, 2018.
- [21] X. C. Wang, R. T. Liu, W. M. Yang et al., "Study on grouting mechanism of horizontal fractures considering the bleeding of cement slurry," *Chinese Journal of Rock Mechanics and Engineering*, vol. 38, no. 5, pp. 1005–1017, 2019.

Research Article

Influence of Three-Dimensional Stress Field Variation on Fracture Evolution Characteristics of a Roof

Xuyang Shi ^{1,2} Zhaolin Li ^{1,2} Qingxiang Cai ^{1,2} Wei Zhou ^{1,2} and Wenshuai Li ³

¹School of Mines, China University of Mining and Technology, Xuzhou, Jiangsu 221116, China

²State Key Laboratory of Coal Resources and Safe Mining, China University of Mining and Technology, Xuzhou, Jiangsu 221116, China

³State Key Laboratory for Geomechanics and Deep Underground Engineering, China University of Mining and Technology, Xuzhou, Jiangsu 221116, China

Correspondence should be addressed to Wei Zhou; loutian1982@126.com

Received 26 June 2020; Revised 10 November 2020; Accepted 30 November 2020; Published 28 December 2020

Academic Editor: Yingchun Li

Copyright © 2020 Xuyang Shi et al. This is an open access article distributed under the Creative Commons Attribution License, which permits unrestricted use, distribution, and reproduction in any medium, provided the original work is properly cited.

Excavation disturbance on the dynamic variation of the three-dimensional stress field is the main cause for the dynamic disasters of the surrounding rock mass of the roof. The stress condition in the surrounding rock mass of the roof during entry excavation and its impact on entry stability are systemically studied in this study. It is found that the surrounding rock mass of the roof is mainly influenced by the combined effect of the stress unloading and stress transference induced by entry excavation. A servo-controlled true triaxial material testing system is used to conduct the true triaxial loading and unloading experiments of rocks under different stress paths. The influence of different stress paths, especially the variation of the principal stress direction, on the mechanical characteristics and fracture characteristics of rocks is investigated. The results indicate that the variation of the principal stress direction has a significant impact on the macroscopic fracture characteristics of the rock. The main macroscopic fracture plane of the rock highly depends on the intermediate principal stress. The fracture evolution of the roof rock mass during entry excavation is analyzed. The results show that the change of the three-dimensional stress field induces the formation of complex fracture networks in the surrounding rock mass of the roof. The roof is likely to dislocate horizontally and collapse. The corners of the entry are seriously damaged. Based on the above findings, a support scheme is proposed to maintain the stability of a gob-side entry. The field experience suggests that the support scheme can achieve good results.

1. Introduction

Dynamic disasters, such as the serious deformation and collapse of the entry roof, have always been major issues restricting the safe, effective mining of coal resources in China [1, 2]. The entry roof tends to fail and become more instable with the increase in mining intensity and mining depths [3]. The failure and instability of the roof result from the formation of the fracture zone in the surrounding rock mass of the entry [4, 5]. It is of great significance in the aspects of theoretical analysis and field applications to understand the fracture pattern and its evolution in the surrounding rock mass of the roof in order to maintain the stability of the roof and prevent dynamic disasters [6].

The excavation of mining entries disturbs the in situ stress balance [7] and induces the dramatic change [8] and dynamic adjustment of the stress field in the roof [9]. This normally leads to the serious deformation and failure of the roof. The mechanical behaviour of the entry roof is closely related to the disturbance caused by entry excavation [10]. Therefore, it is necessary to consider the influence of the stress change in the surrounding rock mass of the entry roof and systematically study the stress disturbance process caused by entry excavation and the mechanical response of the rock mass [11]. Previous studies mainly consider the effect of the change of the vertical stress (i.e., the abutment stress) on the stability of the roof and simply assume that the deformation and failure of the roof result from the one-dimensional loading. Based on field measurement and

numerical modelling results, [12, 13] found that the obvious dynamic adjustment of the three-dimensional stress state in the surrounding rock mass occurs in the driving process of the entry. The individual or the simultaneous variation of each stress component in the three-dimensional stress state is likely to cause the deformation and fracture of the surrounding rock mass.

Many researchers have carried out triaxial compression tests to reveal the mechanical behaviour and the failure process of the surrounding rock mass of the entry under the influence of the complicated three-dimensional stress evolution caused by the disturbance of excavation [14]. These studies mainly focused on the effects of the loading and unloading process in the conventional triaxial compression tests on the strength [15], deformation [16], and failure modes [17] of rocks. Nevertheless, due to the inherent shortcoming of the conventional triaxial compression test that ignores the influence of the intermediate principal stress [18], only the axial stress that differs from the lateral stress can be applied to the cylindrical rock specimen in the laboratory test [19]. Hence, only the strength and deformation characteristics of the rock under the axisymmetric stress condition can be reflected. This is unrepresentative of the stress condition that the rock normally encounters in the realistic situation ($\sigma_1 \neq \sigma_2 \neq \sigma_3$) and differs from the stress evolution characteristics of the entry rock mass induced by excavation disturbance [20, 21]. Based on the three-dimensional stress evolution in the entry roof at the mine site, experimental studies on rocks under true triaxial stress paths can more accurately simulate the failure evolution process of the roof disturbed by gob-side entry driving and disclose the failure mechanism [22]. This is significant for the stability control of the entry roof.

In addition, the traditional theories always considered that the maximum principal stress in the roof strata induced by excavation disturbance has the vertical orientation [23]. Only the stress concentration factor of the abutment stress in the vertical direction was involved in the analysis of the stress state in the surrounding rock mass of the entry influenced by mining excavation [24, 25]. In fact, besides the change of the magnitudes of the principal stresses, the change of the orientations of the principal stresses also occurs during the excavation and construction of underground spaces (e.g., entries) [26, 27]. However, the rotation of the principal stresses in the roof strata is normally ignored in previous studies [28, 29]. Many experimental results in civil engineering indicated that the rotation of the principal stress orientations (assuming that the magnitudes of the principal stresses remain constant) leads to the obvious plastic deformation of the soil [30]. Hence, the complicated evolution of the stress path and the stress orientation induced by entry excavation results in the damage and degradation of the mechanical parameters of the roof. Besides, the dynamic damage evolution process is the fundamental cause for the deformation and fracture of the roof rock mass of the entry.

In view of this, the gob-side entry driving activity at the Dongtan Coal Mine (owned by Yankuang Group) is taken as the engineering background to systematically study the influence of entry excavation on the principal stress path

and the stress principal orientation in the roof rock mass. The mechanism of the dynamic disaster of the roof induced by gob-side entry driving is revealed. The related control technology of the roof rock mass is proposed based on the results. The engineering experience at the Dongtan Coal Mine also offers a reference to the support design of the entries with similar conditions.

2. Engineering Background and Numerical Model

The Dongtan Coal Mine is located in Shandong Province, China (Figure 1(a)). The mining entry in the 3# coal seam at the Dongtan Coal Mine is excavated by gob-side entry driving. The coal pillar between the gob-side entry and the previous panel has a width of 3 m. The dip angle of the 1306 working face in the 3# coal seam ranges from 0° to 12° with an average of 6° (Figure 1(b)). The coal seam has an average thickness of 8.8 m. The 1306 tail entry is located at the -660 m level and is close to the goaf of the 1305 working face (which is at the south of the 1306 tail entry). The entry has a trapezoidal cross section (4.8 m wide at the roof and 5.0 m wide at the floor) with a height of 4 m. In situ stress monitoring was performed in the head entry by the stress relief method. The maximum horizontal in situ stress (σ_H), the minimum horizontal stress (σ_h), and the vertical in situ stress (σ_v) are 19.15 MPa, 10.02 MPa, and 14.64 MPa, respectively.

To study the influence of gob-side entry excavation on the principal stress change and the damage of the roof, the numerical modelling software ABAQUS (based on the finite element method) is used to establish the numerical model in this study (Figure 2(a)). The locations of the mining entries in the 1306 working face in the numerical model are given in Figure 2(b). Both the 1305 head entry and the 1306 tail entry have dimensions of 5 m (in width) \times 4 m (in height). The width of the coal pillar is 3 m. The vertical displacement at the bottom boundary of the model is fixed. A uniform stress of 15 MPa is applied to the top boundary of the model to simulate the overburden stress (the thickness of the overburden rock layers in the numerical model is 660 m). The maximum horizontal in situ stress is 19.5 MPa, which is parallel to the entry axis. The minimum horizontal in situ stress is 10.5 MPa, which is perpendicular to the entry axis. The strain softening model based on the Mohr-Coulomb criterion is used in the numerical simulation. The mechanical parameters of the coal seam and the roof and floor strata in the numerical model are listed in Table 1. Compared with the field measurement results, the numerical simulation can provide good results (Figure 3), which shows the reliability of the numerical model.

Three monitoring points are arranged in the roof rock mass, which are 0 m, 4 m, and 8 m above the roof, respectively (Figure 4). The change of the principal stresses in the roof rock mass is provided in Figure 5. When the working face is 20 m in front of the monitoring section, the rock mass close to the roof suffers from the influence of entry excavation. When the working face is 5 m to the monitoring section, the excavation disturbance becomes quite obvious. Clear

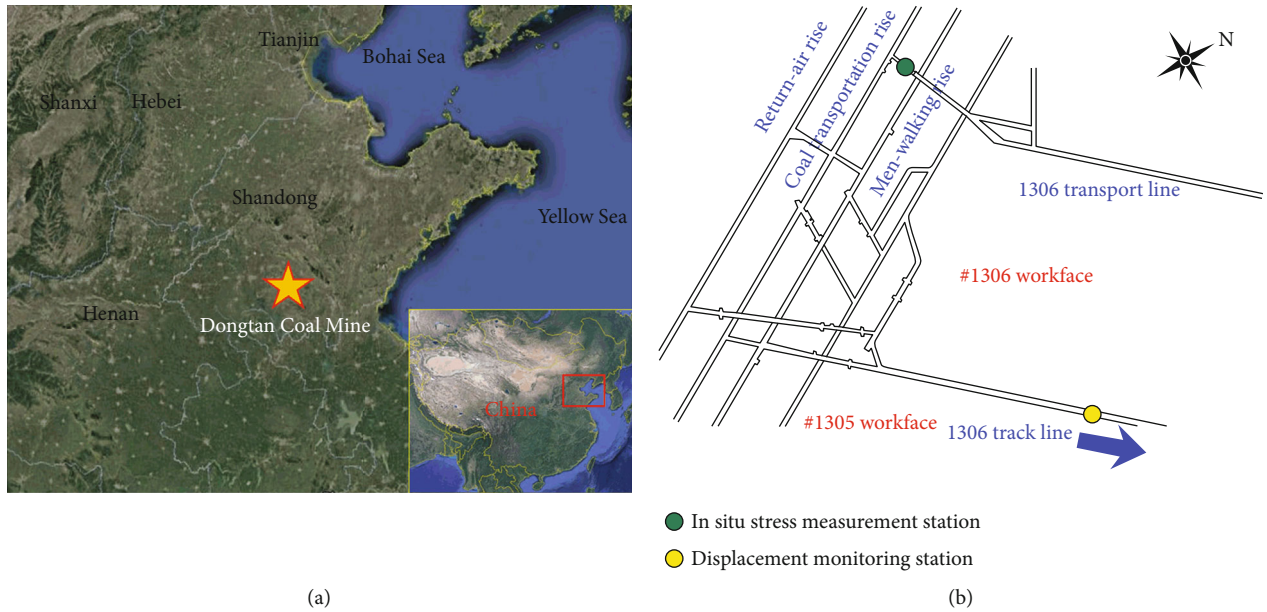


FIGURE 1: (a) Location of the Dongtan Coal Mine, Shandong, China. (b) Plane view of working face arrangement.

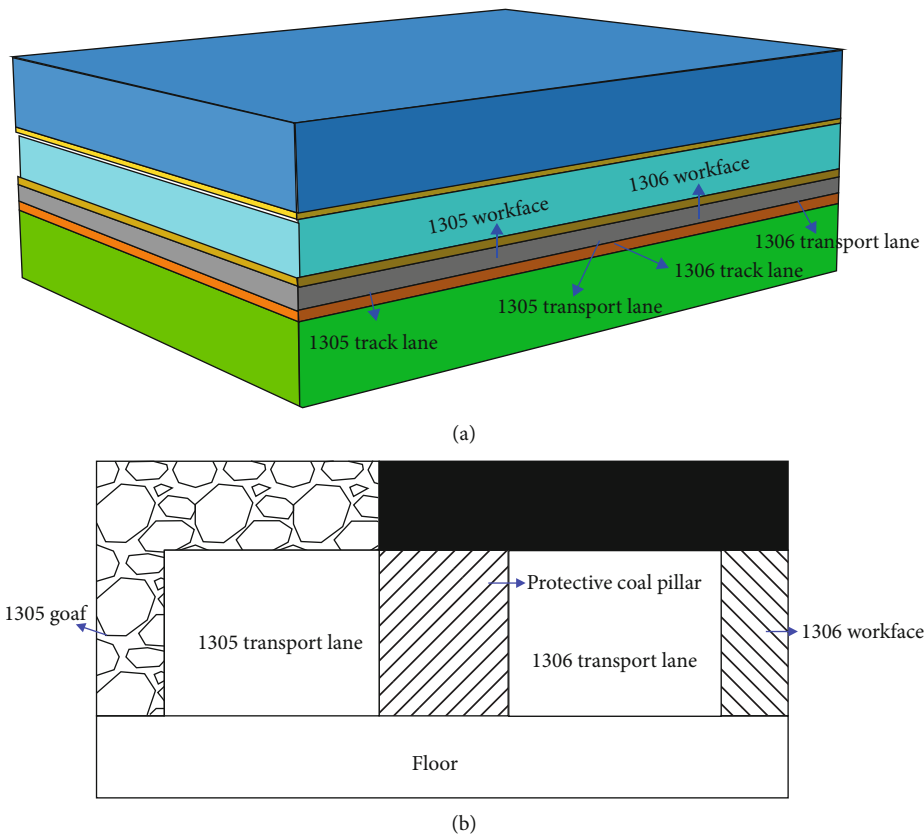


FIGURE 2: (a) Numerical model. (b) Schematic of the mining entries in the 1306 working face.

unloading processes of the three principal stresses occur in the elements at the roof surface. The magnitudes of σ_1 and σ_3 increase first and then decrease, while the σ_2 magnitude is continuous. The change of the principal stresses at the monitoring points 4 m and 8 m above the roof is similar to that at the roof surface. The excavation disturbance becomes

weaker at the rock mass away from the entry roof. When the working face is 10 m behind the monitoring section, the three principal stresses in the roof elements gradually stabilize. This suggests that the influence of the entry excavation on the monitoring section terminates and the stress condition in the roof rock mass redistributes to the equilibrium state.

TABLE 1: Mechanical parameters of coal seam and rock strata.

Stratum	Lithology	Thickness (m)	Elastic modulus (GPa)	Poisson ratio	Density (kg/m ³)	Internal friction angle (°)	Initial cohesion (MPa)	Residual cohesion (MPa)
Roof	Sandstone	110	15	0.3	2560	25	3	2
	Mudstone	2	8	0.35	2480	18	1.2	1
	Middle-fine sandstone	20	9	0.3	2560	24	1.3	1.1
	Argillaceous siltstone	3	8	0.36	2480	18	1.1	0.8
Coal seam	3# coal	8.5	7	0.35	1400	16	1	0.6
Floor	Siltstone	4	8	0.35	2560	18	1.1	0.8
	Fine sandstone	32.5	12	0.3	2560	30	5	4

According to elastic mechanics, when the tangential stress at a surface of an arbitrary point in a three-dimensional space equals to zero, the normal stress at this surface is considered one of the principal stresses at this point and the normal direction of this surface is also the direction of the principal stress. The direction of the principal stress can be calculated by [31]

$$\begin{cases} (\sigma_x - \sigma)l + \tau_{xy}m + \tau_{yz}n = 0, \\ \tau_{xy}l + (\sigma_y - \sigma)m + \tau_{yz}n = 0, \\ \tau_{xz}l + \tau_{yz}m + (\sigma_z - \sigma)n = 0, \end{cases} \quad (1)$$

$$l^2 + m^2 + n^2 = 1, \quad (2)$$

where σ_x is the stress component in the x -axis, σ_y is the stress component in the y -axis, σ_z is the stress component in the z -axis, τ_{xy} is the shear stress at the x - y surface, τ_{xz} is the shear stress at the x - z surface, τ_{yz} is the shear stress at the y - z surface, l is the cosine of the angle between the normal line of the surface and the x -axis, m is the cosine of the angle between the normal line of the surface and the y -axis, n is the cosine of the angle between the normal line of the surface and the z -axis, and σ is the principal stress tensor. According to the elastic mechanics theory, the parallel Equations (1) and (2) can be used to obtain the cosines l_1 , m_1 , and n_1 of the corresponding directions of the principal stress σ_1 . The corresponding direction cosine of the principal stresses σ_2 and σ_3 can also be obtained.

The change of the principal stress directions in the roof rock mass at different stages during entry excavation is given in Figure 6. The entry axis is perpendicular to the paper as shown in Figure 6. The change of the angle between the principal stress at the top surface of the monitoring element and the vertical direction is provided in Figure 7. When the working face moves from the location 5 m in front of the monitoring surface to the location 5 m behind the monitoring surface, the principal stress direction in the entry roof rock mass shows dramatic variation. The principal stress direction at the roof surface exhibits obvious rotation, and the change of the principal stress directions at the monitoring elements 4 m and 8 m above the roof becomes minor. Nevertheless, the reverse of the principal stress direction is observed at all the three monitoring points. The principal stresses at the

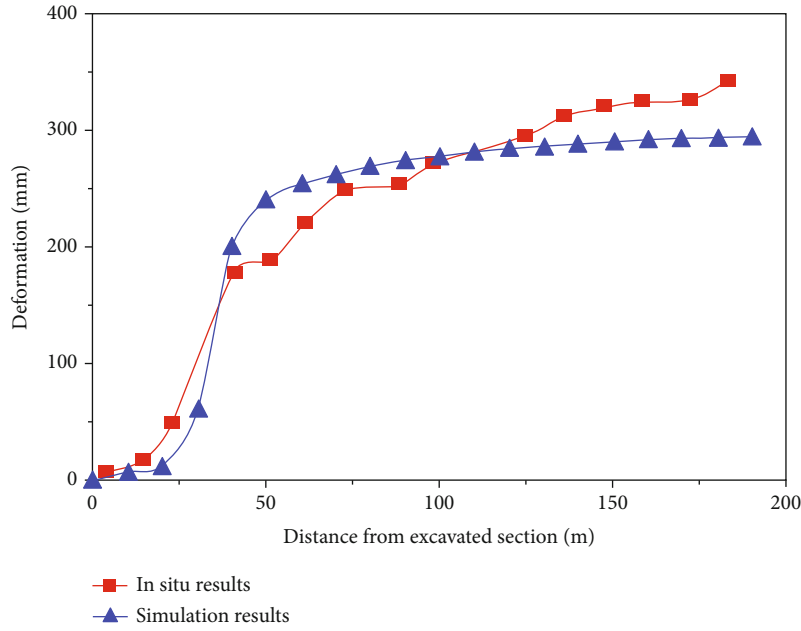
monitoring point 8 m above the roof change earlier than those at the monitoring point 4 m above the roof. This indicates that the entry excavation leads to the transference of the principal stress from the rock mass away from the roof to the rock mass close to the roof.

3. Fracture Characteristics of Rocks under Different Stress Paths

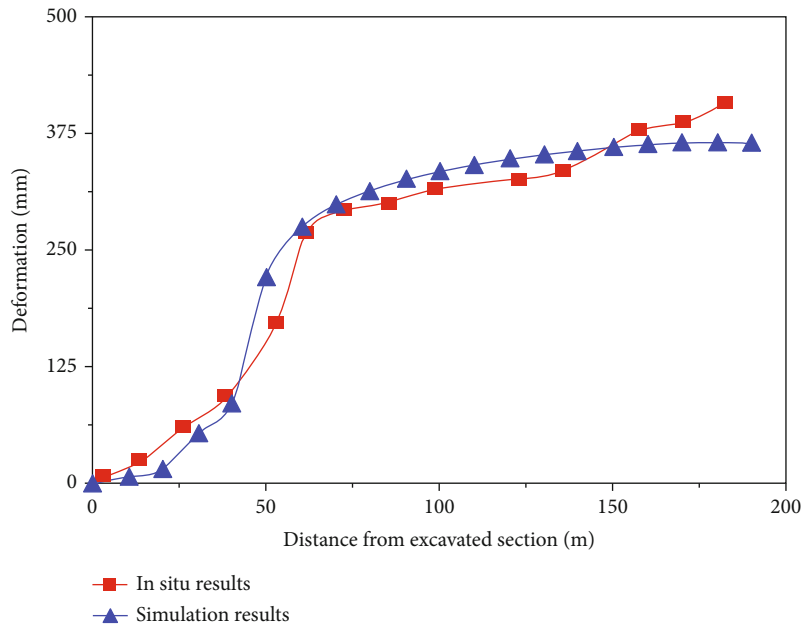
3.1. Stress Path Design. The numerical simulation results in Section 2 show that the roof rock mass sustains complicated stress paths due to the disturbance of the entry excavation. The mechanical characteristics of rocks are closely related to the stress paths they undergo. The fracture characteristics and the fracture mechanism of rocks under complex stress paths can be more accurately described by laboratory experiments on rock specimens under different stress paths. The results can provide a theoretical basis for the entry support at the mine site. To study the fracture characteristics of the roof rock and analyze its fracture mechanism, the following three typical triaxial stress paths are proposed in this section based on the stress paths in the roof rock mass (Table 2).

The underground rock mass is under the in situ stress condition when the entry is unexcavated. With the advance of the working face, the principal stresses in the rock masses with various distances to the entry surface exhibit a certain difference. The maximum principal stress shows variation during the entry excavation and is hence assumed to be constant in this study. The unloading of the intermediate principal stress and the minimum principal stress could occur due to different geotechnical conditions and the variation of the stress conditions. Note that the results in Figures 6 and 7 suggest that entry excavation results in the obvious change of the stress condition in the roof rock mass, especially the exchange of the intermediate principal stress and the minimum principal stress. This is found at all the three monitoring points in the roof rock mass when the working face moves towards the monitoring section (from the location 5 m in front of the monitoring section). This section is aimed at investigating the influence of this stress condition variation on the mechanical characteristics and the fracture characteristics of the rock.

3.2. Specimen Selection and Experimental Schemes. The red sandstone is selected for the experimental study, which



(a)



(b)

FIGURE 3: Comparison between numerical simulation results and in situ measurement results of entry deformation: (a) roof-to-floor convergence; (b) side-to-side convergence.

mainly consists of feldspar and quartz. The sandstone specimen is medium-grained with grain sizes from 0.10 mm to 0.35 mm (Figure 8). Its average density is 2380 kg/m³. Each specimen is cubic with dimensions of 50 mm (in length) × 50 mm (in width) × 100 mm (in height). A grinder is used to flatten the surface of each specimen end.

A servo-controlled true triaxial material testing system [32] is used to conduct the true triaxial compression tests under different loading and unloading stress paths. The influence of three stress paths on the fracture characteristics

of the specimen is studied. Each triaxial test has two stages, including loading the specimen to the expected in situ stress condition (stage 1) and the loading and unloading stage (stage 2) (Figure 9). To get the final fracture pattern of the specimen, the confining pressure and the constant axial stress are increased. The detailed loading and unloading schemes are given as follows.

The three loading and unloading schemes have the same first loading stage (i.e., stage I). First, the specimen is loaded to a hydrostatic stress condition ($\sigma_1 = \sigma_2 = \sigma_3 = 20$ MPa) at

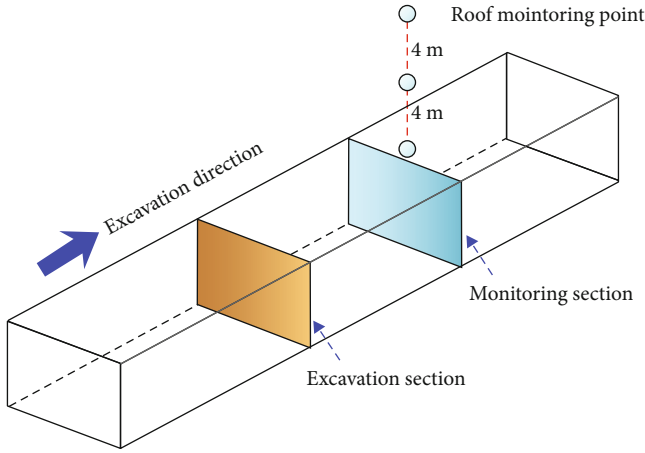


FIGURE 4: Locations of stress monitoring points.

a velocity of 0.1 MPa/s. Then, σ_3 remains constant and σ_1 and σ_2 are increased at the same velocity until σ_2 reaches the expected magnitude ($\sigma_1 = \sigma_2 = 40$ MPa). After that, σ_2 and σ_3 are kept constant and σ_1 is increased to the pre-designed magnitude. Note that the specimen has the average peak strength of about 615 MPa when σ_2 and σ_3 are 40 MPa and 20 MPa, respectively, based on the true triaxial test results. Hence, the σ_1 , σ_2 , and σ_3 magnitudes in the designed in situ stress condition of the specimen are 490 MPa (80% of the peak strength), 40 MPa, and 20 MPa, respectively.

In the second stage (stage II), for path I, the σ_1 magnitude remains constant and σ_2 and σ_3 are decreased at a velocity of 0.1 MPa/s until the specimen fails. In path II, both σ_1 and σ_3 are kept constant and σ_2 is decreased at a velocity of 0.1 MPa/s until the specimen fails. As shown in Figure 9, σ_2 will equal to σ_3 in the unloading process of σ_2 (point *e* in Figure 9). After that, σ_2 and σ_3 exchange with each other. In path III, both σ_1 and σ_2 remain unchanged and σ_3 is decreased at a velocity of 0.1 MPa/s until the specimen fails.

3.3. Characteristics of Strength and Deformation. Figure 10 shows the change of the three principal stresses with the loading time of the specimen under the second stress path (path II). The unloading stage (the *df* stage in Figure 9) is analyzed in this section, which includes the prefailure stage and the postfailure stage. The three principal stress components of the specimen change linearly with the unloading time in the prefailure stage. This suggests that all the three principal stresses vary according to the pre-designed stress path. The σ_1 magnitude drops abruptly when the rock fails. Obvious brittle failure of the specimen is observed. In Figure 10, with the gradual decrease of σ_2 , its magnitude equals to that of σ_3 (point *e* in Figure 9). After that, σ_2 exchanges with σ_3 , which means that the intermediate principal stress becomes the minimum principal stress. The existence of the intersection point *e* in Figure 9 could lead to the variation of the fracture characteristic of the specimen.

Since all the three principal stresses vary during the loading and unloading of the specimen, the octahedral shear

stress τ_{oct} in Equation (3) is used to generalize the strength characteristic of the specimen [33]:

$$\tau_{\text{oct}} = \frac{1}{3} \sqrt{(\sigma_1 - \sigma_2)^2 + (\sigma_2 - \sigma_3)^2 + (\sigma_1 - \sigma_3)^2}. \quad (3)$$

As shown in Figure 11(a), the octahedral shear stresses of the specimens undergo three different unloading stress paths that almost coincide with each other in the prefailure stage and drop abruptly (i.e., brittle failure) in the postfailure stage. The time period between the start of the unloading process and the strength failure of the specimen is termed prefailure unloading duration. The specimens under three unloading paths undergo different prefailure unloading duration, in which the specimen in path I has the shortest prefailure unloading duration and the specimen in path II undergoes the longest. The strains of the specimen under different stress paths are plotted against the loading time in Figure 11(b). The three principal strains of the specimen increases almost linearly against the unloading time at the early stage of the unloading process. Then, the strain rate gradually increases as the unloading time increases. The three principal strains increase, following the power function, in the postfailure stage.

3.4. Acoustic Emission Characteristics. Figure 12(a) gives the typical characteristics of the basic AE parameters of the specimen under path III (the other tests have a similar feature). The AE events are quite active in the early stages of the unloading processes of the specimen under two different stress paths. This suggests that the internal microcracks initiate and propagate before the unloading process commences. The number of the AE events is below 100 before the strength failure of the specimen, which indicates that the microcracks inside the specimen propagate stably. The amount of the AE events increases dramatically in a short time when the peak strength of the specimen is reached, which indicates the start of the unstable propagation of the microcracks and the formation of the macroscopic failure planes.

Figure 12(b) gives the variation of the cumulative AE events against the unloading time under different stress paths [34], which is similar to that of the specimen deformation. The AE events increase stably at the early stage of the unloading process (before the strength failure of the specimen), which suggests the slow propagation of the internal microcracks. The increase in the AE events of the specimen under path II is the slowest compared with that under the other two stress paths. The characteristics of the specimen tend to become that under conventional triaxial compression as the σ_2 magnitude decreases. The intermediate principal stress applies obvious confining to the specimen, and the microcracks develop slowly. The number of the AE events in the specimen under path III rises more quickly since the differential stress between σ_2 and σ_3 increases during the unloading of σ_3 . This enhances the damage effect of the intermediate principal stress and leads to the faster propagation of the microcracks. The AE events in the specimen under the first stress path are highly active, and the microcracks propagate quite fast at the early stage of the unloading process. This indicates that the simultaneous unloading of σ_2 and σ_3

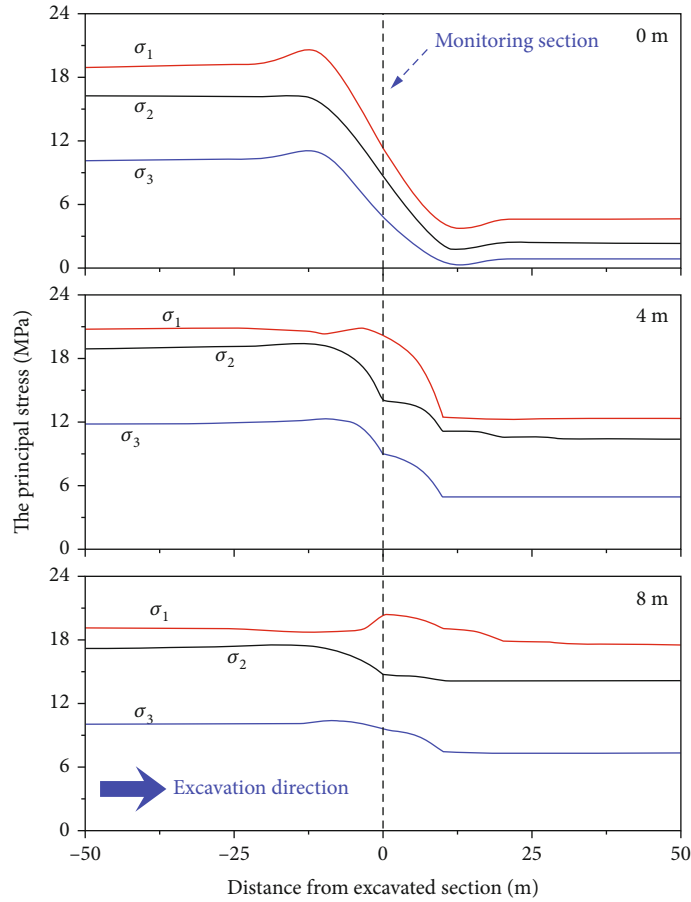


FIGURE 5: Variation of principal stresses.

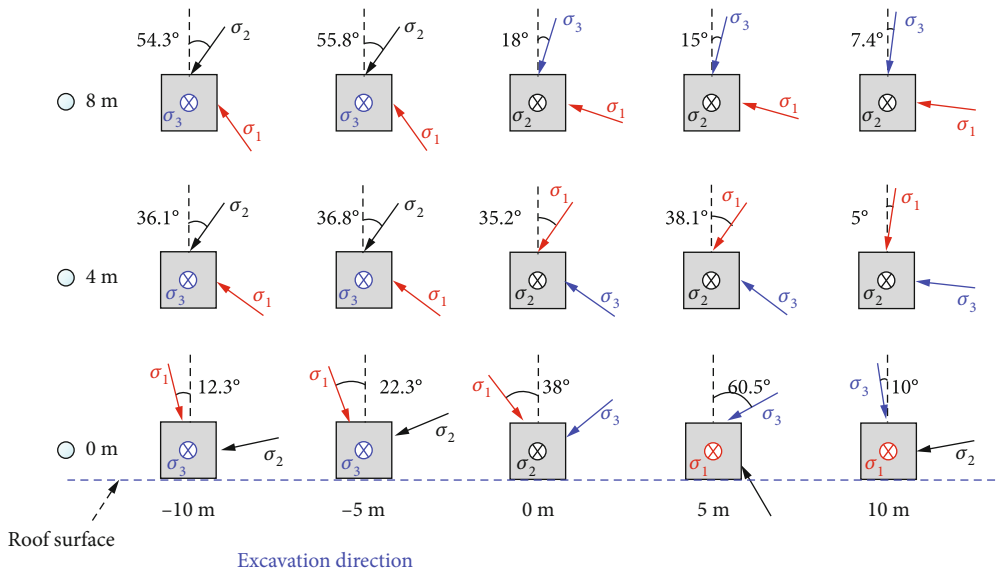


FIGURE 6: Variation of principal stress directions in the entry roof.

exaggerates the propagation of the microcracks and weakens the strength of the rock. When the axial stress reaches the peak strength, dramatic increase in the AE events is found in the specimens under all the three stress paths, which shows the brittle failure characteristic of the specimen.

3.5. *Fracture Characteristics.* Table 3 presents the macroscopic fracture characteristics of the specimens under different loading and unloading stress paths. The σ_2 direction and the σ_3 direction in Table 3 are the initial stress direction of the specimen. Along the σ_2 direction, the macroscopic failure

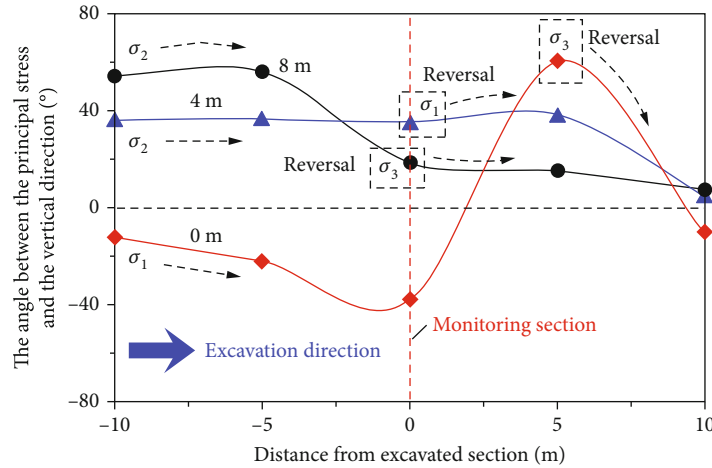
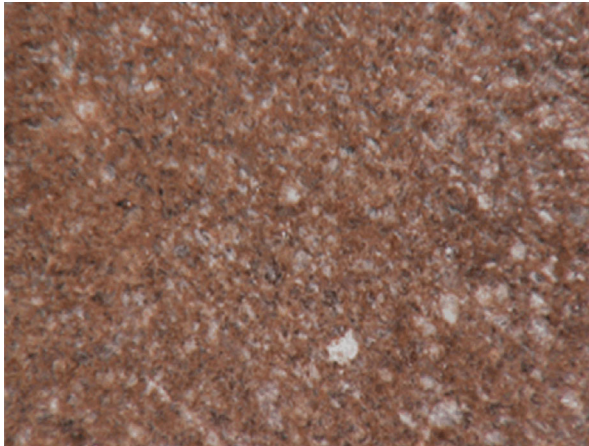


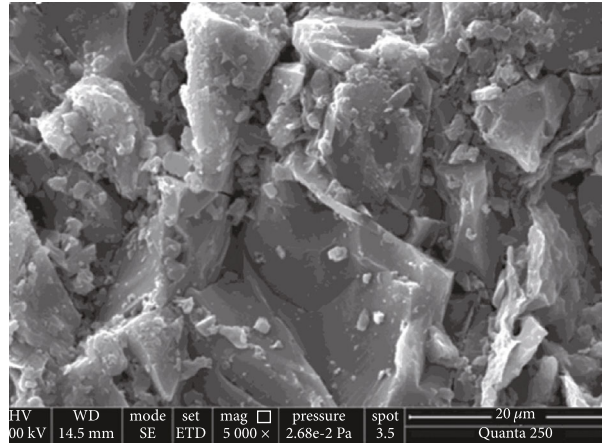
FIGURE 7: Variation of the angle between the principal stress and the vertical direction.

TABLE 2: Typical stress paths.

	Path I	Path II	Path III
Stress path			
Note	4 m away from the roof surface	8 m away from the roof surface	Contrast group



(a)



(b)

FIGURE 8: Optical microscopy and SEM features of red sandstone.

plane has a “V” shape that stretches through the specimen. An obvious brittle failure characteristic is found. Along the σ_3 direction, a quite dense “X”-shaped fracture network is observed in the specimen under path II, while no obvious macroscopic fracture is found in the specimens under the other two stress paths. This indicates that if the intermediate principal stress is always higher than the minimum principal stress in the specimen in the unloading process, the macro-

scopic failure plane only propagates along the σ_2 direction and the specimen looks intact along the σ_3 direction.

Once the stress condition in the specimen has a notable change, such as the reverse of σ_2 and σ_3 in Figures 6 and 7, the fracture characteristics of the specimen will be highly influenced. Hence, this section focuses on the second stress path (path II) in which the σ_2 and σ_3 directions exchange with each other. At the early stage of this stress path in which

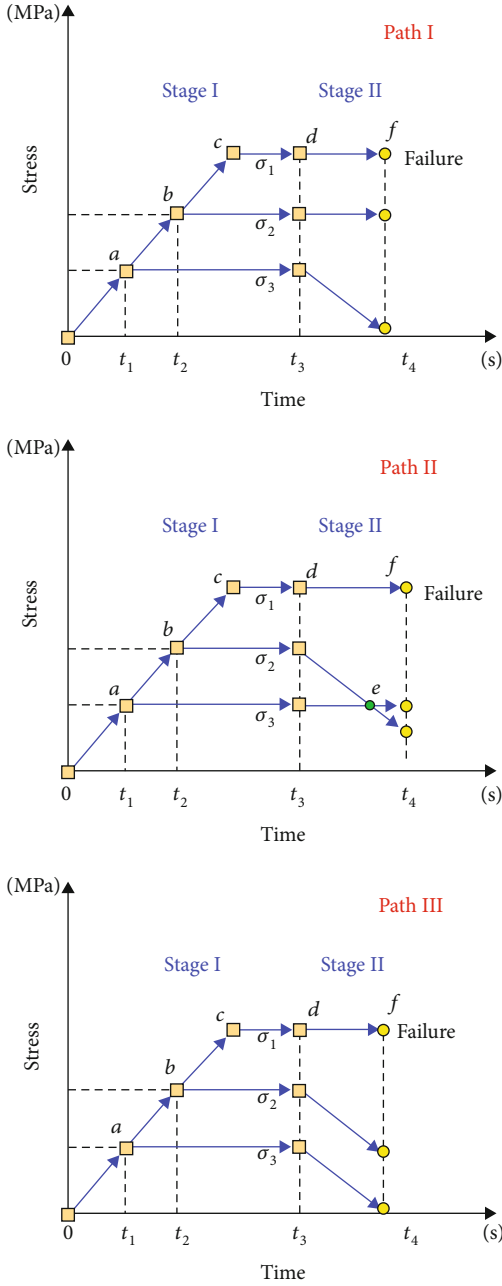


FIGURE 9: Typical loading and unloading scheme.

σ_2 is higher than σ_3 , the fracture type of the specimen is similar to that under the other two stress paths and the macroscopic fracture plane is along the σ_2 direction. As σ_2 gradually decreases and becomes lower than σ_3 , the σ_2 direction changes to the initial σ_3 direction and the complicated fracture network is found in the specimen in the initial σ_3 direction. From the above, the variation of the principal stress direction, especially the σ_2 direction, has a significant impact on the macroscopic failure characteristics of the specimen. The macroscopic failure plane highly depends on the σ_2 direction. This provides an important theoretical basis for the fracture evolution of the rock mass at the field site.

4. Engineering Application

The surrounding rock mass of the underground entry normally contains certain macroscopic and microscopic fractures. Entry excavation changes both the magnitudes and the direction of the principal stress and enhances the development of the fractures in the rock mass. This significantly affects the stability of the entry. The Griffith strength theory assumes that a material contains numbers of randomly distributed internal elliptical microcracks. As shown in Figure 13, a single microcrack is considered. It is deemed that the initiation of the microcracks inside of the rock is caused by the local tensile stress concentration induced at the microcrack tips. The normal stress and the tangential stress at the microcrack surface are calculated by [35]

$$\begin{cases} \sigma_x = \frac{1}{2} [(\sigma_1 + \sigma_3) + (\sigma_1 - \sigma_3) \cos 2\beta], \\ \tau_{xy} = \frac{1}{2} (\sigma_1 - \sigma_3) \sin 2\beta, \end{cases} \quad (4)$$

where β is the tip angle of the microcrack. The tip angle at which the microcrack is most likely to initiate can be derived by

$$\beta = \frac{1}{2} \arccos \frac{\sigma_1 - \sigma_3}{2(\sigma_1 + \sigma_3)}. \quad (5)$$

Based on the true triaxial compression tests in this study, the microcrack plane propagates along the σ_2 direction if σ_2 is higher than σ_3 . This suggests that the rock mainly fractures at the σ_1 - σ_3 surface at the dip angle calculated by Equation (5) during entry excavation. The fracture evolution characteristics of the rock at the roof surface are obtained in Figure 14 based on the Griffith strength theory. Both the magnitude and the direction of the principal stress in the roof rock mass vary due to the advance of the working face. This leads to the change of the dip angle at which the fracture is most likely to initiate. This dip angle gradually rotates towards the horizontal direction, and finally, a horizontal macroscopic fracture forms. In this situation, the roof strata tend to dislocate horizontally and roof collapse is likely to happen. This is similar to that occurring in the roof mass at the field site. The disturbance of entry excavation leads to the gradual interaction of the fractures at the roof surface. These fractures connect with each other to generate macroscopic fracture planes, and complicated fracture networks form due to the change of the dip angle at which the fracture is most likely to initiate. This is the basic reason for the roof failure of underground entries [36].

Based on the above analysis, the change of the stress condition in the roof rock mass during entry excavation is essentially the variation of the magnitudes and the directions of the principal stresses in the roof rock mass. The mechanical parameters of the roof rock mass are affected and degraded due to the complex evolution of the stress path and the stress direction caused by the disturbance of entry excavation. The dynamic damage evolution process is the basic reason for the

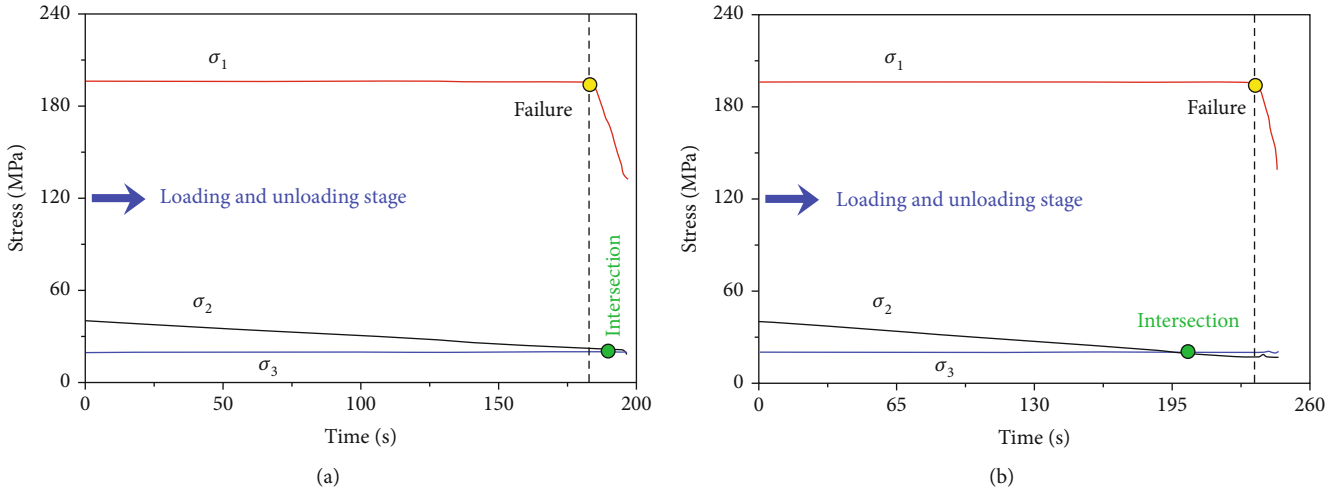


FIGURE 10: Stress-time curves of two groups of rocks in phase II (df) under path II.

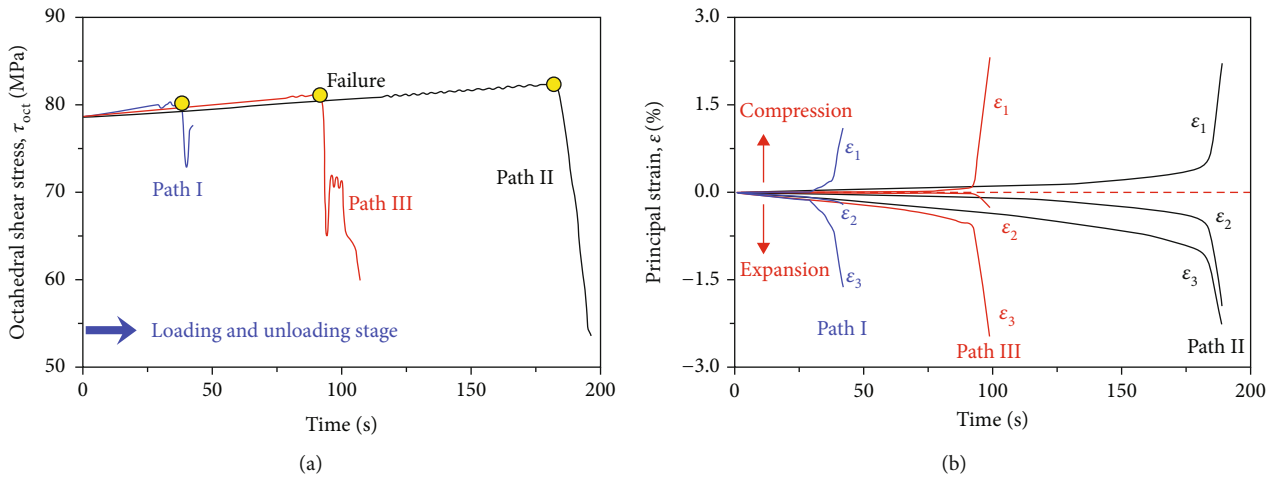


FIGURE 11: Stress-time curves of two groups of rocks during the unloading stage under path II.

deformation and fracture of the surrounding rock mass of the entry. The numerical modelling software ABAQUS is used to establish the two-dimensional numerical model of the mining entry at the 1306 working face. This is to analyze the plastic zone development around the entry induced by the variation of the magnitude and direction of the principal stress in the surrounding rock mass. The stress softening Mohr-Coulomb model is adopted in the numerical simulation. The entry dimensions and the mechanical parameters of the surrounding rock mass are consistent with those in the numerical model in Figure 2. The vertical in situ stress and the horizontal in situ stress are 15 MPa and 10 MPa, respectively.

After the excavation of the 1305 head entry, relatively large plastic zones form at the sides of the entry (Figure 15(a)). With the advance of the working face, the roof rock mass collapses. After that, the 1306 tail entry is excavated (Figure 15(b)). Both the protective pillar and the entry side close to the pillar are seriously damaged. Note that the magnitudes and the directions of the in situ stresses applied to the model boundaries are constant in the numerical simulation. In Figures 15(c) and 15(d), the magnitudes of the in situ stresses remain

unchanged while their directions are rotated by 10° and 20°, respectively. It is found that plastic zones occur at the corners of the entry and the plastic zones extend as the rotation angles increase.

Based on the results in Figures 14 and 15, horizontal failure planes form at the roof due to entry excavation. The roof strata tend to dislocate and collapse due to the rotation of the principal stress directions. The corners of the entry are highly influenced by the principal stress direction rotation, and the support in these areas should be strengthened. According to the dynamic variation of the magnitudes and directions of the principal stresses in the roof rock mass during entry excavation, the fracture characteristics of the surrounding rock mass at the entry roof, and the field condition at the entry excavation working face, the support scheme for the roof and the corners of the entry is given in Figures 16 and 17. The field experience shows that this support scheme achieves good results (Figure 18).

A shallow reinforcement area is generated at the entry roof by metal mesh, steel belts, and rock bolts. Large-diameter cable bolts are installed into the hard rock strata to form the deep reinforcement area. The coupled shallow

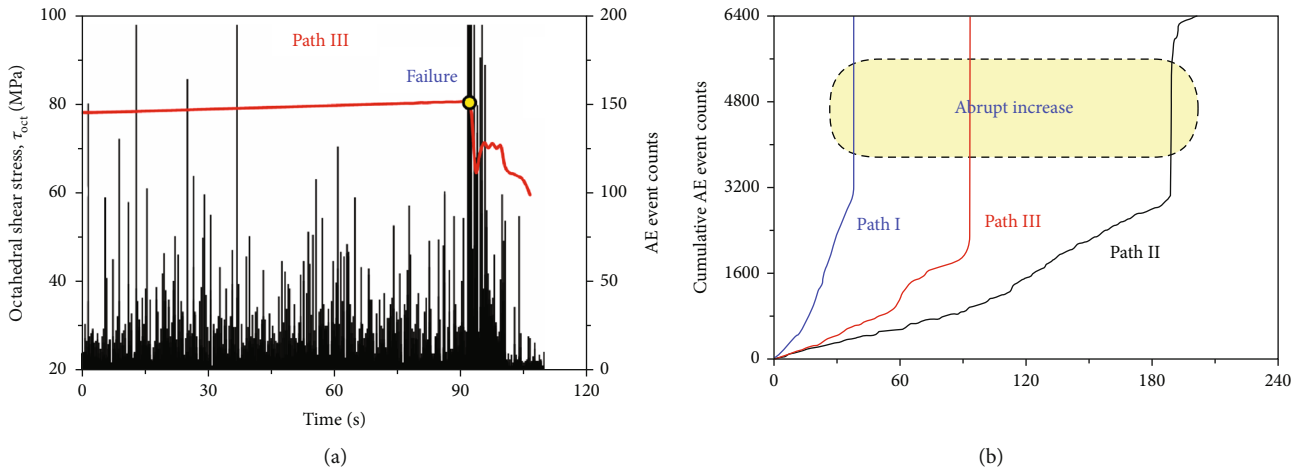


FIGURE 12: Variation of acoustic emission parameters of rocks under typical stress paths.

TABLE 3: Fracture characteristics of rocks under different true triaxial loading and unloading conditions.

	Path I	Path II	Path III
Along the direction of σ_2 (initial direction)			
Along the direction of σ_3 (initial direction)	Invisible crack		Invisible crack

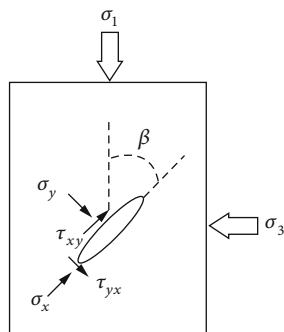


FIGURE 13: Schematic of a single microcrack.

and deep reinforcement prevents the horizontal dislocation and collapse of the roof strata. Rhomboid metal mesh is used to support the roof. Steel belts are arranged at a spacing of 800 mm. In each row, 7 rock bolts with dimensions 22 mm (in diameter) \times 2400 mm (in length) are used with a spacing

of 750 mm. The row spacing of the rock bolts is 800 mm. The rock bolts at the ends of each row have the dip angle of 75°, while others are installed vertically. In each row, two cable bolts are installed. Each cable bolt has dimensions of 22 mm (in diameter) \times 8500 mm (in length) and is 750 mm to the entry center. The row spacing of the cable bolts is 1600 mm.

As for the entry side close to the protective pillar, 5 rock bolts are used in each row with dimensions of 20 mm (in diameter) \times 2000 mm (in length). The top rock bolt in each row is about 200 mm to the steel belt with a dip angle of 15° to 25°, while the bottom rock bolt is about 500 mm to the roof with a depression angle of 15° to 25°. The other rock bolts are installed horizontally into the pillar with a spacing of 800 mm. Two cable bolts with the diameter of 22 mm are installed in each row (between the rock bolt rows) with the row spacing of 1600 mm. In each row, the top cable bolt (5 m in length) is 500 mm to the roof with a dip angle of 25° to 35° and the bottom cable bolt (3.5 m in length) is installed horizontally at the middle of the entry side.

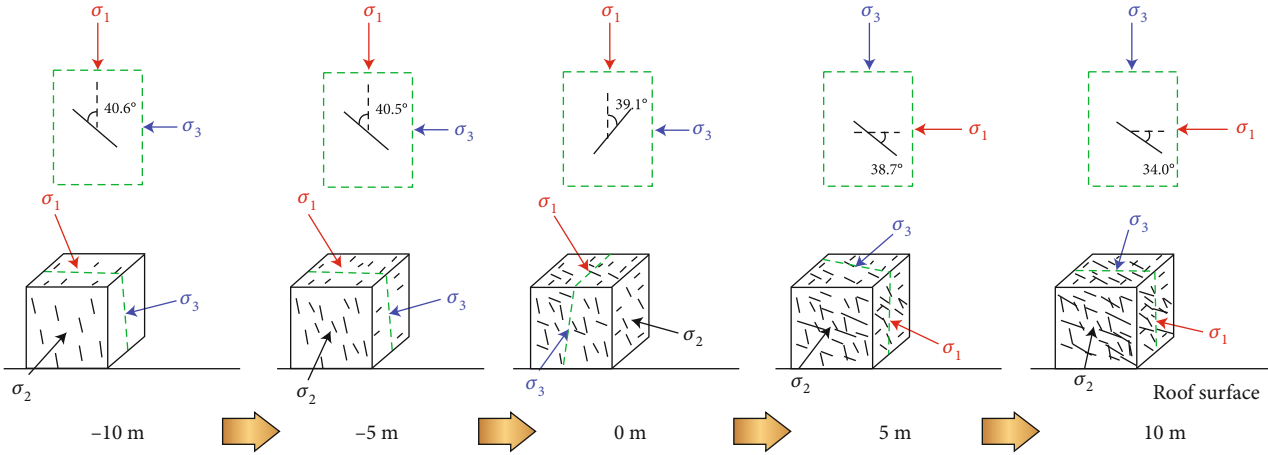


FIGURE 14: Variation of fracture development at the roof surface at different excavation distances.

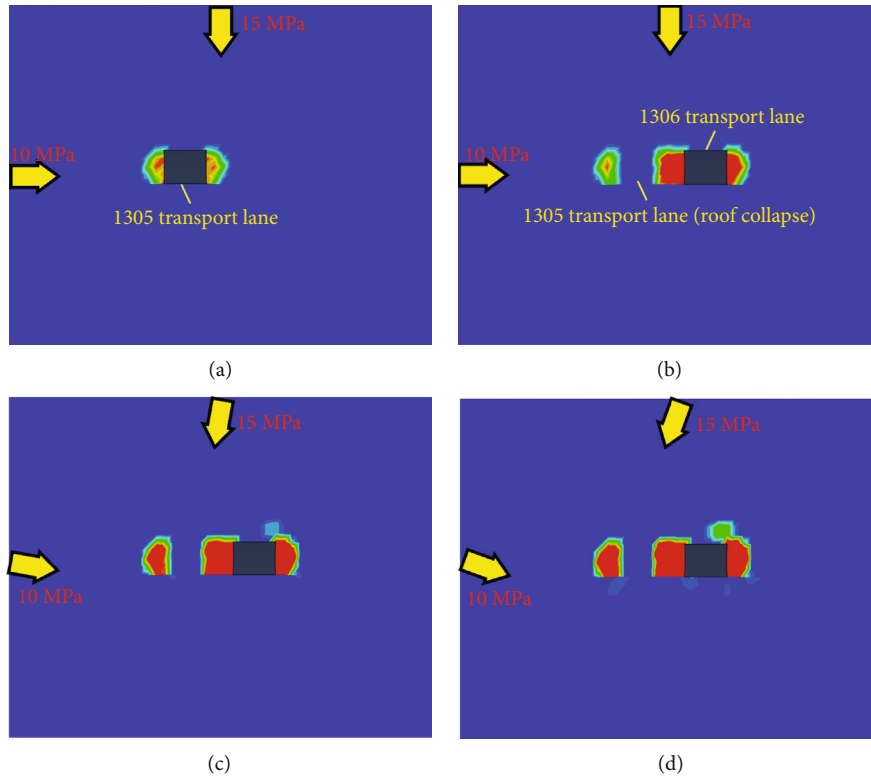


FIGURE 15: Variation of plastic zones in the surrounding rock mass of the entry: (a) damage of the 1305 head entry; (b–d) 1306 transport lane destruction, wherein the angle of the principal stress rotation is 0°, 10°, and 20°, respectively.

The rock bolting at the solid coal side is the same as that at the protective pillar side. In addition, two cable bolts are used in each row with the row spacing of 1600 mm. The cable bolt has dimensions of 22 mm (in diameter) × 8500 mm (in length). In each row, the top cable bolt is 500 mm below the top rock bolt at a dip angle of 15° to 25°. The bottom cable bolt is horizontally installed at the middle of the side.

5. Conclusions

The variation of the stress condition in the roof rock mass during entry excavation and its influence on entry stability

are systematically studied in this study. The impact of the change of the three-dimensional stress field on the fracture evolution of the roof rock mass is disclosed. The following conclusions are made.

- (1) The surrounding rock mass at the entry roof is mainly influenced by the combined effect of the stress unloading and stress transference induced by entry excavation. The magnitude and the direction of the principal stress change notably, and this variation becomes different if the rock mass is away from the roof surface. The rotation of the principal stress

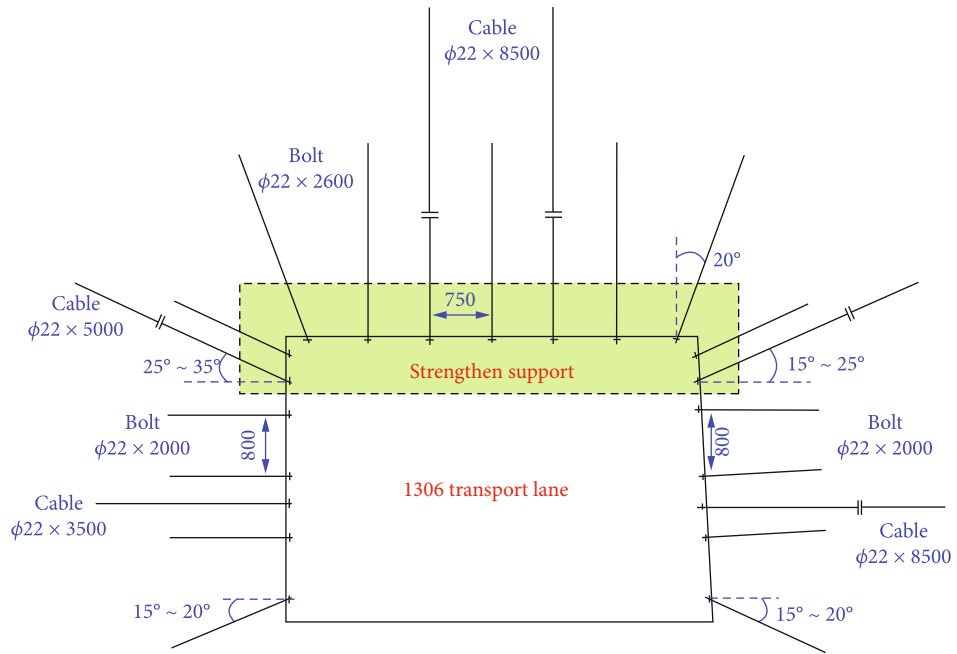


FIGURE 16: Supporting scheme of the gob-side entry.

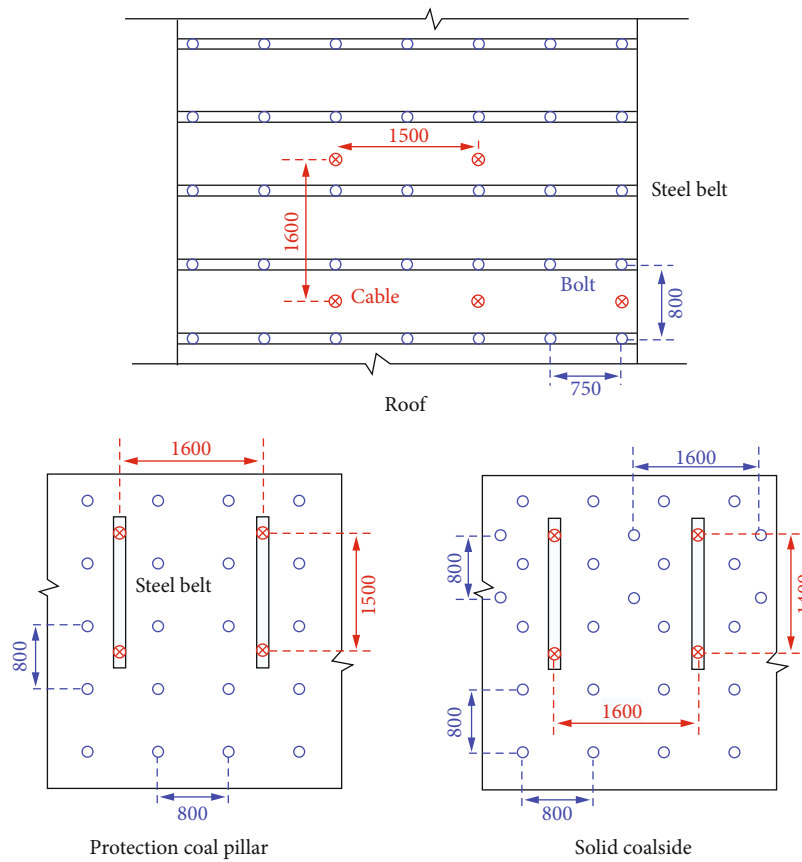


FIGURE 17: Arrangement of rock bolts and cable bolts in the gob-side entry.

directions at the three monitoring elements around the roof surface is observed. A servo-controlled true triaxial material testing system is used to conduct

true triaxial loading and unloading tests under different stress paths. And based on AE monitoring, the AE events are active during the unloading of the



FIGURE 18: Good result of the support scheme.

specimen and obvious brittle failure of the specimen is observed

- (2) The specimens under different stress paths have macroscopic “V”-shaped fracture planes (which stretch through the specimens) along the σ_2 direction, and the brittle failure characteristic of the specimen is obvious. However, when σ_2 and σ_3 exchange with each other (i.e., path II), a quite dense “X”-shaped fracture network is found in the specimen along the σ_3 direction. This indicates that the change of the principal stress direction has a significant impact on the macroscopic fracture characteristics of the specimen. The macroscopic fracture plane highly depends on the intermediate principal stress. This provides an important basis for the investigation on the fracture evolution of the rock mass at the field site
- (3) Based on the stress path experiments and the Griffith strength theory, the fracture evolution of the surrounding rock mass at the entry roof during entry excavation is studied. It is found that the variation of the principal stress direction in the surrounding rock mass of the entry has an extremely negative impact on the stability of the rock mass. The disturbance of entry excavation leads to the interaction of the fractures in the roof rock mass and the formation of the macroscopic fracture planes. Due to the change of the fracture propagation directions, relatively complex fracture networks are generated in the surrounding rock mass of the entry. In this situation, the roof strata are likely to dislocate horizontally and collapse and the corners of the entry are seriously damaged. This is the fundamental reason for the failure of the surrounding rock mass of the entry. Based on the findings, a support scheme is proposed. The field experience shows that the support scheme can achieve good results

Data Availability

The data used to support the findings of this study are available from the corresponding author upon request.

Conflicts of Interest

No conflict of interest exists in the submission of this manuscript.

Authors' Contributions

The manuscript is approved by all the authors for publication.

Acknowledgments

We gratefully acknowledge the support provided by the School Basic Scientific Research Operating Expenses Project (2017XKQY097).

References

- [1] H. Jia, K. Pan, S. Liu, B. Peng, and K. Fan, “Evaluation of the mechanical instability of mining roadway overburden: research and applications,” *Energies*, vol. 12, no. 22, p. 4265, 2019.
- [2] B. Shen, A. King, and H. Guo, “Displacement, stress and seismicity in roadway roofs during mining-induced failure,” *International Journal of Rock Mechanics and Mining Sciences*, vol. 45, no. 5, pp. 672–688, 2008.
- [3] H. Yan, F. He, T. Yang, L. Li, S. Zhang, and J. Zhang, “The mechanism of bedding separation in roof strata overlying a roadway within a thick coal seam: a case study from the Pingshuo Coalfield, China,” *Engineering Failure Analysis*, vol. 62, pp. 75–92, 2016.
- [4] Y. Yuan, W. Wang, S. Li, and Y. Zhu, “Failure mechanism for surrounding rock of deep circular roadway in coal mine based on mining-induced plastic zone,” *Advances in Civil Engineering*, vol. 2018, Article ID 1835381, 14 pages, 2018.
- [5] Z. Zhu, C. Zhu, and H. Yuan, “Distribution and evolution characteristics of macroscopic stress field in gob-side entry retaining by roof cutting,” *Geotechnical and Geological Engineering*, vol. 37, pp. 2963–2976, 2019.
- [6] F. Wang, C. Duan, S. Tu, N. Liang, and Q. Bai, “Hydraulic support crushed mechanism for the shallow seam mining face under the roadway pillars of room mining goaf,” *International Journal of Mining Science and Technology*, vol. 27, no. 5, pp. 853–860, 2017.
- [7] P. K. Kaiser, S. Yazici, and S. Maloney, “Mining-induced stress change and consequences of stress path on excavation stability – a case study,” *International Journal of Rock Mechanics and Mining Sciences*, vol. 38, no. 2, pp. 167–180, 2001.
- [8] B. Wang, F. Dang, W. Chao, Y. Miao, J. Li, and F. Chen, “Surrounding rock deformation and stress evolution in pre-driven longwall recovery rooms at the end of mining stage,” *International Journal of Coal Science & Technology*, vol. 6, no. 4, pp. 536–546, 2019.
- [9] X. Xia, H. B. Li, J. C. Li, B. Liu, and C. Yu, “A case study on rock damage prediction and control method for underground tunnels subjected to adjacent excavation blasting,” *Tunnelling and Underground Space Technology*, vol. 35, pp. 1–7, 2013.
- [10] M. S. Diederichs, P. K. Kaiser, and E. Eberhardt, “Damage initiation and propagation in hard rock during tunnelling and the influence of near-face stress rotation,” *International Journal of Rock Mechanics and Mining Sciences*, vol. 41, no. 5, pp. 785–812, 2004.

- [11] H. Xie, F. Gao, and Y. Ju, "Research and development of rock mechanics in deep ground engineering," *Chinese Journal of Rock Mechanics and Engineering*, vol. 34, pp. 2161–2178, 2015.
- [12] E. Eberhardt, "Numerical modelling of three-dimension stress rotation ahead of an advancing tunnel face," *International Journal of Rock Mechanics and Mining Sciences*, vol. 38, no. 4, pp. 499–518, 2001.
- [13] N. Liu, C. Zhang, X. Chen, J. Hou, and W. Chu, "Monitoring and characteristics study of stress evolution of surrounding rock during deep tunnel excavation," *Chinese Journal of Rock Mechanics and Engineering*, vol. 30, pp. 1729–1737, 2011.
- [14] S.-Q. Yang, P. Ranjith, and Y.-L. Gui, "Experimental study of mechanical behavior and X-ray micro CT observations of sandstone under conventional triaxial compression," *Geotechnical Testing Journal*, vol. 38, pp. 179–197, 2015.
- [15] S. Wang, X. Li, K. Du, S. Wang, and M. Tao, "Experimental study of the triaxial strength properties of hollow cylindrical granite specimens under coupled external and internal confining stresses," *Rock Mechanics and Rock Engineering*, vol. 51, no. 7, pp. 2015–2031, 2018.
- [16] I. Janeček and D. A. Mishra, "Deformational response of rocks to uniaxial, biaxial, and triaxial loading or unloading regimes," *Procedia Engineering*, vol. 191, pp. 332–341, 2017.
- [17] X. Li, F. Feng, D. Li, K. Du, P. G. Ranjith, and J. Rostami, "Failure characteristics of granite influenced by sample height-to-width ratios and intermediate principal stress under true-triaxial unloading conditions," *Rock Mechanics and Rock Engineering*, vol. 51, no. 5, pp. 1321–1345, 2018.
- [18] M. Cai, "Influence of intermediate principal stress on rock fracturing and strength near excavation boundaries—insight from numerical modeling," *International Journal of Rock Mechanics and Mining Sciences*, vol. 45, no. 5, pp. 763–772, 2008.
- [19] Y. Cai, D. Liu, J. P. Mathews, and Z. Pan, "Permeability evolution in fractured coal – combining triaxial confinement with X-ray computed tomography, acoustic emission and ultrasonic techniques," *International Journal of Coal Geology*, vol. 122, pp. 91–104, 2014.
- [20] B.-Y. Jiang, S.-T. Gu, L.-G. Wang, G.-C. Zhang, and W.-S. Li, "Strainburst process of marble in tunnel-excavation-induced stress path considering intermediate principal stress," *Journal of Central South University*, vol. 26, no. 4, pp. 984–999, 2019.
- [21] J. Ptacek, P. Konicek, L. Stas, P. Waclawik, and R. Kukutsch, "Rotation of principal axes and changes of stress due to mine-induced stresses," *Canadian Geotechnical Journal*, vol. 52, no. 10, pp. 1440–1447, 2015.
- [22] X. Li, S. Wang, and S. Wang, "Experimental investigation of the influence of confining stress on hard rock fragmentation using a conical pick," *Rock Mechanics and Rock Engineering*, vol. 51, no. 1, pp. 255–277, 2018.
- [23] Q. Ye, G. Wang, Z. Jia, C. Zheng, and W. Wang, "Similarity simulation of mining-crack-evolution characteristics of overburden strata in deep coal mining with large dip," *Journal of Petroleum Science and Engineering*, vol. 165, pp. 477–487, 2018.
- [24] Y. Li, C. Wu, and B.-A. Jang, "Effect of bedding plane on the permeability evolution of typical sedimentary rocks under triaxial compression," *Rock Mechanics and Rock Engineering*, vol. 53, no. 11, pp. 5283–5291, 2020.
- [25] W. Xu, E. Wang, R. Shen, D. Song, and J. Zhang, "Distribution pattern of front abutment pressure of fully-mechanized working face of soft coal isolated island," *International Journal of Mining Science and Technology*, vol. 22, no. 2, pp. 279–284, 2012.
- [26] C. Zhang, H. Zhou, X. Feng, L. Xing, and S. Qiu, "Layered fractures induced by principal stress axes rotation in hard rock during tunnelling," *Materials Research Innovations*, vol. 15, pp. s527–s530, 2013.
- [27] S. R. Zhang and L. H. Liang, "Analysis on tunnel liner supporting time considering three-dimensional stress rotation," *Journal of Hydraulic Engineering*, vol. 38, pp. 704–709, 2007.
- [28] R. S. Read, N. A. Chandler, and E. J. Dzik, "In situ strength criteria for tunnel design in highly-stressed rock masses," *International Journal of Rock Mechanics and Mining Sciences*, vol. 35, no. 3, pp. 261–278, 1998.
- [29] L. Weng, X. Li, and M. Tao, "Influence of geostress orientation on fracture response of deep underground cavity subjected to dynamic loading," *Shock and Vibration*, vol. 2015, Article ID 575879, 9 pages, 2015.
- [30] R. K. S. Wong, "Sand sheared by stresses with cyclic variations in direction," *Geotechnique*, vol. 36, no. 2, pp. 215–226, 1986.
- [31] H. Jia, G. Li, L. Wang, and A. Qiao, "Characteristics of stress-field environment and roof falling mechanism of mining influenced roadway," *Journal of Mining & Safety Engineering*, vol. 34, pp. 707–714, 2017.
- [32] Z. Li, L. Wang, Y. Lu, W. Li, and K. Wang, "Experimental investigation on the deformation, strength, and acoustic emission characteristics of sandstone under true triaxial compression," *Advances in Materials Science and Engineering*, vol. 2018, Article ID 5241386, 16 pages, 2018.
- [33] X. Ma, J. W. Rudnicki, and B. C. Haimson, "Failure characteristics of two porous sandstones subjected to true triaxial stresses: applied through a novel loading path," *Journal of Geophysical Research: Solid Earth*, vol. 122, no. 4, pp. 2525–2540, 2017.
- [34] Q. He, Y. Li, D. Li, and C. Zhang, "Microcrack fracturing of coal specimens under quasi-static combined compression-shear loading," *Journal of Rock Mechanics and Geotechnical Engineering*, vol. 12, no. 5, pp. 1014–1026, 2020.
- [35] Z. Li, L. Wang, Y. Lu, W. Li, K. Wang, and H. Fan, "Experimental investigation on true triaxial deformation and progressive damage behaviour of sandstone," *Scientific Reports*, vol. 9, p. 3386, 2019.
- [36] Y. Xue, T. Teng, F. Dang, Z. Ma, S. Wang, and H. Xue, "Productivity analysis of fractured wells in reservoir of hydrogen and carbon based on dual-porosity medium model," *International Journal of Hydrogen Energy*, vol. 45, no. 39, pp. 20240–20249, 2019.

Research Article

Effect of Strain-Dependent Hydraulic Conductivity of Coal Rock on Groundwater Inrush in Mining

Haifeng Lu ¹, Nan Shan,² You-Kuan Zhang,^{3,4,5} and Xiuyu Liang ^{3,4,5}

¹School of Earth and Environment, Anhui University of Science and Technology, Huainan, Anhui 232001, China

²Nanjing Institute of Environmental Sciences, Ministry of Ecology and Environment of the People's Republic of China, Nanjing, Jiangsu 210042, China

³School of Environmental Science and Engineering, Southern University of Science and Technology, Shenzhen, Guangdong 518055, China

⁴State Environmental Protection Key Laboratory of Integrated Surface Water-Groundwater Pollution Control, Southern University of Science and Technology, Guangdong 518055, China

⁵Shenzhen Municipal Engineering Lab of Environmental IoT Technology, Southern University of Science and Technology, Shenzhen 518055, China

Correspondence should be addressed to Xiuyu Liang; liangxy@sustech.edu.cn

Received 26 July 2020; Revised 3 December 2020; Accepted 8 December 2020; Published 23 December 2020

Academic Editor: Jingmin Xu

Copyright © 2020 Haifeng Lu et al. This is an open access article distributed under the Creative Commons Attribution License, which permits unrestricted use, distribution, and reproduction in any medium, provided the original work is properly cited.

Hydraulic conductivity is an important parameter for predicting groundwater inrush in coal mining worksites. Hydraulic conductivity varies with deformation and failure of rocks induced by mining. Understanding the evolution pattern of hydraulic conductivity during mining is important for accurately predicting groundwater inrush. In this study, variations of hydraulic conductivity of rock samples during rock deformation and failure were measured using the triaxial servo rock mechanic test in a laboratory. The exponential formula of hydraulic conductivity-volume strain was proposed based on the experimental data. The finite-difference numerical model FLAC^{3D} was modified by replacing constant hydraulic conductivity with the strain-dependent hydraulic conductivity. The coupled water flow and rock deformation and failure were simulated using the modified model. The results indicate that in the early time, the rocks undergo elastic compression with increasing rock strain, resulting in a decrease in hydraulic conductivity; then, the microcracks and fissures appear in the rock after it yields results in a sudden jump in hydraulic conductivity; in the later time, the hydraulic conductivity decreases gradually again owing to the microcracks and fissures that were compacted. The conductivity exponentially decreases with the volumetric strain during the periods of both elastic compression and postyielding. The simulated stress-strain curves using the modified model agree with the triaxial tests. The modified model was applied to the groundwater inrush of a coal mining worksite in China. The simulated water inflow agrees well with the observed data. The original model significantly underestimates the water inflow owing to it to neglect the variations of the hydraulic conductivity induced by mining.

1. Introduction

Coal is a reliable and affordable source of energy in many countries, such as China. It is responsible for approximately 40 percent of the electricity generated globally. The production of coal, however, is constrained by various disasters, such as water inrushes and coal and gas outbursts in working faces during mining [1]. The surrounding aquifers of coal seams are the source of water inrush in the working faces.

The groundwater in the surrounding aquifers will discharge into the working faces during mining. Accurate prediction of the water inflow is important in designing the coal mine drainage system, as well as enhancing coal production efficiency, and hence, was widely studied in previous researches. The methods to predict water inflow from working face include engineering analogy [2], empirical formulas [3, 4], hydrokinetic analysis [5, 6], analytical modeling [7–9], and numerical simulation [10–13]. The analogy and empirical

formula methods are simple and easy to operate. However, due to the different geological environments of the working face, the above two methods lack pertinence and accuracy. The analytical method simplifies the geological model such that the calculation results do not completely reflect the geological and hydrogeological environment in which the working face is located. The numerical simulation method is a suitable method for calculating the water inflow from the working face. It is based on the conceptual model of hydrogeology that reflects the hydrodynamic characteristics and specific boundary conditions of the water-bearing medium in the surrounding rock stope. It can make up for the defect in other methods that have difficulty describing the process of rock mass destruction and groundwater seepage caused by mining.

Hydraulic conductivity is an important parameter for predicting groundwater inrush in mining worksites. The hydraulic conductivity varies with deformation and failure of rocks induced by mining. Understanding the hydraulic conductivity evolution pattern during mining is very important to predict groundwater inrush accurately. However, the influence of mining disturbance on hydraulic conductivity is not considered in the existing numerical models for predicting water inrush. With the exploitation of coal seams, the damage of surrounding rock is gradually developed, and its permeability continues to increase. The hydraulic fracturing experiment points out that with the increase of water pressure, and the development of microfissures, the change in hydraulic conductivity becomes obvious [14, 15]. Souley et al. [16] suggested that the damage of rock will cause increases of hydraulic conductivity. Wang and Park [17] also found that the increase in hydraulic conductivity caused by rock rupture is a controlling factor for water inrush from the mine floor. Schatzel et al. [18] and Adhikary and Guo [19] have carried out an in situ pressure water test on the roof of the longwall working face and measured the hydraulic conductivity changes of strata in the mining overburden fissure zone. The measured hydraulic conductivity increases by three orders of magnitude during mining. The laboratory triaxial test also revealed that the hydraulic conductivity of rock is not a constant but changes with the evolution characteristics of rocks' internal structure during the stress-strain process. The relationship between hydraulic conductivity and stress, for rocks under pressure, shows that the rock pore was compacted and the hydraulic conductivity changes with increasing stress in the elastic stage [20–23]. At this stage, the stress-dependent hydraulic conductivity can be used. However, when the rock enters the plastic stage, the stress did not change significantly while the strain continued to increase. At this time, the stress-dependent hydraulic conductivity cannot be used to represent the changes of hydraulic conductivity. Derek and Mao [24] and Stormont and Daemen [25] suggested using the rock deformation as a valid factor to describe the changes of hydraulic conductivity.

As mentioned above, the existing studies investigated the variations of hydraulic conductivity induced by rock deformation based on the analysis of stress and strain. However, to the best knowledge of the authors, a numerical model having a capacity to consider the variations of hydraulic conduc-

tivity for predicting water inflow in coal working face has not been reported in the existing literatures. This study is aimed at filling this knowledge gap by proposing a formula of hydraulic conductivity-volume strain and modified the existing numerical model to combine this formula. In this study, the formula of hydraulic conductivity-volume strain was established according to the triaxial hydraulic conductivity test. The finite-difference numerical model FLAC^{3D} was modified by replacing constant hydraulic conductivity with the strain-dependent hydraulic conductivity. The modified model was applied to the groundwater inrush of a coal mining worksite in China. This paper is organized as follows. We first present the laboratory experiment and numerical modeling in Section 2, then describe the results and discussion in Sections 3, and apply the modified model to the groundwater inrush of a coal mining worksite in Section 4, followed by summary and conclusions in Section 5.

2. Methodology

2.1. Triaxial Hydraulic Conductivity Test. MTS815.03 electrohydraulic servo rock mechanic test system was used in the triaxial hydraulic conductivity test (Figure 1(a)). The loading system is displayed in Figure 1(b), and the basic principle of the test is presented in Figure 1(c). In Figure 1(c), σ_1 is the axial pressure, σ_3 is the confining pressure, p_1 is the upper water pressure of the rock sample, and p_2 is the lower water pressure of the rock sample. The permeable plates at the upper and lower ends of the rock sample are steel plates with many uniformly distributed holes. Before the experiment, the water pressure was uniformly applied to the bottom of the rock sample. The upper and lower parts were imposed on uppressing and underpressing pressure heads, respectively. The test is carried out according to the following steps. First, the sample was saturated with water in a vacuum immersion device during the test. Then, we used the polytetrafluoroethylene pyrocondensation plastics to seal the surrounding of the rock sample densely, which prevent the fluid leakage from the gap between the protective cover and the rock sample. Finally, the sample was placed in a servo triaxial cylinder for a pressure test.

Two experimental methods are usually used to measure hydraulic conductivity during triaxial compression: the transient flow method (for low hydraulic conductivity) and the steady-state flow method (for high hydraulic conductivity) [5, 6, 26, 27]. In this study, the transient method was adopted, because the initial hydraulic conductivity of the rock sample is very low. According to the ground stress level, the confining pressure was determined to be 5 MPa in the test. Initially, the same water pressure was applied at both top and bottom of the rock sample, i.e., $p_1 = p_2 = 4$ MPa. Then, the water pressure p_2 at the bottom of the rock sample is reduced to generate the water pressure difference between the top and bottom of the sample ($\Delta p = p_1 - p_2 = 1.5$ MPa). With each level of axial stress applied, the process of axial deformation and the change of water pressure with time were measured. The stress, strain, and hydraulic conductivity were measured every 20 s during the test. On the basis of the measured data, the hydraulic conductivity of rock is calculated by the

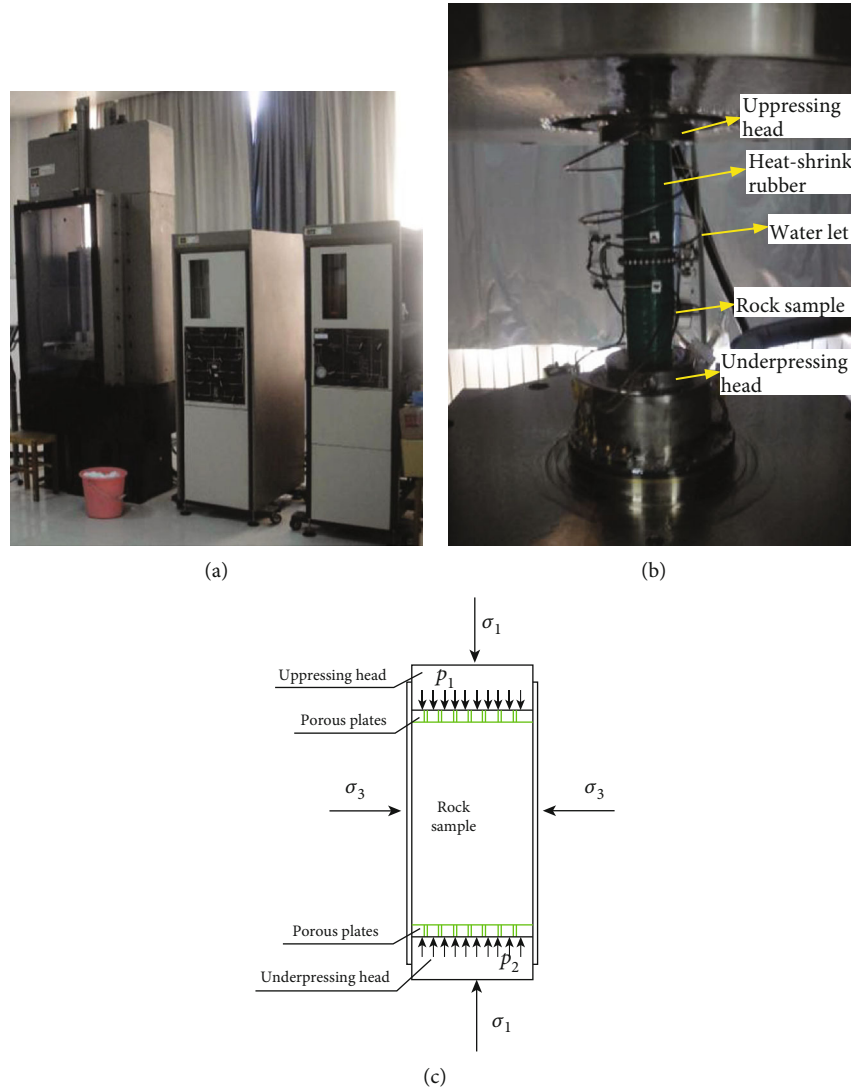


FIGURE 1: MTS rock mechanics testing system and assembled rock sample: (a) testing system, (b) rock sample assembly, and (c) diagram of the triaxial test.

following formula [28]:

$$K = 2.40129 \times 10^9 \times \frac{Llg\Delta p}{A\Delta t}, \quad (1)$$

where K is the hydraulic conductivity, L is the sample height, A is the cross-sectional area, Δp is the pore water pressure difference applied between both end planes of the rock sample, and Δt is the data measurement interval.

The rock samples were taken from a borehole at the Xifeng shaft of Pansan coal mine. The mine is located in Fengtai County, Huainan City, Anhui Province, China. The sampling position was No. 8 coal seam roof and floor. The lithology of the samples collected was siltstone, mudstone, and fine sandstone. Among them, fine sandstone and siltstone had compact and hard lithology, with occasional fissures while mudstone was dense with no fissures. Each rock

sample was divided into three groups. The parameters and the results of the triaxial tests are summarized in Table 1.

2.2. Numerical Modeling. The triaxial hydraulic conductivity test showed that the rock becomes strain softening after the stress reaches peak strength. With the rock gradually deforms, the fissure volume expansion accelerates, and the hydraulic conductivity increases rapidly. The strength of rock also decreases and approaches the residual strength gradually. In this study, we adopted the $FLAC^{3D}$ strain-softening module to describe these processes. Based on the relationship between the volume strain and the hydraulic conductivity (the details are presented in Section 3.2), the coupling fluid-solid modeling was carried out. The strain-softening behavior and hydraulic conductivity evolution process of the rock samples were simulated (the details are presented in Section 3.3).

TABLE 1: Parameters and results of the triaxial hydraulic conductivity test.

Lithology description	Sampling horizon (m)	Sample size (mm)		Confining pressure σ_3 (MPa)	Water pressure difference (MPa)	Average peak stress $\sigma_1 - \sigma_3$ (MPa)	Hydraulic conductivity ($\times 10^{-10}$ cm/s)	
		Height	Diameter				Initial	Peak
Siltstone	461.3-462.2	98.4	49.6	5	1.5	48.7	5.18	24.3
Mudstone	466.2-467.1	99.7	49.6	5	1.5	29.5	1.17	5.31
Fine sandstone	550.2-551.1	99.5	49.5	5	1.5	74.32	8.15	167.7

For the coupling fluid-solid modeling, the rock mass was regarded as a porous medium, and the fluid flow in the porous medium was described by Darcy's law and the Biot fluid-solid equation:

$$\begin{cases} G\nabla^2 u_j - (\lambda + G) \frac{\partial \varepsilon_v}{\partial x_j} - \frac{\partial p}{\partial x_j} + f_{x_j} = 0, \\ K\nabla^2 p = \frac{1}{S} \frac{\partial p}{\partial t} - \frac{\partial \varepsilon_v}{\partial t}, \end{cases} \quad (2)$$

where λ and G are the Lamé constants; p is the pore water pressure; ε_v is the volume strain; χ_i , μ_j , and f_{x_j} are the coordinate, displacement, and volume force in the j direction, respectively. $\partial p/\partial x_j$ reflects the influence of the seepage field on the solid skeleton of the porous medium. The pore pressure affects the effective stress of the solid skeleton, which in turn affects its deformation. Hence, $\partial \varepsilon_v/\partial t$ also reflects the effects of the volume deformation of the solid skeleton on the seepage field. The Biot equation can well reflect the interaction between the pore pressure dissipation and the deformation of the solid skeleton of the porous medium. However, for the Biot equation, the hydraulic conductivity did not change with the stress. Therefore, to investigate the variation of hydraulic conductivity of surrounding rock during mining, we use the exponential equation to describe the changes of the hydraulic conductivity with the volume strain, which is also identified by the triaxial test that will be discussed later. On the other hand, the porosity is also relative to the volume strain. Existing studies suggested that the porosity and the volume strain can be described by the following exponential formula [8, 29, 30]:

$$n = 1 - (1 - n_0)e^{\varepsilon_v}, \quad (3)$$

where n is the porosity and n_0 is the initial porosity. This formula will be adopted by the model of this study. For the FLAC^{3D} model, the strain softening of rock was defined by the degradation of internal friction angle (φ) and cohesion (c) with an increase in plastic strain (ε^{ps}). The plastic strain adopts the following form in FLAC^{3D} [31]:

$$\varepsilon^{ps} = \sqrt{\frac{[(\Delta \varepsilon_1^{ps} - \Delta \varepsilon_m^{ps})^2 + (\Delta \varepsilon_m^{ps})^2 + (\Delta \varepsilon_3^{ps} - \Delta \varepsilon_m^{ps})^2]}{2}}, \quad (4)$$

where $\Delta \varepsilon_m^{ps} = (\Delta \varepsilon_1^{ps} + \Delta \varepsilon_3^{ps})/3$; $\Delta \varepsilon_1^{ps}$ and $\Delta \varepsilon_3^{ps}$ are the plastic

shear strain increment in the first and third main directions, respectively. According to the results of the triaxial hydraulic conductivity test, the changes of internal friction angle and the cohesion degradation with an increase in plastic strain are shown in Figure 2. We adopt the table function of the strain-softening model to calculate and present the internal friction angle (φ) and cohesion (c) reduction.

The FLAC^{3D} model was modified by replacing both constant hydraulic conductivity and porosity with both strain-dependent hydraulic conductivity and porosity using the fish code of FLAC^{3D}. Both strain-dependent hydraulic conductivity and porosity were updated dynamically every 50 steps in the numerical simulation. The model used a rectangular parallelepiped with a length and width of 5 cm and a height of 10 cm. The normal compressive stress of 5 MPa was applied to the side to simulate the confining pressure. The rate of the upper and lower end faces of the rock sample was 4×10^{-8} m/step. The top and bottom of the model were fixed water pressure boundaries. The top water pressure was 1.5 MPa, and the bottom water pressure was 0 MPa. The water pressure difference was 1.5 MPa. The model region was divided into 2000 grids. The parameters of the model are summarized in Table 2.

3. Results and Discussion

3.1. Triaxial Test. Figure 3 shows the measured stress-strain and hydraulic conductivity curves for different lithologies. First, the stress-strain behavior of all three rock samples experienced the following stages: compaction-elastic, deformation-yield, failure-strain, and softening-residual strength. However, for postpeak, the mudstone has stronger plasticity while the sandstone has stronger brittleness, which is caused by the differences in their structural properties. Second, the prepeak variation of rock was mainly compressive deformation, in which the hydraulic conductivity was relatively low. And both pore and fissures are close to the maximum. After the stress reached a peak, the hydraulic conductivity shows a sudden jump. At this time, the fissure inside the rock sample would have expanded, and the rock would have lost the ultimate bearing capacity. In the strain-softening stage, the new fissures would begin to close under the confining pressure, and the hydraulic conductivity of the three rock samples then decreased to varying degrees. Finally, the peak of hydraulic conductivity occurs in the strain-softening stage after rock failure. It indicated that the failure of the rock was not synchronized with the happening of the maximum hydraulic

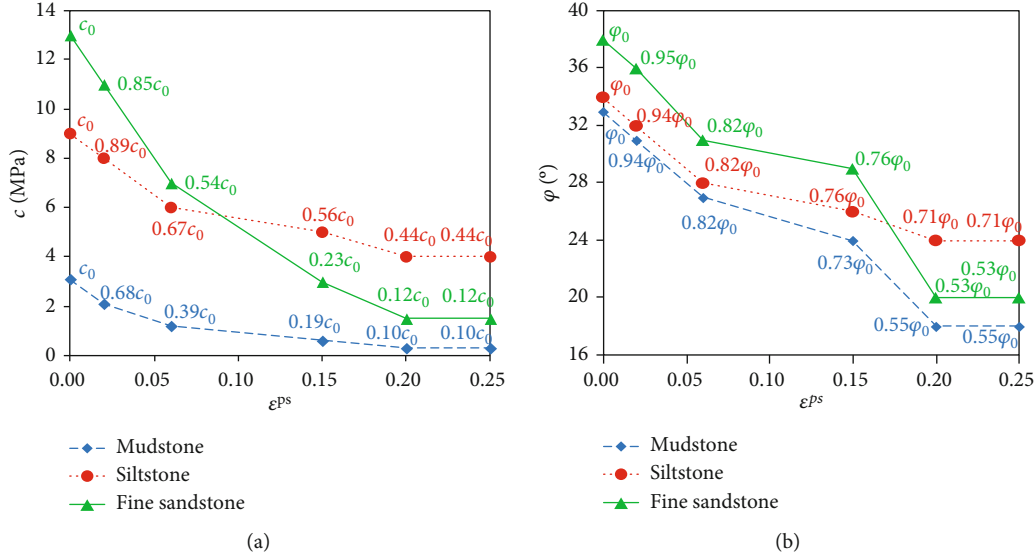


FIGURE 2: Changes of the shear strength parameters with the plastic strain (ϵ^{ps}) for different rocks: (a) cohesion (c) and (b) internal friction angle (ϕ).

TABLE 2: Parameters of the numerical model for the triaxial hydraulic conductivity test.

Lithology	Density (kg/m ³)	Hydraulic conductivity ($\times 10^{-10}$ cm/s)	Porosity	Elastic modulus (GPa)	Poisson's ratio	Cohesion (MPa)	Internal friction angle (°)	Tensile strength (MPa)	Dilatancy angle (°)
Fine sandstone	2600	8.15	0.2	5	0.2	13	38	6	28
Siltstone	2550	5.18	0.15	2.3	0.23	9	34	4	24
Mudstone	2500	1.17	0.12	1.45	0.3	3.1	33	3	22

conductivity. The lowest values of hydraulic conductivity occur in the elastic stage. The test results showed that the hydraulic conductivities of mudstone, siltstone, and fine sandstone increases by 4.54, 4.70, and 20.58 times, respectively. It indicated that the growth rate of hydraulic conductivity of the brittle rocks is significantly higher than that of the plastic rocks.

Figure 4 displays the final fissure pattern of the typical rock samples. Under the action of water pressure and axial compression, the rock mainly splits or produces a high-angle shear fracture. In addition, the rock was ruptured to form an inclined fissure plane that penetrates the entire rock sample when the rock fissure was not developed (Figure 4(a)). When the rock fissure developed, its failure mode was controlled by the structure plane, and the rock was mostly destroyed along the structure plane (Figure 4(b)).

3.2. Formula of Hydraulic Conductivity-Volume Strain. The triaxial test indicated that the larger the void space in the rock, the greater the hydraulic conductivity. Since the solid particles do not easily expand and contract. The expansion and contraction of the rock under triaxial conditions were mainly caused by the expansion and contraction of the void space. The changes in volume strain reflected the changes

of the void space, which can be used to describe the evolution of rock hydraulic conductivity. Figure 5 shows the relationship between volume strain and hydraulic conductivity for the triaxial hydraulic conductivity test. Before yielding, the volume of rock samples decreased, and the volume strain was negative (the compressive strain). At this stage, the hydraulic conductivity generally decreased slowly. After yielding, several microcracks were generated, and the volume expanded. The volume strain increased sharply, resulting in a sudden peak in hydraulic conductivity. With further deformations, the fissure plane was sheared or worn, and the degree of fissure opening reduced. Under the action of confining pressure, the fissure had a certain degree of compaction closure, and the hydraulic conductivity decreased with the increase in volume strain. The variations of hydraulic conductivity of different rock samples after yielding obtained in this test are consistent with other researches [20–23].

To summarize, the volume strain can well reflect the changes in hydraulic conductivity of the rock before and after the stress peak appearing. On the basis of the experimental data, we can obtain the relationship between the volume strain and the hydraulic conductivity, which can be divided into two stages. According to Louis (1974), the hydraulic conductivity as a function of volume strain before the peak

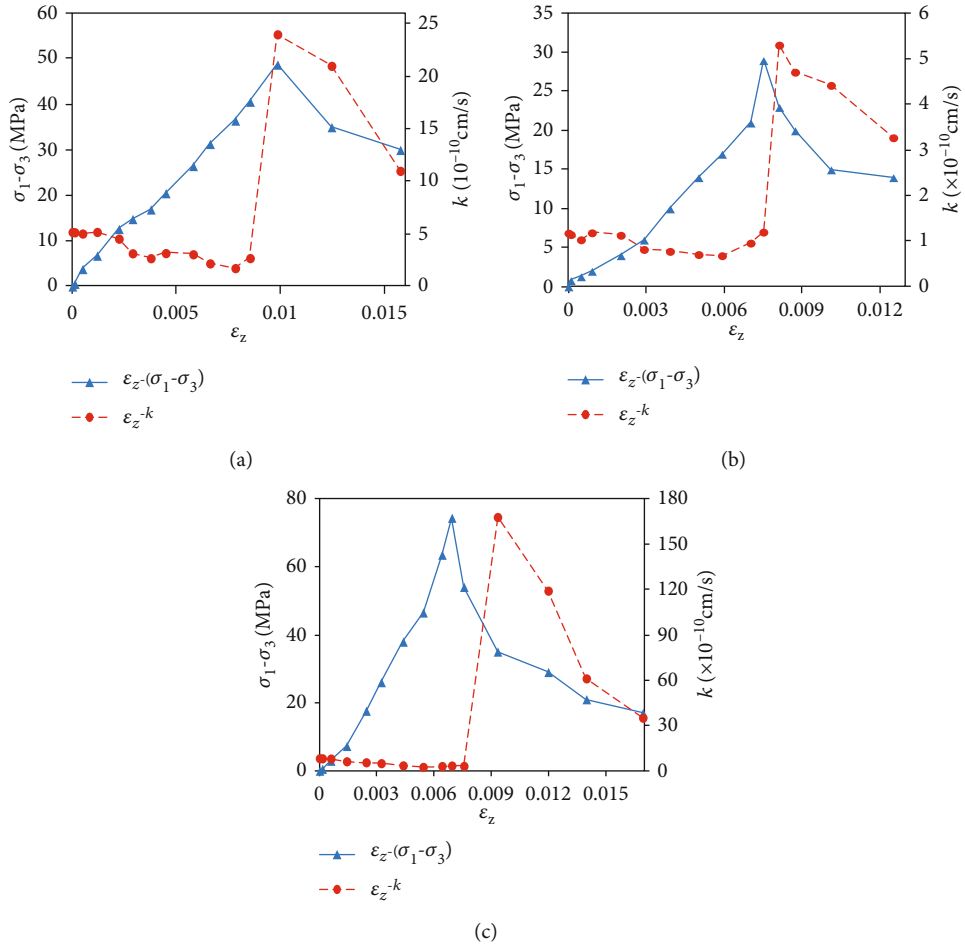


FIGURE 3: Deviatoric stress and hydraulic conductivity versus axial strain: (a) siltstone, (b) mudstone, and (c) fine sandstone.

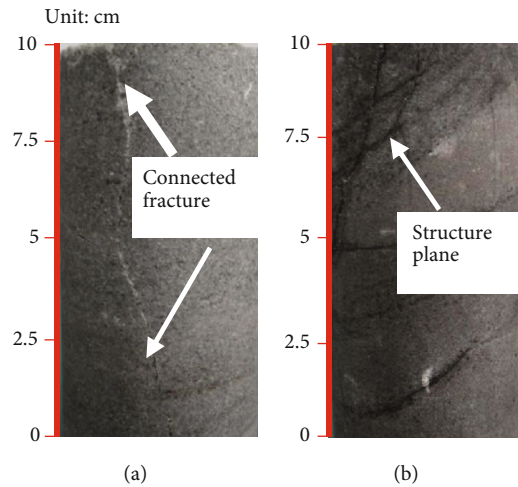


FIGURE 4: Observed cracks of rock samples in the triaxial test for (a) fine sandstone and (b) siltstone.

value appearing is given as

$$K = K_0 e^{\alpha_1 \varepsilon_v}, \quad (5)$$

where K_0 is the initial hydraulic conductivity; α_1 is a constant

to describe the increasing rate of the hydraulic conductivity before its peak value appearing that is determined by the triaxial test. In the postpeak, the rock was destroyed with shear dilatation. Generally, hydraulic conductivity suddenly jumped. We can obtain the relationship between the

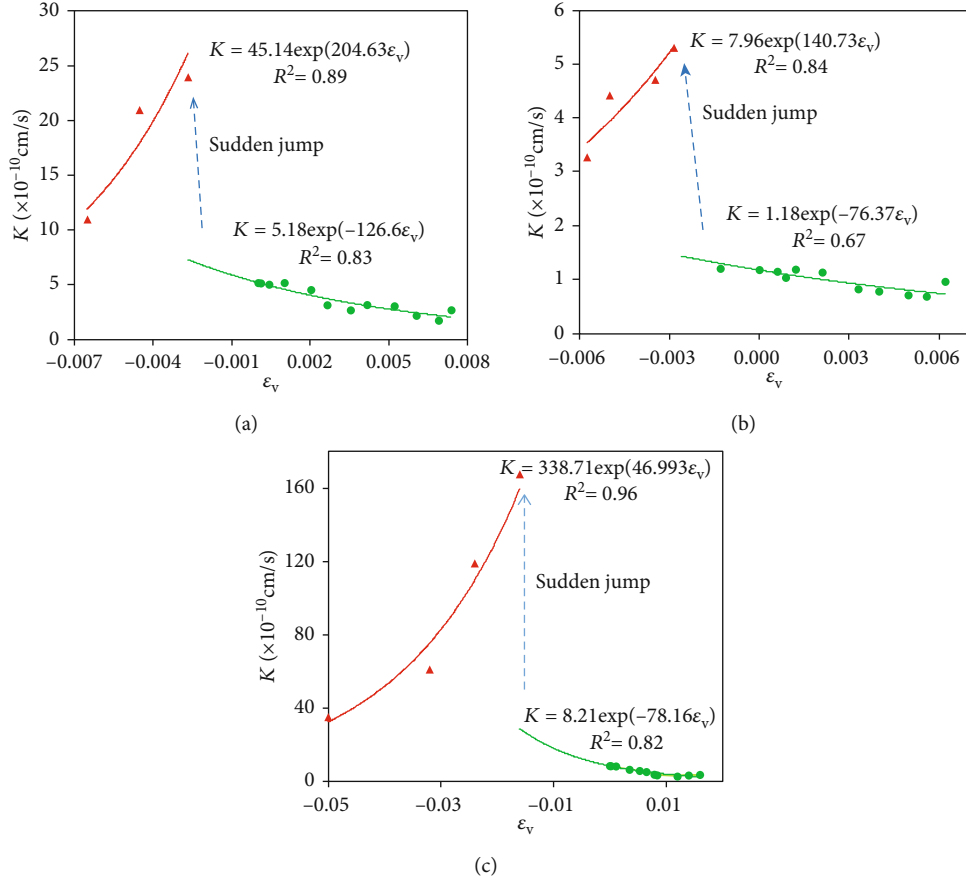


FIGURE 5: Relationship between volume strain and hydraulic conductivity: (a) siltstone, (b) mudstone, and (c) fine sandstone.

postpeak hydraulic conductivity and volume strain using the following formula:

$$K = \xi K_0 e^{\alpha_2 \epsilon_v}, \quad (6)$$

where α_2 is a constant to describe the decreasing rate of the hydraulic conductivity after its peak value appearing that is also determined by the triaxial test; ξ is the sudden jump coefficient of the hydraulic conductivity after yielding. The experimental data are fitted using equations (5) and (6) and are presented in Figure 5, showing that equations (5) and (6) agree well with the experimental data. It indicated that combining this formula into the FLAC^{3D} model is reliable to conduct the coupling fluid-solid modeling for describing the rock failure.

3.3. Numerical Simulation of Triaxial Hydraulic Conductivity Evolution of Rock Samples. Figure 6 displays the comparison of the stress-strain curves using numerical simulation and the triaxial test. It shows that the numerical simulations generally agree with the experimental data for three types of rocks. However, the errors in the prepeak stage were relatively large because the constitutive model used in the numerical model is assumed as a linear model that is not always true for the real case. Even so, the modified model can still reproduce the coupled fluid-solid processes and provide the appropriate

prediction for water inrush in working faces, which will be further discussed in the section of the application.

Figure 7 shows the evolution of the hydraulic conductivity of sandstone sample for different loading stages using the numerical model. In the linear elastic phase (point A), elastic compression closed pore and fissure in the rock sample, and the hydraulic conductivity of the rock sample was lowered. When the stress reaches the yield limit (point B), the internal crack of the rock sample expanded. The hydraulic conductivity increased, and the shear band appeared. As the strain continued to increase, at point C, the rock sample first had a significant shear band at the top. Owing to the dilatancy expansion, the hydraulic conductivity of the rock sample in the shear zone increased sharply. As the fissures continue to grow, X-shaped through fissure was formed at point D. The hydraulic conductivity of the fissure zone was higher than that of the rock, and the maximum increase was 35 times compared with the initial hydraulic conductivity. After yielding, the fissure tended to close gradually, and the range of high hydraulic conductivity decreased step by step because of the confining pressure and is consistent with the previous experimental results. In addition, as seen in Figure 8, the apparent shear zone appeared after yielding, and the water flow converged on the X-shaped crack forming a significant dominant flow channel.

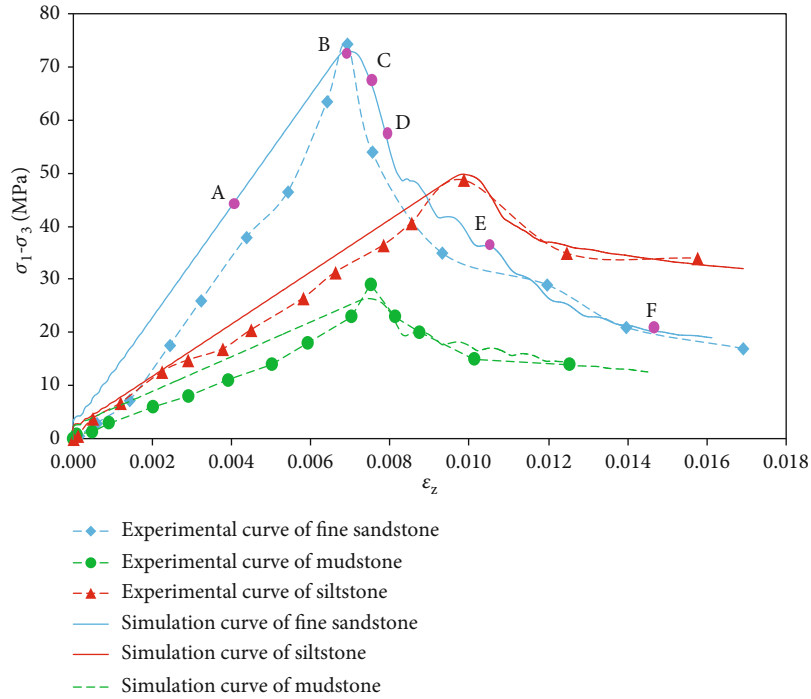


FIGURE 6: Comparison of the observed stress-strain curves with that of the numerical simulation.

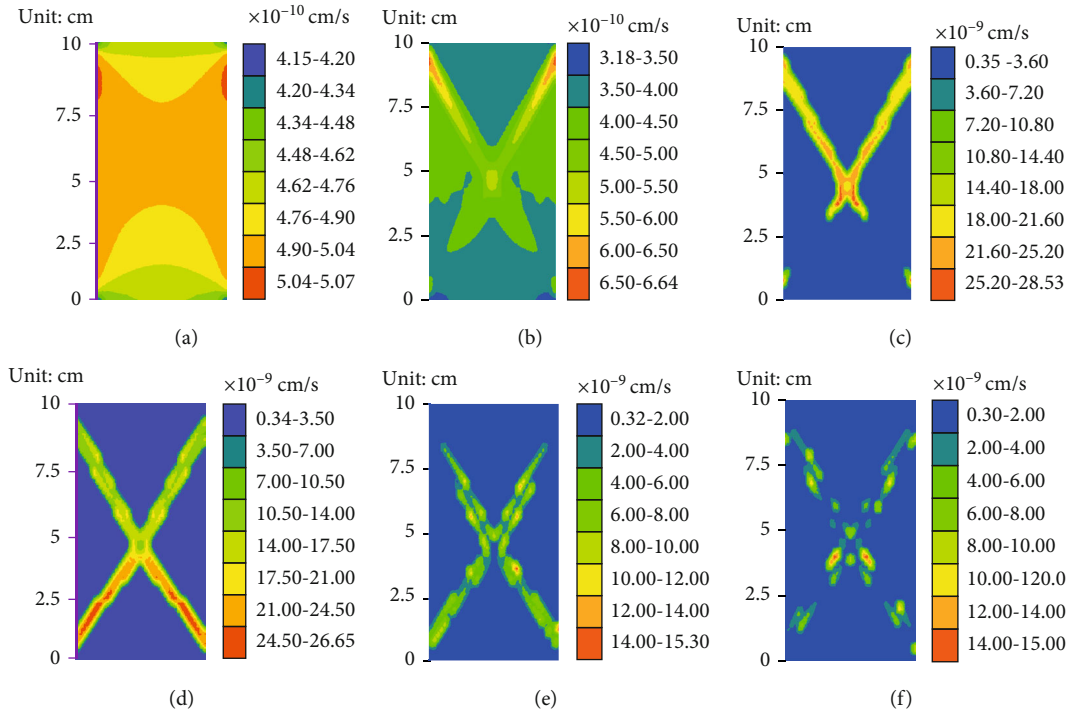


FIGURE 7: Contours of the hydraulic conductivity for the sandstone sample based on the numerical simulation for the different times: (a) point A, (b) point B, (c) point C, (d) point D, (e) point E, and (f) point F in Figure 6.

4. Application

To further demonstrate the capacity of the modified model, it was applied for predicting water inrush in a worksite of Pansan coal mine of Huainan, China.

4.1. Geological Conditions of the Working Face. The 12318 working face is the first working face of the No. 8 coal seam in Pansan coal mine, which is in the east of the Xiyi mining area. The maximum length of the face is 2000 m along the strike, and the length of the tendency is 200 m. The average

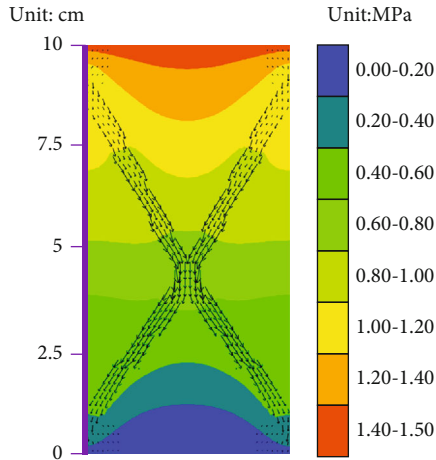


FIGURE 8: Contours of the pore water pressure and the directions of the seepage velocity after the fissure formation of the rock samples based on the numerical simulation.

dip angle and the thickness of the coal seam is 10° and 3.5 m, respectively. The average depth of the working face is 550 m. Most of the seam roof is fine sandstone with an average thickness of 16 m, which is characterized as medium thickness. The color of the roof is gray-white and belongs to the layered structure. Its composition is mainly quartz; the calcium cement is dense and hard with the fissures developed recently. The seam floor is mainly siltstone and fine sandstone.

According to the results of the water pumping test of the sandstone fracture aquifer in the mining area, the buried depth of the static water level is 200 m. The unit water inflow and the hydraulic conductivity are $q = 0.0133 \text{ L}/(\text{s} \cdot \text{m})$ and $K = 1.08 \times 10^{-5} \text{ cm}/\text{s}$, respectively. The sandstone fracture was unevenly developed, and the local water richness was quite different. It is a direct source of water inrush which affects the safe mining of coal seams. Recently, the mining in this face has been affected by roof sandstone water.

4.2. Numerical Model of Water Inflow in the Working Face.

The constitutive model used a strain-softening model with length, width, and height of 400 m, 400 m, and 210 m, respectively. The front, back, left, and right boundary conditions were fixed in the x - and y -direction, while the floor had a full constraint boundary. The upper boundary of the model plus the load of 8.69 MPa was equivalent to the self-weight of the overlying strata. For the prediction of water inflow, the normal compressive stress of 6.6 MPa (crustal stress) was imposed to the side to simulate the confining pressure. Both top and floor of the working face are nonflow boundaries, and the other sides are pressure head boundaries. After the mining, the goaf becomes a drainage boundary. The 3-D model has 55480 units and 60372 nodes (Figure 9). The cohesion of the rock mass in Table 2 was reduced by 1/4 based on previous studies [32] to account for the size effect. The layered thickness and the mechanical and hydraulic parameters of the numerical model are shown in Table 3. The relationship between the surrounding rock strength parameters c and ϕ and the plastic strain ε^{ps} was obtained with reference

to Figure 2. Excavation starts from the left side of the coal seam (x -direction) at 125 m from the left side, and the working face width (y -direction) was 200 m. The hydraulic conductivity of the rock mass and the relationship between the porosity and the volume strain were simulated using the fish language as per equations (3), (5), and (6). The results of the triaxial hydraulic conductivity test were obtained under compression. According to the experimental research, the tensile fracture appeared in the rock, and the hydraulic conductivity increased significantly [23]. If a tensile failure occurred during the mining process, the sudden jump in hydraulic conductivity was considered as five times that of the shear failure.

The daily advancing speed of the working face was 10 m/d. To simulate daily footage, we adopted to excavate 10 m at each step in the numerical simulation. In the calculation process, the fluid module in FLAC^{3D} was first closed to calculate the mining response of the model in a single mechanical field. Next, we opened the fluid part and used the fluid-solid coupling to calculate the seepage field change under the current excavation step. The seepage calculation was completed for 1 day; then, we entered the next step of mining. The results show that the distance of the compaction area in goaf is generally about 100 m. Therefore, a total of 10 steps (100 m) of mining were simulated.

4.3. Analysis of Simulation Results. Mining will affect the distribution of pore water pressure of surrounding rock. Taking the working face pushed to 100 m as an example, the distribution of surrounding rock water pressure was analyzed (Figure 10). The water pressure on the surrounding rock working face suddenly drops to zero after excavation, causing the fluid in the surrounding rock to flow to the goaf. The pore water pressure in the surrounding rock near the working face decreases significantly.

For reflecting on the variation characteristics of pore water pressure in surrounding rock during mining, the middle part of the y -direction of the model and an area 8 m below the coal seam floor was selected. The working face was advanced by 10 m, 30 m, and 50 m to measure variations of the pore water pressure in the x -direction and is shown in Figure 11. With the advancing working face, the goaf gradually increases. The pore water pressure in the vicinity of the goaf decreases obviously; the influence range increases with the goaf area, forming a cone of depression on the goaf. The trend line of pore water pressure on the floor was also advancing. When it is far away from the goaf, the pore water pressure distribution is less affected by mining, and the change is not obvious. However, when the working face passed the measurement point, the pore water pressure dropped rapidly. In addition, considering the change of hydraulic conductivity, the drop of water pressure at the same location was greater than that without considering the change of hydraulic conductivity. This was due to the obvious increase of hydraulic conductivity of roof and floor and the increase of water pressure drop near the working face caused by mining.

The ratio of the hydraulic conductivity of the surrounding rock to its original hydraulic conductivity (K/K_0) in the coal mining process was calculated by using the FLAC^{3D} fish

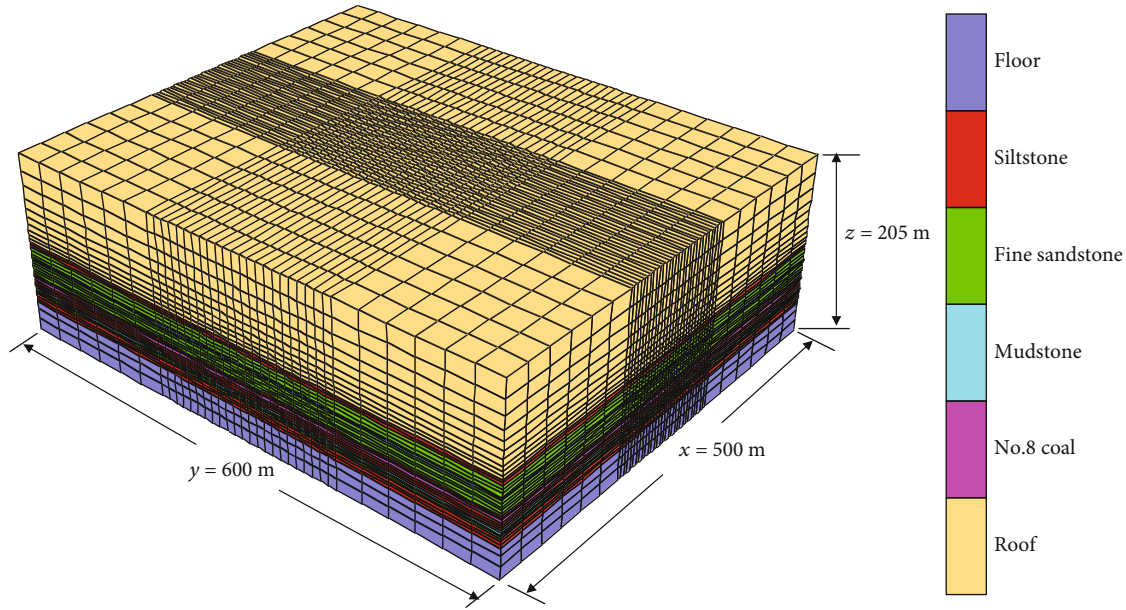
FIGURE 9: Grid mesh of the FLAC^{3D} model.

TABLE 3: Parameters and lithology of the numerical model of water inrush in the working face.

Lithology	Thickness (m)	Density (kg/m ³)	Elastic model (GPa)	Poisson's ratio	Cohesion (MPa)	Tensile strength (MPa)	Internal friction angle (°)	Dilatancy angle (°)	Hydraulic conductivity (×10 ⁻⁶ cm/s)	Porosity
Roof	100	2600	5.00	0.25	3.0	2.6	32	24	10.8	0.2
Siltstone	6	2550	2.30	0.27	2.6	2.5	32	23	3.0	0.15
Fine sandstone	12	2600	5.00	0.25	3.0	2.8	32	24	10.8	0.2
Mudstone	3.5	2500	1.45	0.35	1.3	1.0	30	22	1.0	0.1
Fine sandstone	16	2600	5.00	0.25	3.0	2.8	32	24	10.8	0.2
Siltstone	4	2550	2.30	0.27	2.6	2.5	32	23	3.0	0.15
No. 8 coal	3.5	2000	1.40	0.3	1.2	1.0	28	22	1.0	0.1
Siltstone	8	2550	2.30	0.27	2.6	2.5	32	23	3.0	0.15
Mudstone	4	2500	1.45	0.35	1.3	1.0	30	22	1.0	0.1
Fine sandstone	4	2600	5.00	0.25	3.0	2.8	32	24	10.8	0.2
Siltstone	10	2550	2.30	0.27	2.6	2.5	32	23	3.0	0.15
Floor	34	2600	5.00	0.25	4.0	3.2	32	24	10.8	0.2

language as shown in Figure 12. The distribution diagram in Figure 12(a) shows the variation in hydraulic conductivity in the middle of the working face along the coal seam mining direction. The hydraulic conductivity of each rock mass in the roof and floor of the coal seam has changed greatly before mining because of the damage to the mining rock mass. At the direct roof and floor of the coal seam, due to the influence of tensile failure, the hydraulic conductivity of the siltstone increased to a maximum of approximately 25 times the original value. The variation of the roof hydraulic conductivity was saddle type, and that of the floor was eight shaped. This ratio decremented upwards and downwards from the goaf,

which indirectly reflected the damage of the rock mass in the roof and floor. At different depths in the vertical direction (Figures 12(b)–12(e)), the roof and floor of the coal seam were affected by the mining in a certain range, and the hydraulic conductivity changed greatly. The maximum was usually at the coal wall of the working face. Due to abutment pressure, shear failure occurs here, along with volume strain expansion of rock mass, which results in increased hydraulic conductivity.

For reflecting on the dynamic variation characteristics in hydraulic conductivity of the surrounding rock during the mining, 8 m under the coal seam floor is taken for analysis

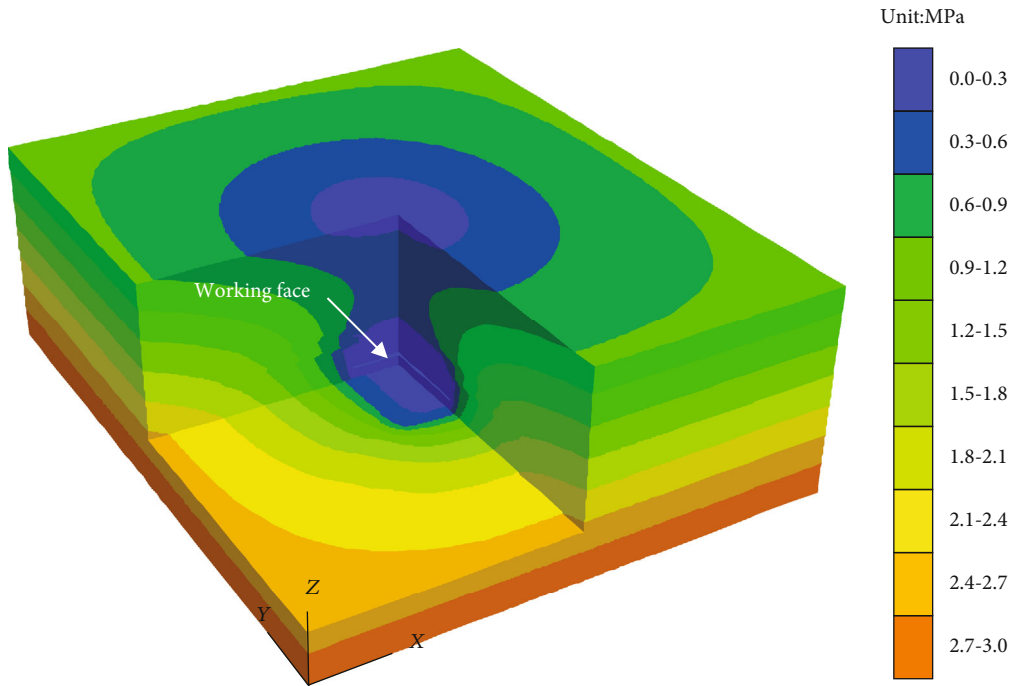


FIGURE 10: Distribution of the pore water pressure in the surrounding rock using the numerical modeling.

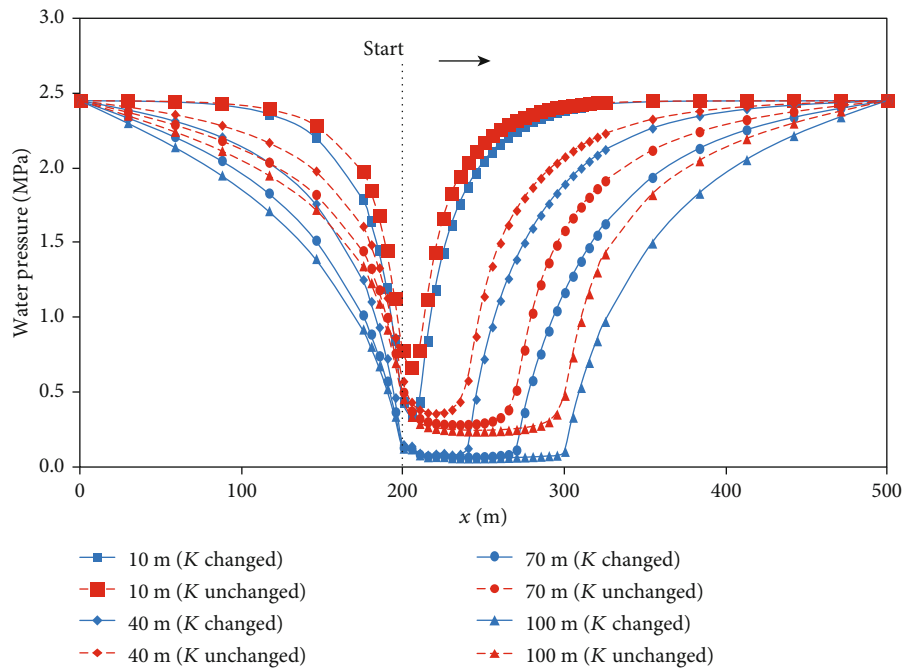


FIGURE 11: Distributions of the water pressure in x -direction using the modified (blue curves) and original (red curves) numerical models for the different lengths of the working face.

(middle section in y -direction of the model). The changing pattern of the hydraulic conductivity (K/K_0) was made when the working face was propelled by 10 m, 40 m, 70 m, and 100 m (Figure 13). It can be seen from Figure 13 that the hydraulic conductivity of the rock mass of the coal seam floor changed regularly with the advancing working face. The rock mass far away from the mining area was less affected by min-

ing, and its hydraulic conductivity changed a little, which shows a declining state. When the working face was advanced by 10 m, the floor rock mass at a depth of 8 m below the goaf was not damaged due to the small disturbance range, and the increase in hydraulic conductivity was not obvious. When the working face advanced distance was large, the hydraulic conductivity of the rock mass increased sharply

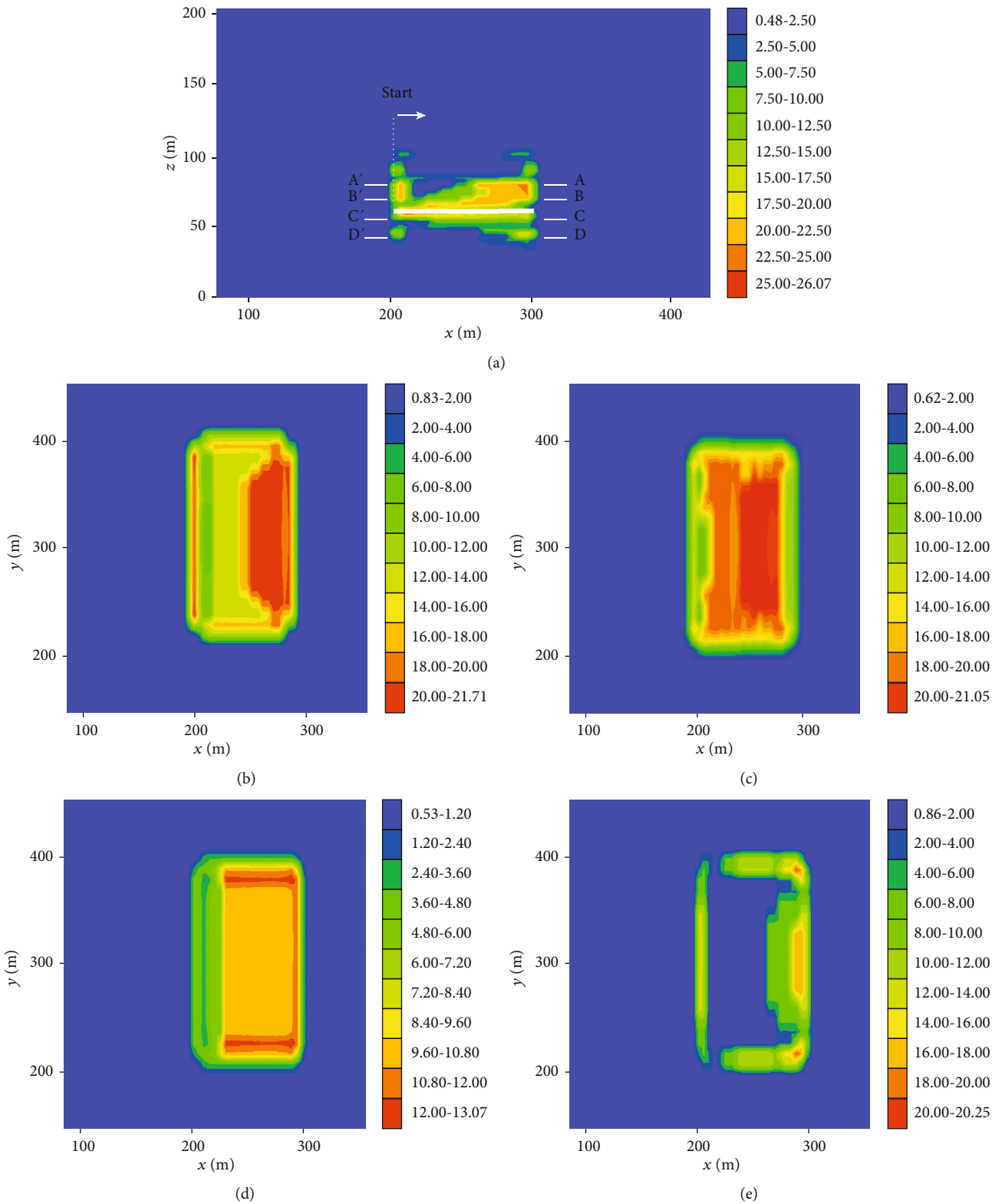


FIGURE 12: Contours of the hydraulic conductivity ratio (K/K_0) using the modified numerical model with 100 m length working face for (a) strike section, (b) $A-A'$ section (the fine sandstone of 17 m above the coal seam), (c) $B-B'$ section (the fine sandstone of 7 m above the coal seam), (d) $C-C'$ section (the siltstone of 4 m below the coal seam), and (e) $D-D'$ section (the fine sandstone of 14 m below the coal seam).

when it was deformed by mining. It should be noted that a small amount of undamaged rock mass appears at a region of $x = 210 \sim 230$ m, and the permeability does not increase

sharply. As the mining distance increased, the range of hydraulic conductivity increased. However, the increase gradually decreased with the advancing working face. As

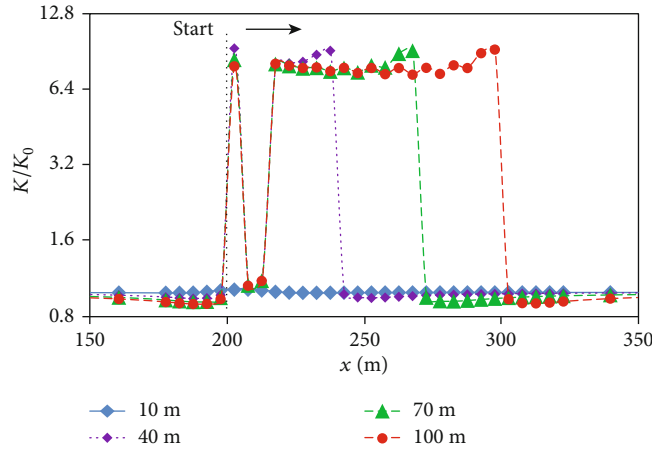


FIGURE 13: Distributions of the hydraulic conductivity of the coal-seam floor in x -direction using the modified numerical model for the different lengths of the working face.

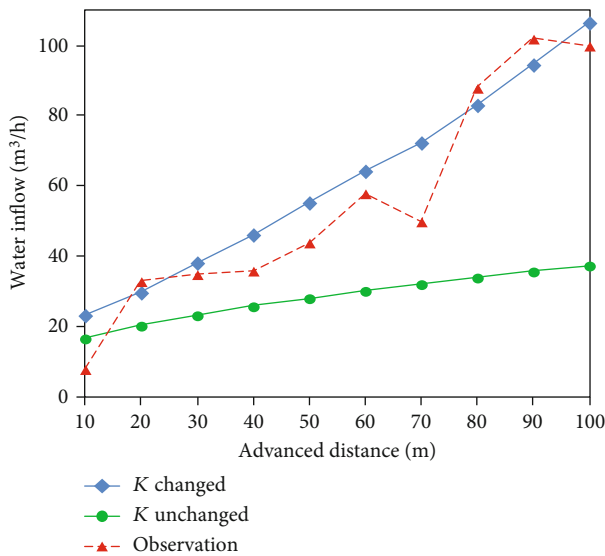


FIGURE 14: Comparisons of the water inflow from the working face of the observation, the original numerical model, and the modified numerical models for the different advanced distance (the length of the working face).

the rock mass fissure gradually closed under the confining pressure after yielding behind the working face, its hydraulic conductivity decreased even when the strain was increased. However, it was much larger than the initial hydraulic conductivity before mining and is consistent with the conclusion of the triaxial hydraulic conductivity test.

For the coupled fluid-solid model, the water inflow rate was calculated using the fish function (gp_flow) of $FLAC^{3D}$, which is displayed in Figure 14. As the excavation area increased step by step, the amount of water inflow increased approximately linearly, from $23\text{ m}^3/\text{h}$ to $106\text{ m}^3/\text{h}$, with the advancing working face. When the influence of the mining disturbance on the hydraulic conductivity of the rock mass was not considered, the value of the water inflow became smaller. The difference gradually increased with the increase in the excavation area. The calculated values agreed with the

measured water inflow values over ten consecutive days, when the hydraulic conductivity change was considered. The calculation accuracy was also higher even without considering changes in hydraulic conductivity.

The above results show that the hydraulic conductivity characteristics of rock mass change under mining conditions are large. However, the calculation results of the fixed value hydraulic conductivity should be used to forecast an actual water inflow to guide the safe production of coal mines correctly.

5. Conclusions

In this study, the hydraulic conductivity variations in rock samples during rock deformation and failure were measured using the triaxial servo rock mechanic test in a laboratory. The formula for the hydraulic conductivity-volume strain was proposed based on the experiment data. The finite-difference numerical model $FLAC^{3D}$ was modified by replacing constant hydraulic conductivity with strain-dependent hydraulic conductivity. The coupled water flow and rock deformation and failure were simulated using the modified model. The modified model was then applied to a coal mining workplace in Huainan, China. The main conclusions drawn from this study are as follows.

- (1) The triaxial hydraulic conductivity test showed that the rock's hydraulic conductivity was not constant but varied with the evolution of the stress-strain process. In the elastic phase, elastic compression caused the pores and fissures in the rock samples to close, and the hydraulic conductivity decreased. When the stress reached the peak value, due to the dilatancy expansion, the hydraulic conductivity also increased sharply by 10–50 times its initial value. After the peak, the fissures tended to close gradually, and the hydraulic conductivity decreased gradually due to the confining pressure

- (2) Based on the test results, the exponential relationship formula between volume strain and hydraulic conductivity was proposed. Before yielding, they show a negative exponential relationship, while after yielding, they show a positive exponential relationship, and the formula has a high degree of fitting. The volume strain can better reflect the evolution of hydraulic conductivity during rock damage
- (3) The coupling relationship between hydraulic conductivity and volume strain was incorporated into the relationship equation between the stress and seepage fields. This provided the governing equation for fluid-solid coupling numerical simulation of water inflow calculation in the coal working face. The FLAC^{3D} rock triaxial seepage coupling model was established, and then, the stress-strain curves of the calculated results were compared with those of the test results. The two were in good agreement, which proved that the fluid-solid coupling model established in this paper was successful
- (4) The hydraulic conductivity and volume strain proposed in this paper was embedded in FLAC^{3D}, and the fluid-solid coupling analysis was carried out for calculating water inflow from 12318 working face in Pansan coal mine of Huainan. The process of the hydraulic conductivity of the surrounding rock and the variation of the water inflow during the mining process were presented in an intuitive image dynamic. The simulation results of water inflow coincide with the actual observed values. In addition, the results are more accurate than that of the seepage model that does not consider mining disturbances

Data Availability

The data used in this study is available from Dr. Haifeng Lu (hflu@aust.edu.cn) upon request.

Conflicts of Interest

The authors declare that they have no conflicts of interest.

Acknowledgments

This work was supported by the National Natural Science Foundation of China (41977165 and 41977253), the major projects of natural science research in Higher Education Institutions of Anhui Province (KJ2019ZD11), the Central Public-interest Scientific Institution Basal Research Fund (GYZX190306), the Guangdong Provincial Key Laboratory of Soil and Groundwater Pollution Control (No. 2017B030301012), the State Environmental Protection Key Laboratory of Integrated Surface Water-Groundwater Pollution Control, and the Shenzhen Municipal Engineering Lab of Environmental IoT Technologies.

References

- [1] L. Yuan, "Scientific problem and countermeasure for precision mining of coal and associated resources," *Journal of China Coal Society*, vol. 44, no. 1, pp. 1–9, 2019.
- [2] X. M. Cheng, T. Z. Zhao, X. Q. Li, C. M. Li, and R. H. Sun, "Prediction of water inflow from the working face with strata bound water," *Coalfield Geology and Exploration*, vol. 4, pp. 34–37, 2007.
- [3] J. J. Duan, H. J. Xu, and R. Prince, "Application of correlation analysis method in prediction of mine water inflow," *Coal Science and Technology*, vol. 41, no. 6, pp. 114–116, 2013.
- [4] H. M. Wang and Y. Huang, "Prediction of mine water inflow by fuzzy hydrogeological analogy method in Changting mining area," *Metal Mine*, vol. 3, pp. 178–182, 2017.
- [5] X. Chen, J. Yu, C. a. Tang, H. Li, and S. Wang, "Experimental and numerical investigation of permeability evolution with damage of sandstone under triaxial compression," *Rock Mechanics & Rock Engineering*, vol. 50, no. 6, pp. 1529–1549, 2017.
- [6] C. Chen, W. Y. Li, and S. G. Xu, "Application of large diameter method in estimation water inflow of coal mine," *Coal Technology*, vol. 36, no. 11, pp. 199–201, 2017.
- [7] L. K. Sahoo, S. Bandyopadhyay, and R. Banerjee, "Water and energy assessment for dewatering in opencast mines," *Journal of Cleaner Production*, vol. 84, pp. 736–745, 2014.
- [8] K. Yang, B. H. Chen, and S. L. Shi, "Short-term prediction model of water inrush from coal mine floor based on HMM," *Safety and Environmental Engineering*, vol. 27, no. 5, pp. 190–196, 2020.
- [9] L. Zhao, R. Ting, and N. B. Wang, "Groundwater impact of open cut coal mine and an assessment methodology: a case study in NSW," *International Journal of Mining Science and Technology*, vol. 27, no. 5, pp. 861–866, 2017.
- [10] X. G. Cheng, W. Qiao, L. Lu, C. W. Jiang, and N. Lei, "Model of mining-induced fracture stress-seepage coupling in coal seam over-burden and prediction of mine inflow," *Journal of China Coal Society*, vol. 45, no. 8, pp. 2890–2900, 2020.
- [11] L. Surinaidu, V. V. S. Gurunadha Rao, N. Srinivasa Rao, and S. Srinu, "Hydrogeological and groundwater modeling studies to estimate the groundwater inflows into the coal mines at different mine development stages using modflow, Andhra Pradesh, India," *Water Resources & Industry*, vol. 7–8, pp. 49–65, 2014.
- [12] H. Lu, X. Liang, N. Shan, and Y.-K. Zhang, "Study on the stability of the coal seam floor above a confined aquifer using the structural system reliability method," *Geofluids*, vol. 2018, 15 pages, 2018.
- [13] W. J. Sun, Q. Wu, H. L. Liu, and J. Jiao, "Prediction and assessment of the disturbances of the coal mining in kailuan to karst groundwater system," *Physics and Chemistry of the Earth, Parts A/B/C*, vol. 89–90, pp. 136–144, 2015.
- [14] P. A. Charlez, *Rock Mechanics Volume 2, Petroleum Applications*, Technical Publisher, Paris, 1991.
- [15] M. M. Tang, H. Y. Zhao, H. F. Ma, S. F. Lu, and Y. M. Chen, "Study on CO₂ huff-n-puff of horizontal wells in continental tight oil reservoirs," *Fuel*, vol. 188, no. 15, pp. 140–154, 2017.
- [16] M. Souley, F. Homand, S. Pepa, and D. Hoxha, "Damage-induced permeability changes in granite: a case example at the url in Canada," *International Journal of Rock Mechanics & Mining Sciences*, vol. 38, no. 2, pp. 297–310, 2001.

- [17] J. A. Wang and H. D. Park, "Fluid permeability of sedimentary rocks in a complete stress-strain process," *Engineering Geology*, vol. 63, no. 3-4, pp. 291-300, 2002.
- [18] S. J. Schatzel, C. Karacan, H. Dougherty, and G. V. R. Goodman, "An analysis of reservoir conditions and responses in longwall panel overburden during mining and its effect on gob gas well performance," *Engineering Geology*, vol. 127, pp. 65-74, 2012.
- [19] D. P. Adhikary and H. Guo, "Modelling of longwall mining-induced strata permeability change," *Rock Mechanics and Rock Engineering*, vol. 48, no. 1, pp. 345-359, 2015.
- [20] X. S. Liu, K. Wang, and M. Xu, "Permeability evolution of low-permeability reservoir sandstone considering hydraulic-mechanical-damage coupling effect during gradual fracturing process," *Chinese Journal of Geotechnical Engineering*, vol. 40, no. 9, pp. 1584-1592, 2018.
- [21] X. Tan, H. Konietzky, and T. Frühwirt, "Laboratory observation and numerical simulation of permeability evolution during progressive failure of brittle rocks," *International Journal of Rock Mechanics & Mining Sciences*, vol. 68, pp. 167-176, 2014.
- [22] W. Wang, X. H. Li, and D. W. Hu, "Permeability evolution of brittle rock in progressive failure process under triaxial compression," *Rock and Soil Mechanics*, vol. 10, pp. 2761-2768, 2016.
- [23] T. H. Yang, J. Liu, W. C. Zhu, D. Elsworth, L. G. Tham, and C. A. Tang, "A coupled flow-stress-damage model for groundwater outbursts from an underlying aquifer into mining excavations," *International Journal of Rock Mechanics & Mining Sciences*, vol. 44, no. 1, pp. 87-97, 2007.
- [24] E. Derek and B. Mao, "Flow-deformation response of dual-porosity media," *Journal of Geotechnical Engineering*, vol. 118, no. 1, pp. 107-124, 1992.
- [25] J. C. Stormont and J. J. K. Daemen, "Laboratory study of gas permeability changes in rock salt during deformation," *International Journal of Rock Mechanics and Mining Science & Geomechanics Abstracts*, vol. 29, no. 4, pp. 325-342, 1992.
- [26] W. F. Brace, J. B. Walsh, and W. T. Frangos, "Permeability of granite under high pressure," *Journal of Geophysical Research*, vol. 73, no. 6, pp. 2225-2236, 1968.
- [27] C. A. Davy, F. Skoczylas, and J. D. Barnichon, "Permeability of macro-cracked argillite under confinement: gas and water testing," *Physics and Chemistry of the Earth*, vol. 32, no. 8-14, pp. 667-680, 2007.
- [28] S. P. Li, Y. S. Li, and Z. Y. Wu, "Permeability-strain equations corresponding to the complete stress-strain path of Yinzhuang sandstone," *International Journal of Rock Mechanics and Mining Sciences & Geomechanics Abstracts*, vol. 31, no. 4, pp. 383-391, 1994.
- [29] F. Cappa and J. Rutqvist, "Modeling of coupled deformation and permeability evolution during fault reactivation induced by deep underground injection of CO₂," *International Journal of Greenhouse Gas Control*, vol. 5, no. 2, pp. 336-346, 2011.
- [30] C. Y. Chin, R. Raghavan, and L. K. Thomas, "Fully coupled geomechanics and fluid flow analysis of wells with stress dependent permeability," *SPE Journal*, vol. 5, p. 48857, 2000.
- [31] ITASCA, *Fast Lagrangian Analysis of Continua, Version 5.0*, Itasca Consulting Group Inc., Minnesota, 2012.
- [32] S. P. Peng and J. A. Wang, *Safe Coal Mining on Confined Water Bodies*, Coal Industry Publishing, Beijing, 2001.

Research Article

Experimental Investigation into the Influences of Weathering on the Mechanical Properties of Sedimentary Rocks

Xiaoshuang Li,^{1,2,3,4} Yingchun Li⁵, and Saisai Wu¹

¹School of Resources Engineering, Xian University of Architecture and Technology, Xian 710000, China

²China Steel Group Ma On Shan Mine Research Institute Co. LTD., Maanshan 243000, China

³State Key Laboratory of Safety and Health in Metal Mines, Maanshan, Anhui 400045, China

⁴Jiangxi Key Laboratory of Mining Engineering, Jiangxi University of Science and Technology, Ganzhou 341000, China

⁵State Key Laboratory of Coastal and Offshore Engineering, Dalian University of Technology, Dalian 116024, China

Correspondence should be addressed to Saisai Wu; saisai.wu@xauat.edu.cn

Received 2 June 2020; Revised 13 October 2020; Accepted 17 November 2020; Published 8 December 2020

Academic Editor: Fabien Magri

Copyright © 2020 Xiaoshuang Li et al. This is an open access article distributed under the Creative Commons Attribution License, which permits unrestricted use, distribution, and reproduction in any medium, provided the original work is properly cited.

The time-dependent behaviors of the sedimentary rocks which refer to the altering of the mechanical and deformable properties of rock elements in the long-term period are of increasing importance in the investigation of the failure mechanism of the rock strata in underground coal mines. In order to obtain the accurate and reliable mechanical parameters of the sedimentary rocks at different weathering grades, the extensive experimental programs including the Brazilian splitting test, uniaxial compression tests, and direct shear tests have been carried out on the specimens that exposed to the nature environments at different durations. The correlation between the weathering grades and mechanical parameters including uniaxial tensile strength, uniaxial compression strength, elastic modulus, Poisson's ratio, cohesion, and friction coefficient was proposed. The obtained results suggested that uniaxial tensile strength, uniaxial compressive strength, elastic modulus, and cohesion dramatically decreased with increasing weathering time, characterized as the negative exponential relationship in general. The influences of various weathering grades on fracture behavior of the rock specimens were discussed. The cumulative damage of the rock by the weathering time decreased the friction coefficient of the specimens which led to the initiation and propagation of microcrack within the rock at lower stress conditions. The obtained results improved the understanding of the roles of weathering on the mechanical properties of sedimentary rocks, which is helpful in the design of the underground geotechnical structures.

1. Introduction

In the underground mining projects, the time-dependent mechanical properties of rock mass are the basic engineering parameters to investigate the rock strata movement as well as the stability of rock mass [1–3]. Due to the differences in compositions, structures, and the ages of formation, the time-dependent mechanical properties or fracture conditions of different rocks are different [4–6]. The mechanical properties of rocks are also affected by other factors including weathering time, temperature, humidity, and the surrounding medium [7, 8]. The difference in the time-dependent mechanical properties of the rock would result in the different failure mechanisms of the rock strata in underground mines [9–11]. For underground coal mines, the rock types

that surrounding the coal seam are generally characterized as the sedimentary rocks, which have the characteristics of low strength, good integrity, and fast weathering [12].

Weathering is a typically time-dependent process and regarded as the procedure of degradation of rocks by physical and chemical effects. The ongoing process of weathering in nature produces progressive but intricate alterations in the petrographical, mineralogical, microstructural, and geomechanical characteristics of rocks [13]. Generally, the weathering process decreases the rock strength by increasing the deformability and degradation of the rock [14]. Since the negative influences of the weathering on the strength and deformational properties of rocks, a critical evaluation of the physical-mechanical behavior of rocks under the effects of weathering are of significant relevance in underground

mines [15, 16]. Previous studies in the assessment of the geotechnical condition of a railway tunnel found that the weathering could cause significant issues and resulted in huge economic losses [17].

A number of studies have been carried to assess the influences of weathering process on the mechanicals of granitoid rocks [18–20]. Heidari et al. [21] reported that the elastic modulus of granodiorite decreased with increasing the weathering time. Based on the correlation between the weathering grades and change in mechanical and petrographic properties, Momeni et al. [22] attempted to propose the weathering classification for granitoid rocks. Alavi Nezhad Khalil Abad et al. [23] studied the characteristics of granitic rock mass in various weathering zones in tropical environments. Other researchers found that the weathering process decreased the elastic modulus of rock by altering the mineralogical characteristics of the rock. For the calcareous rocks, the elastic modulus has a negative exponential relationship with the calcite content [24].

Momeni et al. [25] reported that the difference in the compressive strength and elastic modulus for the fresh and weathered rock is related to their petrographical properties. The appearances of clay minerals with crack density were recognized as the most effective parameters instead of primary mineral composition and textural properties [12]. However, the aforementioned researches mostly focused on studying the effects of weathering on granitoid rocks. Discussions on the time-dependent behavior of sedimentary rocks affected by weathering are found to be reported rarely in the literature. For the underground coal mines, the rock types that surrounding the coal seam are generally characterized as the sedimentary rocks. As one of the typical types of sedimentary rocks, black shale is formed by dehydration and cementation of clay. It is predicted that the mechanical parameters of black shale will be significantly affected by weathering processes. Therefore, it is necessary to study the evolution law of physical and mechanical parameters of black shale in the process of weathering.

In this study, the time-dependent behaviors of sedimentary rocks were examined and assessed at a certain duration of weathering through extensive experimental programs. The correlation between the weathering grades and mechanical parameters including uniaxial tensile strength, uniaxial compression strength, elastic modulus, Poisson's ratio, cohesion, and friction coefficient was proposed. The influences of various weathering grades on the behavior of the rock specimens were discussed, whereby a more reasonable design of the geotechnical engineering structures considering the effects of weathering, especially for the design of slope angle and boundary, could be conducted.

2. Experimental Programs

2.1. Specimens. The tested black shale specimens which are a typical type of sedimentary rocks were collected from an underground mine. The black shale is formed by dehydration and cementation of clay and has the characteristics of fine grain, dense, low strength, good integrity with little small cracks, and fast weathering. The specimens are prepared

through drilling vertically in the direction of the rock layer with good integrity. The diameter of the drilled cylinder core is 50 mm. For the uniaxial compression test, the ratio of height to diameter of the specimens is 2. For the direct shear mechanical test, the ratio of height to diameter is 1. The ratio of height to diameter is 0.5 for the Brazilian split test. The surfaces of the specimens were polished by a grinder. The parallelism deviation of the surfaces at both ends of the specimen was controlled less than 0.1 millimeters. The diameter deviation along the surface of the specimens was less than 0.1 millimeters, which was checked with a cursor caliper. The specimens used for each test are shown in Figure 1.

2.2. Testing Devices. In order to evaluate the influences of the weathering on the uniaxial tensile strength of rock, the Brazilian split tests were carried out on the specimens that were exposed to the environments at different duration. The dimension of the cylinder specimens for the Brazilian split tests is 50 mm × 25 mm. The Brazilian split tests are one of the common methods to determine the uniaxial tensile strength of rock. As shown in Figure 2, the electrohydraulic servo pressure tester was used to perform the Brazilian split tests. During the tests, a relative linear increasing load at 0.50 kN per second in the direction of the diameter was applied, until the failure occurred. A schematic diagram of the loading method is shown in Figure 2(b). The uniaxial tensile strength of the specimens is the ratio applied longitudinal force at the failure time and the cross-sectional area perpendicular to the loading direction.

The uniaxial compression tests were conducted on the cylinder specimens that were exposed to environments with different duration to determine the effects of weathering time on the uniaxial compression strength of rock. The dimension of specimens used for uniaxial compression tests is 50 mm × 100 mm. During the tests, the compression stresses applied on the specimens were increased approximately linearly at 1.0 kN per second until the occurrence of the failure. When compression failure occurred under the action of uniaxial force, the uniaxial compressive strength of rock is the ratio of the maximum load at failure to the cross-sectional area perpendicular to the loading direction. The arrangement of the uniaxial compression testing system is shown in Figure 3.

The influences of the weathering time on the shear strength, internal friction angle, and cohesion of the specimens were determined through conducting the direct shear tests on the specimens with different exposure time to the environments. The dimensions of the cylinder specimens used for the direct shear tests were 50 mm × 50 mm. During the direct shear tests, a relative linear increasing shear load at 0.50 kN per second along the direction of the diameter of the specimens was applied while under different compressive stress, until the failure occurred. The arrangement of the direct shear testing system is shown in Figure 4.

2.3. Testing Procedures. After the specimens were prepared, all specimens were tagged and photographed. The specimens were then carefully placed in the open environment so that the specimens were weathered in the natural state. To accurately determine the effects of weathering on the mechanical

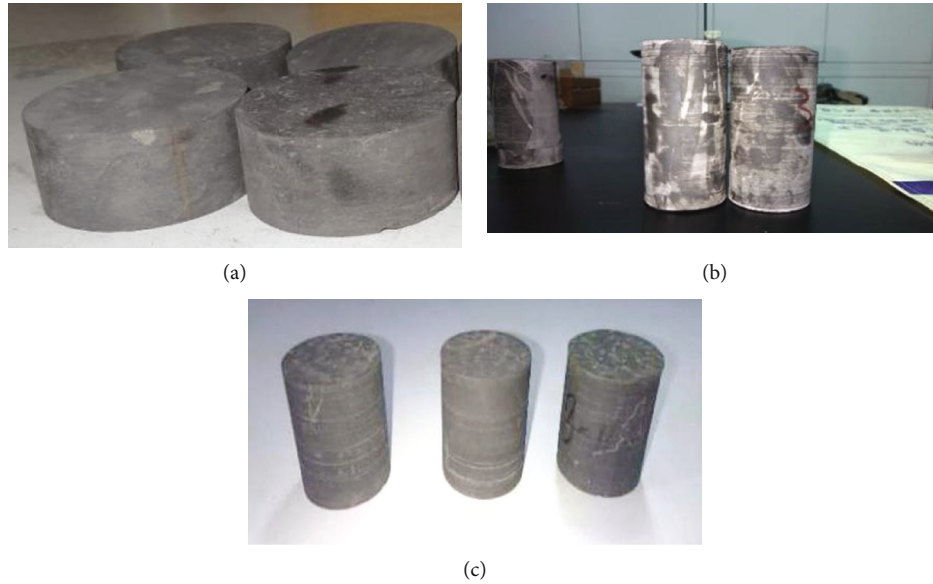


FIGURE 1: Examples of the specimen: (a) Brazilian split test; (b) uniaxial compression test; and (c) direct shear tests.

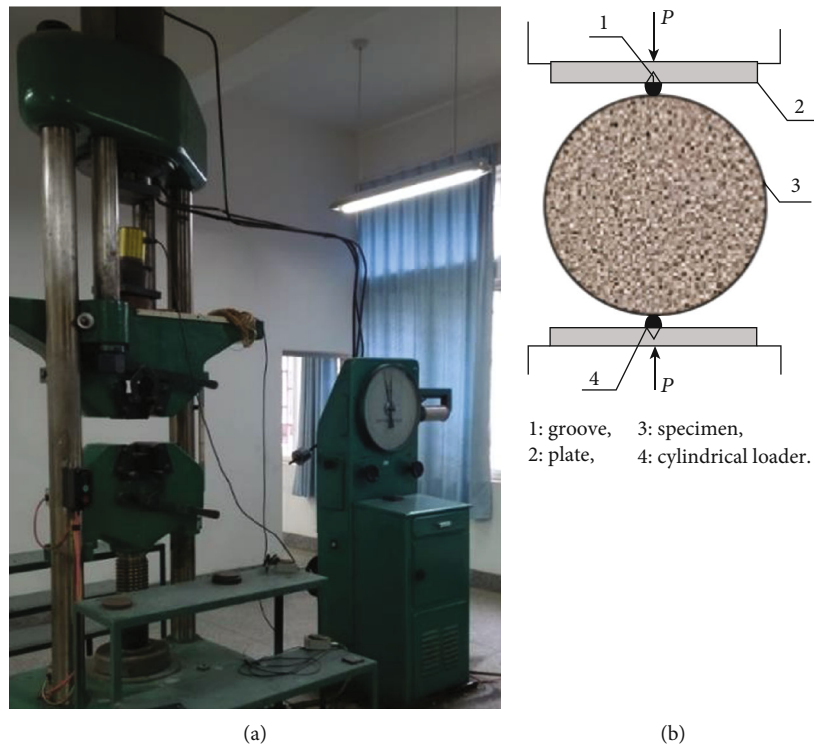


FIGURE 2: Brazilian split test equipment: (a) electro-hydraulic servo pressure tester and (b) schematic diagram of the loading method.

properties of the specimens, the ageing of the rock specimens was examined and evaluated at intervals of one week. The longest duration of the weathering was four weeks. Considering that the black shale has the characteristics of low strength, good integrity, and fast weathering, 28 days' exposure to the environments was considered to be a sufficient period for the occurrence of measurable change on the mechanical properties of the specimens. After each interval, Brazilian split tests, uniaxial compression tests, and direct shear tests were carried

out to determine the relevant physical and mechanical parameters of the specimens. During the tests, the stresses applied on the specimens were increased approximately linearly until the occurrence of the failure. The arrangements of the experimental programs are shown in Table 1. It should be noted that to eliminate the effects of any scatter on the test results, three specimens were tested in each condition. The specimens without the exposure duration to the environments were conducted as the reference tests.

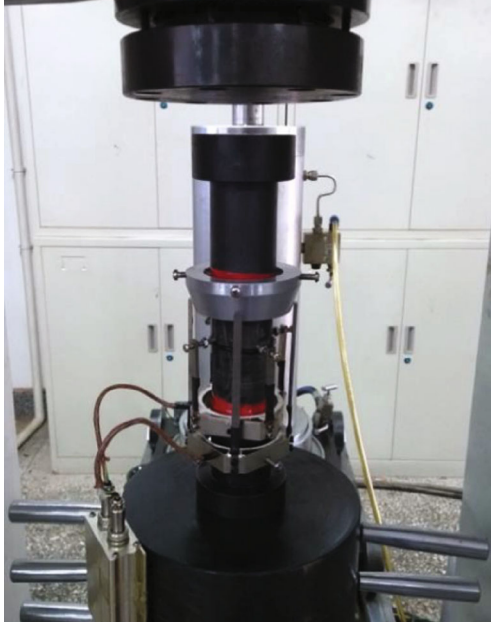


FIGURE 3: Uniaxial compression testing system.



FIGURE 4: The direct shear testing system.

3. Testing Results

3.1. Brazilian Split Tests. During the tests, the stresses applied on the specimens were increased approximately linearly. One of the failed specimens is shown in Figure 5. The failure mode of the specimens in the Brazilian split tests was characterized by a dominant tensile fracture along the vertical direction with little small cracks. The ultimate tensile strength of the specimens could be calculated from the failure load using the following equation (1). The variation in the average ulti-

TABLE 1: The design of the experimental programs.

ID	Weathering period (days)	Number of specimens		
		Brazilian split test	Uniaxial compression tests	Direct shear tests
1	0	3	3	3
2	7	3	3	3
3	14	3	3	3
4	21	3	3	3
5	28	3	3	3

mate tensile strength of the specimens with weathering time is presented in Table 2. The results showed that the ultimate tensile strength of the specimens decreased with the increasing of weathering time. At the weathering time of 28 days, the calculated ultimate tensile strength of the specimens was around 2.98 MPa. While for the specimens without exposure to the environments, the calculated strength was 9.82 MPa which was more than three times of the specimens at the weathering time of 28 days. This indicated that the weathering process could significantly decrease the strength of the specimen within the duration of one month.

$$\sigma_t = \frac{2P}{\pi dt}, \quad (1)$$

where σ_t is the ultimate tensile strength, MPa; P is the ultimate pressure of specimen at failure, N; and d and t are the diameter and thickness of the specimen, mm.

3.2. Uniaxial Compressive Stress. During the tests, the compression stresses applied on the specimens were increased approximately linearly until the occurrence of the failure. One of the failed specimens in the uniaxial compression tests is shown in Figure 6. When the specimen was finally destroyed, an obvious crack was produced along the axial direction with several small horizontal cracks along the horizontal direction. Based on the test results, elastic modulus and Poisson's ratio were calculated. The relationship between the ultimate compression strength, elastic modulus, and Poisson's ratio with weathering time are presented in Table 3. Although the uniaxial compression strength of the specimens varied with the weathering time, the test results at a particular weathering time remained reasonably consistent and repeatable.

It can be seen from the test results that the weathering time has significant influences on the mechanical properties of the specimens under the uniaxial compression test. At the weathering time of 28 days, the average ultimate compression strength, elastic modulus, and Poisson's ratio of the specimens are 12.36 MPa, 3.55 GPa, and 0.39, respectively. While for the specimens without the exposure duration to the environments, the strength, elastic modulus, and Poisson's ratio of the specimens are 66.48 MPa, 13.29 GPa, and 0.16. The significant difference in the mechanical properties of the specimens at the condition of 4 weeks' weathering time and without the weathering also demonstrated the



FIGURE 5: The failed specimen in the Brazilian split tests.



FIGURE 6: The failed specimen in the uniaxial compression tests.

TABLE 2: The variation in the ultimate tensile strength with weathering time.

Weathering time (days)	Test case	Uniaxial tensile strength (MPa)	Mean value (MPa)	Standard deviation (MPa)	Relative standard deviation (%)
0	Case 1-1	9.75	9.82	0.51	5.23
	Case 1-2	9.12			
	Case 1-3	10.59			
7	Case 2-1	6.53	6.91	0.38	5.50
	Case 2-2	6.72			
	Case 2-3	7.48			
	Case 3-1	4.72			
14	Case 3-2	4.81	5.09	0.45	8.84
	Case 3-3	5.74			
	Case 4-1	3.75			
21	Case 4-2	3.98	4.02	0.21	5.15
	Case 4-3	4.33			
	Case 5-1	2.68			
28	Case 5-2	2.97	2.98	0.21	6.94
	Case 5-3	3.29			

direct effects of weathering on the mechanical properties of specimens.

3.3. *Direct Shear Tests.* For the direct shear tests, the shear stress applied on the specimens was increased approximately

linearly while under different compressive stress. Some of the failed specimens in the direct tests are shown in Figure 7. As shown in Figure 7, when the specimen failed, an obvious shear crack was produced in the horizontal direction. The angle between the path of crack growth and the transverse plane was usually around 30 degrees. According to Mohr Coulomb’s law, the relationship between the shear stress and the compressive stress can be characterized as equation (2). From the equation, it can be seen that under a particular weathering time, the correlation between the compressive forces and corresponded shear strength at the same time can be drawn by a straight line. The intercept of the fitted straight line on the ordinate is cohesion, and the inclination of the straight line is the internal friction angle. Using this method, the cohesion and internal friction angle of the specimens under a particular weathering time were calculated.

$$\tau = C + \sigma \tan \Phi, \tag{2}$$

where: τ is the shear strength of specimen, MPa;

C is cohesion, MPa;

σ is the compressive stress applied on the specimen, MPa;

Φ is the angle of internal friction, degree.

The variations in the mechanical parameters with weathering time in the direct shear tests are displayed in Table 4. It should be noted that three specimens were tested in each condition and the test results at a particular testing condition remained reasonably repeatable. Only the average values of the shear strength, the internal friction angle, and cohesions are displayed in Table 4. From the test results, it can be seen that under certain compressive stress, the weathering time has significant effects on the shear strength of the specimens. Under the compressive stress of 10 MPa, the average shear strength of the specimens with weathering a time of 7 and 28 days are 8.48 and 4.49 MPa, respectively. Under the compressive stress of 25 MPa, the shear strength of the specimens with weathering time of 7 and 28 days are 16.14 and 10.73 MPa, respectively.

TABLE 3: The variation of mechanical parameters with weathering time under the uniaxial compression conditions.

Weathering time (days)	Test case	Uniaxial compression strength (MPa)	Mean value (MPa)	Standard deviation (MPa)	Relative standard deviation (%)	Elastic modulus (GPa)	Poisson's ratio
0	Case 1-1	61.15	66.48	4.21	6.33	13.29	0.160
	Case 1-2	65.49					
	Case 1-3	72.80					
7	Case 2-1	36.42	39.51	2.06	5.21	4.70	0.295
	Case 2-2	39.79					
	Case 2-3	42.32					
14	Case 3-1	20.98	24.25	2.18	8.99	4.34	0.339
	Case 3-2	24.89					
	Case 3-3	26.88					
21	Case 4-1	13.52	15.29	1.18	7.72	3.92	0.379
	Case 4-2	17.03					
	Case 4-3	4.33					
28	Case 5-1	8.87	10.09	0.81	8.03	3.55	0.408
	Case 5-2	10.13					
	Case 5-3	11.27					

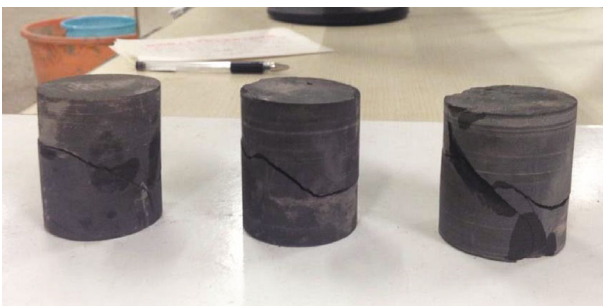


FIGURE 7: Examples of the failed specimen in the direct shear tests.

4. Analysis and Discussion

4.1. Results Analysis. Because of the long time, high cost, and many other influencing factors including the influence of joint fissure, rock mass structure, groundwater, and size effect in rock mass, it is difficult to obtain the macromechanical parameters of the rock mass. Therefore, to provide the basic rock mechanical properties for the design of the engineering project, the mechanical parameters of rock mass are reduced and modified

to the mechanical parameters of rock specimen. In this study, based on the comprehensive experimental tests, the uniaxial tensile strength, uniaxial compressive strength, elastic modulus, Poisson's ratio, cohesion, and angle of internal friction of black shale at different weathering time were obtained through Brazilian split tests, uniaxial compression tests, and direct shear tests. The results of the above tests are summarized in Table 5.

The average uniaxial tensile and uniaxial compressive strength values of the specimen at different weathering times are plotted in Figure 8. From Figure 8, it is clear that with the increasing of the weathering time, both the uniaxial tensile strength and uniaxial compressive strength values of the specimen gradually decreased. Compared to the specimens without exposure to the environments, the uniaxial tensile and uniaxial compressive strength values at weathering time of 28 days decreased by 2.30 times and 5.59 times, respectively. The trendlines are plotted in Figure 8 to represent the variations of the strength values with the weathering time. The determination coefficient (R^2) of the plotted trendlines are provided in Figure 8. Generally, the uniaxial tensile and uniaxial compressive strength values showed negative exponential behavior at the weathering time ranging from 0 to 28 days.

TABLE 4: The variation of mechanical parameters with weathering time in direct shear tests.

Weathering time (days)	Test conditions	Compressive load (kN)	Compressive stress (MPa)	Shear load (kN)	Shear strength (MPa)	Internal friction angle	Cohesion (MPa)	Friction coefficient
0	Condition 1-1	10	5.72	14.84	8.48	42.22	3.28	0.91
	Condition 1-2	15	8.59	19.28	11.05			
	Condition 1-3	20	11.31	23.98	13.56			
	Condition 1-4	25	14.06	26.71	16.14			
7	Condition 2-1	10	5.73	11.84	6.78	42.92	1.60	0.99
	Condition 2-2	15	8.57	17.9	10.22			
	Condition 2-3	20	11.42	19.86	11.34			
	Condition 2-4	25	14.11	26.76	15.10			
14	Condition 3-1	10	5.72	9.96	5.70	40.02	1.07	0.84
	Condition 3-2	15	8.48	15.07	8.52			
	Condition 3-3	20	11.24	18.44	10.36			
	Condition 3-4	25	14.11	22.96	12.90			
21	Condition 4-1	10	5.72	8.87	4.99	40.02	0.67	0.78
	Condition 4-2	15	8.48	13.57	7.63			
	Condition 4-3	20	11.24	16.74	9.41			
	Condition 4-4	25	14.11	20.82	11.7			
28	Condition 5-1	10	5.72	7.98	4.49	40.02	0.38	0.74
	Condition 5-2	15	8.48	12.12	6.81			
	Condition 5-3	20	11.23	15.36	8.63			
	Condition 5-4	25	14.11	19.10	10.73			

TABLE 5: The mechanical parameters of rock specimen.

Rock type	Weathering time (days)	Tensile strength (MPa)	Compression strength (MPa)	Elastic modulus (GPa)	Poisson ratio	Internal friction angle	Cohesion (MPa)	Friction coefficient
Black shale	0	9.82	66.48	13.29	0.160	42.22	3.28	0.91
	7	6.91	39.51	7.96	0.295	42.92	1.60	0.99
	14	5.09	24.25	5.47	0.339	40.02	1.07	0.84
	21	4.02	15.29	4.02	0.379	40.02	0.67	0.78
	28	2.98	10.09	3.55	0.408	40.02	0.38	0.74

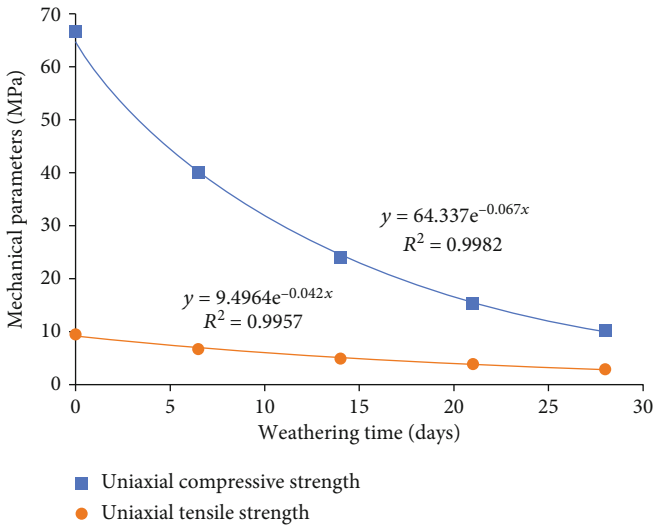


FIGURE 8: Average uniaxial tensile strength of the specimen under different weathering time.

The elastic modulus and Poisson's ratio values of the specimen at different weathering times are plotted in Figure 9. With the increasing of the weathering time, the elastic modulus values of the specimen gradually decreased, while the Poisson's ratio gradually increased. The change in the elastic modulus at the weathering time of zero and 28 days decreased by 2.74 times, while the Poisson's ratio value increased by 2.92 times. The trendlines of the variations of elastic modulus and Poisson's ratio values with the weathering time are plotted in Figure 8, characterized as the quadratic behavior. The determination coefficient (R^2) of the plotted trendlines are also provided.

The variations in the shear strength values at different weathering times while under different compressive stresses are displayed in Figure 10. It is clear that the correlations between shear strength values and the applied compressive at a particular weathering time were near a straight line. At a particular applied compressive stress, the shear strength of the specimens gradually decreased with the increasing of the weathering time. It is observed that the internal friction angle which is the inclination of the straight line remained consistent at different weathering times. The average internal friction angle at a different weathering time was around 42 degrees. The cohesion which is the intercept of the fitted straight line on the ordinate decreased with the increasing of the weathering time. As shown Figure 11, the cohesion of the specimens had a negative exponential relationship with the weather times. The cohesion of the specimen without the exposure to the environments (3.28 MPa) was around 9 times for the specimens at the weathering time of 28 days (0.38 MPa).

According to the comprehensive experimental tests and results analysis, the correlation function between the weathering time and the uniaxial tensile strength, uniaxial compression strength, modulus of elasticity, Poisson's ratio, and cohesion of rock specimens were obtained, as summarized

in Table 6. The determination coefficient (R^2) of each of the correlation function is also provided. The uniaxial tensile strength, uniaxial compression strength, and cohesion of rock specimens were characterized as the negative exponential relationship with the weathering times. The modulus of elasticity has a negative quadratic relationship, while Poisson's ratio had a positive quadratic relationship with the weathering times.

4.2. Discussions. Momeni et al. [25] reported that the difference in the compressive strength and elastic modulus for the fresh and weathered rock is related to their petrographical properties. The existence of clay minerals in the rock was regarded as one of the most important parameters that affected the mechanical properties of the rock through weathering [12]. The black shale specimens used in this study is a typical type of sedimentary rock that formed by dehydration and cementation of clay. The experimental results in this study showed that the rock consisting of clay minerals could be easily softened by the weathering process evidenced by the small deformation modulus and poor antisliding stability. The decrease of compressive strength and elastic modulus of the sedimentary rock with the weathering time confirmed the previous findings and also suggested that the sedimentary rock was sensitive to the weathering grades. In fact, after only 7 days' weathering, the structure of the specimen was significantly damaged evidenced by the obvious decrease of the mechanical parameters.

The cumulative damage of the rock by the weathering time may result in the microcrack coalescence within the rock, which has a great influence on the time-dependent behavior of the rock. Typically, because of the sliding of the initial crack at the elastic deformation stage, microcrack initiated and propagated along the length of the initial crack [26–30]. From this aspect, it was hypothesized that the gradual development of the transverse and longitudinal microcracks coalescence in the specimens during the weathering process led to earlier microcrack initiation compared with the specimens without weathering. The existence of the microcrack coalescence produced during the weathering process could accelerate the crack propagation and result in the macroscopic failure of the rock at low-stress magnitudes. This observation could account for a positive relationship between the Poisson's ratio and weathering time. The development of microcrack coalescence during the weathering process accelerated the radial deformation during the loading process, which resulted in the positive quadratic relationship between the Poisson's ratio and weathering time.

During the failure processes, the direction of the crack initiation and propagation within the rock are randomly distributed. The initiation and propagation of microcracks can be predicted to some extent using the Griffith theory [31]. Other researchers reported that the friction coefficient which is used to describes the sliding friction at microcrack surfaces has important effects on the rock strength and proposed the modified Griffith criterion considering the friction coefficient [32]. The values of the friction coefficient were different along the surface of microcracks, and this value was determined by the extent of wear due to sliding [33–36]. From this aspect,

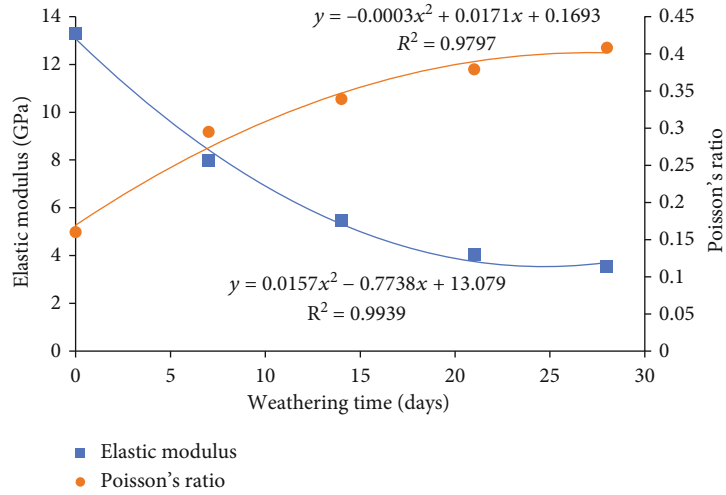


FIGURE 9: The relationship between the elastic modulus and Poisson's ratio with weathering time.

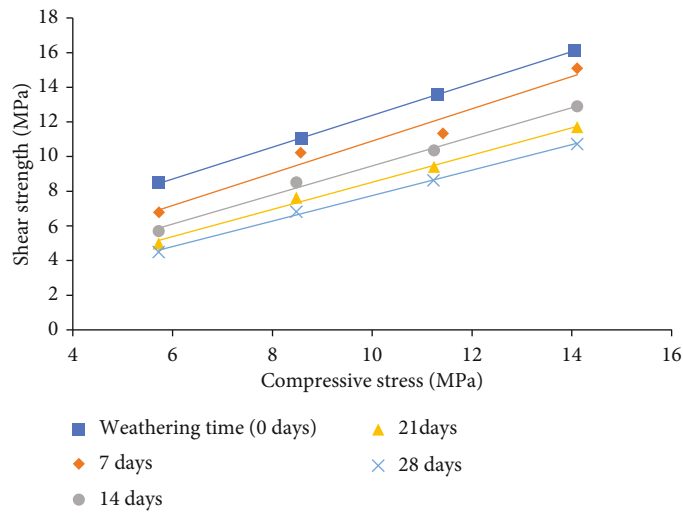


FIGURE 10: Variation in the shear strength under different compressive stress with weathering time.

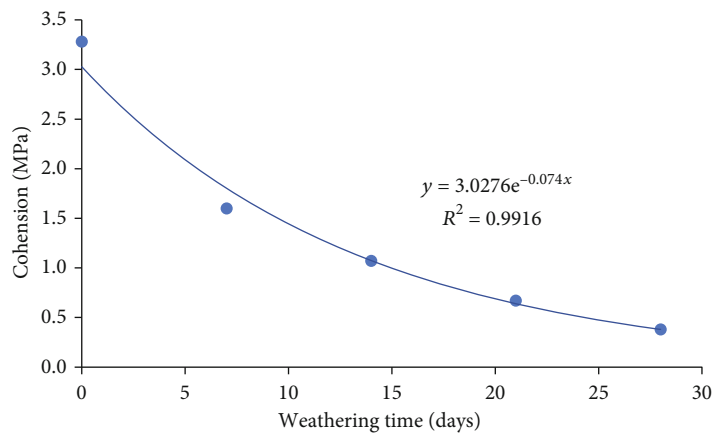


FIGURE 11: Variation in the cohesion of the specimen with weathering time.

TABLE 6: The correlation function between mechanical parameters and weathering time.

Rock type	Parameters	Type of functions	Fitting formula	Correlation coefficient (R ²)
	Uniaxial tensile strength	Exponential	$y = 9.4964e^{-0.042x}$	0.9957
	Uniaxial compression strength	Exponential	$y = 64.337e^{-0.067x}$	0.9982
Black shale	Elastic modulus	Quadratic	$y = 0.0157x^2 - 0.7738x + 13.079$	0.9939
	Poisson's ratio	Quadratic	$y = -0.0003x^2 + 0.0171x + 0.1693$	0.9797
	Cohesion	Exponential	$y = 3.0276e^{-0.074x}$	0.9916

the lower friction coefficient observed in the specimen with higher weathering grades could be attributed to cumulative damage and gradual development of the microcrack coalescence during the weathering process. The lower friction coefficient of the specimen with higher weathering grades led to the initiation and propagation of microcrack at lower stress conditions.

How to obtain accurate and reliable time-dependent behaviors of rock mass has always been an important topic for geotechnical engineering scholars. Conducting the durability tests for evaluating the long-term durability behavior of rock specimens is time-consuming as well as expensive. In this study, the time-dependent durability behaviors of the sedimentary rocks were assessed, and the ageing of the rock specimens that weathered in the natural state was examined. The degradation of the mechanical parameters of rock specimen with different weathering grades was evaluated through the comprehensive experimental programs. However, it should be noted that even though the rock specimen was taken from the site and weathered in the natural state, the selected rock specimens are with good integrity and do not contain or rarely contain the unique weak structural plane of the natural rock mass. The mechanical parameters tested in the laboratory cannot fully represent the mechanical characteristics of the natural rock mass. Therefore, its mechanical parameters need to be reduced in a certain proportion to be applied to the natural rock mass.

5. Conclusions

The paper presented the initial results from the extensive experimental programs to establish the time-dependent behaviors of the sedimentary rocks considering the effects of weathering. The Brazilian split tests, uniaxial compression tests, and direct shear tests have been carried out on the specimens that are exposed to the nature environments at different durations. It was identified that the uniaxial tensile strength, uniaxial compressive strength, and cohesion dramatically decreased with increasing weathering time, characterized as the negative exponential relationship in general. The elastic modulus had a negative quadratic relationship, while the Poisson's ratio had a positive quadratic relationship with the weathering times. It was suggested that the cumulative damage of the rock by the weathering time resulted in the microcrack coalescence within the rock. The existence of the microcrack coalescence facilitated the propagation of the microcracks and accelerated the radial deformation during the loading process. The friction coefficient decreased with

the increasing of the weathering grades. The lower friction coefficient observed in the specimen with higher weathering grades led to the initiation and propagation of microcrack within the rock at lower stress conditions. The results and the proposed correlation between the long-term durability behavior of the sedimentary rocks and weathering grades improved the understanding of the roles of weathering on the mechanical properties which can be used in the design of the underground geotechnical engineering structures.

Data Availability

The data used to support the findings of this study are included within the article, and detailed data are available from the corresponding author upon request.

Conflicts of Interest

The authors declare that they have no conflicts of interest.

Acknowledgments

The work of this paper is financially supported by the National Natural Science Foundation of China (Grant number: 41702327, 41867033, 52004196), China Postdoctoral Science Foundation (Grant number: 2019M650144), State Key Laboratory of Safety and Health of Metal Mines (Grant number: zdsys2019-005), Shanxi Education Department (Grant number: 19JK0454), and Science and Technology Bureau of Beilin, Xi'an (GX2016).

References

- [1] C. R. Windsor, "Rock reinforcement systems," *International Journal of Rock Mechanics and Mining Sciences*, vol. 34, no. 6, pp. 919–951, 1997.
- [2] Z. T. Bieniawski, "Mechanism of brittle fracture of rock," *International Journal of Rock Mechanics and Mining Science and Geomechanics Abstracts*, vol. 4, no. 4, pp. 407–423, 1967.
- [3] E. Hoek and Z. T. Bieniawski, "Brittle fracture propagation in rock under compression," *International Journal of Fracture Mechanics*, vol. 1, no. 3, pp. 137–155, 1965.
- [4] M. H. Ghobadi and A. A. Momeni, "Assessment of granitic rocks degradability susceptible to acid solutions in urban area," *Environmental Earth Sciences*, vol. 64, no. 3, pp. 753–760, 2011.
- [5] S. S. Wu, H. Chen, P. Craig et al., "An experimental framework for simulating stress corrosion cracking in cable bolts,"

- Tunnelling and Underground Space Technology*, vol. 76, pp. 121–132, 2018.
- [6] P. Tapponnier and W. F. Brace, “Development of stress-induced microcracks in westerly granite,” *International Journal of Rock Mechanics and Mining Science and Geomechanics Abstracts*, vol. 13, no. 4, pp. 103–112, 1976.
- [7] S. S. Wu, J. Guo, G. Shi, J. Li, and C. Lu, “Laboratory-based investigation into stress corrosion cracking of cable bolts,” *Materials*, vol. 12, no. 13, p. 2146, 2019.
- [8] S. R. Wang, X. G. Wu, Y. H. Zhao, P. Hagan, and C. Cao, “Evolution characteristics of composite pressure-arch in thin bedrock of overlying strata during shallow coal mining,” *International Journal of Applied Mechanics*, vol. 11, no. 3, article 1950030, 2019.
- [9] Y. C. Li, C. Z. Wu, and B. A. Jang, “Effect of bedding plane on the permeability evolution of typical sedimentary rocks under triaxial compression,” *Rock Mechanics and Rock Engineering*, vol. 53, pp. 5283–5291, 2020.
- [10] Y. C. Li, C. Tang, D. Li, and C. Wu, “A new shear strength criterion of three-dimensional rock joints,” *Rock Mechanics and Rock Engineering*, vol. 53, no. 3, pp. 1477–1483, 2020.
- [11] S. S. Wu, H. L. Ramandi, H. Chen, A. Crosky, P. Hagan, and S. Saydam, “Mineralogically influenced stress corrosion cracking of rockbolts and cable bolts in underground mines,” *International Journal of Rock Mechanics and Mining Sciences*, vol. 119, pp. 109–116, 2019.
- [12] C. Gökçeoğlu, R. Ulusay, and H. Sönmez, “Factors affecting the durability of selected weak and clay-bearing rocks from Turkey, with particular emphasis on the influence of the number of drying and wetting cycles,” *Engineering Geology*, vol. 57, no. 3, pp. 215–237, 2000.
- [13] A. Basu, T. B. Celestino, and A. A. Bortolucci, “Evaluation of rock mechanical behaviors under uniaxial compression with reference to assessed weathering grades,” *Rock Mechanics and Rock Engineering*, vol. 42, no. 1, pp. 73–93, 2009.
- [14] J. Q. Liu, W. Chen, T. Liu, J. Yu, J. Dong, and W. Nie, “Effects of initial porosity and water pressure on seepage-erosion properties of water inrush in completely weathered granite,” *Geofluids*, vol. 2018, Article ID 4103645, 11 pages, 2018.
- [15] S. S. Wu, J. Li, J. Guo, G. Shi, Q. Gu, and C. Lu, “Stress corrosion cracking fracture mechanism of cold-drawn high-carbon cable bolts,” *Materials Science and Engineering*, vol. 769, article 138479, 2020.
- [16] S. Wu, M. Northover, P. Craig, I. Canbulat, P. C. Hagan, and S. Saydam, “Environmental influence on mesh corrosion in underground coal mines,” *International Journal of Mining, Reclamation and Environment*, vol. 32, no. 8, pp. 519–535, 2017.
- [17] D. Arias, L. Pando, C. López-Fernández, L. M. Díaz-Díaz, and Á. Rubio-Ordóñez, “Deep weathering of granitic rocks: a case of tunnelling in NW Spain,” *Catena*, vol. 137, pp. 572–580, 2016.
- [18] M. Heidari, G. R. Khanlari, A. A. Momeni, and H. Jafarholizadeh, “The relationship between geomechanical properties and weathering indices of granitic rocks, Hamedan, Iran,” *Geomechanics and Geoengineering*, vol. 6, no. 1, pp. 59–68, 2011.
- [19] S. Ceryan, K. Zorlu, C. Gokceoglu, and A. Temel, “The use of cation packing index for characterizing the weathering degree of granitic rocks,” *Engineering Geology*, vol. 98, no. 1-2, pp. 60–74, 2008.
- [20] S. S. Wu, X. Zhang, J. Li, and W. Zhao, “Investigation for Influences of Seepage on Mechanical Properties of Rocks Using Acoustic Emission Technique,” *Geofluids*, no. 6693920, 2020.
- [21] M. Heidari, A. A. Momeni, and F. Naseri, “New weathering classifications for granitic rocks based on geomechanical parameters,” *Engineering Geology*, vol. 166, pp. 65–73, 2013.
- [22] A. A. Momeni, G. R. Khanlari, M. Heidari, A. A. Sepahi, and E. Bazvand, “New engineering geological weathering classifications for granitoid rocks,” *Engineering Geology*, vol. 185, pp. 43–51, 2015.
- [23] S. V. Alavi Nezhad Khalil Abad, A. Tugrul, C. Gokceoglu, and D. Jahed Armaghani, “Characteristics of weathering zones of granitic rocks in Malaysia for geotechnical engineering design,” *Engineering Geology*, vol. 200, pp. 94–103, 2016.
- [24] S. Qi, Z. Q. Yue, C. Liu, and Y. Zhou, “Significance of outward dipping strata in argillaceous limestones in the area of the Three Gorges reservoir, China,” *Bulletin of Engineering Geology and the Environment*, vol. 68, no. 2, pp. 195–200, 2009.
- [25] A. Momeni, S. S. Hashemi, G. R. Khanlari, and M. Heidari, “The effect of weathering on durability and deformability properties of granitoid rocks,” *Bulletin of Engineering Geology and the Environment*, vol. 76, no. 3, pp. 1037–1049, 2017.
- [26] L. N. Germanovich, R. L. Salganik, A. V. Dyskin, and K. K. Lee, “Mechanisms of brittle fracture of rock with pre-existing cracks in compression,” *Pure and Applied Geophysics*, vol. 143, no. 1-3, pp. 117–149, 1994.
- [27] S. S. Wu, H. Chen, H. Lamei Ramandi et al., “Investigation of cable bolts for stress corrosion cracking failure,” *Construction and Building Materials*, vol. 187, pp. 1224–1231, 2018.
- [28] N. Erarslan and D. J. Williams, “Mixed-mode fracturing of rocks under static and cyclic loading,” *Rock Mechanics and Rock Engineering*, vol. 46, no. 5, pp. 1035–1052, 2013.
- [29] S. R. Wang, X. G. Wu, J. H. Yang, J. Q. Zhao, and F. L. Kong, “Mechanical behavior of lightweight concrete structures subjected to 3D coupled static-dynamic loads,” *Acta Mechanica*, vol. 231, no. 11, pp. 4497–4511, 2020.
- [30] S. Mo, I. Canbulat, C. Zhang, J. Oh, B. Shen, and P. Hagan, “Numerical investigation into the effect of backfilling on coal pillar strength in highwall mining,” *International Journal of Mining Science and Technology*, vol. 28, no. 2, pp. 281–286, 2018.
- [31] A. M. Ferrero, “The shear strength of reinforced rock joints,” *International Journal of Rock Mechanics and Mining Sciences*, vol. 32, no. 6, pp. 595–605, 1995.
- [32] H. Sonmez, E. Tuncay, and C. Gokceoglu, “Models to predict the uniaxial compressive strength and the modulus of elasticity for Ankara Agglomerate,” *International Journal of Rock Mechanics and Mining Sciences*, vol. 41, no. 5, pp. 717–729, 2004.
- [33] S. Amini, H. N. Hosseinabadi, and S. A. Sajjadi, “Experimental study on effect of micro textured surfaces generated by ultrasonic vibration assisted face turning on friction and wear performance,” *Applied Surface Science*, vol. 390, pp. 633–648, 2016.
- [34] J. Y. Cheng, H. W. Zhang, and Z. J. Wan, “Numerical simulation of shear behavior and permeability evolution of rock joints with variable roughness and infilling thickness,” *Geofluids*, vol. 2018, Article ID 1869458, 11 pages, 2018.

- [35] S. R. Wang, H. G. Xiao, Z. S. Zou, C. Cao, Y. H. Wang, and Z. L. Wang, "Mechanical performances of transverse rib bar during pull-out test," *International Journal of Applied Mechanics*, vol. 11, no. 5, article 1950048, 2019.
- [36] C. C. Wei, C. Zhang, I. Canbulat, A. Cao, and L. Dou, "Evaluation of current coal burst control techniques and development of a coal burst management framework," *Tunnelling and Underground Space Technology*, vol. 81, pp. 129–143, 2018.

Research Article

Evolution Mechanism of Interconnected Vertical Fractures in the Overburden of Longwall Coal Mining

He Changchun ¹, Lu Weiyong ², and Zha Wenhua¹

¹School of Civil Engineering and Architecture, East China University of Technology, Nanchang, Jiangxi 330013, China

²Department of Mining Engineering, Luliang University, Lvliang, Shanxi 033001, China

Correspondence should be addressed to He Changchun; hechangchun87@126.com and Lu Weiyong; 489698551@qq.com

Received 11 June 2020; Revised 17 July 2020; Accepted 20 October 2020; Published 19 November 2020

Academic Editor: Yingchun Li

Copyright © 2020 He Changchun et al. This is an open access article distributed under the Creative Commons Attribution License, which permits unrestricted use, distribution, and reproduction in any medium, provided the original work is properly cited.

Whether a tensile failure fracture will penetrate a stratum is difficult to ascertain at present. In view of this, the method of similar simulation and field verification are used to carry out a systematic study. Similar simulations show that tensile failure fractures will penetrate the layered strata if the compressive stress is greater than the compressive strength. Theoretical analysis points out that whether the tensile failure fractures will penetrate the layered strata can be expressed by the value of criterion of interconnected vertical fractures and the compression-tension ratio. When the value of criterion of interconnected vertical fractures is greater than the compression-tension ratio, the layered strata will break. This criterion was qualitatively verified with a field test. The results of this paper are of great significance for the prevention of water inrush in coal mines, and it can also promote the understanding of the law of strata movement.

1. Introduction

China is a large coal resource country and also a large coal consumption country. Most of the energy supply comes from coal. In 2019, coal still accounts for about 60% of the primary energy consumption ratio [1]. However, a large number of coal mining will also bring many negative impacts, such as ecological damage, surface subsidence, gas outburst, and mine water inrush [2–5]. Mine water inrush is usually fierce, often submerging working faces and tunnels in a short time, bringing harm to mine production and causing casualties. The necessary conditions for mine water inrush are adequate water source and water inrush passage. Most of the mining areas in China are located under the water-rich Quaternary loose aquifer, in which mine water inrush resources are sufficient to meet the source conditions of mine water inrush. The water inrush channel is divided into the primary channel and the secondary channel, and the former channel includes fault, karst, etc. [6, 7]. The secondary channel is the horizontal and mining-induced interconnected vertical fractures [8–

12]. Because the horizontal fractures cannot connect the working face and the aquifer alone, interconnected vertical fractures are the secondary channel of mine water inrush.

After coal seam mining, the overburden is usually divided into the caving zone, the fracture zone, and the bending zone according to the different fracture states [13–19]. Among them, the caving zone has a high degree of fracture development, disordered fracture distribution, and strong permeability, while there are mainly horizontal fractures and interconnected vertical fractures in the fracture zone. Since both the caving zone and the fracture zone have the ability to conduct water, the range of both is the water-flowing fracture zone, and its range is shown in Figure 1. The strata in the bending zone subside as a whole without horizontal fractures or interconnected vertical fractures. If there is a stratum in the bending zone located between the water-flowing fracture zone and the aquifer, the water in the aquifer lacks a transport channel and the water source will not inflow into the coal mining faces. But when interconnected vertical fractures directly develop into the aquifer, the coal mining faces will

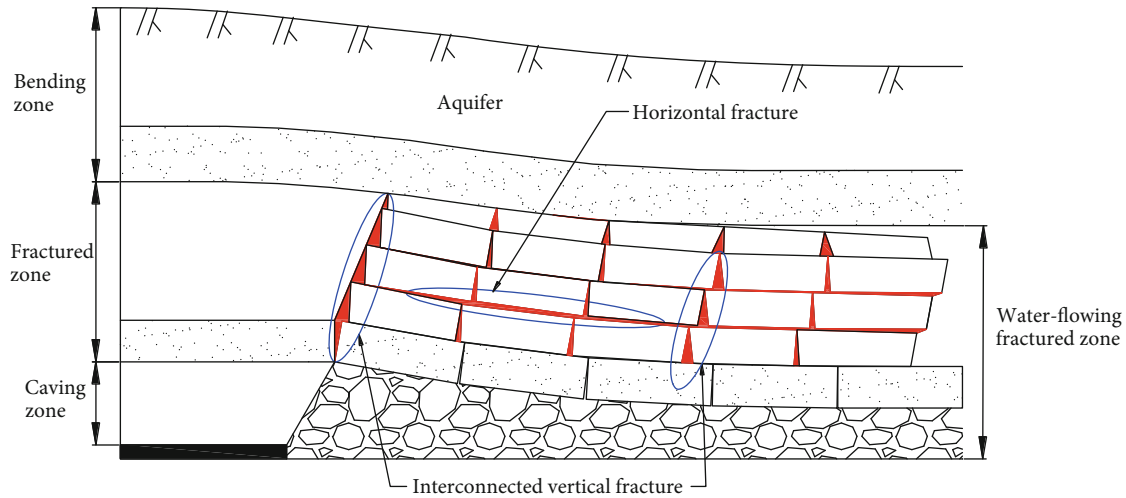


FIGURE 1: Distribution diagram of overburden fracture after coal seam mining.

suffer the threat of water inrush and protective measures should be taken.

In view of the height of interconnected vertical fractures in the overburden, many scholars have carried out researches from different aspects. Wang et al. [20, 21] proposed the “void ratios of fractures” to quantify the separation and fracture evolution in the undermined overburden. On the basis of a lot of practical experience, the former Soviet Union and China put forward several statistical formulae for calculating the height of interconnected vertical fractures and formed a standard [22]. However, the failure characteristics of the overburden under certain special conditions cannot be reflected by the standard formula, by which the measured height of interconnected vertical fractures is significantly higher than that estimated by the standard formula, which leads to many abnormal water inrush accidents [23]. Given the shortcomings of the standard formula, Xu et al. [24, 25] proposed a formula for predicting the height of interconnected vertical fractures based on the position of the primary key strata (PKS), considering the fact of the layered characteristics of overburden and the fracture characteristics of different lithologies. But it is still essentially an empirical formula. There are many mining and geological factors that affect the height of interconnected vertical fractures. Numerous scholars have made predictions of the height of interconnected vertical fractures based on the theory of influencing factors [26–29], which need a large number of measured data, and whether they are universal remains to be verified. The actual measurement method is a direct and effective method for determining the height of interconnected vertical fractures in the overburden. It is generally observed by means of ground drilling [9, 30], as well as other test methods based on modern equipment [31]. These methods can predict the height of interconnected vertical fractures in overburden to a certain extent, but no mechanical mechanism of rock breakage has been involved, and the breaking of a stratum is essentially a result of stress caused by the external environment that exceeds the bearing capacity of the stratum itself. The novelty of this paper is that when a tensile failure fracture will penetrate a stratum is proposed.

In this paper, the characteristics of interconnected vertical fractures in layered strata are firstly studied by similar simulation, and then under certain simplified conditions, the discrimination formula of interconnected vertical fractures in layered strata is obtained by theoretical deduction and calculation. Thirdly, the breaking of each stratum is carried out according to the overburden histogram, and the discriminant method of the height of the water-flowing fracture zone in the overburden is obtained. Finally, the discrimination formula of interconnected vertical fractures is qualitatively verified by an engineering test.

2. Discrimination Formula for Interconnected Vertical Fractures

2.1. Characteristics of Interconnected Vertical Fractures

2.1.1. Model Design. The gravitational planar stress model frame was used in this study to simulate the characteristics of interconnected vertical fractures. The dimensions of the model were 250 cm × 20 cm. In the material mix for each rock layer, sand was used as the aggregate, while plaster and calcium carbonate were used as cements. A layer of mica was placed in the interfaces between the strata to simulate stratification, and the thickness of the soft rock strata was 6–8 cm. The excavation was in steps of 2.5 cm. The simulation was imaged after each excavation to compare the strata breakage and movement before and after the excavation. The mixing ratios that were used are shown in Table 1.

2.1.2. Experimental Results. The distribution of vertical fractures is shown in Figure 2, from which two characteristics of layered strata failure can be found: (1) The mining-induced vertical fractures do not necessarily penetrate the entire thickness of layered strata, that is, the fractures are in a critical state when they extend to a certain extent. The reason for these fractures is that the tensile stress is greater than the tensile strength of the layered strata. (2) Compressive failure occurs at the upper end of the layered strata penetrated by fractures, which indicates that the critical condition for

TABLE 1: Proportion of the similar simulation materials.

Rock strata	Thickness (cm)	Material ratio	Similar materials			
			Sand (kg)	CaCO ₃ (kg)	Gypsum (kg)	Water (kg)
Soft rock	8	473	38.4	6.72	2.88	4.8
Primary key stratum	12	437	30	2.25	5.25	3.75
Soft rock	6	473	28.8	5.04	2.16	3.6
Soft rock	6	473	30	5.25	2.25	3.75
Soft rock	6	473	28.8	5.04	2.16	3.6
Soft rock	6	473	40	7	3	5
Soft rock	8	473	38.4	6.72	2.88	4.8
Soft rock	6	473	30	5.25	2.25	3.75
Soft rock	6	473	28.8	5.04	2.16	3.6
Soft rock	6	473	30	5.25	2.25	3.75
Soft rock	6	473	28.8	5.04	2.16	3.6
Soft rock	6	473	75	13.125	5.625	9.375
Hard rock	15	455	72	9	9	9
Key stratum 2	14	455	40	5	5	5
Soft rock	8	473	38.4	6.72	2.88	4.8
Soft rock	6	473	30	5.25	2.25	3.75
Soft rock	6	473	28.8	5.04	2.16	3.6
Soft rock	6	473	55	9.625	4.125	6.875
Key stratum 1	11	455	52.8	6.6	6.6	6.6
Soft rock	6	473	20	3.5	1.5	2.5
Immediate roof	4	473	19.2	3.36	1.44	2.4
Coal seam	7	773	82.03125	8.203125	3.515625	9.375
Floor	15	455	72	12.6	5.4	9

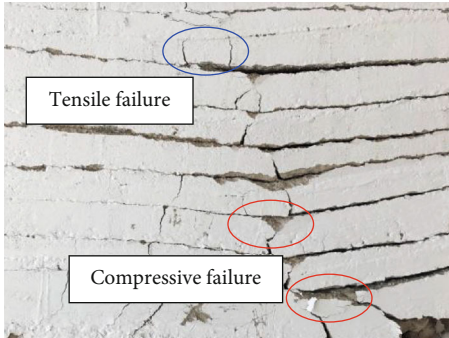


FIGURE 2: Characteristics of vertical fractures in simulated layered strata.

strata breakage is that the compressive stress reaches the compressive strength.

To further illustrate the above two characteristics of layer breakage, a schematic analysis of vertical fracture initiation and propagation is performed. The longitudinal stress development of vertical fracture propagation is shown in Figure 3, and the stress at the crack tip is only for the purpose of display and does not represent the true stress. In addition, h is the thickness of layered strata, σ_t is the tensile strength, and σ_c is the compressive strength. (1) When the longitudinal tensile stress and compressive stress caused by external factors are small, according to material mechanics theory, the

tensile stress and compressive stress are equal and the neutral plane coincides with the central plane, as shown in Figure 3(a). (2) When the change of external factors causes the longitudinal tensile stress and compressive stress to increase, because the compressive strength is greater than the tensile strength, the longitudinal tensile stress will first reach the tensile strength, that is, the rock has a tensile failure fracture, as shown in Figure 3(b). (3) When the external factors continue to change, the vertical fracture begins to expand, and the longitudinal tensile stress at the crack tip has always been equal to the tensile strength, and because the compressive stress is less than the compressive strength, the longitudinal compressive stress continues to increase, as shown in Figure 3(c). (4) When the longitudinal compressive stress increases to the compressive strength, the compressive end of the stratum enters into the plastic state, and the end unit cannot limit the rotation of the section. Therefore, the stress-strain equilibrium state at the crack tip is destroyed, causing the expansion of the fracture, and the subsidence of the stratum also increases, so that more end units in the critical state enter into the plastic state, which is a vicious cycle until the vertical fracture penetrates the stratum, as shown in Figure 3(d).

2.2. Discrimination Formula for Interconnected Vertical Fractures. In order get applicable results, the following assumptions are made:

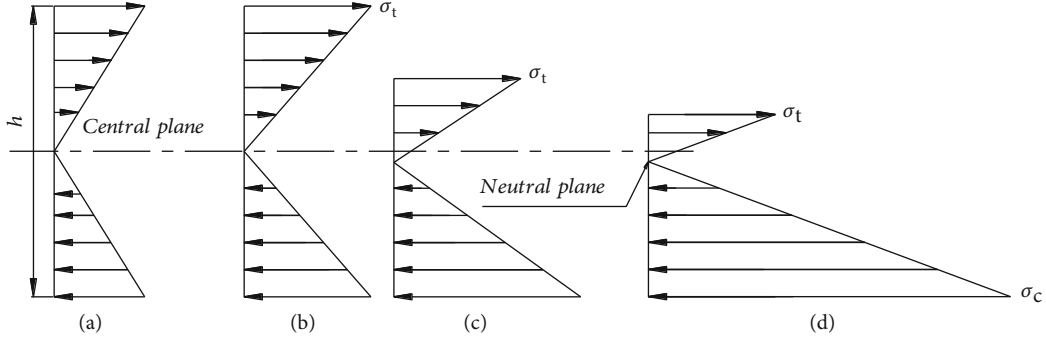


FIGURE 3: Longitudinal stress change in fracture section of the stratum.

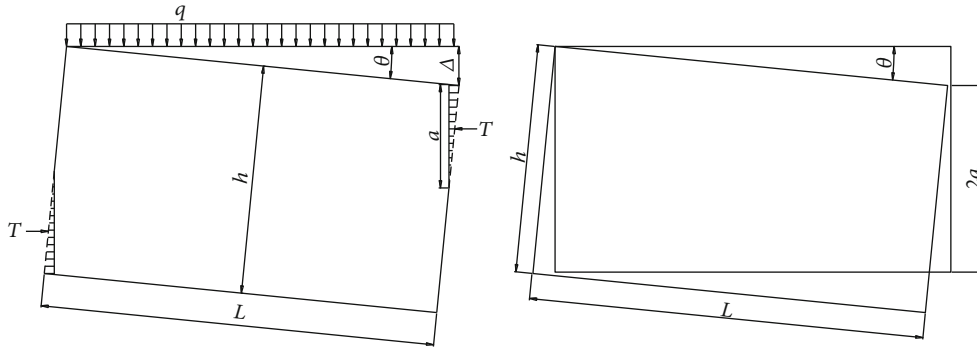


FIGURE 4: Equivalent model of layered strata in the period of first breaking.

- (1) The deposit and rock layers are horizontally stratified
- (2) There is no major geological structural damage to the deposit and rock layers
- (3) The strata are transversely isotropic linear elastomers
- (4) The layered strata are broken into two symmetrical blocks
- (5) A stratum in the plane is simplified as a fixed beam at both ends

According to the above-mentioned characteristics of interconnected vertical fractures of layered strata, when the layered strata rotates to a certain level, under the action of bending moment and axial force, the longitudinal compressive stress at the end of the strata reaches the compressive strength, and the vertical tensile fractures will penetrate the layered strata. When the layered strata are broken for the first time, the cross-sectional shear force in the middle part of the symmetrical strata is zero, which is equivalent to cutting the layered strata with interconnected vertical fractures here. Before the strata break, the stratum will separate with the lower one and only the load will act on the upper surface of the stratum. Therefore, the equivalent model can be represented in Figure 4 where the tensile stress is ignored because it is much smaller compared with the compressive stress. The load q on the layered strata includes the load from the upper strata and self-weight, T is the resultant force of the compressive stress at the extrusion, a is the range of the compressive

stress at the extrusion, h is the thickness of the layered strata, L is the length of the breaking blocks, θ is the rotation angle of the blocks, and Δ is the maximum relative subsidence at the end of the blocks caused by rotation, then the load T can be calculated in the equivalent model [32]:

$$T \left(h - \frac{2a}{3} - \Delta \right) = \frac{qL^2}{2}. \quad (1)$$

When a fracture penetrates a stratum, the range of compressive stress action at the extrusion can be expressed by the thickness of the rock layer according to the geometrical relationship between the blocks, and the range of compressive stress at the extrusion can be obtained [33]:

$$a = \frac{2h - \Delta}{4}. \quad (2)$$

Combined with (1) and (2), horizontal forces during rock block rotation can be obtained:

$$T = \frac{3qL^2}{4h - 5\Delta}. \quad (3)$$

According to the process analysis of the above-mentioned layered stratum fracturing, when the end unit of the layered stratum extrusion enters the plastic state (the compressive stress generated by horizontal thrust is greater than the compressive strength), the layered strata will be

TABLE 2: Compression-tension ratio of common rocks [37].

Test no.	Field naming	Uniaxial compressive strength		Uniaxial tensile strength		Compression-tension ratio		
		Natural	Dry MPa	Saturated	Natural	Dry	Natural	Saturated
ZK33	Granite	/	88.6	44.9	/	8.51	10.4	10.8
ZK34	Granite	/	82.3	39.6	/	6.27	13.1	8.6
ZK35	Granite	/	85.4	44.7	/	9.14	9.3	8.6
ZK36	Granite	/	83.1	36	/	8.93	9.3	6.0
ZK1	Coarse sandstone	72.6	83.1	25.7	4.75	6.43	12.9	8.7
ZK2	Carboniferous coarse sandstone	43.5	52.8	37.4	4.21	5.22	10.3	11.5
ZK3	Fine sandstone	21.4	39.1	20.4	4.03	5.12	5.3	10.1
ZK4	Carbonaceous fine sandstone	37.3	53.9	32.8	3.18	5.64	11.7	19.5
ZK5	Coarse sandstone	76.3	99.3	51.8	7.52	8.79	10.1	11.3
ZK6	Carbonaceous siltstone	27.9	37.2	2.18	2.14	3.21	13.0	3.1
ZK7	Siltstone	25.3	43.7	12.7	2.83	4.36	8.9	6.4
ZK8	Fine sandstone	92.7	97.8	20.6	6.56	9.54	14.1	6.8
ZK9	Coarse sandstone	49.1	84.1	26.5	3.48	6.37	14.1	13.3
ZK10	Conglomerate	43.8	85.1	36.4	5	6.65	8.8	15.1
ZK11	Carboniferous siltstone	44.6	87.2	28.9	6.26	8.86	7.1	8.1
ZK12	Siltstone	32.9	52.7	21.5	3.9	4.93	8.4	9.9
ZK13	Carbonous siltstone	24.5	45	21.8	3.51	4.47	7.0	7.8
ZK14	Carbonous siltstone	9.09	13.3	5.09	1.03	1.32	8.8	8.6
ZK15	Carbonous siltstone	7.63	35.2	2.12	1.75	2.98	4.4	6.6
ZK16	Coarse sandstone	69.6	87.3	43.5	4.88	7.66	14.3	10.5

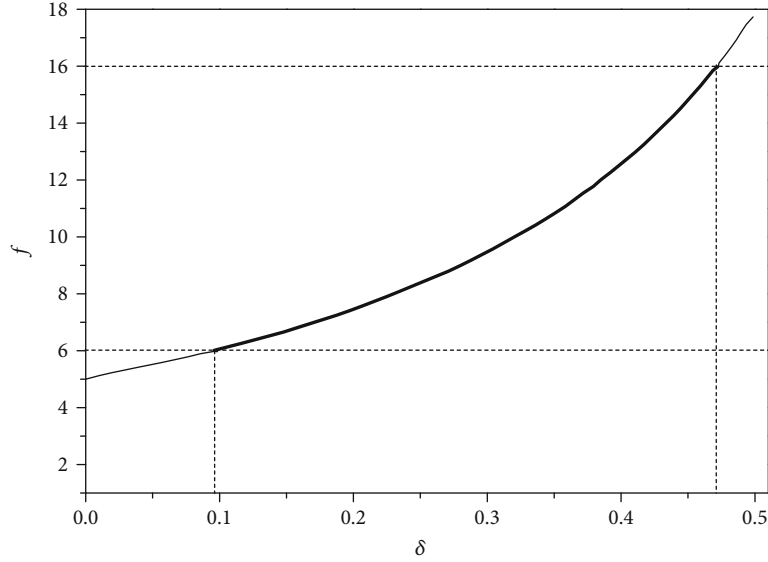


FIGURE 5: Criterion values for different deflection-thickness ratios.

penetrated by the vertical fractures, namely,

$$\frac{24qL^2}{(4h - 5\Delta)(2h - \Delta)} \geq \eta\sigma_c, \quad (4)$$

where η is the extrusion strength coefficient at the end, which is usually 0.3 [34]. According to the fifth hypothesis, the breaking length of rock blocks can be obtained from the relationship between the rock load and tensile strength of the two-end fixed beam in the ultimate bending state, which is

$$L = \frac{h}{2} \sqrt{\frac{2\sigma_t}{q}}. \quad (5)$$

The discrimination formula of interconnected vertical fractures of layered strata is obtained by combining formulae (4) and (5), which is

$$\frac{40h^2}{(4h - 5\Delta)(2h - \Delta)} \geq \frac{\sigma_c}{\sigma_t}, \quad (6)$$

where Δ is the centre subsidence relative to the fixed end of the block and σ_c and σ_t are the uniaxial compressive and tensile strengths of the rock, respectively. The right side of formula (6) is the ratio of compressive stress to tensile stress of layered strata mass (compression-tension ratio). Brook believed that the compression-tension ratio of sandstone is 15 [35], and Sheorey by statistics obtains that the compression-tension ratio of sandstone is between 7 and 39, with an average of 14.9 [36]. Sun [37] has tested the compression-tension ratio of common rocks with different water contents. The measured results are shown in Table 2. The compression-tension ratio of rock blocks in the laboratory is about 10, and in general, the compressive strength of dried rock > natural rock > saturated rock.

3. Height of Water-Flowing Fracture Zone in the Overburden

3.1. Maximum Relative Subsidence. The deflection-thickness ratio δ is defined as the ratio of the maximum relative subsidence of the strata to the thickness of the layered strata. Then, the left side (criterion value) of formula (6) becomes

$$f(\delta) = \frac{40}{(4 - 5\delta)(2 - \delta)}. \quad (7)$$

The relationship between function f and δ is shown in Figure 5. It indicates that the greater the deflection-thickness ratio (maximum relative subsidence), the easier it is for the strata to break and vice versa. The maximum relative subsidence of hard rock is directly related to the mining height and bulking coefficient and is directly proportional to the mining height and inversely proportional to the bulking coefficient. In addition, it can be seen from the range of the rock compression-tension ratio that fractures will vertically penetrate the layered strata in the area indicated by the thick black line in Figure 5.

The key of equation (7) is to calculate the deflection-thickness ratio that is composed of the thickness and the maximum relative subsidence of layered strata. The thickness of layered strata can be obtained from the borehole histogram, which is an easy parameter to get. The maximum relative subsidence is equal to the mining height subtracting the bulking height of the caving zone and the unloading dilation of the layered strata above the caving zone, which are explained separately below.

3.1.1. Bulking Height of the Caving Zone. The bulking height h_p of the caving zone is determined by the height H_k of the caving zone and the bulking coefficient K_p . The height of the caving zone is generally determined by actual measurement. When no measured data is available, the height can

TABLE 3: Empirical formula for calculating the height of caving zone.

Lithology of overburden (uniaxial compressive strength and main rock name) (MPa)	Calculation formula (m)
Hard (40-80, quartz sandstone, limestone, conglomerate)	$(100M/2.1M + 16) \pm 2.5$
Medium-hard (20-40, sandstone, argillaceous limestone, sandy shale, shale)	$(100M/4.7M + 19) \pm 2.2$
Weak (10-20, mudstone, argillaceous sandstone)	$(100M/6.2M + 32) \pm 1.5$
Very weak (<10, bauxite, weathered mudstone, clay, sandy clay)	$(100M/7.0M + 63) \pm 1.2$

TABLE 4: Coefficient of crushing and swelling of loose rock (coal).

Rock	$\varphi \leq 0.5$	$0.5 < \varphi \leq 1.25$	$1.25 < \varphi \leq 2.5$	$2.5 < \varphi \leq 5$	$5 < \varphi \leq 10$
Coal (weak)	1.28	1.22	1.17	1.15	1.14
Sandstone (medium hard)	1.2	1.18	1.15	1.13	1.11
Limestone (hard)	1.25	1.21	1.16	1.14	1.12

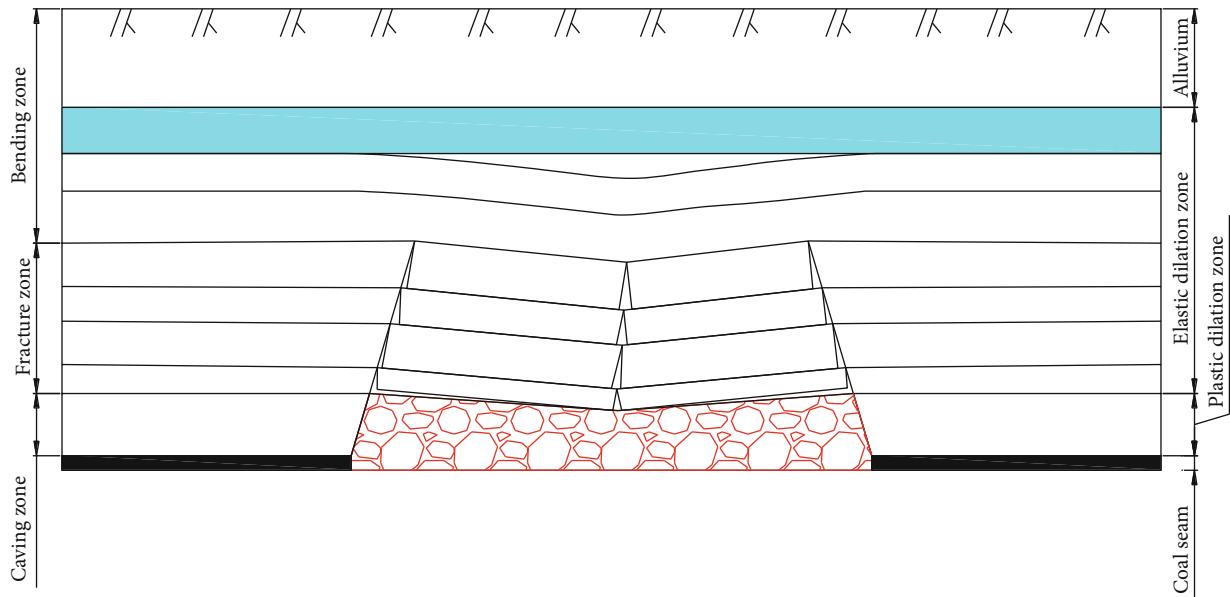


FIGURE 6: Diagram of three zone division.

be calculated according to the empirical formula given in Table 3 [38], in which M is the mining height.

The bulking coefficient of the caving zone can be obtained from laboratory test results as shown in Table 4. The diameter φ (mm) of the block is shown in Table 4, from which it can be seen that the coefficient of the bulking of the caving zone is between 1.1 and 1.3. With the height of the caving zone and the bulking coefficient, the breakage height of the caving zone can be calculated by the following formula:

$$h_p = H_k(K_p - 1). \quad (8)$$

3.1.2. Unloading Dilation of Rock Strata above the Caving Zone. Traditionally, the overburden has been transformed into the caving zone, fracture zone, and bend zone according to the fracture state. The research shows that after coal mining, the rock strata from different layers of coal seam

have different dilation characteristics, and on this basis, the overburden is divided into the plastic dilation zone and the elastic dilation zone [39], as shown in Figure 6. It can be seen that the unloading dilation of rock strata above the caving zone is elastic dilation. Therefore, the unloading dilation of rock strata above the caving zone can be calculated by the coefficient of elastic dilation K_t . If the height of the elastic dilation zone is H_t , the unloading dilation of rock strata above the caving zone is

$$h_t = H_t(K_t - 1). \quad (9)$$

3.2. Height of Water-Flowing Fracture Zone of the Overburden. Fractures are important channels for conducting water in layered strata. After the mining of the coal seam, the overburden will distribute fractures of different states. Among them, interconnected fractures are the way for the overburdened confined aquifer to enter the mining working faces, which will seriously threaten human and

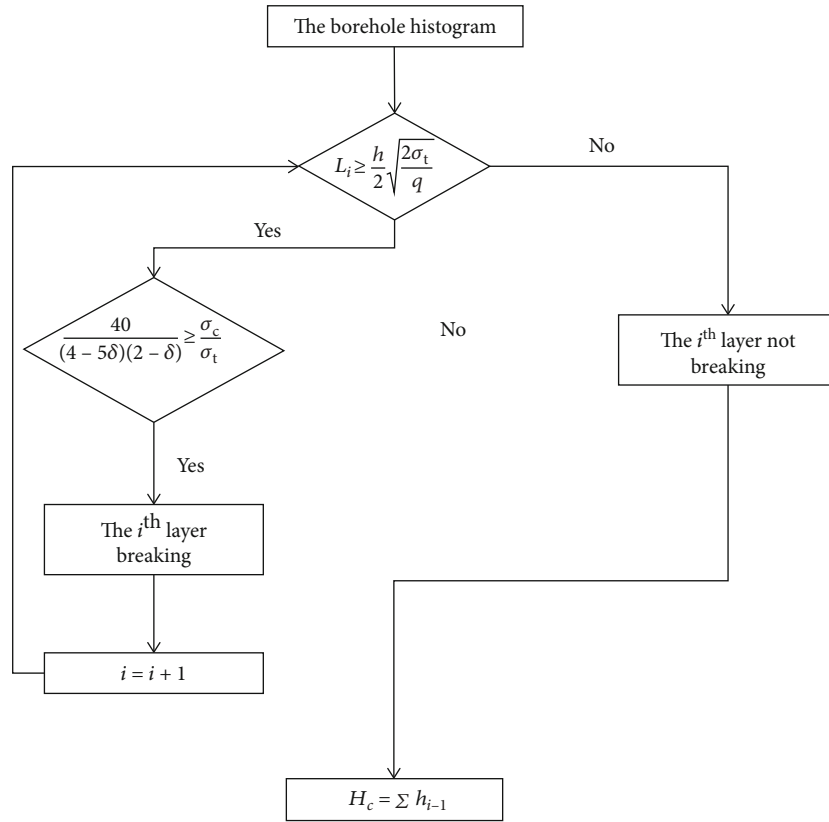


FIGURE 7: Discrimination process of height of water-flowing fracture zone in the overburden.

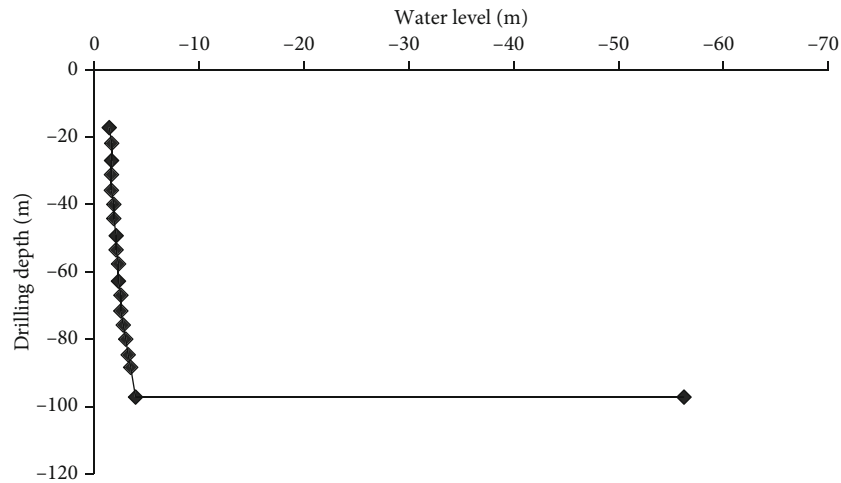


FIGURE 8: The change of water level of the drilling borehole in the water inrush area.

financial safety. Therefore, it is of great significance to predict the height of the water-flowing fracture zone for ensuring safe mining of coal mines.

There are two main methods for predicting the height of the water-flowing fracture zone. The first one is the statistical empirical formula based on a large number of measured data. This method cannot reflect the special overburden structure and breaking characteristics, and the calculation results are too small. The second method is based on the location of the PKS (will be defined fol-

lowing) to predict the height of the water-flowing fracture zone, which is a lack of the interpretation of the fracture mechanics mechanism of the layered strata. In order to predict the height of the water-flowing fracture zone based on the discrimination formula of interconnected vertical fractures in this paper, the fractures of layered strata are explained in terms of mechanical mechanism.

The method of predicting the height of the water-flowing fracture zone based on the discrimination formula of interconnected vertical fractures is as follows: (1) firstly, it needs

No.	h (m)	H (m)	Lithology	KS type	Columnar
1	97.96	97.96	Conglomerate		Orange
2	1.40	99.36	Kern stone		Red
3	3.87	103.23	Kern stone		Red
4	10.62	113.85	Siltstone		Blue
5	8.88	122.73	Argillaceous sandstone		Light Blue
6	3.86	126.59	Post stone		Purple
7	5.90	132.49	Sandy mudstone		Yellow
8	12.92	145.41	Siltstone		Red
9	3.30	148.71	Siltstone		Red
10	32.70	181.41	Medium sandstone	PKS	Grey
11	1.18	182.59	1 ⁻¹ coal		Black
12	0.87	183.46	Sandy mudstone		Yellow
13	0.12	183.58	Seam		Black
14	1.25	184.83	Sandy mudstone		Yellow
15	0.10	184.93	Seam		Black
16	4.30	189.23	Siltstone		Red
17	2.20	191.43	Sandy mudstone		Yellow
18	0.11	191.54	Lack		White
19	2.69	194.23	Sandy mudstone		Yellow
20	0.30	194.53	1 ⁻² up coal		Black
21	9.78	204.31	Siltstone	SKS	Red
22	9.60	213.91	Mudstone		Green
23	1.32	215.23	Mudstone		Green
24	5.92	221.15	1 ⁻² coal		Black

(a)

No.	h (m)	H (m)	Lithology	KS type	Columnar
1	115.45	115.45	Conglomerate		Orange
2	20.06	135.51	Argillaceous siltstone		Light Blue
3	15.30	150.81	Coarse-grained stone	PKS	Red
4	3.15	153.96	Argillaceous siltstone		Light Blue
5	8.20	162.16	Sandy mudstone		Yellow
6	4.40	166.56	Post stone		Purple
7	18.18	184.74	Argillaceous sandstone		Light Blue
8	12.50	197.24	Medium sandstone	SKS	Grey
9	10.64	207.88	Sandy mudstone		Yellow
10	8.55	216.43	Silty claystone		Light Orange
11	5.30	221.73	Post stone		Purple
12	10.47	232.20	Sandy mudstone		Yellow
13	13.77	245.97	Post stone	SKS	Purple
14	4.78	250.75	1 ⁻² coal		Black

(b)

FIGURE 9: Histogram in water inrush and normal areas of 31401 working face of Bulianta Coal Mine [25]: (a) overburden histogram in water inrush area; (b) overburden histogram in normal area.

TABLE 5: Values in water inrush and normal areas in 31401 working face of Bulianta Coal Mine.

Type	M (m)	H_p (m)	K_p (m)	h_p (m)	H_t (m)	K_t (m)	h_t (m)	Δ (m)	h (m)	δ	f
Water inrush	5.92	8.61	1.1	0.86	25.21	1.009	0.23	4.40	32.70	0.14	6.52
Normal	4.78	11.53	1.2	2.36	83.63	1.009	0.75	1.67	15.3	0.11	6.13

to collect the borehole histogram of the mining faces and then (2) judge whether the stratum is broken according to the discrimination formula. If it is not broken, it is not included in the height of the water-flowing fracture zone. If it is broken, it will become part of the water-flowing fracture zone. The flow chart for predicting the height of the water-flowing fracture zone is shown in Figure 7.

However, according to the theory of key strata (KS), the KS refer to the hard strata which control the movement of local layers or all layers up to the surface. The former is called the subkey strata (SKS), and the latter is called the primary key strata (PKS) [32]. According to the definition of the KS, the prediction method of the height of the water-flowing fracture zone based on the discrimination formula of interconnected vertical fractures only needs to judge whether the SKS or the PKS is broken. If the SKS is broken, the strata under its control will also be broken, and the water-flowing fracture zone will develop to the bottom of the upper KS at least. If the PKS is broken, the whole overburden is broken, and the water-flowing fracture zone develops to the surface.

4. Engineering Verification

The Shendong Mining Area, located in the transition zone between the Maowusu Desert and the hilly and gully area of Loess Plateau, belongs to an arid area. The aquifer of the Quaternary Salawusu Formation above the bedrock beneath the desert cover contains valuable diving water, which is the only aquifer in the upper part of the coal seam currently being mined in the mining area.

The 31401 fully-mechanized mining face is the first working face of 1⁻² coal mining in the fourth district, with a designed mining height of 4.5-5.0 m and a comprehensive mechanical mining method of full collapse with longwall retraction. The working face adopts a 4.3/5.5 m two-pillar shielded hydraulic support manufactured by JOY Company with rated working resistance of 8670 kN.

During the period from the cut line to 1600 m in the 31401 working face, the water inflow of the working face is normal, generally 50-80 m³/h, but when the working face is advanced to 1650 m, the water inflow of the working face reaches 200 m³/h. Thereafter, in the range from 1650 m to 2552 m, the roof sprinkler and seepage in the goaf have been continuous. During this period, there were two large water inrushes, and the working face was flooded in a short time, resulting in a 2 m depth of local water inundation, two 48 h shutdowns, and 400 m³/h maximum water inrush.

The borehole flushing fluid loss observation method is a traditional and reliable method to determine the depth of water-flowing fracture zone and caving zone of overlying strata after mining. The height of the water-flowing fracture

zone can be directly measured through the loss of drilling fluid in the drilling process.

The water level in the drilling borehole was instantly lost from 3.85 m to 97.46 m at the bottom of the hole (Figure 8), so all the drilling fluid was lost. Through comprehensive analysis and judgment, the depth of the borehole at the top of the water-flowing fracture zone is 97.10 m. Since the ground elevation before mining is 1305 m, the floor elevation of the coal seam is 1061 m, that is, the mining depth of the coal seam is 244 m. Considering the influence of the 2.0 m surface subsidence and 4.4 m mining height of the coal seam, therefore, the height of the water-flowing fracture zone is 140.5 m.

The research shows that the water inrush is related to the position of PKS in the overburden [25]. The position of PKS is shown in Figure 9.

According to the histogram of the working face in Figure 9, the mining heights of the water inrush and the normal areas in the 31401 working face of the Bulianta Coal Mine are 5.92 m and 4.78 m, respectively. In addition, the lithologies of water inrush and normal areas are medium and hard, respectively, so the height of the caving zone can be calculated separately according to Table 3 without considering its error items. The bulking coefficient of soft rock is less than that of hard rock, so the bulking coefficients of the caving zone in the water inrush zone and normal zone are 1.15 and 1.2, respectively. The height of the elastic dilation zone in the water inrush and normal areas is the distance from the PKS to the top of the caving zone. The literature research shows that the elastic dilation coefficient of different strata is between 1.0090 and 1.0097 under 16 MPa pressure [40], and the elastic dilation coefficient is taken as 1.0090 in this paper. The calculated values of each parameter are shown in Table 5.

According to Table 5, the f value of water inrush area is 6.52, greater than that of the normal area of 6.13, and the PKS of the water inrush area is medium sandstone, while that of normal area is coarse-grained sandstone. According to the experimental results of Table 2, the compression-tension ratio of coarse-grained sandstone is larger than that of medium sandstone, so in the water inrush area, the values more easily meet the discrimination formula (6). It is worth noting that this discrimination formula is only qualitatively verified because the beam was assumed to be two-end fixed, which makes a big difference to the outcome and will be discussed in the future.+

5. Conclusions

Interconnected vertical fractures are the important channel to communicate confined aquifer and the working faces. Water inrush disasters will occur when interconnected

vertical fractures extend from the roof of the working face to the aquifer. Therefore, it is of great significance to study the evolution mechanism of interconnected vertical fractures for preventing and controlling water inrush disasters. This paper draws the following conclusions through similar simulation, theoretical analysis, and field verification methods:

- (1) Vertical fractures in layered strata are initiated because the tensile stress is greater than the tensile strength, but whether fractures penetrate the layered strata is determined by the compressive strength. When the compressive stress is greater than the compressive strength, the vertical fractures will penetrate a stratum
- (2) Whether a vertical fracture penetrates a stratum can be expressed by the value of the criterion of interconnected vertical fractures and compression-tension ratio of layered strata. When the value of the criterion of interconnected vertical fractures is greater than the compression-tension ratio, layered strata are broken. The value of the criterion of interconnected vertical fractures is expressed by maximum relative subsidence. The larger the maximum relative subsidence, the smaller the value of the criterion of interconnected vertical fractures
- (3) The value of the criterion of interconnected vertical fractures in the water inrush area of the 31401 working face of the Bulianta Coal Mine is larger than that in the normal area, while the compression-tension ratio is smaller than that in the water inrush area, so in the water inrush area, the values more easily meet the discrimination formula (6).

Data Availability

The data in the manuscript can be available on request through Changchun He, whose email address is hechangchun1987@126.com.

Conflicts of Interest

The authors declare that they have no known competing financial interests or personal relationships that could have appeared to influence the work reported in this paper.

Acknowledgments

This work was supported by the Research Start-Up Funding of Doctors in East China University of Technology-Prediction Method of Mining Subsidence by Combining Mechanics and Geometry (No. DHBK2019235), Transformation of Scientific and Technological Achievements Programs of Higher Education Institutions in Shanxi (TSTAP) (No. 2020CG050), Special Project of 2019 Plan for the Introduction of High-Level Scientific and Technological Talents in Development Zone of Lvliang City (Development of Automatic Disassembly Platform for Hydraulic Support Pin Shaft) (No. 2019102), Science and Technology Project of Lvliang City in 2019 (Pressure

Relief and Permeability Improvement Technology by Integrated Hydraulic Flushing and Cutting for Low Permeability Coal Seam Containing Methane) (No. GXZZDYF2019080), Natural Science Foundation of Shanxi Province-Mechanical Behaviour and Breaking Mechanism of Three-Axis Fracture of Weak and Fractured Coal Body in Coalbed Methane Mining (No. 201901D111330), and School-Level Teaching Reform and Innovation Projects of Luliang University in 2020 (No. JXGG202039).



References

- [1] Z. Shaotong, "Research on coal supply and demand trend and development intensity of China," *Coal Science and Technology*, vol. 48, no. S1, pp. 85–88, 2020.
- [2] L. Huang, H. Hao, X. Li, and J. Li, "Source identification of microseismic events in underground mines with interferometric imaging and cross wavelet transform," *Tunnelling and Underground Space Technology*, vol. 71, no. 1, pp. 318–328, 2018.
- [3] L. Huang, J. Li, H. Hao, and J. Li, "Micro-seismic event detection and location in underground mines by using convolutional neural networks (CNN) and deep learning," *Tunneling and underground space technology*, vol. 81, no. 11, pp. 265–276, 2018.
- [4] D. Li, "Mining thin sub-layer as self-protective coal seam to reduce the danger of coal and gas outburst," *Natural Hazards*, vol. 71, no. 1, pp. 41–52, 2014.
- [5] L. Shi, M. Qiu, Y. Wang, X. Qu, and T. Liu, "Evaluation of water inrush from underlying aquifers by using a modified water-inrush coefficient model and water-inrush index model: a case study in Feicheng coalfield, China," *Hydrogeology Journal*, vol. 27, no. 6, pp. 2105–2119, 2019.
- [6] B. Zhu, L. Wu, Y. Peng, W. Zhou, and C. Chen, "Risk assessment of water inrush in tunnel through water-rich fault," *Geotechnical & Geological Engineering*, vol. 36, no. 1, pp. 317–326, 2018.
- [7] W. Yang, X. Yang, Z. Fang et al., "Model test for water inrush caused by karst caves filled with confined water in tunnels," *Arabian Journal of Geosciences*, vol. 12, no. 24, pp. 749–760, 2019.
- [8] V. Palchik, "Analysis of main factors influencing the apertures of mining-induced horizontal fractures at longwall coal mining," *Geomechanics and Geophysics for Geo Energy and Geo-Resources*, vol. 6, no. 2, pp. 37–48, 2020.
- [9] H. Wang, D. Zhang, X. Wang, and W. Zhang, "Visual exploration of the spatiotemporal evolution law of overburden failure and mining-induced fractures: a case study of the Wangjialing coal mine in China," *Minerals*, vol. 7, no. 3, pp. 35–51, 2017.
- [10] C. Wang, N. Zhang, Y. Han, Z. Xiong, and D. Qian, "Experiment research on overburden mining-induced fracture evolution and its fractal characteristics in ascending mining," *Arabian Journal of Geosciences*, vol. 8, no. 1, pp. 13–21, 2015.
- [11] V. Palchik, "Experimental investigation of apertures of mining-induced horizontal fractures," *International Journal of Rock Mechanics & Mining sciences*, vol. 47, no. 3, pp. 502–508, 2010.
- [12] Y. Li, C. Wu, and B. Jang, "Effect of bedding plane on the permeability evolution of typical sedimentary rocks under triaxial compression," *Rock Mechanics Rock Engineering*, 2020.

- [13] M. Bai and D. Elsworth, "Some aspects of mining under aquifers in China," *Mining Science and Technology*, vol. 10, no. 1, pp. 81–91, 1990.
- [14] V. Palchik, "Formation of fractured zones in overburden due to longwall mining," *Environmental Geology*, vol. 44, no. 1, pp. 28–38, 2003.
- [15] C. O. Karacan, F. A. Ruiz, M. Cotè, and S. Phipps, "Coal mine methane: a review of capture and utilization practices with benefits to mining safety and to greenhouse gas reduction," *International Journal of Coal Geology*, vol. 86, no. 2-3, pp. 121–156, 2011.
- [16] A. Majdi, F. P. Hassani, and M. Y. Nasiri, "Prediction of the height of destressed zone above the mined panel roof in longwall coal mining," *International Journal of Coal Geology*, vol. 98, no. 62, pp. 62–72, 2012.
- [17] M. Rezaei, M. F. Hossaini, and A. Majdi, "A time-independent energy model to determine the height of destressed zone above the mined panel in longwall coal mining," *Tunneling and underground space technology*, vol. 47, no. 3, article S0886779815000097, pp. 81–92, 2015.
- [18] Y. Chen, G. Zhao, S. Wang et al., "A case study on the height of a water-flowing fracture zone above undersea mining: Sanshandao gold mine," *China Environmental earth sciences*, vol. 78, no. 4, pp. 122.1–122.15, 2019.
- [19] Y. Liu, Q. M. Liu, W. P. Li et al., "Height of water-conducting fractured zone in coal mining in the soil-rock composite structure overburdens," *Environmental Geology*, vol. 78, no. 7, 2019.
- [20] S. Wang, X. Li, and D. Wang, "Mining-induced void distribution and application in the hydro-thermal investigation and control of an underground coal fire: a case study," *Process Safety & Environmental Protection*, vol. 102, article S0957582016300908, pp. 734–756, 2016.
- [21] S. Wang, X. Li, and S. Wang, "Separation and fracturing in overlying strata disturbed by longwall mining in a mineral deposit seam," *Engineering Geology*, vol. 226, pp. 257–266, 2017.
- [22] Y. Sun, Z. Xu, and Q. Dong, "Monitoring and simulation research on development of water flowing fractures for coal mining under Xiaolangdi reservoir," *Chinese Journal of Rock Mechanics and Engineering*, vol. 28, no. 2, pp. 238–245, 2009.
- [23] X. Wang, J. Xu, and W. Zhu, "Influence of primary key stratum structure stability on evolution of water flowing fracture," *Journal of China Coal Society*, vol. 37, no. 4, pp. 606–612, 2012.
- [24] J. L. Xu, X. Z. Wang, W. T. Liu et al., "Influence of primary key stratum location on the height of water flowing fracture zone," *Chinese Journal of Rock Mechanics and Engineering*, vol. 28, no. 2, pp. 381–385, 2009.
- [25] X. Miao, X. Cui, J. Wang, and J. Xu, "The height of fractured water-conducting zone in undermined rock strata," *Engineering Geology*, vol. 120, no. 1-4, pp. 32–39, 2011.
- [26] X. Xie, L. Xibing, S. Xueyi et al., "Prediction of water-bearing fracture zone height by PCA-BP neural network model," *Journal of China Safety Science*, vol. 27, no. 3, pp. 100–105, 2017.
- [27] Z. Hongwei, Z. Zhu, H. Bingjie et al., "An improved FOA-SVM for predicting the height of water-conducted fractures," *Cssea*, vol. 23, no. 10, pp. 9–14, 2013.
- [28] T. Z. Yi, Q. Hongyan, and C. Yizhong, "The DM-L optimization model of water-conducting fracture zone based on sensitivity analysis," *Journal of Central China Normal University (Natural Science)*, vol. 48, no. 5, pp. 673–676, 2014.
- [29] Z. Mao, L. Wenzhe, and H. Chunjuan, "Prediction of height of water flowing fractured zone based on APSO-LSSVM model," *Journal of Liaoning Technical University (Natural Science)*, vol. 39, no. 1, pp. 34–40, 2020.
- [30] Y.-z. Luan, J.-t. Li, X.-h. Ban, C.-y. Sang, C.-q. Zhang, and D.-p. Ma, "Observational research on the height of water flowing fractured zone in repeated mining of short-distance coal seams," *Journal of Mining & Safety Engineering*, vol. 27, no. 1, pp. 139–142, 2010.
- [31] W. Zhang, D. S. Zhang, L. X. Wu, and H. Z. Wang, "On-site radon detection of mining-induced fractures from overlying strata to the surface: a case study of the Baoshan coal mine in China," *Energies*, vol. 7, no. 12, pp. 8483–8507, 2014.
- [32] Q. minggao and S. p. Xu jialin, "Mine pressure and strata control," *China university of mining and technology press*, 2010.
- [33] H. zhongjie, "Dimension of angle contact surface of rotating end of loading fractured rock block," *Mine pressure and roof management*, pp. 29–31, 1999.
- [34] M. Xiexing, "Stability analysis of the main roof during the first weighting in longwall face," *journal of china university of mining and technology*, no. 3, pp. 91–95, 1989.
- [35] N. Brook, "The measurement and estimation of basic rock strength," *Rock Testing and Site Characterization*, pp. 41–66, 1993.
- [36] P. R. Sheorey, "Empirical Rock Failure Criteria," *CRC Press*, 1997.
- [37] S. Li, "Discussion on the relationship between rock tensile strength and uniaxial compressive strength," *Agricultural science and technology and information*, no. 14, pp. 48–49, 2012.
- [38] State Bureau of Coal Industry, *Regulations of buildings, water, railway and main well lane leaving coal pillar and press coal mining*, Beijing: China Coal Industry Publishing House, 2000.
- [39] J. Xu, Q. Wei, X. Dayang et al., "Accumulative effect of overburden strata expansion induced by stress relief," *Journal of China Coal Society*, vol. 45, no. 1, pp. 35–43, 2020.
- [40] Z. Weibing, Y. Shengchao, and X. Jingmin, "Influence of the elastic dilatation of mining-induced unloading rock mass on the development of bed separation," *Energies*, vol. 11, no. 4, pp. 785–801, 2018.

Research Article

Investigation on the Ground Pressure Induced by Hard Roof Fracturing at Different Layers during Extra Thick Coal Seam Mining

Rui Gao ^{1,2}, Jingxuan Yang ³, Tiejun Kuang^{3,2} and Hongjie Liu²

¹College of Mining Engineering, Taiyuan University of Technology, Shanxi 030024, China

²Datong Coal Mine Group Co. Ltd., Datong 037000, China

³State Key Laboratory of Coal Resources and Safe Mining, China University of Mining & Technology, Xuzhou 221116, China

Correspondence should be addressed to Rui Gao; cumtgaorui@163.com and Jingxuan Yang; jxyangcumt@126.com

Received 1 June 2020; Revised 25 July 2020; Accepted 25 September 2020; Published 5 November 2020

Academic Editor: Yingchun Li

Copyright © 2020 Rui Gao et al. This is an open access article distributed under the Creative Commons Attribution License, which permits unrestricted use, distribution, and reproduction in any medium, provided the original work is properly cited.

The fracturing of hard roofs in different layers would result in complex ground pressure on the working face, such as supports collapsed and severe roadway deformation. However, the mechanism of the ground pressure induced by hard roof fracturing in different layers is still unclear. In the paper, a physical model of a 20 m extrathick coal seam mined with hard roofs existing was established based on the physical simulation similarity criterion. The overburden fracturing structure, abutment stress distribution, and failure characteristics of the coal body were monitored by a noncontact strain measurement system and resistance strain gauges, to reveal the mechanism of ground pressure induced by hard roof fracturing. Furthermore, *on-site* measurement was used to monitor and analyze the ground pressure affected by hard roofs in different levels. The results provide a theoretical basis for the control of ground pressure in extrathick coal seam mining with hard roofs.

1. Introduction

In coal seam mining, when hard roofs exist in the overburden, the breaking span is usually huge due to their great strength, thus would result in a strong ground pressure in the mining panel such as support failure and roadway deformation. Through numerical simulation and field measurement, He et al. and Wang et al. found that the large suspended area of hard roofs would easily cause a stress concentration and failure in advanced coal rock mass [1, 2]. When hard roof fracturing, the intensity of the energy release is higher due to the large breaking span. Ning et al. [3] studied the fracture energy of thick hard roofs by means of microseismic monitoring. The results showed that the high energy released by the breaking of thick and hard roofs is the main reason causing strong ground pressure. Bednarek and Majcherczyk [4] discussed the rock mass characteristics which influence the choice of support. Zhao et al. [5] studied the fracture characteristic of an extrathick and hard roof based on the long beam theory. Li et al. [6] studied the periodic

breaking span of a thick and hard roof based on the Vlasov plate theory and the strain energy distribution characteristics of coal seam under a thick hard roof. Shen et al. [7] revealed the strong response for an entry influenced by overlying hard roof and the influence of the hard roof fracture position on the entry. Ju and Xu [8] analyzed the structural characteristics of overlying hard strata and ground pressure in the panel after a 7 m-thick coal seam mining. Xia et al. [9] studied the characteristics and mechanism of ground pressure in the mining panel under the combined action of hard roofs and a coal pillar. It was found in the above research that, because of the high strength and large overhang of hard roofs, the stress concentration is obviously on the hard roofs, which has a significant impact on the working face and roadway in the mining panel.

During the mining of an extrathick coal seam under hard roofs, due to the large mining thickness, the migration range of overburden is wide. The results showed that the failure height could reach 200 to 350 m during a 14 to 20 m-thick coal seam mining [10–12]. Field monitoring showed that

the fracturing of hard roofs in a large space frequently resulted in the occurrence of ground pressure on the working face with a different strength and manifestation [13, 14]. The ground pressure on the working face shows the characteristics of “long and short duration”, of which the “long duration” interval was 30 to 60 m and the “short duration” interval was 12 to 20 m, the pressure intensity increased when the “long duration” occurred. However, there was no obvious regularity in the occurrence of strong ground pressure such as support failure or severe roadway deformation [15, 16]. Li et al. [17] found that the huge mining thickness of an extrathick coal seam results in a larger mobile space of high-level hard roofs, and the sliding instability of the high-level hard roofs would cause strong ground pressure. Singh et al. [18] studied the strata movement during underground mining of a thick coal seam. According to Li et al.’s research [19], the rotational movement of key strata in the overburden had a direct impact on the supports in the working face, and the dynamic loading induced by the instability of the Voussoir beam structure was analyzed. Xie and Xu [20] analyzed the influence law of different thickness and level of hard roofs on the peak value and influencing range of the abutment stress. Yu et al. and Chen et al. conducted field measurement on the deformation characteristics and stress distribution law of a roadway in the process of mining an extrathick coal seam under hard roofs [21, 22]. Guo et al. [23] studied the relationship between the support resistance and the overhanging distance of hard roofs, and criteria for reasonable selection of support resistance were given. Mondal et al. [24] monitored the strata behavior in the destressed zone of a shallow Indian longwall panel with hard sandstone cover using mine-microseismicity and borehole televiewer data. However, other scholars also invest in the hard roof research [25, 26]; the results show that the occurrence of the hard roof has a direct impact on the ground pressure in the working face and is complex.

In terms of the mining conditions of extrathick coal seams with hard roofs, failure and instability of hard roofs will occur gradually within a large space, which may further result in frequent occurrence of ground pressure of different strengths on the working face. Most of the aforementioned scholars focused on the structural characteristics of the overburden or worked from the perspective of mining pressure development but did not do in-depth research on the mechanism of ground pressure induced by the fracturing of hard roofs at different levels. According to the key stratum theory [27, 28], the lower level key stratum is close to the coal seam, and the breaking span is small. With increase in the occurrence level, the breaking span and the strength of the high-level key stratum increase accordingly. Therefore, due to the influence of the distance from the coal seam and the breaking span, the failure and instability of key strata at the low and high levels may have different effects on the ground pressure. In addition, the large breaking span and instability of high-level hard roofs may cause the occurrence of strong ground pressure on the working face and could have interaction with the lower key layers. A physical simulation experiment could reflect the structural characteristics of the overburden and its influence on the abutment stress of a min-

ing panel directly and was considered an effective means to study the overburden structure and ground pressure in coal seam mining [29, 30]. Based on the exploitation of extrathick coal seams with hard roofs, for this paper, the research method of physical simulation was adopted to study the fracture law of key strata and the strength of ground pressure induced by the breakage and instability of strata in different levels.

2. Experimental Model

2.1. Geological Background. The carboniferous #3–5 extrathick coal seams were mainly mined in Tashan coal mine of the Datong mining area, with a thickness of 14 to 20 m. The method of top coal caving mining was adopted. The buried depth of the coal seam is 400 to 800 m, and the overburden is covered with multilayer hard roofs with the compressive strength of 60 to 120 MPa. Due to the large mining thickness of the coal seam, the fracturing of multiple layers in a large space resulted in a frequently strong ground pressure, accompanied by the supports crashed. The floor heave was severe within 10 to 40 m in advanced roadway, and the maximum floor heave was up to 0.8 m. The roof subsidence was up to 0.6 m, the shotcrete of the two sides of the roadway was seriously cracked, and the advanced individual props were seriously damaged, as shown in Figure 1.

Taking the #8216 working face in Tashan coal mine as an example, the Carboniferous #3–5 coal seam was mined, the average thickness of the coal seam was 16 m, and the buried depth and inclination of the coal seam was 418 to 522 m and 1 to 3°, respectively. The length and mining distance of the working face was 230 and 1500 m, respectively, and the coal seam was covered with multiple hard roofs.

Based on the statistics of the strong ground pressure during the mining process, as shown in Table 1, it can be found that the pressure on the working face was relatively strong within the initial mining range of 214 m. The roadway deformation and hydraulic props collapsed were serious in advanced 35 m, the support resistance increased obviously and was even accompanied by safety valve opening. In the later mining process, the strength of the ground pressure was relatively weakened, the influence range was reduced to 10 m in an advanced roadway, and the deformation was also reduced.

2.2. Basic Parameters of the Model. In order to study the effect of key stratum fracturing on the ground pressure in the working face, the method of physical simulation was used in the laboratory. Taking the #8101 working face as the background, the Carboniferous #3–5 coal seam was mined. The thickness and burial depth of the coal seam was 20 and 470 m, respectively. The coal seam dip was 1 to 3°, and the length and mining distance of the working face was 230 and 1500 m, respectively. The frame size of the physical model in the laboratory was 2.5 × 0.2 × 1.9 m (length × width × height). The geometric similitude ratio of the designed model was 150 : 1; the actual height of the model was 1.47 m, which simulated a height of 220 m. Materials including sand, calcium carbonate, and gypsum were used

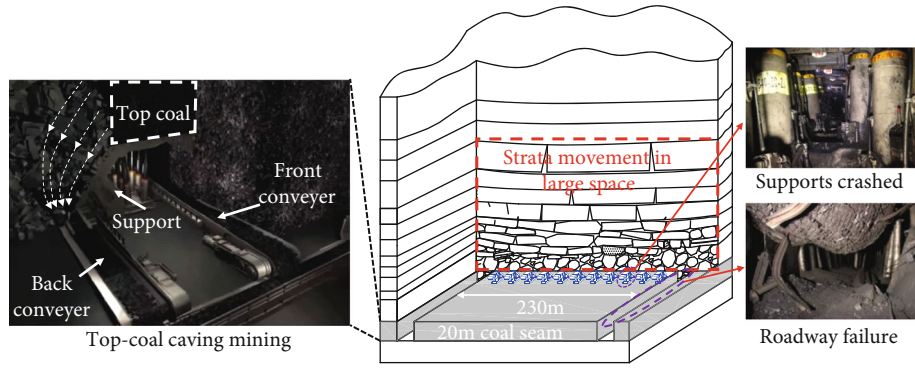


FIGURE 1: Caving mining method and strong ground pressure in the working face.

TABLE 1: Statistics of the strong ground pressure on the working face.

Data	Mining distance (m)	Phenomenal description
2015.11.13	110.2	Strong ground pressure 10 m in advance of the working face, the floor heave was 0.3–0.4 m, rib heave was serious: 0.4 m; the resistance of supports #45 to #67 was high.
2015.11.21	168.8	A stronger ground pressure happened, the advanced range of influence was 10–20 m, roof subsidence and floor heave was severe, ten hydraulic props were dumped, roof subsidence 0.3–0.4 m, floor heave 0.45 m, the resistance of supports #23 to #35 and #56 to #71 were high.
2015.12.30	214.5	A stronger ground pressure occurred 12–35 m in advance of the roadway, thirty hydraulic props were dumped; the roadway deformation in horizontal and vertical direction was 0.5 and 0.8 m, respectively. The resistances of supports in the working face were all higher and the safety valves opened at supports #45 to #67.
2016.1.14	450.0	Strong pressure happened 10 m in advance of the working face, an obvious deformation occurred in the roadway, one hydraulic prop was bent 8 m in advance working face; the resistance of supports increased obviously.
2016.2.13	635.0	Ground pressure occurred, the pressure was concentrated 10 m in advance, the floor heave was 0.2–0.3 m, and roof subsidence was not obvious.
2016.3.18	736.0	Ground pressure occurred. At 15 m in advance, the floor heave was 0.2–0.4 m, rib heave and roof subsidence were not obvious, and five props inclined.

TABLE 2: Basic parameters of the physical similarity model.

Items	Parameters	Items	Parameters
Length of model	2.5 m	Mining distance	2.1 m
Thickness of model	0.2 m	Model boundary	10 cm
Height of model	1.47 m	Excavation steps	45
Coal seam thickness	13.3 cm	Excavate distance once	5 cm
Geometric ratio	150 : 1	Excavate time interval	0.5 h
Weight ratio	1.667 : 1	Excavation time	21 h
Stress ratio	250 : 1	Compensation stress	0.027265 MPa

to simulate the overlying rock. The weight ratio, time ratio, and stress ratio were 1.667 : 1, 12.25 : 1, and 250 : 1, respectively. The actual working time of the working face is 16 hours per day, and the maintenance work time is 8 hours. The advanced distance is about 4 m per day. Therefore, the actual working time and excavation distance on the model can be calculated to be every 78 min and 2.6 cm each time. The thickness of the overlying unladen strata was 272.65 m; then, the weight of the overburden rock is 6.816 MPa, and the magnitude of the compensation stress added to the upper

part of the similar model is 0.027265 MPa. The basic parameters of the model are shown in Table 2.

Table 3 shows the physical and mechanical parameters of the coal and rock mass [31]. According to the similarity ratio, the matching parameters of each rock formation in the model are shown in Table 3. The rock layers No.32, No.27, No.22, No.16, and No.9 above the coal seam are calculated to be the key strata based on the key stratum theory [27, 28], which are the emphasis to be studied in this test.

TABLE 3: Parameters of the coal and rock.

No.	Lithology	Depth (m)	Thickness (m)	Simulated thickness (cm)	Compression strength (MPa)	Simulated strength (KPa)	Matching number	Weight (kg)	Sand (kg)	Calcium carbonate (kg)	Gypsum (kg)	Water (kg)
1	Gritstone	267.01	4.9	3.3	28.34	113.36	373	29.4	22.05	5.15	1.65	4.20
2	Packsand	271.91	12.1	8.1	90.53	362.12	437	72.6	58.08	4.36	8.13	8.07
3	Siltite	284.01	3.7	2.5	33.6	134.4	737	22.2	19.43	0.83	1.70	2.47
4	Gritstone	287.71	2.8	1.9	23.1	92.4	473	16.8	13.44	2.35	0.81	1.87
5	Pebblestone	290.51	4.5	3.0	35.6	142.4	555	27	22.50	2.25	1.88	3.00
6	Gritstone	295.01	5	3.3	25.9	103.6	755	30	26.25	1.88	1.64	3.33
7	Conglomerate	300.01	5	3.3	37.74	150.96	455	30	24.00	3.00	2.40	3.33
8	Siltite	305.01	5	3.3	24.1	96.4	473	30	24.00	4.20	1.44	3.33
9	Packsand	310.01	12.9	8.6	80.21	320.84	337	77.4	58.05	5.81	10.16	11.06
10	Gritstone	322.91	5	3.3	26.6	106.4	755	30	26.25	1.88	1.64	3.33
11	Medium sandstone	327.91	4.8	3.2	30.3	121.2	655	28.8	24.69	2.06	1.76	3.20
12	Siltite	332.71	3	2.0	35.87	143.48	555	18	15.00	1.50	1.25	2.00
13	Conglomerate	335.71	5.2	3.5	25.6	102.4	755	31.2	27.30	1.95	1.71	3.47
14	Pebblestone	340.91	5.4	3.6	32.3	129.2	737	32.4	28.35	1.22	2.48	3.60
15	Siltite	346.31	4	2.7	23.57	94.28	473	24	19.20	3.36	1.15	2.67
16	Packsand	350.31	12.2	8.1	80.27	321.08	337	73.2	54.90	5.49	9.61	10.46
17	Gritstone	362.51	5.7	3.8	32.87	131.48	737	34.2	29.93	1.28	2.62	3.80
18	Conglomerate	368.21	3.3	2.2	22.9	91.6	473	19.8	15.84	2.77	0.95	2.20
19	Siltite	371.51	3	2.0	33.85	135.4	737	18	15.75	0.68	1.38	2.00
20	Medium sandstone	374.51	4.83	3.2	30.24	120.96	655	28.98	24.84	2.07	1.77	3.22
21	Siltite	379.34	5	3.3	23.23	92.92	473	30	24.00	4.20	1.44	3.33
22	Packsand	384.34	10.12	6.7	65.53	262.12	337	60.72	45.54	4.55	7.97	8.67
23	Pebblestone	394.46	5.6	3.7	30.23	120.92	373	33.6	25.20	5.88	1.89	4.80
24	Mudstone	400.06	5.8	3.9	25.3	101.2	755	34.8	30.45	2.18	1.90	3.87
25	Conglomerate	405.86	3.8	2.5	29.13	116.52	373	22.8	17.10	3.99	1.28	3.26
26	Siltite	409.66	5.25	3.5	36.56	146.24	555	31.5	26.25	2.63	2.19	3.50
27	Packsand	414.91	9.1	6.1	55	220	437	54.6	43.68	3.28	6.12	6.07
28	Siltite	424.01	6.4	4.3	30.73	122.92	655	38.4	32.91	2.74	2.35	4.27
29	Conglomerate	430.41	3.2	2.1	23.6	94.4	473	19.2	15.36	2.69	0.92	2.13
30	Medium sandstone	433.61	4	2.7	30.43	121.72	655	24	20.57	1.71	1.47	2.67
31	Gritstone	437.61	5.05	3.4	38.6	154.4	455	30.3	24.24	3.03	2.42	3.37
32	Packsand	442.66	9.44	6.3	55.53	222.12	437	56.64	45.31	3.40	6.34	6.29

TABLE 3: Continued.

No.	Lithology	Depth (m)	Thickness (m)	Simulated thickness (cm)	Compression strength (MPa)	Simulated strength (KPa)	Matching number	Weight (kg)	Sand (kg)	Calcium carbonate (kg)	Gypsum (kg)	Water (kg)
33	Sandy mudstone	452.1	5.65	3.8	33.3	133.2	737	33.9	29.66	1.27	2.60	3.77
34	Conglomerate	457.75	3.2	2.1	23.34	93.36	473	19.2	15.36	2.69	0.92	2.13
35	Siltstone	460.95	4.5	2.9	21.07	84.28	573	26.4	22.00	3.08	1.10	2.93
36	Mudstone	465.35	4.3	2.9	17.36	69.44	773	25.8	22.58	2.26	0.85	2.87
37	#3-5 coal seam	469.65	20	13.3	15.94	63.76	773	120	105.00	10.50	3.94	13.33
38	Gritstone	489.65	3	2.0	43.87	175.48	637	18	15.43	0.77	1.54	2.00

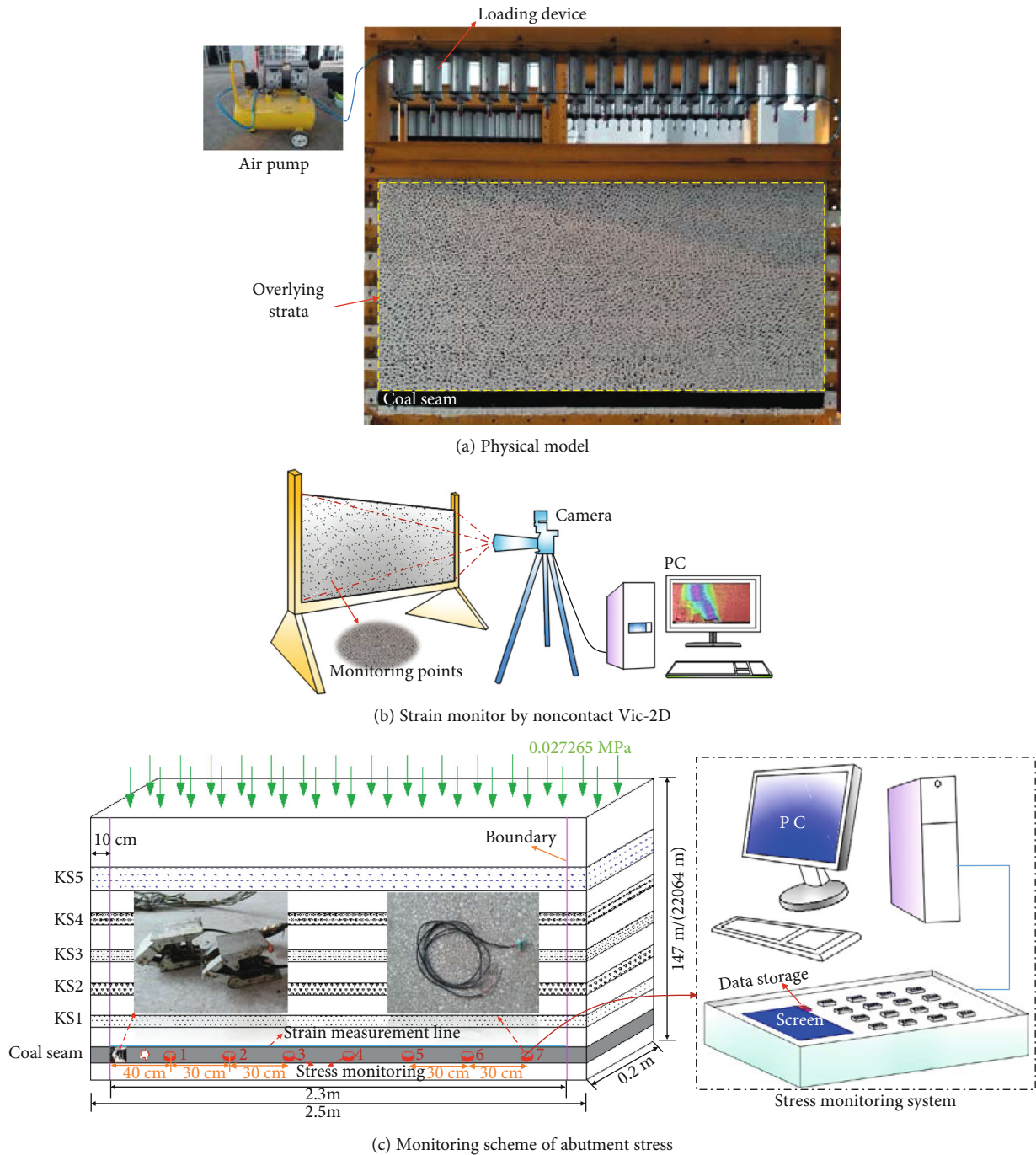
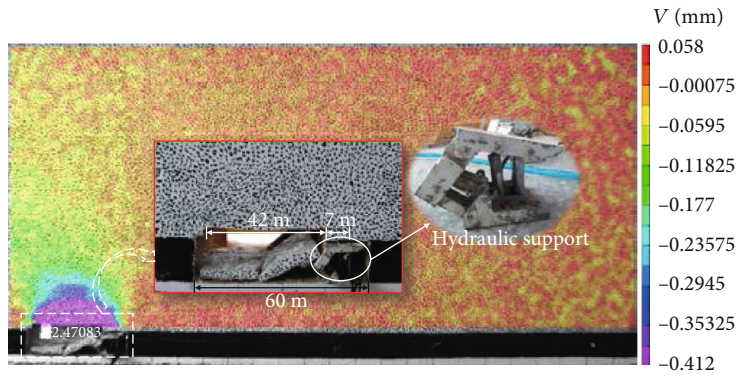


FIGURE 2: Monitoring system of the physical model.

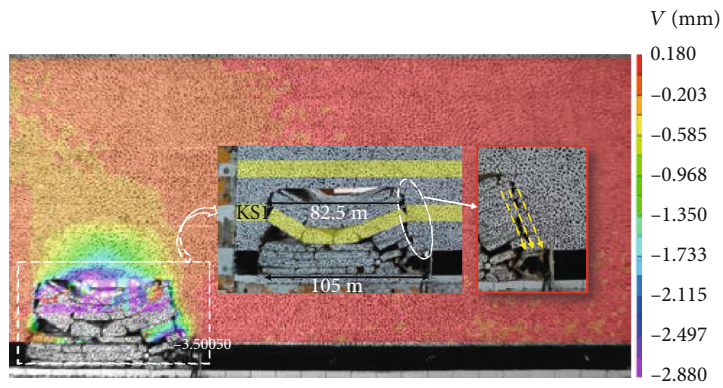
2.3. Monitoring System. The monitoring system schematic is shown in Figure 2. Taking five key strata as the research objects (17, 45, 75, 107, and 146 m vertically above the coal seam), the thickness of each key layer was 9.44, 9.1, 10.12, 12.2, and 12.9 m, respectively. In order to monitor the influence of each key layer breaking on the distribution characteristics of the abutment stress in the coal body, a total of seven strain monitors were arranged at intervals of 30 cm in the coal seam. The first measurement point was 40 cm from the open-off cut of the working face. In order to truly reflect

the structural characteristics of the overburden, a small simulated hydraulic support was placed on the working face.

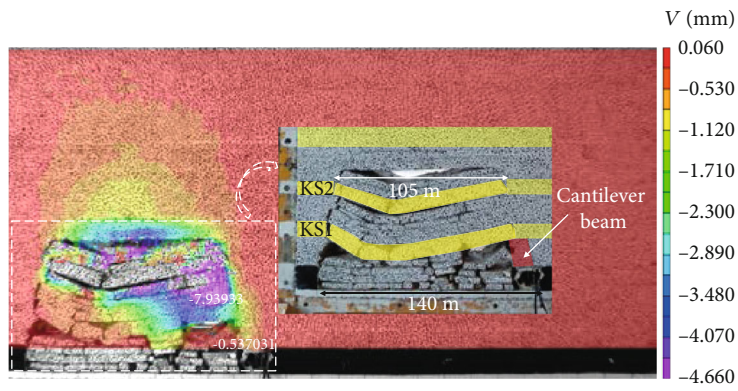
A noncontact strain monitoring system (Vic-2D) was used to monitor the overburden displacement timely, as seen in Figure 2(b). Black flecks were randomly sprayed onto the model surface, and a camera was used to capture movement of the flecks in real time as the overburden moved. The displacement of the flecks was obtained by postprocessing software and was inverted to the displacement-changes law of the overlying strata.



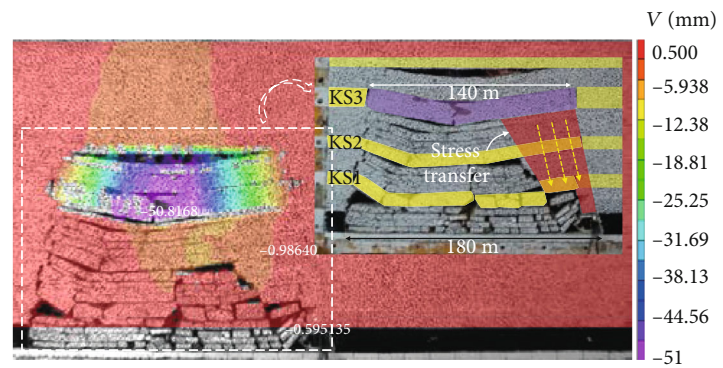
(a) Fracturing of immediate roof



(b) Fracturing of KS1

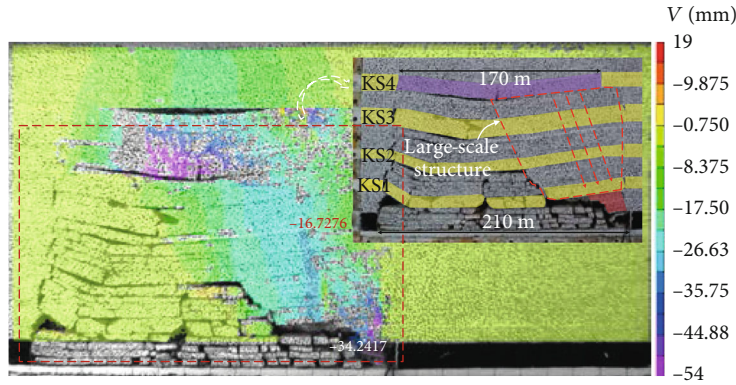


(c) Fracturing of KS2

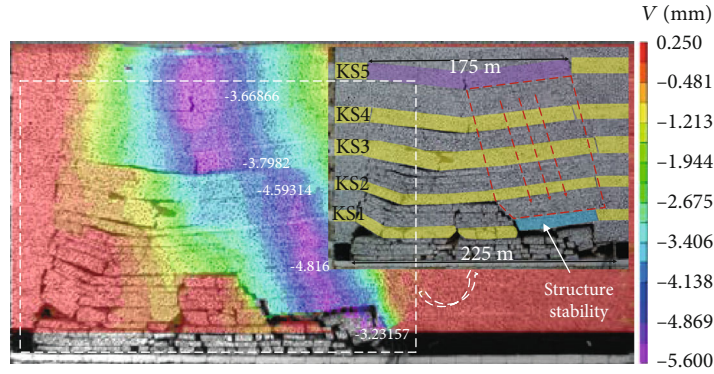


(d) Fracturing of KS3

FIGURE 3: Continued.



(e) Fracturing of KS4



(f) Fracturing of KS5

FIGURE 3: Structure and displacements during the fracturing of strata at different levels.

TABLE 4: The calculated elasticity modulus of strain gauges.

No.	Weight P (N)	Strain ε (10^{-3})	Elasticity modulus E (GPa)
1	32	210	0.121322414
	64.4	412	0.124451178
2	32	230	0.110772639
	64.4	428	0.119798798
3	32	330	0.077205173
	64.4	540	0.09495164
4	32	290	0.087854162
	64.4	690	0.074309979
Avg.			0.101333248

3. Analysis of Experimental Results

3.1. Structural Characteristics of the Overlying Strata. The mined interval of the simulated working face was 5 cm every 30 minutes. The structural characteristics and overburden displacement variation during hard roof fracturing at different levels were obtained, as shown in Figure 3.

When the working face was mined 60 m, the roof broke for the first time, with a breaking span of 42 m. The length of the broken block above the support was 7 m, and its weight was borne by the support. After the roof broke for the first

time, the overlying unbroken strata flexed and sank by 20 cm, as shown in Figure 3(a).

When the working face was mined for 105 m, KS1 broke for the first time, with a breaking span of 82.5 m. The fracturing of KS1 caused synchronous rotation and collapse of lower strata and resulted in vertical variation of 0.42 m in the support. This increased the working resistance of the support, as shown in Figure 3(a).

When the working face was mined for 140 m, KS2 broke for the first time, and the initial fracturing step of KS2 was up to 105 m. The fracturing of KS2 caused synchronous failure and instability of the underlying strata, resulting in rotary movement, as shown in Figure 3(c). The intension was low during the KS2 breakage and the KS1 structure remained stable, which reduced the strength of the KS2 breakage. According to Figure 3(c), we could see that the vertical displacement of the support was only 0.22 m and the rock layer above the support showed the structural characteristics of a composite cantilever beam.

When the working face was mined 180 m, KS3 broke for the first time, with a breaking span of 140 m and a rotary subsidence of 7.5 m. The thickness of KS3 was 10.12 m. Due to its large thickness, breaking span, and rotary subsidence, the energy release intensity was relatively high during the breakage of KS3, thus resulting in synchronous rotary movement of the underlying strata. As shown in Figure 3(d), the drop-off in the support reached 0.9 m.

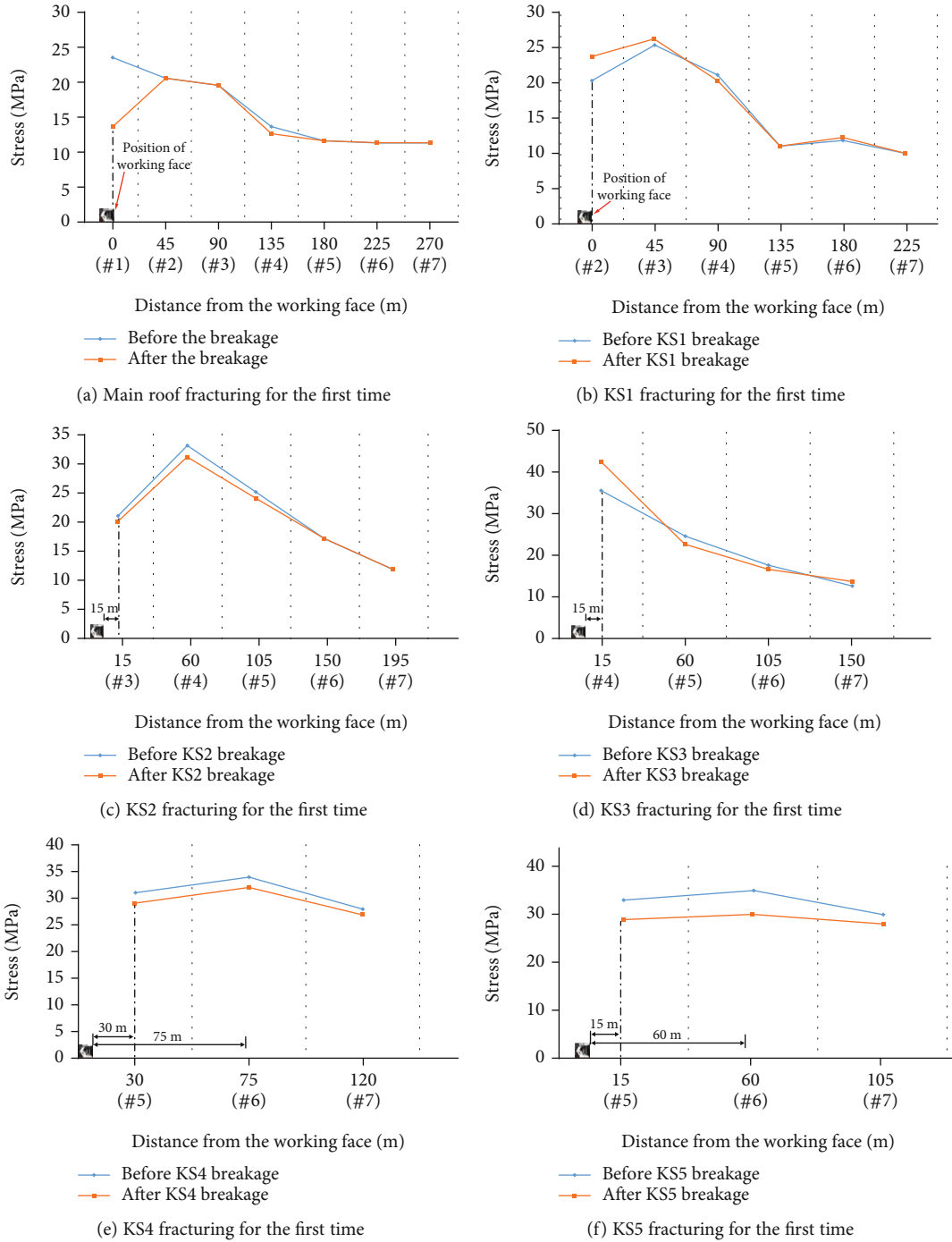


FIGURE 4: Stress distribution during the overburden fracturing.

When the working face was mined to 210 m, KS4 in the high and far field broke for the first time. The breaking step distance was up to 170 m and the thickness of KS4 was 12.2 m. The high intensity of the KS4 fracturing resulted in the synchronous rotation of KS1, KS2, and KS3. The rotary movement of this large rock structure acted on the cantilever beam structure above the support, resulting in a 2.5 m vertical displacement of the cantilever beam structure and intense pressure on the support, as shown in Figure 3(e).

When the working face was mined for 225 m, KS5 broke for the first time. The breaking step distance was 175 m, and the thickness of KS5 was 12.9 m. In the case of the KS5 fracturing, although the intensity was relatively high, due to its long distance from the coal seam, the fracturing of KS5 did not cause instability rotation in all the underlying strata. As shown in Figure 3(f), the cantilever structure of KS1 maintained its own stability, thus having a certain protective effect on the working face. However, due to the high breaking

TABLE 5: Range of stress influence before and after strata fracturing.

	Before breaking		After breaking	
	Peak stress (MPa)	Influence range (m)	Action range (m)	Stress variation (MPa)
KS1	30	45	> 0	24 → 28
KS2	33	60	< 15	—
KS3	25	60	> 15	36 → 43
KS4	34	120	< 30	—
KS5	33	105	> 15	—

intensity of KS5, the vertical displacement at the immediate roof was still up to 0.48 m, and the breaking impact on the support was slightly lower than that of KS4.

Based on the comprehensive analysis of the overlying strata fracturing, it was found that due to the large mining thickness of the coal seam and the wide range of overlying rock migration, the key strata of KS1 to KS5 all broke, and the key strata at different levels had different influences on the working face. The fracturing of KS1 and KS2 in the near field formed a cantilever beam and masonry beam structure, which resulted in a slight ground pressure on the working face. When the far field KS4 broke, due to its great thickness and wide breaking span of 170 m, the ground pressure on the working face was most intense. The intension of the KS5 fracturing was also high with a breaking span of 175 m, but due to the long distance from the coal seam and the stable structure in the lower strata, the effects of KS5 fracturing on the working face was reduced compared to KS4, and the working face showed slightly strong ground pressure.

3.2. Variation of Abutment Stress in the Coal Body. The above analysis was made based on the overburden structural characteristics and displacements when the key strata broke at different layers. The influence of the occurrence and fracturing of key strata on the stress distribution in the coal body could be gained based on the monitored strain value; the calculation process is shown in the following. The strain gauges in the coal seam were numbered 1-7 along the mining direction of the working face, as shown in Figure 2(c). Four strain gauges were selected to decide the elasticity modulus, as shown in Table 4. Thus, based on the elasticity modulus and monitored strain, the stress variation at each monitor point were gained, as shown in Figure 4.

The abutment stress distribution during the first fracturing of the main roof is shown in Figure 4(a), where the No.1 monitoring point is next to the working face. After the main roof breaks, the stress at the No.1 monitoring point decreases from 24 to 14 MPa, indicating that the stress concentration on the coal wall is reduced to a certain extent. When KS1 broke for the first time, the No.2 monitoring point is close to the working face. Due to the rotation of KS1, the stress at the coal wall increases from 24 to 28 MPa, as shown in Figure 4(b). During the first breaking of KS2, the No.3 monitoring point is 15 m from the working face, and the strata fracturing has little impact on the abutment stress, as shown in Figure 4(c). When KS3 first broke, the No.4 monitoring point is 15 m from the working face. As a result of KS3 break-

ing, the stress value at No.4 monitoring point increases from 36 to 43 MPa. Meanwhile, at monitoring points No.5 and No.6, the stress decreases slightly, as shown in Figure 4(d), indicating that the stress concentration in the advanced 60 m is reduced. When KS4 breaks, monitoring points No.5 and No.6 are 30 m and 75 m, respectively, away from the working face. The stress values at monitoring points #5 and #6 are reduced from 31 and 34 MPa to 29 and 32 MPa, respectively, as shown in Figure 4(e). When KS5 broke for the first time, monitoring points No.5 and No.6 is 15 m and 60 m, respectively, away from the working face. The stress change law is similar to that for KS4, as shown in Figure 4(f).

The influence of hard roof fracturing at different layers on the peak stress and the range of the abutment stress in the advanced coal body were obtained statistically (see Table 5).

As shown in Table 5, with the development of the overburden caving height, the abutment stress and the influence range in advanced coal seam increase accordingly. The peak stress in the advanced coal body increases slightly (30 to 34 MPa), and the advanced range of influence increases greatly. Before the critical fracturing of KS4, the range of influence of the advanced abutment stress reaches 120 m.

When the key strata broke, the strata rotations squeezed the coal body near the working face, causing the stress on the coal body to rise. Affected by the strain monitoring layout interval, it was impossible to accurately calculate the range of influence in the advanced coal body affected by the fracturing of each key layer, but we could still find from Table 5 that the fracturing of KS4 resulted in a strong compression zone of 15–30 m in advance of the working face. With the increase of the distance between the key stratum and coal seam, the buffer action of the underlying strata was strengthened, and the strong compression area in the advanced coal body was weakened accordingly (e.g., KS5). As the distance between the key stratum and the coal seam decreased, the breaking span and the range of the advanced compression zone decreased accordingly (e.g., KS3).

3.3. The Advanced Failure Zone. Based on the noncontact strain monitoring system, the strain variation characteristics of the advanced coal body were gained through the strain measurement line to further study the range and degree of influence on strong compression areas caused by the fracturing of each key layer.

Strain measurement lines were arranged at the interface of the coal seam and immediate roof to obtain strain variation of the coal body after the fracturing of KS1 to KS5, as shown in Figure 2; the results are shown in Figure 5. The abscissa represents the location of monitoring points along the mining direction, the leftmost side of the model is the coordinate zero point, and the coordinate axis increases along the mining direction of the working face accordingly. The length of the model is 375 m.

The boundary pillar of 15 m was retained in the model. When the working face was mined to 105 (corresponds to abscissa $x = 120$ m), KS1 broke, and a statistical strain curve of the coal body before and after KS1 was obtained, as shown

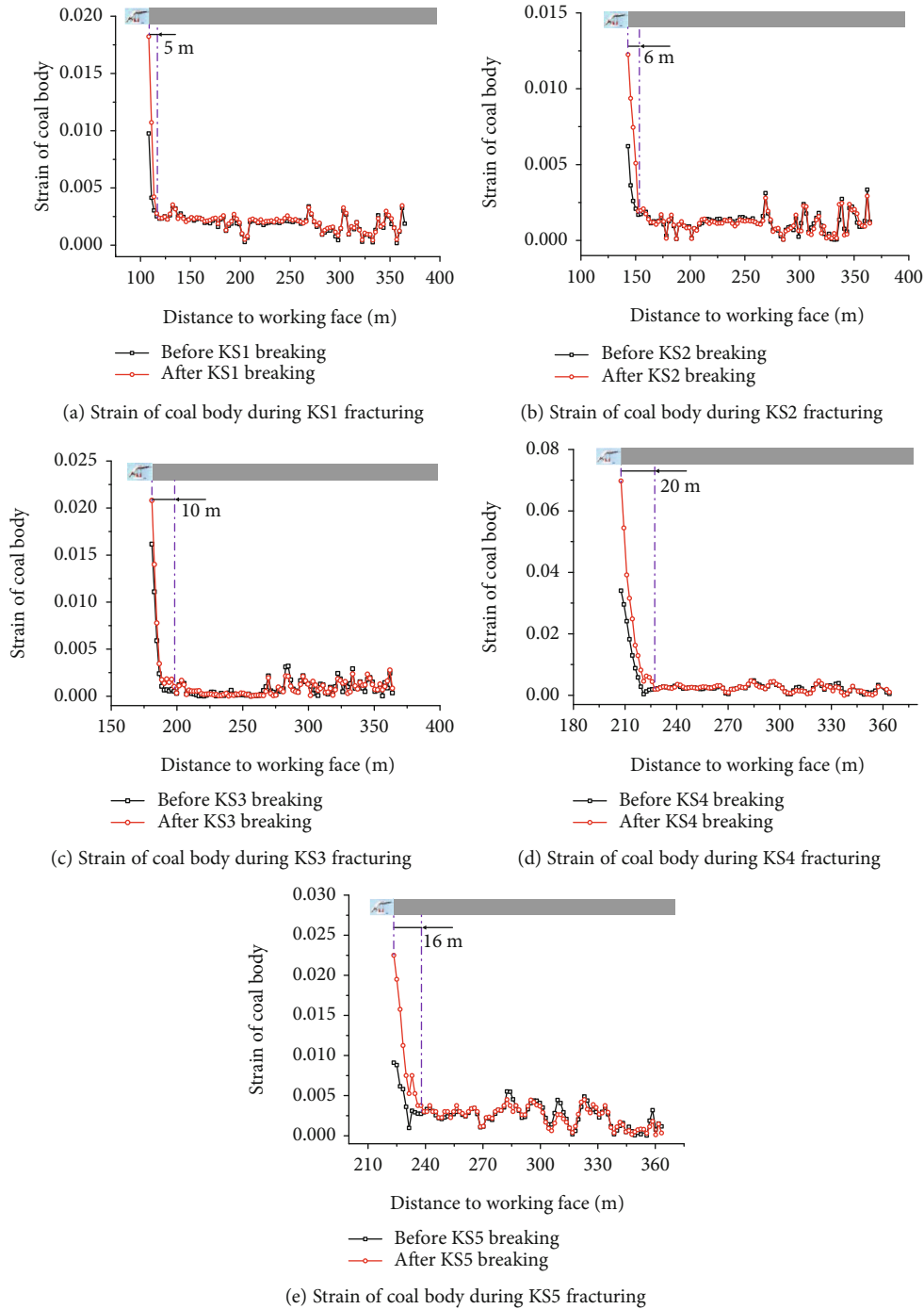


FIGURE 5: Strain of coal body during fracturing of different key strata.

in Figure 5(a). The simulated support is 15 m long. From Figure 5(a), we can find that the coal body is compressed in the advanced 5 m, that is, the impact range of the KS1 fracturing on the advanced coal body is about 5 m. Similarly, the strain curve during KS2 fracturing is obtained as shown in Figure 5(b). Compared with KS1, the compressed zone in the advanced coal body caused by KS2 fracturing slightly increases, reaching 6 m. As shown in Figure 5(c), the compressed range in the advanced coal body during the fracturing of KS3 reaches 10 m. According to the coal body failure

criterion obtained from the test, the fracturing of KS3 resulted in 3 m of advanced coal body failure.

When KS4 broke, due to its high breaking strength and strong impact, the strain on the coal body was greatly increased, as shown in Figure 5(d). The maximum strain variable in the advanced coal body is up to 0.07, which could easily cause the crash of supports and the advanced influence range of 20 m. The coal body is severely compressed in the advanced 20 m. Similar to KS4, the action of KS5 fracturing on the advanced coal body is also relatively serious, but the

range of influence and action intensity are lower than that of KS4, as shown in Figure 5(e). The range of influence from the KS5 fracturing on the advanced coal body is 16 m.

4. Discussion

According to Figure 5, the range of influence and degree of overburden-key-strata fracturing in the advanced coal body are statistically obtained as shown in Figure 6. It can be seen from Figure 6 that, with an increase of the occurrence level of key strata, the impact strength of each key layer fracturing on the coal body increases accordingly. The fracturing of KS4 has the strongest effect on the advanced coal body, with the maximum strain variation of the coal body reaching 0.036 and the influence range reaching 20 m. With further increase of the distance between the key layer and the coal seam, taking KS5 as an example, the action strength of KS5 on the advanced coal body decreases, the change of strain on the coal body is 0.013, and the range of influence decreases to 16 m. As the distance between the key strata and the coal seam gets closer, the intensity of the key strata fracturing will also decrease due to decrease of the breaking span of the key strata. Taking KS3 as an example, the maximum change in the strain on the advanced coal body caused by the KS3 fracturing is 0.005, and the range of influence is 10 m.

Combined with the above studies, we can find that the impact strength of the fracturing of key strata on the mining panel pressure is directly related to the breaking span, occurrence location, and distribution of the underlying strata. The physical simulation studies show that KS4 fracturing had the strongest effect on the mining panel pressure, followed by KS5. The ratio of the distance between KS4 and KS5 from the coal seam and the coal seam thickness are 5.35:1 and 7.3:1, respectively.

From Figure 6, we can see that the compression induced in the coal body by the fracturing of KS4 and KS5 are greater than that of KS1–KS3. This is mainly because during the fracturing of KS1 to KS3, the lower bed-separation space and key layer rotation angle are big. Although the impact velocity of the key strata is larger, the breaking step of key strata is relatively small. In addition, the key strata are more likely to act on the goaf caved rock mass, as shown in Figure 7(a), which has a weak impact on the mining panel pressure.

As the overburden fracture height develops, the bed-separation space under the far field key strata decreases, and the impact velocity after the breaking of key strata decreases accordingly. However, the kinetic energy after a far field key strata break is huge due to its great thickness, high strength, and large breaking interval, coupled with small rotary space. The kinetic energy of strata fracturing mostly acts on the lower overburden, resulting in a synchronous rotary movement of the lower overburden rock strata. This causes strong ground pressure in the advanced coal body and working face, as shown in Figure 7(b).

With further increase of the vertical distance between the key strata and the coal seam, the bed-separation space is further reduced, and the energy transferred from the key strata fracturing to the coal seam is weakened accordingly. Strata fracturing does not necessarily cause instability and synchro-

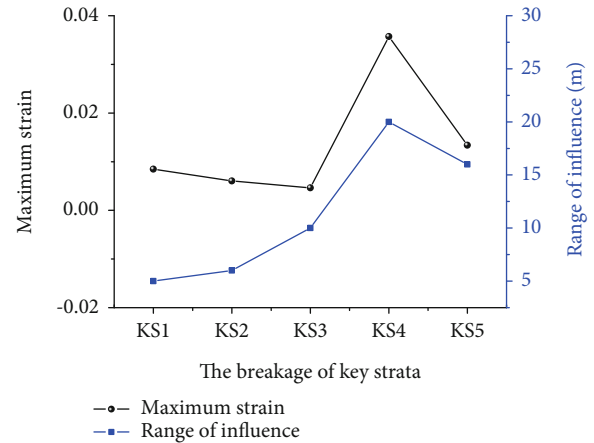


FIGURE 6: Effect on the coal body of fracturing of different levels of hard strata.

nous movement of the underlying strata. According to the above physical simulation analysis, in this geological condition, the KS4 fracturing (in the far field) has the most serious impact on the working face, followed by KS5. The vertical distance from the coal seam of KS4 and KS5 are 107 and 146 m, respectively, and the ratio of the vertical distance to the coal-seam thickness is 5.35 and 7.3, respectively.

At the same time, we also used the method of field measurement to study the ground pressure in the mining of extrathick coal seams with hard roofs [13, 15]. The thickness of the coal seam was 19 m, and the method of top coal caving mining was adopted. The strata movement measurement points were arranged in key strata at different levels (22, 51, and 104 m away from the coal seam). The thickness of the three key strata was 12, 9.8, and 23 m from the bottom up. Meanwhile, the resistance characteristics of the working face support were recorded in real time, as shown in Figure 8. The monitoring results showed that the support resistance in the working face increased with fracturing of the two key strata, which were 22 and 51 m away from the coal seam at the low level, and the dynamic load coefficient of the support was 1.15 and 1.34, respectively. The pressure duration was 7 h and 16 h, respectively, and the working face had no obvious indications of strong ground pressure. When the 23 m-thick key layer (which was 104 m from the coal seam) broke, the #35–95 supports in the working face were crushed, and the dynamic load coefficient of the supports reached 1.54. The pressure duration reached 43 h, and the ratio of the distance between the highest key layer and the coal seam, to the coal seam thickness, was 5.47.

Thus, due to the great thickness of the extrathick coal seam, the range of the overburden movement was huge and the key strata at all different levels broke. Among them, the hard roof in the far field had the largest breaking span and highest energy intensity. This resulted in the synchronous rotation of the underlying strata, which is the main reason of the occurrence of strong ground pressure on the working face. Based on the above studies, it was found that thick, hard strata, with the ratio of the distance from the coal seam to the coal seam thickness between 5.3 and 7.3, have the most

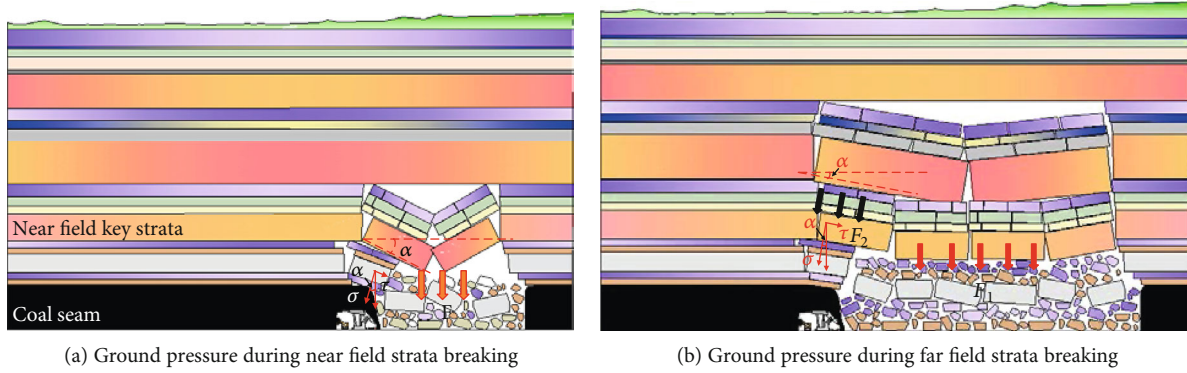


FIGURE 7: Ground pressure during the breaking of strata at different levels.

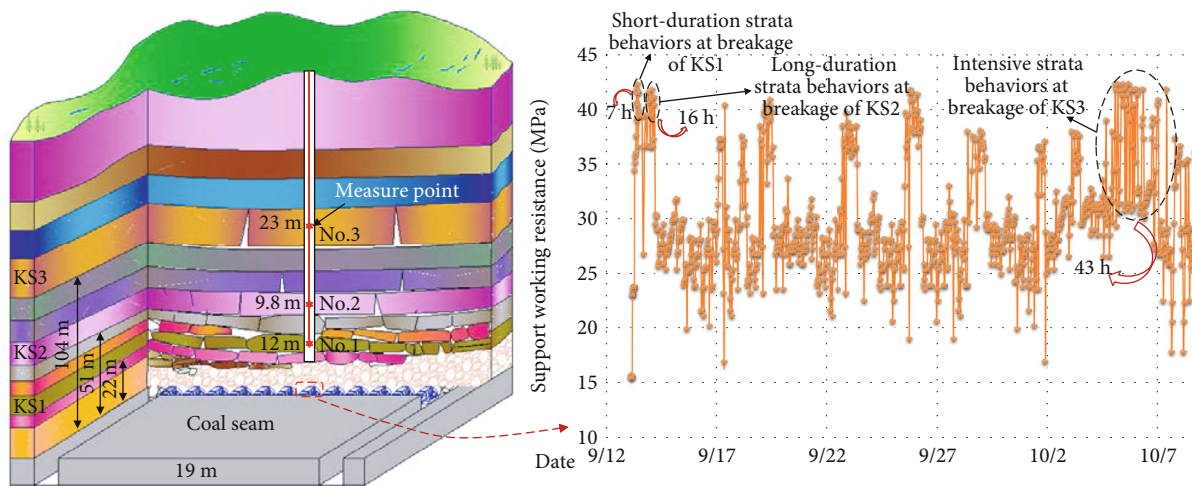


FIGURE 8: Ground pressure during the breaking of strata at different levels.

serious impact on the working face. That is, when a 20 m-thick coal seam is mined, the thick and hard roof, which is within the range of 106 m to 146 m away from the coal seam, has the greatest impact on the mining pressure of the working face. The results provide a theoretical basis for guiding the selection of the hard roof control layer in a large space and improve the reliability of the hard roof control. The results show that the high-level hard strata are the main factor causing strong ground pressure in the stope, which breaks through our idea of control ground pressure by low-level rock weakening and improves the reliability and accuracy of ground pressure control. For the control of high-level hard strata, traditional technical means cannot reach that height. Thus, our team developed a technical method of ground fracturing to control high-level hard strata and achieved success. This will be introduced in the follow-up researches.

5. Conclusions

- (1) Based on physical simulation criterion, a physical model for the mining of an extrathick coal seam with hard roofs was established and the methods of non-contact strain monitor and abutment stress monitoring were used to study the structure characteristics

and the corresponding ground pressure of hard roofs at different levels

- (2) The research showed that the lower key strata mostly collapse into goaf, thus having less impact on the working face and advanced coal body. During the thick, hard key stratum in the far field breaking, the large fracturing span and high strength result in instability and synchronous rotation of the underlying strata, thus causing the supports crashed and advanced coal body damaged, which is the main reason for the occurrence of strong ground pressure
- (3) Combined with the physical simulation and field measurement studies, it is found that the characteristics of ground pressure vary with the levels at which the key strata occur. During the mining of an extrathick coal seam with hard roofs, thick and hard strata with a ratio (of the distance from the coal seam to seam thickness) of 5.3–7.3 have the greatest influence on the working face

Data Availability

The data and material are transparent and included in the paper.

Conflicts of Interest

The authors declare that there is no conflict of interest.

Acknowledgments

We are grateful Yun Zhang, Lixin Lan, Baiyi Li, and Hao Yan for their assistance in physical simulation experiment. This work was supported by the State Key Research Development Program of China (grant numbers 2018YFC0604500, 2018YFC0604506), China Postdoctoral Science Foundation (grant number 2019M651080), applied basic research project of Shanxi Province (grant number 201901D211030), Scientific and Technological Innovation Programs of Higher Education Institutions in Shanxi (STIP) (grant number 2019L0208), Major Program in Shanxi Province (grant number 20191101015), and Independent Research Project of State Key Laboratory of Coal Resources and Safe Mining, CUMT (SKLCRSM18X006).

References

- [1] J. He, L. M. Dou, Z. L. Mu, A. Y. Cao, and S. Y. Gong, "Numerical simulation study on hard-thick roof inducing rock burst in coal mine," *Journal of Central South University*, vol. 23, no. 9, pp. 2314–2320, 2016.
- [2] G. F. Wang, S. Y. Gong, Z. L. Li, L. M. Dou, W. Cai, and Y. Mao, "Evolution of stress concentration and energy release before rock bursts: two case studies from Xingan coal mine Hegang China," *Rock Mechanics and Rock Engineering*, vol. 49, no. 8, pp. 3393–3401, 2016.
- [3] J. G. Ning, J. Wang, L. S. Jiang, N. Jiang, X. S. Liu, and J. Q. Jiang, "Fracture analysis of double-layer hard and thick roof and the controlling effect on strata behavior: a case study," *Engineering Failure Analysis*, vol. 81, pp. 117–134, 2017.
- [4] L. Bednarek and T. Majcherczyk, "An analysis of rock mass characteristics which influence the choice of support," *Geomechanics and Engineering*, vol. 21, no. 4, pp. 371–377, 2020.
- [5] T. Zhao, C. Y. Liu, K. Yetilmeszo, B. S. Zhang, and S. Zhang, "Fractural structure of thick hard roof stratum using long beam theory and numerical modeling," *Environment and Earth Science*, vol. 76, no. 21, p. 751, 2017.
- [6] X. L. Li, C. W. Liu, Y. Liu, and H. Xie, "The breaking span of thick and hard roof based on the thick plate theory and strain energy distribution characteristics of coal seam and its application," *Mathematical Problems in Engineering*, vol. 2017, 14 pages, 2017.
- [7] W. L. Shen, J. B. Bai, X. Y. Wang, and Y. Yu, "Response and control technology for entry loaded by mining abutment stress of a thick hard roof," *International Journal of Rock Mechanics and Mining Sciences*, vol. 90, pp. 26–34, 2016.
- [8] J. F. Ju and J. L. Xu, "Structural characteristics of key strata and strata behaviour of a fully mechanized longwall face with 7.0m height chocks," *International Journal of Rock Mechanics and Mining Sciences*, vol. 58, pp. 46–54, 2013.
- [9] B. W. Xia, J. L. Jia, B. Yu, X. Zhang, and X. L. Li, "Coupling effects of coal pillars of thick coal seams in large-space stopes and hard stratum on mine pressure," *International Journal of Mining Science and Technology*, vol. 27, no. 6, pp. 965–972, 2017.
- [10] B. Yu, J. Zhao, T. J. Kuang, and X. B. Meng, "In situ investigations into overburden failures of a super-thick coal seam for longwall top coal caving," *International Journal of Rock Mechanics and Mining Sciences*, vol. 78, pp. 155–162, 2015.
- [11] B. Yu, J. Zhao, and H. T. Xiao, "Case study on overburden fracturing during longwall top coal caving using microseismic monitoring," *Rock Mechanics and Rock Engineering*, vol. 50, no. 2, pp. 507–511, 2017.
- [12] H. W. Zhang, Z. J. Zhu, L. J. Huo, Y. Chen, and B. J. Huo, "Overburden failure height of superhigh seam by fully mechanized caving method," *Journal of China Coal Society*, vol. 39, no. 5, pp. 816–821, 2014.
- [13] B. Yu, R. Gao, X. B. Meng, and T. J. Kuang, "Near-far strata structure instability and associate strata behaviors in large space and corresponding control technology," *Chinese Journal of Rock Mechanics and Engineering*, vol. 37, no. 5, pp. 1134–1145, 2018.
- [14] J. X. Yang, C. Y. Liu, and B. Yu, "Mechanism of complex mine pressure manifestation on coal mining work faces and analysis on the instability condition of roof blocks," *Acta Geodynamica et Geomaterialia*, vol. 12, no. 1, pp. 101–108, 2015.
- [15] Y. W. Lan, R. Gao, B. Yu, and X. B. Meng, "In situ studies on the characteristics of strata structures and behaviors in mining of a thick coal seam with hard roofs," *Energies*, vol. 11, no. 9, p. 2470, 2018.
- [16] B. Yu, "Behaviors of overlying strata in extra-thick coal seams using top-coal caving method," *Journal of Rock Mechanics and Geotechnical Engineering*, vol. 8, no. 2, pp. 238–247, 2016.
- [17] H. M. Li, D. J. Jiang, and D. Y. Li, "Analysis of ground pressure and roof movement in fully-mechanized top coal caving with large mining height in ultra-thick seam," *Journal of China Coal Society*, vol. 39, no. 10, pp. 1956–1960, 2014.
- [18] R. Singh, P. K. Mandal, A. K. Singh, R. Kumar, J. Maiti, and A. K. Ghosh, "Upshot of strata movement during underground mining of a thick coal seam below hilly terrain," *International Journal of Rock Mechanics and Mining Sciences*, vol. 45, no. 1, pp. 29–46, 2008.
- [19] Z. Li, S. C. Yu, W. B. Zhu et al., "Dynamic loading induced by the instability of voussoir beam structure during mining below the slope," *International Journal of Rock Mechanics and Mining Sciences*, vol. 132, article 104343, 2020.
- [20] J. L. Xie and J. L. Xu, "Effect of key stratum on the mining abutment pressure of a coal seam," *Geosciences Journal*, vol. 21, no. 2, pp. 267–276, 2017.
- [21] B. Yu, Z. Zhang, T. J. Kuang, and J. R. Liu, "Stress changes and deformation monitoring of longwall coal pillars located in weak ground," *Rock Mechanics and Rock Engineering*, vol. 49, no. 8, pp. 3293–3305, 2016.
- [22] Y. Chen, S. Q. Ma, and Y. Yu, "Stability control of underground roadways subjected to stresses caused by extraction of a 10-m-thick coal seam: a case study," *Rock Mechanics and Rock Engineering*, vol. 50, no. 9, pp. 2511–2520, 2017.
- [23] W. B. Guo, H. S. Wang, G. W. Dong, L. Li, and Y. G. Huang, "A case study of effective support working resistance and roof support technology in thick seam fully-mechanized face mining with hard roof conditions," *Sustainability*, vol. 9, no. 6, p. 935, 2017.
- [24] D. Mondal, P. N. S. Roy, and M. Kumar, "Monitoring the strata behavior in the distressed zone of a shallow indian longwall panel with hard sandstone cover using mine-microseismicity and borehole televiewer data," *Engineering Geology*, vol. 271, article 105593, 2020.
- [25] D. Szurgacz and J. Brodny, "Analysis of the influence of dynamic load on the work parameters of a powered roof

- support's hydraulic leg," *Sustainability*, vol. 11, no. 9, article 2570, 2019.
- [26] P. Konicek and P. Waclawik, "Stress changes and seismicity monitoring of hard coal longwall mining in high rockburst risk areas," *Tunnelling and Underground Space Technology*, vol. 81, pp. 237–251, 2018.
- [27] M. G. Qian, X. X. Miao, and J. L. Xu, "Theoretical study of key stratum in ground control," *Journal of China Coal Society*, vol. 21, no. 3, pp. 225–230, 1996.
- [28] X. X. Miao and M. G. Qian, "Advance in the key strata theory of mining rockmass," *Journal of China University of Mining and Technology*, vol. 1, pp. 25–29, 2000.
- [29] H. Yan, J. X. Zhang, S. Zhang, and N. Zhou, "Physical modeling of the controlled shaft deformation law during the solid backfill mining of ultra-close coal seams," *Bulletin of Engineering Geology and the Environment*, vol. 78, pp. 3741–3754, 2019.
- [30] J. F. Ju and J. L. Xu, "Surface stepped subsidence related to top-coal caving longwall mining of extremely thick coal seam under shallow cover," *International Journal of Rock Mechanics and Mining Sciences*, vol. 78, pp. 27–35, 2015.
- [31] R. Gao, B. J. Huo, H. C. Xia, and X. B. Meng, "Numerical simulation on fracturing behaviour of hard roofs at different levels during extra-thick coal seam mining," *Royal Society Open Science*, vol. 7, no. 1, article 191383, 2020.

Research Article

Analysis and Modeling of Particle Velocities in Premixed Abrasive Water Jets

Wei qin Zuo ^{1,2}, Cheng Huang,^{1,2} Yanwei Liu,^{1,2} Hongkai Han ^{1,2}, Fuchang Hao,^{1,2}
Fajun Zhao,^{1,2} and Fei Huang³

¹State Key Laboratory Cultivation Base for Gas Geology and Gas Control, Henan Polytechnic University, Jiaozuo, 454000 Henan Province, China

²School of Safety Science and Engineering, Henan Polytechnic University, Jiaozuo, 454000 Henan Province, China

³School of Resources & Environment and Safety Engineering, Hunan University of Science and Technology, Xiangtan, 411100 Hunan Province, China

Correspondence should be addressed to Hongkai Han; hkh@hpu.edu.cn

Received 22 July 2020; Revised 18 September 2020; Accepted 3 October 2020; Published 25 October 2020

Academic Editor: Guozhong Hu

Copyright © 2020 Wei qin Zuo et al. This is an open access article distributed under the Creative Commons Attribution License, which permits unrestricted use, distribution, and reproduction in any medium, provided the original work is properly cited.

The premixed abrasive jet possesses a strong strike ability and is widely used in oil and gas exploitation, machining, rust removal, and other fields. The superstrong, forceful impact of the premixed abrasive jet is mainly provided by high-speed abrasive groups. Hence, the abrasive velocity is the basis of this research, by applying the distribution law of abrasive impact force. In this paper, the particle velocity of the premixed abrasive jet is analyzed theoretically, and the corresponding particle velocity model is established. The real-time contrast interpolation method is employed to solve the problem of the variable drag coefficient. Factors such as the nozzle structure, average abrasive diameter, abrasive density, and jet flow are utilized to determine the abrasive velocity of the nozzle outlet. The numerical solution for the abrasive velocity is obtained by dividing the high-pressure pipe and nozzle into several sections, along the axis. Finally, the calculated particle velocity is compared with the particle image velocity measurement (PIV), to verify the correctness of the established model. These results demonstrate that the model calculation is in effective agreement with the experimental results. The deviation between the theoretical value and the experimental mean is 0.18 m/s. The standard deviation of the experimental results is 3.81–4.22 m/s, while the average error is less than 4%.

1. Introduction

Abrasive water jet technology has seen rapid development in modern times. It is widely used in industrial cutting, tunneling, surface cleaning, and drilling applications [1–3] due to characteristics that include cold state, spot cutting, universality, good cutting quality, and strong cutting performance; this technology is also environmentally protective and pollution-free. It is well known that the striking force of the premixed abrasive jet is provided primarily by the abrasive itself and that the striking force is closely related to the speed of the abrasive. The velocity field of the premixed abrasive jet is studied to provide support for the analysis of the distribution law in abrasive jet hitting force; based on this work, the

acceleration process and acceleration mechanism of the abrasive jet are analyzed in-depth.

There are complex pulsation mechanisms in an abrasive water jet, which are affected by various forces in the process of acceleration. Research on abrasive jets has previously focused on experimental means and numerical abrasive assessments; however, this theoretical research does not provide a thorough understanding of these mechanisms. Hlaváč et al. [4, 5] and Liu et al. [6] conducted stress analysis on a single abrasive and then established a motion equation for the abrasive; although these results were useful, the stress analysis of the abrasive jet in the flow field was not comprehensive. Chen and Siores [7], Haj Mohammad Jafar et al. [8], Laniel et al. [9], Wang et al. [10], and Liu et al. [11]

studied the abrasive jet flow field by using the numerical simulation method and achieved good results. However, due to the complex pulsation phenomenon of the abrasive jet, the results obtained from numerical simulation were still far from the actual flow field of the abrasive jet. Stevenson and Hutchings [12] and Huang et al. [13, 14] conducted research on abrasive jets using experimental methods and reached some beneficial conclusions. Swanson et al. [15] and Miller and Archibald [16] used two electromagnetic induction coils to measure the movement process of abrasive particles in a postmixing collimator. This method was limited in that it could only measure the average velocity of abrasive particles in a certain section and failed to obtain the radial position of abrasive particles in the jet. Momber and Kovacevic [17] calculated the time integral of the jet impact force according to the impact momentum relationship and obtained the relationship between jet velocity and jet impact force. This method was simple to execute but was only capable of measuring jet velocity after the jet penetrated the workpiece. However, these previous studies mostly treated the drag coefficient, a key parameter, as a constant and did not consider the influence of the Basset force on the abrasive acceleration; thus, it was difficult to comprehensively analyze the problem of abrasive stress.

In recent years, domestic and foreign scholars have conducted in-depth research on various flow fields by using PIV technology (particle image velocimeter) and, in doing so, have achieved productive results [18]. This technology provides for a type of noncontact measurement with large testing ranges and high precisions, which is widely used in various flow field tests. The measurement principle is as follows: under the premise of reasonably assigning pulse time, the flow field illuminated by the pulse-type laser plate light source is captured by a camera, and a series of images of the flow field tracer particles are obtained. The images are analyzed for correlation, and the velocity of the flow field is represented by the displacement of the tracer particles. To ensure a high correlation coefficient for correlation analysis, it is necessary to ensure that each image query interval has 5-10 tracer particles. For ordinary liquid flow field, trace particles at specific concentrations can be added to the fluid. For an abrasive jet, tracer particles cannot represent abrasive displacement, and since abrasive particles are large in size, it is difficult to reach a concentration of 5-10 particles within each query interval. Therefore, it remains difficult to test the abrasive velocity field directly with PIV technology alone. To this end, this paper proposes using PIV technology in combination with an independent abrasive center recognition program, thus realizing a noncontact testing method and using real-time comparison interpolation analysis. The influence of the resistance coefficient and the Basset force on abrasive acceleration can then be assessed, and an abrasive movement differential equation can be developed, which is solved by an iterative algorithm to achieve a more comprehensive and accurate interpretation of the abrasive mechanism of acceleration.

2. Abrasive Force Analysis

The abrasive is subjected to the following main forces during acceleration: viscous resistance, virtual mass, Basset force, pres-

sure gradient force, Magnus force, and Saffman force. According to Newton's second law of motion, the Euler form of the differential equation for abrasive motion can be expressed as

$$\begin{aligned} \frac{4\pi}{3} r_p^3 \rho_p \frac{dV_p}{dt} = & C_D \frac{1}{2} \rho_f |V_f - V_p| (V_f - V_p) S \\ & + \frac{2}{3} \pi \cdot r_p^3 \rho_f \frac{d}{dt} (V_f - V_p) \\ & + 6r_p^2 \sqrt{\pi \mu \rho_f} \int_{t_{p0}}^{t_p} \frac{1}{\sqrt{t_p - \tau}} \left(\frac{d}{dt} (V_f - V_p) \right) \\ & \cdot d\tau - \left(\frac{4}{3} \pi r_p^3 \right) \frac{\partial p}{\partial x} + F_{ML} + F_S, \end{aligned} \quad (1)$$

where r_p is the abrasive radius, subscript f is the liquid phase, subscript p is the abrasive, ρ is the density, V is the velocity, t is the time, C_D is the drag coefficient, S is the windward area of the abrasive, and t_{p0} indicates that the particle begins to accelerate at the moment, t_p is the iteration termination time, P is the liquid pressure, and x is the displacement.

The first item is the viscous resistance, the second item is the virtual mass force, the third item is the Basset force, the fourth item is the pressure gradient force, the fifth item is the Magnus force, and the sixth item is the Saffman force.

3. Acceleration Mechanism of the Abrasive in a High-Pressure Pipeline

3.1. Iterative Algorithms. In the premixed abrasive jet, the abrasive particles are fluidized in the high-pressure abrasive tank and passed from the control valve, through the mixing chamber, and into the main flow of the high-pressure pipeline. An interaction force is generated due to unequal flow rates of the abrasive particles and the high-pressure water. The abrasive particles are subjected to the first acceleration. At this point, the following assumptions are made:

- (1) The volume of the premixed abrasive jet studied in the paper is approximately 5%. Considering the very sparse, solid-liquid two-phase flow, the interaction force between the abrasive particles is neglected
- (2) The abrasive is a rigid sphere

Abrasives are mainly affected by viscous drag, virtual mass, and Basset forces in high-pressure pipelines. Therefore, the Euler form of the differential equation for the movement of abrasive particles in a high-pressure pipe is

$$\begin{aligned} \frac{4\pi}{3} r_p^3 \rho_p \frac{dV_p}{dt} = & C_D \frac{1}{2} \rho_f |V_f - V_p| (V_f - V_p) S \\ & + \frac{2}{3} \pi \cdot r_p^3 \rho_f \frac{d}{dt} (V_f - V_p) \\ & + K_B \sqrt{\pi \mu \rho_f} r_p^2 \int_{t_{p0}}^{t_p} \frac{1}{\sqrt{t_p - \tau}} \left(\frac{d}{dt} (V_f - V_p) \right) d\tau, \end{aligned} \quad (2)$$

where the i step is set and the speed of the abrasive is V_i .

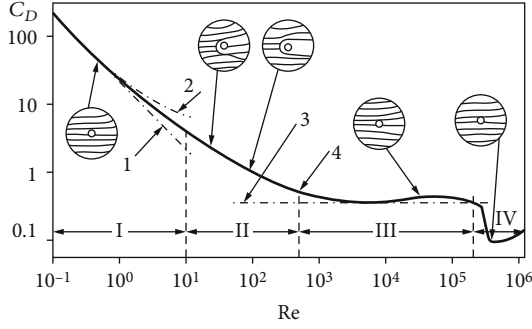


FIGURE 1: The relationship between the viscous resistance coefficient of the sphere and the Reynolds number. 1: Stokes' law; 2: Ossen's formula; 3: Newton's formula; 4: standard resistance curve.

The drag coefficient C_D is a key parameter in the calculation of resistance. The accuracy of this parameter directly affects the result of the resistance calculation. Since the boundary layer of the spherical particle surface is very complicated, there are only a few special cases where the C_D can be derived from the equations. At present, the drag coefficient is mainly determined experimentally. The relationship between the drag coefficient and the Reynolds number of a single rigid sphere, which was obtained by a large number of experiments in a stationary, isothermal, incompressible, and infinite flow field of fluid (referred to as the standard resistance curve), is shown in Figure 1.

Previous research often designated the drag coefficient as a constant or replaced it with a certain formula, which affected the calculation accuracy to some extent. To eliminate this effect, this study uses a real-time contrast interpolation method for analysis. The study utilizes MATLAB to identify the function depicted in Figure 1 and to establish a database of C_D values that change with the Reynolds number. The current Reynolds number is calculated according to the abrasive speed V_i and is compared to those in the database. Three sets of data are selected both before and after the current Reynolds number. According to the six sets of data and using the cubic spline interpolation method to find the resistance coefficient C_{Di} corresponding to the current Reynolds number, the viscous resistance can be expressed as

$$F_{di} = C_{Di} \frac{1}{2} \rho_f |V_f - V_{pi}| (V_f - V_{pi}) S. \quad (3)$$

The Basset force is a force related to the acceleration of abrasives. Let $t_{p0} = 0$, when calculating to the i th step, $t_{pi} = i \times \Delta t$, $\tau = n \times \Delta t$, then:

$$F_{Bi} = -K_B \sqrt{\pi \mu \rho_f} r_p^2 \times \sum_{n=1}^{i-1} \frac{1}{\sqrt{i \times \Delta t - n \times \Delta t}} \times a_i \times \Delta t. \quad (4)$$

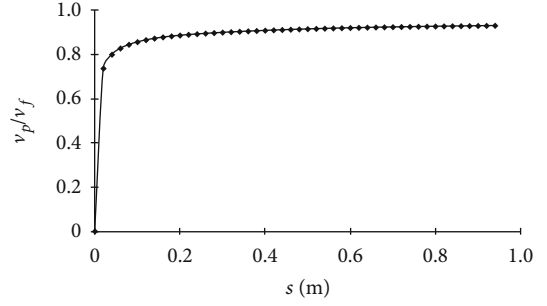


FIGURE 2: The distribution of velocity ratio of abrasive to water phase in the high-pressure pipe.

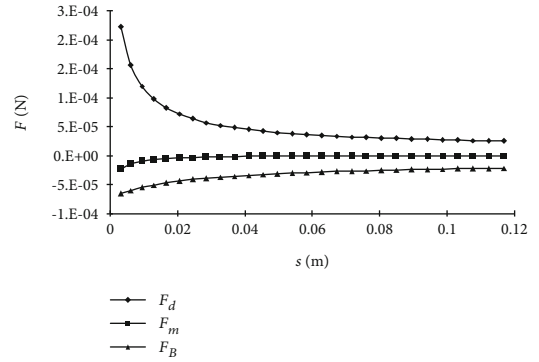


FIGURE 3: Abrasive stress distribution in the high-pressure pipe.

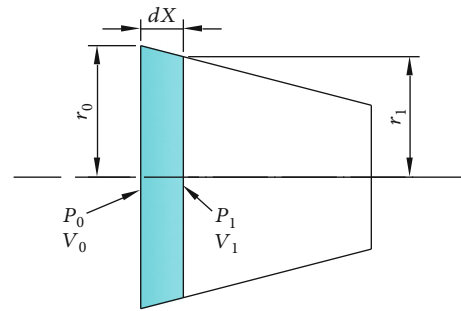


FIGURE 4: The sketch map of the pressure change in the nozzle's convergence section.

In the high-pressure pipeline, it can be assumed that the velocity V_f of the high-pressure water is constant, and the virtual mass force can be expressed as

$$F_{mi} = -\frac{2}{3} \pi \cdot r_p^3 \rho_f a_i. \quad (5)$$

For the simultaneous type 2 and the formula (5), the obtained acceleration expression is as follows:

$$a_i = \frac{F_{di} + F_{Bi}}{4/3\pi \cdot r_p^3 \rho_p + 2/3\pi \cdot r_p^3 \rho_f}. \quad (6)$$

The speed V_{i+1} and the displacement s_{i+1} of the abrasive at the $i+1$ th step are calculated according to the

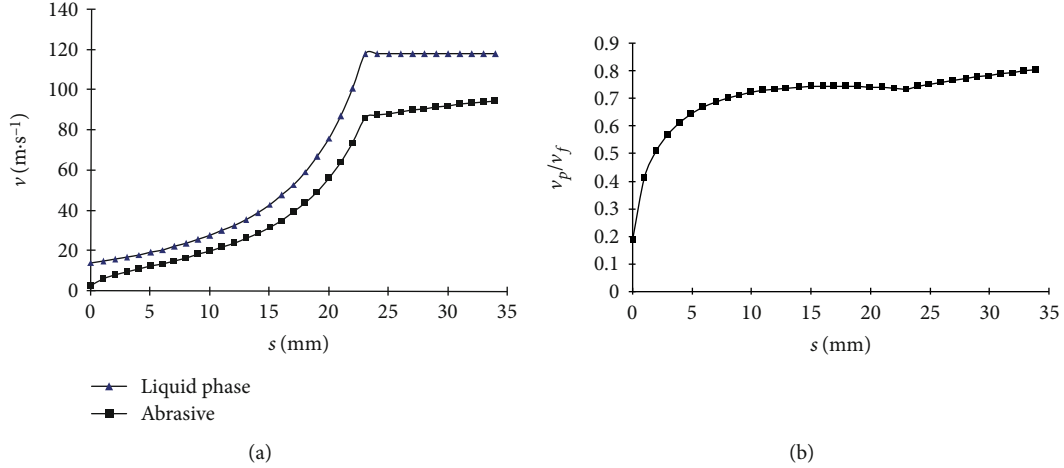


FIGURE 5: The velocity contrast curve of abrasive to water phase in the nozzle.

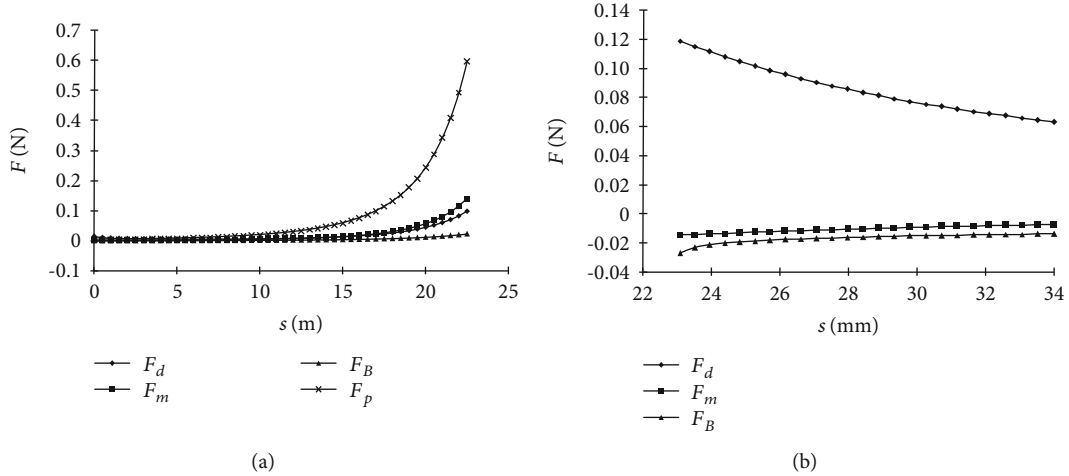


FIGURE 6: The stress distribution of abrasive in the nozzle.

acceleration, and the relevant parameters are brought into the iterative algorithm to continue the loop calculation.

3.2. Case Analysis. The high-pressure pipe in this study had a flow rate of 50 L/min and a diameter of 20 mm. The abrasive used was ceramsite, which has a size of 20 mesh, an abrasive apparent density of 2.7 kg/L, and a dynamic viscosity coefficient of $1.14 \times 10^{-3} \text{ kg}\cdot\text{m}^{-1}\cdot\text{s}^{-1}$. The time step was set at 0.00002 s, and the total step size was 20,000. The calculation result is shown in Figure 2.

It can be seen from Figure 2 that the abrasive accelerated to 0.2% of the liquid phase after 0.2 m of acceleration; after 0.8 m of acceleration, the speed had reached 92.6% of the liquid phase. The abrasive continued to accelerate until the speed was infinitely close to the speed of the liquid phase. Figure 3 shows the relationship between the forces and the displacement during the acceleration of the abrasive.

It can be seen from Figure 3 that the viscous resistance F_d coincides with the direction of the abrasive movement when the abrasive is accelerated in the pipeline and plays a major role in the acceleration of the abrasive. Depending on the mass force F_m and the Basset force F_B , the direction of the

abrasive movement is opposite, which acts to hinder the acceleration of the abrasive. During the acceleration of the abrasive, the virtual mass force F_m decays rapidly and gradually approaches zero. Although the viscous drag and the Basset are also attenuating, the decay rate is not fast. In the later stage of acceleration, the abrasive movement is mainly affected by viscous drag and Basset forces, but the two directions are opposite. As the difference between the abrasive accelerations gradually decreases, the abrasive acceleration also decays rapidly, but the speed of the abrasive and liquid phase at this point is infinitely close.

4. Acceleration Mechanism of the Abrasive in the Nozzle

The abrasive accelerated for the first time within the high-pressure pipeline; however, the kinetic energy obtained by the abrasive was small because of the small flow velocity in the pipeline. The second acceleration of the abrasive was accomplished in the nozzle. In this paper, the common conical convergent nozzle is taken as the research object.

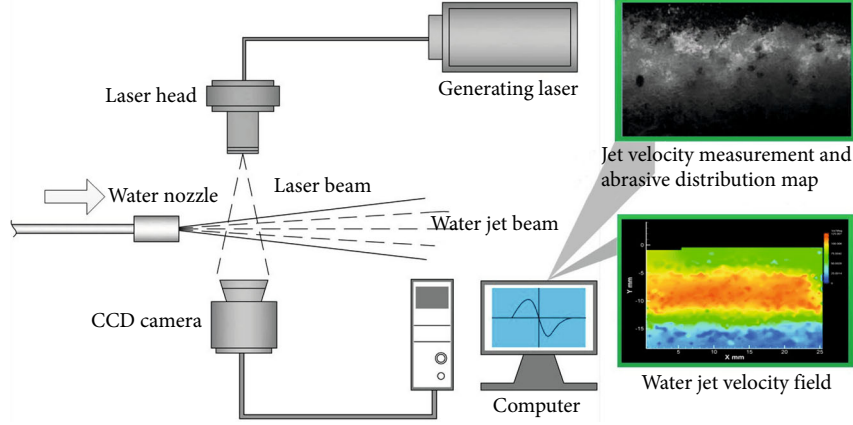


FIGURE 7: System diagram of velocity measurement with an abrasive jet.

4.1. Iterative Algorithm. The abrasive is mainly affected by viscous resistance, virtual mass force, and Basset force in the straight section of the nozzle. Its algorithm is consistent with that of abrasive in the pipeline, which is not discussed here. Abrasives are affected not only by the above three forces but also by the pressure gradient force in the convergence section of the nozzle. The Eulerian form of the differential equation for motion can be expressed as follows:

$$\begin{aligned} \frac{4\pi}{3}r_p^3\rho_p\frac{dV_p}{dt} &= C_D\frac{1}{2}\rho_f|V_f-V_p|(V_f-V_p)S \\ &+ \frac{2}{3}\pi\cdot r_p^3\rho_f\frac{d}{dt}(V_f-V_p) \\ &+ K_B\sqrt{\pi\mu\rho_f}r_p^2\int_{t_{p0}}^{t_p}\frac{1}{\sqrt{t_p-\tau}}\left(\frac{d}{dt}(V_f-V_p)\right) \\ &\cdot d\tau - \left(\frac{4}{3}\pi r_p^3\right)\frac{\partial p}{\partial x}. \end{aligned} \quad (7)$$

In step 1, the velocity of the abrasive is V_i , and the calculation of viscous resistance, Basset force, and virtual mass force is as follows. Step 2 will not be repeated here. In this paper, the pressure gradient force was analyzed in detail. The pressure gradient force is a force formed by nonuniformity of the additional pressure distribution caused by the pressure gradient, which is the key parameter of the force. As shown in Figure 4, a schematic of the pressure change is given for displacement dx .

Assuming that water is incompressible and the change of gravitational potential energy of liquid phase in the nozzle can be neglected, it can be seen from the law of conservation of mass and Bernoulli equation:

$$P_0 - P_1 = \frac{1}{2}\rho_f V_0^2 \left(\frac{r_0}{r_1} - 1\right) \left(\frac{r_0}{r_1} + 1\right) \left[\left(\frac{r_0}{r_1}\right)^2 + 1\right]. \quad (8)$$

TABLE 1: Parameter settings for the experiment.

Type	Cylindrical
Nozzle length of straight segment (mm)	5, 7, 9, 11
Nozzle length of convergence section (mm)	14, 17, 20, 23
Nozzle inner diameter (mm)	3
Nozzle inlet flow (L/min)	50
Abrasive	Ceramsite
Abrasive mean diameter (mm)	0.425-0.85
Abrasive density (kg/m ³)	2.7

TABLE 2: The descriptive statistics of abrasive's velocity.

	Mean	Standard deviation	Standard error of mean
V (abrasive speed)	94.70	3.74	0.563

Since it is infinitesimal, formula (8) can be simplified to

$$P_0 - P_1 = \frac{\rho_f V_0^2 dx \tan(\theta/2)}{2r_0}. \quad (9)$$

Therefore, the pressure gradient force can be expressed as

$$F_{pi} = \frac{4}{3}\pi r_p^3 \frac{\rho_f V_{fi}^2 \tan(\theta/2)}{2r_{pi}}. \quad (10)$$

Then, the expression of acceleration is as follows:

$$a_i = \frac{F_{di} + F_{pi} + F_{Bi}}{\left(\frac{4}{3}\pi \cdot r_p^3 \rho_p + \frac{2}{3}\pi \cdot r_p^3 \rho_f\right)}. \quad (11)$$

According to the acceleration calculation, the velocity of the abrasive V_{i+1} and the displacement s_{i+1} are calculated at step $i+1$. When the displacement s_{i+1} of the abrasive is larger than the length of the convergence section of the nozzle, the calculation stops. When the displacement s_{i+1} of the

TABLE 3: *T*-test of abrasive's velocity sample.

	<i>t</i>	df	Sig (bilateral)	Mean difference	Lower limit	Upper limit
V (abrasive speed)	0.352	46	0.726	0.198	93.19	96.21

abrasive is smaller than the length of the convergence section of the nozzle, the cycle calculation continues. When the abrasive accelerates in the straight section of the nozzle, the calculation is carried out according to the iteration algorithm in step 3. When the abrasive displacement is greater than the length of the straight section of the nozzle, the iteration ends.

4.2. Example Analysis. The conditions of the numerical example analysis are as follows: the flow rate is 50 L/min, the diameter of the high-pressure pipeline is 20 mm, the abrasive type is ceramsite, the abrasive size is 20 mesh, the apparent density of the abrasive is 2.7 kg/L, the dynamic viscous coefficient is $1.14 \times 10^{-3} \text{ kg m}^{-1} \text{ s}^{-1}$, the time step is 0.00002 s, the total step length is 20,000, the nozzle diameter is 3 mm, the convergence length is 23 mm, the linear segment length is 11 mm, and the convergence angle is 14 degrees. Assuming that the abrasive accelerates sufficiently in the high-pressure pipeline, the velocity of the liquid phase in the pipeline can be regarded as the initial velocity of the abrasive at the nozzle entrance. The above parameters are substituted into the iteration program for calculation, and the results are shown in Figure 5.

As seen from Figure 5(a), the liquid phase acceleration in the convergence zone is accompanied by a significant increase in the abrasive speed. In the first half of the convergence section of the nozzle, the liquid velocity is not substantial, and the abrasive velocity is not increasing rapidly. In the second half of the convergence stage, the liquid phase velocity increases sharply, and the abrasive velocity also increases sharply. From Figure 5(b), it can be seen that the velocity of the abrasive rapidly approaches that of the liquid phase when the displacement is less than 10 mm, indicating that the acceleration of abrasive is greater than that of the liquid phase. In the first half of the convergence stage, the change in the flow area is slow, the liquid phase acceleration is slow, and the initial abrasive velocity is low. There is a notable difference between the abrasive velocity and the liquid phase velocity, which suggests that the abrasive acceleration is greater than the liquid phase acceleration. In the second half of the convergence stage, the liquid velocity increases sharply and the abrasive acceleration delays, so the velocity ratio decreases after 15 mm. In the straight-line section, the liquid phase velocity remains unchanged, and the abrasive velocity at the nozzle outlet reaches 80% of the liquid phase. Thus, there is still a certain gap between the abrasive velocity and the liquid phase velocity. Figure 6 shows the relationship between forces and displacements in the process of abrasive acceleration.

Figure 6(a) shows that the pressure gradient force, virtual mass force, viscous drag force, and Basset force are applied to the abrasive in the convergence section of the nozzle from large to small. The pressure gradient force plays a particularly major role. Figure 6(b) shows that the force acting on the

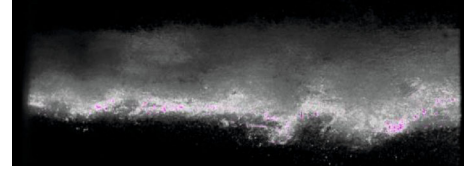


FIGURE 8: The pure water jet picture taken by PIV.

abrasive in the straight line of the nozzle is viscous resistance, Basset force, and virtual mass force, in turn. The viscous resistance is consistent with the direction of abrasive motion and plays a major role in the acceleration process. The virtual mass force and Basset force are opposite to the direction of acceleration, which hinders acceleration. Equation (7) shows that the viscous resistance is related to the velocity difference between the abrasive and the liquid phase, so the viscous resistance decreases with the acceleration of the abrasive. The virtual mass force and Basset force are related to the acceleration of the abrasive, while the acceleration of the abrasive in the straight section changes little; thus, the virtual mass force and Basset force change little. The summary analysis shows that the acceleration of abrasive is slow in the straight section of the nozzle.

5. Experimental Verification

5.1. Experimental Equipment and Methods. The models were assessed by comparing the calculated and experimental particle velocities measured using a particle image velocimetry (PIV) system. PIV is a nonintrusive laser-optical method for fast flow field measurement. In a PIV system, a laser generates a thin light sheet inside the flow. With a pulsed laser, a cross-correlation camera acquires two consecutive images of the particles transported with the flow. The particles have a displacement proportional to the flow velocity. With the known pulse distance and the calibrated scaling factor of the camera, the flow velocity can be calculated by the specialized software with the system. A detailed description of the PIV measurement technique can be found in one paper by Zuo et al. [19].

The PIV system used in this paper is produced by TSI Company. The specific information is as follows: (1) laser model: PIV00461, output energy: $2 \times 120 \text{ mJ/pulse}$; (2) light arm and light source lens group model: 610015-SOL; (3) synchronizer model: 610034; (4) CCD camera model: 630057, resolution: $1.6 \text{ K} \times 1.2 \text{ K}$, frame rate: 32 frames per second.

The abrasive speed test system diagram used in the experiment is shown in Figure 7. The system consists of two parts, a premixed abrasive generator and an abrasive speed tester.

The major parameter settings for the abrasive air jet are given in Table 1. The descriptive statistics of abrasive velocity are given in Table 2. The statistics of abrasive velocity at the nozzle exit can be seen in Table 3.

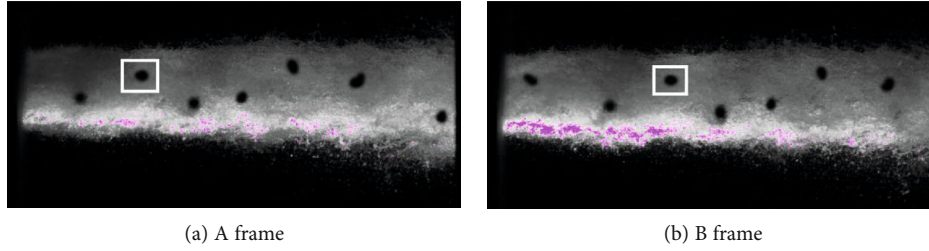


FIGURE 9: The picture of the abrasive water jet taken by PIV.

As shown in Figure 7, the jet is injected from left to right by nozzle 8, and the lamp light source 9 is irradiated from top to bottom. The irradiation surface is a vertical plane passing through the jet axis. The CCD camera is arranged perpendicular to the irradiation surface and photographs the irradiation surface from inside to outside. The range of the CCD camera is $19.94 \text{ mm} \times 14.85 \text{ mm}$, and the pixels are 1600×1192 . The size of each pixel is $12.46 \mu\text{m}$. The time interval between two photos in the same frame is $20 \mu\text{s}$. The obtained images are shown in Figures 8 and 9. The shooting range is 19.94 mm from the nozzle outlet to the target distance.

Figure 8 presents the results obtained for a pure water jet and Figure 9 for an abrasive jet. In Figures 9(a) and 9(b), the black spot circled by the white rectangle is the same abrasive, which clearly shows the direction of the abrasive movement. When the interval time between two pictures is known, the velocity of the abrasive can be obtained by calculating the displacement of the black spot.

5.2. Comparative Analysis. Four groups of nozzles with convergence section lengths of 23 mm , convergence angles of 14 degrees, and straight section lengths of 5 mm , 7 mm , 9 mm , and 11 mm were selected for experiments. The experimental flow rate was 50 L/min . PIV shooting conditions remain unchanged, with a shooting range from the nozzle outlet to the target distance of 19.94 mm and a shooting width of 14.85 mm . The Laida criterion was used to eliminate abnormal test data. The parameter hypothesis test was carried out for a nozzle with an 11 mm straight length. An abrasive theoretical velocity of 94.51 was the original hypothesis, while an alternative hypothesis of 94.5 was also considered. Given a significance level $= 0.01$, the test results returned by the statistical software SPSS are as follows:

Since the value $p = 0.726 \geq 0.01$ falls within the acceptance domain, the original hypothesis cannot be rejected; that is, there is no significant difference between the abrasive velocity parameter and the test value of 94.51 . Further, the 99% confidence interval tells us that there is a 99% chance that the abrasive velocity value is between $(93.19, 96.21)$, and 94.51 is included in this confidence interval, which also confirms the above inference; thus, the theoretical calculation and experimental results are satisfied.

Using the same method, based on the parameter hypothesis test, the abrasive velocity test results and theoretical values at the nozzle outlet with different linear lengths are verified, as shown in Table 4.

After the parameter hypothesis test, the experimental and theoretical values are compared and analyzed, and the results

TABLE 4: The statistics of abrasive's velocity at the exit of the nozzle.

Nozzle straight section length (mm)	Mean (m/s)	Standard deviation	Theoretical value (m/s)	Consistency
5	90.70	4.32	90.87	Satisfy
7	92.43	4.46	92.24	Satisfy
9	93.57	3.80	93.44	Satisfy
11	94.70	3.74	94.51	Satisfy

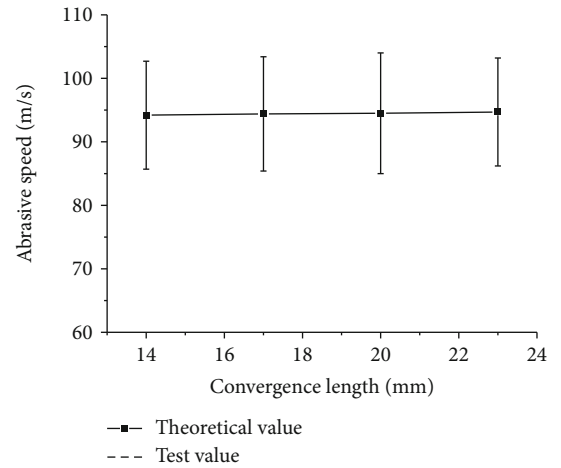


FIGURE 10: The velocity contrast figure of abrasive at the exit of the nozzle with different lengths of a straight segment.

show that the experimental and theoretical values meet the consistency. Figure 10 is a comparison between the theoretical and experimental results of abrasive velocity at the nozzle outlet.

From Figure 10, the theoretical value of abrasive velocity agrees well with the experimental value. The deviation between the theoretical value and the experimental mean value is 0.19 m/s , and the standard deviation is $3.74\text{--}4.46 \text{ m/s}$. The experimental results are in good agreement with the calculated results.

Four groups of nozzles with linear lengths of 11 mm , convergence angles of 14 degrees, and convergence section lengths of 14 mm , 17 mm , 20 mm , and 23 mm were selected for the same experiment. Using the Laida criterion to eliminate abnormal test data, the mean and standard deviation of the abrasive velocity at the nozzle outlet, with different lengths of convergence sections, were obtained and validated

TABLE 5: The statistics of abrasive's velocity at the exit of the nozzle.

Nozzle straight section length (mm)	Mean (m/s)	Standard deviation	Theoretical value (m/s)	Consistency
14	94.20	3.93	94.28	Satisfy
17	94.40	4.22	94.38	Satisfy
20	94.51	3.81	94.48	Satisfy
23	94.69	3.82	94.51	Satisfy

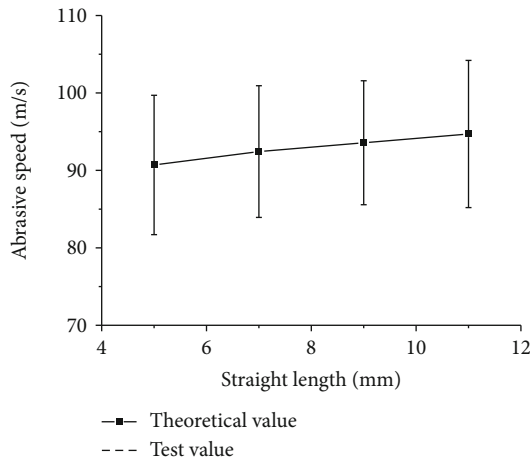


FIGURE 11: The velocity contrast figure of abrasive at the exit of the nozzle with different lengths of the convergence section.

by the parameter hypothesis test and theoretical value, as shown in Table 5.

After the parameter hypothesis test, the experimental and theoretical values were compared and analyzed, and the results show that the experimental and theoretical values are consistent. Figure 11 is a comparison between the theoretical and experimental results of abrasive velocity at the nozzle exit.

Figure 11 shows that the theoretical value of the abrasive velocity is in good agreement with the experimental value. The deviation between the theoretical value and the experimental mean is 0.18 m/s, and the standard deviation is 3.81–4.22 m/s. The experimental results are in good agreement with the revariation trend of the calculated results.

6. Conclusion

The theoretical analysis and corresponding mathematical model of the velocity of the premixed abrasive jet have been put forward. The real-time contrast interpolation method is utilized to solve the problem of the variable drag coefficient. In this paper, a numerical method is proposed to calculate the particle velocity, by discretizing the high-pressure pipe and nozzle into several small sections, along the axial direction. By comparing the calculated and measured particle velocity data, the model is verified experimentally. The results prove that the model prediction is in effective agreement with the experimental results, and the average error is less than 4%.

Nomenclature

V : Jet velocity
 C_D : Drag coefficient
 ρ : Liquid density
 t : Time
 τ : Duration of the peak pressure
 S : Windward area of abrasive.

Data Availability

As for the data availability statement, some or all data, models, or code generated or used during the study are available from the corresponding author by request (list items).

Conflicts of Interest

No conflict of interest exists in the submission of this manuscript.

Authors' Contributions

The manuscript is approved by all authors for publication.

Acknowledgments

This work is jointly supported by the National Natural Science Foundation of China (Nos. 51604092, 51774119, 51704096, and 51804115), the China Postdoctoral Science Foundation (No. 2018M642749) Key Scientific Research Project of Colleges and Universities in Henan Province (No. 21A44009), and the Natural Science Foundation of Henan Province (No. 182300410128). Zuo Weiqin received his B.S. and Ph.D. degrees from Chongqing University, China, in 2007 and 2012. He is now an associate professor at Henan Polytechnic University.

References

- [1] R. Melentiev and F. Fang, "Recent advances and challenges of abrasive jet machining," *CIRP Journal of Manufacturing Science and Technology*, vol. 22, pp. 1–20, 2018.
- [2] J. G. Kim and J. J. Song, "Abrasive water jet cutting methods for reducing blast-induced ground vibration in tunnel excavation," *International Journal of Rock Mechanics and Mining Sciences*, vol. 75, pp. 147–158, 2015.
- [3] Y. Xue, H. Si, D. Xu, and Z. Yang, "Experiments on the microscopic damage of coal induced by pure water jets and abrasive water jets," *Powder Technology*, vol. 332, pp. 139–149, 2018.
- [4] L. M. Hlaváč, I. M. Hlavacova, F. Arleo, F. Vigano, M. P. G. Annoni, and V. Geryk, "Shape distortion reduction method for abrasive water jet (AWJ) cutting," *Precision Engineering*, vol. 53, pp. 194–202, 2018.
- [5] R. S. Kumar, S. Gajendran, and R. Kesavan, "Estimation of optimal process parameters for abrasive water jet machining of marble using multi response techniques," *Materials Today: Proceedings*, vol. 5, no. 5, pp. 11208–11218, 2018.
- [6] Y. Liu, J. Zhang, J. Wei, and X. Liu, "Optimum structure of a Laval nozzle for an abrasive air jet based on nozzle pressure ratio," *Powder Technology*, vol. 364, no. 3, pp. 343–362, 2020.

- [7] F. L. Chen and E. Siores, "The effect of cutting jet variation on striation formation in abrasive water jet cutting," *International Journal of Machine Tools & Manufacture*, vol. 41, no. 10, pp. 1479–1486, 2001.
- [8] R. H. M. Jafar, H. Nouraei, M. Emamifar, M. Papini, and J. K. Spelt, "Erosion modeling in abrasive slurry jet micro-machining of brittle materials," *Journal of Manufacturing Processes*, vol. 17, pp. 127–140, 2015.
- [9] R. Laniel, O. Bouchareb, A. Brient, and M. Miroir, "Discrete elements model of an abrasive water-jet through the focal canon to the work-piece," *Procedia CIRP*, vol. 58, pp. 529–534, 2017.
- [10] F. Wang, R. Wang, W. Zhou, and G. Chen, "Numerical simulation and experimental verification of the rock damage field under particle water jet impacting," *International Journal of Impact Engineering*, vol. 102, pp. 169–179, 2017.
- [11] X. Liu, S. Liu, and H. Ji, "Numerical research on rock breaking performance of water jet based on SPH," *Powder Technology*, vol. 286, pp. 181–192, 2015.
- [12] A. N. J. Stevenson and I. M. Hutchings, "Scaling laws for particle velocity in the gas-blast erosion test," *Wear*, vol. 181–183, pp. 56–62, 1995.
- [13] F. Huang, S. Li, Y. Zhao, and Y. Liu, "Study on lateral jetting range during an arc-curved jet impacting nonplanar solid surfaces," *Journal of Fluids Engineering*, vol. 140, no. 10, article 101201, 2018.
- [14] F. Huang, S. Li, Y. Zhao, and Y. Liu, "A numerical study on the transient impulsive pressure of a water jet impacting nonplanar solid surfaces," *Journal of Mechanical Science and Technology*, vol. 32, no. 9, pp. 4209–4221, 2018.
- [15] R. K. Swanson, M. Kilman, and S. Cerwin, "Study of particle velocities in water driven abrasive jet cutting," in *Proceedings of the 4th US Water Jet Conference*, pp. 103–107, Berkeley, CA, USA, 1987.
- [16] A. L. Miller and J. H. Archibald, "Measurement of particle velocities in an abrasive jet cutting system," in *Proceedings from the 6th American Water Jet Conference*, pp. 291–304, Houston, TX, USA, 1991.
- [17] A. W. Momber and R. Kovacevic, "Energy dissipative processes in high speed water-solid particle erosion," in *Annual Meeting of American Society of Mechanical Engineers*, pp. 243–256, New York, NY, USA, 1995.
- [18] Y. J. Choo and C. H. Song, "PIV measurements of turbulent jet and pool mixing produced by a steam jet discharge in a sub-cooled water pool," *Nuclear Engineering and Design*, vol. 240, no. 9, pp. 2215–2224, 2010.
- [19] W. Zuo, X. Wang, F. Hao, Y. Lu, and M. Liu, "Research on acceleration mechanism of abrasive in pre-mixed abrasive water-jet based on iterative algorithm," *Journal of China University of Petroleum (Edition of Natural Science)*, vol. 40, no. 4, pp. 104–109, 2016.

Research Article

Model of Heat and Mass Exchange between a Downcast Shaft and the Air Flow to the Mine

WenJing Li,^{1,2} ShengHua Zou¹ ,³ WanXin Yang,³ and Qi Hu³

¹School of Resource & Environment and Safety Engineering, Hunan University of Science and Technology, Xiangtan Hunan 411201, China

²Architectural Engineering College, Hunan Institute of Engineering, Xiangtan Hunan 411104, China

³Civil Engineering College, Hunan University of Science and Technology, Xiangtan Hunan 411201, China

Correspondence should be addressed to ShengHua Zou; shzou@hnust.edu.cn

Received 1 June 2020; Revised 26 August 2020; Accepted 9 September 2020; Published 8 October 2020

Academic Editor: Jingmin Xu

Copyright © 2020 WenJing Li et al. This is an open access article distributed under the Creative Commons Attribution License, which permits unrestricted use, distribution, and reproduction in any medium, provided the original work is properly cited.

Mining activities have increased owing to the rise in the social demand for minerals. Thermal hazards have become a major health and safety consideration in mines. The thermal environment of a working face is related to the air parameters at the bottom of shaft. The objective of this study is to accurately predict the air temperature at the bottom of a shaft in a mine with the ventilation time over 3 years. For this purpose, a mathematical model of the heat and mass exchange between the surrounding rock of the shaft and the downcast air is established by utilizing the finite volume method. The C++ languages are used for numerical calculations. The results are in agreement with the measured data. The effects of the relative humidity of air at the inlet of the shaft, the surface moisture coefficient of the shaft surface, and the physical parameters of the rock on the air parameters at the shaft bottom are studied in detail. Equations for calculating the enthalpy increase of air per 100 m in shaft with the depth of 1300 m were established by using cluster analysis. This equation provides a theoretical basis for predicting the air parameters along the shaft with the ventilation time over 3 years.

1. Introduction

The number of high-temperature mines is increasing with mining depth. According to statistics [1], there were almost 100 mines with a depth of more than 1000 m in China by 2015, among which approximately 47 were coal mines with an average mining depth of 1086 m. In the next 10 to 15 years, 50% of iron ore resources, 33% of nonferrous metal resources, and 53% of coal resources will be mined below 1000 m. The geothermal gradient distribution in China is high in the east and south and low in the west and north. The geothermal gradient within a depth of 1000 m (1.8–4.3°C/100 m) is linear and varies negligibly. The surface temperature at a depth of 1000 m is generally 40–45°C in north-east China and the southeast coast and 35–45°C in the central

Sichuan Basin. The geothermal temperatures at a depth of 2000 m typically reach 70–80°C [2]. Therefore, thermal hazards are becoming an increasing concern in deep mines. It is crucial to effectively judge the thermal hazards of the working face of a mine and accurately predict the temperature and relative humidity of air.

The calculation of the heat and mass exchange between the surrounding rock of an air supply shaft and the airflow in the shaft can provide a basis for the prediction of the temperature and relative humidity of air on the working face.

Numerous studies have investigated the heat and mass transfer between airflow and excavation roadways and working surfaces. As early as 1919, South Africa began to study the thermodynamic law of mine air flow, and Jappe [3] puts forward the basic idea of the wind temperature calculation.

Lambrechts [4] analyzed a large number of measured temperature changes in shafts with an average depth of 1258.8 m. They studied the relationship between the wet-bulb temperature of airflow in a roadway and natural rock temperature, initial wet-bulb temperature, distance, air velocity, and wall moisture content. Starfield [5] used the finite difference method to calculate the wall temperature of a roadway, and a formula was established using mathematical fitting to rapidly predict the dry-bulb and wet-bulb temperatures of airflow in the roadway. The formula can be used in practice. Ross [6] predicted the temperature, humidity, and other related climate parameters by numerical simulation. Lowndes and Hargreaves [7, 8] developed the ventilation and climate model of the fast tunneling roadway. Onder [9] studied the change of air supply volume and its influence on ventilation in the long-distance tunneling roadway. Kertikov [10] calculated the air flow temperature and humidity of the local ventilation roadway. Sasmito [11] established a three-dimensional unsteady local thermal nonequilibrium model to evaluate thermal storage and the heat transfer between ventilation air and rock pit. In 2020, based on the similarity theory, Zhu [12] designed a facility to investigate effects of airflow velocity, thermal diffusion coefficient, moisture content, and thermal insulation material on the temperature field distribution in the surrounding rock. In order to save the energy and control mine environment, many scholars began to study how to use surrounding rocks or abandoned mines for thermal storage. Ghoreishi–Madiseh [13] and Zhu [14] studied the heat storage and heat regulation of surrounding rocks; Loredó [15] studied the heat storage ability of the isolated surveyed mine voids.

Most of the researches focus on the underground space, and there are few researches on the heat exchange process between the downcast air and shaft. In China, the method of differences and regression analysis, which were first proposed by Cen and Hou [16], was used to predict the air temperature at a shaft in 1989. At present, the simple difference iterative method [16], measured statistical method [4, 17], and PSO-BP neural network prediction method [18] are primarily used to calculate the air temperature at a shaft. However, these methods are too simple or geographically limited to estimate the air temperature accurately. And they neglect the latent heat effect of water vapor. In this work, according to the characteristics of coupled heat and mass exchange in the fluid–solid systems, the finite volume method is adopted to establish a mathematical model of the heat and water vapor exchange between the surrounding rock of an air supply shaft and the downcast air in the shaft. The formula that can accurately calculate the air parameters of the shaft bottom in different geological conditions and inlet air condition is given by using the C++ languages.

2. Mathematical Model

The bottom of the vertical shaft is an important node of the entire mine ventilation network. The temperature and relative humidity of the airflow in the shaft are related to the thermal environment of the entire mine. The heat and mass exchange between the shaft and the downcast air in the mine are different from those in a horizontal tunnel, and they have

the following characteristics: (1) the airflow produces auto-compression heat as it moves to the bottom of the shaft because of height difference. (2) The temperature of the shaft wall surface changes because of the geothermal gradient. (3) The shaft may pass through the underground aquifers. In this case, there is infiltration water on the shaft wall, and this water participates in the heat and mass exchange. (4) There may be heat dissipation by equipment and drainage pipes in the shaft.

The following assumptions are proposed to simplify the problem to be studied:

- (1) The air supply shaft is a hollow cylinder. The surrounding rock is isotropic and homogeneous, and the original temperature of the surrounding rock changes linearly with the depth
- (2) Only the heat and mass exchange between the downcast air and surrounding rock is considered, and the influence of infiltration water and other heat dissipation is neglected
- (3) The temperature and humidity of air are evenly distributed on the cross section of the shaft, and the change in the kinetic energy of the airflow is not considered

Based on these assumptions, the heat and mass exchange between the shaft and the airflow are shown in Figure 1. The equations of the heat and mass balance between the airflow and surrounding rock can be established as follows:

$$Gc_p \frac{\partial H}{\partial \tau} = Q_y + Gg\Delta z - G[c_p(t_{\text{out}} - t_{\text{in}}) + 0.001(d_{\text{out}} - d_{\text{in}})r], \quad (1)$$

$$Q_y = Q_x + Q_q = hA(T_w - t) + h_{md}A(d_w - d)r. \quad (2)$$

Equations (1) and (2) consider the surface of the shaft wall to be completely wet, but this is not the case. Therefore, the above equations must be revised. Japanese scholars first put forward the moisture coefficient of the wet wall rock [19], and most Chinese scholars have adopted the moisture coefficient to calculate the moisture exchange of the wet wall rock [20]. The value ranges from 0.05 to 0.4, in which the complete wet wall is 0.4 and the wet wall in one quarter (i.e., 0.1). After introducing the moisture coefficient of the roadway surface, equation (2) can be written as

$$Q_y = Q_x + Q_q = hA(T_w - t) + h_{md}A(d_w - d)rf. \quad (3)$$

2.1. Finite Volume Meshing. As shown in Figure 2, based on the assumption that the temperature and humidity of air are uniformly distributed on the cross section of the shaft in the axial direction, it can be considered that airflow parameters change only in the axial direction. The axial direction from the entrance of the shaft is set as Δz in the meshing space.

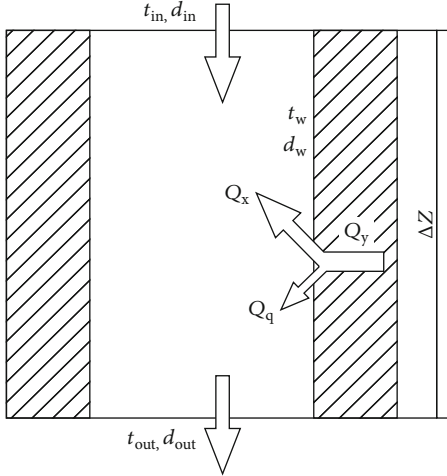


FIGURE 1: Heat and mass exchange between the surrounding rock and airflow.

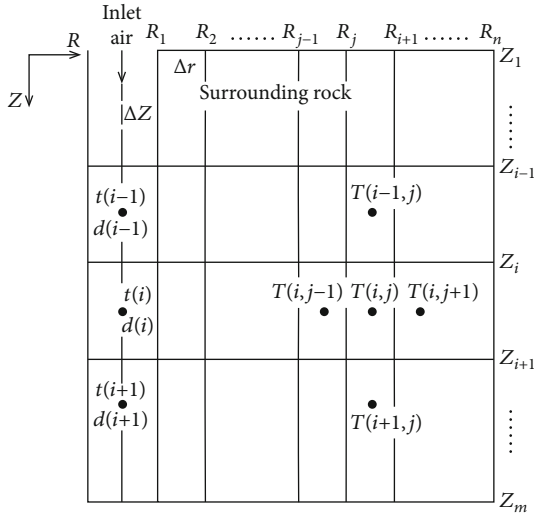


FIGURE 2: Finite difference grid.

As the temperature field of the surrounding rock is axisymmetric, the determination of the thermal conductivity of the surrounding rock can be simplified to a two-dimensional problem in the radial and axial directions. The finite difference grid is shown in Figure 2, where the meshing space is set as Δr and Δz .

2.2. Mathematical Model

2.2.1. Equations of Airflow Parameters. Air velocity and density are assumed to be 1 m/s and 1.2 kg/m^3 , respectively. The relative strength of convection and diffusion at adjacent nodes can be measured based on the grid Peclet number (Pe), which is defined as

$$Pe = \frac{\rho v}{\lambda_a / \Delta z} = \frac{1.2 \times 1}{0.0267 / 10} = 449.3. \quad (4)$$

The thermal conduct of air between adjacent nodes is negligible. According to the principle of energy and mass balance, the change in air temperature in the shaft is equal to the convective heat transfer between the downcast air and the surface of the surrounding rock and the autocompression. Additionally, the change in the humidity ratio of air is equal to the mass exchange between the airflow and the surface of the surrounding rock. Therefore, the equations of air parameters at different nodes are as follows:

$$Gc_p \frac{\partial t}{\partial \tau} = h[T_w(i-1) - t(i-1)]2\pi R_1 \Delta z + Gg\Delta z - Gc_p[t(i) - t(i-1)], \quad (5)$$

$$G \frac{\partial d}{\partial \tau} = h_{md}[d_w(i-1) - d(i-1)]2\pi R_1 \Delta z f - G[d(i) - d(i-1)]. \quad (6)$$

The evaporation coefficient is based on the Lewis relation.

$$h_{md} = \frac{h}{c_p Le^{2/3}}. \quad (7)$$

The equation can be applied to gases or liquids with Sc ranging from $0.6-2500$ and Pr ranging from $0.6-100$. h_{md} can be approximately considered as $h_{md} = h/c_p$ when $Le = 0.857$.

2.2.2. Equations for the Surrounding Rock. The differential equation of heat conduction in a two-dimensional cylindrical coordinate system is given by equation (8).

$$\frac{\partial^2 T}{\partial R^2} + \frac{1}{R} \frac{\partial T}{\partial R} + \frac{\partial^2 T}{\partial z^2} = \alpha \frac{\partial T}{\partial \tau}. \quad (8)$$

2.2.3. Boundary Conditions for the Surrounding Rock. The boundary conditions in the radial direction are as follows: the inner interface is the convective heat transfer interface between the surrounding rock surface and downcast air. This is regarded as the fourth type boundary condition. The outer surface is the surface of the cooling zone surface. It is a given temperature interface which is regarded as the first type boundary condition. The temperature is the original rock temperature.

The boundary conditions in the axial direction are as follows: the entrance of the shaft in the axial direction is set as the soil layer of constant temperature. Thus, the temperature at the section at $z = 0$ can be regarded as a temperature in the soil layer of constant temperature. Based on literature [16], the thickness of the stable cooling zone is considered as approximately $10-20 \text{ m}$, and the rock temperature within the cooling zone is a power function distribution. The radial temperature gradient close to the shaft surface is considerably larger than the axial temperature gradient. The surrounding rock temperature rapidly approaches the original rock temperature as the radius increases. Therefore, the axial heat transfer can be neglected compared

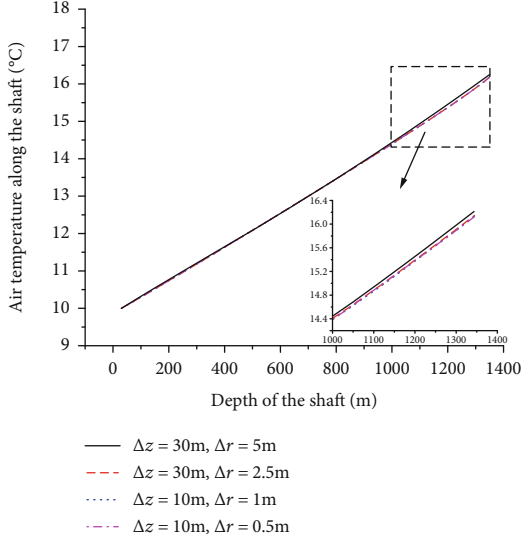


FIGURE 3: Grid independence verification.

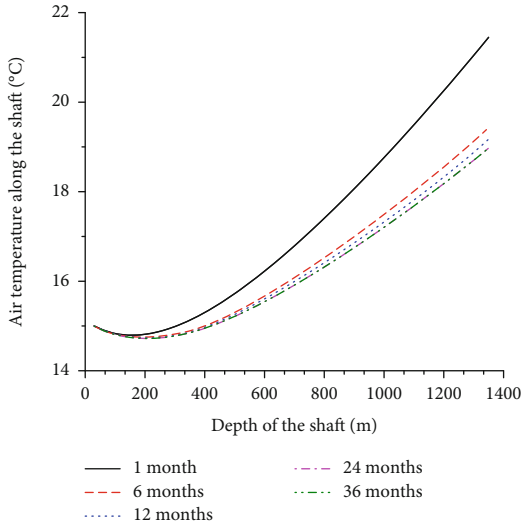


FIGURE 4: The variation of the air temperature along the shaft with the ventilation time.

to the radial heat transfer at the shaft bottom. The bottom of the interface between the shaft wall and rock can be considered as an adiabatic surface. The mathematical model of the surrounding rock temperature is as follows:

$$\begin{cases} \frac{\partial^2 T}{\partial R^2} + \frac{1}{R} \frac{\partial T}{\partial R} + \frac{\partial^2 T}{\partial z^2} = \alpha \frac{\partial T}{\partial \tau} \\ T|_{\tau=0} = T_{gu}; T|_{R=\infty} = T_{gu} \\ \lambda \left. \frac{\partial T}{\partial R} \right|_{R=R_1} = hA(T_w - t) + h_{md}A(d_w - d)rf \end{cases} \quad (9)$$

The finite volume method is used to discretize differential equation (9). According to the energy conservation equation,

it is assumed that the temperature at a node represents the temperature of the control volume for internal node (i, j) , which can be written as

$$\begin{aligned} & \frac{T^n(i-1, j) - T^n(i, j)}{\Delta z} (R_{j+1}^2 - R_j^2) \pi + \frac{T^n(i+1, j) - T^n(i, j)}{\Delta z} \\ & \times (R_{j+1}^2 - R_j^2) \pi + \frac{T^n(i, j-1) - T^n(i, j)}{\Delta r} 2\pi R_j \Delta z \\ & + \frac{T^n(i, j+1) - T^n(i, j)}{\Delta r} 2\pi R_{j+1} \Delta z \\ & = \frac{T^{n+1}(i, j) - T^n(i, j)}{\alpha \Delta \tau} (R_{j+1}^2 - R_j^2) \pi \Delta z. \end{aligned} \quad (10)$$

This can also be written as

$$\begin{aligned} T^{n+1}(i, j) = \alpha \Delta \tau & \left[\frac{T^n(i-1, j) + T^n(i+1, j)}{\Delta z^2} \right. \\ & \left. + \frac{T^n(i, j-1) 2R_j + T^n(i, j+1) 2R_{j+1}}{\Delta r (R_{j+1}^2 - R_j^2)} \right] \\ & + \left[1 - \alpha \Delta \tau \left(\frac{2}{\Delta z^2} + \frac{2R_j + 2R_{j+1}}{\Delta r (R_{j+1}^2 - R_j^2)} \right) \right] T^n(i, j). \end{aligned} \quad (11)$$

Its stability condition is $1 - \alpha \Delta \tau ((2/\Delta z^2) + (2R_j + 2R_{j+1}/\Delta r (R_{j+1}^2 - R_j^2))) \geq 0$.

2.2.4. Temperature of the Shaft Surface. The temperature of the shaft surface can be obtained using equation (5). Before solving equation (5), it is necessary to determine the density of saturated water vapor on the shaft surface, which is a single-value function of temperature. There are numerous empirical formulas for calculating the partial pressure of saturated water vapor; most of them are complex functional relations. To simplify the calculation, the relationship between the density of saturated water vapor and temperature between 10–45°C is expressed as the following linear equation:

$$d = 4.217e^{0.062t}. \quad (12)$$

The relative error between the calculated value calculated by equation (12) and the exact value is within 2.3%. Then, the surface temperature of the shaft can be calculated as

$$\begin{aligned} T_w(i) = & \left[\lambda T(i, 1) \left(R_1 + \frac{\Delta r}{4} \right) + 0.5 \Delta r h R_1 t(i) \right. \\ & \left. - \frac{Gfr(d(i+1) - d(i))}{4\pi \Delta z} \right] / [0.5 \Delta r h R_1 + \lambda (R_1 + 0.25 \Delta r)]. \end{aligned} \quad (13)$$

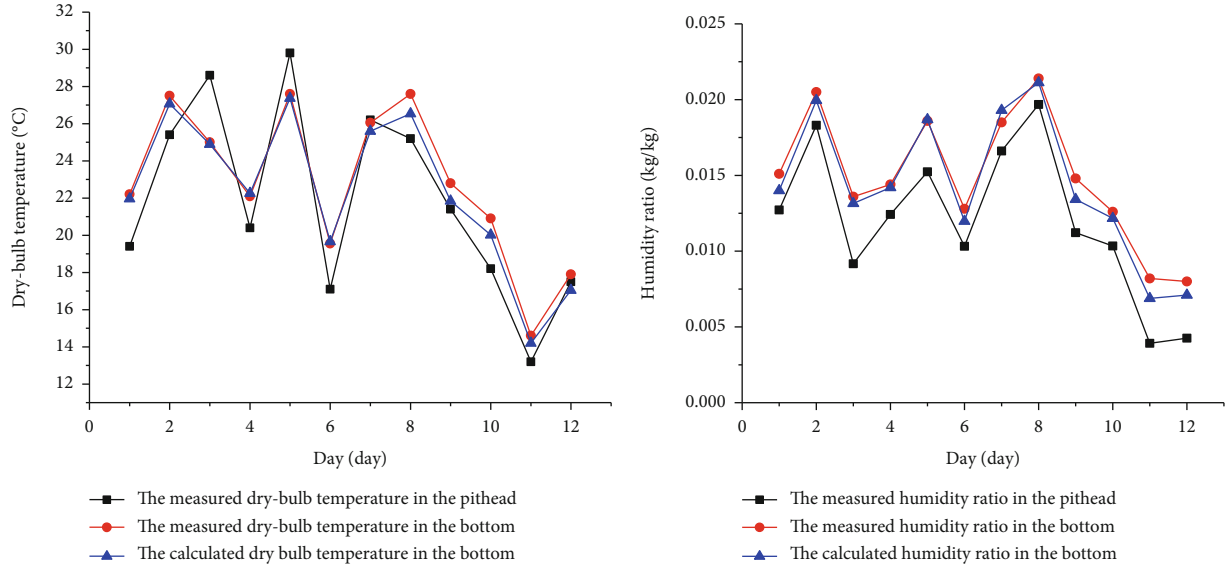


FIGURE 5: Comparison between the dry-bulb temperature and the humidity ratio of the calculated and measured in literature [24] at the shaft bottom.

The convective heat transfer coefficient, h , is calculated using the formula proposed by Sherbani [21].

$$h = 2.33 \frac{\epsilon G^{0.8} U^{0.2}}{F} \quad (14)$$

3. Results and Discussion

3.1. Grid Independence Verification and Ventilation Time Selection. The geological conditions of a gold mine in Laizhou in the Shandong province in China are considered. According to the geological survey results of the Fourth Institute of Geology and Mineral Exploration of Shandong Province, the main composition of the surrounding rock is metagabbro when the depth is less than 1300 m. The thermal conductivity of metagabbro is $2.2 \text{ W/m}^\circ\text{C}$ [22]. The temperature in the soil layer of constant temperature is 15°C , and the geothermal gradient is $2.2^\circ\text{C}/100 \text{ m}$ [23]. The radius of the air supply shaft is 2.5 m, and the air supply rate is 30 kg/s .

In order to select the appropriate space step size, mesh independence verification is carried out. As shown in Figures 3 and 4, grids are selected to calculate the air flow temperature in the shaft, when the step sizes are considered as $\Delta r = 0.5\text{-}1\text{m}$ and $\Delta z = 10$, and the air flow curve almost coincides. The variation of the air temperature in the inlet shaft with the ventilation time is also calculated. As shown in Figure 4, when the inlet air temperature is 15°C , the air temperature along the shaft gradually decreases with the increase of the ventilation time and tends to be consistent. The temperature curves of the ventilation time at 2 and 3 years are almost coincident. At the beginning of ventilation, the shaft wall temperature is higher, and the heat releases into the air are higher. As the ventilation time increases, the shaft wall is gradually cooled, and the heat release to the air is reduced, so the airflow temperature along the shaft decreases with time. And the radius of the heat adjusting circle expands continuously, but the radius expands more slowly with the

time increases and approaches to the steady state gradually. So, the temperature curves of the ventilation time at 2 and 3 years are almost coincident. In the following calculation, the step sizes are considered as $\Delta r = 0.5\text{-}1\text{m}$ and $\Delta z = 10\text{m}$, and the ventilation time is considered 3 years.

3.2. Validation of the Model. The comparison of the calculation results and the measured data obtained from the literature [24] is shown in Figure 5. The calculation condition in literature [24] is as follows: the constant temperature layer with a value of 15.7°C ; the mean value of the geothermal gradient is $2.91^\circ\text{C}/100 \text{ m}$. The shaft radius is 3.5 m, and the speed of the airflow is 3 m/s. The physical properties of the wall rock are as follows: the underground 0-99 m is a mudstone layer with a thermal conductivity of $2.1 \text{ W}/(\text{m}^\circ\text{C})$; the sandstone layer is distributed at 100-500 m underground, and its thermal conductivity is $4.1 \text{ W}/(\text{m}^\circ\text{C})$; the limestone layer is distributed at 501-666 m underground, and its thermal conductivity is $3.1 \text{ W}/(\text{m}^\circ\text{C})$. The calculated values exhibit strong agreement with the measured values. Therefore, the results obtained using the model are reliable. Thus, the model is used to calculate the air parameters at the shaft bottom under different inlet air parameters and different thermophysical characteristics of the rock. The results are described below.

3.3. Effect of Temperature and Relative Humidity of Inlet Air on Temperature and Enthalpy of Air along the Intake Shaft. As in literature [24], in this work, it is assumed that f is 0.05, the inlet air temperature is $10\text{-}25^\circ\text{C}$, and relative humidity is 50-80%. As shown in Figures 6 and 7, the temperature and relative humidity of air in the shaft are evidently correlated with the inlet air temperature. The variation in the air temperature in the shaft depends on the heat dissipation of the surrounding rock and the auto-compression.

The heat dissipation of the surrounding rock is composed of the sensible heat transfer and latent heat transfer between

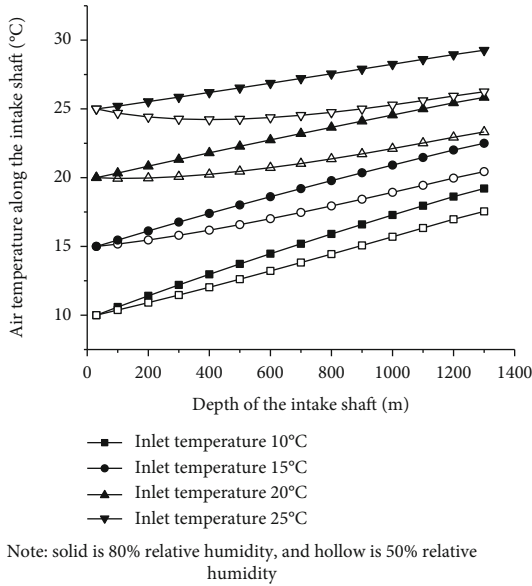


FIGURE 6: Effect of temperature and humidity of inlet air on the air temperature along the shaft.

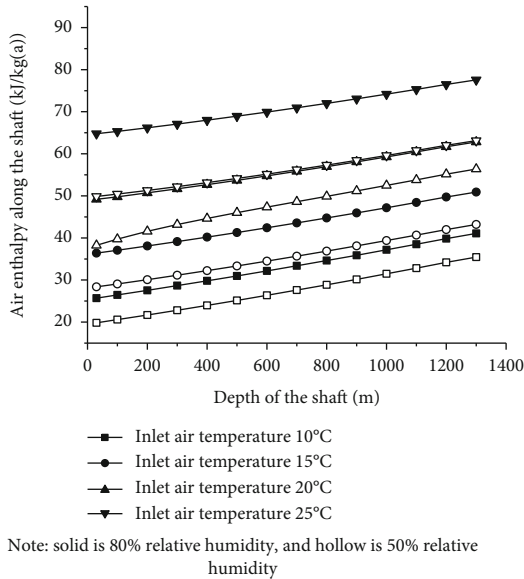


FIGURE 7: Effect of temperature and humidity of inlet air on air enthalpy along the shaft.

the air and surrounding rock surface. The sensible heat transfer may be negative when the inlet air temperature is higher than the temperature of the surrounding rock surface. The air dry-bulb temperature decreases when the absolute value of the sensible heat transfer is more than the auto-compression. The air dry-bulb temperature starts increasing when the value of the sensible heat transfer is positive or the absolute value of the sensible heat transfer is less than the auto-compression. However, the enthalpy of the airflow along the intake shaft increases because of air self-compression and wall heat dissipation.

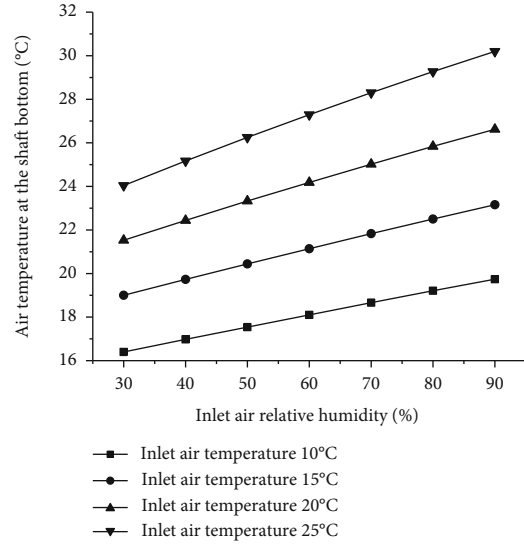


FIGURE 8: Effect of the inlet air temperature and humidity of inlet air on the air temperature at the shaft bottom.

3.4. Effect of Temperature and Relative Humidity of Inlet Air on the Air Temperature at the Shaft Bottom. The working efficiency and thermal comfort of workers depend on the air parameters on the working face, which are related to the air parameters at the bottom of the shaft. The influence of the temperature and relative humidity of inlet air on the air temperature at the shaft bottom is analyzed when $f = 0.05$, as shown in Figure 8. The air temperature at the shaft bottom increases with the temperature and relative humidity of inlet air. As relative humidity increases, the evaporation of water on the intake shaft wall decreases and the latent heat decreases. This increases the air temperature at the shaft bottom. Figure 6 shows that the relative humidity of inlet air significantly influences the airflow temperature along the shaft. However, as the depth reaches 600 m, the air temperature in the shaft increases linearly with the shaft depth.

3.5. Effect of the Surface Moisture Coefficient on Air Parameters at the Shaft Bottom. In addition to the relative humidity of inlet air, the surface moisture coefficient of the wall surface is related to the amount of water vapor that enters the airflow from the wall. Therefore, the surface moisture coefficient of the wall surface strongly affects the air temperature at the shaft bottom. The inlet air at 15°C is considered as an example to calculate the change in the air temperature at the shaft bottom with f varying from 0–0.3, as shown in Figure 9. There is no water evaporation when the surface moisture coefficient is 0, and the heat transferred from the surrounding rock is converted into the sensible heat of air. Under the influence of rock heat dissipation and auto-compression, the air temperature at the shaft bottom is up to 28.73°C, and it is not affected by the relative humidity of inlet air. As the surface moisture coefficient increases, the air temperature at the shaft bottom decreases. The air temperature at the shaft bottom does not change significantly after the surface moisture coefficient becomes more than 0.2.

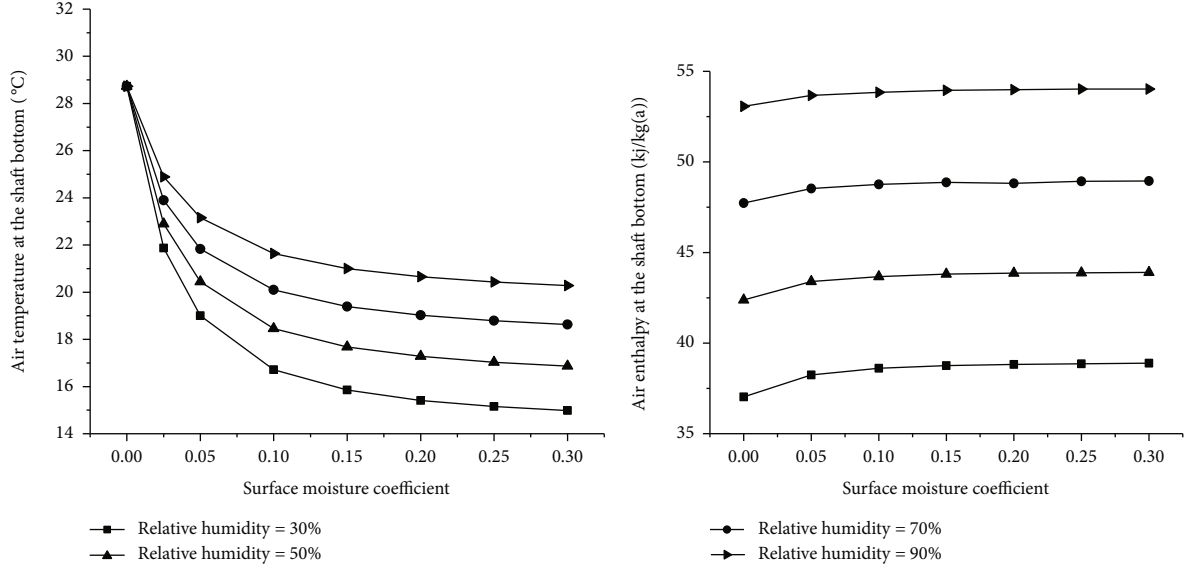


FIGURE 9: Effect of the surface moisture coefficient on the air temperature and enthalpy at the shaft bottom.

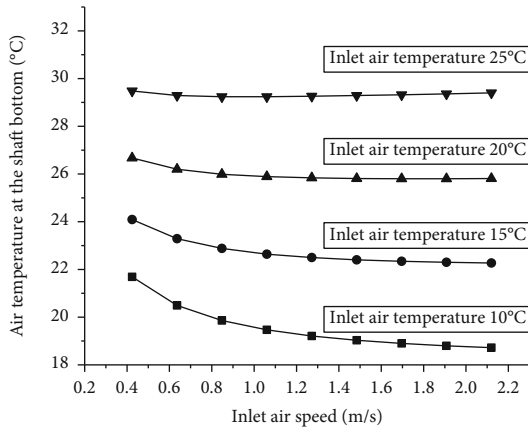


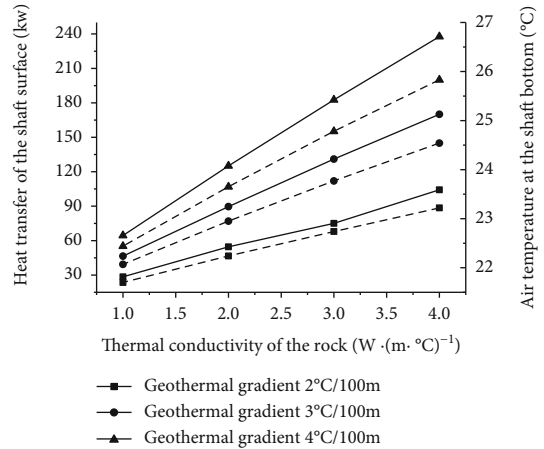
FIGURE 10: Effect of inlet air speed on the air temperature at the shaft bottom.

The effect of the surface moisture coefficient on the air enthalpy at the shaft bottom is analyzed, as shown in Figure 9. When the inlet air temperature is 15°C, the air enthalpy at the shaft bottom increases slightly from the dry wall surface to the wet wall surface. However, the change is not as evident as the increase in the surface moisture coefficient. The air enthalpy at the shaft bottom changes negligibly after the surface moisture coefficient becomes greater than or equal to 0.1.

Heat conduction and transfer are expressed in cylinder coordinates by the following equations:

$$Q = \frac{2\pi(t_{gu} - t)}{(1/R_1\xi h) + (1/\lambda) \ln(R_n/R_1)}, \quad (15)$$

$$\xi = \frac{Q_y}{Q_x} = \frac{h(t_w - t) + h_{md}(d_w - d) \cdot r \cdot f}{h(t_w - t)}$$



Note: the solid line is the heat transfer, and the dotted line is the air temperature.

FIGURE 11: Effect of rock thermophysical properties on the air temperature at the shaft bottom.

TABLE 1: The calculating parameter range.

	Value of parameters
Inlet air temperature (°C)	10, 15, 20, 25
Inlet air relative humidity (%)	30, 50, 70, 90
Geothermal gradient (°C/100 m)	2, 3, 4
Rock thermal conductivity (w/m·°C)	1, 2, 3, 4
Surface moisture coefficient	0, 0.05, 0.1, 0.2

ξ is in a range of 1.36–2.34 when the inlet air temperature is 15°C. However, it has been reported in literature [19] that the evaporation heat transfer of the actual underground roadway is approximately 0.2 to 1.57 times the sensible heat of the completely dry roadway surface. This implies that the range of ξ is 1.2–2.57. Thus, the results of

TABLE 2: The formula of the difference enthalpy per 100 m along of the intake shaft.

Surface moisture coefficient (f)	The difference enthalpy per 100 m	Error
0	$\Delta H = 0.00323\lambda(t_{gu} - t_{in}) + 0.98$	$\pm 2\%$
0.05/0.1/0.2	$\Delta H = -5.395 \times 10^{-7}\lambda(H_{gus} - H_{in})^2 + 0.0005227\lambda(H_{gus} - H_{in}) + 1.004$	$\pm 8\%$

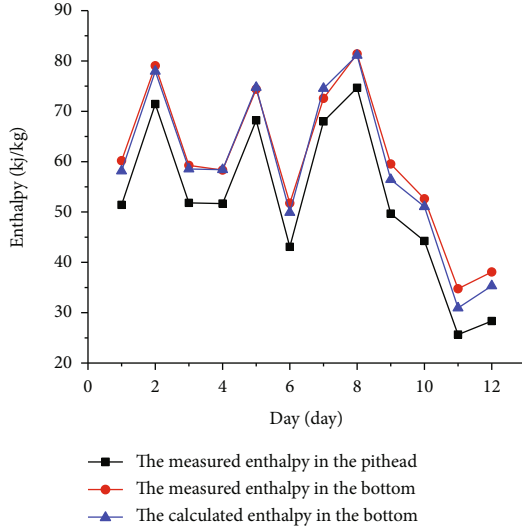


FIGURE 12: Comparison between the enthalpy of the calculated and measured in literature [24] at the shaft bottom.

our study agree with literature. The effect of ξ on heat transfer is not evident in the case of $1/R_1\xi h \ll (1/\lambda) \ln(R_n/R_1)$. The main reason for the increase in heat transfer is that the air temperature along the shaft decreased as the latent heat of evaporation increases. Thus, the change in the air enthalpy at the shaft bottom is negligibly affected by the surface moisture coefficient.

3.6. Effect of Air Velocity on the Air Temperature at the Shaft Bottom. The relative humidity of mine supply air is generally high. Therefore, the effect of the air velocity on the air temperature at the shaft bottom is calculated at a relative humidity of 80% and different temperatures when $f = 0.05$, as shown in Figure 10. The increase in the air velocity significantly affects the air temperature at the shaft bottom when the air velocity is small. This effect is stronger when the inlet air temperature is low and vice versa. When the inlet air temperature is 25°C, the air velocity negligibly affects the air temperature at the shaft bottom. When the inlet air velocity increases to 1.70 m/s (air volume: 40 kg/s), the air temperature at the shaft bottom does not change significantly with the air velocity at all temperatures. Therefore, when the inlet air temperature is low, the air temperature at the shaft bottom decreases considerably as the air velocity increases. However, when the inlet air temperature is high, air velocity does not affect the air temperature at the shaft bottom.

3.7. Effect of Rock Thermophysical Properties on the Air Temperature at the Shaft Bottom. The temperature at the same depth of the surrounding rock increases with the geo-

thermal gradient. Additionally, the thermal conductivity of the rock influences rock heat dissipation. Inlet air temperature, relative humidity, and the surface moisture coefficient are set as 15°C, 80%, and $f = 0.05$, and the air supply rate is 30 kg/s to calculate. The results are shown in Figure 11. When the geothermal gradient increases from 2°C/100 m to 4°C/100 m, the heat transfer from the surface of the shaft increases by about 2.28 times. When the thermal conductivity of the rock increases from 1 W/m°C to 4 W/m°C, the heat transfer from the surface of the shaft increases by about 3.6 times. Moreover, the effect of the thermal conductivity of the rock is stronger in rocks with a larger geothermal gradient. As the thermal conductivity of the rock increases from 1 W/m°C to 4 W/m°C, the heat transfer from the surface of the shaft increases by 75.8KW and 173.3KW when the geothermal gradient is 2°C/100 m and 4°C/100 m, respectively. The geothermal gradient and thermal conductivity of the rock have similar effects on the air temperature at the shaft bottom.

3.8. Comprehensive Effect and Equation Fitting. The effect of the abovementioned factors on the air parameters at the shaft bottom is further examined. The previous analysis results show that when the wind speed exceeds 1.7 m/s, the airflow parameter changes very little, while the wind speed in the inlet shaft often exceeds 3 m/s [4, 24], so the wind speed is set as 3 m/s in the calculation. According to the literature [3], the main geothermal gradient of China is 1.8-4.38°C/100 m, and the rock thermal conductivity is 0.2-4.2 w/m°C [16], so the calculated parameters are set as shown in Table 1. And the radius of the shaft is set as 2.5 m. C++ languages is used to calculate the temperature and enthalpy of air along the shaft under the conditions listed in Table 1. As shown in Table 2, the equations for calculating the difference enthalpy per 100 m of air along the shaft of the depth less than 1300 m are obtained using the clustering analysis method.

According to Figure 9, although the surface moisture coefficient can affect the air temperature, it has little influence on air enthalpy. Therefore, the equations can be combined into a unified equation when the surface moisture coefficients are different. It can also be seen from the equation that in the vertical shaft excluding other heat sources, the influence of autocompression is dominant, and the heat transfer of the surrounding rock only has significant influence when the geothermal gradient and rock thermal conductivity are both high. With the increase of the depth, the original rock temperature of the rock increases so in the deep mine, the heat dissipated in the surrounding rock of the shaft will also increase gradually.

The equations in Table 2 show the difference enthalpy per 100 m along shaft. When the shaft radius is 2.5 m, the error of the enthalpy difference calculated by the fitting formula and the program under the dry condition is within 2%, and the error under the wet condition is within 8%. The enthalpy of the flow at the bottom of the inlet parameter in literature [24] is also calculated by formula in Table 2. The calculated results are in good agreement with the measured value in literature [24] as shown in Figure 12. The results of the fitting equations can provide a reference for designers to estimate the air parameters at the bottom of the intake shaft in different.

4. Conclusions

A mathematical model is built according to the heat and the mass exchange principle between a shaft and the downcast air with the ventilation time of 3 years by employing the finite volume method. C++ languages is utilized to calculate the heat and mass exchange. The calculated results are in agreement with the measured data in literature [24]. Equations for calculating the enthalpy increase of air per 100 m in shaft of the depth less than 1300 m were established by using cluster analysis. This equation provides a theoretical basis for predicting the air parameters at the shaft bottom with the ventilation time over 3 years.

The main conclusions of this study are as follows:

- (1) The parameters of inlet air affect the parameters of downcast air along the intake shaft. The influence of relative humidity on the air temperature along the intake shaft is stronger at a high inlet air temperature
- (2) There is an evident positive relationship between the air temperature at the shaft bottom and the temperature and relative humidity of inlet air. The surface moisture coefficient affects the air temperature at the shaft bottom. However, the air temperature at the shaft bottom does not change significantly when the surface moisture coefficient becomes greater than or equal to 0.2. The surface moisture coefficient negligibly affects the air enthalpy at the shaft bottom
- (3) The increase in air velocity evidently affects the air temperature at the shaft bottom when the inlet air temperature is low. However, when air velocity increases to 1.70 m/s, the air temperature at the shaft bottom does not change significantly as air velocity increases
- (4) The air temperature at the shaft bottom and the heat released from the surface of the shaft increase with the geothermal gradient and thermal conductivity of the rock

Nomenclature

A: area, m²
 c_p : specific heat of air, J/kg·K
d: air moisture, g/kg(a)

f : moisture coefficient
 F : area of the roadway section, m²
 g : gravitational acceleration, m/s²
 G : air mass flow of the shaft, kg/s
 h : convective heat transfer coefficient, w/m²·K
 h_{md} : Evaporation coefficient, kg/m²·s
 H : the enthalpy of air, kJ/kg(a)
 H_{gus} : the enthalpy of saturated air at original rock temperature, kJ/kg(a)
 Le : Lewis number
 Pe : Peclet number
 Pr : Prandtl number
 Q_y : total heat exchange, w
 Q_x : significant heat exchange, w
 Q_q : latent heat exchange, w
 r : latent heat of vaporization of water, kJ/kg
 R_1 : shaft radius, m
 R_n : cooled zone radius, m
 Sc : Schmidt number
 t : air temperature, °C
 T : rock temperature, °C
 T_{gu} : original rock temperature, °C
 T_h : temperature in soil layer of constant temperature, °C
 ΔT : geothermal gradient, °C/100 m
 ΔH : the difference enthalpy of air per 100 m, kJ/100 m
 U : circumference of the roadway, m
 v : air speed, m/s
 z : depth of the shaft, m.

Greek Symbols

α : surrounding rock thermal diffusivity, m²/s
 λ : thermal conductivity of rock, W/m·°C
 λ_a : thermal conductivity of air, W/m·°C
 ε : roughness coefficient of roadway
 Φ : relative humidity, %
 ρ : air density, kg/m³
 ξ : moisture separation coefficient
 τ : time, s.

Subscript

in: inlet air
out: outlet air
 w : the surrounding rock surface.

Data Availability

The data used to support the findings of this study are available from the corresponding author upon request.

Conflicts of Interest

The authors declare that there is no conflict of interest regarding the publication of this paper.

Acknowledgments

This work was supported by the National Natural Science Foundation of China (No. 51134005 and No. 52174098)

and Human Engineering Research Centre of Energy Efficiency and Material Technology in green and low-carbon building.

References

- [1] H. Xie, "Research ideas and expected results of "deep rock mass mechanics and mining theory"," *Engineering Science and Technology*, vol. 2, pp. 1–16, 2017.
- [2] J. Wang, *Basic characteristics of geotemperature distribution in China*, vol. 7, Geological Publishing House, Beijing, 1990.
- [3] C. W. Biccard Jeppe, "The estimation of ventilation air temperatures in deep mines," *Journal of the Chemical Metallurgical and Mining Society of South Africa*, vol. 40, no. 1, 1939.
- [4] J. d. V. Lambrechts, "The Estimation of Ventilation Air Temperatures in Deep Mines," *Journal of the Chemical Metallurgical & Mining Society of South Africa*, vol. 50, pp. 184–198, 1950.
- [5] A. M. Starfield, "A rapid method of calculating temperature increases along mine airways," in *Clays in crustal environments*, Springer-Verlag, 1969.
- [6] M. Stokes, A. J. Ross, M. A. Tuck, and I. S. Lowndes, "Computer Simulation of Climatic Conditions in Rapid Development Drivages," in *Proceedings of 6th International Mine Ventilation Congress, SME*, pp. 283–288, Littleton, CO, 1997.
- [7] I. S. Lowndes, A. J. Crossley, and Z. Y. Yang, "The ventilation and climate modelling of rapid development tunnel drivages," *Tunnelling and Underground Space Technology*, vol. 19, no. 2, pp. 139–150, 2004.
- [8] D. M. Hargreaves and I. S. Lowndes, "The computational modeling of the ventilation flows within a rapid development drive," *Tunnelling and Underground Space Technology*, vol. 22, no. 2, pp. 150–160, 2007.
- [9] M. Onder, S. Sarac, and E. Cevik, "The influence of ventilation variables on the volume rate of airflow delivered to the face of long drivages," *Tunnelling and Underground Space Technology*, vol. 21, no. 5, pp. 568–574, 2006.
- [10] V. Kertikov, "Air temperature and humidity in dead-end headings with auxiliary ventilation," in *Proceedings of 6th International Mine Ventilation Congress, SMME*, pp. 269–276, Littleton, CO, USA, 1997.
- [11] A. P. Sasmito, J. C. Kurnia, E. Birgersson, and A. S. Mujumdar, "Computational evaluation of thermal management strategies in an underground mine," *Applied Thermal Engineering*, vol. 90, pp. 1144–1150, 2015.
- [12] S. Zhu, J. Cheng, Z. Wang, and M. Borowski, "Physical simulation experiment of factors affecting temperature field of heat adjustment circle in rock surrounding mine roadway," *Energy Sources, Part A: Recovery, Utilization, and Environmental Effects*, pp. 1–18, 2020.
- [13] S. A. Ghoreishi-Madiseh, A. P. Sasmito, F. P. Hassani, and L. Amiri, "Performance evaluation of large scale rock-pit seasonal thermal energy storage for application in underground mine ventilation," *Applied Energy*, vol. 185, pp. 1940–1947, 2017.
- [14] S. Zhu, J. Cheng, W. Song et al., "Using seasonal temperature difference in underground surrounding rocks to cooling ventilation airflow: a conceptual model and simulation study," *Energy Science & Engineering*, pp. 1–19, 2020.
- [15] C. Loreda, D. Banks, and N. Roqueni, "Evaluation of analytical models for heat transfer in mine tunnels," *Geothermics*, vol. 69, pp. 153–164, 2017.
- [16] C. Yanqiang and H. Qizong, *Thermal environment engineering in mine*, Wuhan Industrial Humanities Press, Wuhan, 1989.
- [17] J. Hu, *Calculation of Airflow Heat and Moisture Exchange and Air Distribution in High Temperature Deep Mine*, Shandong University of Science and Technology, 2004.
- [18] X. Zhang and B. S. Wang, "Predicting of air flow temperature of shaft with water dropping based on PSO-BP neural network, Saf," *Coal Mines*, vol. 43, pp. 178–181, 2012.
- [19] L. Heqing, *Research on Heat and Mass Exchange Theory and Cooling Technology of High Temperature Mine Lane*, Central South University, 2009.
- [20] J. Gao, W. Xu, and X. Zhang, "Treatment of water evaporation during calculation of temperature and humidity of airflow," *Journal of China Coal Society*, vol. 6, pp. 951–955, 2010.
- [21] A. H. Sherbani, *Mine cooling guide*, vol. 2, Coal Industry Press, Beijing, 1982.
- [22] H. Xiao, X. Wu, and J. Zhou, "Research on thermal conductivity calculation of geotechnical materials," *Subgrade Engineering*, vol. 3, pp. 54–56, 2007.
- [23] Z. Xingdong, X. Guolin, Y. Zhuzhou, H. Haiyang, L. Zicheng, and L. Wei, "Tests of the temperature gradient of surrounding rockmass and analysis of the engineering thermal circumstance at Sanshandao gold mine," *Metal Mine*, vol. 6, pp. 109–113, 2013.
- [24] T. Gao, F. T. Yue, M. Sun, J. S. Wei, and Y. J. Wang, "A steady calculation model on heat and humidity parameters of airflow in heat hazard MINES," *Interfacial Phenomena and Heat Transfer*, vol. 7, no. 4, pp. 331–344, 2019.

Research Article

Preliminary Study on High-Energy and Low-Energy Microfracture Event Evolution Characteristics in the Development Process of Rock Failure

Guofeng Yu,^{1,2} Guanwen Cheng ,³ Lianchong Li,³ Chunan Tang,⁴ Bo Ren,² and Yunchun Han³

¹School of Energy and Safety, Anhui University of Science and Technology, Huainan 232001, China

²State Key Laboratory of Deep Coal Mining and Environmental Protection, Huainan Mining (Group) Co., Ltd., Huainan 232001, China

³Center for Rock Instability and Seismicity Research, Northeastern University, Shenyang 110819, China

⁴State Key Laboratory of Coastal and Offshore Engineering, Dalian University of Technology, Dalian 116023, China

Correspondence should be addressed to Guanwen Cheng; chengguanwen@mail.neu.edu.cn

Received 20 May 2020; Revised 6 July 2020; Accepted 21 August 2020; Published 14 September 2020

Academic Editor: Jingmin Xu

Copyright © 2020 Guofeng Yu et al. This is an open access article distributed under the Creative Commons Attribution License, which permits unrestricted use, distribution, and reproduction in any medium, provided the original work is properly cited.

The evolution characteristics of high-energy and low-energy microfracture events play an important role in the brittle failure mechanism of rock and reasonable microseismic (MS) monitoring and acoustic emission (AE) monitoring. The bimodal distribution (BMD) model is commonly used to observe the evolution characteristics of high-energy and low-energy MS events; however, its precise mechanism remains unclear. The evolution characteristics of high-energy and low-energy microfracture events are assessed in this study based on a BMD model. MS monitoring results from the No. 22517 working face of the Dongjiahe Coal Mine are studied, and AE monitoring results of a biaxial compression experiment of a granite specimen are analyzed. High-energy MS events in the No. 22517 working face are found to be generated by an increase in the failure scale of the overlying rock mass upon exiting the insufficient mining stage and entering the sufficient mining stage. The change characteristics of the high-energy AE hits are positively correlated with crack evolution characteristics in the granite specimen and negatively correlated with changes in the Gutenberg-Richter b value. A precise high-energy and low-energy AE hit evolution mechanism is analyzed based on the microscopic structure of the granite specimen. Similarities and differences between high-energy MS events and low-energy AE hits are determined based on these results. Both are found to have bimodal characteristics; an increase in the failure scale is identified as the root cause of the high-energy component. The bimodal distribution of AE hits is far less obvious than that of MS events.

1. Introduction

In a study on the recurrence of large seismic events in Polish mines, Gibowicz and Kijko [1] found that the pattern of empirical distributions of the largest seismic events is more complex than expected based on the most general theoretical considerations (e.g., Gumbel distributions) [2]. The observed distributions possess bimodal distribution (BMD) characteristics, as shown in Figure 1 BMD has also been observed in the underground coal mines of Upper Silesia, Poland, at the

Doubrava coal mine of the Ostrava-Karvina Coal Field, Czechoslovakia, and in the copper ore mines of Lubin Copper Basin, Poland [1]. The seismicity associated with the eruption of Mount St. Helens, Washington, in May 1980 obeyed the BMD as confirmed by the distribution of characteristic periods in the maximum amplitude signals and by the frequency-magnitude relations [3]. Another striking example of BMD was found in New Madrid, Missouri, and interpreted as a result of the superposition of two distinct seismogenic source types observed in the area [4].

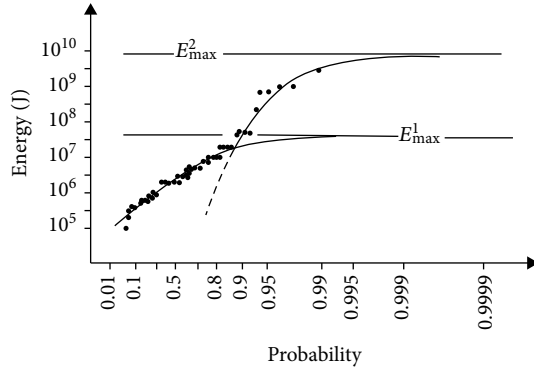


FIGURE 1: Probability distribution of the monthly occurrence of maximum magnitude tremors at the Lubin copper mine, Poland, for the period 1972-1980 [6].

The BMD results from the mixing of random variables generated by two different phenomena. The first phenomenon is responsible for the low-energy component and the second one for the high-energy component of the distribution. At present, the BMD is considered an important method for observing the evolution characteristics of high-energy and low-energy microseismic (MS) events.

Despite many valuable contributions to the literature, the precise mechanism of the BMD is not yet known. The traditional view is that the BMD obeys at least three statistical distributions. The first was proposed by Stankiewicz [5], who assumed that at any moment, the state of the rock mass can be described by a stress that increases linearly in time in the absence of a seismic event and drops to a certain value from the interval if an event occurs. The other two statistical distributions were proposed by Gibowicz and Kijko [1]. Under the second statistical distribution, high- and low-energy seismicity are independent of each other. Under the third statistical distribution, the high-energy seismicity is dependent on the low-energy seismicity. Monitoring data can be well fitted to these three statistical distributions, but none fully characterizes the BMD mechanism.

There are two hypotheses as to the nature of the two sets of events discussed above [6]. The first states that BMD is a result of the inhomogeneous and discontinuous structure of the rock mass. The second states that the low-energy component of the distribution is a result of mine-induced stress release, while the high-energy component is a result of the interaction between mine-induced and residual tectonic stresses in the area. The first hypothesis is acceptable in certain mining districts and the second hypothesis in others, where geologic factors play by far the most important role in the generation of seismic events in mines.

The early warning mechanism of mine disaster is closely related to the rock and fissures, and the evolution characteristics of high-energy and low-energy microfracture events monitored by microseismic early warning are of great significance to the failure mechanism of rocks [7, 8]. Many previous researchers have conducted laboratory and in situ research by acoustic emission (AE) and MS monitoring technologies. In the field of MS monitoring, Xiao et al. [9], Feng et al. [10], Xu et al. [11], and Yu et al. [12, 13] studied the rela-

tionships between monitored MS activities and rockburst events in tunnels; rockburst events can be predicted by capturing MS events produced during the excavation of a rock. Zhang et al. (2017), Wang et al. [14], and Cheng et al. [15] studied the relationship between the MS event distribution and strata movement caused by underground mining. Cao et al. [16, 17] and Li et al. [18] investigated the relationship between MS activities and rockburst events to predict possible rockburst locations in coal mines. Lu et al. [19] and Li et al. [20] studied the relationship between the distribution of MS events and coal-gas outburst in a coal mine. Li et al. [7], Zhang et al. [21], and Wang et al. [14] studied the relationship between MS monitoring results and water inrush. They found that fractured zones in rock masses, which may form water inrush channels, can be determined according to the spatial distribution of MS events.

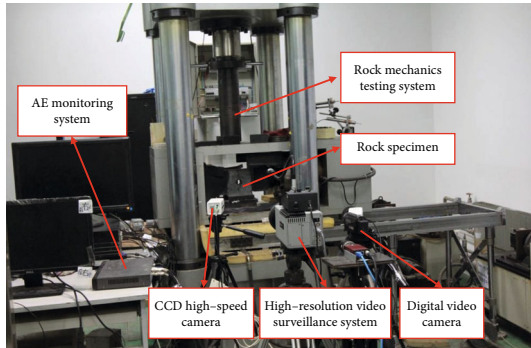
Xu et al. [22], Dai et al. [23], and Salvoni et al. [24] carried out MS monitoring during the excavation of slopes and to find that ground deformation and MS data reflect rock damage at various depths as well as mechanisms of rock mass instability. Previous studies have also shown that the occurrence of MS events is closely related to failure rock mass and related disasters. AE evolution characteristics have been analyzed based on six main factors: number and energy [25–27], frequency [28, 29], spatial location [30–32], spatial correlation length [33], fractal dimension [34, 35], and moment tensor [36]. Dixon et al. [37, 38] and Smith [39, 40] used AE monitoring for slope deformation and stability predictions. These previous studies provide a workable basis for studying the evolution characteristics of high-energy and low-energy microfracture events related to the BMD mechanism.

Inspired by previous research results, MS monitoring was carried out in No. 22517 working face in the Dongjiahe Coal Mine in this study. A biaxial compression experiment was also performed with a granite specimen in the laboratory. The MS monitoring and experimental results were analyzed to determine the evolution characteristics of high- and low-energy microfracture events. The relationship between the evolution characteristics and various failure scales were observed to determine the BMD mechanism. Finally, the similarities and differences between high-energy MS event and low-energy AE hit evolution characteristics were determined as discussed in detail below.

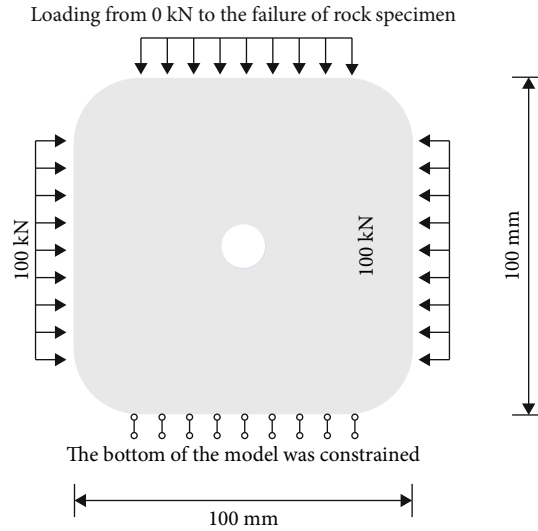
2. Evolution Characteristics of High-Energy and Low-Energy AE Hits

2.1. Experimental System. The biaxial compression experimental system used in this study is composed of a rock mechanic testing system, an AE monitoring system, and an observation system (Figure 2(a)). The experiment was conducted on a servocontrolled rock testing machine (RLW-3000). The loading was applied in both horizontal and vertical directions. The maximum axial loading was 3000 kN, the maximum horizontal loading was 1000 kN, and the measurement error of loading force was less than 1%.

The AE activities were recorded on an eight-channel PCI-2 AE monitoring system (Physical Acoustic Corporation). The bandwidth of the AE acquisition card is 3 kHz-



(a) Biaxial compression experimental system



(b) Size and loading conditions of experiment

FIGURE 2: Biaxial compression experiment using AE monitoring.

3 MHz. An R6a sensor was used which has working temperature from -65-175 degrees Celsius, size of 19*22 mm, frequency range of 35-100 kHz, and center frequency of 60 kHz. The magnification is adjustable to 20, 40, and 60 dB over three gears. The observation system consists of a CCD high-speed camera, a high-resolution video surveillance system, and a digital video camera which can obtain images during crack development and rock failure.

The test granite specimen in this experiment was a cube with side length of 100 mm and a 15 mm-diameter circular opening in the middle (Figure 2(b)). Before AE monitoring began, the horizontal and vertical loads were gradually loaded to 10 kN by stress loading. The vertical load was stopped as the horizontal load continued to 100 kN and was held unchanged by the servocontrol system. AE sensors with 40 dB threshold and 1 MHz sampling frequency were then arranged on the specimens for AE monitoring. The loading applied at the upper side increased from 10 kN until failure of the granite specimen. The bottom end was prevented from displacement in the vertical direction. The sampling frequency of the high-speed video was 100 frames per second.

2.2. Experimental Results

2.2.1. Axial Load-Displacement Curve and Fracture Evolution Process. The axial load-displacement curve was determined as shown in Figure 3. Based on the biaxial compression load-displacement curve, three feature points (A, B, and C) were identified. Point A is the critical point from the compaction stage to elastic deformation, point B is the critical point from elastic deformation to inelastic deformation, and point C is the peak stress of the load-displacement curve. At Point A, the axial loading force of the granite specimen was equal to the lateral loading force. Li et al. [18] showed that when the stress increases to 78.2% of the peak loading value, critical cracks initiate in the tensile stress concentration zones under uniaxial loading conditions; similar results were also reached

by Zhong et al. [41]. Based on previous research, the axial loading force at Point B was determined to be 80% of the peak stress under biaxial loading.

As shown in Figure 3, the axial force was 100.14 kN at Point A, 677.29 kN at Point B, and 846.59 kN at Point C. The ratio of the lateral loading force to the axial loading force was defined as the lateral pressure coefficient. During the experiment, the lateral pressure coefficient decreased as the axial load force increased continuously. In region OA, the lateral pressure coefficient was greater than 1. The axial load-displacement curve of the granite specimen shows deformation characteristics in the compaction stage. In region AB, the lateral pressure coefficient decreased from 1 to 0.148 and the axial load-displacement curve of the granite specimen exhibited elastic deformation characteristics. In region BC, the lateral pressure coefficient decreased from 0.148 to 0.120 and the axial load-displacement curve of the granite specimen showed plastic deformation characteristics.

2.2.2. AE Hit and Energy Distribution Characteristics. The number and total energy of AE hits in each time window were counted over the course of the experiment as shown in Figure 4. Both indicators increased until reaching a peak at about 30 s, then decreased until 100 s. From 100 s to 360 s, they remained basically unchanged. The selection of Point A could be revised at 100 s; the axial force was 15% of the peak stress, 130 kN.

As shown in Figure 4, the number of AE hits increased in a fluctuant manner while the total energy of AE dropped slightly from 560 s to 590 s, which is congruous with the characteristics of the number and total energy of AE hits. The number of AE hits decreased rapidly and the total energy released by AE hits increased rapidly after 590 s. The selection of Point B could be revised accordingly at 590 s; the axial force was 85% of the peak stress, 720 kN.

The region AB can be divided into three phases. In the first phase (from 100 s to 360 s), the number and total energy

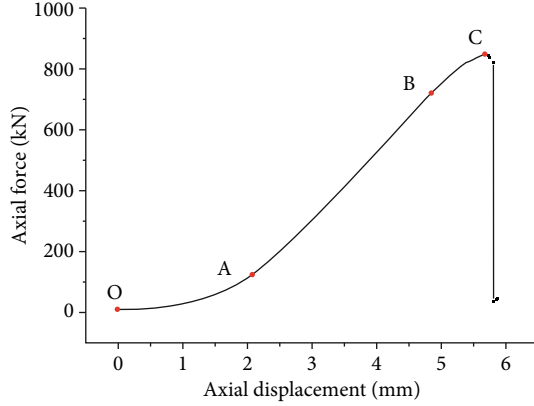


FIGURE 3: Curve of axial force versus axial displacement.

of AE hits was small and relatively constant. In the second phase (from 360 s to 510 s), the number and total energy of AE hits increased in a fluctuant manner. In the third phase (from 510 s to 590 s), the number of AE hits increased in a fluctuant manner while the total energy of AE slightly decreased. The region BC extended from 590 s to 699 s. Gao et al. [42, 43] carried out similar stress-strain curves and generation characteristics of AE, which confirms the repeatability of these experimental results.

Ai et al. (2011) examined the spatial-temporal evolution of AE locations under triaxial compression to find that the number of and energy released by the AE hits first increases and then decreases as axial stress reaches the confining pressure value. This is the so-called “confining pressure effect” of AE. The peak of the number and total energy of AE hits during the OA stage should be also attributed to the confining pressure.

2.3. Evolution Characteristics of High-Energy and Low-Energy AE Hits

2.3.1. Definition of High-Energy and Low-Energy AE Hits

(1) *Average Energy Logarithm Evolution Characteristics of AE Hits.* Ten seconds were selected as a time window and the AEL was calculated to analyze the AE hit energy evolution over the course of the rock specimen failure process. The change curve of AEL versus time during the biaxial compression experiment is shown in Figure 5. This curve can be divided into three stages. In the first stage (from 0 s to 360 s, corresponding to the region OA and the first phase in the region AB), AEL fluctuated around 3.75. In the second stage (from 360 s to 590 s, corresponding to the second and third phases in the region AB), the AEL fluctuated while trending upward. In the third stage (from 590 s to 705 s, corresponding to the region BC), the AEL began to increase rapidly from 4 to 8.23. The average energy corresponding to a given AE hit in the time window increased with some fluctuation after 360 s and significantly increased after 590 s.

(2) *Energy Distribution Evolution Characteristics of AE Hits.* The energy distribution evolution characteristics of AE hits were analyzed as shown in Figure 6. As shown in Figure 7, the density of AE hits versus the logarithm of AE energies obeys a Burr distribution from 0 s to 670 s. However, it did not obey the Burr distribution from 670 s to 705 s. The density function of the Burr distribution can be expressed as follows:

$$f(x | a, c, k) = \frac{(kc/a)(x/a)^{c-1}}{[a + (x/a)^c]^{k+1}}, \quad x > 0, a > 0, c > 0, k > 0, \quad (1)$$

where a is a scale parameter, c is a parameter of inequality, x is the logarithm of energy, and k is a shape parameter.

The peak density as per the AE hit energy distribution increased from $10E2.4$ aJ to $10E3.0$ aJ between 0 s and 670 s. Although the density of AE hits versus the logarithmic AE energies did not obey the Burr distribution from 670 s to 700 s, the peak density increased from $10E3.0$ aJ to $10E5.6$ aJ. The energy of AE hits ranged from $10E1.8$ aJ to $10E5.6$ aJ before 490 s (corresponding to the region OA and the first/second phases in the region AB). After 490 s (corresponding to the third phase in the region AB and the region BC), AE hits with energy larger than $10E5.6$ aJ began to appear, then increased in proportion as the loading time progressed. The AEL evolution characteristics are closely related to the number of AE hits with energy larger than $10E5.6$ aJ.

(3) Evolution Characteristics of Cracks in Granite Specimen.

The evolution of cracks during the biaxial compression experiment is shown in Figure 8. As shown in Figure 8, no obvious microcracks were observed before 477 s. Between 477 s and 587 s, microcracks emerged and developed along the primary structural planes (e.g., interfaces between the groundmass and phenocryst) but did not connect with each other (Figure 6). After 587 s, these microcracks expanded into tensile cracks (PTC), remote cracks (RC), and shear cracks (SC) around the circular opening due to the stress concentration around the opening. The SC continuously expanded and gradually connected with the RC and PTC over the loading time, as similarly observed by Dzik et al. [44], Martin et al. [45], and Zhu et al. [46].

By comparing the energy distribution evolution characteristics of AE hits and the evolution characteristics of cracks, the increase in AE hits with energy $>10E5.6$ aJ was found to be attributable to the evolution and growth of microcracks and cracks in the granite specimen. Thus, AE hits with energy $<10E5.6$ aJ were defined as “low-energy AE hits” and those $>10E5.6$ aJ as “high-energy AE hits.”

2.3.2. Evolution of High-Energy and Low-Energy AE Hits

(1) *Evolution Characteristics of High-Energy and Low-Energy AE Hits.* The energy distribution of AE hits over the course of the experiment is shown in Figure 9(a). The energy of AE hits was mainly distributed in the low-energy range during the experiment. The energy distribution of high-energy AE hits

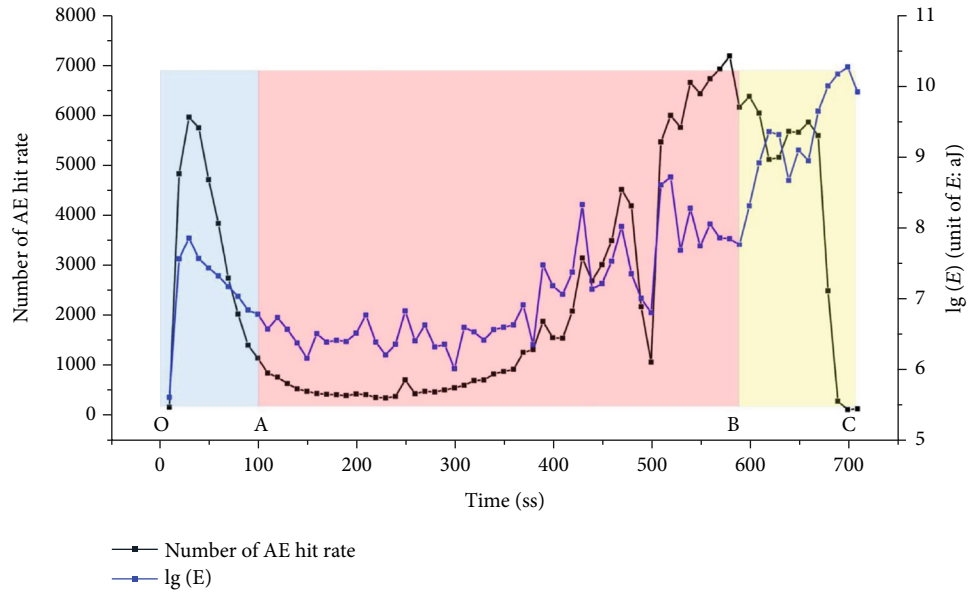


FIGURE 4: Curves of AE hit rate and energy during loading process.

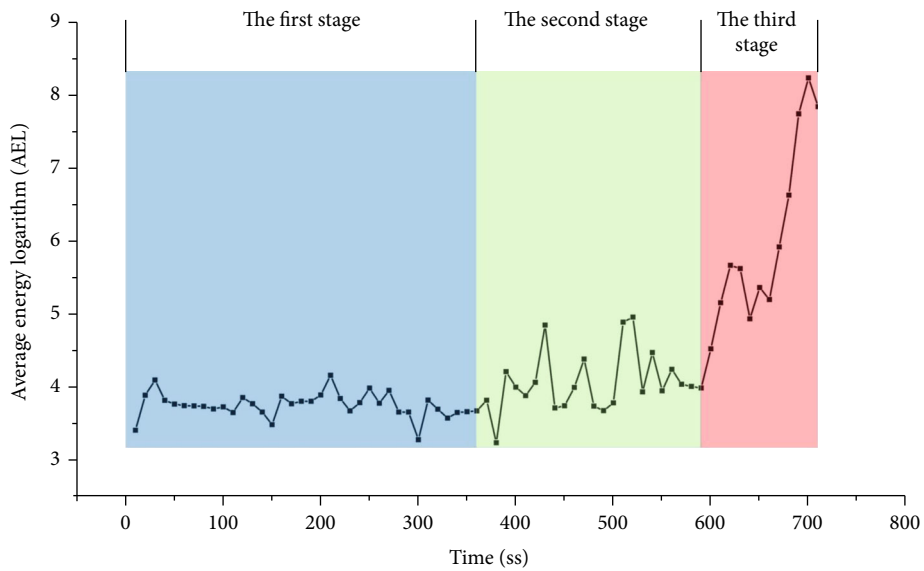


FIGURE 5: Change curve of AEL during the experiment process.

is shown in Figure 9(b). There were fewer high- than low-energy hits, but some did remain in the later stages of the experiment.

AE hits with energy ranging from $10E2.4$ aJ to $10E2.6$ aJ were selected to analyze the low-energy hit evolution characteristics during the experiment; hits ranging from $10E5.8$ aJ to $10E6.0$ aJ were selected to analyze the high-energy hit evolution characteristics during the experiment. As shown in Figure 10(a), the energy evolution characteristics of low-energy AE hits was approximately the same as that of all AE hits. As shown in Figure 8(b), the energy evolution characteristics of high-energy AE hits were quite different from that of low-energy hits and can be divided into three stages: basically negligible in the first loading

stage (before 360 s), increasing slightly in the second loading stage (from 360 s to 490 s), and increasing rapidly in the third loading stage (after 490 s).

The distribution of AE hits and energy monitored during the experiment were mainly dependent on the low-energy AE hits. There also were some similarities among the evolution characteristics of high-energy AE hits and the AEL evolution characteristics of the hits; an increase in the number of the high-energy AE hits is the root cause of an increase in AEL. The evolution characteristics of high-energy AE hits also are in close agreement with the evolution characteristics of cracks in the granite specimen.

(2) *Evolution Mechanism of High-Energy and Low-Energy AE Hits.* The granite specimen used in the experiment has a

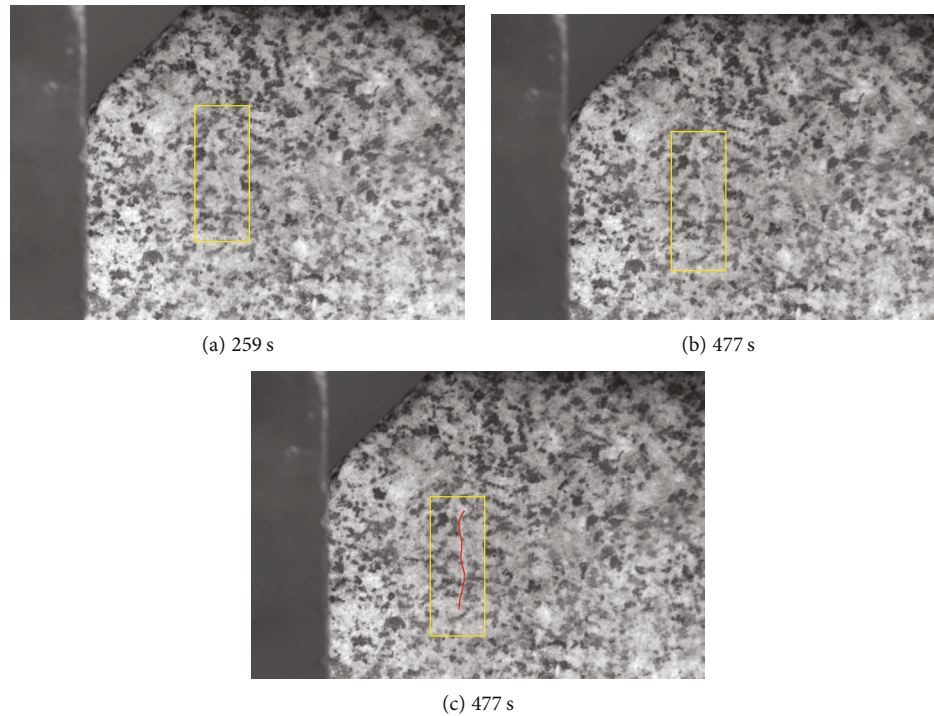


FIGURE 6: Trace of an example microcrack.

porphyritic texture and is composed of two different sizes of granules. Large granules (or “phenocrysts”) were scattered among the small granules (groundmass). The groundmass is composed of microlite, crystallite, cryptocrystalline, or glassy material. In the local region, there were several closely packed, interconnected phenocrysts. Phenocrysts and their interfaces constituted the framework of the granite specimen. The diameter of phenocrysts ranges from 1 mm to 5 mm while that of groundmass granules is less than 1 mm. The evolution mechanism of high-energy and low-energy AE hits can be summarized as per the microscopic structure of the granite specimen, evolution characteristics of cracks in the granite specimen, and the evolution mechanism of high-energy and low-energy AE hits.

In the early stage of the loading process (before 490 s, corresponding to the region OA and the first/second phases in the region AB), low-energy AE hits caused by failure of the small groundmass occurred in the granite specimen. Though groundmass failure had little effect on the damage of the granite specimen, it led to the stress concentration in the specimen’s framework (which did not fail in this stage). As the loading increased, the interfaces of one phenocryst to another phenocryst or to the groundmass failed and produced high-energy AE events. The granite specimen entered the midstage of the loading process at this point (from 490 s to 590 s, corresponding to the third phase in the region AB), where the number of low-energy AE hits was much higher than that of high-energy AE hits.

As the number of the failed interfaces continued to increase, stress transferred to the phenocrysts in the granite specimen and caused them to fail alongside the emergence of high-energy AE events. Failure of both the interfaces and phenocrysts damaged the granite specimen. Once a certain amount of damage had accumulated, the granite specimen entered the later stage of the loading process (from 590 s to 705 s, corresponding to the region BC). Phenocrysts inside the specimen failed and quickly penetrated the primary structural planes, which ultimately led to the failure and instability of the whole specimen. A rapid increase in the number of high-energy AE hits (with still relatively few low-energy hits) is an important indicator that this stage has begun. The evolution mechanism of high energy and low energy AE hits explains this phenomenon that the closer to failure AE data are used as initial input into the AE data-driven model to simulate the rock failure process, the better the model predictions of failure are by Wei et al. [47].

(3) *Relationship between Evolution Mechanism and Gutenberg-Richter b Value.* The Gutenberg-Richter b value was calculated over the loading process. Ten seconds was selected as a time window representative of the whole biaxial compression experiment. The b value in each time window was calculated to determine its variations with time as shown in Figure 11. The b value fluctuated around 0.83 before 490 s (corresponding to the region OA and the first/second phases in the region AB) and decreased slightly from 490 s to 590 s (corresponding to the third phase in the region AB), then

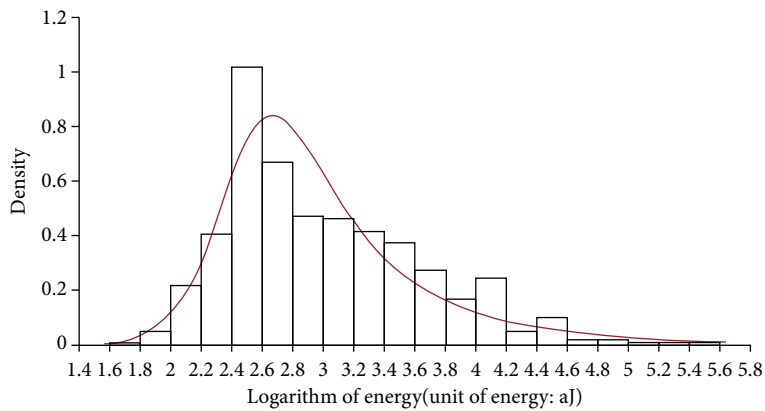
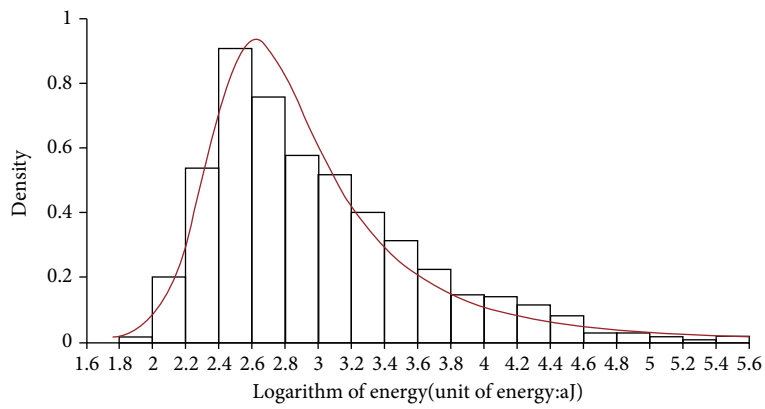
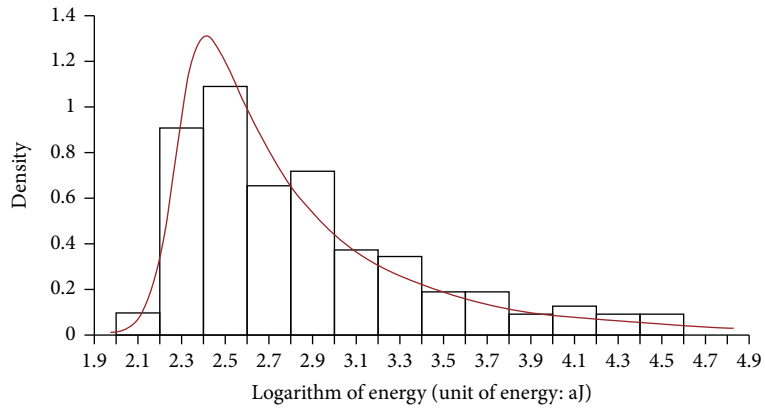


FIGURE 7: Continued.

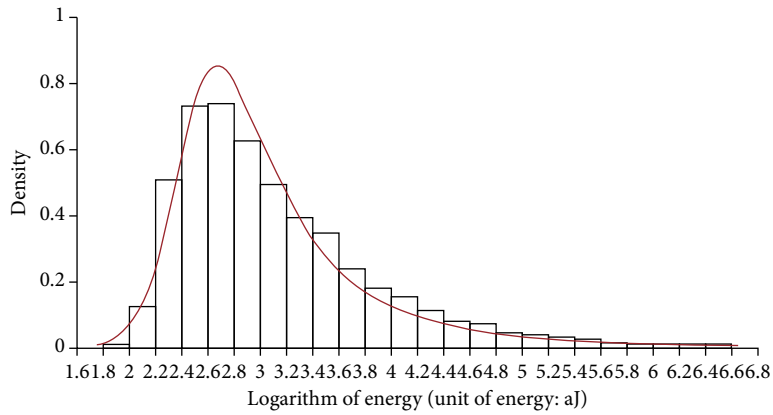
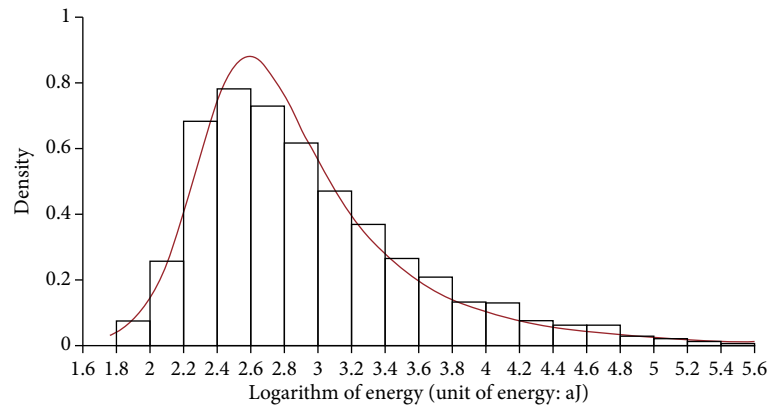
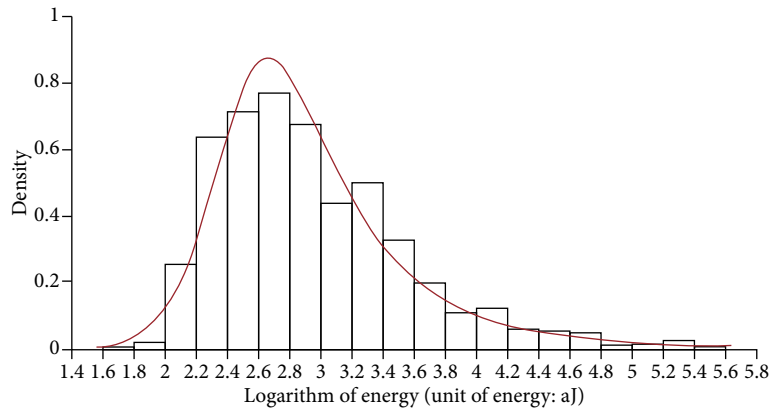
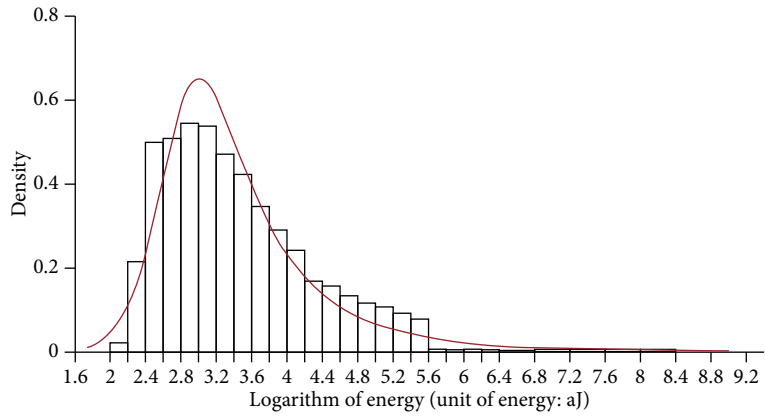
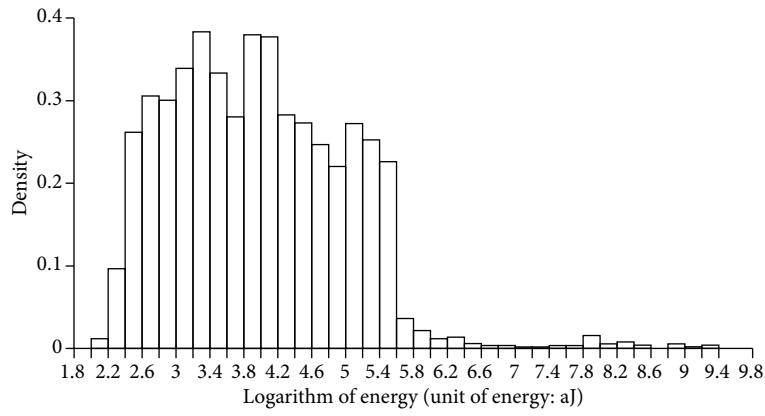


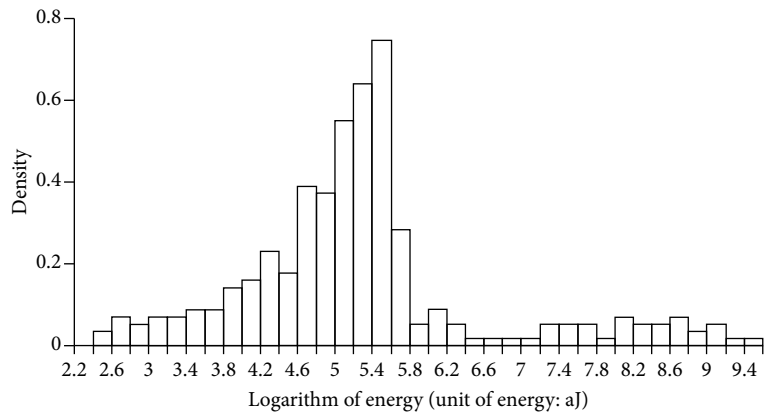
FIGURE 7: Continued.



(g) Density of AE hits (from 660 s to 670 s)

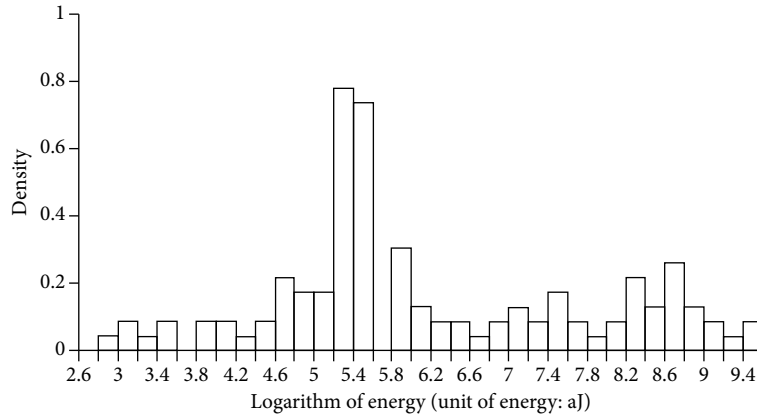


(h) Density of AE hits (from 670 s to 680 s)



(i) Density of AE hits (from 680 s to 690 s)

FIGURE 7: Continued.



(j) Density of AE hits (from 690 s to 700 s)

FIGURE 7: Energy distribution of AE hits (note: the red curve is the fitting result with the Burr distribution model).

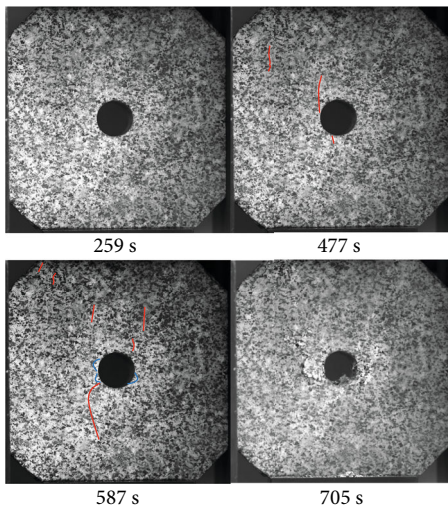


FIGURE 8: Crack evolution characteristics during biaxial compression experiment (note: microcracks marked with red lines, macrocracks marked with blue lines).

declined rapidly after 590 s (corresponding to the region BC). At 490 s, the axial loading force increased to 72% of the peak loading value. At 590 s, the axial loading force increased to 85% of the peak loading value (corresponding to Point C in the axial load-displacement curve).

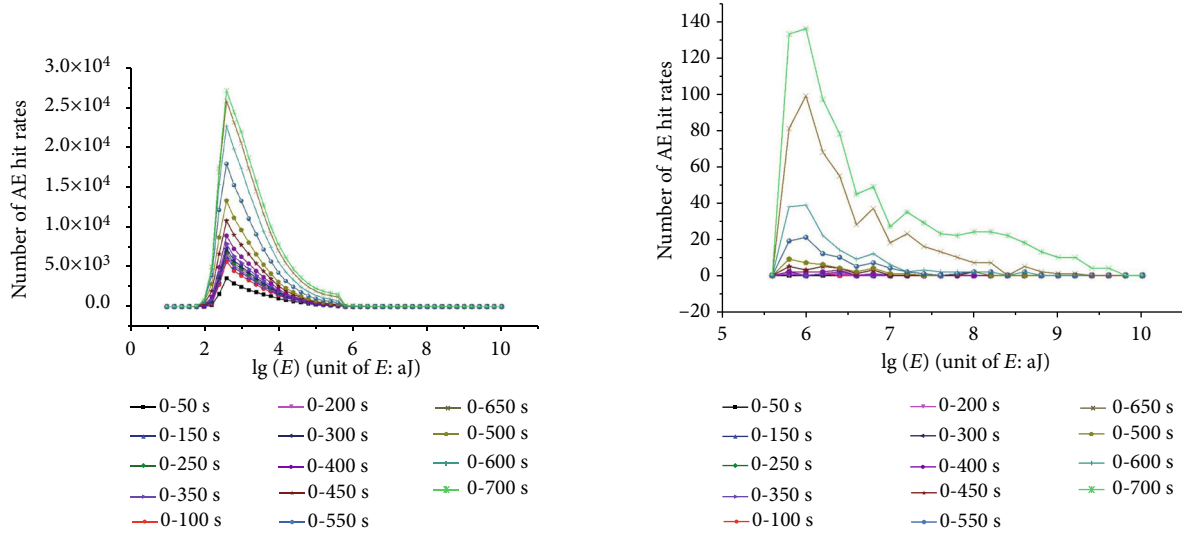
The high-energy AE hit evolution characteristics were inversely proportional to the Gutenberg-Richter b value of the granite specimen during the loading process. The increase in low-energy AE hits did not cause the Gutenberg-Richter b value to change, but the increase in high-energy hits caused the Gutenberg-Richter b value to decrease. A larger b value decreasing rate created a larger increasing high-energy AE hit rate. This further validates the high- and low-energy AE hit evolution mechanism presented above.

3. High-Energy and Low-Energy MS Event Evolution Characteristics

3.1. Engineering Geology and MS Monitoring System. General geological information for the Dongjiahe Coal Mine and MS monitoring system used in this study is given in a previous publication by Cheng et al. [15]. Briefly, the Dongjiahe Coal Mine is located in northwestern China. The No. 22517 working face is a typical advancing mining face which has a length of 1217 m, width of 185 m, and dips from east to west. The inclination angle of the working face is approximately 3° , making it nearly horizontal. The open cut is located at 1217 m and the mining stop line at 100 m. The coal seam in the working face varies in thickness from 2.5 m to 4.1 m with an average thickness of 3.3 m. The schematic sketch of the No. 22517 working face is shown in Figure 12. The advancement schedule of the No. 22517 working face is given in Table 1.

According to the drill histogram of No. 22517 (Figure 13), the rock mass strata around the working face is, according to the ages of formation from old to new, as follows: middle Ordovician System, Fengfeng Formation; upper Carboniferous System, Taiyuan Formation; lower Permian System, Shanxi Formation; lower Permian System, Xiashihezi Formation; and Quaternary System overburden soil.

Geophones with 43.3 V/m/s sensitivity were adopted in the MS monitoring system used in this study. The response frequency of geophones ranges from 15 to 1000 Hz. The geophone placement scheme for MS monitoring is given in detail by Cheng et al. [15]. The Geiger location method was used here to localize the MS. The P-wave velocity was estimated at 2800 m/s and the S-wave velocity at 1800 m/s based on artificial blasting tests. The ESG microseismic monitoring system is used for signal acquisition, including Paladin underground digital signal acquisition system, Hyperion surface digital signal processing system, and MMVTS-3D visualization software. The system can monitor continuously 24 hours in real time. Many focal parameters such as time-



(a) Energy distribution of all AE hits during the experiment process (b) Energy distribution of high-energy AE hits during the experiment process

FIGURE 9: Energy distribution of AE hits during the experiment process.

space coordinates, errors, magnitude, and energy of microseismic events can be obtained. The collected data can be filtered, and the complete waveform and spectrum analysis chart of source information can be provided. At the same time, it can automatically identify the type of microseismic events and eliminate noise events by filtering, threshold setting and bandwidth detection.

3.2. Evolution Characteristics of High-Energy and Low-Energy MS Events. Basic MS monitoring results are given in the previous publication by Cheng et al. [15]. The energy and moment magnitude of MS events over coal seams caused by mining activities were analyzed based on this information; the results are shown in Figure 14. As shown in Figures 14(a) and 14(b), the energy distribution and the moment magnitude distribution of MS events conformed in this case to the BMD. The energy of low-energy MS events was less than 158.5 J, while the energy of high-energy MS events was greater than 158.5 J (Figure 14(a)). The moment of low-energy MS events was less than -0.1, while the energy of high-energy MS events was greater than -0.1 (Figure 14(b)).

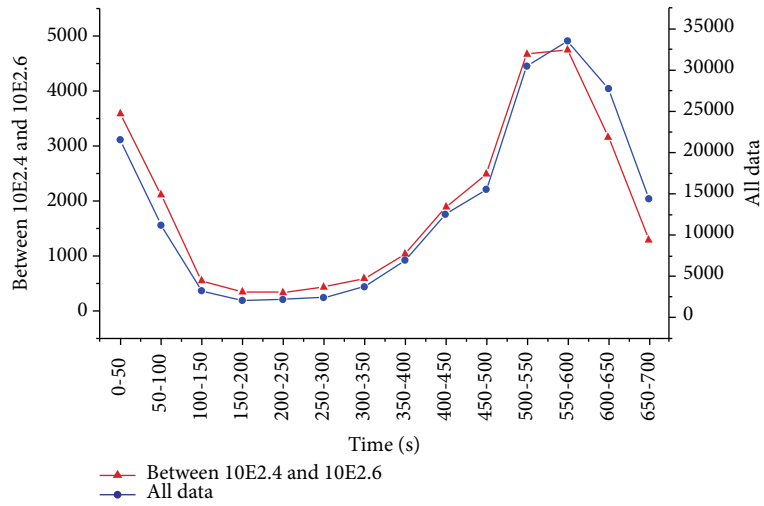
The average energy logarithm (AEL) was defined to further analyze the difference between high- and low-energy MS event components. The AEL is a logarithm of the ratio of the total energy to the number of all MS events in a one-day period (Formula (2)). Its physical meaning corresponds to the average energy of MS events in a given day. The curve of AEL versus time is given in Figure 14(c), where AEL mainly varied between 0.5 and 2.0 from Nov. 25, 2014, to Feb. 25, 2015, and between 2.8 and 4.1 from Feb. 25, 2015, to Oct. 10, 2015. The high-energy MS event components appear to have increased rapidly after Feb. 25.

$$AEL = \lg(E_w/N_w), \quad (2)$$

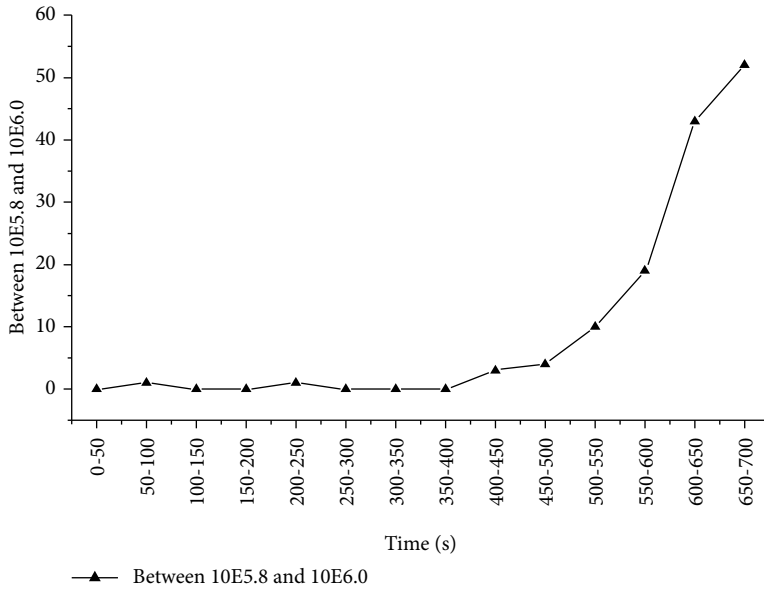
where AEL is the average energy logarithm, N_w is the number of MS events in a day, and E_w is the sum of energy of MS events in a day.

Cheng et al. [15] introduced time-, location-, and energy-related evolution characteristics of MS events in the roof of the Dongjiahe Coal Mine. Based on their monitoring results, new MS events added monthly fell into the region from 30 m behind the mining face to 220 m in front of the mining face along the horizontal direction and in the region from the elevation of +320 m to +500 m along the vertical direction after Mar. 6, 2015 [15]. Most of the new MS events added monthly were concentrated in the coal pillar supporting zone, the support and bed-separation zone along the horizontal direction, and from the top of the fractured zone to the bottom of the continuous zone along the vertical direction. Based on the conceptual model proposed by Qian et al. [48], the rock mass was in a state of near failure or had already failed in the zone where these new monthly MS events occurred. By Feb. 25, 2015, the working face had advanced 360 m (about twice the width of the working face) from the open cut to the stopping line.

The MS monitoring data suggests that the working face was in the insufficient mining stage (in the stage, only the collapse zone is formed but the fracture zone is not formed in the process of rock failure; the maximum subsidence value of the strata continues to increase) before Feb. 25 and that the height of the fracture zone caused by mining did not develop to the final height. After Feb. 25, the working face was in the sufficient mining stage (in this stage, the size of the goaf is large enough and the maximum subsidence value of the strata does not increase) and the fracture zone developed to the final height. Thus, the high-energy MS events occurred beginning on Feb. 25, because the failure scale of the overlying rock mass increased upon the working face entering the sufficient mining stage.



(a) Energy evolution characteristics of low-energy AE hits



(b) Energy evolution characteristics of high-energy AE hits

FIGURE 10: Energy evolution characteristics of low-energy and high-energy AE hits.

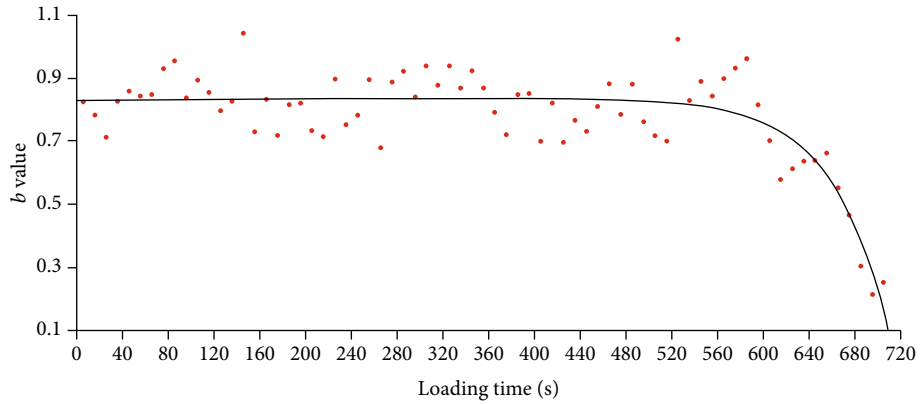


FIGURE 11: Change of b value of Gutenberg-Richter during loading process.

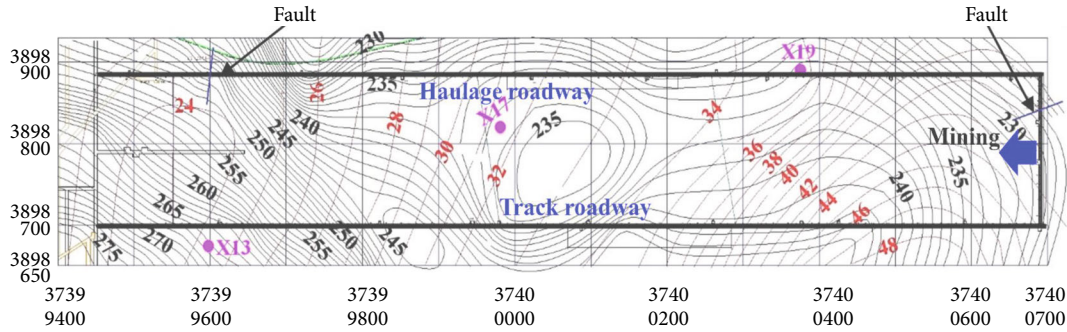


FIGURE 12: Schematic sketch of coal seam of No. 22517 working face.

TABLE 1: Mining schedule, No. 22517 working face of Dongjiahe Coal Mine [15].

Date (year/month/day)	The mining face (pitch distance)
2014/12/23	1005 m
2015/01/09	981 m
2015/01/19	942 m
2015/01/30	917 m
2015/02/09	885 m
2015/02/15	856 m
2015/02/27	847 m
2015/03/09	803 m
2015/03/19	779 m
2015/03/30	760 m
2015/04/09	714 m
2015/04/18	700 m
2015/04/29	694 m
2015/05/08	688 m
2015/05/19	681 m
2015/05/30	750 m
2015/06/09	745 m
2015/06/19	736 m
2015/06/29	730 m
2015/07/09	720 m
2015/07/18	677 m
2015/07/30	665 m
2015/08/08	657 m
2015/08/15	648 m
2015/08/19	642 m
2015/08/30	628 m
2015/09/08	615 m
2015/09/19	603 m
2015/09/29	592 m
2015/10/09	578 m

4. Discussion

There are some similarities among the evolution characteristics of high-energy MS events and low-energy AE hits. Both

have bimodal characteristics and can be divided into the high-energy and low-energy components. An increase in the failure scale is the root cause of an increase in the high-energy component. There is also a significant difference between the two: the bimodal distribution of AE hits is far less obvious than that of MS events. There are two potential reasons for this.

The first reason involves differences in the monitoring equipment. The frequency range of the R6a sensor in the AE monitoring system extends from 35 kHz to 100 kHz while that of the geophone in the MS monitoring system is from 15 Hz to 1000 Hz. The bandwidth of the AE monitoring system is much larger than that of the MS monitoring system. In addition, the scale of the AE monitoring system monitoring object is far smaller than that of the MS monitoring system monitoring object. Therefore, the AE monitoring system serves to detect AE events caused by the full-scale microcracks of rock specimens during the experiment while the MS monitoring system cannot detect the MS events caused by small-scale microcracks, which are the main components of low-energy MS events.

The second reason involves differences in the monitoring object. In this study, the object of the AE monitoring system is a granite specimen while that of the MS monitoring system is sandstone/mudstone. Granite is an igneous rock; sandstone and mudstone are sedimentary. The diagenesis of igneous rock material differs from that of sedimentary rock materials, so there are substantial differences between the microstructures of granite and sandstone and mudstone. The rock specimen used in the laboratory was not designed with consideration of its structural plane, though the in situ rock mass contains a large number of original structural planes. These factors may have made the BMD of AE hits less obvious than that of MS events.

5. Conclusions

Microseismic and acoustic emission monitoring are always carried out in engineering rock masses and experimental rocks, and the evolution characteristics of high-energy and low-energy events occurring in the deformation of the rock are instructive for optimizing monitoring and understanding the failure mechanism. In this study, combining the granite specimen biaxial compression experiment and the MS monitoring results of the 22517 working face in the Dongjiahe

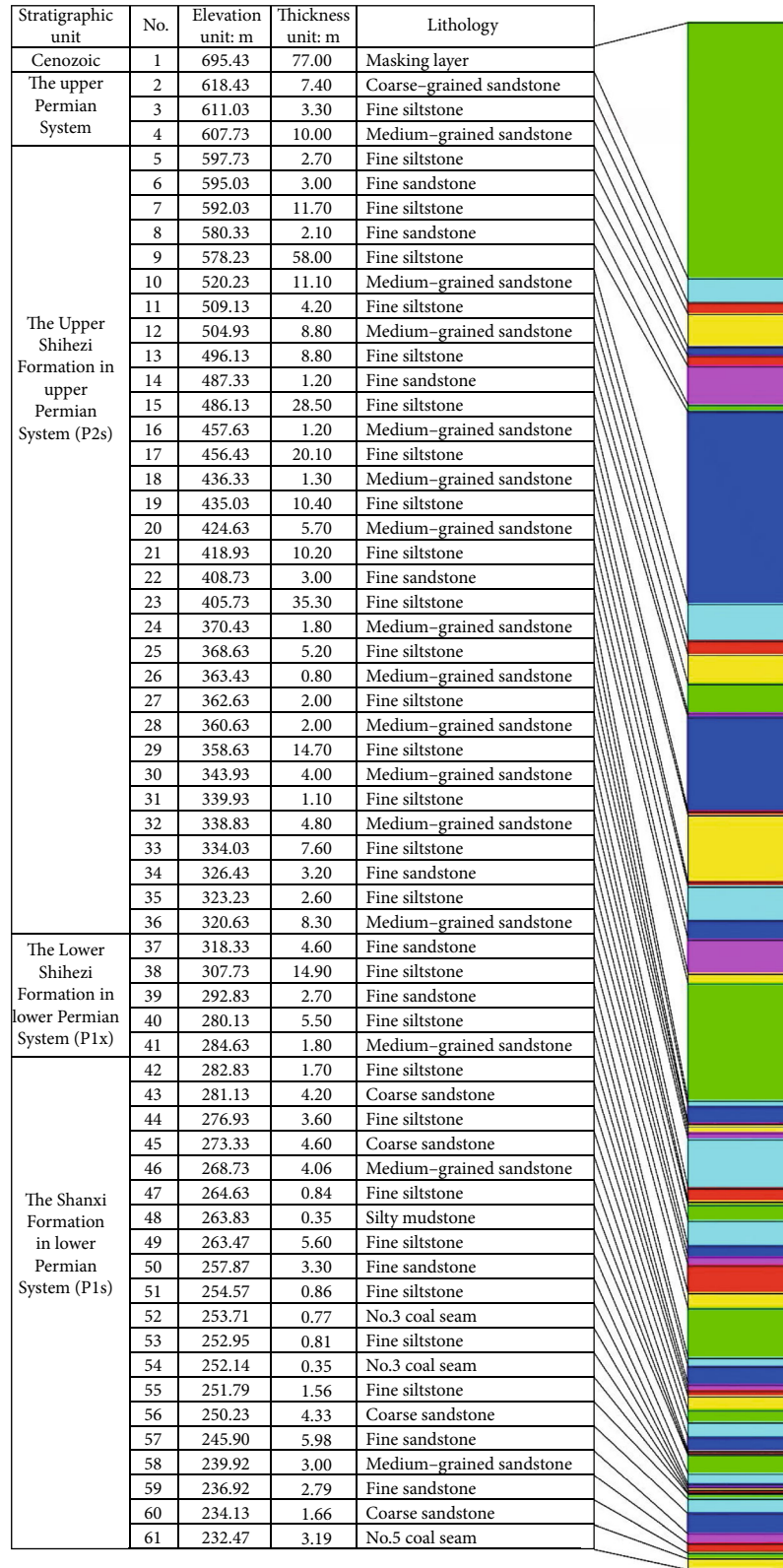
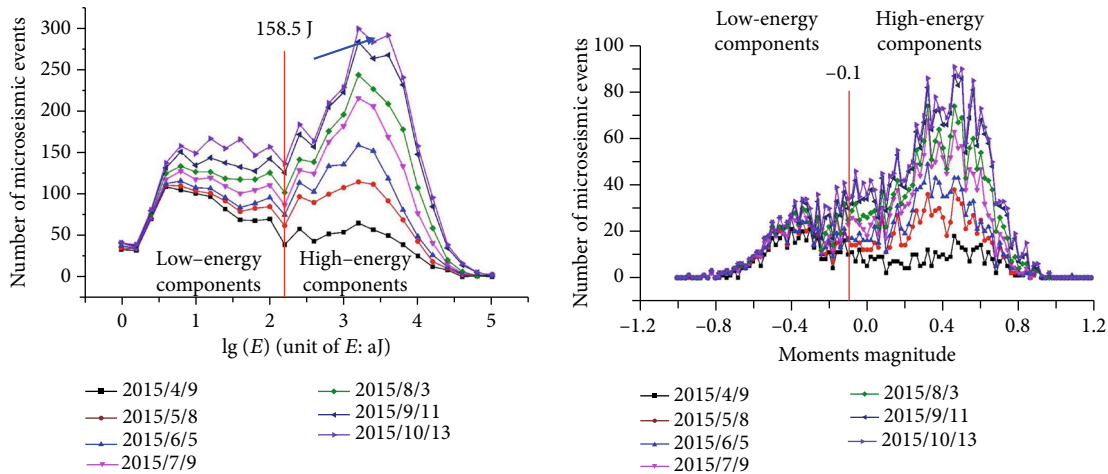


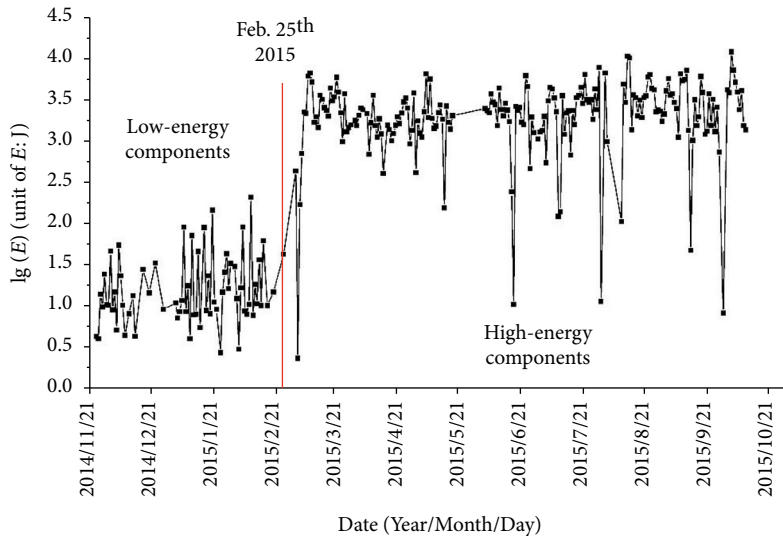
FIGURE 13: Drill histogram of No. 22517 working face [15].

Coal Mine, the evolution characteristics of microseismic events were analyzed based on the bimodal distribution (BMD) model, and the following conclusions were obtained:

- (1) The MS monitoring results of No. 22517 working face in Dongjiahe Coal Mine show unimodal energy and moment magnitude distributions from Nov. 25,



(a) Energy distribution characteristic of microseismic events in No. 22517 working face (b) Moment magnitude distribution characteristic of microseismic events in No. 22517 working face



(c) Curve of energy index with time in No. 22517 working face

FIGURE 14: Energy and moment magnitude distribution of MS events.

2014, to Feb. 25, 2015; the distributions were bimodal from Feb. 25, 2015, to Oct. 10, 2015. High-energy MS events were generated due to an increase in the failure scale of the overlying rock mass once the working face crossed into the sufficient mining stage from the insufficient mining stage

(2) Biaxial compression experiments were conducted on a granite specimen to observe various characteristics of low- and high-energy AE hits. The whole loading process was divided into three stages. In the first loading stage, only low-energy AE hits occurred. In the second loading stage, high-energy AE hits began to appear and slowly grew more common. In the third loading stage, the quantity of high-energy AE hits increased rapidly until the specimen failed. Low-energy AE hits were more common than high-energy AE hits throughout the whole loading process, but the change characteristics

of the high-energy hits appeared to be positively correlated with the evolution of cracks in the granite specimen and negatively correlated with changes in the Gutenberg-Richter *b* value. The high-energy and low-energy AE hit evolution mechanism was defined here based on the microscopic structure of the granite specimen

(3) This paper discussed the similarities and differences between the evolution of high-energy MS events and low-energy AE hits. Both were found to have bimodal characteristics and can be divided into high-energy and low-energy components. An increase in the failure scale is the root cause of the increase observed in the high-energy component. The bimodal distribution of AE hits was far less obvious than that of MS events, which is likely attributable to differences in the monitoring equipment and monitoring object

Data Availability

As for the data availability statement, some or all data, models, or code generated or used during the study are available from the corresponding author by request (list items).

Conflicts of Interest

No conflict of interest exists in the submission of this manuscript.

Authors' Contributions

The manuscript is approved by all authors for publication.

Acknowledgments

We thank Shaanxi Coal and Chemical Technology Institute Co., Ltd. for approving our publication, and the personnel at the Dongjiahe coal mine. We thank Dalian University of Technology for facilitating our project and personnel at the State Key Laboratory of Coastal and Offshore Engineering in Dalian University of Technology. The project was funded by the National Science Foundation of China (Grant Nos. 51909032, 51627804, and U1710253) and Department of Science and Technology of Anhui Province (Nos. 2008085ME145 and 17030901023).

References

- [1] S. Gibowicz and A. Kijko, *An Introduction to Mining Seismology*, Elsevier, 1994.
- [2] A. Kijko, M. Dessokey, E. Głowacka, and M. Kazimierczyk, "Periodicity of strong mining tremors in the Lubin copper mine," *Acta Geophysica Polonica*, vol. 30, pp. 221–230, 1982.
- [3] I. Main, "A characteristic earthquake model of the seismicity preceding the eruption of Mount St. Helens on 18 May 1980," *Physics of the Earth and Planetary Interiors*, vol. 49, no. 3–4, pp. 283–293, 1987.
- [4] I. Main and P. Burton, "Physical links between crustal deformation, seismic moment and seismic hazard for regions of varying seismicity," *Geophysical Journal International*, vol. 79, no. 2, pp. 469–488, 1984.
- [5] T. Stankiewicz, *Stochastic Model of Seismic Activity and its Application to Seismic Hazard Estimates in Mines*, Institute of Geophysics, Polish Academy of Sciences, Warsaw, 1989.
- [6] A. Kijko, B. Drzezla, and T. Stankiewicz, "Bimodal character of the distribution of extreme seismic events in Polish mines," *Acta Geophysica Polonica*, vol. 35, no. 2, pp. 157–166, 1988.
- [7] T. Li, T. Mei, X. Sun, Y. Lv, J. Sheng, and M. Cai, "A study on a water-inrush incident at Laohutai coalmine," *International Journal of Rock Mechanics and Mining Sciences*, vol. 59, pp. 151–159, 2013.
- [8] K. Zhang, T. Yang, H. Bai, and R. Pathegama Gamage, "Long-wall mining-induced damage and fractures: field measurements and simulation using FDM and DEM coupled method," *International Journal of Geomechanics*, vol. 18, no. 1, article 04017127, 2018.
- [9] Y. Xiao, X. T. Feng, J. A. Hudson, B. R. Chen, G. L. Feng, and J. P. Liu, "ISRM suggested method for in situ microseismic monitoring of the fracturing process in rock masses," *Rock Mechanics and Rock Engineering*, vol. 49, no. 1, pp. 343–369, 2016.
- [10] G. Feng, X. Feng, B. Chen, Y. X. Xiao, and Y. Yu, "A microseismic method for dynamic warning of rockburst development processes in tunnels," *Rock Mechanics and Rock Engineering*, vol. 48, no. 5, pp. 2061–2076, 2015.
- [11] N. Xu, T. Li, F. Dai, R. Zhang, C. A. Tang, and L. X. Tang, "Microseismic monitoring of strainburst activities in deep tunnels at the Jinping II hydropower station, China," *Rock Mechanics and Rock Engineering*, vol. 49, no. 3, pp. 981–1000, 2016.
- [12] Y. Yu, B. Chen, C. Xu, X. H. Diao, Tong, and Y. F. Shi, "Analysis for microseismic energy of immediate rockbursts in deep tunnels with different excavation methods," *International Journal of Geomechanics*, vol. 17, no. 5, article 04016119, 2017.
- [13] Y. Yu, D. Geng, L. Tong, X. S. Zhao, X. H. Diao, and L. H. Huang, "Time fractal behavior of microseismic events for different intensities of immediate rock bursts," *International Journal of Geomechanics*, vol. 18, no. 7, article 06018016, 2018.
- [14] J. Wang, J. Liu, H. Liu, Z. Tian, and F. Cheng, "Modeling and locating underground water pipe leak with microseismic data," *Journal of Applied Geophysics*, vol. 136, pp. 1–8, 2017.
- [15] G. Cheng, T. Ma, C. Tang, H. Liu, and S. Wang, "A zoning model for coal mining-induced strata movement based on microseismic monitoring," *International Journal of Rock Mechanics and Mining Sciences*, vol. 94, pp. 123–138, 2017.
- [16] A. Cao, L. Dou, W. Cai, S. Gong, S. Liu, and G. Jing, "Case study of seismic hazard assessment in underground coal mining using passive tomography," *International Journal of Rock Mechanics and Mining Sciences*, vol. 78, pp. 1–9, 2015.
- [17] A. Cao, L. Dou, C. Wang, X. X. Yao, J. Y. Dong, and Y. Gu, "Microseismic precursory characteristics of rock burst hazard in mining areas near a large residual coal pillar: a case study from Xuzhuang coal mine, Xuzhou, China," *Rock Mechanics and Rock Engineering*, vol. 49, no. 11, pp. 4407–4422, 2016.
- [18] D. Li, Q. Zhu, Z. Zhou, X. Li, and P. G. Ranjith, "Fracture analysis of marble specimens with a hole under uniaxial compression by digital image correlation," *Engineering Fracture Mechanics*, vol. 183, pp. 109–124, 2017.
- [19] C. Lu, L.-M. Dou, H. Liu, H.-S. Liu, B. Liu, and B.-B. Du, "Case study on microseismic effect of coal and gas outburst process," *International Journal of Rock Mechanics & Mining Sciences*, vol. 53, pp. 101–110, 2012.
- [20] T. Li, M. Cai, and M. Cai, "Earthquake-induced unusual gas emission in coalmines-A km-scale in-situ experimental investigation at Laohutai mine," *International Journal of Coal Geology*, vol. 71, no. 2–3, pp. 209–224, 2007.
- [21] P. Zhang, T. Yang, Q. Yu, T. Xu, W. Shi, and S. Li, "Study of a seepage channel formation using the combination of microseismic monitoring technique and numerical method in Zhangmatun Iron Mine," *Rock Mechanics & Rock Engineering*, vol. 49, no. 9, pp. 3699–3708, 2016.
- [22] N. Xu, C. A. Tang, L. C. Li et al., "Microseismic monitoring and stability analysis of the left bank slope in Jinping first stage hydropower station in southwestern China," *International Journal of Rock Mechanics and Mining Sciences*, vol. 48, no. 6, pp. 950–963, 2011.
- [23] F. Dai, B. Li, N. Xu, G. Meng, J. Wu, and Y. Fan, "Microseismic monitoring of the left bank slope at the Baihetan Hydropower Station, China," *Rock Mechanics and Rock Engineering*, vol. 50, no. 1, pp. 225–232, 2017.

- [24] M. Salvoni and P. Dight, "Rock damage assessment in a large unstable slope from microseismic monitoring-MMG Century mine (Queensland, Australia) case study," *Engineering Geology*, vol. 210, pp. 45–56, 2016.
- [25] H. Alkan, Y. Cinar, and G. Pusch, "Rock salt dilatancy boundary from combined acoustic emission and triaxial compression tests," *International Journal of Rock Mechanics & Mining Sciences*, vol. 44, no. 1, pp. 108–119, 2007.
- [26] S. Hall, F. Sanctis, and G. Viggiani, "Monitoring fracture propagation in a soft rock (Neapolitan tuff) using acoustic emissions and digital images," *Pure and Applied Geophysics*, vol. 163, no. 10, pp. 2171–2204, 2006.
- [27] X. Zhao, J. Wang, M. Cai et al., "Influence of unloading rate on the strainburst characteristics of Beishan granite under true-triaxial unloading conditions," *Rock Mechanics and Rock Engineering*, vol. 47, no. 2, pp. 467–483, 2014.
- [28] M. He, J. Miao, and J. Feng, "Rock burst process of limestone and its acoustic emission characteristics under true-triaxial unloading conditions," *International Journal of Rock Mechanics and Mining Sciences*, vol. 47, no. 2, pp. 286–298, 2010.
- [29] H. Ji, H. Wang, S. Cao, Z. Hou, and Y. Jin, "Experimental research on frequency characteristics of acoustic emission signals under uniaxial compression of granite," *Chinese Journal of Rock Mechanics and Engineering*, vol. 31, no. 1, pp. 2900–2905, 2012.
- [30] P. Benson, B. Thompson, P. G. Meredith, S. Vinciguerra, and R. P. Young, "Imaging slow failure in triaxially deformed Etna basalt using 3D acoustic-emission location and X-ray computed tomography," *Geophysical Research Letters*, vol. 34, no. 3, article L03303, 2007.
- [31] J. Fortin, S. Stanchits, G. Dresen, and Y. Gueguen, "Acoustic emissions monitoring during inelastic deformation of porous sandstone: comparison of three modes of deformation," *Pure and Applied Geophysics*, vol. 166, no. 5-7, pp. 823–841, 2009.
- [32] S. Yang, H. Jing, and S. Wang, "Experimental investigation on the strength, deformability, failure behavior and acoustic emission locations of red sandstone under triaxial compression," *Rock Mechanics and Rock Engineering*, vol. 45, no. 4, pp. 583–606, 2012.
- [33] Y. Li, J. P. Liu, X. D. Zhao, and Y. J. Yang, "Experimental studies of the change of spatial correlation length of acoustic emission events during rock fracture process," *International Journal of Rock Mechanics and Mining Sciences*, vol. 47, no. 8, pp. 1254–1262, 2010.
- [34] H. Xie, J. F. Liu, Y. Ju, J. Li, and L. Z. Xie, "Fractal property of spatial distribution of acoustic emissions during the failure process of bedded rock salt," *International Journal of Rock Mechanics and Mining Sciences*, vol. 48, no. 8, pp. 1344–1351, 2011.
- [35] R. Zhang, F. Dai, M. Gao, N. W. Xu, and C. P. Zhang, "Fractal analysis of acoustic emission during uniaxial and triaxial loading of rock," *International Journal of Rock Mechanics & Mining Sciences*, vol. 79, pp. 241–249, 2015.
- [36] S. Chang and C. Lee, "Estimation of cracking and damage mechanisms in rock under triaxial compression by moment tensor analysis of acoustic emission," *International Journal of Rock Mechanics & Mining Sciences*, vol. 41, no. 7, pp. 1069–1086, 2004.
- [37] N. Dixon and M. Spriggs, "Quantification of slope displacement rates using acoustic emission monitoring," *Canadian Geotechnical Journal*, vol. 44, no. 8, pp. 966–976, 2007.
- [38] N. Dixon, M. P. Spriggs, A. Smith, P. Meldrum, and E. Haslam, "Quantification of reactivated landslide behaviour using acoustic emission monitoring," *Landslides*, vol. 12, no. 3, pp. 549–560, 2015.
- [39] A. Smith, N. Dixon, R. Moore, and P. Meldrum, "Photographic feature: acoustic emission monitoring of coastal slopes in NE England, UK," *Quarterly Journal of Engineering Geology and Hydrogeology*, vol. 50, no. 3, pp. 239–244, 2017.
- [40] A. Smith, N. Dixon, and G. Fowmes, "Early detection of first-time slope failures using acoustic emission measurements: large-scale physical modelling," *Géotechnique*, vol. 67, no. 2, pp. 138–152, 2017.
- [41] Z. Zhong, R. Deng, L. Lv, X. Fu, and J. Yu, "Fracture mechanism of naturally cracked rock around an inverted U-shaped opening in a biaxial compression test," *International Journal of Rock Mechanics and Mining Sciences*, vol. 103, pp. 242–253, 2018.
- [42] X. Gao, S. Liu, and J. Huang, "Acoustic emission characteristics of different areas in the fracture process of perforated granite," *Journal of Northeastern University*, vol. 39, no. 11, pp. 136–140, 2018.
- [43] X. Gao, S. Liu, J. Huang, Z. Yang, W. Mao, and L. Wu, "The influence of strain rate on AE characteristics during rock deformation," *Chinese Journal of Rock Mechanics and Engineering*, vol. 37, no. 4, pp. 887–897, 2018.
- [44] E. Dzik and E. Lajtai, "Primary fracture propagation from circular cavities loaded in compression," *International Journal of Fracture*, vol. 79, no. 1, pp. 49–64, 1996.
- [45] C. Martini, R. Read, and J. Martino, "Observations of brittle failure around a circular test tunnel," *International Journal of Rock Mechanics and Mining Sciences and Geomechanics Abstracts*, vol. 34, no. 7, pp. 1065–1073, 1997.
- [46] W. Zhu, J. Liu, C. Tang, X. D. Zhao, and B. H. Brady, "Simulation of progressive fracturing processes around underground excavations under biaxial compression," *Tunnelling and Underground Space Technology*, vol. 20, no. 3, pp. 231–247, 2005.
- [47] J. Wei, W. Zhu, K. Guan, J. Zhou, and J. J. Song, "An acoustic emission data-driven model to simulate rock failure process," *Rock Mechanics and Rock Engineering*, vol. 53, no. 4, pp. 1605–1621, 2020.
- [48] M. Qian and H. Li, "The movement of overlying strata in long-wall mining and its effect on ground pressure," *Journal of China Coal Society*, vol. 2, pp. 1–12, 1982.

Research Article

Research on the Influence of Slurry Filling on the Stability of Floor Coal Pillars during Mining above the Room-and-Pillar Goaf: A Case Study

Zhu Li, Guorui Feng , and Jiaqing Cui

College of Mining Engineering, Taiyuan University of Technology, Shanxi 030024, China

Correspondence should be addressed to Guorui Feng; guorui_feng_tyut@163.com

Received 10 May 2020; Revised 30 June 2020; Accepted 11 August 2020; Published 12 September 2020

Academic Editor: Guozhong Hu

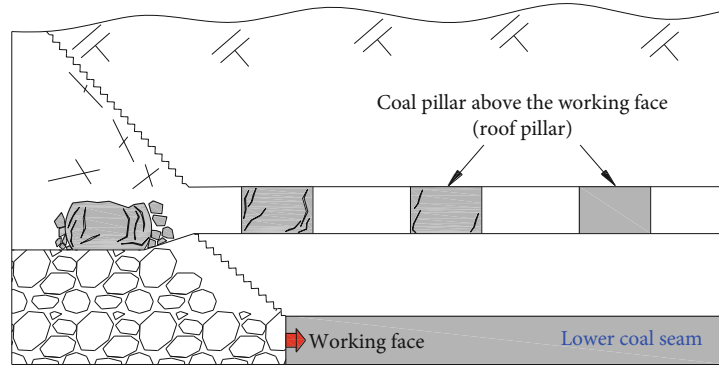
Copyright © 2020 Zhu Li et al. This is an open access article distributed under the Creative Commons Attribution License, which permits unrestricted use, distribution, and reproduction in any medium, provided the original work is properly cited.

Room-and-pillar mining is a commonly used mining method in previous practice in northwest China mining area. Due to priority selection of high-quality resources, coal mines in northwest China generally have to face upward mining above goaf. Thus, the stability of a floor coal pillar influenced by mining activities plays an essential role in upward mining above goaf. The results indicated that a floor coal pillar kept stable before coal excavation in the no. 6107 working face in the Yuanbaowan coal mine; however, the plastic zone in the floor coal pillar expanded sharply and the elastic core zone reduced suddenly on the influence of abutment pressure. Finally, the floor coal pillar supported failure. Accordingly, the paper proposed a floor coal pillar reinforcing technique through a grout injection filling goaf area. As physically limited by a different-height filling body on the double sides, the plastic zone scope and horizontal displacement and loading capacity of the floor coal pillar were studied, working out that the critical height of the filling body should be about 6 m which can ensure safe mining when upward mining above goaf. Case practice indicated that the fractures induced by mining in the floor coal pillar, filling body, and floor can be restrained effectively when the filling body height is 6 m, which can ensure floor coal pillar stability and safe mining of the no. 6107 working face in the Yuanbaowan coal mine. The research can provide theoretical and technical guidance for upward mining above goaf and have a critical engineering practice value.

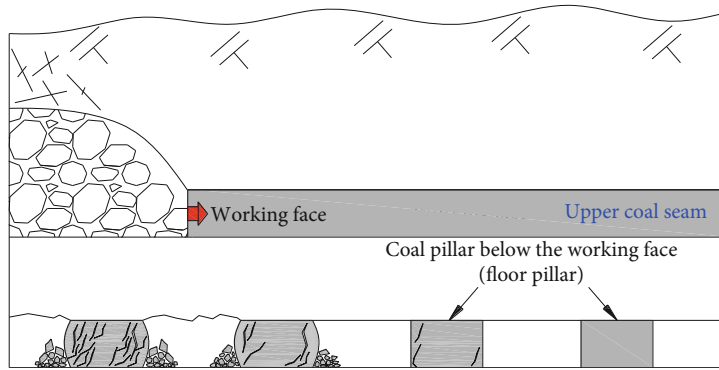
1. Introduction

As the largest coal production base and a well-known demonstration project of a modern mine with production capacity over 10 million tons per year in China [1], the northwestern mining area's coal production accounts for 68% of the coal production of the whole country according to 2018 statistics. In the northwestern mines, a room-and-pillar mining method was widely used in the early stage of coal mining practice [2, 3], leaving abundant coal pillars in the goaf, which puts a huge hidden threat to the safe mining of longwall working faces of adjacent coal seams. The spatial relationship between coal pillars and the longwall working faces of adjacent coal seams is mainly divided into two types: roof coal pillars and floor coal pillars, as shown in Figures 1(a) and 1(b), which indicates that the coal pillars are located above the longwall working faces and below the

longwall working faces, respectively. The research results on roof coal pillars are mainly focused on the following four aspects: the occurrence mechanism of support crushing accidents in the longwall working faces under the roof coal pillars and its control measures [4–6], the stress distribution pattern of the roof coal pillars and its influence on the mining and the layout of roadways in underlying coal seams [7, 8], the calculation methods of dynamic and static loading on roof coal pillars [9–12], and the analysis and evaluation of coal pillar stability [13–16]. The research on floor coal pillars is mainly focused on their stability under the influence of the front abutment pressure to avoid the collapse of the working face and the coal and rock mass ahead caused by the failure of the floor coal pillar [17, 18]. Therefore, the key to safely mining of the longwall working face above the room-and-pillar goaf is to ensure that the floor coal pillars remain stable under the influence of mining-induced stress.



(a)



(b)

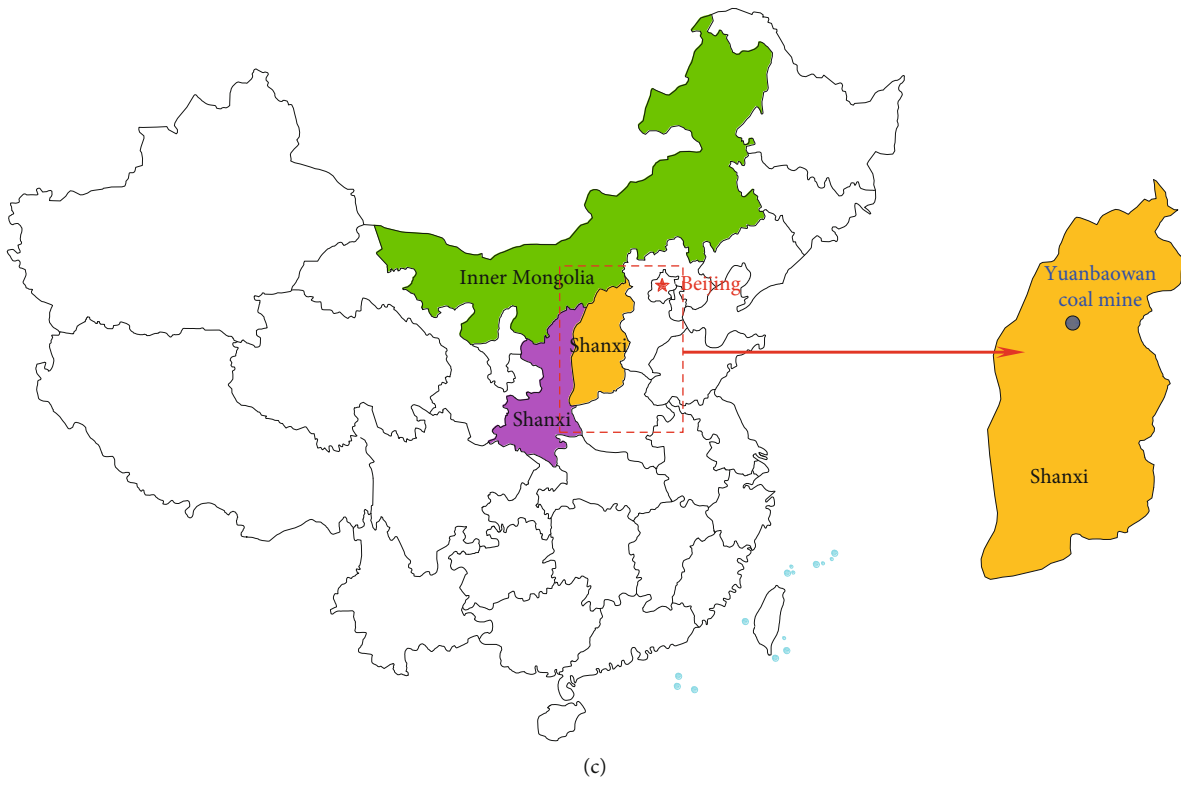


FIGURE 1: Continued.

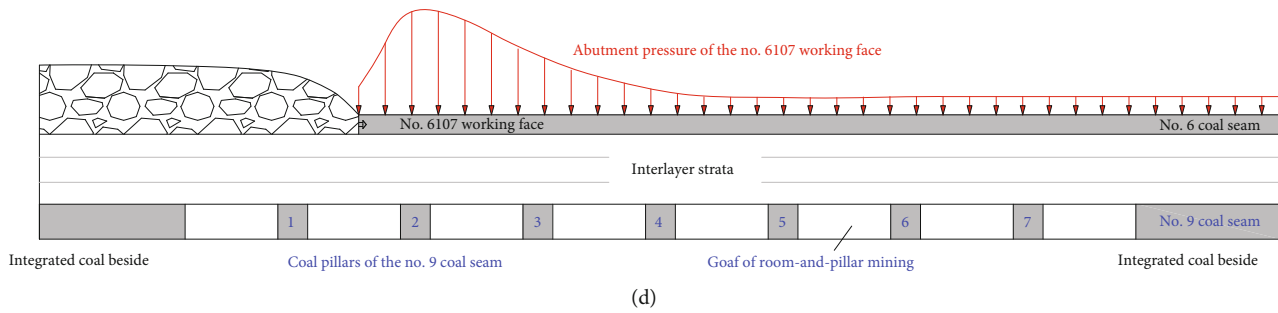


FIGURE 1: The location of the Yuanbaowan coal mine and the schematic diagram of mining above the goaf: (a) roof pillar; (b) floor pillar; (c) geographic location; (d) schematic diagram of no. 6107 working face mining above the goaf.

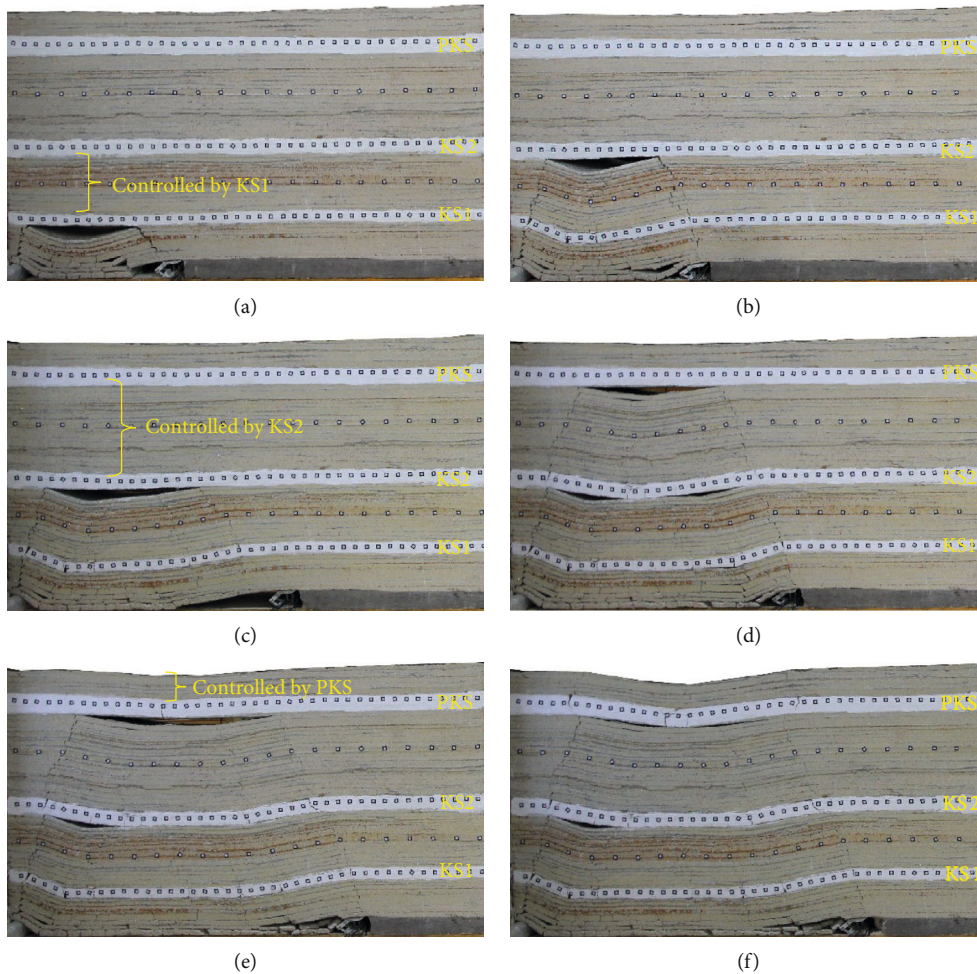


FIGURE 2: The control effect of the key stratum: (a) before the breakage of KS1; (b) after the breakage of KS1; (c) before the breakage of KS2; (d) after the breakage of KS2; (e) before the breakage of PKS; (f) after the breakage of PKS.

With regard to the theory and technology of safe mining of the longwall working faces above the room-and-pillar goaf, many scholars have conducted massive researches. Liu studied the influence of lithological combinations between coal seams on ascending mining [19]. Sun and Wang demonstrated the feasibility of ascending mining by adopting methods such as mining influence multiples, method of balancing the surrounding rocks, and mathematical statistical

analysis [20]. Huang analyzed the stability of the floor strata of the longwall working faces above the strip goaf by using similar simulations and numerical simulations [21]. Feng et al. considered that the failure scope of the floor strata is less than the thickness of the rock interlayers as the prerequisite for safe mining of longwall working faces, and the method for determining the feasibility of ascending mining in the strip mining area was given [22–24]. Bai et al. studied the

No.	Thickness (m)	Depth (m)	Lithology	Key strata	Legend
32	38.50	38.50	Loose layer		
31	1.90	40.40	Siltstone		
30	4.00	44.40	Coarse sandstone		
29	7.60	52.00	Sandy mudstone		
28	5.80	57.80	Fine sandstone	PKS	
27	8.00	65.80	Sandy mudstone		
26	3.50	69.30	Fine sandstone		
25	0.80	70.10	Mudstone		
24	0.40	70.50	Coal		
23	2.80	73.30	Sandy mudstone		
22	1.00	74.30	Fine sandstone		
21	4.60	78.90	Sandy mudstone		
20	8.05	86.95	Siltstone	KS4	
19	4.35	91.30	Coal		
18	6.60	97.90	Mudstone		
17	1.40	99.30	Coal		
16	4.00	103.30	Sandy mudstone		
15	1.60	104.90	Fine sandstone		
14	5.50	110.40	Coarse sandstone	KS3	
13	2.00	112.40	Fine sandstone		
12	1.00	113.40	Coarse sandstone		
11	6.10	119.50	No. 4 coal		
10	2.60	122.10	Mudstone		
9	2.80	124.90	Sandy mudstone		
8	3.70	128.60	Fine sandstone		
7	7.10	135.70	Coarse sandstone	KS2	
6	3.80	139.50	No. 6 coal		
5	4.00	143.50	Mudstone		
4	3.00	146.50	Sandy mudstone		
3	5.40	151.90	Fine sandstone	KS1	
2	0.50	152.40	Mudstone		
1	8.30	160.70	No. 9 coal		

FIGURE 3: Location of key strata of the no. 6107 working face.

distribution law of the mining-induced stress on the middle coal seam when above and below the working face lie the room-and-pillar mining goafs by applying a numerical simulation method [25, 26]. By reviewing the existing literature, it can be found that the research results above are mainly focused on the feasibility evaluation of mining above goaf and that the failure scope of the floor rock is less than the thickness of the rock interlayers, which has been considered as the standard for mining above goaf. However, the mining damage scope of the floor strata is significantly greater than

the thickness of the interlayer strata when mining in extremely close coal seams, and few studies have given safe mining techniques under such conditions. Therefore, the safe mining technology of the upper coal seam needs further study in the case of extremely close-distance coal seams.

Based on the mining conditions of the Yuanbaowan coal mine in Shanxi Province, this article proposes a new engineering technology to safely mine the upper coal seams by strengthening the bearing capacity of the floor coal pillars with the method of backfilling the room-and-pillar mining

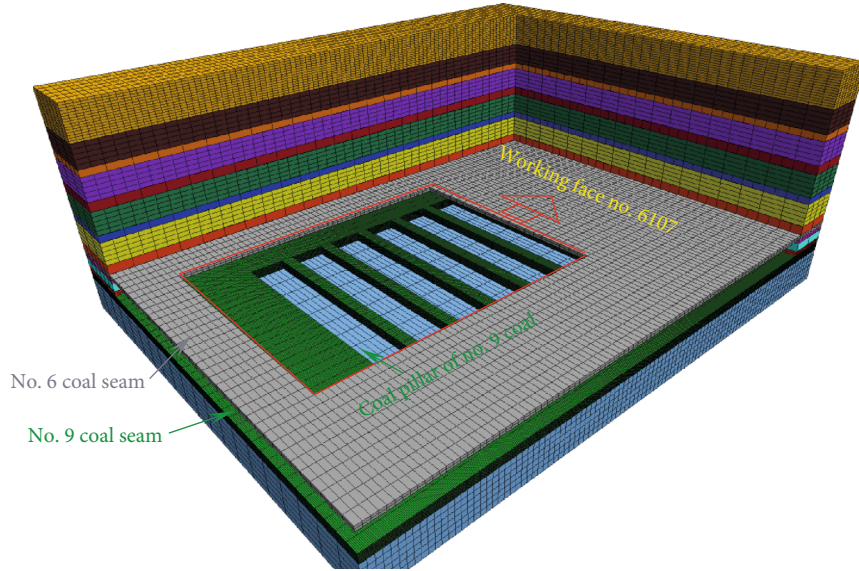


FIGURE 4: Schematic diagram of no. 6107 working face mining above the room-and-pillar goaf.

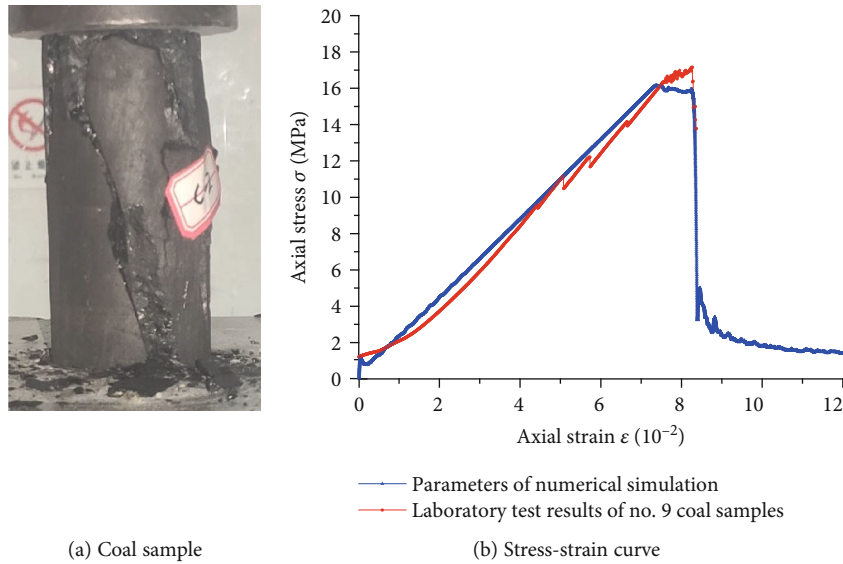


FIGURE 5: Calibration result of the coal seam simulation parameter.

TABLE 1: Parameters in FLAC3D numerical simulation.

Layers	Bulk modulus b (Pa)	Shear modulus s (Pa)	Cohesion c (MPa)	Internal friction angle f ($^{\circ}$)	Tensile strength t (MPa)
Soft rock	$5.00E + 09$	$3.40E + 09$	$3.40E + 06$	24	$1.80E + 06$
Coal seam	$4.00E + 09$	$3.00E + 09$	$2.20E + 06$	18	$1.50E + 06$
Key strata	$7.50E + 09$	$4.50E + 09$	$4.30E + 06$	32	$2.50E + 06$

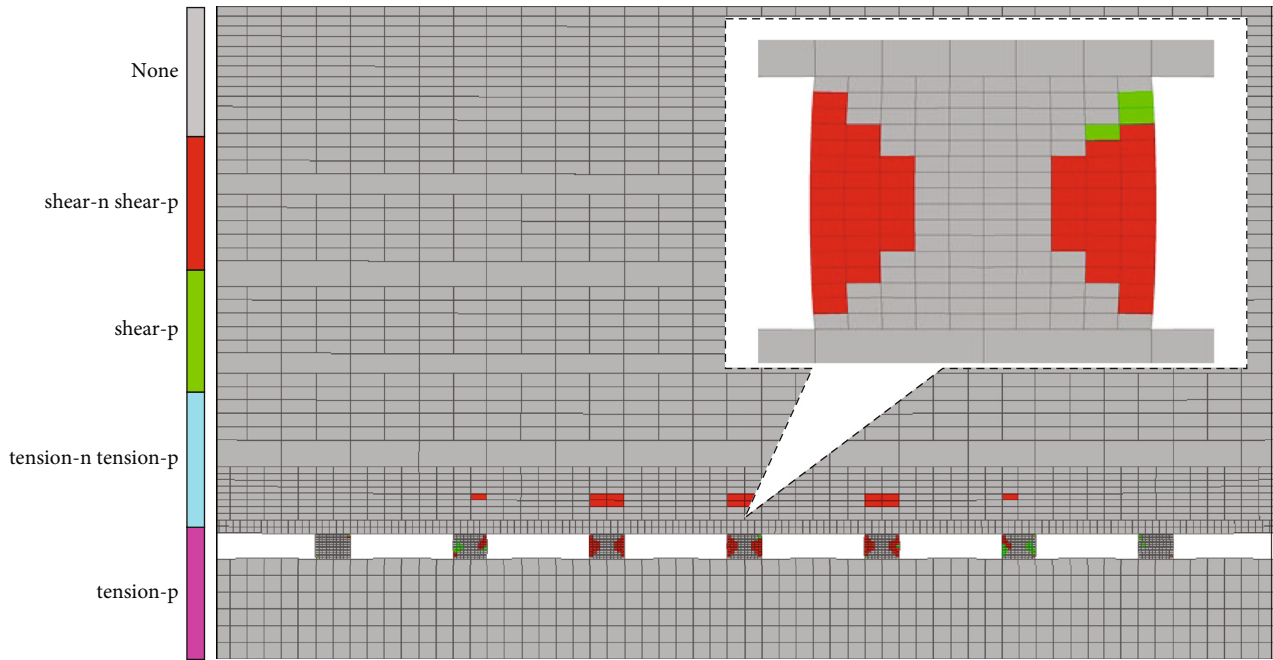
goaf. The filling body formed by the concretion of the cement slurry has a lateral clamping effect on the floor coal pillars. And the effects of difference in filling bodies' heights on the suppression of the expansion of the floor coal pillars' plastic area and on strengthening the bearing capacity of the floor coal pillars are also different. Accordingly, the critical height of filling bodies to ensure the stability of the floor coal pillars is given in this paper. The research results can provide impor-

tant theoretical and engineering technical support for the safe mining of longwall working faces above the goaf.

2. Geological Conditions

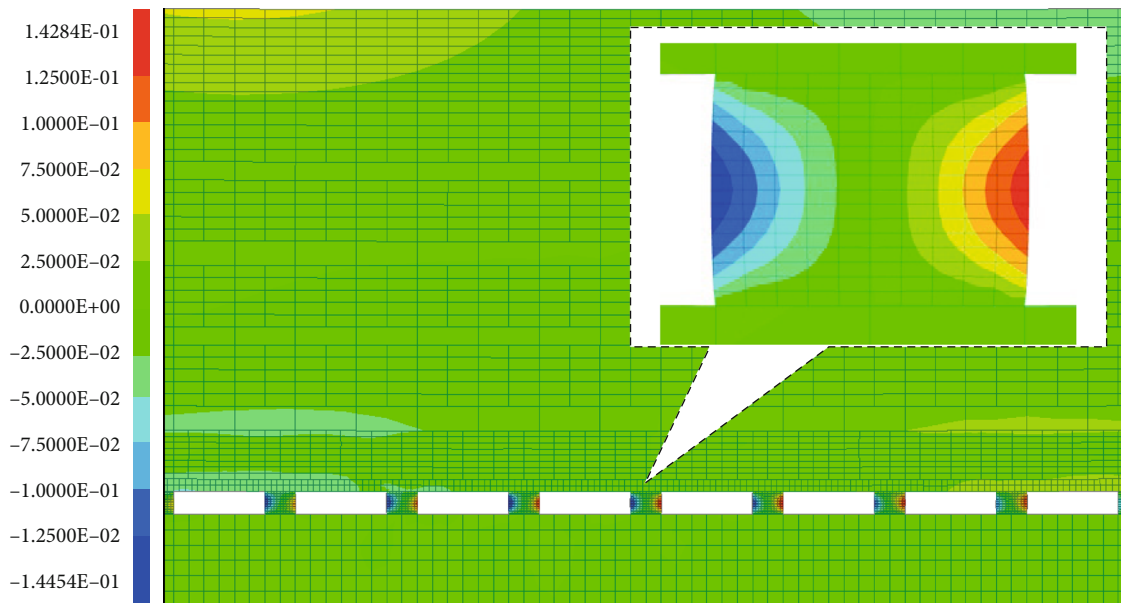
2.1. *General Situation of the Working Face.* The Yuanbaowan coal mine is located in Shuozhou City, Shanxi Province, China, of which the no. 6107 working face is the first coal

FLAC3D 5.01
©2014 Itasca Consulting Group, Inc.
Demonstration Model
Zone:
Plane: active on
Colorby: State - Average



(a)

FLAC3D 5.01
©2014 Itasca Consulting Group, Inc.
Demonstration Model
Contour of X Displacement
Plane: active on



(b)

FIGURE 6: Continued.

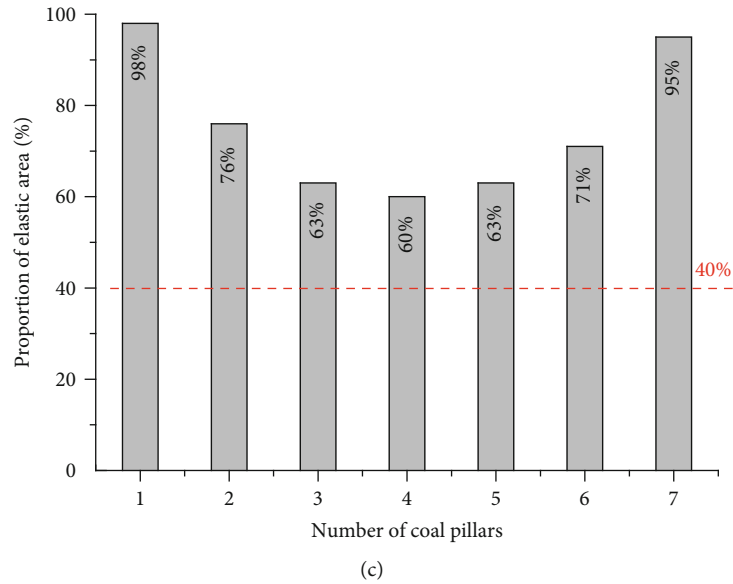


FIGURE 6: Initial stability of coal pillars below the no. 6107 working face before mining: (a) elastic-plastic regional distribution of the no. 4 coal pillar; (b) heave of the left and right side of the no. 4 coal pillar; (c) proportion of elastic core areas of each coal pillar.

mining face in the first panel. The no. 6107 working face is deployed in the no. 6 coal seam. The no. 6 coal seam dip angle is 0° – 6° , with an average mining height of 3.6 m. The width of the no. 6107 working face is 240 m, with an accumulated advancement distance of about 600 m. Below the no. 6 coal seam lies the no. 9 coal seam, with an average thickness of about 8.0 m. As of May 2005, the no. 9 coal seam had been fully mined out by the room-and-pillar mining method. In the no. 9 coal seam appears the room-and-pillar mining goaf when the no. 6107 working face advances between 200 m and 400 m. Affected by both the early mining design and planning and the unauthorized cross-border mining, mining above the room-and-pillar goaf is not a specific case for the Yuanbaowan coal mine but a relatively common type of mining conditions for shallow coal seams in northwestern China. Achieving safe mining of the longwall working faces above the room-and-pillar goafs is a major technical problem remaining urgently to be solved not only in the Yuanbaowan coal mine but also in most mines in northwestern China.

For the room-and-pillar goafs below the no. 6107 working face in the Yuanbaowan coal mine, the width of the coal pillar is about 10–12 m and the space between pillars is about 25–30 m. The geographical location of the Yuanbaowan coal mine and the mining situation of the no. 6107 working face are shown in Figures 1(c) and 1(d).

2.2. Columnar Overburden Stratum of the Working Face

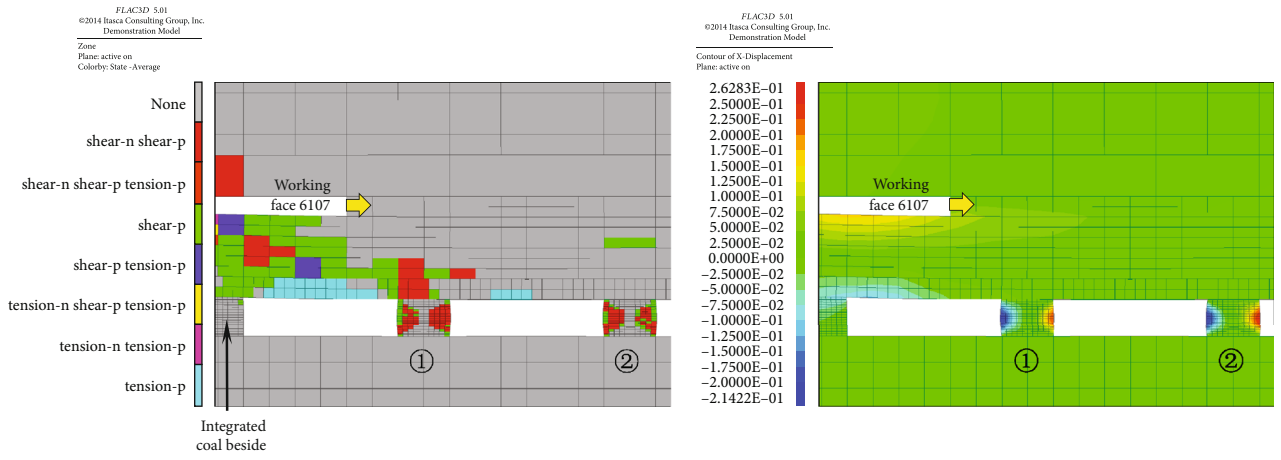
2.2.1. Key Stratum Theory. The stratification of the coal system strata leads to differences in the motions of each stratum; In particular, thick and hard strata control these motions, while thin and soft strata act as loads. Based on the recognition of these facts, the Chinese scientist Minggao Qian proposed the “key stratum theory in ground control” in 1990. The theory treats the stratum that controls some or all of the strata above it up to the ground surface as the key stratum.

This implies that deformation or breakage of the key stratum would simultaneously cause deformation or breakage of the strata under its control. One or more key strata exist in the overlying strata of a coal mine. Because the top-most key stratum controls the stratum movement up to the ground surface, it is referred to as the primary key stratum (PKS), while all other key strata are referred to as a subkey stratum (SKS). This “controlling effect” of the key strata is illustrated in Figure 2. The key stratum theory provides a sound foundation on understanding the progressive caving behavior of strata. The strata behavior is primarily controlled by the breakage and movement of the KS. The theory has been widely used and demonstrated in the mining industry in China [27–32]. This study is also preceded on the basis of this theory.

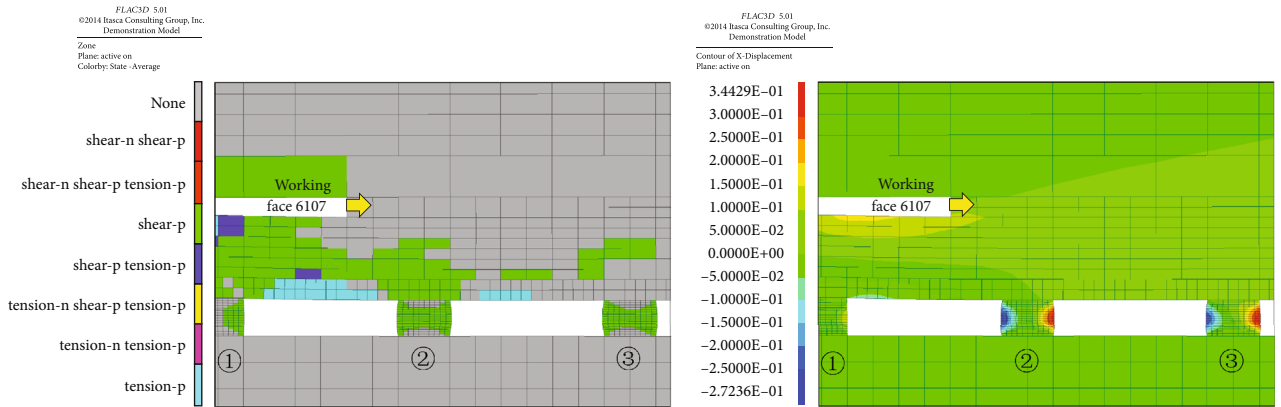
2.2.2. Key Stratum of the No. 6107 Working Face. According to the key stratum theory of stratum control, the key strata in the overlying strata of the no. 9 coal seam are identified with the help of key stratum identification software. The results are shown in Figure 3. It can be seen that there are altogether 5 key strata in the overlying strata of the no. 9 coal seam. From bottom to top, they are fine sandstone with a burial depth of 151.90 m and a thickness of 5.4 m, coarse sandstone with a burial depth of 136.10 m and a thickness of 7.5 m, coarse sandstone with a burial depth of 110.40 m and a thickness of 5.5 m, siltstone with a burial depth of 86.95 m and a thickness of 8.05 m, and fine sandstone with a burial depth of 57.80 m and a thickness of 5.8 m, respectively. The distinguishing method of the key stratum in overburden can be seen in Reference 29, which is limited to space and will not be repeated here.

3. Numerical Simulation

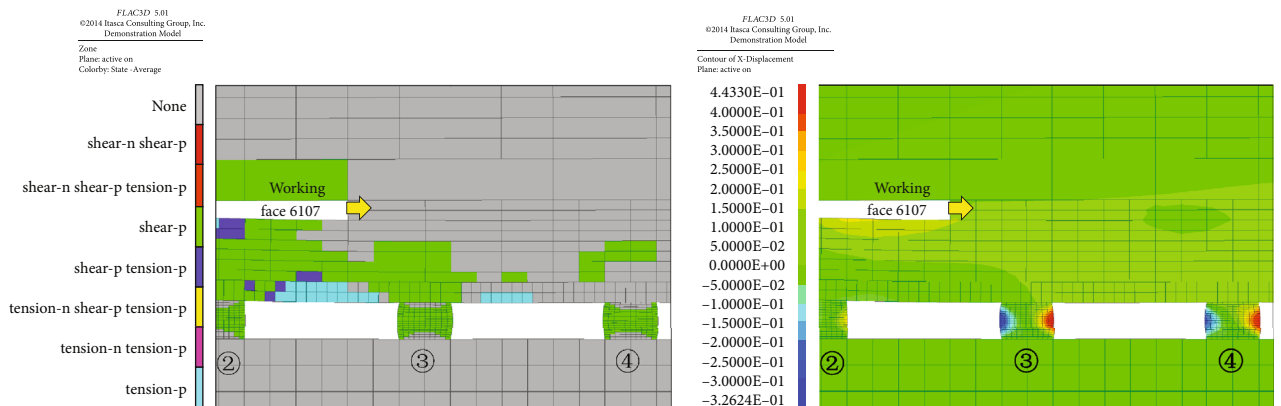
3.1. Modelling and Mining Scheme. The FLAC3D numerical calculation model is established, as shown in Figure 4,



(a) Advancing distance 80 m



(b) Advancing distance 120 m



(c) Advancing distance 160 m

FIGURE 7: Continued.

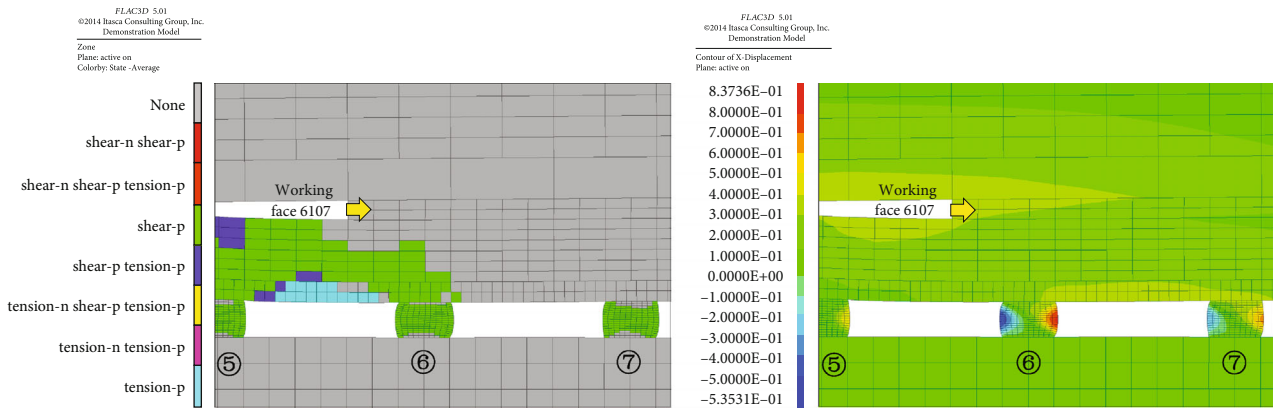
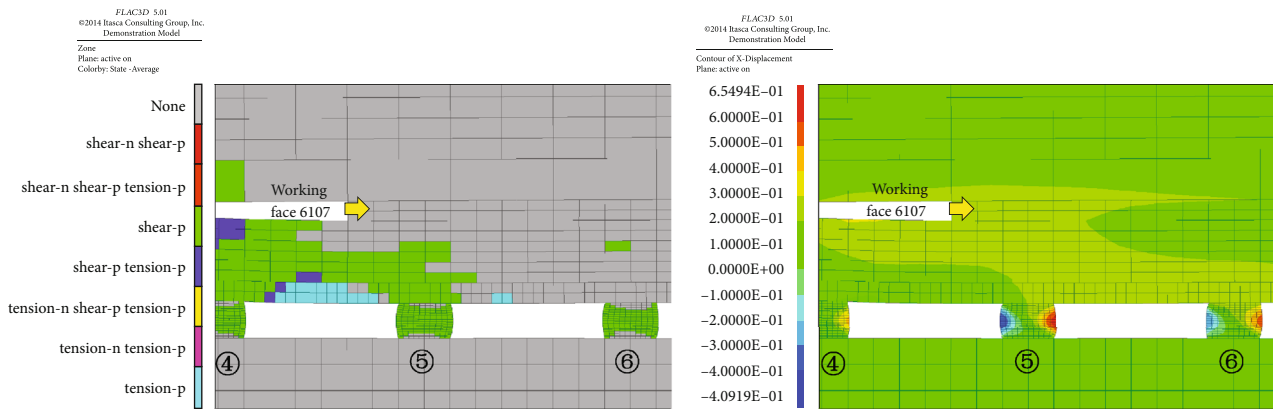
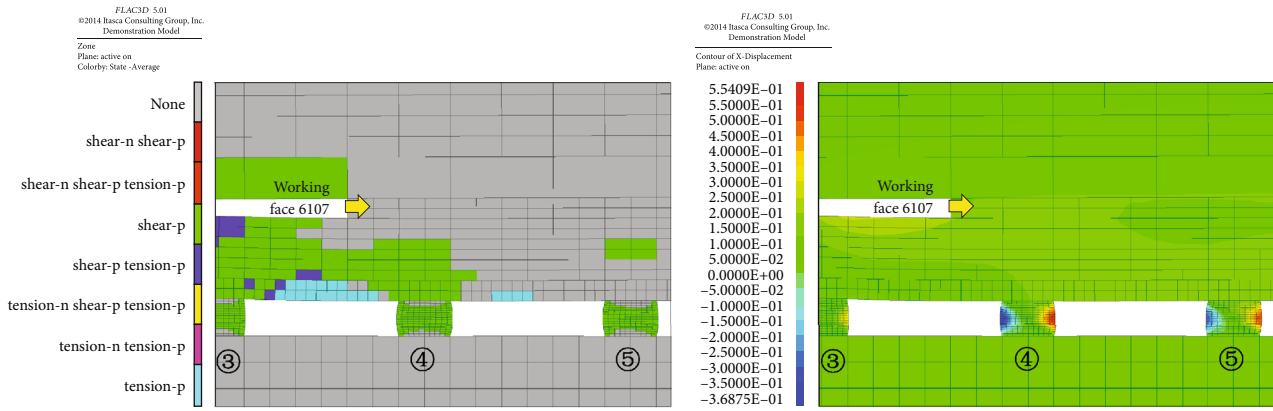
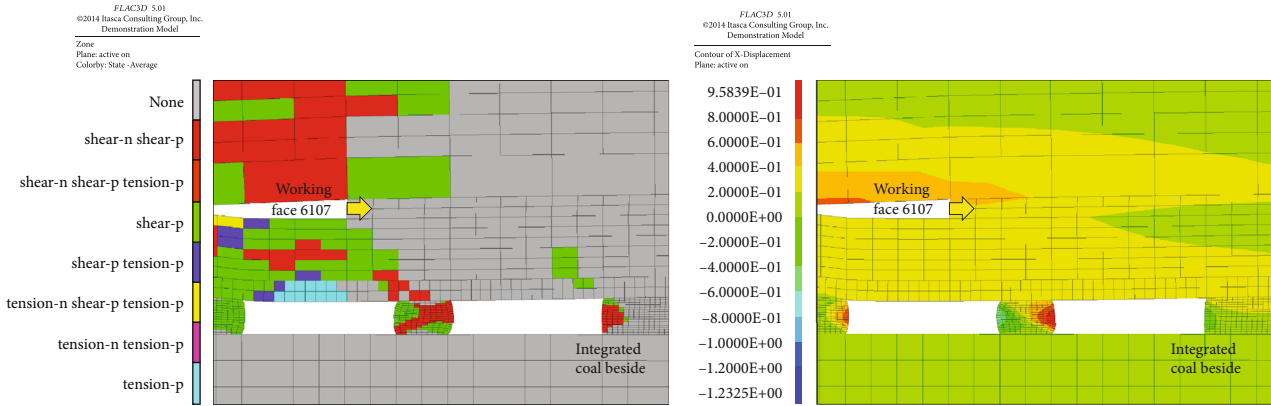
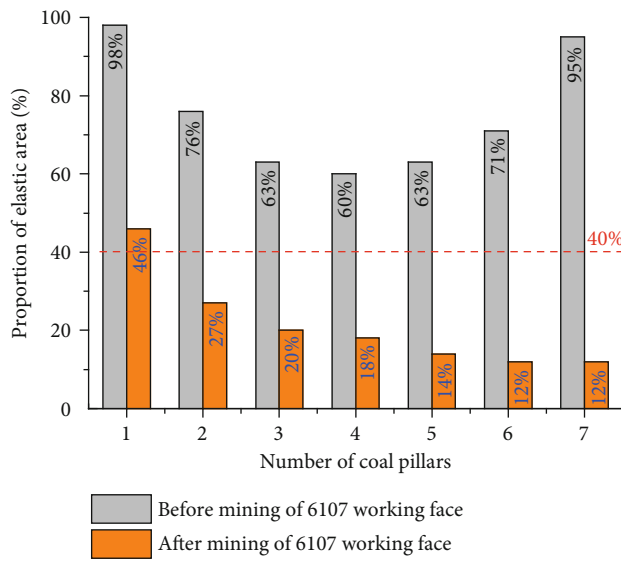


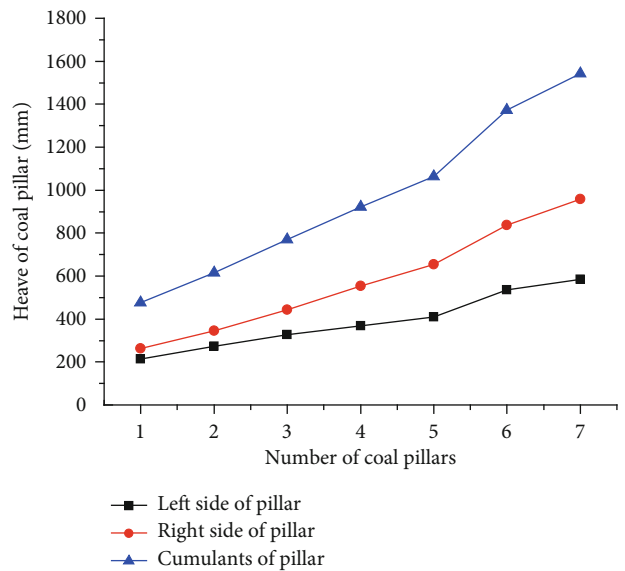
FIGURE 7: Continued.



(g) Advancing distance 320 m



(h) Proportion of the elastic core area of each coal pillar



(i) Heave of the left and right side of the coal pillar

FIGURE 7: Evolution law of the elastic-plastic property and the amount heave of the left and right side of the coal pillar under different advancing distances of the no. 6107 working face.

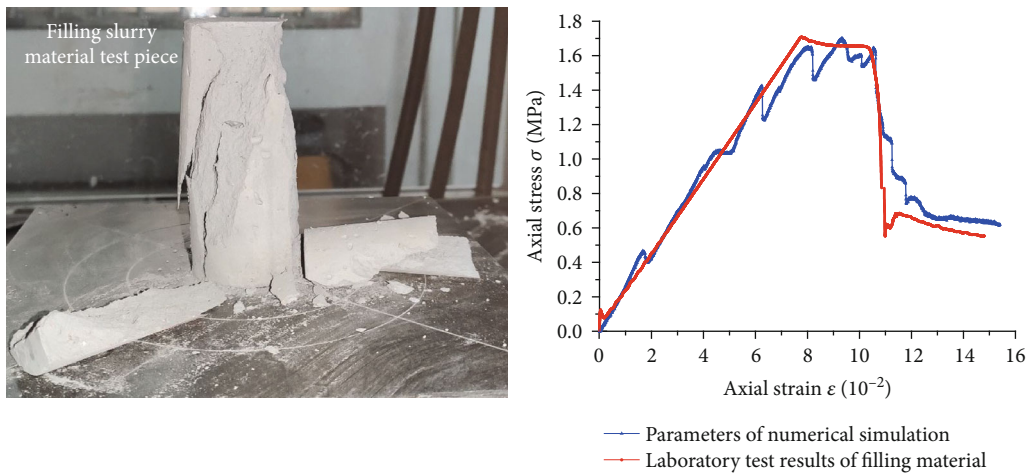
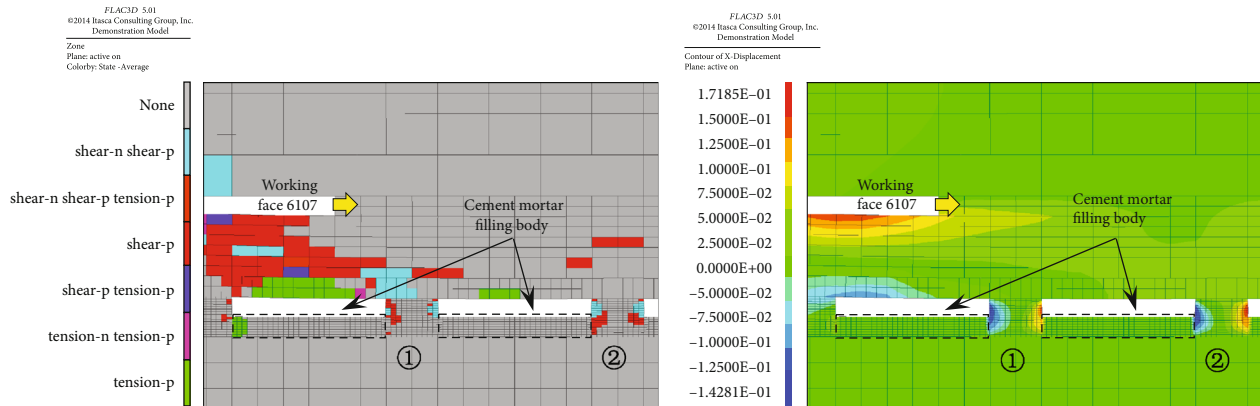
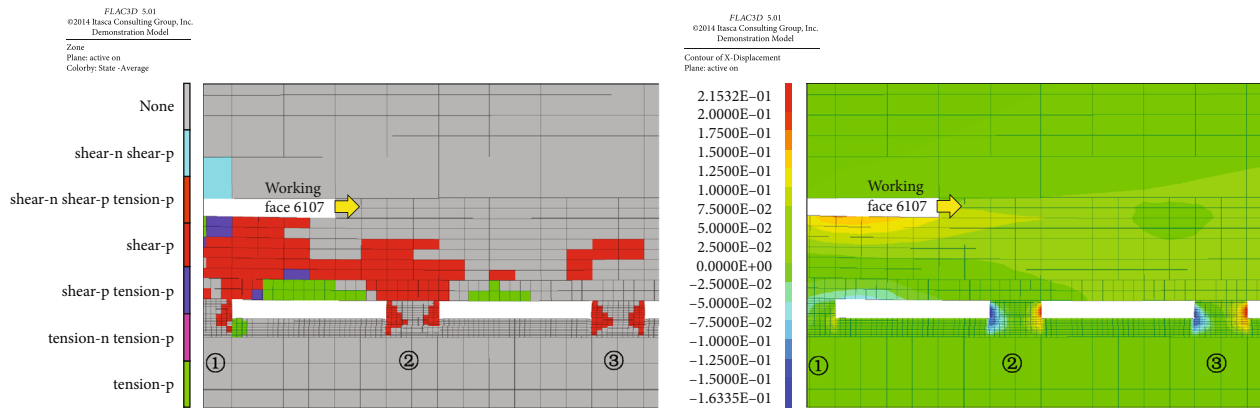


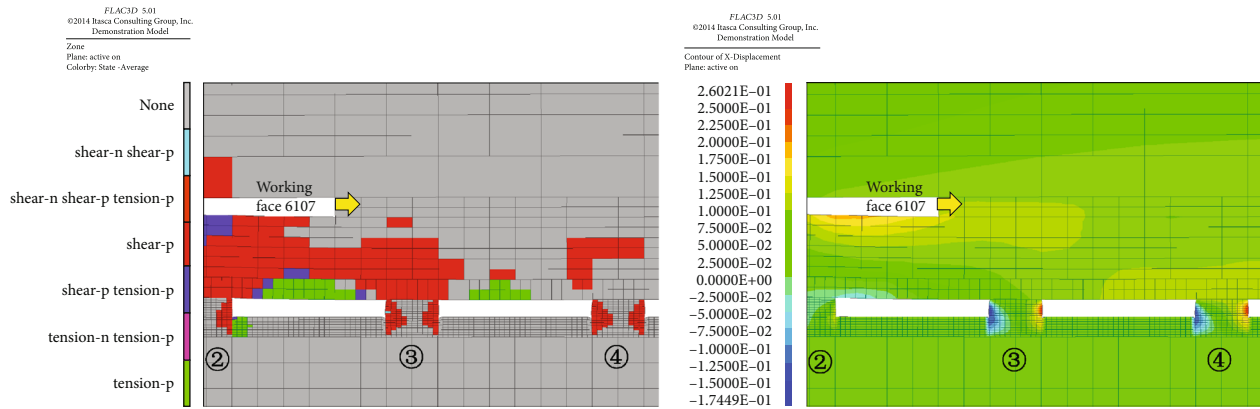
FIGURE 8: Calibration result of the filling material simulation parameter.



(a) Advancing distance 80 m

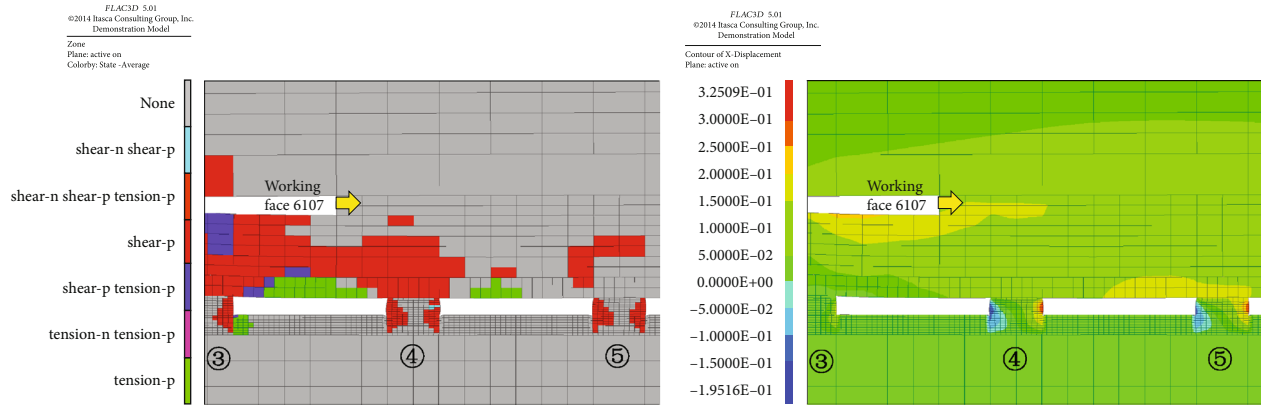


(b) Advancing distance 120 m

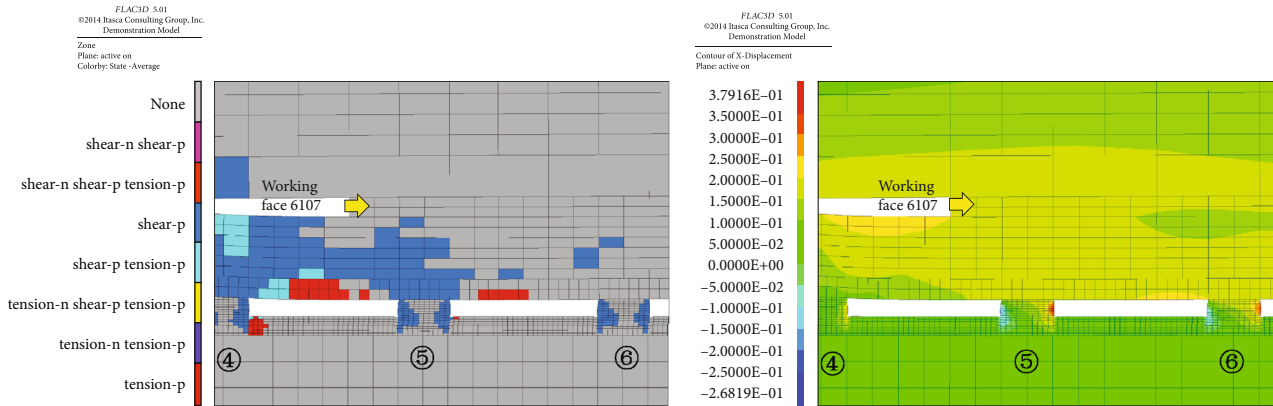


(c) Advancing distance 160 m

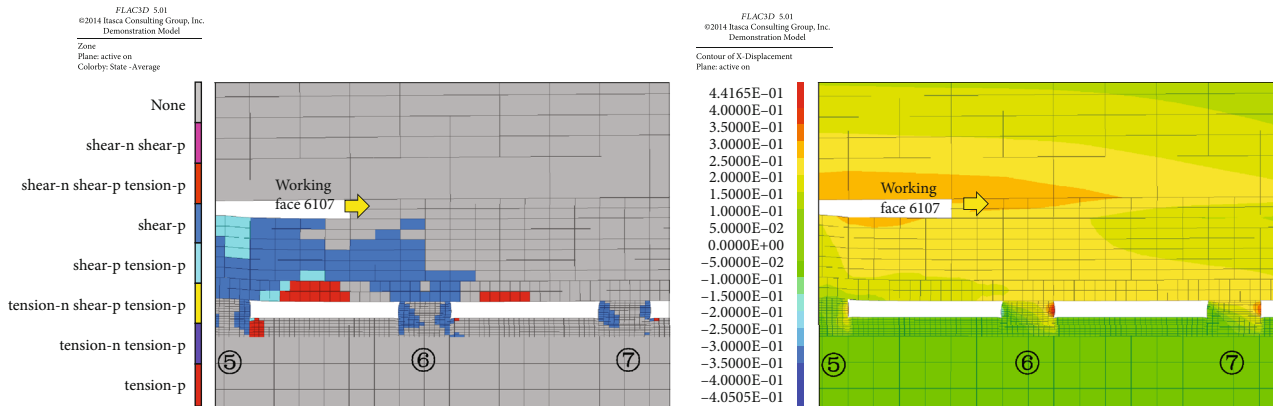
FIGURE 9: Continued.



(d) Advancing distance 200 m

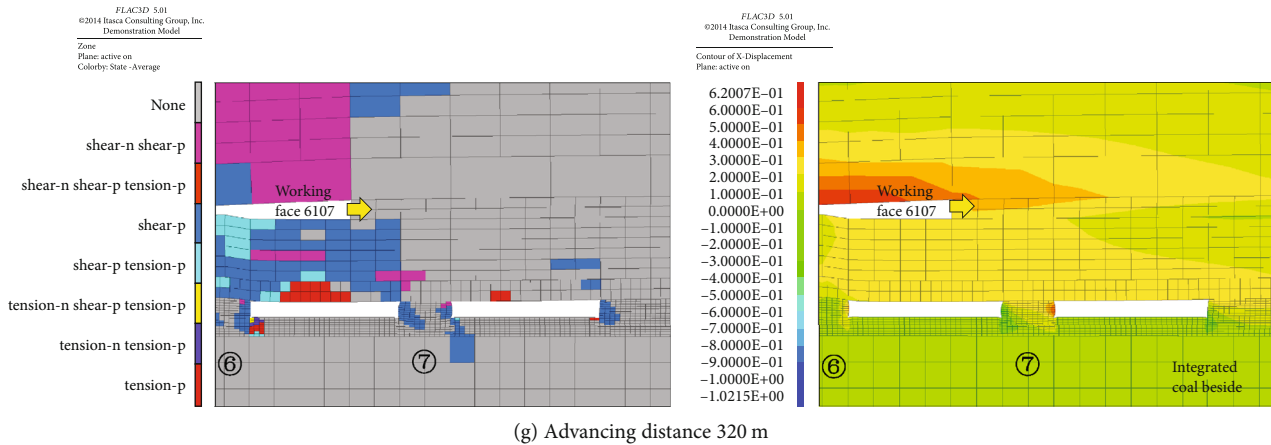


(e) Advancing distance 240 m



(f) Advancing distance 280 m

FIGURE 9: Continued.



(g) Advancing distance 320 m

FIGURE 9: The elastoplastic expansion and the amount of the horizontal bulge of each coal pillar with a filling body height of 4 m.

according to identification results of the key strata in the overlying strata. And the KS1, KS2, KS3, KS4, and PKS in the figure refer to the key strata of the overlying strata of the no. 9 coal seam.

The simulation research work is carried out in the following three steps. First, room-and-pillar goaf is formed in the no. 9 coal seam in the model under the premise of the balance of the geostatic stress field. Secondly, the stability of the floor coal pillars with the condition that its goaf is unfilled in the no. 9 coal seam is investigated under the influence of mining of the no. 6107 working face. Finally, the stability of the floor coal pillar, during the advancement of the no. 6107 working face, was studied with the condition that room-and-pillar goaf has been filled in the no. 9 coal seam. Based on this, the effect rules of difference in filling bodies' heights on the suppression of the expansion of the floor coal pillars' plastic area and on strengthening the bearing capacity of the floor coal pillars were revealed. Accordingly, the critical height of filling bodies for the no. 9 room-and-pillar goaf is obtained to ensure safe mining in view of the geological conditions of the no. 6107 working face.

3.2. Calibration of Coal Seam Simulation Parameters. Correctly selecting material parameters in numerical simulation is not only a key prerequisite for accurately investigating the stability of the coal pillars below the no. 6107 working face but also the basis for ensuring that the numerical simulation results are consistent with the actual situation. Accordingly, the no. 9 coal seam is sampled and the physical and mechanical parameters are obtained through laboratory tests. In the uniaxial compression experiment, according to the international rock mechanics test experiment specification, a cylindrical specimen with a geometric size of $\phi 50\text{mm} \times 100\text{mm}$ was selected, and the loading speed of the electrohydraulic servo universal testing machine was $0.02\text{ mm/s} \sim 0.05\text{ mm/s}$. And then, uniaxial compression curve experiments are performed in FLAC3D, and the strain softening model is applied to obtain simulated parameters relatively consistent with the laboratory test results. As shown in Figure 5, the red curve is the uniaxial compression curve (obtained from the laboratory tests) of the coal sample of the no. 9 coal seam and the blue curve is the numerical simulation result of FLAC3D, and the

simulation parameters are shown in Table 1. There is much consistency in the elasticity modulus and peak strength of both. It can be seen that the simulated parameters of the blue curve can be used as the parameters of the no. 9 coal seam, which can accurately reflect the stress evolution, elastic and plastic expansion, and failure modes of the coal pillars in the no. 9 coal seam under the influence of mining-induced stress of the no. 6107 working face.

4. Stability of Floor Pillars

4.1. Stability of Floor Pillars before the Mining of the No. 6107 Working Face. The vertical stress, horizontal displacement, and elastic-plastic area of the coal pillar in the goaf of the no. 9 coal seam before mining of the no. 6107 working face are shown in Figures 6(a)–6(c), respectively. It can be seen that the no. 4 coal pillar has the largest horizontal side heaves among all the coal pillars, and its value is 145 mm. The elastic core area of each coal pillar accounts for 98%, 76%, 63%, 60%, 63%, 71%, and 95% of the total volume of the coal pillar, as shown in Figure 6(c). It is worth noting that both the proportion of the elastic core area of coal pillars in the room-and-pillar goaf in northwestern China and its relationship with the stability of the coal pillars have been carefully studied in literature [33]. It has been pointed out that when the elastic core area of the coal pillars accounts for 40% of the total volume, the coal pillar is considered to be in a stable state. In order to ensure the safety mining of the no. 6107 working face to the greatest extent, the identification standard, where the elastic core area makes up 40% of the total volume of coal pillars, for the stability of the coal pillar has been set. It can be known that the coal pillar of the no. 9 coal seam was in a stable state before mining of the no. 6107 working face.

4.2. Stability of Floor Pillars during the Mining of the No. 6107 Working Face. During the mining of the no. 6107 working face, both the horizontal side heave and the plastic area of the coal pillar further expanded due to the influence of the abutment pressure, and the proportion of the elastic core area of the coal pillar further reduced. According to the existing research results, it is generally considered that the peak value

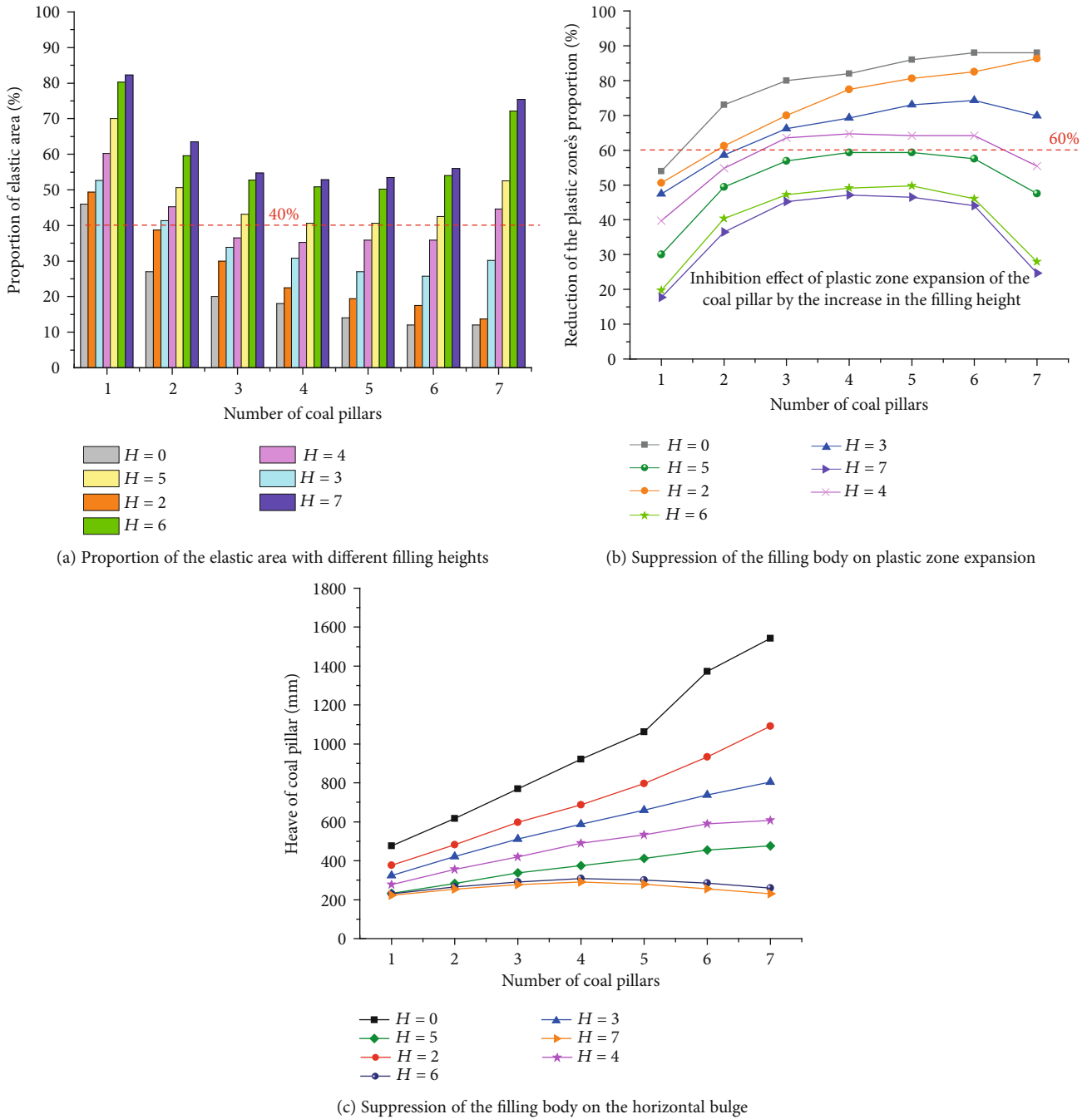
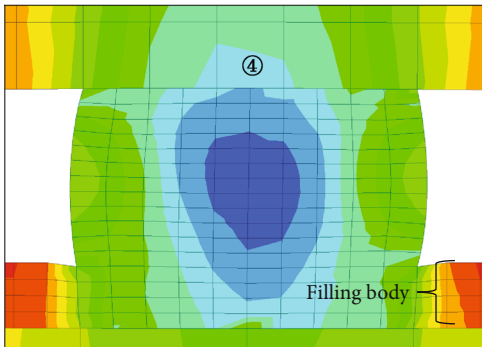
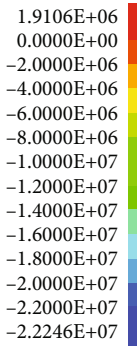


FIGURE 10: Suppressing effect of different filling body heights on the expansion of the plastic zone and the amount of the horizontal bulge of each coal pillar.

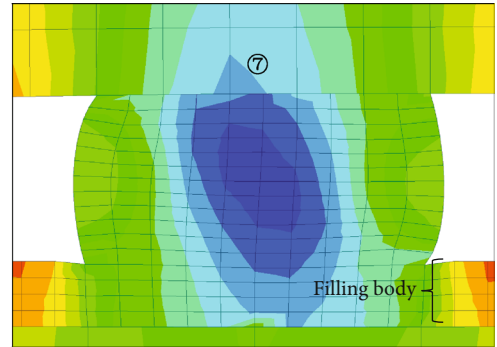
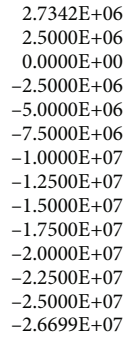
of front abutment pressure is located 0-10 m in front of the coal mining working face [34–36]. Therefore, the floor coal pillar is most likely to be destroyed when it is at the position of the peak value of front abutment pressure. The proportion of elastic/plastic areas, horizontal side heaves, and bearing capacity of each coal pillar are studied in this case. The evolutionary process of both elastic-plastic area expansion and the horizontal side heave of each floor coal pillar is shown in Figures 7(a)–7(g) during the advancing of the no. 6107 working face.

It can be seen from Figure 7 that under the influence of the abutment pressure of the no. 6107 working face, the proportions of the elastic area of each floor pillar have been reduced to 46%, 27%, 20%, 18%, 14%, 12%, and 12%, respectively. And the volume of the horizontal side heave of each floor coal pillar increases from 220 mm, 241 mm, 268 mm, 275 mm, 271 mm, 247 mm, and 220 mm to 476 mm, 616 mm, 769 mm, 922 mm, 1063 mm, 1372 mm, and 1543 mm, respectively. The dramatic reduction of the elastic core area will definitely cause the instability of the coal

FLAC3D 5.01
©2014 Itasca Consulting Group, Inc.
Demonstration Model
Contour of ZZ-Stress
Plane: active on
Calculated by: Volumetric Averaging

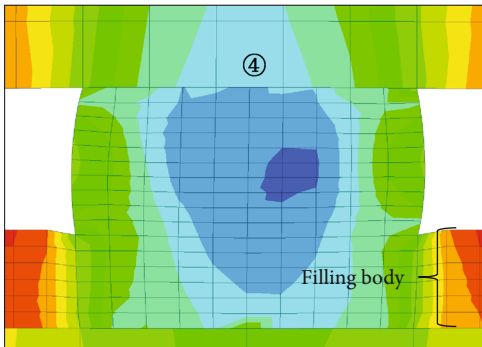
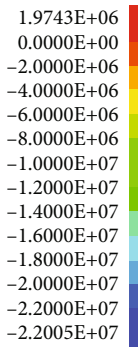


FLAC3D 5.01
©2014 Itasca Consulting Group, Inc.
Demonstration Model
Contour of ZZ-Stress
Plane: active on
Calculated by: Volumetric Averaging

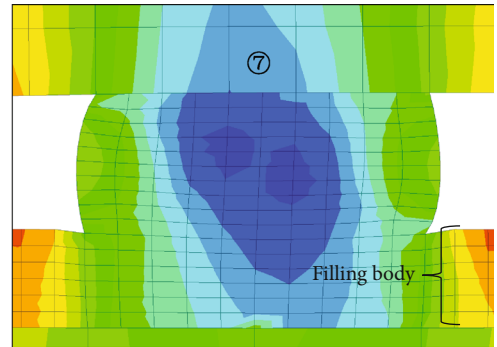
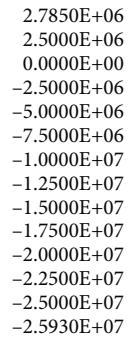


(a) Filling body heights 2 m

FLAC3D 5.01
©2014 Itasca Consulting Group, Inc.
Demonstration Model
Contour of ZZ-Stress
Plane: active on
Calculated by: Volumetric Averaging

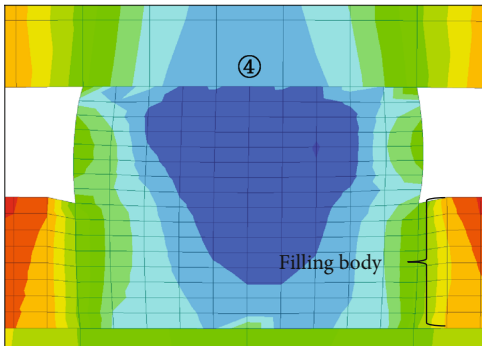
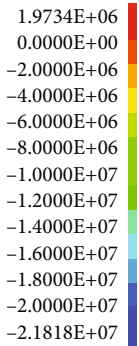


FLAC3D 5.01
©2014 Itasca Consulting Group, Inc.
Demonstration Model
Contour of ZZ-Stress
Plane: active on
Calculated by: Volumetric Averaging

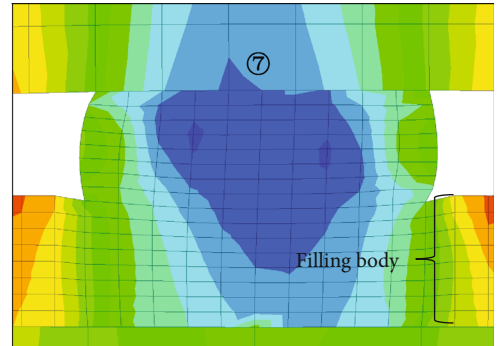
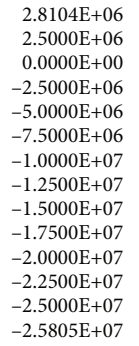


(b) Filling body heights 3 m

FLAC3D 5.01
©2014 Itasca Consulting Group, Inc.
Demonstration Model
Contour of ZZ-Stress
Plane: active on
Calculated by: Volumetric Averaging



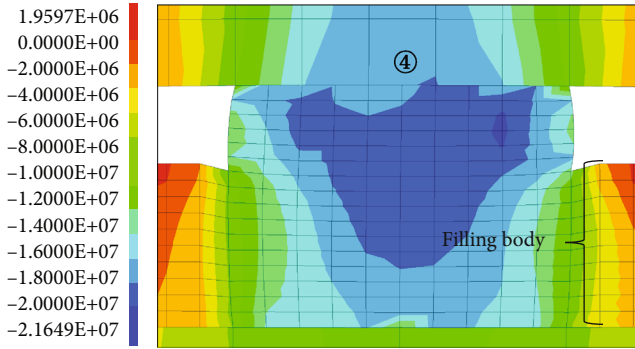
FLAC3D 5.01
©2014 Itasca Consulting Group, Inc.
Demonstration Model
Contour of ZZ-Stress
Plane: active on
Calculated by: Volumetric Averaging



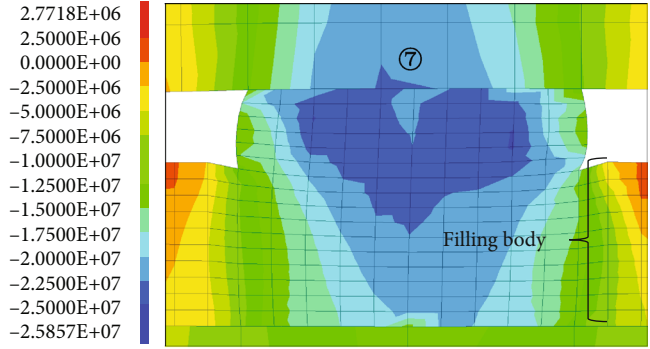
(c) Filling body heights 4 m

FIGURE 11: Continued.

FLAC3D 5.01
©2014 Itasca Consulting Group, Inc.
Demonstration Model
Contour of ZZ-Stress
Plane: active on
Calculated by: Volumetric Averaging

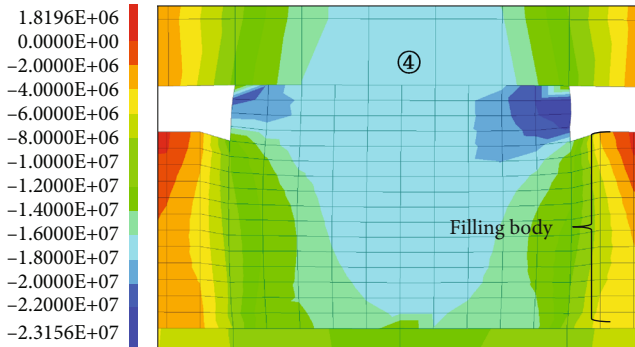


FLAC3D 5.01
©2014 Itasca Consulting Group, Inc.
Demonstration Model
Contour of ZZ-Stress
Plane: active on
Calculated by: Volumetric Averaging

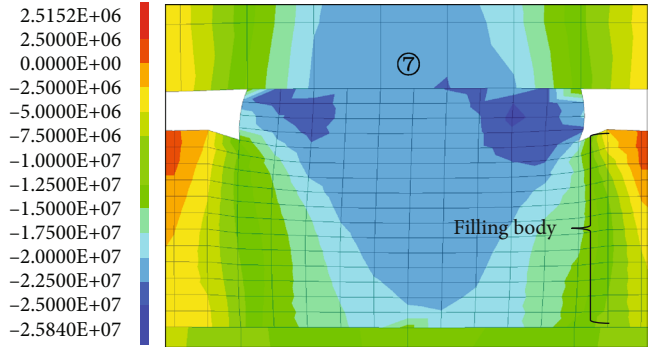


(d) Filling body heights 5 m

FLAC3D 5.01
©2014 Itasca Consulting Group, Inc.
Demonstration Model
Contour of ZZ-Stress
Plane: active on
Calculated by: Volumetric Averaging

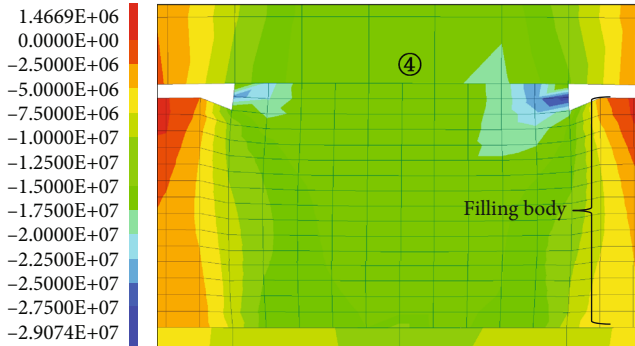


FLAC3D 5.01
©2014 Itasca Consulting Group, Inc.
Demonstration Model
Contour of ZZ-Stress
Plane: active on
Calculated by: Volumetric Averaging

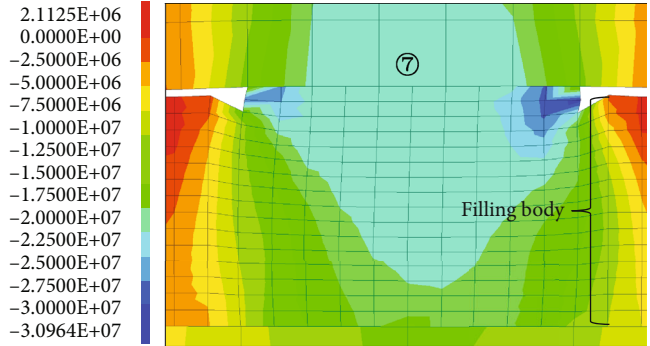


(e) Filling body heights 6 m

FLAC3D 5.01
©2014 Itasca Consulting Group, Inc.
Demonstration Model
Contour of ZZ-Stress
Plane: active on
Calculated by: Volumetric Averaging



FLAC3D 5.01
©2014 Itasca Consulting Group, Inc.
Demonstration Model
Contour of ZZ-Stress
Plane: active on
Calculated by: Volumetric Averaging



(f) Filling body heights 7 m

FIGURE 11: Vertical stress of coal pillars with different filling heights.

pillars. If certain reinforcement measures for the coal pillar are not taken, instability of the coal pillars below the no. 6107 working face will occur, causing the collapse of the no. 6107 working face and posing a huge threat to safe mining. Therefore, it is necessary to take reasonable measures to ensure the safe mining of the no. 6107 working face.

4.3. Influence Law of Filling Bodies on the Stability of Coal Pillars. Considering the mining conditions of the Yuanbaowan coal mine, the proposal of drilling on the floor of the no. 6107 working face and then grouting the goaf below the no. 6107 working face through these boreholes has been put forward. In order to ensure the safe mining, the effect of different heights of filling bodies on the stability of coal

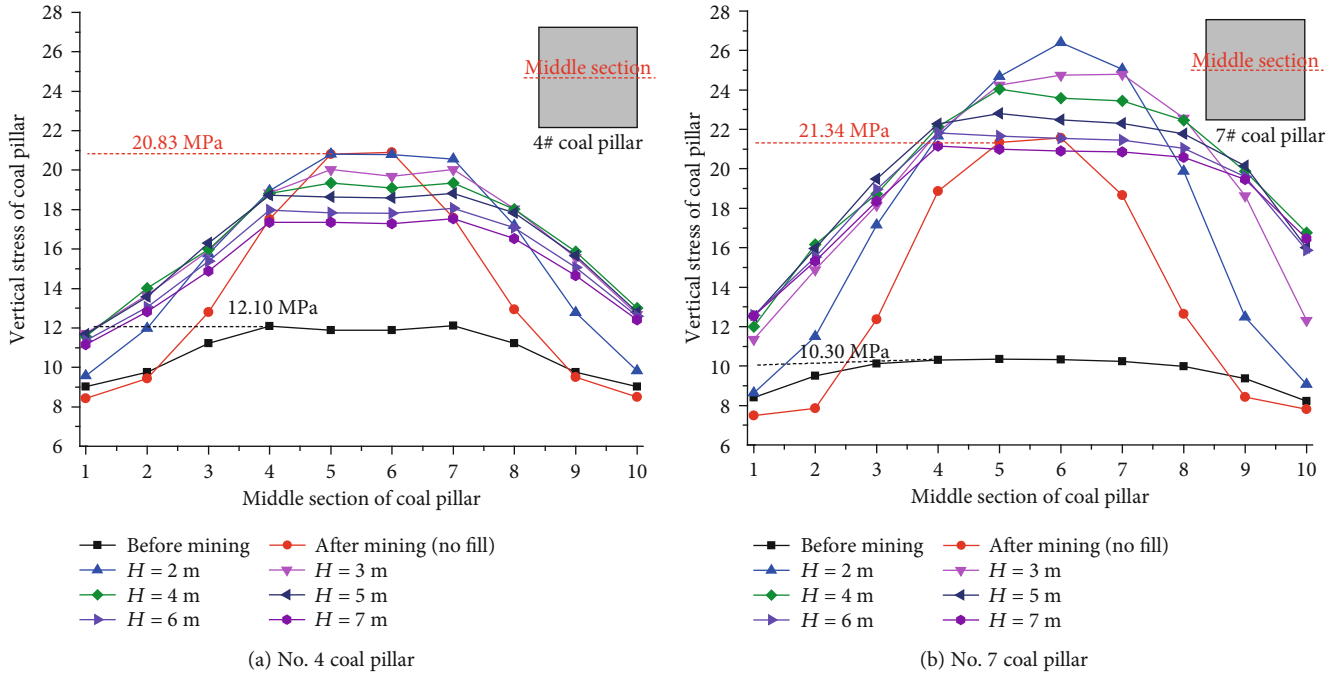


FIGURE 12: Strengthening effect of different filling body heights on coal pillar's bearing capacity.

pillars is studied. The research is mainly divided into two aspects: (1) the effect of different filling bodies' heights on the suppression of the expansion of the coal pillars' plastic area and (2) the effect of difference in filling bodies' heights on strengthening the bearing capacity of the coal pillars. The grouting filling material used in the Yuanbaowan coal mine was encapsulated and brought to the laboratory to conduct the measurement of the physical and mechanical parameters. At the same time, to accurately reflect the interaction between the floor pillars and the filling bodies, the parameters of the filling materials in the numerical simulation are also calibrated to ensure that the mechanical properties reflected by the simulated parameters are consistent with the true mechanical characteristics of the grouting material. And the calibration results are shown in Figure 8.

4.3.1. Suppressing Effect of Filling Bodies on the Expansion of the Coal Pillars' Plastic Area. Under the influence of the clamping effect of the filling bodies, the proportion of the plastic zone and the horizontal side heaves of coal pillars are effectively suppressed. The suppression effect when the height of the filling body is 4 m is shown in Figure 9.

The elastoplastic expansion law of the coal pillars below the no. 6107 working face and the change law of the horizontal side heaves corresponding to different grouting heights are shown in Figure 10. As shown in Figures 10(a) and 10(b), the proportion of the plastic zone of the no. 1 to no. 7 coal pillars has been reduced to 18%, 36%, 45%, 47%, 46%, 44%, and 25% rapidly when the height of filling bodies reaches 2 m, 3 m, 4 m, 5 m, 6 m, and 7 m, respectively, compared to the unfilled state. The horizontal side heave of the no. 1 to no. 7 coal pillars rapidly has been reduced from 476 mm, 616 mm, 769 mm, 622 mm, 1063 mm, 1372 mm,

and 1543 mm to 223 mm, 253 mm, 278 mm, 290 mm, 280 mm, 256 mm, and 230 mm, respectively, as shown in Figure 10(c). With the increase in the height of the filling bodies, the lateral clamping effect of the filling bodies on coal pillars below the no. 6107 working face tends to be more obvious, and the filling bodies have a significant suppressing effect on the expansion of both the plastic zone and the horizontal side heave of the floor coal pillars.

4.3.2. Strengthening Effect of the Filling Body on the Bearing Capacity of the Coal Pillar. The filling bodies of different heights form different clamping pressures on the coal pillars, which effectively improves the bearing capacity of the coal pillars, as shown in Figure 11.

In view of the limited space, taking the no. 4 and no. 7 coal pillars as examples, the strengthening effect of different heights of filling bodies on the bearing capacity of the floor coal pillars will be illustrated, as shown in Figure 12. It can be seen that before the mining of the no. 6107 working face, the vertical stresses of the no. 4 and no. 7 coal pillars are 12.10 MPa and 10.30 MPa, respectively, and the elastic core area accounts for 60% and 95%, respectively. Thus, the coal pillars are in a stable state. When mining is conducted without filling, the vertical stresses of the no. 4 and no. 7 coal pillars increase to 20.83 MPa and 21.34 MPa, respectively, and during which time, the proportions of the elastic core area of the two dramatically drop to 18% and 12%, causing instability for both these two coal pillars. While if the mining work of the working face 6107 is carried out after filling, the filling bodies support the overlying strata to a certain extent, reducing the overburden load of the coal pillars and increasing the proportion of the elastic core area of coal pillars, then the bearing capacity of coal pillars will be effectively improved.

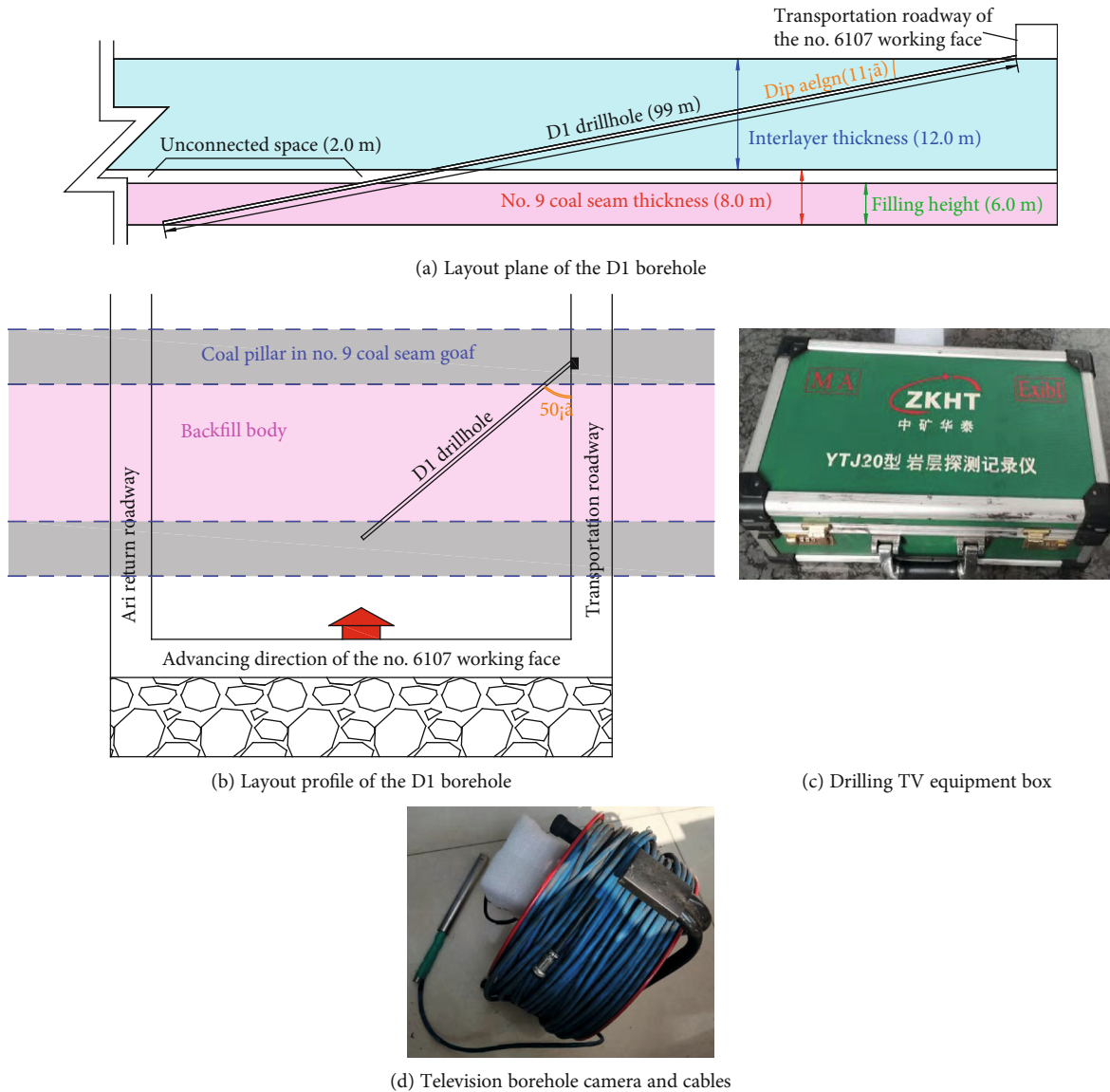


FIGURE 13: D1 borehole layout diagram and borehole TV observation equipment.

The strengthening effect of the filling bodies on the bearing capacity of the floor pillars becomes more obvious with the increasing height of the filling bodies.

5. Engineering Practice

Based on the research results above, it can be found that when the height of the filling bodies reaches 5 m, 6 m, or 7 m, the coal pillars can be kept stable under the influence of abutment pressure of the no. 6107 working face. However, when the height of the filling body is 5 m, the elastic core area of no. 4 and no. 5 coal pillars accounts for 40.625%, which is in a critically stable state. The filling body may suffer from certain shrinkage in size during the consolidation process, causing fissures between the body and the coal pillar, and the lateral clamping effect of the filling body on the coal pillar will be weakened. When the height of the filling body is 6 m or 7 m, the proportion of the elastic core area of each floor

pillar is higher than 50%, which can maintain the stability of the floor pillar. In summary, to ensure the safe mining of the no. 6107 working face with minimum filling cost, the height of the filling body is finally determined to be 6 m, and accordingly, on-site filling experiment work has been carried out.

5.1. Observation Hole Layout and Observation Equipment. Drilling on the floor is applied to test the on-site filling result and to evaluate the disturbance and damage caused by the mining-induced stress during the mining process of the no. 6107 working face. A floor sight borehole (hereinafter referred to as the D1 borehole), whose diameter and length are 65 mm and about 99 m, respectively, has been arranged in the transporting roadway in the no. 6107 working face. The angle between the D1 borehole and transporting roadway is about 50°, and the horizontal angle of the drilling hole is about 11°. To ensure that the probe can be smoothly

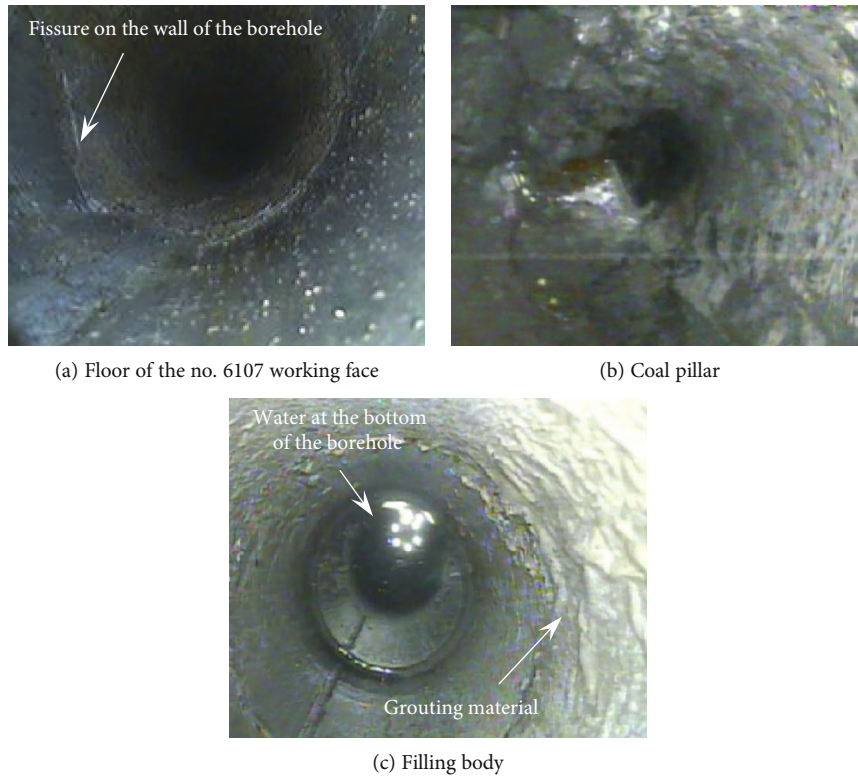


FIGURE 14: D1 borehole TV observation results at different depths.

lowered and determine the lowering distance of the probe, the connectable push rod is used to connect with the television borehole camera. As each part of the push rod is 1 m long, the lowering distance can be measured by the number of rods pushed into the drilling hole. The position of the borehole, D1, and drilling observation equipment are shown in Figure 13.

5.2. Field Observation Results. After the completion of the filling work and the consolidation of the filling slurry, developing rules of mining-induced fissures of the floor of the no. 6107 working face, the coal pillars, and the filling bodies have been investigated by using the borehole D1 and TV observation equipment, and their stability has been evaluated. On September 19, 2019, the underground borehole TV observation was conducted. At this time, the no. 6107 working face was about 30 m away from the borehole. The borehole successively goes through the floor, filling bodies, and coal pillars. The development conditions of fissures at different depths in the borehole D1 have been shown in Figure 14. The wall of the borehole D1 remains intact in the floor pillars and the filling bodies. There is much water in the bottom of D1, of which the seepage flow is relatively slow, and there is no obvious damage or water-conducting fissures. This also confirms that although the positions of the floor coal pillars, filling bodies, and floor coal pillars are located in the influence area of the peak value of abutment pressure of the no. 6107 working face, their stability is still maintained. It can be seen that the safe mining of the no. 6107 working face can be ensured when the height of the filling bodies reaches 6 m.

6. Discussion

- (1) On the basis of ensuring that the physical and mechanical parameters of simulated materials are consistent with those of coal pillars and the filling bodies, the effects of difference in filling bodies' heights on the suppression of the expansion of the coal pillars' plastic area below the no. 6107 working face and on strengthening the bearing capacity of the coal pillars have been mainly investigated, and the influence laws of different grouting heights of filling bodies on the stability of coal pillars have been revealed. However, the consolidation process of the filling slurry, the degree of adhesiveness/bonding between the filling bodies and the side wall of the coal pillars, and the size of the clearance between the two remain to be studied. In addition, the variation of the lateral clamping of coal pillars with different bonding levels needs to be further studied.
- (2) The filling materials of the Yuanbaowan coal mine are used, and accordingly, parameter calibration and simulation research is conducted in this paper. The effects of difference in the materials and the material ratio of filling bodies on the suppression of the expansion of the coal pillars' plastic area and on strengthening the bearing capacity of the coal pillars also remain to be investigated. Accordingly, research on the materials will be performed to find out the optimal combination of mining economic benefits

and coal pillar's controlling effects. The economic investment of the filling process will be minimized on the premise of ensuring safe mining.

7. Conclusion

- (1) Before the mining of the no. 6107 working face, the elastic core areas of no. 1 to no. 7 coal pillars, which are all stable, accounted for 98%, 76%, 63%, 60%, 63%, 71%, and 95%, respectively. When mining is conducted without filling the goaf, the plastic zone of the no. 1 to no. 7 coal pillars expands rapidly as influenced by the front abutment pressure, and the proportions of the elastic core area of the seven dramatically drop to 46%, 27%, 20%, 18%, 14%, 12%, and 12%, respectively, causing instability for no. 2 to no. 7 coal pillars. Thus, filling the goaf in the no. 9 coal seam is the prerequisite for safe mining of the no. 6107 working face.
- (2) The filling bodies have a certain lateral clamping effect on the coal pillars, which can effectively improve the stability of the coal pillars under the influence of the mining-induced pressure of the no. 6107 working face. The filling body has not only a suppressing effect on the expansion of the plastic zone of the coal pillars and the horizontal side heave but also a strengthening effect on the bearing capacity of the coal pillars. This phenomenon becomes more obvious with the increasing height of the filling bodies. When the height of the filling bodies reaches 6 m, the proportion of the plastic zone declines from 88% to 25% and the amount of the horizontal side heave reduced from 1534 mm to 230 mm. So the suppression effect on the plastic zone and the amount of the horizontal side heave is as high as 72% and 85%, respectively.
- (3) Drilling on the floor of the no. 6107 working face and then grouting the goaf have been carried out. The research shows that when the height of the filling bodies is 6 m, the occurrence and expansion of mining-induced fissures in the floor strata, filling bodies, and the floor pillars below the no. 6107 working face have been effectively restrained. So the floor pillars remain stable under the influence of the front abutment pressure, and the safe mining above the goaf of the no. 6107 working face can be ensured by grouting the goaf first.

Data Availability

Research data can be seen in the relevant images and tables in the text.

Conflicts of Interest

The authors declare that they have no conflicts of interest.

Acknowledgments

Financial support from the National Natural Science Foundation of China (No. 51904201), Fundamental Research Program of Shanxi (201901D211035), and Scientific and Technological Innovation Programs of Higher Education Institutions in Shanxi (2019L0245) is greatly appreciated.

References

- [1] J. H. Wang, "Present status and prospects of modernized mining technology and equipment in China coal mine," *Coal Science and Technology*, vol. 39, no. 1, pp. 1–5, 2011.
- [2] J. F. Ju, J. L. Xu, and W. B. Zhu, "Longwall chock sudden closure incident below coal pillar of adjacent upper mined coal seam under shallow cover in the Shendong coalfield," *International Journal of Rock Mechanics and Mining Sciences*, vol. 77, pp. 192–201, 2015.
- [3] J. L. Xu, J. F. Ju, and W. B. Zhu, "Support crushing types in the longwall mining of shallow seams," *Journal of China Coal Society*, vol. 39, no. 8, pp. 1625–1634, 2014.
- [4] J. F. Ju, J. L. Xu, W. B. Zhu, and K. Liu, "Influence of cut-hole position on support crushing during mining out coal pillar at the side of upper goaf in close distance of shallow seams," *Chinese Journal of Rock Mechanics and Engineering*, vol. 33, no. 10, pp. 2018–2029, 2014.
- [5] J. F. Ju, *Mechanisms and Prevention of Support Crushing Disaster while Mining out of the Upper Coal Pillar in Close Distance Shallow Seams*, China University of Mining and Technology, Xuzhou, China, 2013.
- [6] J. F. Ju, J. L. Xu, and W. B. Zhu, "Hydraulic powered support jammed mechanism and prevention technology of fully mechanized coal mining face 22103 in Daliuta mine," *Coal Science and Technology*, vol. 40, no. 2, pp. 4–7, 2012.
- [7] B. Yu, C. Y. Liu, J. X. Yang, and J. R. Liu, "Mechanism of strong pressure reveal under the influence of mining dual system of coal pillar in Datong mining area," *Journal of China Coal Society*, vol. 39, pp. 40–46, 2014.
- [8] T. Xiao, B. Jianbiao, X. Lei, and Z. Xuebin, "Characteristics of stress distribution in floor strata and control of roadway stability under coal pillars," *Mining Science and Technology*, vol. 21, no. 2, pp. 243–247, 2011.
- [9] B. A. Poulsen, "Coal pillar load calculation by pressure arch theory and near field extraction ratio," *International Journal of Rock Mechanics and Mining Sciences*, vol. 47, no. 7, pp. 1158–1165, 2010.
- [10] R. Singh, T. N. Singh, and B. B. Dhar, "Coal pillar loading in shallow mining conditions," *International Journal of Rock Mechanics and Mining Sciences & Geomechanics Abstracts*, vol. 33, no. 8, pp. 757–768, 1996.
- [11] A. K. Singh, R. Singh, J. Maiti, R. Kumar, and P. K. Mandal, "Assessment of mining induced stress development over coal pillars during depillaring," *International Journal of Rock Mechanics and Mining Sciences*, vol. 48, no. 5, pp. 805–818, 2011.
- [12] R. Singh, A. K. Singh, J. Maiti, P. K. Mandal, R. Singh, and R. Kumar, "An observational approach for assessment of dynamic loading during underground coal pillar extraction," *International Journal of Rock Mechanics and Mining Sciences*, vol. 48, no. 5, pp. 794–804, 2011.

- [13] A. Jaiswal and B. K. Shrivastva, "Numerical simulation of coal pillar strength," *International Journal of Rock Mechanics and Mining Sciences*, vol. 46, no. 4, pp. 779–788, 2009.
- [14] G. Murali Mohan, P. R. Sheorey, and A. Kushwaha, "Numerical estimation of pillar strength in coal mines," *International Journal of Rock Mechanics and Mining Sciences*, vol. 38, no. 8, pp. 1185–1192, 2001.
- [15] Z. L. Zhou, Y. Zhao, W. Z. Cao, L. Chen, and J. Zhou, "Dynamic response of pillar workings induced by sudden pillar recovery," *Rock Mechanics and Rock Engineering*, vol. 51, no. 10, pp. 3075–3090, 2018.
- [16] W. B. Zhu, L. Chen, Z. L. Zhou, B. T. Shen, and Y. Xu, "Failure propagation of pillars and roof in a room and pillar mine induced by longwall mining in the lower seam," *Rock Mechanics and Rock Engineering*, vol. 52, no. 4, pp. 1193–1209, 2019.
- [17] M. L. Wang, H. X. Zhang, and G. Y. Zhang, "Safety assessment of ascending long wall mining over old rib pillar gobs," *Journal of Mining & Safety Engineering*, vol. 25, no. 1, pp. 87–90, 2008.
- [18] Z. L. Zhou, X. B. Li, and G. Y. Zhao, "Evaluation of cascading collapse for private mined zone groups," *Journal of Natural Disasters*, vol. 16, no. 5, pp. 91–95, 2007.
- [19] T. Q. Liu, "The possibility of mining using the upward method," *Journal of China Coal Society*, vol. 3, no. 1, pp. 18–28, 1981.
- [20] G. J. Sun and Y. T. Wang, "Upward mining to improve complex roof control of seam," *Coal Science and Technology*, vol. 32, no. 5, pp. 15–18, 2004.
- [21] Q. X. Huang, "Analysis of floor stability of ascending mining in the contiguous seam," *Journal of Xi'an Mining Institute*, vol. 16, no. 4, pp. 291–294, 1996.
- [22] G. R. Feng, X. Yan, X. X. Wang, L. X. Kang, and Y. D. Zhai, "Determination of key positions of strata controlling in rocks between coal seams for upward mining," *Chinese Journal of Rock Mechanics and Engineering*, vol. 28, no. 2, pp. 3721–3726, 2009.
- [23] G. R. Feng, X. Y. Zhang, J. J. Li, S. S. Yang, and L. X. Kang, "Feasibility on the upward mining of the left-over coal above goaf," *Journal of China Coal Society*, vol. 34, no. 6, pp. 726–730, 2009.
- [24] G. R. Feng, J. Zheng, Y. F. Ren, X. X. Wang, L. X. Kang, and H. F. Liu, "Decision theory and method on feasibility on the upward fully mechanized mining of the left-over coal above gob area mined with caving method with pillar supporting method," *Journal of China Coal Society*, vol. 35, no. 11, pp. 1863–1868, 2010.
- [25] J. W. Bai, G. R. Feng, S. Y. Wang et al., "Vertical stress and stability of interburden over an abandoned pillar working before upward mining: a case study," *Royal Society Open Science*, vol. 5, no. 8, article 180346, 2018.
- [26] J. W. Bai, G. R. Feng, M. Zhang et al., "Influence of upper-bottom pillar mining on temporal and spatial evolution of stress in rock strata around middle residual coal seam," *Journal of China Coal Society*, vol. 41, no. 8, pp. 1896–1903, 2016.
- [27] M. G. Qian, X. X. Miao, J. L. Xu, and X. B. Mao, *Study of Key Strata Theory in Ground Control*, China University of Mining and Technology Press, Xuzhou, China, 2003.
- [28] Z. Li, S. C. Yu, W. B. Zhu et al., "Dynamic loading induced by the instability of voussoir beam structure during mining below the slope," *International Journal of Rock Mechanics and Mining Sciences*, vol. 132, article 104343, 2020.
- [29] J. F. Ju and J. L. Xu, "Surface stepped subsidence related to top-coal caving longwall mining of extremely thick coal seam under shallow cover," *International Journal of Rock Mechanics and Mining Sciences*, vol. 78, pp. 27–35, 2015.
- [30] Z. Li, J. L. Xu, J. F. Ju, W. B. Zhu, and J. M. Xu, "The effects of the rotational speed of voussoir beam structures formed by key strata on the ground pressure of stopes," *International Journal of Rock Mechanics and Mining Sciences*, vol. 108, pp. 67–79, 2018.
- [31] Y. Li, C. Tang, D. Li, and C. Wu, "A new shear strength criterion of three-dimensional rock joints," *Rock Mechanics and Rock Engineering*, vol. 53, no. 3, pp. 1477–1483, 2020.
- [32] T. J. Kuang, Z. Li, W. B. Zhu et al., "The impact of key strata movement on ground pressure behaviour in the Datong coalfield," *International Journal of Rock Mechanics and Mining Sciences*, vol. 119, pp. 193–204, 2019.
- [33] Z. Li, J. L. Xu, S. C. Yu, J. F. Ju, and J. M. Xu, "Mechanism and prevention of a chock Support failure in the longwall top-coal caving Faces: a case study in Datong Coalfield, China," *Energies*, vol. 11, no. 2, p. 288, 2018.
- [34] W. B. Zhu, J. L. Xu, L. Chen, Z. Li, and W. T. Liu, "Mechanism of disaster induced by dynamic instability of coal pillar group in room-and-pillar mining of shallow and close coal seams," *Journal of China Coal Society*, vol. 44, no. 2, pp. 358–366, 2019.
- [35] J. L. Xie, J. L. Xu, and F. Wang, "Mining-induced stress distribution of the working face in a kilometer-deep coal mine—a case study in Tangshan coal mine," *Journal of Geophysics and Engineering*, vol. 15, no. 5, pp. 2060–2070, 2018.
- [36] Y. Pan and S. T. Gu, "Analysis of bending moment, shear force, deflection and strain energy of hard roof at initial stage of cracking during periodic pressures," *Chinese Journal of Rock Mechanics and Engineering*, vol. 33, no. 6, pp. 1123–1134, 2014.

Research Article

Influence of Key Strata on the Gas Downward Leakage Law in Dual-System of Coal Seam

Feng Du,¹ Kun Jiao,¹ and Zhanyuan Ma²

¹School of Energy Science and Engineering, Henan Polytechnic University, Jiaozuo, 454000 Henan, China

²Datong Coal Mine Group Co. Ltd., Datong, 037003 Shanxi, China

Correspondence should be addressed to Zhanyuan Ma; 455985723@qq.com

Received 24 May 2020; Revised 28 June 2020; Accepted 27 August 2020; Published 10 September 2020

Academic Editor: Guozhong Hu

Copyright © 2020 Feng Du et al. This is an open access article distributed under the Creative Commons Attribution License, which permits unrestricted use, distribution, and reproduction in any medium, provided the original work is properly cited.

In Datong mining area, CO and other harmful gases were discharged from the gob in the Jurassic overburden strata to the panel of Carboniferous coal seam. To this end, panel 8309 of Tongxin coal mine in Datong mining area was taken as the engineering background; the change law of CO concentration in the upper corner of the panel and the law of mining pressure were studied through field measurement, and the influence of periodic movement of key strata on the downward leakage law of harmful gases was analyzed. In this paper, the fracture law of the key strata and fracture development characteristics of overburden strata were further studied by the similar simulation test, and the influence of the periodic movement of the key strata on the pathway formation of gas downward leakage was analyzed. The results show that the main cause of harmful gas downward leakage in the Jurassic gob is through the fracture produced by the fracture of the higher key strata. If the higher key strata fractures in the coal mining in the Carboniferous system, through fracture connecting the Jurassic gob above the open-off cut and the upper part of the panel are formed, and effective pathways for gas downward leakage are generated. The fracture and rotation of the higher key strata are accompanied by the formation and disappearance of the effective pathway for gas downward leakage above the panel. Then the periodic change of harmful gas discharging to the panel is caused and consistent with the law of mining pressure.

1. Introduction

Datong mining area has both Jurassic and Carboniferous coal seams. At present, the upper Jurassic coal resources are almost exhausted, and the lower Carboniferous ultra-thick coal seam has become the main coal seam for the mining [1, 2]. Carboniferous coal seam is usually mined with a large thickness, and the damage area of the rock strata is usually enlarged with the highly developed mining fractures [3]. As a result, fractures are easily interacted with the gob in Jurassic coal seam (abbreviated as Jurassic gob) and Carboniferous coal seam; and the downward leakage of harmful gases (such as CO) can be caused from the Jurassic gob, which seriously affects the safe and efficient mining of the Carboniferous coal seam [4].

The downward leakage of harmful gas in the Jurassic gob is mainly caused by the mining-induced fracture in the interval strata of the dual-system coal seam. Many scholars have studied the development law of overburden breakage charac-

teristics and mining-induced fracture in overburden strata. Bai and Lsworth [5] and Palchik [6] verified that there were three different moving zones in longwall mining overburden rock, namely, the caving zone, the fracture zone, and the bending deformation zone. Liu [7] systematically studied and summarized the deformation and failure of mining-induced overburden strata in coal mines of China. Besides, the calculation equations of the development height of water-conducting fracture zone were obtained [8–10]. Singh and Kendorski [11] put forward the importance of the water-retaining rock formation between water body and gob in 1981. This work plays an important guiding role in the safe mining of coal seam under water body. However, the influence of the overburden structure, fracture type, and the whole movement of the strata on the development of the water-conducting fracture are not considered in these researches. Qian et al. [12] proposed the theory of key strata control and concluded that the key strata play a decisive role in controlling the strata movement and the development of

mining fracture. Ju and Xu [13] and Li et al. [14] studied the structural characteristics of the key strata of longwall face in fully mechanized mining and its influence on mine pressure. Zhang et al. [15] and Kuang et al. [16] determined the law of fracture and movement of key strata through in situ investigation. Based on the key strata theory, Miao et al. [17], Wang et al. [18] and Feng et al. [19] proposed the concept and principle of the water-resisting key strata for the mining with water preservation, established a mechanical model of the composite water-resisting key strata, and successfully applied it to the prevention and control of water inrush disaster of roof and floor and the protection of water resources in mining area [20]. Based on the theory of key strata, Xu et al. [21] and Wang et al. [22] studied the influence of the location of the main key strata of the overburden strata on the development height of the water-conducting fracture and proposed a prediction method for the height of the water-conducting fracture zone by the location of the key strata of the overburden strata [23]. Du et al. [24] analyzed the development patterns of fractured water-conducting zones in longwall mining of thick coal seams according to the safety mining of Zhuozhang river. Tu and Fu [25], Qu et al. [26], and Wu [27] performed the research on the gas migration pathway in the coal seam and obtained the influence of key strata on the effect and scope of gas drainage. Besides, the reliability of key strata theory applied in gas extraction was verified by field engineering application. In addition, Ma et al. [28] studied the characteristics of water flow in mining fractured rock mass. Si et al. [29], Zhao et al. [30], and Wang et al. [31] presented a systematic investigation into the permeability characteristics of flow field in mining area.

At present, many scholars have studied the development law of overburden breakage characteristics and mining-induced fracture in overburden strata, and the mining thickness of coal seam is below 8 m [32, 33]. However, the average thickness of Carboniferous ultra-thick coal seam in Datong mining area is 15 m, and the damage area of the rock strata is usually enlarged with the highly developed mining fractures [34, 35]. The downward leakage of harmful gas in the Jurassic gob is mainly caused by the mining-induced fracture in the interval strata of the dual-system coal seam [36–38]. Therefore, the research on the development law of overburden breakage characteristics and mining-induced fracture in Datong mining area should be carried out systematically.

To summarize, the key strata theory has been well applied in the development law of water-conducting fracture zone and the mining-induced fracture evolution related to gas drainage. In view of the occurrence and mining conditions of the dual-system coal seams in Datong mining area, panel 8309 of Tongxin mine, Datong mining area was taken as the research background; the key strata theory, physical experiment, and field measurement were used to study the fracture law and fracture development characteristics of the interval strata of the dual-system coal seam. Besides, the influence of the periodic movement of the key strata on the gas downward leakage pathway and gas drainage law was analyzed, so as to ensure the safe and efficient mining of the dual-system coal seams. This study provides a theoretical guidance for coal mining in the dual-system coal seam.

2. Introduction of Panel and Identification of Key Strata

2.1. Overview of the Panel. Panel 8309 of Tongxin mine is located in the third mining area of Tongxin mine in Datong mining area. The 3-5# coal seams of the Carboniferous system were mined. The average thickness of the coal seam was 14.88 m, the average buried depth was 580 m, and the dip angle was 0-3°. The length of the panel was 2843 m, and the dip length was 200 m. Longwall mining and the extraction ventilation method was adopted. Jurassic gob in 14# coal seam was overlaid on the panel 8309, with a spacing of 200-240 m. There were a lot of water and harmful gas in the Jurassic gob, which seriously affected the safe and efficient mining of the panel. The goaf in Jurassic coal seam above the panel 8309 from the open-off cut to 1283 m includes the panel 81003, the panel 81005, the panel 81006, and the panel 81008; besides, the goaf in Jurassic coal seam above the panel 8309 from 1809 m to the nonmining line includes the panel 8902-3, the panel 8902-2, the panel 8908, and the panel 8906.

2.2. Key Strata Identification. According to the key strata theory of strata control and the water-resisting key strata theory for mining with water conservation [8], the stability of key strata in the interval strata of dual-system coal seam plays a decisive role in the gas drainage in the overburden gob. The key strata refer to the strata which control the whole or partial overburden movement from the overburden to the surface. If the structural key strata do not fracture after mining, the fracture cannot expand, develop, or form an effective gas drainage pathway. Therefore, the structural key strata is the gas-resisting key strata. To study the influence of the key strata between the dual-system coal seams on the harmful gas downward leakage of the overburden gob, the core drilling holes were arranged in the middle of the panel 8309. Mechanical parameters of the standard coal rock samples were tested by RMT-150B rock mechanics experiment system, and the position of the key strata of the overburden strata on the panel was determined according to the key strata discrimination condition [7], as shown in Table 1.

It can be seen from Table 1 that the immediate floor of the panel is composed of sandy mudstone with a thickness of 4 m, and the immediate roof is mainly composed of coarse-grained sandstone and sandy mudstone. There is the Jurassic gob in 14# coal seam and 220.89 m above the panel, and there are two key strata in the overburden strata. The higher key strata are 123.08 m away from the 3-5# coal seams, which is less than 10 times of the mining height. According to the prediction method for the height of the water-conducting fracture zone proposed by Xu et al. [21], the harmful gas of Jurassic gob in 14# coal seam will be discharged to the panel 8309 after the key strata are broken.

3. Experimental Analysis of Periodic Movement of Key Strata and Gas Downward Leakage

3.1. CO Observation Schemes of Panel 8309. To study the gas downward leakage law of the Jurassic gob in 14# coal seam

TABLE 1: Physical and mechanical parameters of 1# drill hole column and coal seams.

	Lithology	Thickness (m)	Buried depth (m)	Unit weight ($\text{kN}\cdot\text{m}^{-3}$)	Tensile strength (MPa)	Elastic modulus (GPa)	Key strata location
Jurassic system	Fine-grained sandstone	6.44	346.13	27.00	6.40	44.65	
	Siltstone	8.21	354.34	26.04	4.89	37.29	
	Coal seam 14	2.90	357.24	14.26	4.20	4.20	
	Siltstone	8.57	365.81	26.04	4.89	37.29	
	Sandy mudstone	6.48	372.29	26.81	4.40	38.07	
	Medium-grained sandstone	4.30	376.59	26.54	5.72	38.90	
	Mudstone	4.20	380.79	27.52	2.72	29.40	
	Coarse-grained sandstone	3.64	384.43	25.40	2.56	18.28	
	Medium-grained sandstone	3.35	387.78	26.54	5.72	38.90	
	Mudstone	9.06	396.84	27.52	2.72	29.40	
	Fine-grained sandstone	1.60	398.44	27.00	6.40	44.65	
	Mudstone	2.03	400.47	27.52	2.72	29.40	
	Fine-grained sandstone	4.30	404.77	27.00	6.40	44.65	
	Mudstone	17.31	422.08	27.52	2.72	29.40	
	Fine-grained sandstone	5.27	427.35	27.00	6.40	44.65	
	Siltstone	42.01	469.36	27.52	2.72	29.40	Higher key strata
	Sandy mudstone	7.27	476.63	26.81	4.40	38.07	
	Fine-grained sandstone	3.00	479.63	27.00	6.40	44.65	
	Sandy mudstone	2.04	481.67	26.81	4.40	38.07	
	Coarse-grained sandstone	6.37	488.04	25.40	2.56	18.28	
	Coarse sandstone with gravel	4.57	492.61	25.28	3.20	15.33	
	Coarse-grained sandstone	3.23	495.84	25.40	2.56	18.28	
	Coarse sandstone with gravel	2.80	498.64	25.28	3.20	15.33	
	Coarse-grained sandstone	5.54	504.18	25.40	2.56	18.28	
	Coarse sandstone with gravel	12.74	516.92	25.28	3.20	15.33	Lower key strata
	Coarse-grained sandstone	5.84	522.76	25.40	2.56	18.28	
	Coarse sandstone with gravel	6.97	529.73	25.28	3.20	15.33	
	Mudstone	5.20	534.93	27.52	2.72	29.40	
	Sandy mudstone	3.57	538.50	26.81	4.40	38.07	
	Coarse-grained sandstone	6.17	544.67	25.40	2.56	18.28	
	Sandy mudstone	4.10	548.77	26.81	4.40	38.07	
	Medium-grained sandstone	2.37	551.14	26.54	5.72	38.90	
Dyas system							

TABLE 1: Continued.

	Lithology	Thickness (m)	Buried depth (m)	Unit weight ($\text{kN}\cdot\text{m}^{-3}$)	Tensile strength (MPa)	Elastic modulus (GPa)	Key strata location
Carboniferous system	Coarse-grained sandstone	2.40	553.54	25.40	2.56	18.28	
	Sandy mudstone	5.94	559.48	26.81	4.40	38.07	
	Coarse-grained sandstone	3.10	562.58	25.40	2.56	18.28	
	Mudstone	6.74	569.32	27.52	2.72	29.40	
	Sandy mudstone	1.87	571.19	26.81	4.40	38.07	
	Coarse-grained sandstone	5.34	576.53	25.40	2.56	18.28	
	Sandy mudstone	1.60	578.13	26.81	4.40	38.07	
	Coal seams 3-5	14.05	592.18	14.26	4.20	4.20	
	Sandy mudstone	4.00	596.18	26.81	4.40	38.07	

above the panel 8309, CO was taken as the monitoring object of the discharged gas, and 8 observation points for CO concentration were designed and arranged in panel 8309, headgate 2309, and tailgate 5309. As shown in the Figure 1, 4 measuring points for CO concentration are uniformly arranged in the 200 m long panel. The exact time for field measurement is from June 14, 2018, to July 13, 2018. Measuring points 1 and 4 correspond to the upper and lower corners of the panel, and two measuring points are arranged 50 m and 100 m away from the upper and lower corners of headgate 2309 and tailgate 5309. CO concentration of each measuring point is monitored in real time through the CO volume concentration sensor, as shown in Figure 2.

3.2. Effect of Periodic Movement of Key Strata on Gas Downward Leakage. Through the CO concentration of each observation point, it is found that CO of the Jurassic gob in 14# coal seam is discharged to panel 8309 under the negative pressure effect. Since the upper corner is located at the return side of the panel and close to the triangle area of the upper side of the return air lane and the edge of the gob, the CO concentration of the upper corner is significantly affected. Based on the monitoring results of CO concentration in the upper corner of the panel from June 13 to 14 and the mining pressure curve obtained by the 58# support in the middle of the panel, the influence of periodic movement of key strata on gas downward leakage is analyzed. As shown in Figure 3, there are large and small periods of mining pressure in the advance of the panel. The small periodic mining pressure steps are measured as 24 m, 40 m, 34 m, etc., and the average pressure steps are 33 m; the large periodic pressure steps are measured as 64 m, 58 m, etc., and the average pressure steps are 61 m. The large periodic mining pressure steps are about twice of the small periodic mining pressure. The change of CO concentration in the upper corner presents periodic change, which is consistent with the law of mining pressure law. In the case of nonperiodic and small periodic mining pressure, CO concentration is low, while in the large periodic mining pressure, CO concentration increases significantly.

According to the drilling column in Table 1 and the theory of mining pressure and strata control [7], the main reason for the large and small periodic mining pressure in the panel is that there are two key strata in the overburden strata of the panel. When the lower key strata are broken, a small periodic mining pressure is formed, and when the lower key strata and the higher key strata are broken simultaneously, the large periodic mining pressure is formed. In the mining process of the dual-system coal seam, mining-induced fractures are generated in the interval strata, and harmful gas can be discharged to the Carboniferous panel through the gas leakage pathway formed by mining fractures. Because the key strata control the evolution of mining fractures, it can be inferred that the periodic fracture of the higher key strata will change the gas leakage pathway, thus causing the periodic leakage of the harmful gas from the Jurassic gob.

4. Similar Simulation Experiments of Fracture and Fracture Development in Key Strata

4.1. Design of Similar Simulation Experiments. To further study the influence of the periodic movement of the key strata on the evolution characteristics of the gas leakage pathway and the gas leakage law, a similar simulation experiment of the key strata fracture and fracture development law was performed based on the project background of the panel 8309. In this similar simulation experiment, a similar model frame with the size of $2.5 \times 1.3 \times 0.2$ m (length \times height \times width) was selected. The geometric similarity ratio of the model was 200:1, the actual laying height was 1.28 m, and the simulated laying height was 256.49 m. The unit weight ratio of the model was 1.5:1, so the stress similarity ratio of the model was 300:1, the thickness of the nonsimulated overburden was 339.69 m, and the load on the upper part of the model was 0.028 MPa. For test materials, sand was taken as aggregate; cement, calcium carbonate, and gypsum as cementing materials; borax as retarder; and mica as layered materials.

The theoretical basis for the similar simulation experiment includes the geometric similarity, the kinematic

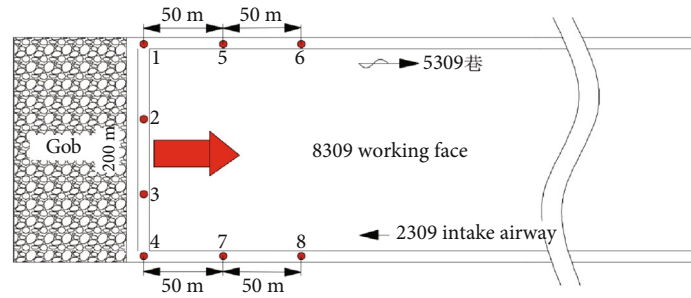


FIGURE 1: Layout of CO measuring points in panel 8309.



FIGURE 2: CO volume concentration sensor.

similarity, and the dynamic similarity. The similar simulation model is shown in Figure 4. To clearly observe the fracture development characteristics of 3-5# coal seams and interval strata of 14# coal seam during the excavation, after the model was laid, the coal seam and key strata were colored with black paint and yellow paint, respectively, on the front of the model, and the remaining strata were whitewashed with lime. At the same time, the grid lines with a spacing of 10 cm were drawn with ink bucket.

4.2. Experimental Processes and Experimental Results. Before the excavation, the model was loaded with a loading of 0.028 MPa. To reduce the boundary effect of the model platform, 30 cm protective pillars were reserved at both ends of the coal seam. In the model, 14# coal seam was first mined, then 3-5 # coal seams, all of which were excavated from the left side of the model at 5 cm every 30 minutes.

Similar simulation experiment results show that during the excavation of 3-5# coal seams, the fracture of the key strata is accompanied by the movement of the loaded overburden strata and the fracture development. As shown in Figure 5, when the lower key strata is fractured, and a through fracture is formed, the overburden strata controlled

by the key strata break synchronously, and the fracture develops rapidly to the lower part of the higher key strata; when the higher key strata fractures, longitudinal cracks are developed from the overburden strata to 14 # coal floor. Through the analysis of the experimental results, it is believed that the lower layer of the key strata directly collapses during the advance of the panel, and the stability of the key strata is determined by the fracture and fracture development of the interval strata in the dual-system coal seam. Therefore, the two key stages of the fracture of the lower and higher key strata are analyzed based on experimental results.

4.2.1. Fracture of Lower Key Strata. When the panel is mined 60 m from the open-off cut, the first collapse of the direct roof occurs. With the panel advances to 120 m, the fracture height of overburden strata reaches to the lower key strata, and separation zone appears at the bottom of the panel and gradually expands with the advance of the panel. When the panel is mined to 160 m, the lower key strata fractures for the first time. As shown in Figure 6(a), due to the long settlement time in the separation zone near the open-off cut and the large compaction degree of the rock layer, the lower key strata presents an asymmetric fracture structure, and some of the above rock layer collapse. With the primary fracture of the lower key strata, longitudinal fracture runs through the lower key strata and develops to the lower part of the unbroken layer with the separation zone. At this time, the longitudinal fractures and separation zones on both sides are connected with each other, resulting in trapezoidal-shaped collapse in the model.

When the panel is mined to 200 m, the first periodic fracture occurs in the lower key strata, and the overburden strata collapse completely. At the same time, the separation zone and longitudinal fracture develop rapidly to the lower part of the higher key strata, as shown in Figure 6(b). With the advance of the panel, the periodic fracture continues to occur in the lower key strata, with an average periodic fracture step distance of 30 m. Because the higher key strata are not broken, the development of the fracture upward is hindered, and the trapezoidal-shaped collapse area of the rock strata evolves towards the panel instead of the higher key strata. The floor failure in Jurassic coal seam has the important effect on gas downward leakage, because the mining fractures caused by the floor failure in Jurassic coal seam are the main leakage channel for the harmful gas.

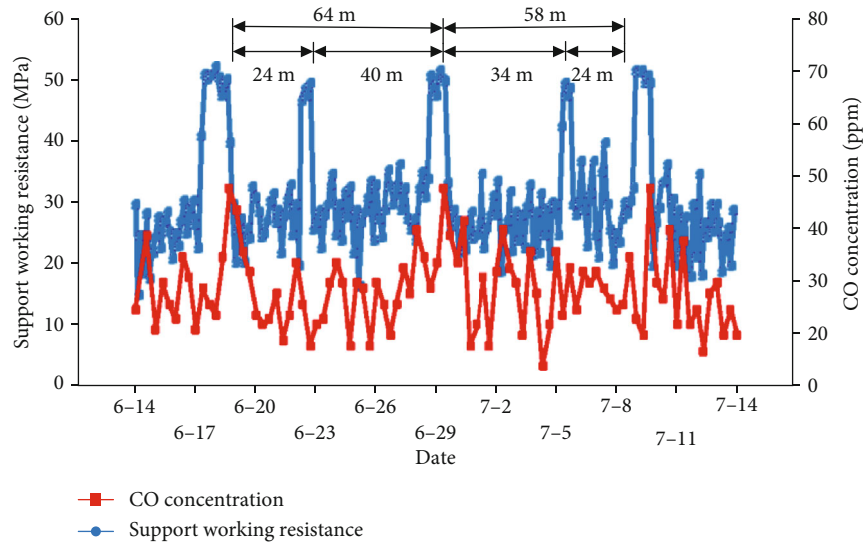


FIGURE 3: CO concentration and mining pressure curve in the upper corner of the panel.

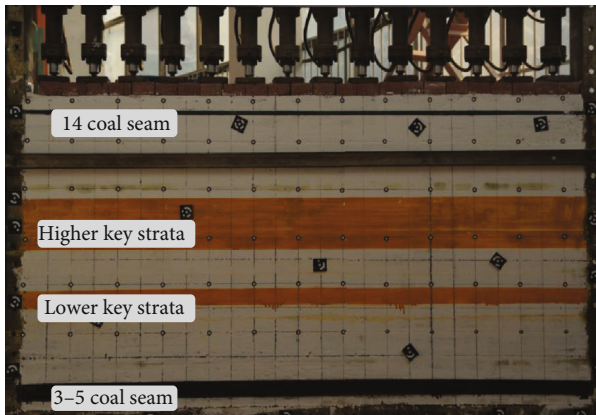


FIGURE 4: Similar simulation model.

4.2.2. Higher Key Strata Fracture. The fracture characteristics of the higher key strata in the mining process of the panel are shown in Figure 7. When the panel is mined to 300 m, the higher and the lower key strata fracture simultaneously. With the first fracture of the higher key strata, the bottom strata of the gob in 14# coal seam, which is controlled by the higher key strata, are fractured simultaneously. Meanwhile, the cracks in the overburden strata of the higher key strata develop rapidly to the bottom of the gob in the 14# coal seam, and three longitudinal through cracks connecting the gob in 14# coal seam are formed above the cut-out hole and the panel, as shown in Figure 7(a). Due to the large compaction degree of rock at the cut-out hole side, through crack 2 is inclined to the one side of the cut-out hole. When the panel advances to 360 m, the first periodic fracture occurs in the higher key strata, with a step distance of about 60 m. At the same time, a new through fracture is formed above the panel, as shown in Figure 7(b).

According to the main characteristics of fracture and fracture development of key strata in the excavation process of model, it is obtained that the periodic fracture step

distance of the lower and higher key strata in the mining process of panel 8309 is about 30 m and 60 m, respectively; the fracture step distance of higher key strata is twice that of lower key strata, which is basically consistent with the large and small periodic mining pressure curve of 58# support in the middle of panel.

In the coal mining of Carboniferous system, through fractures caused by the fracture of the higher key strata is the main cause of the downward leakage of harmful gas in Jurassic gob. The phenomenon of key layer rotation and crack closure occurs in the similar simulation experiment results, which is controlled by the higher key strata. If the higher key strata fracture after the panel of Carboniferous system is fully mined, a through fracture connecting the Jurassic gob will be formed above the cut-out hole and the upper part of the panel, resulting in the generation of harmful gas leakage pathway. With the periodic fracture of the higher key strata, a new through fracture appears above the panel, becoming a new gas downward leakage pathway.

5. Analysis of the Influence of the Key Strata on the Gas Downward Leakage Law in the Mining of Dual-System Coal Seam

5.1. Influence of Key Strata on Evolution Law of Gas-Conducting Fractures. In general, there are multiple key strata in the coal seam of the dual-system. Based on the theory of key strata, the evolution law of the gas-conducting fracture is analyzed when there are two key strata in the overburden. In the excavation of 3-5# coal seams of Carboniferous system, when the lower key strata fractures with the advance of the panel, the lower key strata are located in the open-off cut, and the broken rock block above the panel rotates. The two ends of the gyratory block are occluded with the adjacent key strata or broken rock block to form four gas-conducting fractures. With the fracture of the lower key strata, the soft rock layer in the control area overlying the

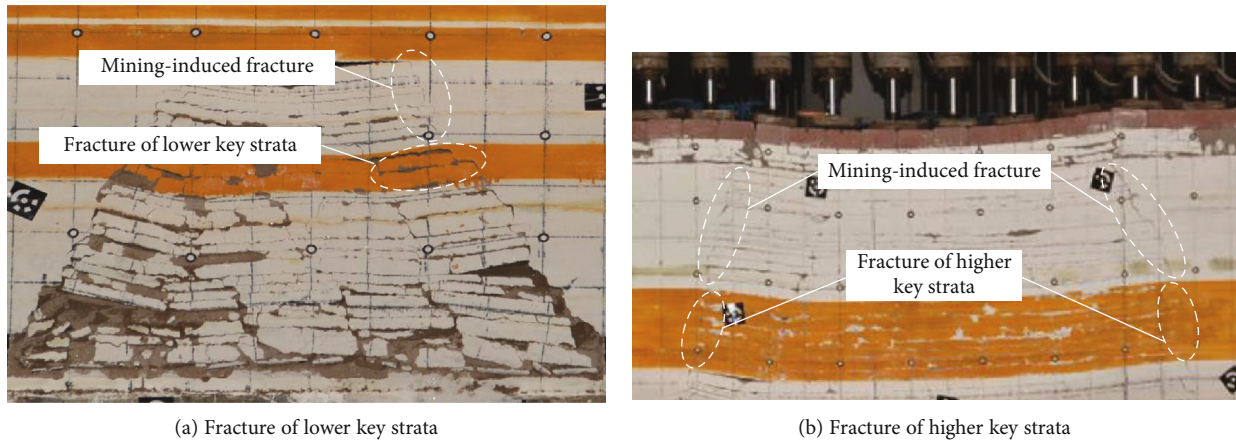


FIGURE 5: Simultaneous fracture of key strata and overburden strata.

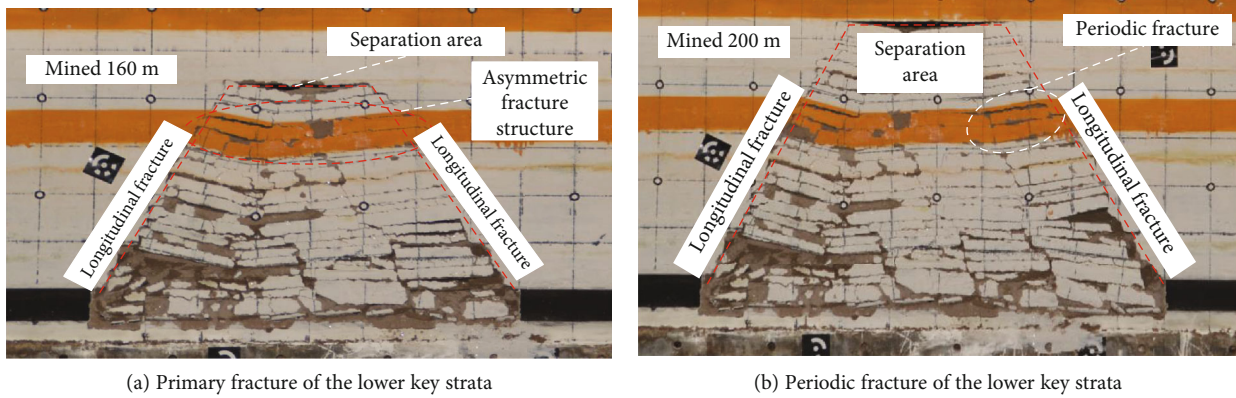


FIGURE 6: Fracture characteristics of lower key strata.

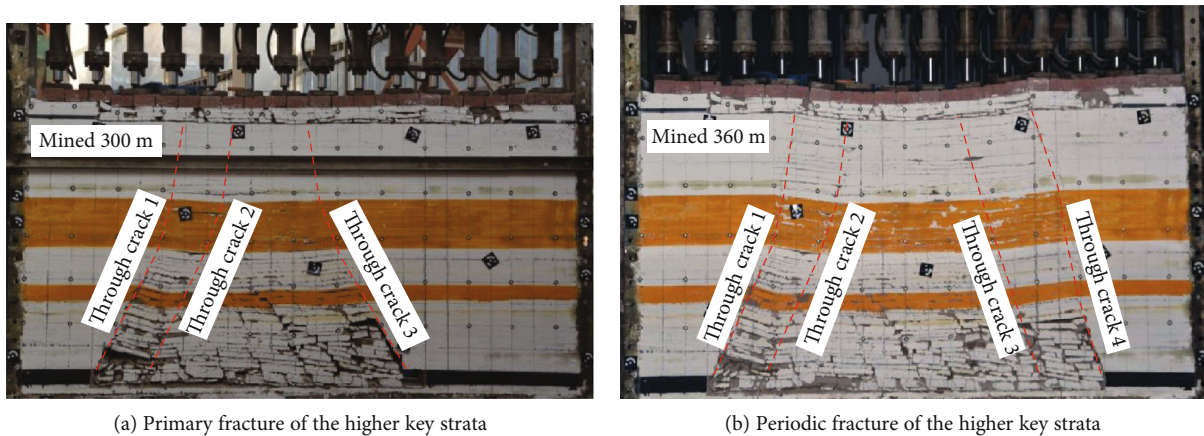


FIGURE 7: Fracture characteristics of the higher key strata.

lower key strata fractures synchronously, and the gas-conducting fracture develops in the soft rock layer and extends to the bottom of the higher key strata. If the higher key strata does not fracture or lose stability (the distance of panel advance is insufficient), the gas-conducting fracture in the higher key strata and its control soft rock layer cannot

connect with the Jurassic gob, and the gas downward leakage will not be caused, as shown in Figure 8.

With the continuous advance of the panel, if the higher key strata is fractured along with the mining, the soft rock layer at the upper part of the higher key strata is simultaneously fractured along with the higher key

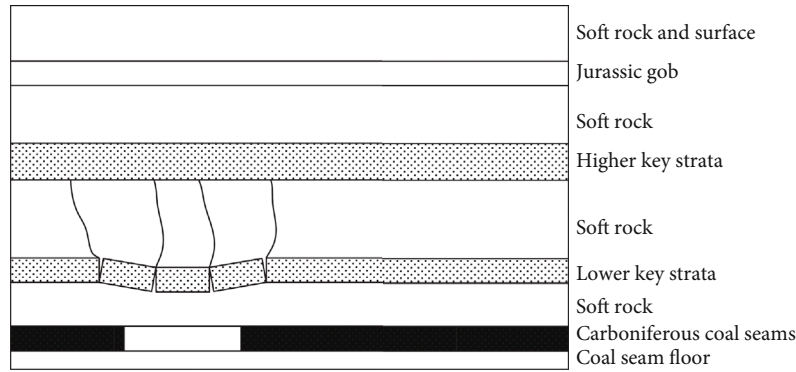


FIGURE 8: Distribution diagram of gas-conducting fracture field before fracture of the higher key strata.

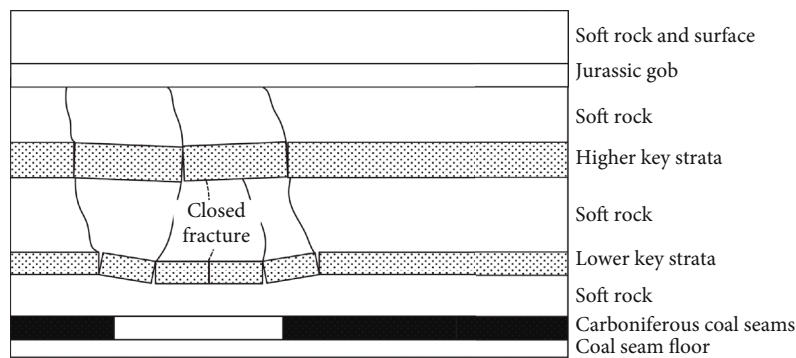


FIGURE 9: Distribution diagram of gas-conducting fracture field in the first fracture of the higher key strata.

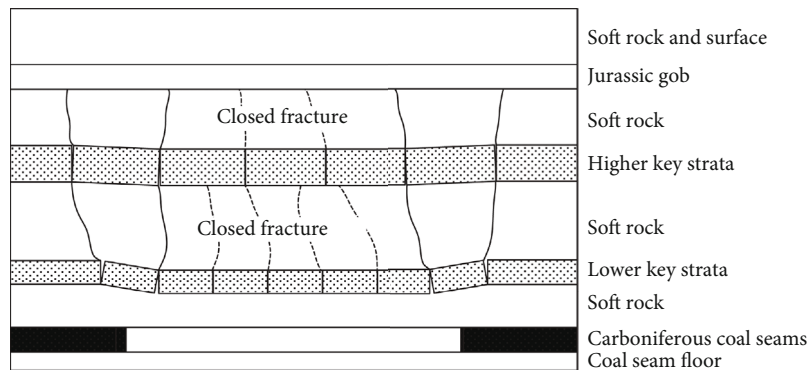


FIGURE 10: Distribution diagram of gas-conducting fracture field during periodic fracture of the higher key layer.

strata, the fracture field at the upper part of the higher key strata connects the Jurassic gob and forms an effective gas pathway together with the fractures in the control area of the lower key strata, and the harmful gas in the Jurassic gob enters downward along with the effective gas pathway to the gob open-off cut and the panel, as shown in Figure 9. It should be noted that with the development of mining activities, the lower key strata has a periodic fracture and settlement rotation. The gas-conducting fracture (including the gas-conducting fracture in the upper control soft rock layer) behind the panel is closed with the settlement contact, and the gas-conducting capacity is sharply reduced. However, the new broken rock block

forms the new gas-conducting fracture in front of the panel. If the closed fracture is not considered, with the periodic fracture of the lower key strata, the number and capacity of the effective gas-conducting fractures in the lower key strata and its overburden strata do not decrease with the closing of the latter fractures.

When the higher key strata fractures periodically with the mining, the gas-conducting fracture in the soft layer, lower, and higher key strata in the middle of the gob gradually close and disappear, and the gas-conducting ability decreases sharply. The mining fracture of the overburden strata near the open-off cut and the panel are developed, and four effective gas leakage pathways are formed in the lower key strata,

the higher key strata, and the soft strata controlled by the overburden strata, as shown in Figure 10.

5.2. Analysis of the Influence of Key Strata on the Gas Downward Leakage Law. Under the mining condition of dual-system coal seam in Datong mining area, the main reason for periodic downward leakage of harmful gas in Jurassic gob is the fracture and rotation of the higher key strata. Under the condition of nonpressure and small mining pressure, the blocks in the higher key strata above the panel turn in the reverse direction, the higher key strata and its upper gas-conducting fracture close rapidly, resulting in the disappearance of the effective gas pathway. Harmful gases in the Jurassic gob are mainly discharged into the gob of carboniferous coal seam through the effective gas pathway above the open-off cut. In the closed state, there is stable harmful gas discharge into the panel through the gob of Carboniferous system. In the large periodic mining pressure, the rotation and fracture of the higher key strata result in the formation of new effective gas-conducting pathways, and the harmful gas in the panel of Carboniferous system increases sharply.

To sum up, under the condition of dual-system coal seam mining in Datong mining area, when the Carboniferous coal seam is mined to the lower part of the Jurassic gob, if there is strong mining pressure in the panel, effective measures such as the use of pressure equalizing ventilation system should be taken timely to eliminate the hidden danger of harmful gas downward leakage from the Jurassic gob to the panel.

6. Conclusions

- (1) The change of CO concentration in the upper corner of panel 8309 shows periodic change, which is consistent with the mining pressure law. In the case of non-pressure and small periodic mining pressure, CO concentration is low, while in the case of large periodic mining pressure, CO concentration increases significantly.
- (2) The main cause of harmful gas downward leakage in the Jurassic gob is through fractures produced by the fracture of the higher key strata. If the higher key strata fractures in the coal mining in the Carboniferous system, the through fracture connecting the Jurassic gob will be formed above the open-off cut and the panel.
- (3) Under the mining condition of dual-system coal seam in Datong mining area, the main reason for periodic downward leakage of harmful gas in Jurassic gob is the fracture and rotation of higher key strata. When the Jurassic gob is overlying on the Carboniferous coal seam in the mining process, once the strong mine pressure appears in the panel, effective measures should be taken timely to eliminate the hidden danger of harmful gas downward leakage from the Jurassic gob to the panel.

Data Availability

The data used to support the findings of this study are included within the article.

Conflicts of Interest

The authors declare that they have no conflicts of interest.

Acknowledgments

This work was supported by the National Natural Science Foundation of China (U1904128 and 51774110, 51704095) and Program for Science & Technology Innovation Talents in Universities of Henan Province (19HASTIT047), the Fundamental Research Funds for the Universities of Henan Province (NSFRF200302), and the Foundation for Higher Education Key Research Project by Henan Province (19A130001).

References

- [1] B. Yu, "Study on fully mechanized coal mining technology in passed 40 years in Datong mining area," *Journal of China Coal Society*, vol. 32, pp. 1772–1777, 2010.
- [2] B. Yu, "Behaviors of overlying strata in extra-thick coal seams using top-coal caving method," *Journal of Rock Mechanics and Geotechnical Engineering*, vol. 8, no. 2, pp. 238–247, 2016.
- [3] D. Ma, J. Wang, X. Cai et al., "Effects of height/diameter ratio on failure and damage properties of granite under coupled bending and splitting deformation," *Engineering Fracture Mechanics*, vol. 220, p. 106640, 2019.
- [4] Y. Chen, H. W. Zhang, Z. J. Zhu, B. Yu, and L. J. Huo, "Research on the law overburden movement and failure under the influence of double period coal seam mining," *The Chinese Journal of Geological Hazard and Control*, vol. 32, pp. 67–73, 2014.
- [5] M. Bai and D. Elsworth, "Some aspects of mining under aquifers in China," *Mining Science and Technology*, vol. 10, no. 1, pp. 81–91, 1990.
- [6] V. Palchik, "Influence of physical characteristics of weak rock mass on height of caved zone over abandoned subsurface coal mines," *Environmental Geology*, vol. 42, no. 1, pp. 92–101, 2002.
- [7] T. Q. Liu, *Theory and technology of optimal design of outcrop coal pillar*, Coal Industry, Beijing, 1981.
- [8] State Bureau of Coal Industry, *Rules for coal pillar reservation and coal pressure mining in buildings, gas, railways and main shafts*, Coal Industry, Beijing, 2000.
- [9] D. Ma, J. Wang, and Z. Li, "Effect of particle erosion on mining-induced water inrush hazard of karst collapse pillar," *Environmental Science and Pollution Research*, vol. 26, no. 19, pp. 19719–19728, 2019.
- [10] W. Xu, Y. C. Xia, and R. J. Du, "Study on three properties of the empirical formula for estimating the height of water-flowing fractured zone," *Mining Research and Development*, vol. 33, pp. 63–67, 2013.
- [11] M. M. Singh and F. S. Kendorski, "Strata disturbance prediction for mining beneath surface water and waste impoundments," *International Journal of Rock Mechanics and Mining Sciences & Geomechanics Abstracts*, vol. 20, no. 1, p. a13, 1983.

- [12] M. G. Qian, S. P. Wu, and J. L. Xu, *Mine pressure and strata control*, China University of Mining and Technology, Xuzhou, 2010.
- [13] J. Ju and J. Xu, "Structural characteristics of key strata and strata behaviour of a fully mechanized longwall face with 7.0m height chocks," *International Journal of Rock Mechanics and Mining Sciences*, vol. 58, pp. 46–54, 2013.
- [14] Z. Li, J. Xu, J. Ju, W. Zhu, and J. Xu, "The effects of the rotational speed of voussoir beam structures formed by key strata on the ground pressure of stopes," *International Journal of Rock Mechanics and Mining Sciences*, vol. 108, pp. 67–79, 2018.
- [15] Z. Zhang, J. Xu, W. Zhu, and Z. Shan, "Simulation research on the influence of eroded primary key strata on dynamic strata pressure of shallow coal seams in gully terrain," *International Journal of Mining Science and Technology*, vol. 22, no. 1, pp. 51–55, 2012.
- [16] T. Kuang, Z. Li, W. Zhu et al., "The impact of key strata movement on ground pressure behaviour in the Datong coalfield," *International Journal of Rock Mechanics and Mining Sciences*, vol. 119, pp. 193–204, 2019.
- [17] X. X. Miao, H. Pu, and H. B. Bai, "Principle of water-resisting key strata and its application in water-preserved mining," *Journal of China University of Mining and Technology*, vol. 37, pp. 1–4, 2008.
- [18] L. WANG, X. MIAO, Y. WU, J. SUN, and H. YANG, "Discrimination conditions and process of water-resistant key strata," *Mining Science and Technology (China)*, vol. 20, no. 2, pp. 224–229, 2010.
- [19] M. M. Feng, X. B. MAO, H. B. Bai, and X. X. Miao, "Analysis of water insulating effect of compound water-resisting key strata in deep mining," *Journal of China University of Mining and Technology*, vol. 17, no. 1, pp. 1–5, 2007.
- [20] D. Ma, M. Rezaia, H. S. Yu, and H. B. Bai, "Variations of hydraulic properties of granular sandstones during water inrush: effect of small particle migration," *Engineering Geology*, vol. 217, pp. 61–70, 2017.
- [21] J. L. Xu, W. B. Zhu, and X. Z. Wang, "New method to predict the height of fractured water-conducting zone by location of key strata," *Journal of China Coal Society*, vol. 37, pp. 762–769, 2012.
- [22] X. Z. Wang, W. T. Liu, and Z. G. Wang, "Effects of primary key stratum location on height of water flowing fracture zone," *Chinese Journal of Rock Mechanics and Engineering*, vol. 28, pp. 380–385, 2009.
- [23] D. Ma, H. Duan, W. Liu, X. Ma, and M. Tao, "Water- sediment two-phase flow inrush hazard in rock fractures of overburden strata during coal mining," *Mine Water and the Environment*, vol. 39, no. 2, pp. 308–319, 2020.
- [24] F. Du and R. Gao, "Development patterns of fractured water-conducting zones in longwall mining of thick coal seams—a case study on safe mining under the Zhuozhang river," *Energies*, vol. 10, no. 11, p. 1856, 2017.
- [25] M. Tu and B. J. Fu, "Analysis of the effect of key strata structure on relief-pressure mining in protective seam," *Journal of Mining and Safety Engineering*, vol. 28, pp. 536–541, 2011.
- [26] Q. D. Qu, J. L. Xu, and M. G. Qian, "Study on the influence of key strata movement on gas emission of adjacent layers," *Chinese Journal of Rock Mechanics and Engineering*, vol. 26, pp. 1478–1484, 2007.
- [27] R. L. Wu, "Effects of key stratum on the scope of the "three zones" of gas pressure relief and migration in coal seam group mining," *Journal of China Coal Society*, vol. 38, pp. 924–929, 2013.
- [28] D. Ma, H. Duan, X. Li, Z. Li, Z. Zhou, and T. Li, "Effects of seepage-induced erosion on nonlinear hydraulic properties of broken red sandstones," *Tunnelling and Underground Space Technology*, vol. 91, p. 102993, 2019.
- [29] G. Si, S. Durucan, J.-Q. Shi, A. Korre, and W. Cao, "Parametric analysis of slotting operation induced failure zones to stimulate low permeability coal seams," *Rock Mechanics and Rock Engineering*, vol. 52, no. 1, pp. 163–182, 2019.
- [30] Z. Yangsheng, Q. Fang, W. Zhijun, Z. Yuan, L. Weiguo, and M. Qiaorong, "Experimental investigation on correlation between permeability variation and pore structure during coal pyrolysis," *Transport in Porous Media*, vol. 82, no. 2, pp. 401–412, 2010.
- [31] G. X. Wang, P. Massarotto, and V. Rudolph, "An improved permeability model of coal for coalbed methane recovery and CO₂ geosequestration," *International Journal of Coal Geology*, vol. 77, no. 1-2, pp. 127–136, 2009.
- [32] Y. Xue, T. Teng, F. Dang, Z. Ma, S. Wang, and H. Xue, "Productivity analysis of fractured wells in reservoir of hydrogen and carbon based on dual-porosity medium model," *International Journal of Hydrogen Energy*, vol. 45, no. 39, pp. 20240–20249, 2020.
- [33] Z. Z. Cao, P. Xu, Z. H. Li, M. X. Zhang, Y. Zhao, and W. L. Shen, "Joint bearing mechanism of coal pillar and backfilling body in roadway backfilling mining technology," *CMC-Computers Materials & Continua*, vol. 54, no. 2, pp. 137–159, 2018.
- [34] W. L. Shen, J. B. Bai, W. F. Li, and X. Y. Wang, "Prediction of relative displacement for entry roof with weak plane under the effect of mining abutment stress," *Tunnelling and Underground Space Technology*, vol. 71, pp. 309–317, 2018.
- [35] J. Liu, X. Liang, Y. Xue, K. Yao, and Y. Fu, "Numerical evaluation on multiphase flow and heat transfer during thermal stimulation enhanced shale gas recovery," *Applied Thermal Engineering*, vol. 178, p. 115554, 2020.
- [36] Y. Xue, P. G. Ranjith, F. Dang et al., "Analysis of Deformation, Permeability and Energy Evolution Characteristics of Coal Mass Around Borehole After Excavation," *Natural Resources Research*, vol. 29, 2020.
- [37] D. Ma, H. Y. Duan, Q. Zhang et al., *A Numerical Gas Fracturing Model of Coupled Thermal, Flowing and Mechanical Effects*, CMC-Computers Materials & Continua, 2010.
- [38] Y. Li, L. She, L. Wen, and Q. Zhang, "Sensitivity analysis of drilling parameters in rock rotary drilling process based on orthogonal test method," *Engineering Geology*, vol. 270, p. 105576, 2020.

Research Article

Effect of Stress and Moisture Content on Permeability of Gas-Saturated Raw Coal

Junhui Wang,¹ Zhijun Wan ,¹ Yi Wang ,² Zhixiang Liu,³ Sifei Liu,¹ Hongwei Zhang ,⁴ and Qiuyan Pei⁵

¹Key Laboratory of Deep Coal Resource Mining (CUMT), Ministry of Education of China; School of Mines, China University of Mining and Technology, Xuzhou, Jiangsu 221116, China

²College of Safety and Emergency Management Engineering, Taiyuan University of Technology, Taiyuan, Shanxi 030024, China

³Planning and Research Institute, Norinco Group, Beijing 100053, China

⁴School of Energy and Mining Engineering, China University of Mining and Technology (Beijing), Beijing 100083, China

⁵University of Science and Technology of China, Hefei, Anhui 230031, China

Correspondence should be addressed to Zhijun Wan; zhjwan@cumt.edu.cn and Yi Wang; wangyi@tyut.edu.cn

Received 9 April 2020; Accepted 17 June 2020; Published 7 September 2020

Academic Editor: Jingmin Xu

Copyright © 2020 Junhui Wang et al. This is an open access article distributed under the Creative Commons Attribution License, which permits unrestricted use, distribution, and reproduction in any medium, provided the original work is properly cited.

Hydraulic fracturing and premining gas drainage are important to safe mining and coalbed methane extraction. These technical processes cause the redistribution of in-situ stress and the regional variation of moisture contents within the affected zone. Therefore, we investigated the coupled effect of variable stresses (from 9 MPa to 27 MPa) and moisture contents (from 0.22% to 4.00%) on the permeability evolution of gas-saturated raw coal. The results show that (1) the relationship between the mean effective stress and the permeability can be described by a power function according to the permeability evolution model of the porous matrix established in this study. Besides, the influence mechanisms of moisture on fitting coefficients in the function were analyzed. (2) The permeability decreases with the increase of in-situ stress (e.g., confining pressure or volumetric stress) in a negative exponential manner. (3) The curves of permeability variations with moisture content are not always linear, and the permeability is more sensitive to the moisture content than the volumetric stress in the test range. Moreover, the sensitivity of permeability varies in different regions. These results would be beneficial for permeability prediction and surface well parameters design.

1. Introduction

Coalbed methane (CBM) is an abundant valuable resource in underground coal mines. It is estimated that China bears approximately 36.8 trillion m³ of CBM in its reservoirs shallower than 2 km, ranking the third country in the world [1]. Qinshui Basin whose CBM reserve accounts for 1.08% of the total CBM reserve in China is one of the largest CBM reservoirs [2]. However, the reservoir is generally characterized by low permeability, which seriously inhibits efficient CBM extraction [3]. In-situ surface well extraction is a technique for enhancing the permeability and relieving the pressure of coal seams. Permeability is a key parameter for surface well design, and its temporal and spatial variations remarkably

affect the occurrence state, migration, and extraction of CBM [4]. Scholars have conducted extensive researches on the factors influencing permeability, including in-situ stress field [5], gas pressure [6], Klinkenberg effect [7], geothermal field [8], geoelectric field [9], acoustic field [10], and physical properties [11]. These findings have allowed the mechanics of permeability evolution to be deliberated and also provided an adequate data volume and dimension for machine learning which has been proven to be a powerful tool for permeability prediction [12, 13]. Specifically, the process of fracturing, drainage, and gas extraction in surface wells destroys the original stress distribution balance and results in the existence of stress concentration or relief region [14]. Besides, the large amount of fracturing fluids leads to

TABLE 1: Proximate analysis results and adsorption constants of coal samples.

Proximate analysis			True density (t/m^3)	Bulk density (t/m^3)	Porosity (%)	Absorption constant	
$M_{ad}(\%)$	$A_{ad}(\%)$	$V_{daf}(\%)$				a (cm^3/g_{daf})	b (MPa^{-1})
0.49	10.31	16.01	1.46	1.43	2.05	34.14	0.80

regional differences in water-bearing conditions. Therefore, special attention needs to be paid to in-situ stress and moisture content of coal seam for the sake of permeability evolution investigation and prediction, gas flow simulation around the wells, and parameter design of CBM surface wells.

The development of uniaxial and triaxial loading devices has actively promoted the knowledge of permeability evolution characteristics under different stress conditions [15, 16]. The permeability-strain curve of coal corresponds well to its full stress-strain curve. To be specific, the permeability drops first and then rises as a coal sample gets loaded, deformed, and destructed [5]. The peak value of coal permeability lags behind that of stress and strain, suggesting that the characteristics of CBM flow are closely related to the evolution of coal damage generated in the loading process. In addition, scholars have carried out abundant researches on seepage tests under complex loading/unloading paths and loading/unloading rates and on the establishment of permeability models in the case of multifield coupling [17], but these researches are mostly focused on dry coal. The permeability evolution of water-bearing coal in the case of moisture-stress coupling is rarely reported.

The influence of moisture on the permeability of CBM reservoirs is primarily reflected in coal deformation, gas desorption, and migration [18]. Pan et al. [19] believed that moisture in the coal matrix would cause coal swelling/shrinkage and mechanical property alteration that would impact on coal permeability under reservoir conditions. Zhao et al. [20] and Gai et al. [21] investigated the desorption law of coal subjected to high-pressure water injection and made a comparison with the natural desorption state. Guo and Su [22] conducted laboratory tests on the starting pressure gradient and permeability under different water saturation conditions. The test results showed that the permeability gradually declined and the starting pressure gradient gradually rose with the increase of water saturation degree. Nie et al. [23] explored the microscopic mechanism of gas adsorption on coal samples with different moisture contents in light of molecular thermodynamics and surface physicochemical theories. Wang et al. [24] probed into the relationship among moisture content, porosity, and permeability of fractured coal. Yin et al. [25], Liu et al. [26], Wei et al. [27], and Yuan and Jiang [28] analysed the seepage characteristics of gas-bearing coal with different moisture contents and found that the moisture content and permeability shared a linear negative relationship or negative exponential variation law. Hao et al. [29] performed axial and radial gas seepage experiments and revealed that the axial and radial permeabilities of coal first increased and then decreased with the rise of moisture content. Nevertheless, these researches failed to achieve a unified understanding, and the varied research results imply

the difficulty in clearly explaining the effect of coupling terms on gas adsorption, diffusion, and seepage.

This study is focused on investigating the permeability evolution of gas-saturated raw coal samples with different moisture contents under varying stresses. Firstly, the experimental conditions were simplified by setting constant temperature and gas pressure, unidirectional loading path, and resaturated adsorption after the break of balance, so as to avoid irrelevant factors. Then, the relationship between effective stress and permeability was described by a new function that has a clear physical meaning based on the established permeability evolution model of the porous matrix. Furthermore, the mutual effect of moisture content and volumetric stress on permeability were obtained, and conclusions different from the abovementioned ones were drawn. Finally, a sensitivity analysis was performed in the test region.

2. Materials and Methods

2.1. Engineering Background. Yuwu Coal Mine is located in the south of Qinshui Basin, China. The buried depth of S2107 working face of the mine lies in the range of 480-543 m. No. 3 coal seam that is being mined belongs to a high-gas and low-permeability coal seam with a gas content of $7.71 m^3/t$, a gas emission initial volume from a 100-meter-long borehole of $1.42 m^3/min \cdot h$, and a permeability coefficient of $0.28-0.42 m^2/(MPa^2 \cdot d)$. The proximate analysis results and adsorption constants of coal samples from the No. 3 coal seam are listed in Table 1.

Surface wells #1-52 and #1-54 were constructed for conducting permeability-enhancing fracturing on S2107 working face before gas extraction. No. 1-No. 12 gas extraction drilling sites were arranged along the tailentry, and the single-hole gas flow rate was recorded within 50 d. During this period, the drilling sites were not affected by mining activities. The analysis results show that the influence radii of surface wells #1-52 and #1-54 are 85-100 m and 39-42 m, respectively. Coal samples YW1-YW4 were taken from the affected zone in Figure 1.

2.2. Coal Sample Preparation. The steps of coal sample preparation are shown in Figure 2. (1) Standard raw coal samples with the size of $\phi 50 \times (100 \pm 2)$ mm were prepared with the aid of a wire cutting machine (Figure 2(a)), and relative homogeneity of the samples was ensured through density measurement and wave velocity measurement (PDS-SW ultrasonic detector). Samples YW1-YW3 almost bear no cracks (wave velocity range 1921.8-2050.8 m/s), while Sample YW4 owns obvious cracks on its surface (wave velocity range 1826.8-2033.8 m/s). (2) Preparation of coal samples with different moisture contents Φ : YW1 ($\Phi = 1.98\%$), the samples that

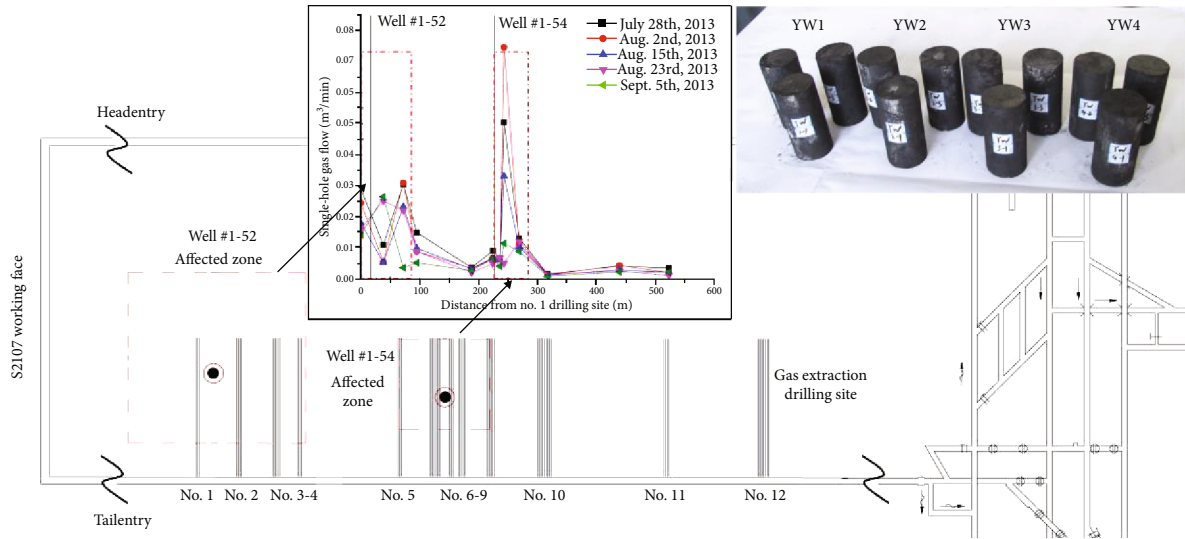


FIGURE 1: Affected zone of surface wells where samples were taken.

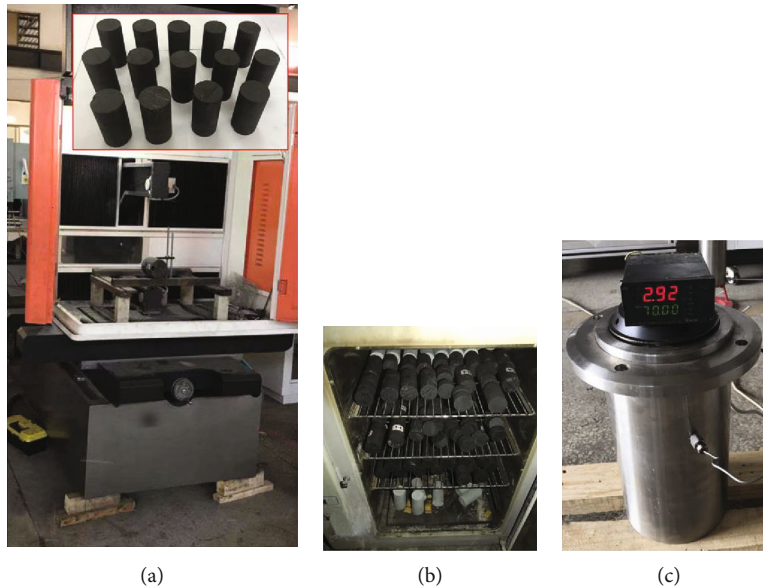


FIGURE 2: Coal sample preparation: (a) wire cutting; (b) drying oven; (c) pressure container.

had experienced hydraulic measures, did not receive any treatment; YW2 ($\Phi = 0.22\%$), the samples with an ultra-low moisture content (lower than the original moisture content 0.49%), were prepared by controlling the drying time of drying oven (Figure 2(b)); YW3 ($\Phi = 3.24\%$), the samples with a high moisture content, were prepared by controlling the pressure holding time of pressure container (Figure 2(c)); YW4 ($\Phi = 4\%$) were the crack-containing sample with a high moisture content.

2.3. Testing Apparatus. The testing apparatus is mainly composed of a loading frame, a servo hydraulic station, an air path system, a triaxial chamber, a constant-temperature oil bath, and a data acquisition system. The schematic diagram of the apparatus is displayed in Figure 3. The main technical parameters are as follows: axial stress range 10-800 KN,

confining pressure range 0-15 MPa, gas pressure range 0-15 MPa, and temperature range from room temperature to 260°C. The chamber equipped with a temperature sensor (PT100, $\pm 0.01^\circ\text{C}$) and a circumferential extensometer (Epsilon 3544, made in USA) was placed in the constant-temperature oil bath for maintaining a constant temperature.

2.4. Experimental Contents and Procedures. The experimental conditions were simplified by setting constant temperature and gas pressure. The temperature was maintained at 20°C. In the process of gas pressure determination, the Klinkenberg effect needs to be avoided, because a small gas pressure difference can cause gas slippage. More specifically, the Klinkenberg effect refers to the slip phenomenon that the gas flow velocity at the wall does not equal zero when the average molecular free path of gas approximates the pore size

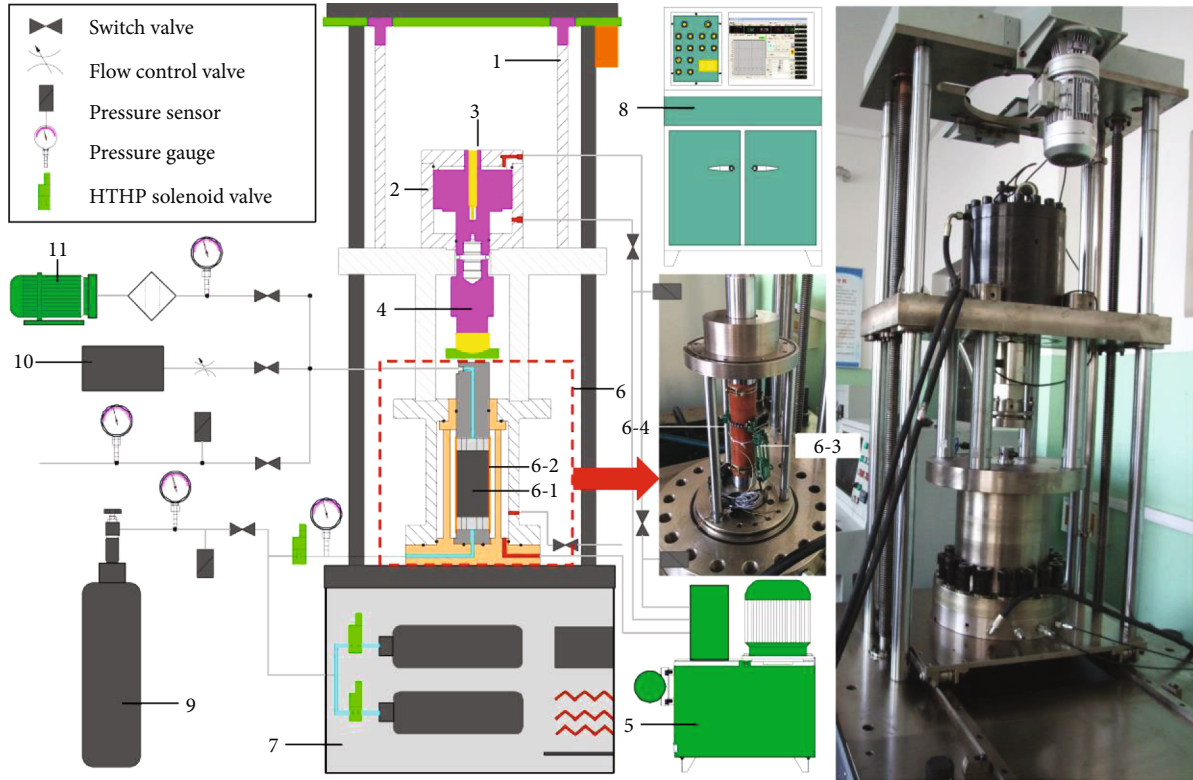


FIGURE 3: Schematic diagram of the testing apparatus. 1. Loading frame; 2. Axial loading hydro-cylinder; 3. Displacement sensor; 4. Stress sensor; 5. Servo hydraulic station; 6. Triaxial compression chamber; 6-1. Coal sample; 6-2. Heat shrinkable tube; 6-3. Circumferential extensometer; 6-4. Temperature sensor; 7. Constant-temperature oil bath; 8. Data acquisition system; 9. Gas cylinder; 10. Gas mass flow meter; 11. Vacuum pump;

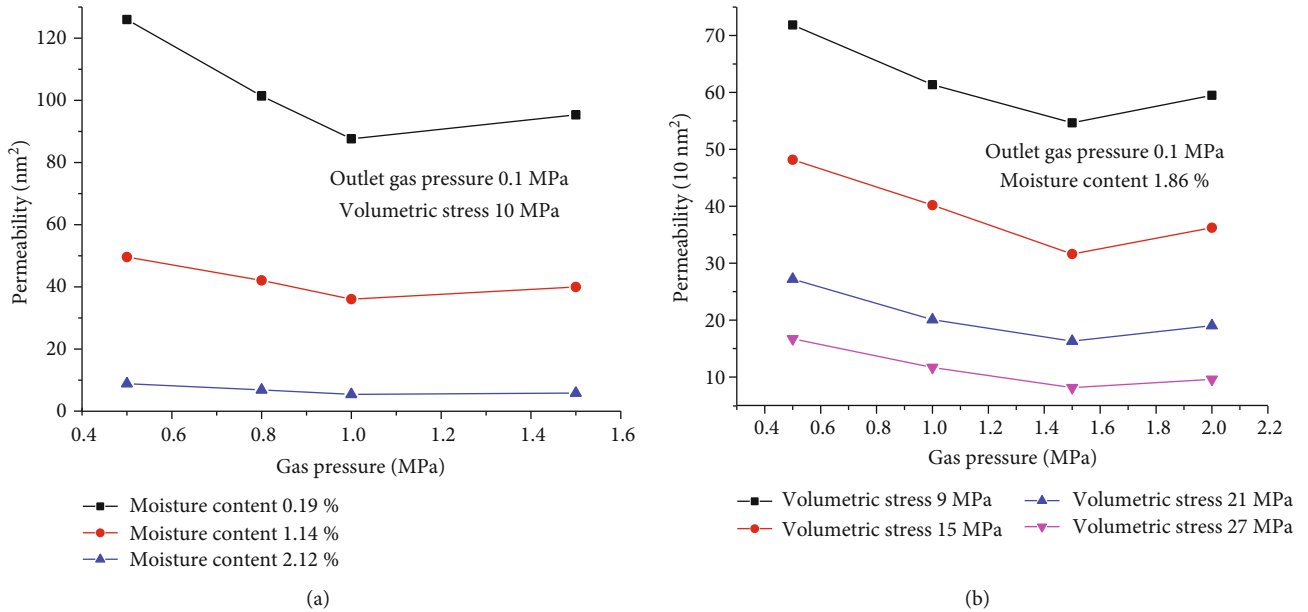


FIGURE 4: Influence of gas pressure on raw coal permeability: (a) Guandi Coal Mine in Qinshui Coalfield; (b) Malan Coal Mine in Qinshui Coalfield.

of a porous medium. It is manifested in varying ways under different effective stresses [5, 6, 30, 31], moisture contents [27, 28, 32], and temperatures [33, 34]. In view of this fact,

the permeabilities of coal samples from Qinshui coalfield were tested at 20°C under variable gas pressures. As presented in Figure 4, the Klinkenberg effect disappears when

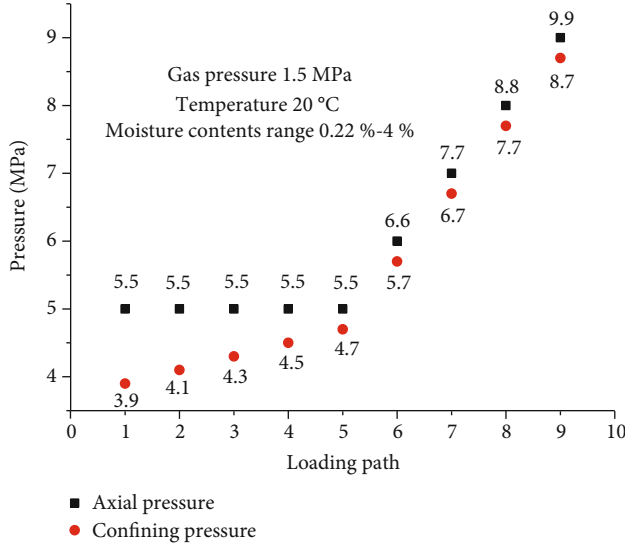


FIGURE 5: The loading path of the prepared samples with different moisture contents.

the gas pressure exceeds 1.0-1.5 MPa, and its influence on the permeability becomes weaker with the rise of moisture content or volumetric stress.

Therefore, considering the in-situ stress value of No. 3 coal seam and the test results of Klinkenberg effect inflection point, the volumetric stress range and gas pressure were set as 9-27 MPa and 1.5 MPa, respectively, in this experiment. The prepared samples with different moisture contents were loaded in accordance with the path in Figure 5, which can ensure that the axial pressure is higher than the confining pressure and the applied unidirectional external stress is lower than the peak strength. Gas pressure at the outlet was 0.1 MPa. Saturated adsorption treatment was conducted on the samples when the stress condition was altered, in order to prevent the adsorption/desorption process from entangling the result analysis.

Experimental procedures: (1) Sample installation: First, the side of the sample was coated with 704 silicone rubber. Then, the sample was wrapped in a heat-shrinkable tube and placed in the chamber. Afterwards, the chamber was put in the 20°C oil bath. (2) Initial adsorption and seepage test: The in-situ stress was raised to the initial value, and 1.5 MPa of CH₄ was injected. Next, the outlet valve was closed to allow the sample to adsorb CH₄ until the equilibrium state was reached, i.e., until gas pressure in the chamber ceased changing. Finally, the outlet valve was opened to record the steady flowrate. (3) The sample was allowed to re-adsorb CH₄ for 2 h under an altered stress, after which the steady flowrate was recorded. Step (3) was repeated along the loading path. (4) Steps (1)-(3) were repeated for another sample.

3. Permeability of Coal Samples: Theoretical Backgrounds

3.1. Calculation Method for Permeability. According to the theory of geotechnical mechanics, the mean effective stress (MES) can be calculated by Eq. (1) [35, 36]:

$$\sigma_0 = \frac{1}{3}(\sigma_1 + 2\sigma_2) - \frac{1}{2}(P_1 + P_2), \quad (1)$$

where σ_0 is the MES, MPa; σ_1 is the axial stress, MPa; σ_2 is the confining pressure, MPa; P_1 is the gas pressure at the inlet, MPa; P_2 is the gas pressure at the outlet, MPa, and it takes the value 0.1 MPa.

Regardless of the starting pressure gradient, the permeability of the coal sample is calculated by Eq. (2) according to Darcy's law [37, 38]:

$$K = \frac{2QP_a\mu L}{A(P_1^2 - P_2^2)}, \quad (2)$$

where K is the permeability of coal sample, $10^{-3} \mu\text{m}^2$; Q is the gas flow rate at the outlet, cm^3/s ; P_a is the atmospheric pressure, 0.1 MPa; μ is the dynamic viscosity coefficient of gas, $\text{Pa}\cdot\text{s}$; L is the length of deformed coal sample, cm; A is the area of deformed coal sample, cm^2 ; P_1 is the gas pressure at the inlet, Pa.

$$L = L' - l_1, \quad (3)$$

$$A = \frac{1}{4}\pi \left(d + \frac{l_2}{\pi} \right)^2, \quad (4)$$

where L and A are the length and area of deformed coal sample; L' and d are the original height and diameter of coal sample, mm; l_1 is the axial deformation of coal sample after the force loading, mm; l_2 is the radial deformation of coal sample after the force loading, mm.

3.2. Permeability Evolution Model of Porous Matrix. The Warren-Root model of coal is presented in Figure 6 [39]. The porous matrix, which comprises pore clusters supported by skeletons, is the main gas storage space of coal (Figure 6(a)), while cracks, which completely separate the matrix, are the primary gas migration channel [40]. Figure 6(b) shows the seepage model of pores, in which the matrix is equivalent to parallel capillary tubes with equal diameter and skeletons.

Space of cracks or pores will be significantly reduced if deformation or stagnant water exists. Effective porosity is not only a key indicator for measuring the size of the space, but also an important factor that determines the adsorption/desorption and permeability of coal. The effective porosity of coal is related to its structural deformation and bulk deformation. Structural deformation refers to compression deformation of the skeleton caused by external stress, or the relative dislocation between tubes which make the tubes more closely arranged. It is usually unrecoverable. Bulk deformation refers to tube expansion caused by thermal stress or adsorption swelling, or compression deformation of tubes under the action of gas pressure [41]. Such elastic deformation caused by internal stress can be recovered.

In this study, the permeability evolution model of porous matrix considering moisture is established because Samples YW1-YW3 contain few cracks. Since the matrix will undergo

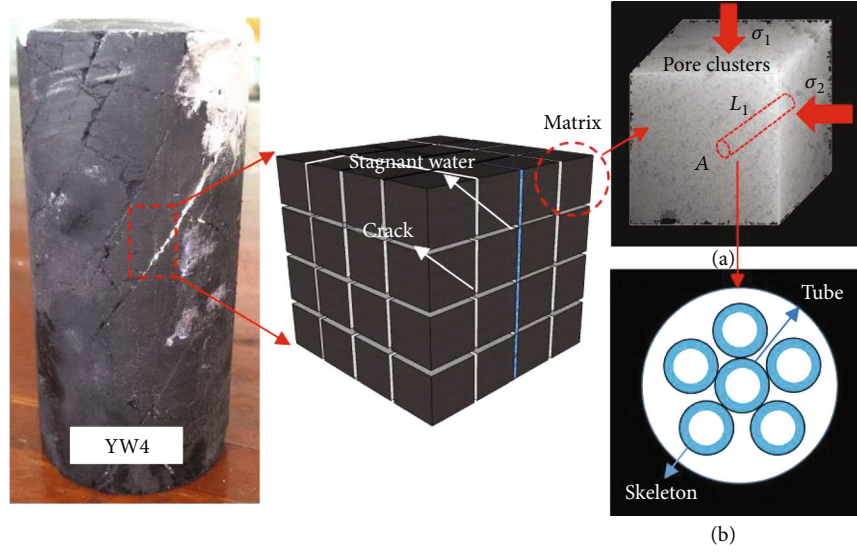


FIGURE 6: The Warren-Root model of coal: (a) pore clusters in porous matrix; (b) seepage model of pores comprising capillary tubes and skeletons.

structural deformation (external stress compression) and bulk deformation (adsorption swelling and gas pressure extrusion) under the condition of constant temperature and gas pressure, the dynamic evolution model of porosity φ_d of the dry matrix is [14, 41–44]:

$$\begin{aligned}\varphi_d &= 1 - \frac{1 - \varphi_0}{1 + e} \left(1 + \frac{\varepsilon_p}{1 - \varphi_0} - K_Y \Delta P_1 \right) \\ &= \frac{\varphi_0 + e - \varepsilon_p + K_Y \Delta P_1 (1 - \varphi_0)}{1 + e},\end{aligned}\quad (5)$$

where φ_d is the porosity of dry matrix, %; φ_0 is the initial porosity of matrix, %; e is the volumetric strain, of which the value is negative under compression; ε_p is the adsorption expansion strain per unit volume of coal; K_Y is the volumetric compression coefficient, MPa^{-1} .

The $A * L_1$ unit in the matrix is taken and regarded to be equivalent to the capillary tubes (Figure 6(b)). Given the fact that water distributed in macropores (pore diameter $> 1 \mu\text{m}$) and mesopores (pore diameter $= 0.1 - 1 \mu\text{m}$) occupies the space, the porosity of the water-containing matrix is [14]:

$$\varphi_w = \varphi_d \left(1 - \frac{\rho_s w}{n \rho_w \pi r^2} \right), \quad (6)$$

where ρ_s is the density of matrix, kg/m^3 ; w is the moisture content of matrix pores; n is the number of capillary tubes per unit area A , tubes/ m^2 ; ρ_w is the density of water in capillary tubes, kg/m^3 ; and r is the radius of a tube, m.

By integrating Eq. (5) with Eq. (6), the effective porosity evolution model of water-containing matrix can be obtained:

$$\varphi_w = \left(1 - \frac{\rho_s w}{n \rho_w \pi r^2} \right) \left(\frac{\varphi_0 + e - \varepsilon_p + K_Y \Delta P_1 (1 - \varphi_0)}{1 + e} \right), \quad (7)$$

The relationship between permeability and porosity is given in the Kozeny-Carman equation established on the basis of the capillary tubes model [44]. Ignoring the change in the total surface area of coal particles per unit volume, a permeability evolution model that takes into account the moisture content in pores can be obtained:

$$K = \frac{K_0}{1 + e} \left(1 + \frac{e - \varepsilon_p + K_Y \Delta P_1 (1 - \varphi_0)}{\varphi_0} \right)^3 \left(1 - \frac{\rho_s w}{n \rho_w \pi r^2} \right), \quad (8)$$

where K_0 is the initial permeability of coal sample, $10^{-3} \mu\text{m}^2$.

4. Results and Discussion

4.1. Effect of Mean Effective Stress on Permeability. Changes in flow rates Q and permeabilities K of coal samples with moisture contents of 0.22%, 1.98%, and 3.24% under mean effective stress (MES) values of 4.2–8.3 MPa are disclosed in Figures 7(a)–7(c). The flow rates of coal samples decrease nonlinearly at a reduced rate with the increase of MES, and the relationship between flow rate and MES can be expressed by a quadratic function $Q = a_1 \sigma_0^2 + b_1 \sigma_0 + c_1$ where a_1 , b_1 , and c_1 are fitting coefficients.

The permeabilities and flow rates of samples with different moisture contents vary in similar trends (Figure 7(d)). The variation trend of permeability with MES can be fitted by the power function $K = a \cdot (1 + b \sigma_0)^3 / (1 + c \sigma_0)$ which agrees with the form of Eq. (8). In the function, a , b , and c are the fitting coefficients with clear physical meanings (see Table 2 for their values), and the influence mechanisms of moisture on the values of a , b , and c differ.

The fitting coefficient a is related to the initial permeability of the matrix with specified moisture content. The value of a drops sharply with the rise of moisture content, and the effect of water on the value of a is mainly reflected in the

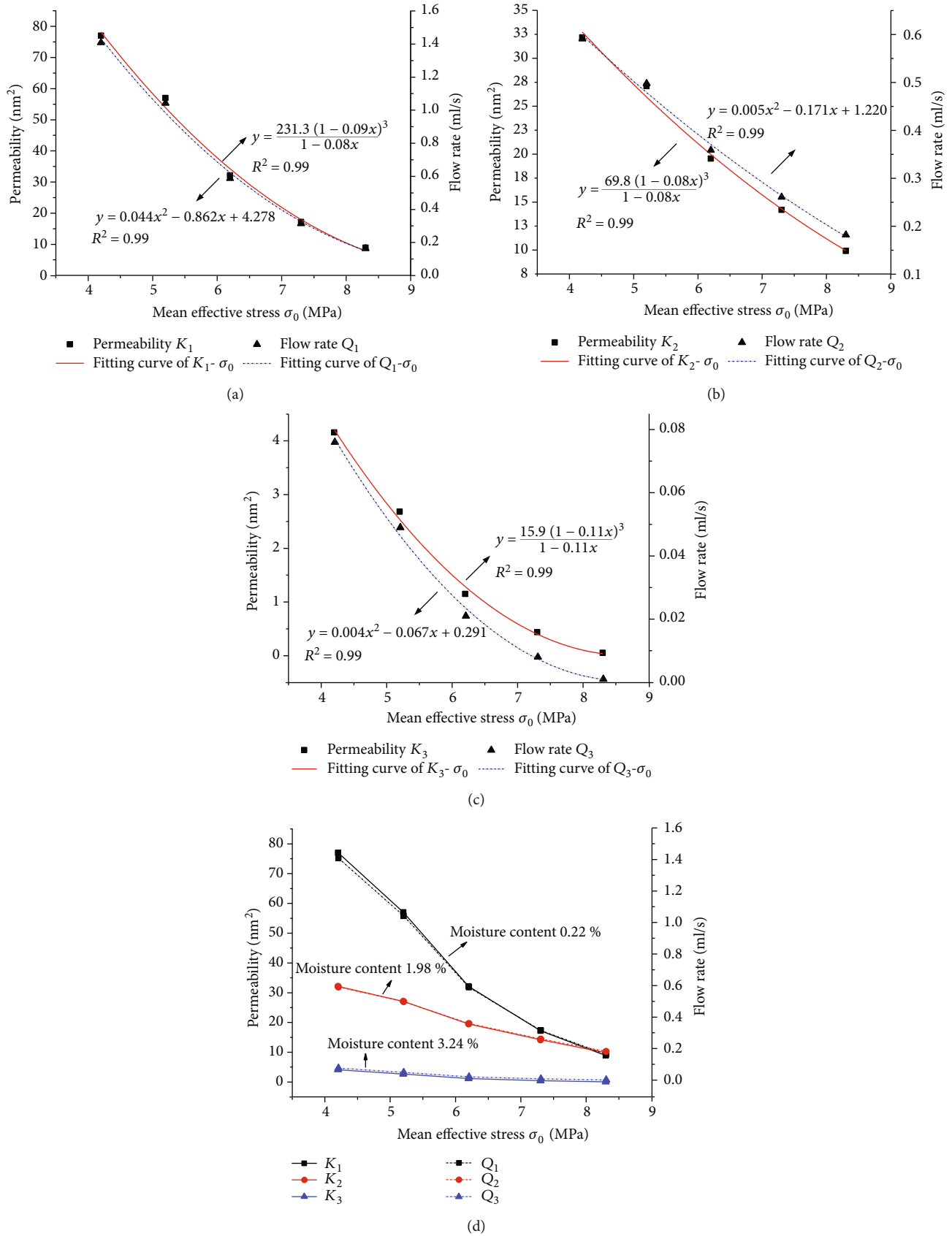
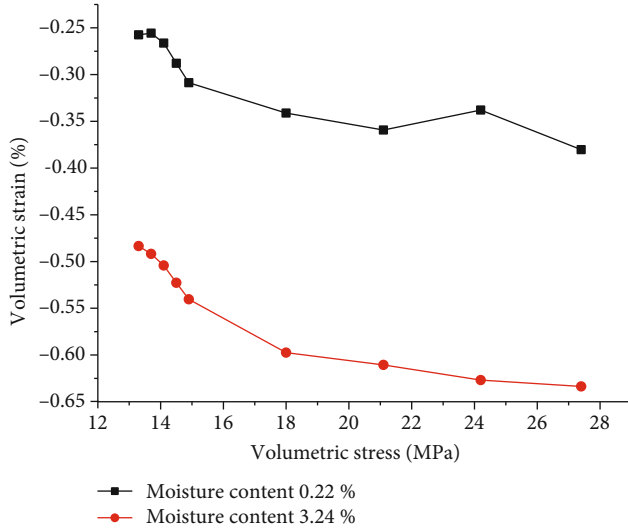


FIGURE 7: $K - \sigma_0$ and $Q - \sigma_0$ curves of samples with different moisture contents: (a) moisture content 0.22%; (b) moisture content 1.98%; (c) moisture content 3.24%; (d) total trend.

TABLE 2: Fitting coefficients of K - σ_0 curves.

Value Φ	a	b	c	R^2
0.22%	231.3	-0.09	-0.08	0.99
1.98 %	69.8	-0.08	-0.08	0.99
3.24 %	15.9	-0.11	-0.11	0.99

FIGURE 8: Volumetric stress Θ -strain e curves of samples with different moisture contents.

following two nondeformation aspects of matrix: (1) Free water, adhered water, and film water in macropores and mesopores occupy the gas flow channel, thus lowering the effective porosity of coal. In addition, a water film formed on the pore surface generates a certain vapor pressure, thus raising the viscous resistance of gas migration [45, 46]. (2) Within the main space for CH_4 adsorption and desorption, namely, micropores (0.01-0.1 μm) and molecules structural pores (<0.01 μm), capillary resistance formed by water hinders gas desorption and exhibits a water-locking effect.

The fitting coefficient b is related to the bulk deformation, structural deformation, and initial porosity of the coal matrix. By conducting wave velocity measurement, the initial permeabilities ϕ_0 of Samples YW1-YW3 are considered to be consistent, so the variation of b value is mainly affected by structural deformation (external stress) and bulk deformation (adsorption swelling and gas pressure extrusion) of the matrix in this test. As the moisture content increases, the volumetric compressive strain $|e|$ goes up (Figure 8); the volumetric compression coefficient K_Y grows [47]; and the adsorption expansion strain ε_p does down [26, 42, 43, 48], because water molecules possess stronger adsorption competitiveness on the coal matrix surface compared with CH_4 molecules [49, 50]. Thereby, with the rise of moisture content, the effective adsorption sites of gas on the pore surface decrease, so does the adsorption expansion strain ε_p . As revealed by the analysis on the values of $|e|$, ε_p , K_Y , and b

with the change of moisture content, with the rise of moisture content, the effective porosity of matrix increases in terms of bulk deformation, but meanwhile the existence of external stress makes the structural deformation of the matrix with a high moisture content more obvious. As a result, the effective porosity is reduced because of the larger structural deformation.

The fitting coefficient c is related to the structural deformation of the coal matrix caused by external stress. Figure 8 displays the curves of volumetric strain variation measured in the test. It can be seen that as the moisture content rises, the absolute value of volumetric strain increases, so does the absolute value of c .

4.2. Effect of In-Situ Stress on Permeability. Figure 9(a) demonstrates the permeability variations of samples with moisture contents of 0.22%, 1.98%, and 3.24% under a constant axial pressure of 5.5 MPa and confining pressures of 3.9, 4.1, 4.3, 4.5, and 4.7 MPa. Figure 9(b) shows the permeability variations of samples with moisture contents of 0.22%, 1.98%, and 3.24% under volumetric stresses of 13.3-27.3 MPa.

Obviously, permeability K goes downward nonlinearly at a reduced rate with the increase of in-situ stress (e.g., confining pressure σ_2 or volumetric stress Θ). The above downward trend can be fitted with a negative exponential function $K = a \cdot \exp(-bx)$ where a and b are the fitting coefficients and a is related to the initial permeabilities of coal samples with different moisture contents. This finding corresponds to previous research results [27, 35, 51]. The reason can be explained as follows. The initial permeabilities of coal samples with different moisture contents differ. Specifically, the higher the moisture content is, the lower the initial permeability is. First, the stagnant water and the seal off the effect of water reduce the effective porosity of coal [29]. Second, with the increase of external stress, the structural deformation of coal brings about further shrinkage of gas seepage channel.

Sample YW4 ($\Phi = 4\%$) contains evident microcracks (Figure 6). The test result shows that its permeability is up to 60% higher than the value in Figure 9 under the same in-situ stress condition. The result fully proves that although the moisture content seriously weakens coal permeability, cracks, as the dominant factor affecting coal permeability [52], will effectively weaken the negative impact of water on coal permeability.

4.3. Mutual Effect of Moisture Content and Volumetric Stress on Permeability

4.3.1. Relationship between Permeability and Moisture Content under Applied In-Situ Stress. Figure 10 exhibits the variation of permeability K with the moisture content Φ and the volumetric stress Θ . The $K - \Phi$ curves are not always linear. In the whole region ($\Phi = 0.22\text{-}3.24\%$), under low volumetric stresses ($\Theta < 15$ MPa), K decreases nonlinearly with the increase of Φ ; as the volumetric stress grows (e.g., $\Theta = 18$ MPa), it becomes linearly correlated with Φ , which agrees with the conclusions of Liu et al. [26], Yin et al. [25, 53], and Yuan and Jiang [28]; under high volumetric stresses

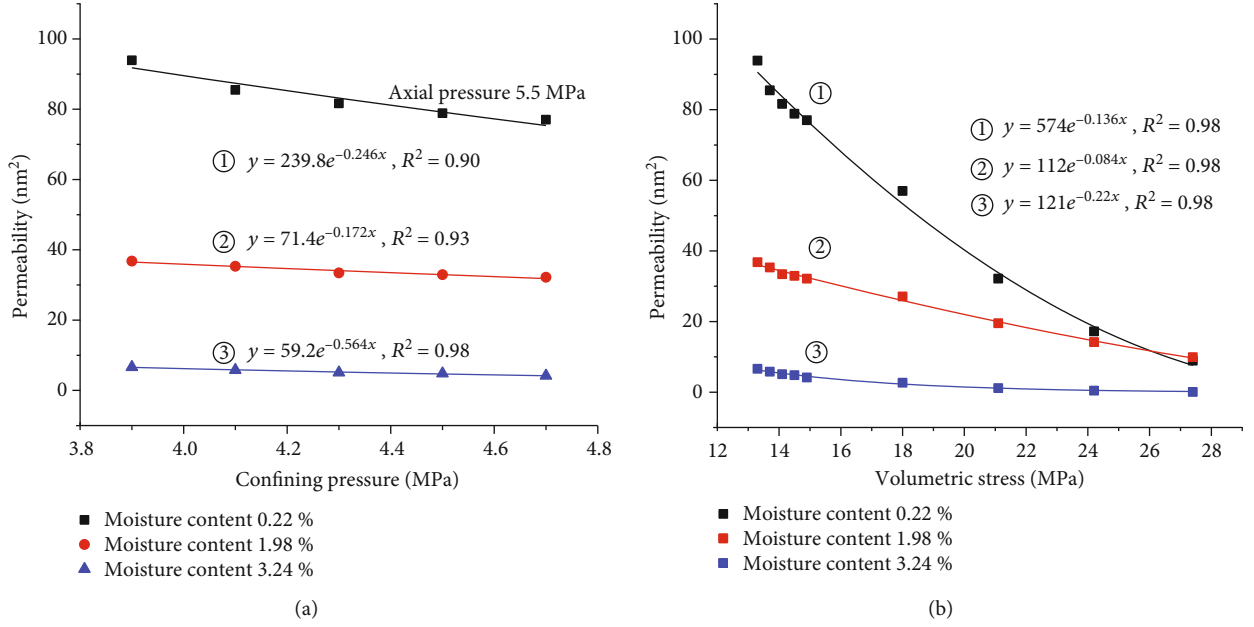


FIGURE 9: Effect of in-situ stress on permeability: (a) confining pressure; (b) volumetric stress.

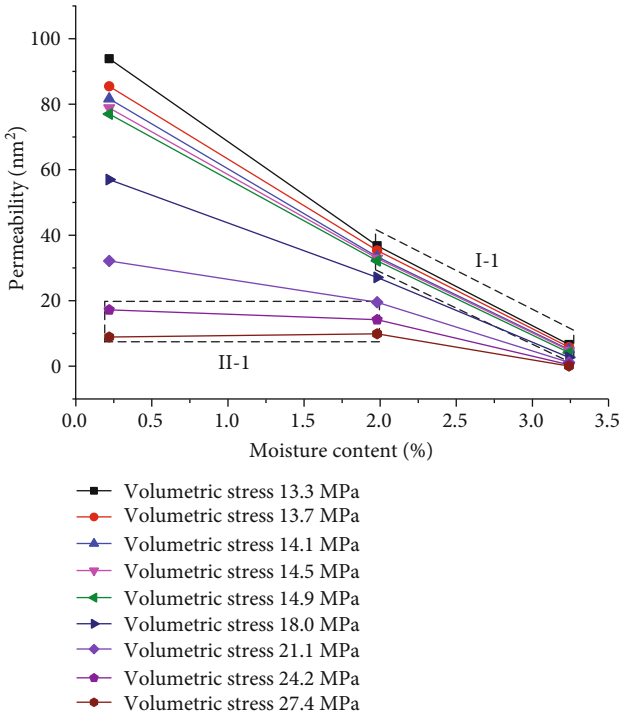


FIGURE 10: Effect of moisture content and volumetric stress on permeability.

($\Theta > 18$ MPa), it is no longer linearly correlated with Φ , the slope of $K - \Phi$ curve altering evidently in the vicinity of $\Phi = 1.98\%$. Moisture occupies pores and external stress causes structural deformation of the pore, both reducing the effective porosity of matrix and thus resulting in a decrease in permeability.

In different regions ($\Phi = 0.22 - 1.98\%$ and $\Phi = 1.98 - 3.24\%$), the slope of $K - \Phi$ curve decreases with the increase of Θ , because influence of Φ on K weakens with the increase of Θ . It is noteworthy that in Zone I-1 where Φ is high and Θ is low, the slope of $K - \Phi$ curve remains basically constant with the increase of Θ ; in Zone II-1 where Φ is low and Θ is high, the slope of $K - \Phi$ curve remains basically unchanged with the increase of Φ . The variation trend reflects the differences in permeability sensitivity to volumetric stress and moisture content in different regions.

4.3.2. *Sensitivity Analysis of the Test Regions.* To determine the influence degrees of moisture content Φ and volumetric stress Θ on permeability K , the sensitivity coefficients of permeability to moisture content and volumetric stress were defined as C_Φ and C_Θ , respectively. The meanings of $C_{\Phi,1,2}$ and $C_{\Theta,1,2}$ were defined in the same way as above.

First, the correlation between variables was analysed. The Pearson correlation coefficient $\rho_{X,Y}$ (PPMCC) shown in Eq. (9), which is the quotient of the product of covariance and standard deviation of two variables [54], is widely used for measuring the correlation between two variables. Through calculation, the correlation between the moisture content Φ and the permeability K is -0.782 (highly significant, $P < 0.01$), while that between the volumetric stress Θ and the permeability K is -0.470 (significant, $P < 0.05$). In addition, Φ and Θ are two independent variables.

$$\rho_{X,Y} = \frac{\text{cov}(X, Y)}{\sigma_X \sigma_Y} = \frac{E(XY) - E(X)E(Y)}{\sqrt{E(X^2) - E^2(X)} \sqrt{E(Y^2) - E^2(Y)}}, \quad (9)$$

where cov is the covariance; and E is the mathematical expectation.

TABLE 3: Calculation results of regression coefficients.

Coefficient	Value	Standard error	T value	$P > T $	Confidence interval
β_1	-0.782 ($P < 0.01$)	0.084	-9.35	0	[-0.95, -0.61]
β_2	-0.470 ($P < 0.01$)	0.084	-5.63	0	[-0.64, 0.30]
β_0	-0.001	0.082	0	1	[-0.17, 0.17]

TABLE 4: Calculation results of regression coefficients.

Coefficient	Value	Standard error	T value	$P > T $	Confidence interval
β_1	-52.679 ($P < 0.01$)	2.120	-24.85	0	[-57.06, -48.29]
β_2	-6.287 ($P < 0.01$)	0.250	-25.1	0	[-6.8, -5.77]
β_3	1.909 ($P < 0.01$)	0.114	16.74	0	[1.67, 2.14]
β_0	175.984	4.655	37.81	0	[166.36, 185.61]

(1) *Sensitivity analysis in the whole test region.* Based on the correlation analysis, a multiple regression model was established to calculate the sensitivity coefficients C_Φ and C_Θ . The data in Figure 10 were subjected to Z-Score standardization via Stata software and then substituted into the regression equation $Y_K = \beta_0 + \beta_1 X_\Phi + \beta_2 X_\Theta + \mu_I$ where β_0 , β_1 , and β_2 are the regression coefficients and μ_I is the error term.

The permeability K is more sensitive to the moisture content Φ in the whole test region. The overall sensitivity coefficients $C_{\Phi 1} = dY_K/dX_\Phi = \beta_1$ and $C_{\Theta 1} = dY_K/dX_\Theta = \beta_2$ were defined. Their values $C_{\Phi 1} = -0.782$ (highly significant, $P < 0.01$) and $C_{\Theta 1} = -0.470$ (highly significant, $P < 0.01$) can be found in Table 3. In the whole test region, $|C_{\Phi 1}| > |C_{\Theta 1}|$, that is, permeability is more sensitive to moisture content on the whole.

(2) *Sensitivity analysis in different regions.* The interaction variable [55–57] $\beta_3 X_\Phi X_\Theta$ was added into the regression equation $Y_K = \beta_0 + \beta_1 X_\Phi + \beta_2 X_\Theta + \beta_3 X_\Phi X_\Theta + \mu_2$ for comparing the values of C_Φ and C_Θ in different regions. The regional sensitivity coefficients $C_{\Phi 2} = dY_K/dx_\Phi = \beta_1 + \beta_3 * X_\Theta$ and $C_{\Theta 2} = dY/dx_\Theta = \beta_2 + \beta_3 * X_\Phi$ were defined.

As given in Table 4, the interaction term coefficient is 1.909 (highly significant, $P < 0.01$), suggesting that although moisture content and volumetric stress are independent variables, they exert a mutual effect on permeability. $C_{\Phi 2} = -52.679 + 1.909 * X_\Theta$ and $C_{\Theta 2} = -6.287 + 1.909 * X_\Phi$ demonstrate that the sensitivity coefficient $C_{\Phi 2}$ decreases gradually with the increase of volumetric stress while $C_{\Theta 2}$ decreases gradually with the increase of moisture content (Figure 11). Therefore, the sensitivity coefficient $C_{\Phi 2}$ decreases with the increase of volumetric stress Θ so that the slope of $K - \Phi$ curve becomes smaller and smaller in the ranges of $\Phi = 0.22 - 1.98\%$ and $\Phi = 1.98 - 3.24\%$ (Figure 10), which indicates the weakening influence of moisture content on permeability.

Figure 12(a) is a three-dimensional diagram of the data in Figure 10. As can be observed in Figure 12(b), $|C_{\Phi 2}| > |C_{\Theta 2}|$ in Zone I ($X_\Theta < 24.37 + X_\Phi$), that is, permeability is more

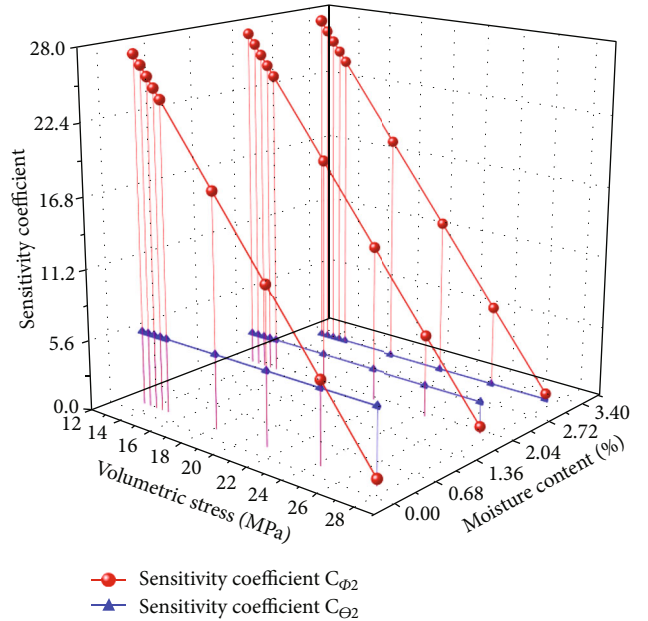


FIGURE 11: Calculation of sensitivity coefficient of each experimental condition.

sensitive to moisture content in this region; $|C_{\Phi 2}| < |C_{\Theta 2}|$ in Zone II ($X_\Theta > 24.37 + X_\Phi$), that is, permeability is more sensitive to volumetric stress in the region. The constant slopes of $K - \Phi$ curves in Zone I-1 and Zone II-1 in Figure 10 indicate the absolute influence of high volumetric stress or high moisture content on permeability.

The value of $C_{\Phi 2}$ is larger than that of $C_{\Theta 2}$ when the volumetric stress is lower than 15 MPa (Figure 11). At this time, coal permeability is not simply linearly correlated but shares a negative exponential relationship with moisture content (Figure 12(a)). This finding differs from the research results of Yin et al. [25, 53], probably because the briquette samples used by Yin et al. possess a homogeneous internal structure while the complex pore structure of raw coal samples used in this test decides the more complex influence mechanism

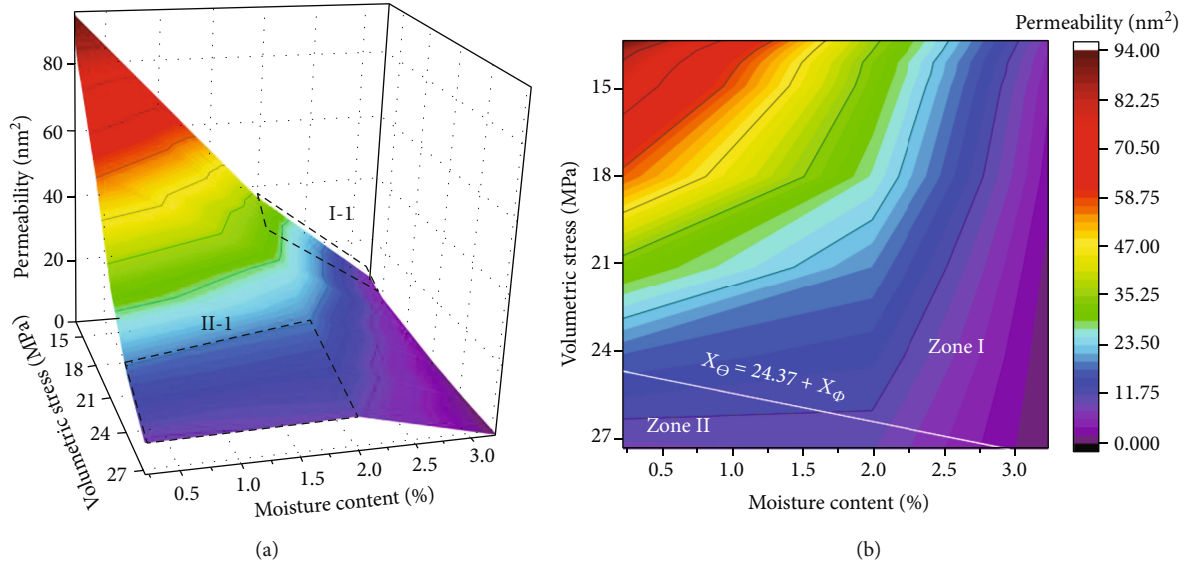


FIGURE 12: Division of sensitive regions under the test conditions: (a) Three-dimensional diagram of Figure 10; (b) Top view.

of moisture on raw coal permeability. Under a low volumetric stress, the pores in coal are slightly affected by stress, and the coal is strongly hydrophilic. As a result, the increased water adsorbs on the pore surface easily and meanwhile occupies the effective gas seepage channel. Since the porosity of coal is an important parameter affecting gas permeability, the permeability of coal falls rapidly with the rise of moisture content under a low volumetric stress. With the increase of volumetric stress, the sensitivity of permeability to moisture content decreases, so that permeability becomes linearly correlated with moisture content. After volumetric stress continues to increase to 24 MPa, the coal sample gets more sensitive to volumetric stress (Zone II in Figure 12(b)), which is reflected by the phenomenon that the increase of moisture content fails to notably lower permeability under a low moisture content.

5. Conclusions

In this study, a series of experiments were performed for grasping the permeability evolution of gas-saturated raw coal under the coupled influences of moisture contents and in-situ stress. The main conclusions reached are as follows.

- (1) A permeability evolution model of a porous matrix was established. On the basis of this mode, it is found that the power function $K = a \cdot (1 + b\sigma_0)^3 / (1 + c\sigma_0)$ can be used to describe the relationship between MES σ_0 and permeability K . In this function, the fitting coefficient a is related to the initial permeability with specified moisture content; b is related to the bulk deformation, structural deformation, and initial porosity of coal matrix; and c is related to the structural deformation of coal matrix caused by external stress. The influence mechanisms of moisture on these coefficients were analysed according to the experimental results afterwards

- (2) Permeability decreases nonlinearly with the increase of in-situ stress (e.g., confining pressure σ_2 or volumetric stress Θ), which can be fitted by a negative exponential function $K = a \cdot \exp(-bx)$, where a is related to the initial permeabilities of coal samples with specified moisture content Φ
- (3) The mutual influences of moisture content and volumetric stress on permeability were analysed. In different regions, the slope of $K - \Phi$ curve decreases with the increase of Θ , because the increase of Θ would weaken the influence of Φ on K . Overall, the $K - \Phi$ curves are not always linear. The variation reflects the differences in permeability sensitivity to volumetric stress and moisture content in different regions

Data Availability

The data used to support the findings of this study are available from the corresponding author upon request.

Conflicts of Interest

The authors declare no conflicts of interest.

Acknowledgments

The authors are grateful to Professor Yaojiang Zhao from Taiyuan University of Technology for his support and contribution in this study. This work has been supported by the Fundamental Research Funds for the Central Universities (2017XKZD06).

References

- [1] H. Wang, Y. Cheng, W. Wang, and R. Xu, "Research on comprehensive CBM extraction technology and its applications in

- China's coal mines," *Journal of Natural Gas Science & Engineering*, vol. 20, pp. 200–207, 2014.
- [2] Z. Meng, J. Zhang, and R. Wang, "In-situ stress, pore pressure and stress-dependent permeability in the southern Qinshui Basin," *International Journal of Rock Mechanics and Mining Sciences*, vol. 48, no. 1, pp. 122–131, 2011.
 - [3] J. Fan, P. Liu, J. Li, and D. Jiang, "A coupled methane/air flow model for coal gas drainage: Model development and finite-difference solution," *Process Safety and Environmental Protection*, vol. 141, pp. 288–304, 2020.
 - [4] J. Lin, T. Ren, G. Wang, and J. Nemeik, "Simulation investigation of N₂-injection enhanced gas drainage: model development and identification of critical parameters," *Journal of Natural Gas Science & Engineering*, vol. 55, pp. 30–41, 2018.
 - [5] D. Wang, R. Lv, J. Wei et al., "An experimental study of seepage properties of gas-saturated coal under different loading conditions," *Energy Science & Engineering*, vol. 7, no. 3, pp. 799–808, 2019.
 - [6] S. Cao, P. Guo, Y. Li, and Y.-J. Bai, "Effect of gas pressure on gas seepage of outburst coal," *Journal of China Coal Society*, vol. 35, no. 4, pp. 595–599, 2010.
 - [7] K. Wang, F. Du, and G. Wang, "Investigation of gas pressure and temperature effects on the permeability and steady-state time of Chinese anthracite coal: an experimental study," *Journal of Natural Gas Science and Engineering*, vol. 40, pp. 179–188, 2017.
 - [8] X. Li, X. Yan, and Y. Kang, "Effect of temperature on the permeability of gas adsorbed coal under triaxial stress conditions," *Journal of Geophysics and Engineering*, vol. 15, no. 2, pp. 386–396, 2018.
 - [9] E. Wang, L. Zhang, X. He, and Z. Liu, "Electric field response of gas permeability of coal," *Journal of China University of Mining & Technology*, vol. 33, no. 1, pp. 62–65, 2004.
 - [10] J. Yan and L. Li, "Experimental study of acoustic effects on coal gas permeability," *Journal of China Coal Society*, vol. 35, pp. 81–85, 2010.
 - [11] C. R. Clarkson and R. M. Bustin, "Variation in permeability with lithotype and maceral composition of Cretaceous coals of the Canadian Cordillera," *International Journal of Coal Geology*, vol. 33, no. 2, pp. 135–151, 1997.
 - [12] O. Sudakov, E. Burnaev, and D. Koroteev, "Driving digital rock towards machine learning: predicting permeability with gradient boosting and deep neural networks," *Computers & Geosciences*, vol. 127, pp. 91–98, 2019.
 - [13] A. Erofeev, D. Orlov, A. Ryzhov, and D. Koroteev, "Prediction of porosity and permeability alteration based on machine learning algorithms," *Transport in Porous Media*, vol. 128, no. 2, pp. 677–700, 2019.
 - [14] Y. Zhao, S. Cao, Y. Li et al., "The occurrence state of moisture in coal and its influence model on pore seepage," *RSC Advances*, vol. 8, no. 10, pp. 5420–5432, 2018.
 - [15] Y. Li, C. A. Tang, D. Li, and C. Wu, "A new shear strength criterion of three-dimensional rock joints," *Rock Mechanics and Rock Engineering*, vol. 53, no. 3, pp. 1477–1483, 2019.
 - [16] Z. Li, S. Yu, W. Zhu et al., "Dynamic loading induced by the instability of voussoir beam structure during mining below the slope," *International Journal of Rock Mechanics and Mining Sciences*, vol. 132, p. 104343, 2020.
 - [17] D. Zhang, Y. Yang, H. Wang, X. Bai, C. Ye, and S. Li, "Experimental study on permeability characteristics of gas containing raw coal under different stress conditions," *Royal Society Open Science*, vol. 5, no. 7, article 180558, 2018.
 - [18] A. Liu, S. Liu, X. Hou, and P. Liu, "Transient gas diffusivity evaluation and modeling for methane and helium in coal," *International Journal of Heat and Mass Transfer*, vol. 159, p. 120091, 2020.
 - [19] Z. Pan, L. D. Connell, M. Camilleri, and L. Connelly, "Effects of matrix moisture on gas diffusion and flow in coal," *Fuel*, vol. 89, no. 11, pp. 3207–3217, 2010.
 - [20] D. Zhao, Z. Feng, and Y. Zhao, "Experimental study of effects of high pressure water injection on desorption characteristic of coal-bed methane (CBM)," *Chinese Journal of Rock Mechanics and Engineering*, vol. 30, no. 3, pp. 547–555, 2011.
 - [21] N. Gal, V. Lagneau, and A. Charmoille, "Experimental characterization of CH₄ release from coal at high hydrostatic pressure," *International Journal of Coal Geology*, vol. 96, pp. 82–92, 2012.
 - [22] H. Guo and X. Su, "Research on the mechanism of gas emission inhibition in water-flooding coal seam," *Journal of China Coal Society*, vol. 35, no. 6, pp. 928–931, 2010.
 - [23] B. Nie, X. Liu, S. Yuan et al., "Sorption characteristics of methane among various rank coals: impact of moisture," *Adsorption*, vol. 22, no. 3, pp. 315–325, 2016.
 - [24] S. Wang, D. Elsworth, and J. Liu, "Permeability evolution in fractured coal: the roles of fracture geometry and water-content," *International Journal of Coal Geology*, vol. 87, no. 1, pp. 13–25, 2011.
 - [25] G. Yin, C. Jiang, J. Xu, S. Peng, and W. Li, "Experimental study of influences for water content in coalbed gas reservoirs on methane seepage," *Chinese Journal of Rock Mechanics and Engineering*, vol. 30, pp. 3401–3406, 2011.
 - [26] Q. Liu, L. Zhang, H. Li, and Z. Deng, "Effect of moisture content on CBM seepage," *Journal of China Coal Society*, vol. 39, no. 9, pp. 1840–1844, 2014.
 - [27] P. Wei, L. Wei, and D. Wang, "Experimental study of moisture content influences on permeability of coal containing gas," *Journal of China Coal Society*, vol. 39, no. 1, pp. 97–103, 2014.
 - [28] X. Yuan and D. Jiang, "Experimental study of gas permeability of coal under different moisture state," *Journal of Mining & Safety Engineering*, vol. 35, no. 3, pp. 649–656, 2018.
 - [29] D. Hao, L. Zhang, Z. Ye, S. Tu, and C. Zhang, "Experimental study on the effects of the moisture content of bituminous coal on its gas seepage characteristics," *Arabian Journal of Geosciences*, vol. 11, no. 15, p. 436, 2018.
 - [30] B. Li, J. Wei, K. Wang, and Y. Jia, "Experimental study of non-linear motion law for gas seepage in coal seams," *Chinese Journal of Rock Mechanics and Engineering*, vol. 33, pp. 3219–3224, 2014.
 - [31] G. Zhang, Y. Hu, and D. Jiang, "Study on the factors affecting gas permeability of coal," *Journal of Chongqing University (Natural Science Edition)*, vol. 18, no. 3, pp. 27–30, 1995.
 - [32] F. Ma, Y. Wang, L. Wang, S. Zhang, and Q. Zhang, "Influence of moisture content in coal rock on permeability," *Lithologic Reservoirs*, vol. 25, no. 3, pp. 97–101, 2013.
 - [33] C. Zhang, Y. Zhao, and X. Zheng, "Coupled model of deformation and gas flow process with temperature and slippage effect," *Journal of Hebei University of Science and Technology*, vol. 36, no. 3, pp. 306–312, 2015.
 - [34] J. Xu, M. Zhang, S. Peng, B. Li, and X. Wu, "Experimental study of migration laws of gas during loading-unloading

- process at different temperatures,” *Rock and Soil Mechanics*, vol. 37, no. 6, pp. 1579–1587, 2016.
- [35] Y. S. Zhao, *Multi-Field Coupling in Porous Media and its Engineering Response*, Science press, Beijing, 2010.
- [36] K. Terzaghi, “Principles of soil mechanics, IV—settlement and consolidation of clay,” *Engineering News-Record*, vol. 95, no. 3, pp. 874–878, 1925.
- [37] A. E. Scheidegger, “The physics of flow through porous media,” *Soil Science*, vol. 86, no. 6, p. 355, 1958.
- [38] C. Wang, Y. Zang, L. Wang et al., “Interaction of cleat-matrix on coal permeability from experimental observations and numerical analysis,” *Geofluids*, vol. 2019, Article ID 7474587, 15 pages, 2019.
- [39] N. M. Dmitriev and V. M. Maksimov, “Models of flow through fractured-porous anisotropic media,” *Fluid Dynamics*, vol. 42, no. 6, pp. 937–942, 2007.
- [40] E. Ranjbar and H. Hassanzadeh, “Matrix-fracture transfer shape factor for modeling flow of a compressible fluid in dual-porosity media,” *Advances in Water Resources*, vol. 34, no. 5, pp. 627–639, 2011.
- [41] Y. Tao, J. Xu, M. Cheng, S. Li, and S. Peng, “Theoretical analysis and experimental study on permeability of gas-bearing coal,” *Chinese Journal of Rock Mechanics and Engineering*, vol. 28, Supplementary 2, pp. 3364–3370, 2009.
- [42] B. Li, J. Li, K. Yang, C. Ren, J. Xu, and M. Zhang, “Deformation and permeability model of coal and rock considering moisture content,” *Journal of China Coal Society*, vol. 44, no. 4, pp. 1076–1083, 2019.
- [43] X. Li, Y. Guo, and X. Wu, “Analysis of the relation of porosity, permeability and swelling deformation of coal,” *Journal of Taiyuan University of Technology*, vol. 36, no. 3, pp. 264–266, 2005.
- [44] Y. Tao, J. Xu, D. Liu, and Y. Liang, “Development and validation of THM coupling model of methane-containing coal,” *International Journal of Mining Science and Technology*, vol. 22, no. 6, pp. 879–883, 2012.
- [45] J. Wei, H. Qin, and D. Wang, “Seepage characteristics of coal mass containing gas considering moisture effect in loading-unloading confining pressure test,” *Journal of Mining and Safety Engineering*, vol. 31, no. 6, pp. 987–994, 2014.
- [46] Z. Liu, Z. Li, Y. Yang, and H. Ji, “Experimental study of effect of water on sorption and radial gas seepage of coal,” *Chinese Journal of Rock Mechanics & Engineering*, vol. 33, no. 3, pp. 586–593, 2014.
- [47] C. Jiang, G. Yin, J. Xu, S. Peng, and W. Li, “The effect of original moisture content in coal beds on coal and gas outburst risk level,” *Journal of Chongqing University*, vol. 37, no. 1, pp. 91–95, 2014.
- [48] D. Chen, Z. Pan, J. Liu, and L. D. Connell, “Modeling and simulation of moisture effect on gas storage and transport in coal seams,” *Energy & Fuels*, vol. 26, no. 3, pp. 1695–1706, 2012.
- [49] J. Jing, W. Liang, B. Zhang, and L. Li, “Experimental investigation on coal permeability under water injection,” *Journal of Taiyuan University of Technology*, vol. 47, no. 4, pp. 450–454, 2016.
- [50] Z. Gao and W. Yang, “Adsorption mechanism of water molecule on different rank coals molecular surface,” *Journal of China Coal Society*, vol. 42, no. 3, pp. 753–759, 2017.
- [51] B. Lin and S. Zhou, “Experimental investigation on the permeability of the coal samples containing methane,” *Journal of China University of Mining & Technology*, vol. 16, no. 1, pp. 21–28, 1987.
- [52] Z. Feng, Y. Zhao, and Z. Wen, “Percolation mechanism of fractured coal rocks as dual-continua,” *Chinese Journal of Rock Mechanics and Engineering*, vol. 24, no. 2, pp. 236–240, 2005.
- [53] G. Yin, C. Jiang, J. Xu, L. Guo, S. Peng, and W. Li, “An experimental study on the effects of water content on coalbed gas permeability in ground stress fields,” *Transport in Porous Media*, vol. 94, no. 1, pp. 87–99, 2012.
- [54] S. Prion and K. A. Haerling, “Making sense of methods and measurement: Pearson product-moment correlation coefficient,” *Clinical Simulation in Nursing*, vol. 10, no. 11, pp. 587–588, 2014.
- [55] L. E. Toothaker, “Multiple regression: testing and interpreting interactions,” *Journal of the Operational Research Society*, vol. 45, no. 1, pp. 119–120, 1994.
- [56] C. Coulton and J. Chow, “Interaction effects in multiple regression,” *Journal of Social Service Research*, vol. 16, no. 1–2, pp. 179–199, 1993.
- [57] H. K. Chan, R. W. Y. Yee, J. Dai, and M. K. Lim, “The moderating effect of environmental dynamism on green product innovation and performance,” *International Journal of Production Economics*, vol. 181, pp. 384–391, 2016.

Research Article

Experimental Study of Slurry Flow in Mining-Induced Fractures during Longwall Overburden Grout Injection

Dayang Xuan,¹ Jian Li ,¹ Kaidan Zheng,¹ and Jialin Xu^{1,2}

¹School of Mines, China University of Mining and Technology, Xuzhou, Jiangsu 221116, China

²State Key Laboratory of Coal Resources and Safe Mining, China University of Mining and Technology, Xuzhou, Jiangsu 221116, China

Correspondence should be addressed to Jian Li; li_jian@cumt.edu.cn

Received 30 July 2020; Revised 22 August 2020; Accepted 26 August 2020; Published 4 September 2020

Academic Editor: Yingchun Li

Copyright © 2020 Dayang Xuan et al. This is an open access article distributed under the Creative Commons Attribution License, which permits unrestricted use, distribution, and reproduction in any medium, provided the original work is properly cited.

Slurry flow in mining-induced overburden fractures is an important theoretical concept for the grouting design of longwall overburden grout injection engineering. In this study, a visual experimental simulation system of longwall overburden grouting was designed to study the flow, pressure distribution, consolidation, and fill thickness of fly ash slurry in overburden bedding separation. Experiments showed that the slurry generates a radial and bidirectional flow during nonpressure grouting and presents itself as an approximately elliptical dominant flow channel under pressure injection. This channel expanded horizontally along the strike direction and gradually became tabular. The slurry pressure increased as the grouting time increased. Although the pressure curves at different locations exhibited similar trends, their values did not decrease as the distance from the borehole center decreased during observations. Bleeding and consolidation occurred in the slurry as soon as it flowed out of the borehole to the fracture, and the degree of consolidation increased as a function of the distance from the injection borehole. The bleeding water gathered continually to the boundary of the bedding separation fracture and was then seeped to and stored by the underlying strata based on the injection pressure. The final injection fill is manifested as a half pace with a large thickness at the center. This research provides a theoretical basis for the design and optimization of overburden grout injection in underground longwall mining.

1. Introduction

Underground longwall coal mining causes movements and breakage of strata, thus inducing vertical and horizontal fractures in the overburden [1–6]. The mining-induced fractures propagate gradually from the gob area to the ground surface and induce surface subsidence and corresponding environmental damage [7, 8]. Meanwhile, these fractures are the flow paths of geofluids, such as methane [9], water [10, 11], and slurry [12–14]; corresponding surface subsidence can be reduced by filling these fractures during mining. Grout injection into the overburden bedding fractures is one such method and is used to control mining subsidence [15–18]. Overburden grout injection involves injecting grout into mining-induced bedding fractures through surface boreholes as the longwall advances. These separations are horizontal fractures formed at the interface of strong and weak rock

layers during mining. The injected fill supports the ground and reduces surface subsidence. In particular, this technology has been successfully utilized in the protection of surface infrastructures [18–22].

The dynamic flow of slurry in the overburden is the basis of injection design, such as grout take estimation, grouting pressure determination, and borehole layout. In this regard, previous research has covered the vertical injection horizon and flow radius. For example, borehole drilling [8], ground penetration radar [23], and fluorescent approach [24] have been used to locate the final injection horizon (or injection layer) in the overburden. Specifically, Xuan et al. [8] found that the injection fill is manifested as a primary injection horizon below a strong and thick rock layer (key stratum) above the injection borehole. Additionally, the flow radius of fly ash slurry was tested experimentally through two parallel disks without the simulation of mining [25, 26]. The

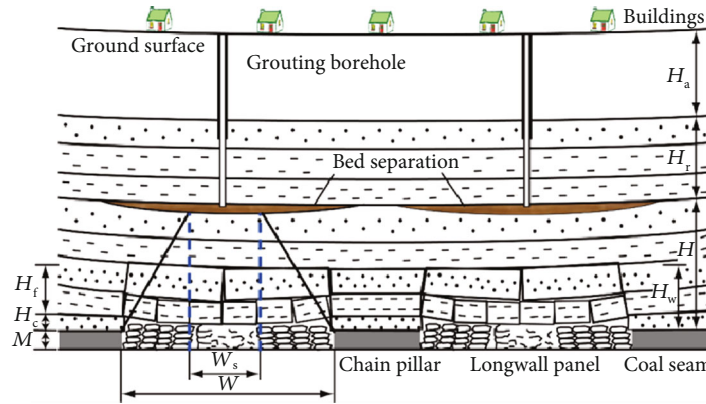


FIGURE 1: Principle of isolated overburden grout injection [21].

practical flow radius of a single borehole was determined for longwall overburden injection by using methods of borehole connectivity [21] and borehole imaging [23]. Studies also covered the theoretical model of the final injection fill distribution that was used to estimate the injection ratio [27].

These studies have prompted the understanding of the final fill in overburden following longwall mining with grouting. However, there is still insufficient research on the dynamic slurry flow in mining-induced overburden fractures. For the fractured rock grouting, extensive research has been conducted on grout flow with respect to experimenting and modeling [28–30]; however, the aperture of the fractures in this area differs considerably from that in longwall overburden injection engineering. The longwall-injected target is a fracture associated with underground mining; it is highly dependent on the mining height and can reach the meter level that is much larger than that in fractured rock grouting. Thus, the flow model in fractured rock is considered inapplicable to longwall overburden grout injection.

Presently, slurry flow is still unclear for the longwall injection, at least in terms of the flow channel and slurry pressure distribution in the bedding separation. Additionally, the bleeding and consolidation of the commonly used fly ash slurry that is a typical solid–liquid, two-phase flow, also need investigation in longwall overburden injection. Geophysical prospecting methods are considered insufficient to locate the slurry flow because of a large depth (usually 400–500 m below ground surface), while borehole drilling can only reveal the final fill distribution at some points instead of the entire underground bedding separation fracture.

With these issues in mind, this study utilizes an experimental methodology to (a) emulate the process of longwall overburden grout injection, (b) determine the dynamic flow, pressure distribution, and consolidation, and (c) fill the thickness of the slurry with different monitoring methods.

2. Materials and Methods

2.1. Theoretical Background. Isolated overburden grout injection is an improved technology for traditional longwall overburden injection [17, 18, 31]. It involves drilling surface boreholes to the selected key strata followed by the injection of slurry into the separation fracture below the strata with

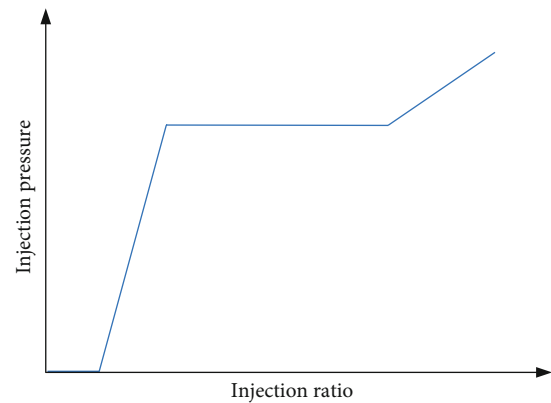


FIGURE 2: Four stages of borehole injection pressure during longwall overburden grout injection [19].

high pump pressure. The high pressure generates a load-transfer effect that supports the overlying ground and compacts underlying caved and fractured rocks, thus inducing a support system that bears the ground, and controls surface subsidence (Figure 1). This technology can increase the subsidence reduction ratio because of an improved injection ratio of up to 50–60%.

Fly ash slurry, a typical solid–liquid two-phase fluid is used as the grouting material in injection engineering, and the borehole grouting pressure can reach 5–6 MPa. Following the filling in the separation zone, the slurry undergoes bleeding and consolidation under the action of grouting pressure and finally forms a compacted fill body [32]. Because a mining-induced bedding separation defines the dynamic process of the initial formation and enlargement, the injection pressure changes correspondingly, and the flow, bleeding, and consolidation of the slurry also evolve. In this regard, Teng [33] summarized the overburden grouting pressure in four stages based on actual engineering data: nonpressure, increased pressure, stabilized pressure, and overpressure (Figure 2). The grouting pressure is zero at first. This corresponds to the initial formation stage of the bedding separation. Subsequently, the grouting pressure begins to increase, thus indicating the difference between the filling speed and the formation speed of the separation fracture gradually decreases. Furthermore, the pressure reaches the weight of

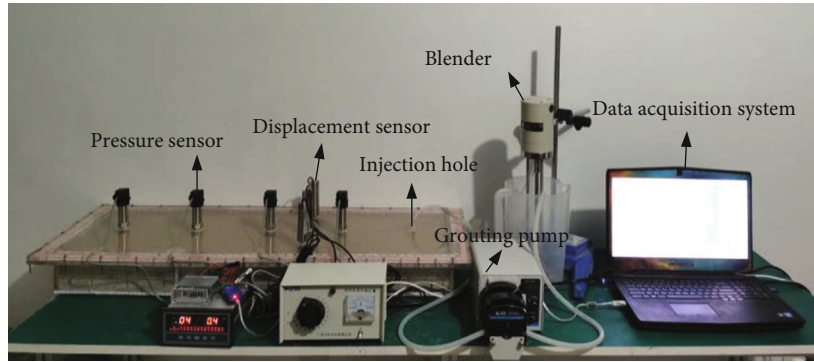


FIGURE 3: Experimental system.

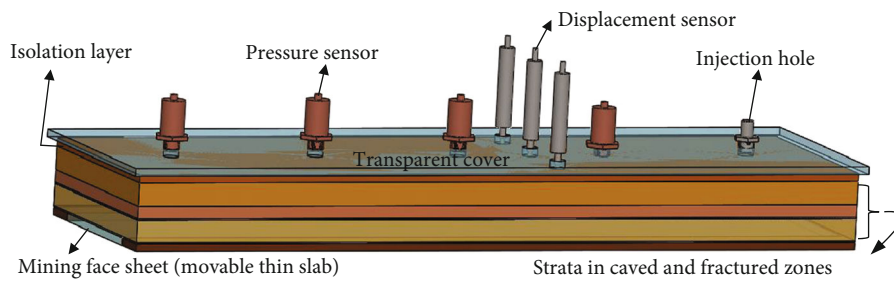


FIGURE 4: Schematic of experimental system used for the emulation.

TABLE 1: Model laying parameters.

Lithology	Thickness (cm)	Material	Ratio	Layers	Strength (kPa)
Isolation layer	1	Paraffin : hydraulic oil : talcum powder : river sand : straw powder	1 : 2 : 5.7 : 34.2 : 1	2	95
Soft rock layer	3	Sand : calcium carbonate : gypsum : water	3.5 : 3.5 : 1.5 : 1	3	70
Key strata	2	Sand : calcium carbonate : gypsum : water	3 : 3.5 : 1.5 : 1	2	78
Immediate roof	3	Sand : calcium carbonate : gypsum : water	3.5 : 3.5 : 1.5 : 1	3	70

the overlying strata, thus indicating that a stable balance is formed between the grouting and separation. The overpressure stage that usually occurs at the end stage of grouting indicates that the grouting speed is greater than the separation rate. The pressure stage provides a basis for experimental research on fluid flow.

2.2. Experimental System. To study the reproduce of grout flow in the overburden, we established a similar simulation system to emulate the overburden grouting process during underground mining with grouting. The system includes the main frame, grouting system, monitoring sensor, and acquisition software (Figure 3).

The main frame is made of a transparent Perspex sheet which can visualize the slurry flow. The inner dimensions of the frame are $1000 \times 300 \times 100$ mm in length, width, and height. It is used to emulate coal seams, overlying strata, and the bedding separation fracture intended to be injected. At the bottom of the main frame is a movable thin slab with length, width, and thickness of 100, 20, and 1 cm, respectively, which is used to emulate coal seam. The move of the

thin slab emulates the coal-mining process and the formation of the gob area. A width of 5 cm is left between the two sides of the thin plate and the inner boundary of the frame to emulate the coal pillars on both sides of the longwall panel. Similar materials are laid above the thin slab in layers. These include the immediate roof, the main roof, the soft rock layer, and the isolation layer from bottom to top, with the thicknesses of 3, 2, 3, and 1 cm, respectively (Figure 4).

The immediate roof, main roof, and soft rock layers are made of sand, calcium carbonate, gypsum, and water. These layers are used to emulate the caved and fractured zones above the gob area. The isolation layer is made of paraffin wax, hydraulic oil, talcum powder, river sand, straw powder, and water, with a solid-phase material ratio of 1 : 2 : 5.7 : 34.2 : 1. The isolation layer directly below the separation fracture allows for nondisintegration, thus preventing the bleeding water from entering the lower rock layers and causing disintegration. The material ratio and characteristics of each rock layer are listed in Table 1. When laying each rock layer, mica was placed between layers to emulate the bedding. A space with a height of 0.5 cm was placed

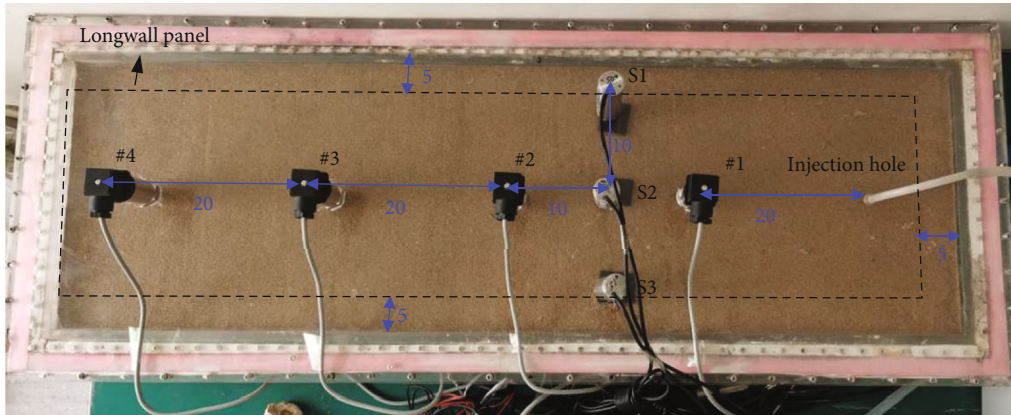


FIGURE 5: Locations of the sensors, borehole, and longwall panel (unit: cm).



FIGURE 6: Injection material. (a) Fly ash and (b) injection slurry.

between the isolation layer and the upper cover plate of the main frame to emulate the initial separation zone that was intended to be injected.

The grouting system included a slurry mixer, a grouting pump, pipelines, and a borehole. The borehole is located at the top of the main frame. To monitor the slurry pressure at different positions in the separation fracture, four pressure sensors (#1–4 in Figure 5) are evenly arranged on the center line of the upper cover plate of the main frame. Their distances to the holes are 20, 40, 60, and 80 cm and are used to reflect the pressure difference at different positions. The thickness of the injection fill body was determined by monitoring the displacement of the lower isolation layer subject to the separation fracture. For this reason, three displacement sensors (S1–S3 in Figure 5) are arranged at equal intervals in the inclination direction of the main frame and are used to reflect the thickness differences in the boundary and the middle of the fracture. The relative positions of the pressure displacement sensor, borehole, and longwall working face are shown in Figure 5.

2.3. Experimental Methods. According to an engineering of isolated overburden grout injection, the fly ash slurry was selected as the injection material with a water-to-fly ash ratio of 1.6:1 (Figure 6). The grouting flow rate was determined to be 300 ml/min. Before the extraction of the longwall face, grout was injected into the preset separation fracture until the injection pressure is formed, so as to simulate the flow

of slurry in the nonpressure stage. Once the pressure develops, grouting during mining begins. The thin plate was extracted at a distance of 15 cm from the frame every 10 min to emulate the mining distance, and the coal seam was mined for six times. During this process, grouting in the bedding separation zone was performed simultaneously, and the slurry pressure and displacement of the isolation layer were monitored. To monitor the flow channel and consolidation of the slurry, a camera was used to capture pictures on the upper surface of the model for observation continually. In the grouting process, a colored tracer was added to the slurry to enhance the display of the results.

3. Results and Discussion

3.1. Slurry Flow. The slurry flow under the nonpressure and pressure stages are described based on the photographic monitoring results. During the nonpressure stage, the slurry flow manifested in two successive stages, namely, radial and bidirectional. During the radial flow stage, the slurry presented an approximate circular flow centered on the grouting hole, and the radius of the slurry diffusion increased as a function of the grouting time. When the front part of the slurry reached the boundary of the bedding separation zone, the slurry was transferred to the bidirectional flow because of the boundary constraint, that is, a planar flow along the left and right sides of the borehole (Figure 7). When the front

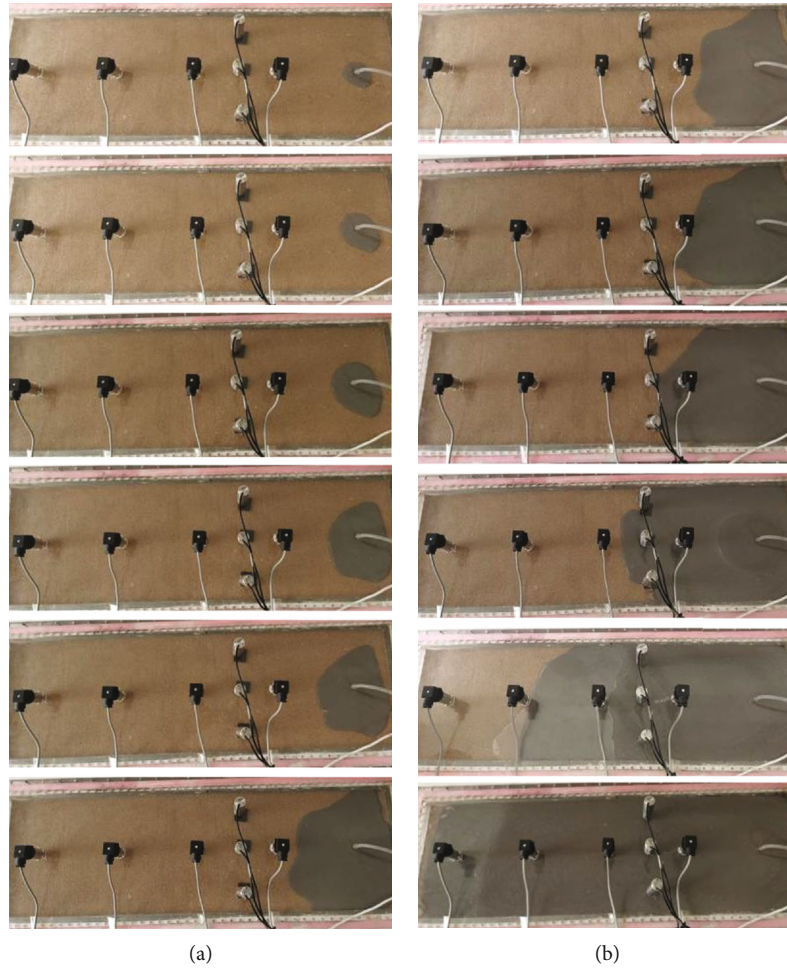


FIGURE 7: Slurry flow during nonpressure injection. (a) Radial flow (0–90 s). (b) Bidirectional flow (90–630 s).

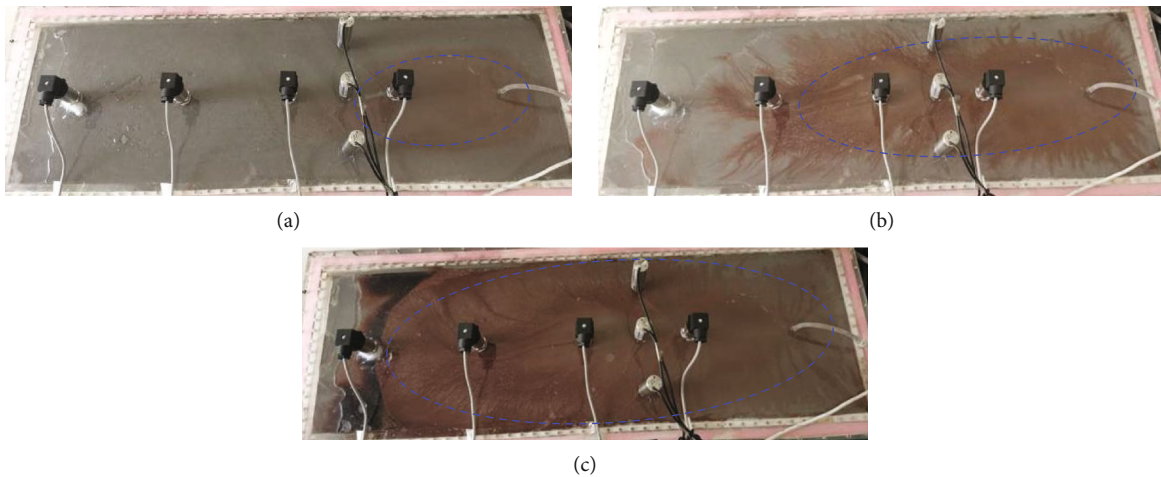


FIGURE 8: Slurry flow channel during pressurized injection. (a) 810 s, (b) 1170 s, and (c) 1770 s.

of the slurry reached the right boundary, the slurry changed to one-sided flow owing to the boundary constraint.

Subject to the applied pressure, the slurry flow was no longer the plan flow, as in the case of nonpressure stage, but a dominant flow channel appeared. The channel was

approximately elliptic with respect to the center of the grouting. As the grouting volume increased, the size of the channel expanded (Figure 8). The dominant flow channel expanded along the strike direction (i.e., face advance direction), and the channel width was smaller than its length before it

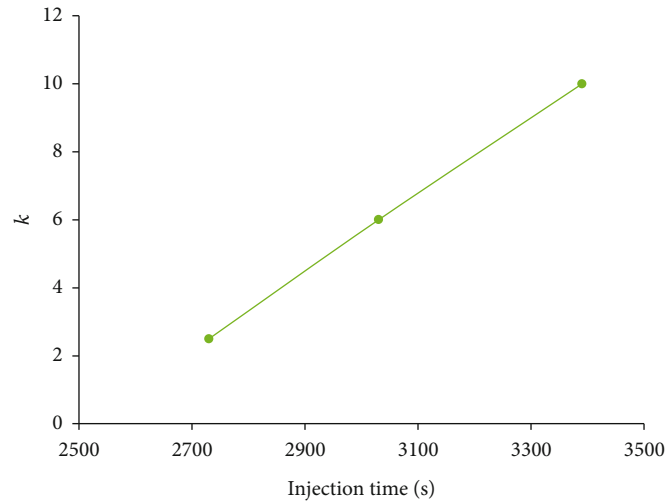


FIGURE 9: Flow channel coefficient k vs. time.

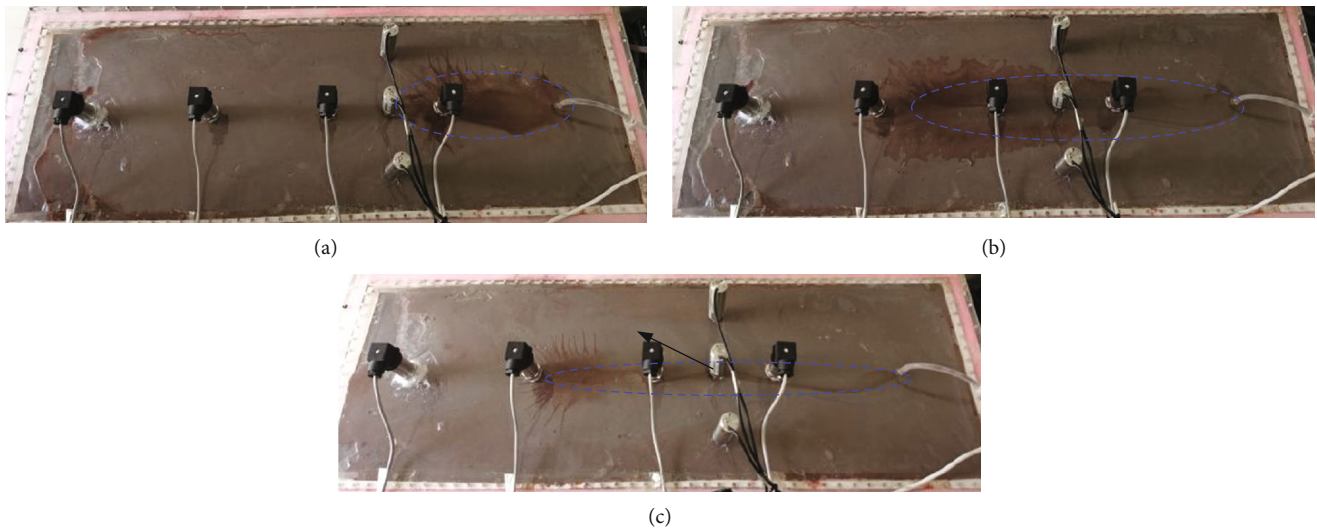


FIGURE 10: Evolution of slurry flow channel. (a) 2730 s, (b) 3030 s, and (c) 3390 s.

reached the strike boundary of the separation zone. To characterize the dominant flow channel, we defined a flow channel coefficient k as the ratio of the channel length to its width.

As the grouting volume and pressure continued to increase, the newly injected grout exerted the induced stress on the existing grout so that a shear channel was formed in the early-filled grout and allowed the new grout to flow along this channel. Meanwhile, the dominant flow channel was evolving: the value of k continued to increase as the grouting time elapsed and is approximately linearly correlated with time (Figure 9). That is, the dominant flow channel gradually developed into a tabular shape (Figure 10). This is because the consolidation and deposition of the grout at the trend boundary occurred continually (refer to section 3.3).

3.2. Grouting Pressure Distribution. The grouting pressure distribution in the bedding separation fracture is an important factor that affects the slurry flow. It was found that the

pressure at any point in the bedding separation increased as a function of the grouting time, and the pressure curves at different positions exhibited similar trends (Figure 11(a)). However, the pressure at different points in the separation was not equal. The grouting pressure decreased as a function of distance from the grouting hole, but the reduction was not large. In particular, the pressure differences for different positions gradually decreased as the injection time elapsed (Figure 11(b)). Setting of the grouting time at 1200 s (initial injection stage) generated the following pressures at sensors #1–4 of 82%, 43%, 36%, and 7% of the hole pressure, respectively, while the pressure at #4 (farthest from the borehole) was just 9% of that at #1 (nearest to the borehole). If the grouting time was set at 3000 s (the end of grouting), the pressures at sensors #1–4 reached 98%, 93%, 92%, and 28%, of the hole pressure, and the pressures at sensors #1–3 were almost the same. The results showed that the grouting pressure decreased along the direction of slurry flow, but the differences were limited. It also indicated that the pressure at

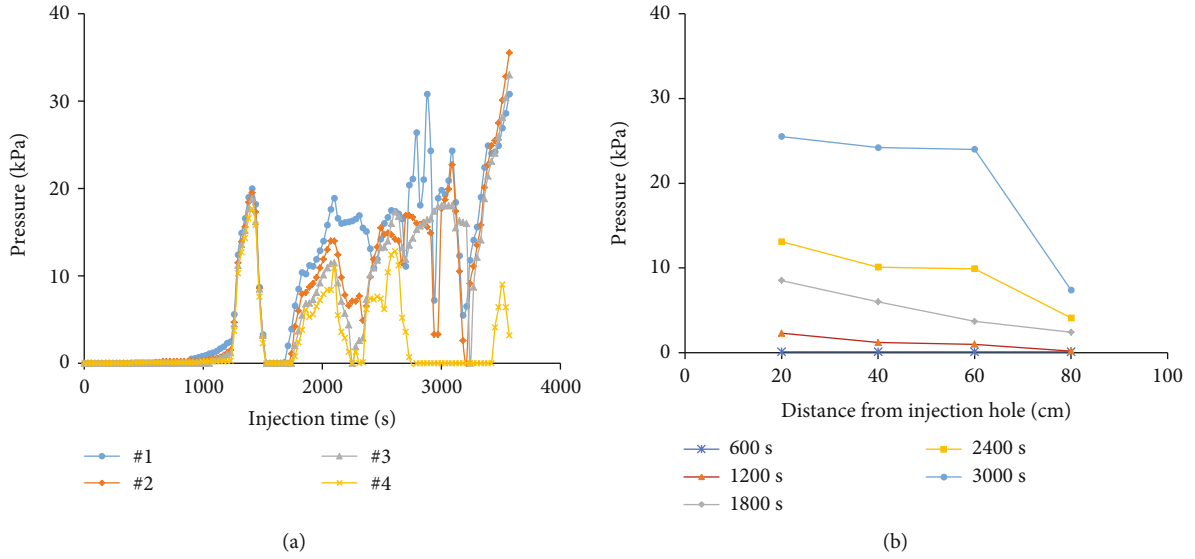


FIGURE 11: Slurry pressure as a function of (a) injection time and (b) distance.

any position can reflect the pressure trend in the entire bedding separation fracture.

3.3. Slurry Consolidation and Fill Distribution. To determine the consolidation characteristics of the slurry, it is necessary to determine the deposition rate of solid particles in the slurry. Water in the fly ash slurry serves as a carrier of solid particles. The flow velocity of the solid particles gradually decreases because of the bleeding of the slurry and final deposition. To prevent solid particles from depositing, the flow velocity should be greater than the critical nonsilting velocity [34]:

$$v_c = 0.2(1 + 3.4C_w^{1/3}D^{1/4})\beta, \quad (1)$$

where v_c is the critical nonsilting velocity, C_w is the specific concentration of the solid mass, D is the width of the flow channel, and β is a coefficient that satisfies

$$\beta = (r_s - 1)/1.7, \quad (2)$$

where r_s is the density of the ash particles. By substituting Equation (2) in Equation (1), we obtain

$$v_c = 0.12(1 + 3.4C_w^{1/3}D^{1/4})(r_s - 1). \quad (3)$$

According to Equation (3), the critical nonsilting velocity of solid particles in fly ash slurry was determined to be 0.4 m/s.

The flow velocity of the slurry injected into the bedding separation fracture was constrained by the flow rate and the size of the separation fracture, and satisfied

$$v = Q/wh, \quad (4)$$

where Q is the grouting flow, w is the separation fracture width, and h is the separation fracture height. According to

Equation (4), the velocity of the injected slurry at the bedding separation fracture was 0.0033 m/s, or just 0.8% of the critical nonsilting velocity. This indicates that the solid particle deposits (or the bleeding of slurry) occurred quickly following its entry into the borehole to the fracture. This was also verified in the experiment of the slurry flow.

The consolidation rate of the slurry at different positions of the bedding separation zone was not the same and was closely related to the slurry velocity. If the flow rate was low, the solid particles were expected to deposit fast; otherwise, the consolidation rate would be slower. Owing to the restriction of the boundary in the width direction, the flow velocity was smaller than that along the strike direction, and both were less than the critical nonsilting velocity. Therefore, the bleeding velocity in the width direction was greater than that in the strike direction. At distances closer to the boundary, the velocity was smaller. Therefore, the consolidation degree increased as the distance from the center increased along the width direction. The bleeding water gathered in the most anterior part of the slurry and formed a “water belt.” The “water belt” moved to the boundary of the bedding separation zone subject to continuous pushing of the newly injected slurry. Finally, because of the action of the grouting pressure, the water in the “water belt” flowed to the underlying rock mass and was stored. Figure 12 shows the consolidation of the slurry in the separation fracture zone.

The fill thickness distribution in the width direction was determined with displacement sensors. In the initial stage of grouting (0–1200 s), there was no significant difference in the fill thickness, and the boundary fill thickness accounted for 84% of that in the center (Figure 13). As the gob volume increased, the amount of grouting also increased. Subject to the combined action of the mining effect and grouting pressure, the isolation layer began to exhibit deflection deformation that further allowed a large injectable space. At the end of mining (3000 s), the fill thickness direction was different along the width direction. The thickness was approximately

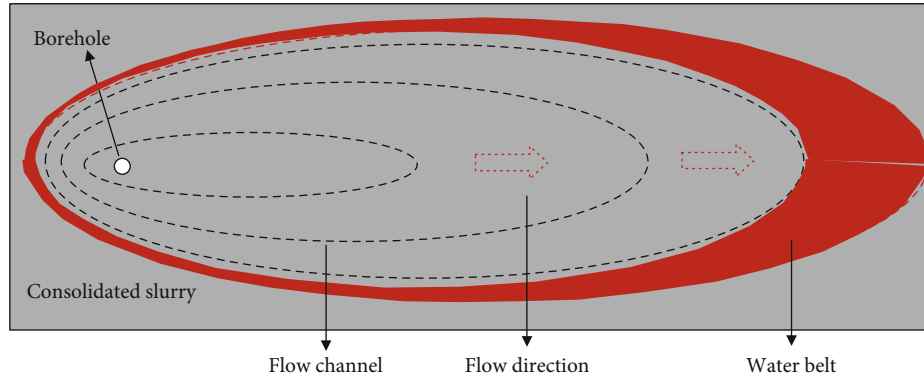


FIGURE 12: Schematic of slurry flow rule.

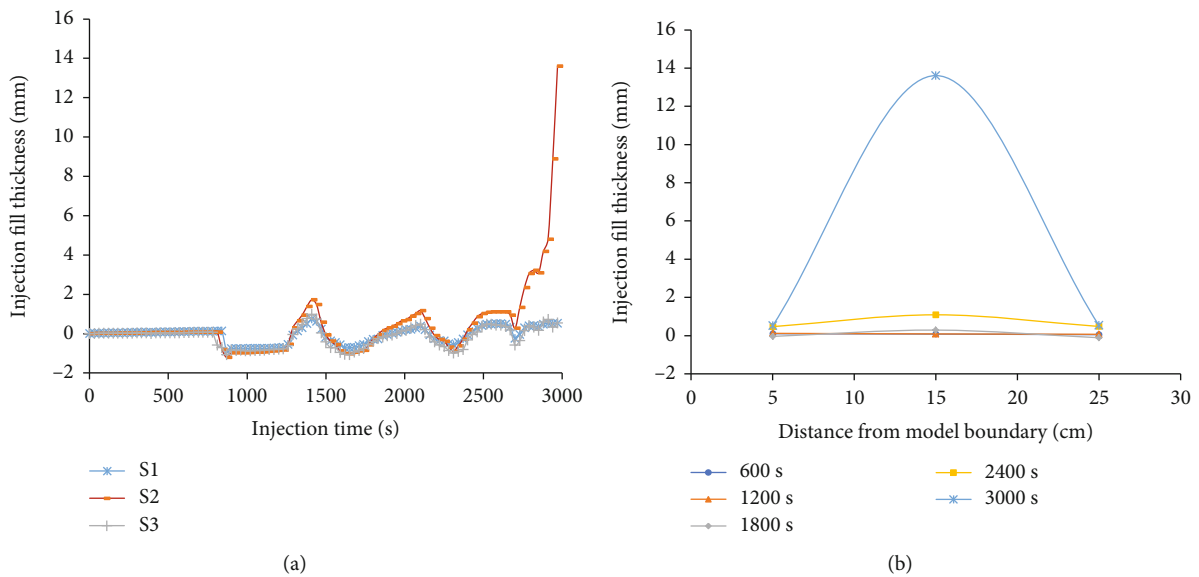


FIGURE 13: Distribution of injection fill. Fill thickness as a function of (a) time and (b) distance.

0.53 mm on both sides (and accounted for 5.3% of the mining height), whereas that in the center reached 13.61 mm, and accounted for 86.1% of the mining height. Thus, the thickness of the boundary fill was only 3.8% of that in the center, and the injection fill thickness distribution manifested as half pace, which is consistent with the model as described in [27]. This also indicates that the caved and fractured rocks are further compacted when subjected to the action of grouting pressure, thus allowing a larger injectable space above the isolation layer.

4. Conclusions

Mining-induced fractures formed in overburden by longwall mining are the key reasons for surface subsidence. Overburden grout injection technology uses these fractures to control mining subsidence. In this study, the flow of slurry in overburden fractures was studied experimentally.

The characteristics of slurry flow subject to nonpressure and pressure were obtained by photographic monitoring. In the nonpressure stage, slurry flows were manifested in the

radial and bidirectional stages successively. In the pressure stage, the flow was presented as an almost elliptic dominant flow channel with its center on the grouting hole. This channel expanded gradually along the strike direction, and its size increased continually. The flow channel coefficient was proposed to represent the dominant channel at different pressure conditions. This increased in an efficient manner as the grouting time elapsed. This was attributed to the consolidation of the slurry at the boundary.

The distribution of the slurry pressure in the mining separation fracture was also revealed. The pressure at any point in the bedding separation increased as a function of grouting time. However, the pressure at different points in the separation was not equal. The grouting pressure decreased away from the grouting hole, but the reduction was not large. Nevertheless, it is interesting that the pressure curves at different positions exhibited similar trends. This provided the basis for the determination of borehole connectivity and pressure monitoring during longwall overburden grout injection.

The consolidation characteristics of the slurry were obtained. After entering the separation fracture, the flow

velocity decreased significantly. This resulted in the deposition of solid particles and in the bleeding of the slurry. The slurry consolidation rate was not the same at each position, and it was greater in the width direction than that in the strike direction. In particular, the closer the slurry was to the boundary, the smaller the velocity. That is, the farther from the borehole, the greater the degree of slurry consolidation. The bleeding water gathered at the anterior part of the slurry and formed a “water belt,” which moved to the boundary of the bedding fracture. Finally, the water in the “water belt” flowed toward the underlying rock mass and was stored because of the action of the grouting pressure. The fill thickness increased as a function of the grouting and mining times. This indicated that the caved and fractured rock mass was further compacted that allowed a large injectable space above the isolation layer. This finding may improve the estimation of the injection ratio.

Data Availability

The research data used to support the findings of this study may be released upon request addressed to the corresponding author who can be contacted at Li_Jian@cumt.edu.cn. Some or all data, models, or code generated or used during the study are available from the corresponding author upon request (experimental equipment parameters, laboratory experimental results data, field experimental results, etc.).

Conflicts of Interest

The authors declare that there are no conflicts of interest regarding the publication of this paper.

Acknowledgments

This work was supported by the National Natural Science Foundation of China (51604258) and the China Scholarship Council (201906425004).

References

- [1] V. Palchik, “Formation of fractured zones in overburden due to longwall mining,” *Environmental Geology*, vol. 44, no. 1, pp. 28–38, 2003.
- [2] C. Ö. Karacan and R. A. Olea, “Inference of strata separation and gas emission paths in longwall overburden using continuous wavelet transform of well logs and geostatistical simulation,” *Journal of Applied Geophysics*, vol. 105, pp. 147–158, 2014.
- [3] V. Palchik, “Localization of mining-induced horizontal fractures along rock layer interfaces in overburden: field measurements and prediction,” *Environmental Geology*, vol. 48, no. 1, pp. 68–80, 2005.
- [4] V. Palchik, “Experimental investigation of apertures of mining-induced horizontal fractures,” *International Journal of Rock Mechanics and Mining Sciences*, vol. 47, no. 3, pp. 502–508, 2010.
- [5] D. P. Adhikary and H. Guo, “Modelling of longwall mining-induced strata permeability change,” *Rock Mechanics and Rock Engineering*, vol. 48, no. 1, pp. 345–359, 2015.
- [6] Y. Li, C. Wu, and B. A. Jang, “Effect of bedding plane on the permeability evolution of typical sedimentary rocks under triaxial compression,” *Rock Mechanics and Rock Engineering*, 2020.
- [7] S. G. Chen and W. Hu, “A comprehensive study on subsidence control using COSFLOW,” *Geotechnical Geological Engineering*, vol. 27, no. 3, pp. 305–314, 2009.
- [8] D. Xuan, J. Xu, B. Wang, and H. Teng, “Borehole investigation of the effectiveness of grout injection technology on coal mine subsidence control,” *Rock Mechanics and Rock Engineering*, vol. 48, no. 6, pp. 2435–2445, 2015.
- [9] G. Wang, Y. Guo, C. a. du et al., “Experimental study on damage and gas migration characteristics of gas-bearing coal with different pore structures under sorption-sudden unloading of methane,” *Geofluids*, vol. 2019, Article ID 7287438, 11 pages, 2019.
- [10] X. Peng, S. Zhu, Z. You et al., “Numerical simulation study of fines migration impacts on an early water drainage period in undersaturated coal seam gas reservoirs,” *Geofluids*, vol. 2019, Article ID 5723694, 16 pages, 2019.
- [11] F. Wang, W. Wang, B. Wu, Q. Bai, and M. S. A. Perera, “Mechanism, cause, and control of water, solutes, and gas migration triggered by mining activities,” *Geofluids*, vol. 2019, Article ID 5789152, 4 pages, 2019.
- [12] H. Guo, D. P. Adhikary, and M. S. Craig, “Simulation of mine water inflow and gas emission during longwall mining,” *Rock Mechanics and Rock Engineering*, vol. 42, no. 1, pp. 25–51, 2009.
- [13] G. Hu, W. He, and C. Lan, “Sealing behavior and flow mechanism of expandable material slurry with high water content for sealing gas drainage boreholes,” *Geofluids*, vol. 2018, Article ID 2954306, 15 pages, 2018.
- [14] Q. Qu, J. Xu, R. Wu, W. Qin, and G. Hu, “Three-zone characterisation of coupled strata and gas behaviour in multi-seam mining,” *International Journal of Rock Mechanics and Mining Sciences*, vol. 78, pp. 91–98, 2015.
- [15] S. G. Chen and H. Guo, “Numerical simulation of bed separation development and grout injecting into separations,” *Geotechnical and Geological Engineering*, vol. 26, no. 4, pp. 375–385, 2008.
- [16] B. Shen and B. Poulsen, “Investigation of overburden behaviour for grout injection to control mine subsidence,” *International Journal of Mining Science and Technology*, vol. 24, no. 3, pp. 317–323, 2014.
- [17] D. Xuan and J. Xu, “Longwall surface subsidence control by technology of isolated overburden grout injection,” *International Journal of Mining Science and Technology*, vol. 27, no. 5, pp. 813–818, 2017.
- [18] J. Xu, J. Ni, D. Xuan, and X. Wang, “Coal mining technology without village relocation by isolated grout injection into overburden,” *Coal Science and Technology*, vol. 43, pp. 8–11, 2015.
- [19] H. Teng, J. Xu, D. Xuan, and B. Wang, “Surface subsidence characteristics of grout injection into overburden: case study of Yuandian No. 2 coalmine, China,” *Environmental Earth Sciences*, vol. 75, no. 6, p. 530, 2016.
- [20] B. Wang, J. Xu, and D. Xuan, “Time function model of dynamic surface subsidence assessment of grout-injected overburden of a coal mine,” *International Journal of Rock Mechanics and Mining Sciences*, vol. 104, pp. 1–8, 2018.
- [21] D. Xuan and J. Xu, “Grout injection into bed separation to control surface subsidence during longwall mining under

- villages: case study of Liudian coal mine, China,” *Natural Hazards*, vol. 73, no. 2, pp. 883–906, 2014.
- [22] D. Xuan, J. Xu, and W. Zhu, “Dynamic disaster control under a massive igneous sill by grouting from surface boreholes,” *International Journal of Rock Mechanics and Mining Sciences*, vol. 71, pp. 176–187, 2014.
- [23] H. Guo, B. Shen, and S. Chen, “Investigation of overburden movement and a grout injection trial for mine subsidence control,” in *Rock Mechanics: Meeting Society’s Challenges and Demands*, pp. 1559–1566, American Rock Mechanics Association, 2007.
- [24] Y. Chen, T. Nishiyama, M. Terada, and Y. Iwamoto, “A fluorescent approach to the identification of grout injected into fissures and pore spaces,” *Engineering Geology*, vol. 56, no. 3-4, pp. 395–401, 2000.
- [25] H. Alehossein, “Viscous, cohesive, non-Newtonian, depositing, radial slurry flow,” *International Journal of Mineral Processing*, vol. 93, no. 1, pp. 11–19, 2009.
- [26] H. Alehossein, B. Shen, Z. Qin, and C. Huddleston-Holmes, “Flow analysis, transportation, and deposition of frictional viscoplastic slurries and pastes in civil and mining engineering,” *Journal of Materials in Civil Engineering*, vol. 24, no. 6, pp. 644–657, 2012.
- [27] D. Xuan, J. Xu, B. Wang, and H. Teng, “Investigation of fill distribution in post-injected longwall overburden with implications for grout take estimation,” *Engineering Geology*, vol. 206, pp. 71–82, 2016.
- [28] M. J. Yang, Z. Q. Yue, P. K. K. Lee, B. Su, and L. G. Tham, “Prediction of grout penetration in fractured rocks by numerical simulation,” *Canadian Geotechnical Journal*, vol. 39, no. 6, pp. 1384–1394, 2002.
- [29] S. C. Li, Z. Zheng, R. T. Liu, X. C. Wang, L. Z. Zhang, and H. B. Wang, “Analysis of the grouting diffusion mechanism of micro-fractures considering the coupling effect of grouting and rock,” *Chinese Journal of Rock Mechanics and Engineering*, vol. 36, pp. 812–820, 2017.
- [30] X. C. Wang, R. T. Liu, W. M. Yang et al. , “Study on grouting mechanism of horizontal fractures considering the bleeding of cement slurry,” *Chinese Journal of Rock Mechanics and Engineering*, vol. 38, pp. 1005–1017, 2019.
- [31] J. Xu, D. Xuan, W. Zhu, and X. Wang, “Partial backfilling coal mining technology based on key strata control,” *Journal of Mining and Strata Control Engineering*, vol. 1, pp. 135041–135048, 2019.
- [32] L. Zhang, J. Xu, D. Xuan, and M. Gan, “Experimental and applied research on compression properties of slurry used for isolated overburden grout injection,” *Journal of China Coal Society*, vol. 42, pp. 1118–1123, 2017.
- [33] H. Teng, *Formation Mechanism of Compacting Area in the Gob with Grouting Into Overburden of Isolated Panels during Longwall Mining*, China University of Mining and Technology, Xuzhou, China, 2017.
- [34] C. Wang, J. Xu, and D. Xuan, “Blockage mechanism of ground transport pipeline for isolated overburden grout injection,” *Journal of China Coal Society*, vol. 43, pp. 2703–2708, 2018.

Research Article

Failure Behavior of Thin Disc Sandstone under Coupled Bending-Seepage Condition

Luzhen Wang¹ and Hailing Kong^{1,2} 

¹College of Civil Engineering, Yancheng Institute of Technology, Yancheng, Jiangsu 224051, China

²Institute of Coastal Ultra-Soft Soil, Yancheng Institute of Technology, Yancheng, Jiangsu 224051, China

Correspondence should be addressed to Hailing Kong; hailkong@126.com

Received 8 April 2020; Revised 22 June 2020; Accepted 8 July 2020; Published 28 August 2020

Academic Editor: Yingchun Li

Copyright © 2020 Luzhen Wang and Hailing Kong. This is an open access article distributed under the Creative Commons Attribution License, which permits unrestricted use, distribution, and reproduction in any medium, provided the original work is properly cited.

A floor aquifuge usually bends and fails when mining above a confined aquifer, which may lead to water inrush disaster. The floor aquifuge was simplified as a thin disc model in this paper, and a series of coupled bending-seepage tests of sandstone were carried out by a patent test system. The variation characteristics of load-displacement, load-time, and permeability-time were analyzed. The deflection and stress in the thin disc rock samples were deduced; the initiation and propagation of cracks were analyzed. The failure behavior of the thin disc rock samples was described. It shows the following: (1) The bending failure behavior relates to the stress distribution and crack evolution inside the thin disc. (2) The main cause of crack initiation is a tension-shear failure. (3) The 5 mm thickness thin discs form petal-shaped cracks, due to tensile stress, while petal-shaped cracks only appear at the cap block of the 10 mm discs, which are sheared into two pieces along the conical surface with an inclination about 45°. (4) Water inrush occurs after bending failure in the floor aquifuge, and it is an opportune moment to grout along the crack propagation trend lines to prevent the water inrush disasters.

1. Introduction

Due to the gradual depletion of shallow mineral resources, mining activities are shifted to the deep. In deep mining activities, geological conditions become complex; confined water pressure increased. Continuous deep mining may result in bending deformation and failure of the floor aquifuge, which may link the groundwater to the working face, and induce water inrush accidents [1–4]. Hence, the bending failure of the floor above a confined aquifer is one of the reasons to induce water inrush.

Scholars began to study the mechanism of floor breakage and water inrush since the last century. Some important theories have been proposed successively, such as the key stratum theory, three-underlying belts theory, in situ rifting and zero failure theory, relative aquifuge thickness and water inrush coefficient method, and water inrush critical index method [5–9]. In recent years, due to the complex geological background and mining conditions, the floor breakage and water inrush mechanisms have been extensively and deeply

studied based on the above theories, and new achievements emerged endlessly.

A large-scale model test is one of the effective means to reproduce the process of water inrush from floor breakage. Zhao et al. [10, 11] developed a large-scale three-dimensional solid-fluid coupling simulation experimental equipment, analyzed the wall rock distortion and breakage process, and described the variation law of stress and water pressure and their influence on water inrush. Li et al. [12] divided the mining-induced floor stresses into three distinct stages with the help of a fluid-solid coupling model test system. Chen et al. [13] described the crack formation and evolution law in the floor aquifuge by the solid-fluid coupling similar simulation test system and found that most mining cracks were vertical tensile cracks, shear cracks, and layer cracks. Kang et al. [14] studied the failure law of the floor after mining using a large-scale simulation test system and divided the floor fracture belt into an open-off-cut fracture zone, central goaf compaction zone, and working-face fracture zone. Liu et al. [15] found that the failure range

morphological map of the mining floor was approximately a spoon shape and obtained the maximum failure depth of the floor aquifuge by similar simulation tests. Based on the multifunctional simulation test apparatus, Hua et al. [16] pointed out that the floor heave was mainly composed of the compression bending type, shear dislocation type, and extrusion fluidity type, and the floor heave was mainly caused by the tensile failure or tensile-shear failure.

The similar model test can reproduce the process of floor's breakage and water inrush, but it still has some disadvantages; for example, the model sizes are usually too large, cost too much, and last for long test periods. Therefore, theoretical research and numerical calculation are essential.

Miao et al. [17] simplified the floor aquifuge to a rock beam model with both ends fixed and loaded uniformly and analyzed the strength characteristics and water-resisting performance of the floor aquifuge. Sun and Wang [18] regarded the floor aquifuge as a square elastic thin plate with fixed constraints on four sides and deduced an instability mechanics criterion of the inclined floor water-resisting key strata using the elastic thin plate theory. Gao et al. [19] established a fracture mechanics model based on the thin plate theory and regarded that the essence of water inrush in the mining field was the result of the accumulation of microcracks and propagation of macrocracks in the floor aquifuge caused by mining-induced stress and confined water pressure. Wang et al. [20] established a plate model subjected to horizontal extrusion force, deduced the critical load of floor buckling failure based on the thin plate yield theory, and obtained that the floor thickness was the main factor affecting the critical load. Guo et al. [21] analyzed the distribution of displacement and pore water pressure on the floor using Comsol Multiphysics and pointed out that the key cause of water inrush was the release of energy from the floor above the confined water aquifer when mining. Pang [22] simplified the layered floor to homogeneous elastic plates, calculated the floor failure depth by means of the average modulus method, and considered that the lithology and composite structure of the floor are two important factors affecting the failure depth. Xie [23] used Flac3D to analyze the damage law of elastic modulus of the floor aquifuge caused by mining qualitatively and found that the floor crack rate controlled the stress distribution in the floor and the thickness of floor aquifuge played an important role in controlling the displacement and failure depth of the floor. Obviously, the mechanism of water inrush can be clarified by mastering the failure behavior in the floor aquifuge.

The research above studied the stress distribution [10–12, 17, 23], displacement change [10, 11, 21, 23], crack evolution [13, 14, 19, 23], and failure law [15, 16, 18, 20, 22] in the floor aquifuge. The achievements reach a consensus that (1) the essence of water inrush from the floor aquifuge is the result of the combined action of mining-induced stress and confined water pressure, (2) the stress variation and crack evolution in the floor may lead to water inrush, and (3) the thickness and lithology of the floor aquifuge are two important factors affecting the failure behavior of the floor. However, the above studies ignored the correlation between the distribution of stress and the propagation of cracks when

the floor aquifuge was bending, and the formation and propagation of cracks have not been described in-depth, so the bending failure characteristics and the induced water inrush behavior in the floor aquifuge need to be studied further.

To this end, this paper established a thin disc model, conducted the bending-seepage tests of different thicknesses and lithology under the coupled bending-seepage condition, calculated the deflection and stresses inside the thin disc gray sandstone and red sandstone, revealed the formation and propagation mechanism of the cracks in the thin disc rock with different thicknesses and lithology, and described the bending failure behavior in the floor aquifuge, as well as the bending-failure-induced water inrush behavior. This research is expected to provide references for the description of floor failure and the prevention of water inrush.

2. Simplified Model and Experimental Process

2.1. Simplified Model. With coal extraction continuing, the confined water pressure and the mining-induced stress become the force sources. Subject to their joint action, the floor aquifuge undergoes bending deformation. In the bending floor aquifuge, the cracks are formed, developed, and penetrated, and water flow changes from seepage to turbulence and rushes into the working face, which may cause water inrush disaster.

A simplified model is shown in Figure 1, established based on the following assumptions:

- (1) The floor aquifuge in practical engineering is assumed as a circular thin plate relative to the stratum; the self-weight of the thin disc rock sample is ignored.
- (2) Owing to the strength and stiffness of the surrounding rock mass that are far greater than those of the floor aquifuge, the constraint of the thin disc rock sample is peripheral clamping.
- (3) The floor aquifuge is assumed above the confined aquifer. The confined water pressure is regarded as a uniformly distributed pore pressure, q , distributed on the lower surface of the thin disc rock sample.
- (4) Excavation disturbances induce floor heave; the upward bending deformation is applied to the thin disc rock sample, which is realized by applying an upward concentrated force, P , on the lower surface of the thin disc rock sample by a conical indenter.

As shown in Figure 1(c), the peripheral clamping is equivalent to a force couple, M , and a force, $F/2\pi a$. a is the radius of the thin disc rock sample, F is a circumferential load applied by the Material Testing Machine, and a retaining ring is used to act on the annular upper surface of the thin disc rock sample.

2.2. Testing System. In order to simulate the heave and breakage of the floor aquifuge and realize the coupled bending deformation and water flow applied on the floor aquifuge, a testing system that can conduct the coupling bending-seepage test is designed and manufactured [3, 24]. It consists of an axial loading subsystem, a pore pressure loading and

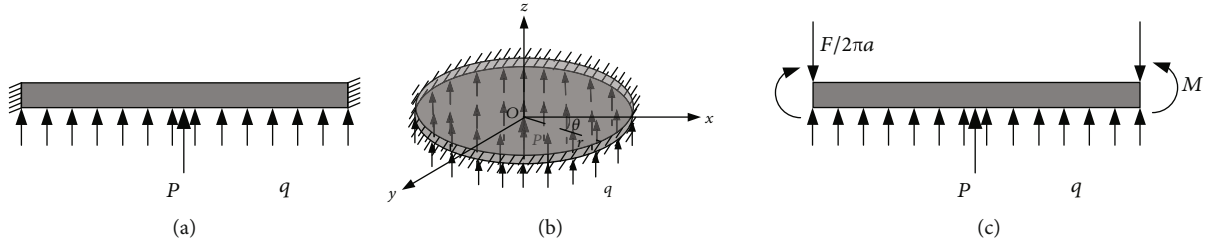


FIGURE 1: Simplified model for floor aquifuge.

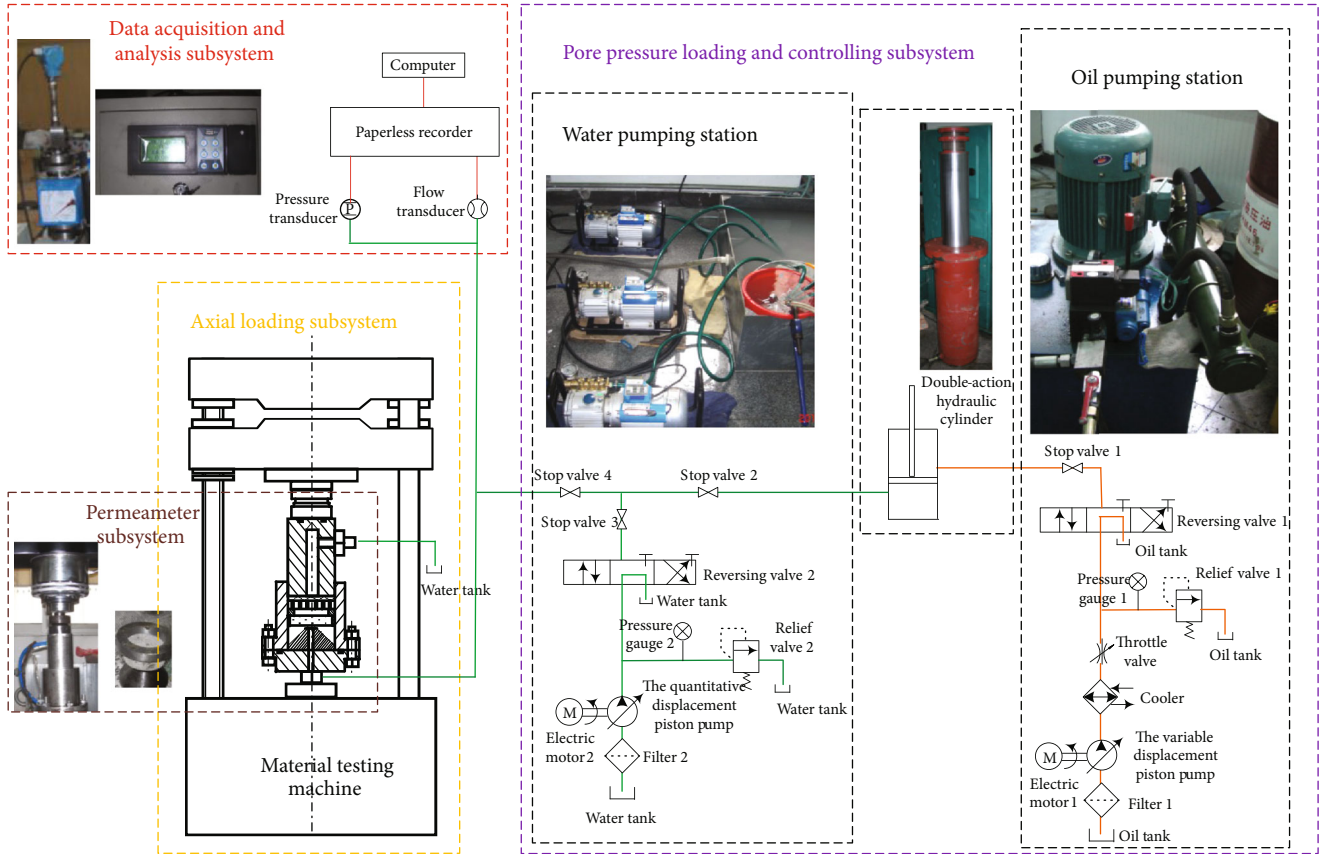


FIGURE 2: Testing system.

controlling subsystem, a permeameter subsystem, and a data acquisition and analysis subsystem. The overall design of the testing system is shown in Figure 2.

As the core of the testing system, the permeameter subsystem contains a bottom plate, a cylinder, a permeable piston, a conical indenter, a retaining ring, seals, etc., shown in Figure 3. The thin disc rock sample is fixed between the retaining ring and the conical indenter. It is critical to tightly seal the interspace between the outer boundary of the sample and the cylinder wall using high water materials and to ensure that the liquid only flows within the rock sample but not seeps out from surrounding voids before and during the loading process.

The test adopted the steady-state permeation method. Stable pore water pressure was provided by driving oil pressure in the pore pressure loading and controlling subsystem. Water flowed through the pressure transducer, flow trans-

ducer, and the inlet at the bottom plate, entered the conical indenter, and evenly distributed on the lower surface of the thin disc rock sample to simulate the action of the confined water pressure on the floor aquifuge. An axial load was applied onto the piston of the permeameter, then loaded on the upper surface of the thin disc rock sample through the retaining ring as circumferential load. Under the bidirectional actions of concentrated force from the conical indenter and circumferential load from the retaining ring, the rock sample underwent bending deformation, which was used to simulate the floor heave bending deformation of the floor aquifuge due to excavation disturbances.

2.3. Testing Scheme

2.3.1. Material Characterization and Sample Preparation. The floor aquifuge in Pan mine in Sichuan is taken as the

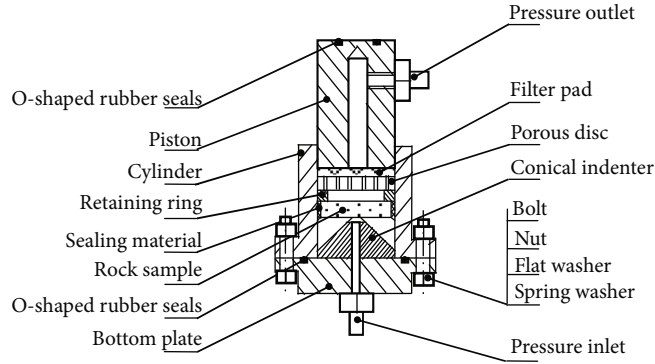


FIGURE 3: Schematic of the permeameter.

example in this paper, which is mainly gray sandstone and red sandstone. All samples were acquired from a single rock block to ensure their similar physical properties, respectively. The physical and mechanical properties are listed in Table 1.

Based on the simplified model of the floor aquifuge and the diameter of the permeameter cylinder, the rock sample was processed as a 50 mm diameter disc. According to the definition of the thin plate theory, the thickness-diameter ratio should be less than 1/5. Therefore, two thicknesses, 5 mm and 10 mm, are selected in this research.

Samples were examined before testing to exclude those with obvious macroscopic defects and to ensure the testing values free from the impacts of macrojoints and fissures. The structures of the selected thin disc rock samples were compact, and there was no visible natural microfissure. Then, thin disc rock samples were polished to keep the surface smooth at two ends.

Taking lithology and thickness as the influencing factors, four independent tests were carried out, marked GS05, GS10, RS05, and RS10. Three samples were tested in each independent test.

2.3.2. Testing Design. At the beginning of testing, water was injected into the permeameter to saturation at least half an hour. Then, the pore pressure was loaded, and the sealing performance of the system was timely checked. According to relevant geological data, the pore pressure was set as 2 MPa in this test. When the pore pressure was completely stable at 2 MPa, the rock sample was loaded by the axial loading subsystem in the displacement control mode at a loading rate of 0.5 mm/min till the rock sample failed.

In addition, the pore pressure q and water flow Q were simultaneously acquired from the beginning of loading; the load F and displacement u during bending deformation were real-time recorded.

Permeability, k , can be calculated by Darcy's law as below:

$$k = \frac{\mu v}{q/l\delta}, \quad (1)$$

where μ is the dynamic viscosity of water, v is the seepage speed calculated from $v = Q/\pi a^2$, q is the pore pressure, and δ is the thickness of the thin disc rock sample.

3. Experimental Results

3.1. Variation Characteristics of Load-Displacement Curves. Figure 4 shows the load-displacement ($F-u$) curves of the gray sandstone and red sandstone with two different thicknesses. They have similar variation characteristics, which can be divided into four stages $OA-AB-BC-CDE$, as shown in Figure 5.

The section of the OA segment is shorter and steeper. This section contains adaptive adjustment and elastic deformation of the thin disc structure under uniform water pressure and bending load. Obviously, the thin disc samples have low elastic deformation.

The AB segment is a line with a very small slope; the deformation increases significantly while the load-carrying capacity increases very small in this stage. The structure produces large plastic deformation, and microcracks in the disc germinate and develop; floor heave occurs in the AB section [16, 25, 26].

The BC section has a great slope. With the increase of deformation, the load increases sharply, and the bearing capacity of the thin disc structure is strengthened. In this stage, the crack propagation inside the thin disc changes qualitatively, microcracks develop and grow continuously, forming macrocracks, and the internal structure of the thin disc is damaged gradually. Although the thin disc structure is still in the overall state, the internal cracks penetrate rapidly. The bearing capacity of the thin disc structure reaches its peak value at point C , which is listed in Table 2. It presents that the thicker disc rock sample has a greater peak load, the peak value of red sandstone with the same thickness is larger than that of gray sandstone, and the displacement of gray sandstone is less than that of red sandstone.

After the peak value, CDE is the postfracture stage. In this stage, cracks intersect each other, under the action of splitting expansion of pore water pressure, the macrofracture surface is united and formed, and rock blocks slide along the fracture surface, which may cause water inrush [27, 28]. The bearing capacity of the sample decreases slowly with the increase of deformation in CD and then drops rapidly in DE , and the thin disc structure collapses till its bearing capacity loses completely. Generally, if the deformation and heave behavior of the floor have not been dealt with in time before the peak value in the project, it can be remedied in the CD section.

TABLE 1: Physical and mechanical properties of gray sandstone and red sandstone.

Lithology	Gray sandstone	Red sandstone
Uniaxial compressive strength (σ_c , MPa)	54.7	51.2
Tensile strength (σ_t , MPa)	5.02	4.71
Elastic modulus (E , GPa)	32.0	29.2
Poisson ratio (ν)	0.23	0.16
Density (ρ , kgm^{-3})	2473	2574
Internal friction angle (ϕ , $^\circ$)	47.8	43.0
Cohesion (C , MPa)	21.2	22.9

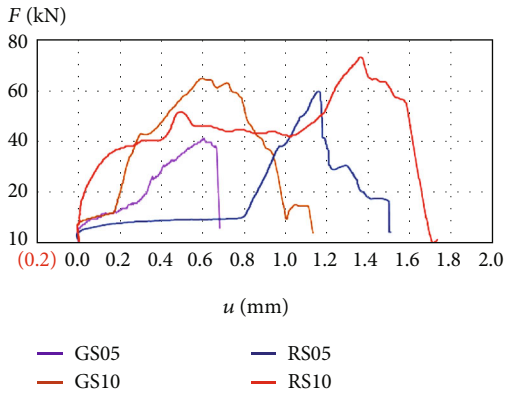


FIGURE 4: Load-displacement curves of four different sandstone samples.

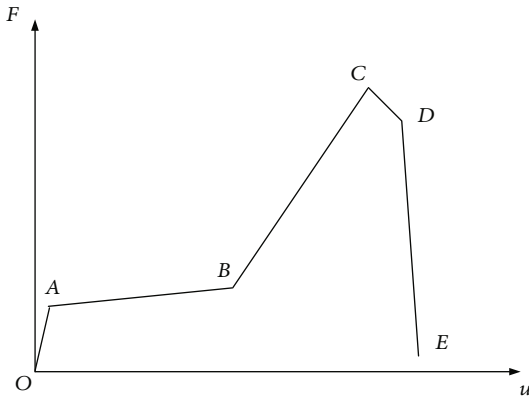


FIGURE 5: Four-stage dividing sketch of load-displacement curves.

Because the floor still has its bearing capacity, it is not too late to control the floor deformation and heave behavior by means of grouting. Mastering the characteristics of crack initiation and propagation can better guide grouting.

3.2. Time-Varying Characteristics of Load and Permeability.

Figure 6 shows the load-time ($F-t$) curves and permeability-time ($k-t$) curves of the gray sandstone and red sandstone with two different thicknesses.

The permeability of the intact thin disc rock sample is about 10^{-17} m^2 at the beginning of the experiments, which

TABLE 2: The peak values for different samples.

Sample number	GS05	GS10	RS05	RS10
Peak load (kN)	4.065	6.419	5.915	7.283
Displacement on the peak load (mm)	0.609	0.603	1.162	1.363

is consistent with the testing result of standard intact rock samples [29–37]. It increases rapidly after bending failure occurred several seconds, water flow changes from seepage to turbulence simultaneously, and then, water inrush may occur. In this process, permeability evolved from 10^{-17} m^2 up to 10^{-11} m^2 , increasing six orders of magnitude. Its evolution rule is obviously different from standard rock samples [32], in which permeability usually increases three to four orders of magnitude after the postpeak strength. Obviously, the permeability of the thin disc structure changes greatly with stronger mutation, because the stress distribution and crack evolution of the thin disc are different from that of the standard rock sample.

As shown in Figure 6, the peak permeability always lags the peak load, indicating that it still has time and opportunity to take measures to prevent water inrush disaster, which is consistent with the CD section in Figure 5. Table 3 lists the occurrence time of peak load and peak permeability, as well as the lagging time.

The sample GS05 experienced the longest time; this is because the sealing material between the outer boundary of the sample and the cylinder wall was compacted for a long time. The compression of the sealing material only prolongs the test time but does not affect the deformation measurement of the sample. Because of the difference in experimental operation, the peak load and permeability occurrence times of four samples cannot be compared separately. Only the lagging time can be analyzed; it shows that the lagging time of gray sandstone is longer than that of red sandstone. It is because the brittle behaviors of the thin disc in the postfracture stage are different, which relates to the crack propagation. The longer the lagging time is, the longer the time that can be used for water inrush prevention and control is, the more effective the water inrush risk can be reduced.

3.3. Bending Failure Pattern. Figure 7 shows the bending failure patterns of the four thin disc rock samples. The 5 mm thickness disc rock samples formed petal-shaped cracks after bending failure, as shown in Figures 7(a) and 7(c). For the 10 mm thickness disc samples, a cap block was cut out along a conical surface with an inclination about 45° , as shown in Figures 7(b) and 7(d), and petal-shaped cracks also appear in the cap block.

Obviously, when the thin disc rock samples are under the coupled bending-seepage condition, their failure behaviors belong to the problem of structural failure. It is related not only to material properties but also to the structural properties and external force characteristics. In order to analyze the bending failure behavior in-depth, the stress distribution and crack evolution in the thin disc rock structures should be studied further.

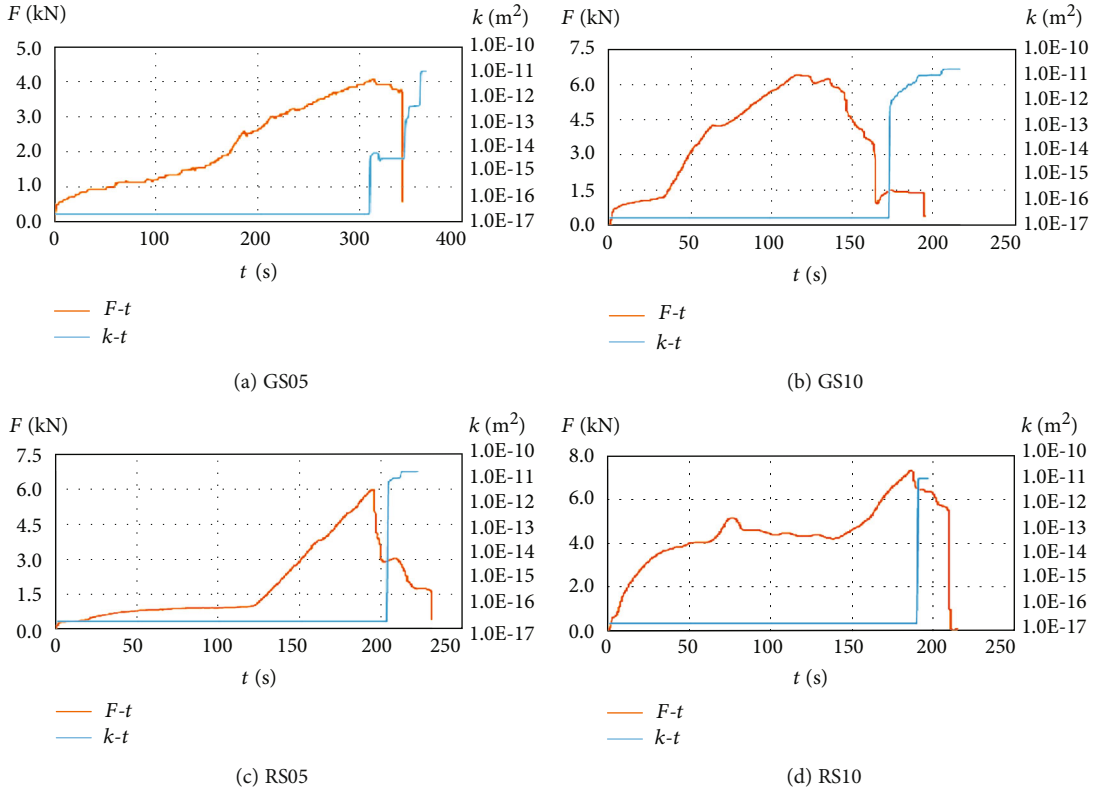


FIGURE 6: Time-varying characteristics of load and permeability.

TABLE 3: The lagging times for different samples.

Sample number	GS05	GS10	RS05	RS10
Time on the peak load occurrence (s)	310	118	193	186
Time on the peak permeability occurrence (s)	356	174	203	190
Lagging time (s)	46	56	10	4

4. Discussion

The hard rock floor aquifuge is mainly a local plastic failure, and the stability coefficient is generally high; it can be solved with the elastic solution [38].

4.1. Deflection Calculation and Distribution in Thin Disc Rock Samples. Based on the simplified model in Figure 1(c), circumferential load, F , and pore pressure, q , can be measured timely during the test; the concentrated force, P , and the force couple, M , can be calculated as

$$P = F - q\pi a^2, \quad (2)$$

$$M = \frac{a}{2} \left(\frac{F}{2\pi} - qa \right).$$

In polar coordinates, as shown in Figure 1, the transverse loads on the thin disc rock sample are symmetrical around the z -axis, which is a vertical plate face up. The deflection, w , of the elastic thin disc is also symmetrical around the z

-axis, and it is a function of r but does not change with θ . When the thin disc rock sample bends axial-symmetrically, the differential equation of the deflection is

$$\left(\frac{d^2}{dr^2} + \frac{1}{r} \frac{d}{dr} \right) \left(\frac{d^2 w}{dr^2} + \frac{1}{r} \frac{dw}{dr} \right) = \frac{q}{D}, \quad (3)$$

where $D = E\delta^3/12(1 - \nu^2)$ is the bending stiffness of thin disc and E and ν are elastic modulus and Poisson's ratio, respectively.

A semi-inverse method is used to solve the differential Equation (3); the general solution for the deflection of the thin disc rock sample is

$$w = \frac{q}{64D} r^4 + A_1 r^2 + A_2 r^2 \ln \frac{r}{a} + A_3 \ln \frac{r}{a} + A_4, \quad (4)$$

where $A_1, A_2, A_3,$ and A_4 are coefficients, determined by the boundary conditions.

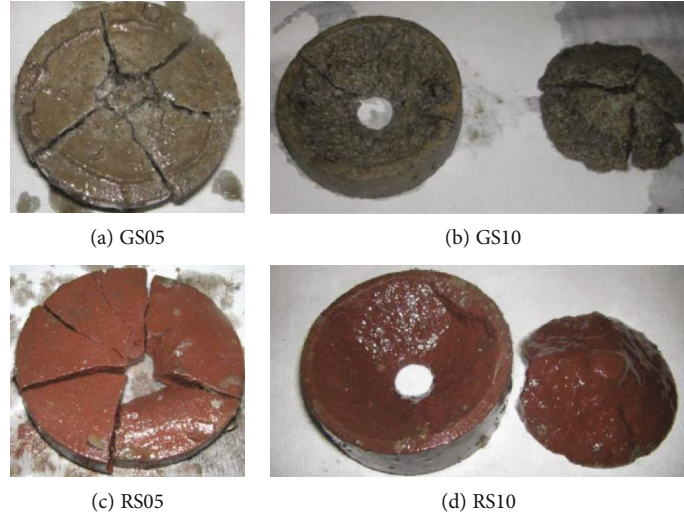


FIGURE 7: Bending failure patterns.

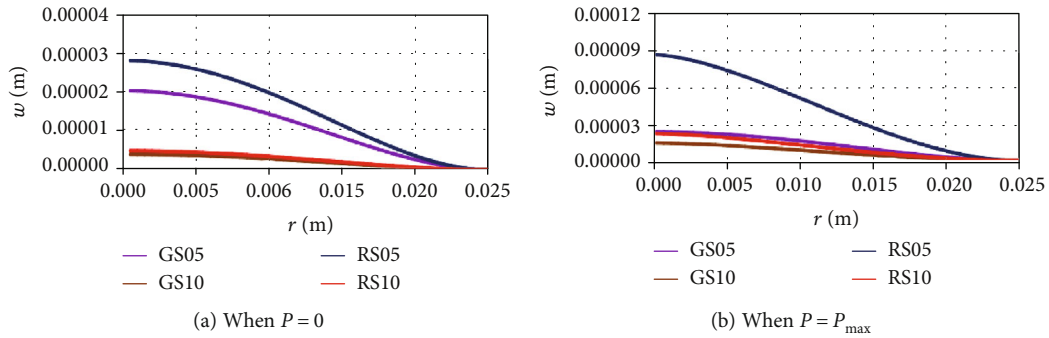


FIGURE 8: Deflection distribution curves.

Based on the boundary conditions in the mechanical model, the deflection is expressed as

$$w = \frac{q}{64D} (a^2 - r^2)^2 + \frac{P}{8\pi D} \left[\frac{1}{2} (a^2 - r^2) + r^2 \ln \frac{r}{a} \right]. \quad (5)$$

Applying Equation (5), the deflection distribution inside the thin disc rock sample along the radius direction at different loading times could be obtained.

The deflection distributions along the radius direction when $P = 0$ are shown in Figure 8(a). It shows that when the thin disc rock sample is only under the action of pore pressure, the maximum deflections of samples GS05, GS10, RS05, and RS10 are 0.0191, 0.00374, 0.0264, and 0.0046 mm, respectively. It can be inferred that the thinner the floor aquifuge, the larger the deformation caused by the confined water pressure.

Figure 8(b) shows the deflection distributions at the time of peak load appearance, $P = P_{max}$, the maximum deflections of samples GS05, GS10, RS05, and RS10 are 0.0218, 0.0132, 0.0797, and 0.0203 mm, respectively. Mining disturbance induces further bending deformation of the floor. Under the combined action of mining-induced stress and confined

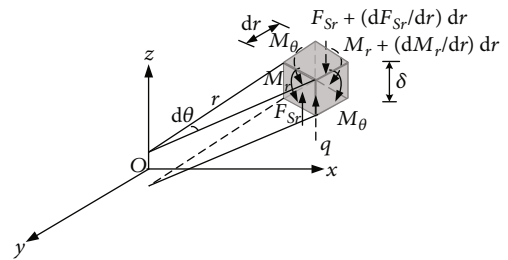


FIGURE 9: Internal force distribution of microelement in the thin disc rock sample.

water pressure, the deflection of the floor aquifuge is 1.2 to 4 times of that under the alone confined water pressure.

It is worth noting that these deflections are the elastic ultimate load-bearing displacements. The displacements are different from the values in Table 2, which includes not only the deformation of the thin disc rock sample but also the deformation of the sealing material and the displacement of the sample after being fractured.

The maximum deflections both occur at the center of the thin disc rock sample when $P = 0$ and $P = P_{max}$; as a result, the center of the disc is the dangerous position that the disc may break from here.

Sandstone is a typical brittle material at room temperature; its elastic deformation is weak. The bending failure of the thin disc rock sample mainly results from the strength, but not the stiffness. Therefore, in addition to analyzing the deformation in the disc, stress distribution should be emphasized.

4.2. *Stress Calculation and Distribution in Thin Disc Rock Samples.* As Figure 9 shows, through the analysis of the microelement in the thin disc rock sample, the internal force equation of the element is calculated as follows:

$$\left\{ \begin{array}{l} M_r = -D \left(\frac{d^2 w}{dr^2} + \frac{v}{r} \frac{dw}{dr} \right) = -\frac{P}{4\pi} \left(1 + \ln \frac{r}{a} + v \ln \frac{r}{a} \right) + \frac{q}{16} [(1+v)(a^2 - r^2) - 2r^2], \\ M_\theta = -D \left(\frac{1}{r} \frac{dw}{dr} + v \frac{d^2 w}{dr^2} \right) = -\frac{P}{4\pi} \left(v + \ln \frac{r}{a} + v \ln \frac{r}{a} \right) + \frac{q}{16} [v(a^2 - 3r^2) + (a^2 - r^2)], \\ M_{r\theta} = 0, \\ F_{Sr} = -D \left(\frac{d^3 w}{dr^3} + \frac{1}{r} \frac{d^2 w}{dr^2} \right) = -\frac{P}{4\pi r} \left(2 + \ln \frac{r}{a} \right) + \frac{q}{16r} (a^2 - 9r^2), \\ F_{S\theta} = 0. \end{array} \right. \quad (6)$$

Using Equation (6), the distribution of internal forces along the radius direction can be solved and drawn, as shown in Figure 10.

As seen in Figure 10(a), the reverse bending point of M_r is about 0.01 m away from the center of the disc. When $r < 0.01$ m, the upper surface of the disc is in tension and the lower surface is in compression, and when $r > 0.01$ m, it is just the opposite. All the samples except for GS05 have the maximum value of M_r at the center, where it is the most dangerous cross-section. Particularly, the maximum value of M_r occurs at the edge in the sample of GS05. The value in the center is slightly less than that in the edge; both the center and edge cross-sections are dangerous sections.

It can be seen from Figure 10(b) that the M_θ distribution curves are similar to the distribution curves of M_r , but the

reverse bending point is different, which is about 0.022 m away from the center. When $r < 0.022$ m, the upper surface of the disc rock sample is in tension and the lower surface is in compression, and when $r > 0.022$ m, the upper surface is compressed and the lower surface is tensed. The maximum value of M_θ occurs at the center, so the central cross-section is the most dangerous point.

It can be seen from Figure 10(c) that when $r \approx 0.004$ m, the shear force F_{Sr} in the disc changes from positive to negative. The maximum value of F_{Sr} occurs at the center of the disc, so it is the most dangerous cross-section; the direction of the shear force at the dangerous section is downward.

From Equations (5) and (6), the stress at every cross-section of the thin disc rock sample can be calculated as follows:

$$\left\{ \begin{array}{l} \sigma_r = -\frac{Ez}{1-\nu^2} \left(\frac{d^2 w}{dr^2} + \frac{v}{r} \frac{dw}{dr} \right) = \frac{12M_r}{\delta^3} z = -\frac{3}{\delta^3} \left\{ \frac{P}{\pi} \left(1 + \ln \frac{r}{a} + v \ln \frac{r}{a} \right) - \frac{q}{4} [(1+v)(a^2 - r^2) - 2r^2] \right\} z, \\ \sigma_\theta = -\frac{Ez}{1-\nu^2} \left(\frac{1}{r} \frac{dw}{dr} + v \frac{d^2 w}{dr^2} \right) = \frac{12M_\theta}{\delta^3} z = -\frac{3}{\delta^3} \left\{ \frac{P}{\pi} \left(v + \ln \frac{r}{a} + v \ln \frac{r}{a} \right) - \frac{q}{4} [v(a^2 - 3r^2) + (a^2 - r^2)] \right\} z, \\ \tau_{r\theta} = \tau_{\theta r} = 0, \\ \tau_{rz} = \frac{6F_{Sr}}{\delta^3} \left(\frac{\delta^2}{4} - z^2 \right) = -\frac{3}{\delta^3} \left[\frac{P}{2\pi r} \left(2 + \ln \frac{r}{a} \right) - \frac{q}{8r} (a^2 - 9r^2) \right] \left(\frac{\delta^2}{4} - z^2 \right), \\ \tau_{\theta z} = \tau_{z\theta} = 0. \end{array} \right. \quad (7)$$

Using Equation (7), the stress distribution at the central dangerous cross-section along the direction of the disc thickness (i.e., the z -axis direction) is shown in Figure 11(a). For the sample of GS05, the edge cross-section is dangerous

too; its stress distribution along the direction of the disc thickness is shown in Figure 11(b).

As seen in Figure 11, both σ_r and σ_θ are linearly distributed along the thickness direction, forming the bending

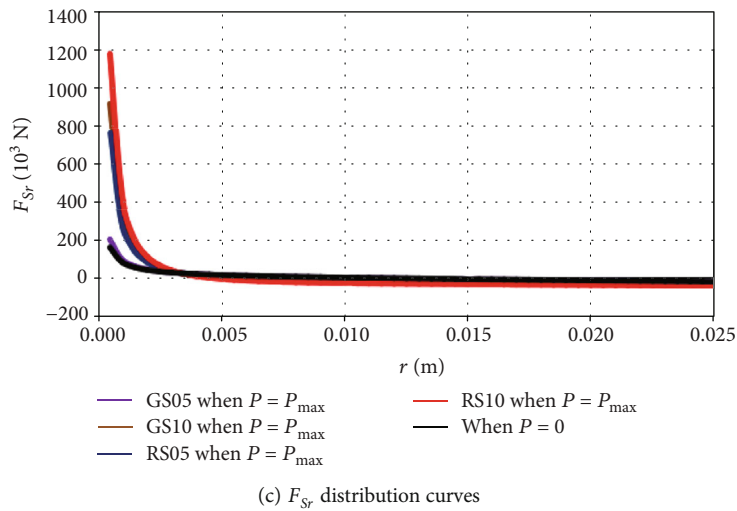
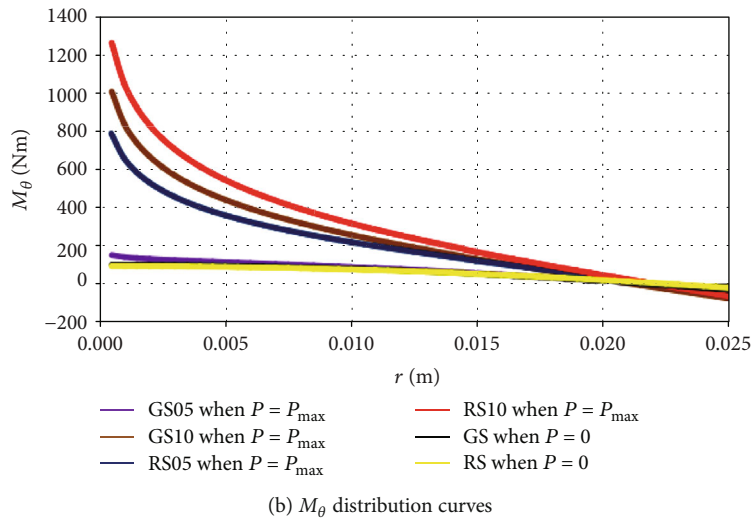
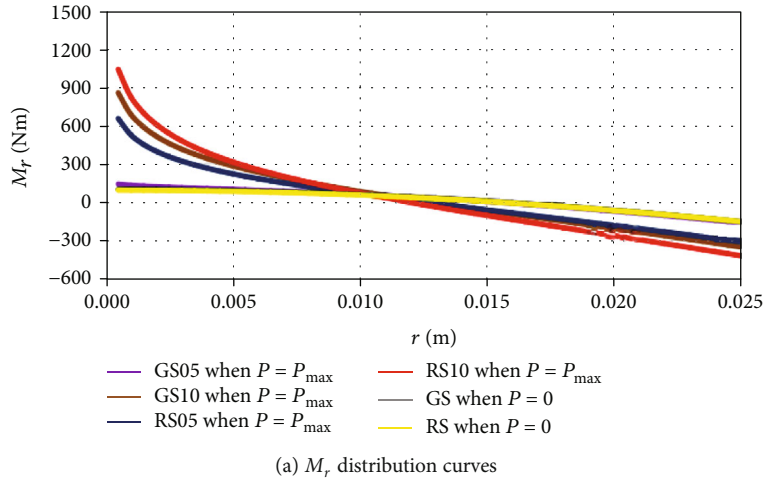


FIGURE 10: Internal force distribution curves.

moments M_r and M_θ , respectively. The maximum values of σ_r and σ_θ occur at the upper and lower points of the dangerous cross-sections. τ_{rz} is parabolically distributed along the thickness direction, constituting the shear force F_{Sr} . The maximum value τ_{rz} occurs at the neutral point of the dangerous cross-section.

Summing up, the location and stresses of the dangerous points in the thin disc rock samples can be calculated and are shown in Table 4.

As illustrated in Table 4, for sample GS05, $\sigma_{r \max}$ at the upper and lower points of the edge cross-section is very large, and the thin disc rock sample may be damaged from the

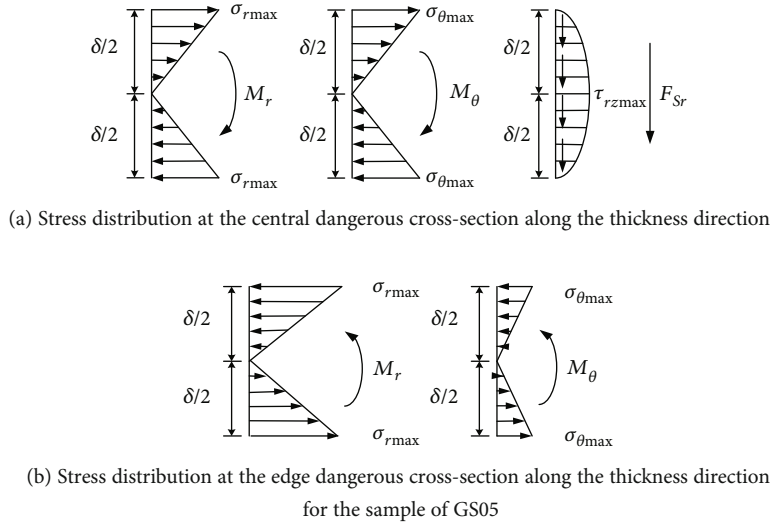


FIGURE 11: Stress distribution at the dangerous cross-section.

TABLE 4: The location and stresses of the dangerous points in the thin disc rock samples.

Samples	Location/stresses
GS05	The upper and lower points of the central cross-section/ $\sigma_{r \max} = 22.3$ MPa
	The upper and lower points of the edge cross-section/ $\sigma_{r \max} = 27.0$ MPa
	The upper and lower points of the central cross-section/ $\sigma_{\theta \max} = 23.7$ MPa
	The neutral point of the central cross-section/ $\tau_{rz \max} = 48.8$ MPa
GS10	The upper and lower points of the central cross-section/ $\sigma_{r \max} = 46.4$ MPa
	The upper and lower points of the central cross-section/ $\sigma_{\theta \max} = 54.7$ MPa
	The neutral point of the central cross-section/ $\tau_{rz \max} = 130.5$ MPa
RS05	The upper and lower points of the central cross-section/ $\sigma_{r \max} = 120.2$ MPa
	The upper and lower points of the central cross-section/ $\sigma_{\theta \max} = 144.8$ MPa
	The neutral point of the central cross-section/ $\tau_{rz \max} = 199.9$ MPa
RS10	The upper and lower points of the central cross-section/ $\sigma_{r \max} = 59.8$ MPa
	The upper and lower points of the central cross-section/ $\sigma_{\theta \max} = 72.7$ MPa
	The neutral point of the central cross-section/ $\tau_{rz \max} = 173.3$ MPa

edge. For samples GS05, GS10, RS05, and RS10, both $\sigma_{r \max}$ and $\sigma_{\theta \max}$ occur at the upper and lower points of the central cross-section, and $\tau_{rz \max}$ occurs at the neutral point of the central cross-section. $\sigma_{\theta \max}$ is larger than $\sigma_{r \max}$ at the upper and lower points of the central cross-section, and the thin disc rock sample may be damaged mainly by $\sigma_{\theta \max}$ from the center.

It also shows that the sample RS05 has the largest $\sigma_{r \max}$, $\sigma_{\theta \max}$, and $\tau_{rz \max}$, followed by RS10, GS10, and GS05. The thin disc red sandstone has higher stress than the gray one. The greater the stress is, the faster the cracks develop in the thin disc, and the shorter the time of water inrush passage through. This is consistent with the experimental phenomenon that the lagging time of red sandstone is shorter than that of gray sandstone in Table 3.

The stress state of dangerous points in the thin disc rock samples can be described as shown in Figure 12.

Figure 13 and Table 5 show the specific locations of the dangerous points on the thin discs and the corresponding stress states.

Based on the description for the location and stress state of the dangerous points on the thin discs, these dangerous points are in the biaxial tensile/compressive stress state, the uniaxial tensile/compressive stress state, and the pure shear stress state, respectively. The structural failure of the thin disc rock sample is mainly due to the stress reaching or exceeding its strength limit, and therefore, the strength condition should be established to reveal the failure mechanism.

4.3. Crack Initiation and Propagation in Thin Disc Rock Samples. Sandstone is a kind of brittle material so that we use the Maximum Tensile Stress Theory and Mohr-Coulomb Strength Theory to analyze the bending failure behavior.

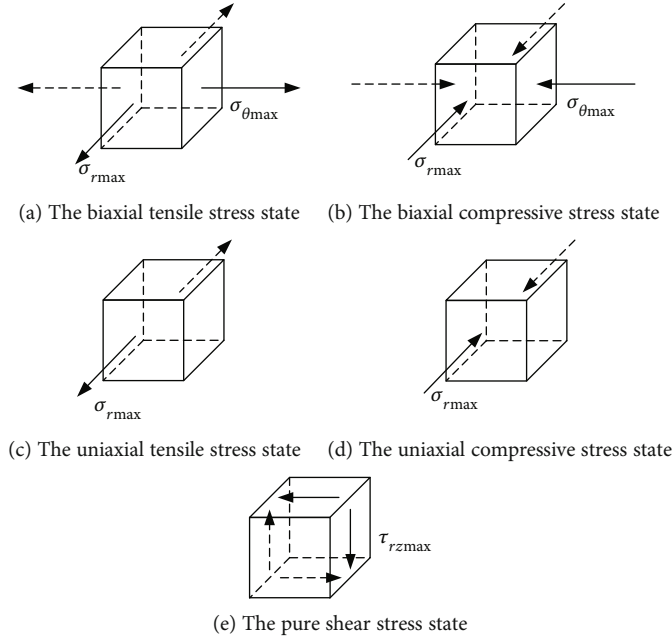


FIGURE 12: Stress state of dangerous points.

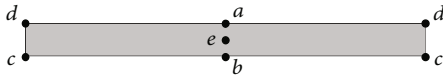


FIGURE 13: The location of the danger points on thin discs.

4.3.1. *The Cause of the Crack Initiation.* Combining Figures 12 and 13, the upper points of the central cross-section in the four samples are the dangerous points. They are in the biaxial tensile stress state, and the principal stresses of the dangerous points are $\sigma_{\theta \max}$, $\sigma_{r \max}$, and 0. According to the Maximum Tensile Stress Theory, when bending failure occurs, the maximum tangential tensile stress reaches and exceeds the allowable tensile stress. So, the upper points of the central cross-section in the disc, i.e., the points a in Figure 13, are the points of crack initiation, and the disc rock sample is tensed at these points along the tangential direction.

Meanwhile, the lower points of the edge cross-section in sample GS05 are also the dangerous points. They are in the uniaxial tensile stress state, and the principal stresses of the dangerous points are $\sigma_{r \max}$, 0, and 0. When bending failure occurs in sample GS05, the maximum radial tensile stress reaches and exceeds the allowable tensile stress. Therefore, for the sample GS05, besides the upper points of the central cross-section, the lower points of the edge cross-section, i.e., the points c in Figure 13, are the points of crack initiation, too. That is to say, the sample GS05 is tensed simultaneously at the location a along the tangential direction and at location c along the radial direction.

In addition, the neutral points of the central cross-section in the four thin disc rock samples are also dangerous points, which are in the pure shear stress state, and the principal stresses of the dangerous points are $\tau_{rz \max}$, 0, and $-\tau_{rz \max}$.

According to the Mohr-Coulomb Strength Theory, it is obviously obtained that shear is the main cause of the bending failure. It shows that the four kinds of discs also suffer from shear failure from the neutral points of the central cross-section, i.e., the points e in Figure 13; this location is also the points of crack initiation.

In summary, the crack initiation points for the samples GS10, RS05, and RS10 are a and e as shown in Figure 13; the crack develops resulting from the upper point a of the central cross-section which is tensed along the tangential direction and the neutral point e of the central cross-section which is sheared. The crack initiation points for sample GS05 are a , c , and e in Figure 13; they are caused by the upper points a of the central cross-section and the lower points c of the edge cross-section that are tensed simultaneously along the tangential direction at the center and radial direction at the edge and the neutral points e of the central cross-section that is sheared. Briefly, tension-shear failure is the main reason for crack initiation.

4.3.2. *The Cause of Crack Propagation.* As seen in Table 4, there are two dangerous locations in sample GS05. One is at the disc center, where $\tau_{rz \max}$ and $\sigma_{\theta \max}$ play major roles, and $\tau_{rz \max}$ is about 2.06 times of $\sigma_{\theta \max}$. The other is at the lower points of the disc edge, which is the uniaxial tensile stress state dominated by $\sigma_{r \max}$. Crack propagation in this disc is caused by the tangential tensile stress and shear stress at the center and the radial tensile stress at the edge. The cracks are developed oppositely by the tension-shear failure at the center and tension failure at the edge, producing the petal-shaped cracks shown in Figure 14(a).

For sample RS05, the cracks propagate from the center, where $\tau_{rz \max}$ is only 1.38 times $\sigma_{\theta \max}$. Crack propagation

TABLE 5: The details of the stress state at the dangerous points.

Stress state	Location of the dangerous points
<i>a</i> : the biaxial tensile stress state	The upper points of the central cross-section in samples of GS05, GS10, RS05, and RS10.
<i>b</i> : the biaxial compressive stress state	The lower points of the central cross-section in samples of GS05, GS10, RS05, and RS10.
<i>c</i> : the uniaxial tensile stress state	The lower points of the edge cross-section in the sample of GS05.
<i>d</i> : the uniaxial compressive stress state	The upper points of the edge cross-section in the sample of GS05.
<i>e</i> : the pure shear stress state	The neutral points of the central cross-section in samples of GS05, GS10, RS05, and RS10.

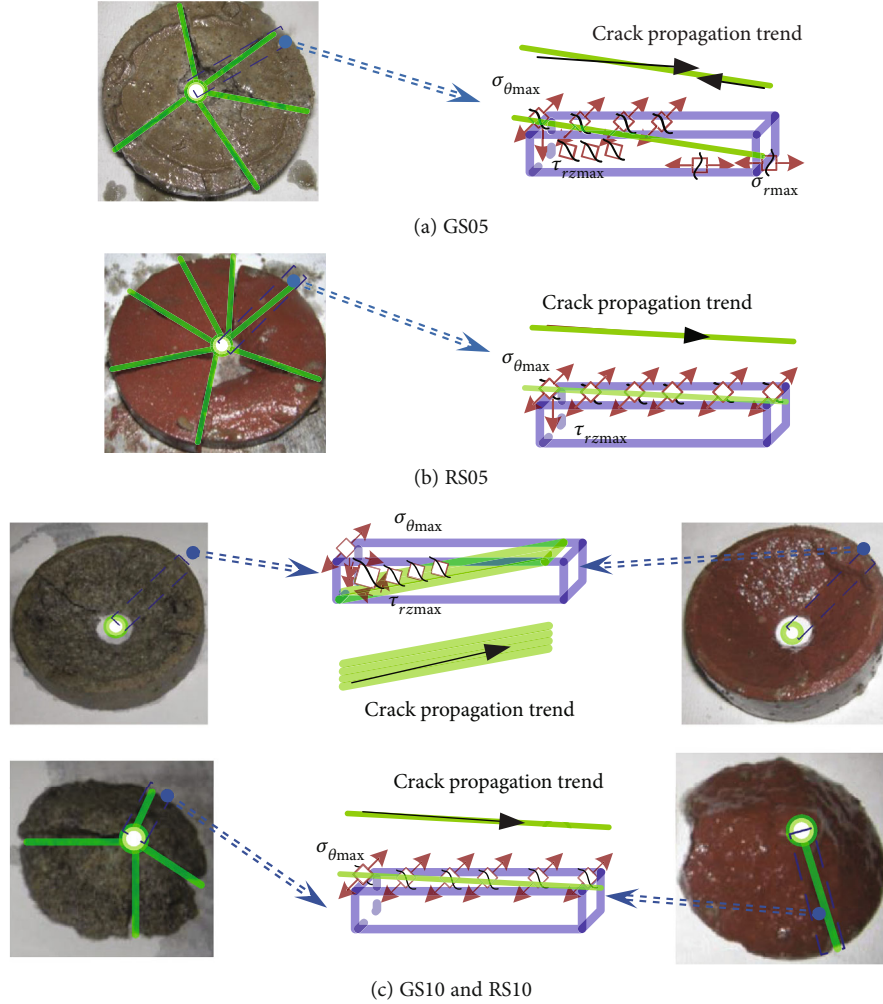


FIGURE 14: The mechanism of crack propagation.

of this disc is mainly due to the tension failure, which is perpendicular to the radius direction and caused by the tangential tensile stress. The cracks develop from the center to the edge; petal-shaped cracks are formed, as shown in Figure 14(b).

For samples GS10 and RS10, $\tau_{rz \max}$ is about 2.38 times $\sigma_{\theta \max}$. Due to the thicker thickness, crack propagation in the disc is mainly caused by shear failure; meanwhile, the tension failure plays a secondary role. As shown in Figure 14(c), the cracks rise along a conical surface with an inclination about 45° from the center to the edge, and the disc rock sample is sheared into two pieces. The cap block is accompanied

by petals with tension cracks caused by the tangential tensile stress.

4.4. Bending-Failure-Induced Water Inrush Behavior in the Floor Aquifuge. During mining activities, the floor aquifuge is bending; the deflection and stress are changing timely. It is safe when the deflection and stress are far less than the allowable values. The cracks initiate and propagate with the increase of stress, and the confined water pressure split and expand the cracks continuously. When bending failure occurs, the maximum tensile stress exceeds the allowable values; the cracks propagate to penetrate.

Although the occurrence of bending failure is really very dangerous, the water inrush disaster does not happen immediately, because of the water inrush lagging. There is a short time to take measures to grout the cracks and to prevent the water inrush accident. According to the crack initiation and propagation (Figure 14), the grouting should be at the center or the edge of the floor aquifuge along the crack propagation trend lines.

5. Conclusions

A simplified thin disc model was introduced to study the bending failure of the floor aquifuge. Based on a self-designed experimental system, thin disc gray and red sandstone samples were tested under coupled bending-seepage condition to study the failure behavior. The failure behavior in thin disc sandstone with two different lithologies and thicknesses were analyzed. The main conclusions can be drawn as follows:

- (1) The failure process of thin disc sandstone can be divided into four stages: adaptive adjustment and elastic deformation stage, plastic deformation and microcrack development stage, bearing capacity strengthening and macrocrack formation stage, and postfracture stage, of which water inrush disaster occurs at the postfracture stage.
- (2) The permeability changes from 10^{-17} m^2 to 10^{-11} m^2 in the thin disc structure, and the sharp increase leads to more sudden and intense water inrush. The peak permeability always lags the peak load, and the lagging time of water inrush in gray sandstone is longer than that in red sandstone owing to the difference of crack propagation.
- (3) The crack initiation point occurred at the center because of the tangential tensile stress and shear stress. The crack propagation is related to disc thickness and lithology.
- (4) Water inrush accident occurs after the bending failure in the floor aquifuge. It is an opportune moment to grout along the crack propagation trend lines to prevent the water inrush disasters.

Abbreviations

a :	Radius of the thin disc rock sample (L)
A_1, A_2, A_3, A_4 :	Coefficients (-)
C :	Cohesion ($\text{ML}^{-1}\text{T}^{-2}$)
D :	Bending stiffness of thin disc (ML^2T^{-2})
E :	Elastic modulus ($\text{ML}^{-1}\text{T}^{-2}$)
F :	Circumferential load (MLT^{-2})
$F_{Sr}, F_{S\theta}$:	Shearing internal forces (MLT^{-2})
k :	Permeability (L^2)
M :	Force couple (ML^2T^{-2})
$M_r, M_{r\theta}, M_\theta$:	Internal force couples (ML^2T^{-2})
P :	Concentrated force (MLT^{-2})
P_{\max} :	Peak load (MLT^{-2})

q :	Confined water pressure/pore pressure ($\text{ML}^{-1}\text{T}^{-2}$)
Q :	Water flow (L^3T^{-1})
r :	Radial direction in polar coordinates (-)
t :	Testing time (T)
u :	Displacement (L)
v :	Seepage speed (LT^{-1})
w :	Deflection (L)
z :	Symmetrical axis (-)
δ :	Thickness of the disc (L)
θ :	Tangential direction in polar coordinates (-)
μ :	Dynamic viscosity of water ($\text{ML}^{-1}\text{T}^{-1}$)
ν :	Poisson ratio (-)
ρ :	Density (ML^{-3})
σ_c :	Uniaxial compressive strength ($\text{ML}^{-1}\text{T}^{-2}$)
σ_r :	Radial stress ($\text{ML}^{-1}\text{T}^{-2}$)
$\sigma_{r \max}$:	Maximum radial stress ($\text{ML}^{-1}\text{T}^{-2}$)
σ_t :	Tensile strength ($\text{ML}^{-1}\text{T}^{-2}$)
σ_θ :	Tangential stress ($\text{ML}^{-1}\text{T}^{-2}$)
$\sigma_{\theta \max}$:	Maximum tangential stress ($\text{ML}^{-1}\text{T}^{-2}$)
$\tau_{rz}, \tau_{r\theta}, \tau_{\theta z}$:	Shear stresses ($\text{ML}^{-1}\text{T}^{-2}$)
$\tau_{rz \max}$:	Maximum shear stress ($\text{ML}^{-1}\text{T}^{-2}$)
ϕ :	Internal friction angle (-).

Data Availability

The data used to support the findings of this study are available from the corresponding author upon request.

Conflicts of Interest

The authors declare that they have no conflict of interest.

Acknowledgments

The authors gratefully acknowledge the support provided by the National Natural Science Fund (11502229), the Natural Science Foundation of Jiangsu Province of China (BK20160433), the Program of Yellow Sea Elite in Yancheng Institute of Technology (2019), the Program of Outstanding Young Scholars in Yancheng Institute of Technology (2014), the Program of Yellow Sea Team in Yancheng Institute of Technology (2019), and the Program of innovative training program for College Students in Yancheng Institute of Technology (2020).

References

- [1] J. Wang and H. D. Park, "Coal mining above a confined aquifer," *International Journal of Rock Mechanics and Mining Sciences*, vol. 40, no. 4, pp. 537–551, 2003.
- [2] J. Zhang and B. Shen, "Coal mining under aquifers in China: a case study," *International Journal of Rock Mechanics and Mining Sciences*, vol. 41, no. 4, pp. 629–639, 2004.
- [3] L. Wang, Z. Chen, H. Kong, and H. Shen, "Effects of pore pressure on permeability of sandstone during bending deformation," *International Journal of Rock Mechanics and Mining Sciences*, vol. 70, pp. 26–32, 2014.
- [4] D. Ma, J. Wang, X. Cai et al., "Effects of height/diameter ratio on failure and damage properties of granite under coupled bending and splitting deformation," *Engineering Fracture Mechanics*, vol. 220, article 106640, 2019.

- [5] L. Shi, *Study of the Water-Inrush Mechanism and Prediction of the Water-Resisting Floor*, Shandong University of Science and Technology, Taian, China, 1999.
- [6] Z. Wang and H. Liu, *Coal Mining above the Confined Aquifer*, China Coal Industry Publishing House, Beijing, China, 1993.
- [7] M. Qian, X. Miao, and J. Xu, *Theory of Key Stratum in Ground Control*, University of Mining and Technology Press, Xuzhou, China, 2003.
- [8] J. Zhang and Y. Zhang, *Seepage in Rock Fissures and Water-Inrush from the Floor of the Coal Seam*, Geology Press, Beijing, China, 1997.
- [9] S. Peng and J. Wang, *Safe Coal Mining above Confined Aquifers*, Coal Industry Publishing House, Beijing, China, 2001.
- [10] P. Gong, Y. Hu, Y. Zhao, and D. Yang, "Three-dimensional simulation study on law of deformation and breakage of coal floor on mining above aquifer," *Chinese Journal of Rock Mechanics and Engineering*, vol. 24, no. 23, pp. 4396–4402, 2005.
- [11] Y. Hu, Y. Zhao, and D. Yang, "Simulation theory and method of 3D solid-liquid coupling," *Journal of Liaoning Technical University*, vol. 26, no. 2, pp. 204–206, 2007.
- [12] Z. Li, S. Zhang, and F. Du, "Novel experimental model to investigate fluid-solid coupling in coal seam floor for water inrush," *Technical Gazette*, vol. 25, no. 1, pp. 216–223, 2018.
- [13] J. Chen, L. Yin, W. Sun, C. Lu, S. Zhang, and X. Sun, "Development and application for new solid-fluid coupling similar material of deep floor aquifuge," *Chinese Journal of Rock Mechanics and Engineering*, vol. 34, Supplement 2, pp. 3956–3964, 2015.
- [14] Q. Kang, W. Zhang, P. Han, and D. Zhang, "Experimental study of mine-induced underlying strata failure regularity in three dimensional stress condition," *Chinese Journal of Underground Space and Engineering*, vol. 13, no. 3, pp. 612–618, 2017.
- [15] S. Liu, W. Liu, and J. Shen, "Stress evolution law and failure characteristics of mining floor rock mass above confined water," *KSCE Journal of Civil Engineering*, vol. 21, no. 7, pp. 2665–2672, 2017.
- [16] X. Hua, M. Yang, Q. Liu, and P. Yang, "Model test on evolution mechanism of floor heave in gob-side retaining entry of deep mine," *Journal of Mining and Safety Engineering*, vol. 35, no. 1, pp. 1–9, 2018.
- [17] X. Miao, R. Chen, and H. Bai, "Fundamental concepts and mechanical analysis of water-resisting key strata in water-preserved mining," *Journal of China Coal Society*, vol. 32, no. 6, pp. 561–564, 2007.
- [18] J. Sun and L. Wang, "Instability mechanics criterion of inclined water-resisting key strata in coal seam floor," *Journal of China Coal Society*, vol. 39, no. 11, pp. 2276–2285, 2014.
- [19] Y. Gao, S. Liu, B. Lyu, and K. Li, "Mechanism study of floor water inrush around mining field based on micro-crack extension," *Journal of Mining and Safety Engineering*, vol. 33, no. 4, pp. 624–629, 2016.
- [20] S. Wang, K. Zhang, J. Jiang, J. Xia, and G. Zhu, "Damage and control mechanism of thick and hard floor of large chamber in deep mines," *Chinese Journal of Geotechnical Engineering*, vol. 38, no. 7, pp. 1316–1323, 2016.
- [21] W. Guo, J. Zhao, L. Yin, and D. Kong, "Simulating research on pressure distribution of floor pore water based on fluid-solid coupling," *Arabian Journal of Geosciences*, vol. 10, no. 1, 2017.
- [22] X. Pang, *Calculation and analysis of the failure depth of the structure bottom*, Shandong University of Science and Technology, Qindao, China, 2017.
- [23] X. Xie, *Study on floor water inrush mechanism and its application in grouting reinforcement working face under high water pressure and large mining height*, China University of Mining and Technology, Beijing, China, 2018.
- [24] X. Miao, Z. Chen, S. Li, and Y. Liu, "A Permeation Testing Device for Shear Rock Samples," 2011, China Patent 201110046283.X.
- [25] S. Li, *Study on the mechanism and control of floor heave of soft rock roadway in Gequan mine*, Central South University, Changsha, China, 2004.
- [26] F. Zhang, *The research on space-time evolution of confined water in mining coal floor fractures*, Anhui University of Science and Technology, Huainan, China, 2014.
- [27] L. Shi, "The mechanical analysis of water-inrush from mining floor," *Coal Geology & Exploration*, vol. 5, pp. 37–39, 1998.
- [28] S. Li, K. Wang, L. Li, Z. Zhou, S. Shi, and S. Liu, "Mechanical mechanism and development trend of water-inrush disasters in karst tunnels," *Chinese Journal of Theoretical and Applied Mechanics*, vol. 49, no. 1, pp. 22–30, 2017.
- [29] J. Heiland, "Permeability of triaxially compressed sandstone: influence of deformation and strain-rate on permeability," *Pure and Applied Geophysics*, vol. 160, no. 5, pp. 889–908, 2003.
- [30] S. I. Mayr, H. Burkhardt, Y. Popov, and A. Wittmann, "Estimation of hydraulic permeability considering the micro morphology of rocks of the borehole YAXCOPOIL-1 (impact crater Chicxulub, Mexico)," *International Journal of Earth Sciences*, vol. 97, no. 2, pp. 385–399, 2008.
- [31] J. E. Elkhoury, A. Niemeijer, E. E. Brodsky, and C. Marone, "Laboratory observations of permeability enhancement by fluid pressure oscillation of in situ fractured rock," *Journal of Geophysical Research: Solid Earth*, vol. 116, article B02311, 2011.
- [32] S. Wang, D. Elsworth, and J. Liu, "Permeability evolution during progressive deformation of intact coal and implications for instability in underground coal seams," *International Journal of Rock Mechanics and Mining Sciences*, vol. 58, pp. 34–45, 2013.
- [33] S. Wang, D. Elsworth, and J. Liu, "Mechanical behavior of methane infiltrated coal: the roles of gas desorption, stress level and loading rate," *Rock Mechanics and Rock Engineering*, vol. 46, no. 5, pp. 945–958, 2013.
- [34] Q. Kong, H. Wang, and W. Xu, "Experimental study on permeability and porosity evolution of sandstone under cyclic loading and unloading," *Chinese Journal of Geotechnical Engineering*, vol. 37, no. 10, pp. 1893–1900, 2015.
- [35] Z. Chao, H. Wang, W. Xu, L. Yang, and K. Zhao, "Variation of permeability and porosity of sandstones with different degrees of saturation under stresses," *Chinese Journal of Rock Mechanics and Engineering*, vol. 36, no. 3, pp. 665–680, 2017.
- [36] J. Zhang, Z. Song, W. Fan, and D. Huang, "Experimental study on mechanical behavior and permeability characteristics of sandstone under stress-seepage coupling," *Chinese Journal of Rock Mechanics and Engineering*, vol. 38, no. 7, pp. 1364–1372, 2019.
- [37] C. Ding, Y. Zhang, X. Yang, D. Hu, H. Zhou, and J. Lu, "Permeability evolution of tight sandstone under high confining

pressure and high pore pressure and its microscopic mechanism,” *Rock and Soil Mechanics*, vol. 40, no. 9, pp. 3300–3308, 2019.

- [38] H. Lu, X. Xiangshuai, W. Yan, and D. Yao, “Circular sliding solution for mining stability and failure depth of the layered structure of floor in coal face,” *Rock and Soil Mechanics*, vol. 41, no. 1, pp. 1–9, 2020.

Research Article

A Discussion of Reinforcement Timing Optimization for Main Inclined Shaft Roadway with Water Seepage

Minglei Zhang , Chaoyu Chang, and Wen Cao

Institute of Disaster Prevention, Langfang 065201, China

Correspondence should be addressed to Minglei Zhang; zml@cidp.edu.cn

Received 28 May 2020; Revised 17 July 2020; Accepted 24 July 2020; Published 13 August 2020

Academic Editor: Jingmin Xu

Copyright © 2020 Minglei Zhang et al. This is an open access article distributed under the Creative Commons Attribution License, which permits unrestricted use, distribution, and reproduction in any medium, provided the original work is properly cited.

The infiltration and physical and chemical effects of fissure water often have a degrading effect on the strength and bearing capacity of the surrounding rock of the roadway. With the increase of the time of water infiltration, the roadway deformation increases exponentially, resulting in a higher risk of roadway destruction. In this paper, targeting at the supporting and protection issues associated with the main inclined shaft during the water-drenching, a numerical simulation method was established to evaluate the impact of the fissure water on the deformation of the surrounding rock of the roadway, and a solution to control the top water in main inclined shafts by grouting was proposed. Through the numerical simulation method, the effective penetration range of the slurry in the surrounding rock and the variation of the tunnel deformation with the grouting timing were studied. A method of combining numerical simulation with on-site monitoring to determine a reasonable grouting timing was proposed. The field application suggests that grouting at a reasonable timing can effectively control the influence of seepage water from the roof crack of the main inclined shaft on the deformation of the roadway surrounding rock, improve the integrity of the roadway surrounding rock, increase the bearing capacity of the support, and maintain the safety and stability of the roadway surrounding rock of the main inclined shaft. Furthermore, this study can provide insightful references to the grouting reinforcement adopted by similar main inclined shafts.

1. Introduction

With the continuous increase in mining scale and mining intensity, the threat of coal mine roof water hazards has become increasingly prominent, resulting in serious safety hazards to mine production [1, 2]. When the groundwater, as a chemical solution with a complex composition, is exposed to the rocks, complex physical and chemical reactions often occur, resulting in damages to the mechanical properties of the rock mass, such as the softening and hydraulic erosion of rocks. Rock softening is a typical physical property of rock, and the strength deterioration severity depends on the water content of the rock [3]. The hydraulic pressure intensifies the development of the internal cracks in the softened rock mass, gradually reducing the integrity of the rock mass and changing the macromechanical properties of the rock mass [4]. The redistribution of chemical elements caused by water-rock chemistry and changes in rock

microstructure further exacerbate the deterioration of rock mechanical properties [5].

During the roadway excavation, with the existences of the fissure water in the surrounding rock, the physical and chemical reactions between the water and the rock mass have a degrading effect on the bear capacity of the roadway surrounding rock, resulting in safety hazards and other risks, which should be either drained or contained effectively to prevent further damage [6]. Under the circumstance that proper drain is not possible, grouting is often adopted to control the fissure water in the roadway surrounding rock and strength the roadway accordingly. Many scholars have conducted in-depth studies on the roadway grouting technologies. In terms of grouting materials, due to the engineering needs and advances in material science, the common materials adopted in the grouting process include cement slurry, loess, fly ash, and other chemical grouting materials [7–10]. In terms of grouting technologies, various grouting methods

are developed such as the adoption of the grouting pipes, grouting anchors, and grouting anchor cables [11–14]. In terms of grouting mechanism, multiple grouting theories have been proposed by different scholars such as porous media grouting, continuous media grouting, and fractured media grouting to study the diffusion law and influencing factors of grouting slurry in rock mass [15–19]. In order to evaluate the strengthening performances of the grouting, article [20] sampled and tested the grouting body mixed with coal and mudstone, respectively. The test results suggest that the residual strengths of the rocks after cement grouting and chemical slurry grouting can be increased by 0.7 to 2 times and 1.5 to 6 times, respectively. According to New Austrian Tunneling Method, the timing to add roadway support should be determined based on “the premium compatibility between the roadway surrounding rock release stress and its self-bearing capacity,” which can fully release the deformation energy of the surrounding rock and appropriately reduce the support intensity [21]. Based on New Austrian Tunneling Method, some researchers proposed the timing determination methods of adding primary and secondary support to the deep soft rock roadway, which greatly enriched the surrounding rock grouting reinforcement theory [22–24]. However, the aforementioned studies focus on the single roadway with severe deformation and overlooks the reinforcement needs of the roadway under the influences of the fissure water for an extended period of time. In this paper, studies were conducted to focus on the supporting needed by the roadway of the main inclined shaft. After the analysis to the impacts of the fissure water on the mechanical properties and deformation of the roadway surrounding rock, through the strain and softening structural model included in the FLAC3D numerical simulation software, numerical simulations were established to determine the optimum timing for adding grouting reinforcement to the main inclined shaft. Furthermore, the methods and technical schemes for determining the reasonable grouting timing of the main inclined shaft roadway with fissure water were discussed, which can provide some insightful references for the grouting reinforcement of similar conditions.

2. The Impact of Roof Fissure Water on the Stability of the Roadway Surrounding Rocks

2.1. The Project Overview. The main inclined shaft of the Gucheng has a total length of 2,019 meters with an inclined degree of 15° and a penetration depth of 92 meters underground. The fracture surface of the roadway in the bedrock section takes a shape of a straight wall semicircular arch with a width of 6.4 meters and a height of 1.2 meters. The support was constructed with anchor bolts, anchor cables, and sprayed cement. The total thickness of the coated cement is about 200 mm. No water seepage is founded in the surface soil layer of the main inclined shaft. On the other hand, in the bedrock section, due to the skip of determining the water contents and proper draining, water seepage occurred during the layout of the anchor cables. Water seepage was observed in the bolt holes. Some bolt holes suffered with severe water seepage, as well as the surrounding area of the roof displace-

ment monitors. The severe water seepage has jeopardized the support effects of the roadway and field construction. In order to ensure the construction progress, no more anchor bolt hole is drilled at the point of 580 meters. Instead, anchor mesh and coating cement were installed. No anchor cable was installed from 580 meters to 880 meters. Anchor cables were installed after 880 meters. The supporting parameters of the roadway section with water seepage and the appearances of the roadway are provided in Figures 1 and 2 below.

Underground water is a complexed chemical solution. Under the interaction between the underground water and the rock, the physical and chemical properties of the rock tend to change including the macrostructure and the increased porosity, resulting in severe damages to the rock. Simultaneously, the increasement of the permeability and the water pressure at the pores lower the effective stress of the rock, resulting in lower resistances of the surrounding rocks to the deformation. The macrostrength and the rigidity of the surrounding rock are further reduced accordingly. On the other hand, under the pressure of the infiltration water, the underground water enters the roadway surrounding rock through the fissures developed dynamically and weakens the bear capacity of the surrounding rock and the supporting structure, resulting in failure of the bolting structure and safety hazards. From the long-term perspective, the underground water poses as a threat to the supporting structure, especially to the metal anchor bolts and cables such as the rust and erosion, increasing the failure risks of the supporting structure and jeopardizing the safety of the main inclined shaft.

2.2. The Numerical Simulation of the Roadway Surrounding Rock Deformation. FLAC3D numerical simulation software was adopted to build model to evaluate the impact of the water seepage to the deformation of the roadway surrounding rock. The model was built based on the rock layer distribution, and the physical properties of the main inclined shaft obtained from the Gucheng coal mine. The parameters of the rock layers are presented in Table 1 below. The size of the model is 300 × 100 × 40 m. The rock damage is estimated based on the Mohr-Coulomb criterion and the strain-softening model. 2.58 MPa was applied to the top part of the model with no restriction applied. Restrictions were applied to both the left side and right side of the model. A perpendicular restriction was applied to the bottom of the model. According to relevant studies, the roadway with water seepage was divided into two conditions including the roadway with the short-term seepage (grouting was added within half a year after the construction) and the roadway with long-term seepage (no grouting after the construction). Strength reduction was used to indicate the damage to the roadway strength, until the strength was reduced to the 80% and 50% of the initial roadway strength [25].

Figure 3 shows the roadway displacement distribution and statistics. Under normal circumstances, the main inclined shaft roadway demands more to the deformation control of the surrounding rock with a higher level of the support, which often leads to limited roadway deformation. Comparing with regular roadway, both the bottom and top deformations of the

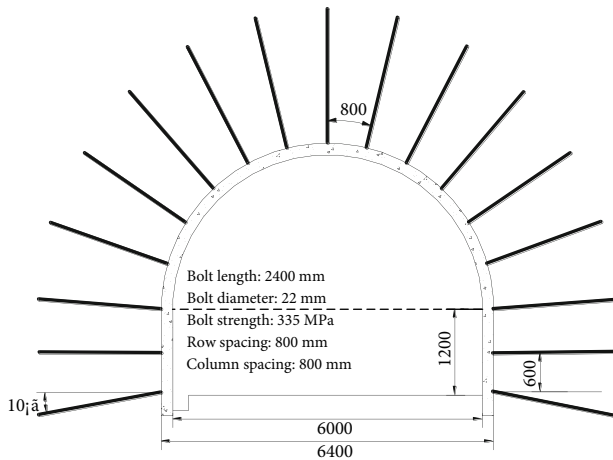


FIGURE 1: The supporting parameters and appearance of the roadway.



FIGURE 2: Roadway appearance (without anchor cable).

roadway exposed to the short-term water seepage were increased by 2.63 times and 4.07 times for the lateral deformation. In contrast, both the bottom and top deformations of the roadway exposed to the long-term water seepage were increased by 11.8 times and 12.7 times for the lateral deformation. The test indicates that the short-term water seepage has a limited impact on the roadway strength. However, the long-term water seepage can severely degrade the roadway strength. Most of the main inclined shaft often have a long service life, as long as 50 to 60 years. The negative impact of the water seepage on the strength of the roadway is mostly likely to occur and last for an extended period of time, demanding effective measures to control the water seepage in the roadway.

No major strata behavior was noticed within a short period of time. However, the main inclined shaft located at the Gucheng coal mine is required to have a long service life, demanding a high level of support. The anchor cables play a vital role in the supporting system of the main inclined shaft. During the survey, a large amount of mudstone with low strength were detected, which can easily crack during the excavation due to the original stress of the rocks. The cracks will allow the water seepage developed, jeopardizing the sup-

porting, and the construction progress. Often, the preferred solution is to drain the water from the roof. However, due to the large amount of water and tight schedule, the support of combining the grouting and the anchor cables were selected for the roof section with water seepage of the main inclined shaft.

3. The Numerical Simulation of the Timing to Grout in the Roadway Section with Water Seepage of the Main Inclined Shaft

The grouting timing refers to the time interval between the second support of the grouting anchor cable and the installation of the anchor bolts and the sprayed cement. The field experiences suggest that newly excavated roadway is not suitable to grout within a few days after the excavation. After the excavation, the roadway is still in the process of stress distribution, exposing the surrounding rock to the easy development of the damage and deformation. If the grouting is conducted too early, the fissures are too small to accept the grouting. Also, the continuous release of the stress and deformation of the surrounding rock can possibly damage the solidified grouting. If the grouting is conducted too late, the deformation of the surrounding rock has been developed excessively. Despite the good diffusion of the grouting slurry in the fissures, the surrounding rock has lost its bear capacity, resulting in a limited effect of reinforcement. Therefore, a good timing for the grouting is critical for the effectiveness of the supporting system.

3.1. The Impact of the Grouting Time on the Thickness and Stability of Effective Permeation Circle of Grouting Slurry in Surrounding Rock. Essentially speaking, the deformation of the surrounding rock is a process of stress release and transfer, as well as a strength reduction process. The grouting is designed to solidify the broken and fractured rocks after the peak. FLAC3D numerical simulation software was adopted to simulate the solidifying process of the grouting of the roadway with water seepage. A strain and softening model is used to simulate the after peak damage suffered by the rock [26, 27]. The fracture degree of the rock after the peak is indicated with equivalent plastic shear strain [28–30]. As the equivalent plastic shear strain increased, the rock strength after the peak reduced drastically. The general cohesion was reduced significantly, while the general friction angles experienced less changes. Assuming that the grouting was carried out when the rocks were still in the process of fracture development, the grouting can spread to the fracture areas of the rock, achieving a highly effective permeation status. The fracture area achieved effective permeation status is labeled as an effective permeation circle. To evaluate the impact of grouting timing on the solidifying effect of the grouting, the grouting was carried out at the following equivalent plastic shear strain including 0.01, 0.08, 0.16, 0.24, 0.32, 0.40, 0.48, 0.56, 0.64, and 0.72. Considering that different damage levels in various locations within the rock, the maximum value in the fracture area was selected as the equivalent plastic shear strain. The impacts of the grouting time on the effective permeation circles of grouting slurry,

TABLE 1: The physical parameters of the rock layers.

Rock layer	Thickness/m	Density/kg.m ³	Bulk Modulus/GPa	Shear Modulus/GPa	Tensile strength/MPa	Cohesion/MPa	Internal friction angle/°
Overlying rock	30	2300	2.65	1.47	3.81	4.69	32
Sandstone	4	2350	16.24	11.15	4.69	6.79	35
Mudstone	3.5	2150	2.32	1.09	1.81	2.19	30
Sandstone	2.5	2350	16.24	11.15	4.69	6.79	35
Mudstone	5	2150	2.32	1.09	1.81	2.19	30
Sandy mudstone	6.5	2300	2.66	1.46	2.11	2.49	33
Mudstone	13.5	2150	2.32	1.09	1.81	2.19	30
Siltstone	3	2450	15.72	9.81	3.62	5.91	33
Mudstone	2	2150	2.32	1.09	1.81	2.19	30
Underlying bed	30	2300	2.65	1.47	3.81	4.69	32

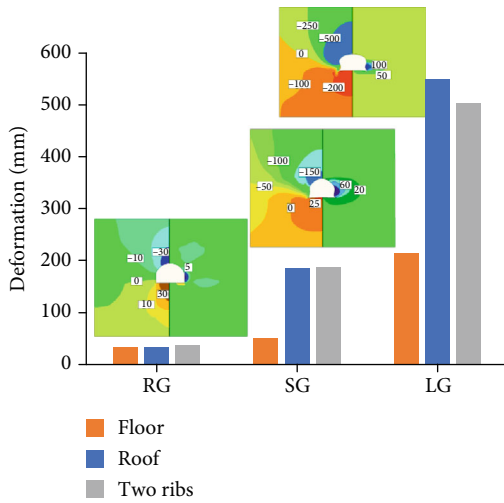


FIGURE 3: The roadway displacement distribution and statistics (RG represents for routine group, SG represents for short-term water seepage group, and LG represents for long-term water seepage group).

the deformation, and the damage were analyzed through the calculation. In the numerical simulation, the internal cohesion and the internal friction angles were increased to simulate the grouting effect. According to the relevant researches, the strength of grouted rocks was assumed as 1.8 times of that before the grouting.

The flow and penetration range of the slurry in the surrounding rock depends on the crack development within the surrounding rock. Therefore, the grouting performed differently under different damage states after the peak and so was the effective penetration range of the slurry. Meanwhile, due to the different fracture state of the surrounding rock during grouting, the residual strengths of the rock in the effective grouting circle varied, affecting the strength of grouting and resulting in different reinforcement effects to the roadway surrounding rock. Figure 4 shows the distribution characteristics of the grouting slurry effective permeation circle in the surrounding rock under different grouting timings. The thickness of the slurry effective perme-

ation circle and the deformation of the roadway surrounding rock at various grouting timings are presented in Figure 4 as well.

The simulation results indicate that the permeation range of the grouting slurry was increased along with the delay of the grouting. At the early fracture stage, the increasing of the equivalent plastic shear strain led to the fast development of the fractures, resulting in more fracture space. The thickness of the slurry effective permeation circle was increased from 0.3 m to 1.4 m. At the middle fracture stage, the fracture space increased at a lower rate. The thickness of the slurry effective permeation circle was increased from 1.4 m to 2.8 m. At the residual deformation stage of the surrounding rock, the stress redistribution was complete, and the fracture area expanded slowly, resulting in a stable thickness of slurry effective permeation circle. The thickness of the slurry effective permeation circle stands for the permeation and diffusion effect of the grouting slurry. A higher thickness of the slurry effective permeation circle indicates a wider range of permeation and diffusion of the grouting slurry. However, the range of grouting slurry permeation and diffusion is not the sole deciding factor in the strength of the slurry solidification, which also depends on the strength of the surrounding rock during the grouting process. Normally, a higher strength of the surrounding rock during the grouting process leads to a stronger grouting body. An early grouting timing leads to a smaller range of permeation and diffusion and a stronger grouting body. On the other hand, a delayed grouting timing leads to a wider range of permeation and diffusion and a weaker grouting body. Therefore, a turning point was observed in the deformation curve of the roadway surrounding rock corresponding to the grouting time. A U shape was developed as the grouting timing was postponed, suggesting a reduction followed by an increase in the deformation of the roadway surrounding rock. This change suggests that an optimum timing range does exist to strive for a balance between the effective permeation range and the strength of the grouting slurry, resulting in an effective control to the deformation of the roadway surrounding rock.

3.2. *The Determination of the Optimum Support.* Based on the analysis mentioned above, the optimum grouting timing

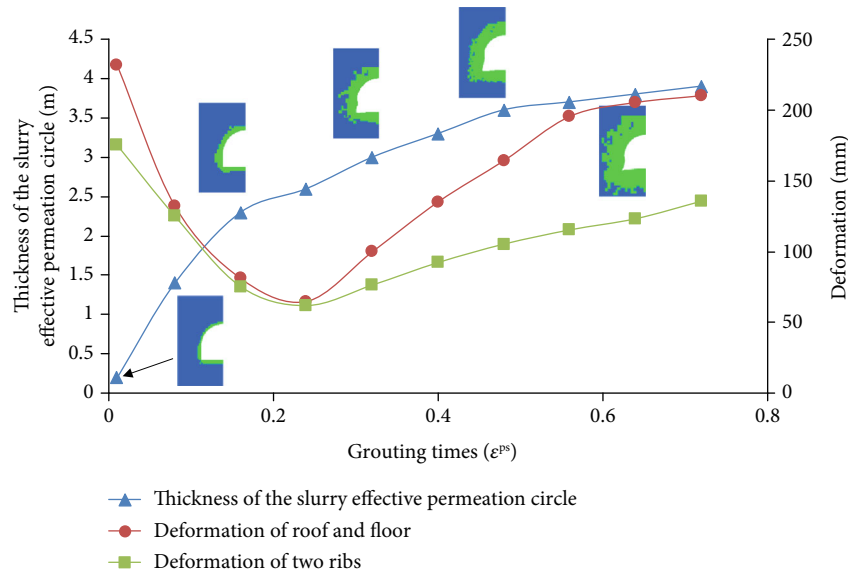


FIGURE 4: The thickness of the slurry effective permeation circle and the deformation of the roadway surrounding rock at various grouting timings.

is between 0.16 and 0.32 ($\epsilon^{ps} = 0.16 \sim 0.32$). However, the maximum equivalent plastic shear strain could not be obtained from the field measurement. The roadway deformation can be measured easily, which is a frequently needed parameter in the field, which can be used as an indicator to determine the grouting timing of the roadway. According to the simulation results, when the maximum equivalent plastic shear strain of the surrounding rock is between 0.16 and 0.32 ($0.16 < \epsilon^{ps} \leq 0.32$), the roadway roof deformation (U_r), the lateral deformation (U_l), and the bottom deformation (U_f) were $48.5 \text{ mm} < U_r \leq 65.2 \text{ mm}$, $54.8 \text{ mm} < U_l \leq 70.6 \text{ mm}$, and $12.1 \text{ mm} < U_f \leq 15.4 \text{ mm}$, respectively, suggesting an optimum timing range for grouting.

During the field application, the specific engineering geological conditions should be included to obtain the roadway surface deformation corresponding to the best grouting timing of the roadway, followed by the field monitoring of the deformation of the roadway surrounding rock. When the deformation of the roadway surrounding rock reaches the deformation corresponding to the optimum grouting timing, the grouting should be carried out.

4. The Field Application and Reinforcement Effect

According to the analysis above and the field monitoring to the roadway deformation of the main inclined shaft, grouting should be conducted 4 to 5 months after the excavation to achieve the effective control to the roadway deformation. Without disruption to the construction progress, the main inclined shaft should be reinforced with the anchor bolts and the sprayed concrete. The secondary reinforcement should be added 4 months after the excavation by the adoption of the latest hollow grouting anchor cables which was fabricated with eight wound 7 mm-diameter metal tubes.

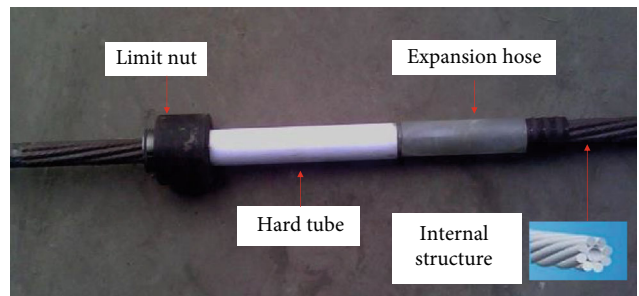


FIGURE 5: Grouting cable anchor.

The sealing package includes seal clamps, expandable flexible hoses, and hard plastic tubes.

The dimension of the hollow grouting anchor cable is 8300 mm at length and 22 mm at diameter, as shown in Figure 5. Each row was installed with three grouting anchor cables with a distance of $2000 \times 1600 \text{ mm}$ in-between. The sprayed slurry was mainly cement (#42.5 standard Portland cement with a water and ash ratio of 1:1.5). ACZ-1 agent was also added to the slurry, which contains 8% cement. The sealing clamp has been assembled on the anchor cable body when the anchor cable was delivered from the factory. When installing the anchor cable, the expansion soft rubber tube shall be sleeved first, and then, the plastic hard tube shall be sleeved. It shall be confirmed that the hard tube is 50-80 mm away from the hole opening. After that, the plastic hard tube shall be pushed through the special pushing device, until the soft rubber tube can be pressurized and expanded to seal the hole. The layout of grouting cable anchor is shown in Figure 6. Before grouting, multiple sprayed cement spots had been permeated with water. After the installation of the grouting anchor cables, fissure water was drained along the anchor cable holes, as demonstrated in Figure 7. After the grouting, the fissure water migrated beyond the area of the grouting area

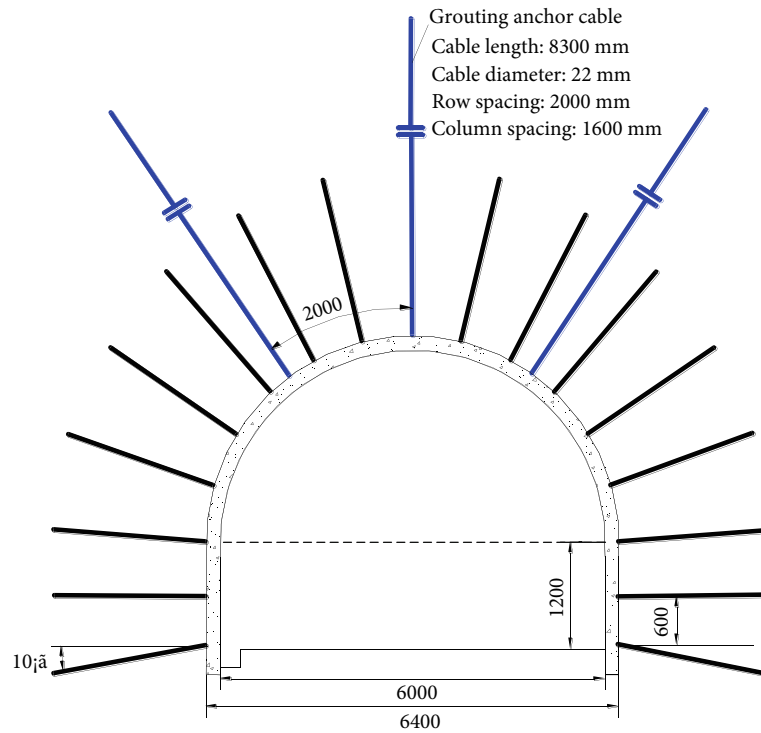


FIGURE 6: Layout of grouting cable anchor.



Left (before grouting)



Middle (before grouting)



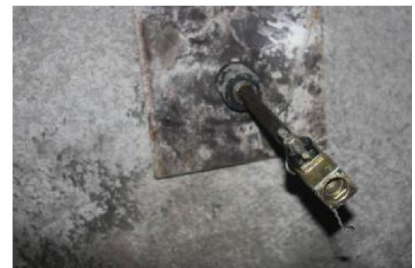
Right (before grouting)



Left (after grouting)



Middle (after grouting)



Right (after grouting)

FIGURE 7: Comparison of water flow in anchor hole before and after grouting.

and no more water seepage was detected. After a while, the permeated water in the sprayed cement was evaporated, and no water seepage was observed visually, as demonstrated in Figure 8.

As shown in Figure 9, the maximum deposition in roof was 8 mm with a maximum of 6 mm bulging at the bottom.

The roof displacement was about 14 mm. The roof deposition was slightly higher than the bulging at the bottom; which suggests that due to the roof fissures under the water impact, the roof rock was weakened, resulting in more deposition than the bottom. The maximum displacements of the roadway at the left and right were 4 mm and 7 mm, respectively.



FIGURE 8: Grouting effect.

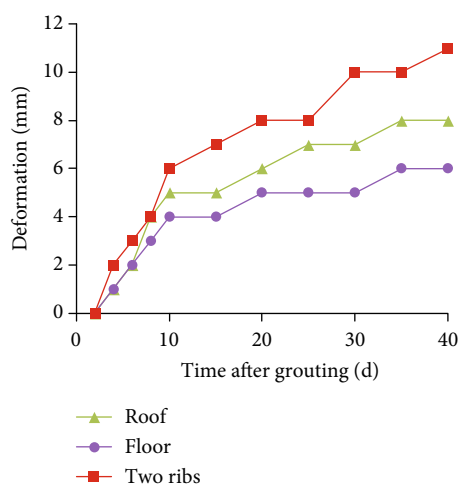


FIGURE 9: The roadway deformation after grouting.

The total lateral displacement reached a total of 11 mm. The limited roadway deformation occurred 9 days after the installation of the grouting anchor cables, suggesting that a quality reinforcement provided by the grouting anchor cables to the roadway roof.

5. Conclusion

- (1) The permeation effect and the physical and chemical effect of the flowing water tend to degrade the strength of the roadway surrounding rock and bear capacity. The degrading effect increases exponentially as the water penetration extends, resulting in the increased risks of roadway failures
- (2) The effective permeation range increases as the grouting timing delays, but not the strength of the grouting body, which leads to the decreasing of the roadway deformation, followed by the increasing deformation. Therefore, an optimum grouting timing should be selected to achieve a preferred grouting slurry permeation range and the strength of the grouting body, resulting in effective control of the surrounding rock deformation

- (3) Combining the numeric simulation and the field monitoring, a grouting timing determination method based on the surrounding rock deformation of the roadway is proposed for the main inclined shaft. The field application demonstrates a proper grouting time can effectively control the roof fissure water permeation effect on the deformation of the roadway surrounding rock in the main inclined shaft, improve the integrity of the roadway surrounding rock, increase the bearing capacity of the supporting structure, and maintain the safety and stability of the roadway surrounding rock of the main inclined shaft

Data Availability

The data used to support the findings of this study are available from the corresponding author upon request.

Conflicts of Interest

The authors declare that there is no conflict of interest regarding the publication of this paper.

Acknowledgments

This work is supported by the Fundamental Research Funds for the Central Universities (grant no. ZY20200203), the Key tasks for earthquake emergency youth of China Seismological Bureau (CEA_EDEM-202029), and Self financing project of scientific research and development plan of Langfang science and Technology Bureau (grant no. 2020013046).

References

- [1] Q. Wu, M. Wang, and X. Wu, "Investigations of groundwater bursting into coal mine seam floors from fault zones," *International Journal of Rock Mechanics and Mining Sciences*, vol. 41, no. 4, pp. 557–571, 2004.
- [2] Y. Zhang, S. Cao, N. Zhang, and C. Zhao, "The application of short-wall block backfill mining to preserve surface water resources in northwest China," *Journal of Cleaner Production*, vol. 261, article 121232, 2020.
- [3] C. Y. Zhou, N. Liang, and Z. Liu, "Multifractal characteristics of pore structure of red beds soft rock at different saturations," *Journal of Engineering Geology*, vol. 28, no. 1, pp. 1–9, 2020.
- [4] Z. Zhang, H. Cao, T. Y. Wang, and Z. L. Ni, "Experimental investigation on swelling inhibition of shale in northwestern Hunan under the interaction of shale-fluid," *Bulletin of Science and Technology*, vol. 35, no. 12, pp. 6–11, 2019.
- [5] Y. P. Xie, Q. N. Chen, X. C. Huang, and P. Luo, "An experimental study of microstructure and uniaxial compression test of carbonaceous slate in a deep buried tunnel," *Hydrogeology and Engineering Geology*, vol. 47, no. 1, pp. 96–102, 2020.
- [6] Z. J. Gao, J. T. Liu, Y. Z. Li et al., "Hydro chemical characteristics and hydrogeochemical simulation of pore groundwater in Lhasa valley area," *Journal of Shandong University of Science and Technology (Natural Science)*, vol. 39, no. 1, pp. 1–10, 2020.
- [7] T. F. Gu, Z. D. Sun, F. T. Luo, Y. M. Liu, K. Guo, and L. Feng, "Experimental research on loess grouting material for coal gob

- filling,” *Journal of Engineering Geology*, vol. 22, no. 1, pp. 98–105, 2014.
- [8] G. C. Yan, L. J. Bai, Z. Q. Zhang, T. Yang, and J. H. Liu, “Experimental and applied study on PU modified chloroaluminate cement grouting material,” *Journal of China Coal Society*, pp. 1–7, 2020.
- [9] H. Liang, L. Fan, H. Wei, and Y. Z. Li, “Study on influencing factors of strength of polyether polyurethane grouting material,” *Journal of Wuhan University of Technology*, vol. 44, no. 1, pp. 172–176, 2020.
- [10] X. M. Guan, H. B. Zhang, Z. P. Yang et al., “Research of high-performance inorganic-organic composite grouting materials,” *Journal of China Coal Society*, vol. 45, no. 3, pp. 902–910, 2020.
- [11] S. Y. Guo, “Historic opportunity, development predicament and some suggestions for tunnel and underground works in China,” *Tunnel Construction*, vol. 39, no. 10, pp. 1545–1552, 2019.
- [12] J. Li, Z. H. Li, and X. D. Hu, “Analysis on water sealing effect of freezing-sealing pipe roof method,” *Chinese Journal of Underground Space and Engineering*, vol. 11, no. 3, pp. 751–758, 2015.
- [13] Q. Wang, Y. D. Xu, S. Xu, B. Jiang, R. Pan, and B. H. Liu, “Study and application of bolt-grouting slurry diffusion and reinforcement mechanism in broken surrounding rock,” *Journal of Mining and Safety Engineering*, vol. 36, no. 5, pp. 916–923, 2019.
- [14] G. Y. Wang and L. Jin, “Study on the dynamic response of the tunnel under the action of dynamic load,” *Chinese Journal of Applied Mechanics*, vol. 34, no. 5, pp. 881–886, 2017.
- [15] Z. L. Zhou, Y. L. Zhao, Z. Chen, X. M. Du, and Z. B. Wu, “Meso-mechanism of compaction grouting in soil based on particle flow method,” *Journal of Central South University (Science and Technology)*, vol. 48, no. 2, pp. 465–472, 2017.
- [16] L. Wen, Z. Q. Luo, Y. G. Qin, W. Wang, and K. H. Zheng, “Effective diffusion range of exponential fluids based on Navier-stokes equation in collapse area,” *Journal of Southwest Jiaotong University*, vol. 55, no. 1, pp. 193–201, 2020.
- [17] L. Z. Zhang, Q. S. Zhang, R. T. Liu, and S. C. Li, “Grouting mechanism in fractured rock considering slurry-rock stress coupling effects,” *Chinese Journal of Geotechnical Engineering*, vol. 40, no. 11, pp. 2003–2011, 2018.
- [18] J. P. Wei, B. H. Yao, Y. Liu, D. K. Wang, P. F. Cui, and S. Yao, “Grouting fluid diffusion law and variable model for fractured coal mass seepage,” *Journal of China Coal Society*, vol. 45, no. 1, pp. 201–212, 2020.
- [19] Q. Wang, L. Wang, B. H. Liu, B. Jiang, H. J. Zhang, and S. Xu, “Study of void characteristics and mechanical properties of fractured surrounding rock grout,” *Journal of China University of Mining and Technology*, vol. 48, no. 6, pp. 1197–1205, 2019.
- [20] X. Y. Yu, *Mining Failure Mechanism and Grouting Reconstruction Technology of Coal Wall in the Lag Section of Gob Side Entry*, China University of Mining and Technology, Xuzhou, China, 2014.
- [21] S. X. Lei and W. Zhao, “Study on the mechanism of circumferential yielding support for soft rock tunnel with large deformation,” *Rock and Soil Mechanics*, vol. 41, no. 3, pp. 1–8, 2020.
- [22] K. Wu, Z. S. Shao, and S. Qin, “Investigation on the mechanical behavior of tunnel supported by yielding supports in rheological rocks,” *Chinese Journal of Theoretical and Applied Mechanics*, vol. 52, no. 3, pp. 890–900, 2020.
- [23] Y. Zhang, F. X. Shen, X. M. Sun, M. C. He, J. Wang, and M. Du, “Stress and deformation law of surrounding rock in the second reuse of roadway formed by roof cutting in the “three-soft” coal seam,” *Journal of China University of Mining and Technology*, vol. 49, no. 2, pp. 247–254, 2020.
- [24] X. Sun, B. Zhang, L. Gan, Z. Tao, and C. Zhao, “Application of constant resistance and large deformation anchor cable in soft rock highway tunnel,” *Advances in Civil Engineering*, vol. 2019, Article ID 4347302, 19 pages, 2019.
- [25] S. Y. Zhu, S. G. Song, Q. Sun, B. Yan, and C. T. Wang, “Characteristics of interaction process between deep rock of lower coal seam floor and water under different test conditions,” *Chinese Journal of Rock Mechanics and Engineering*, vol. 33, Supplement 1, pp. 3231–3237, 2014.
- [26] Z. Li, S. Yu, W. Zhu et al., “Dynamic loading induced by the instability of voussoir beam structure during mining below the slope,” *International Journal of Rock Mechanics and Mining Sciences*, vol. 132, article 104343, 2020.
- [27] Y. Li, C. Tang, D. Li, and C. Wu, “A new shear strength criterion of three-dimensional rock joints,” *Rock Mechanics and Rock Engineering*, vol. 53, no. 3, pp. 1477–1483, 2020.
- [28] Y. L. Lu, L. G. Wang, B. Zhang, and Y. J. Li, “Optimization of bolt-grouting time for soft rock roadway,” *Rock and Soil Mechanics*, vol. 33, no. 5, pp. 1395–1402, 2012.
- [29] L. Ma, F. Yang, H. Xu, and Z. Xie, “Post-yield properties of rock salt using the concept of mobilized strength components and the dilation angle,” *Geotechnical and Geological Engineering*, vol. 35, no. 6, pp. 2841–2849, 2017.
- [30] X. Zhu, L. Tang, and H. Tong, “Effects of high-frequency torsional impacts on rock drilling,” *Rock Mechanics and Rock Engineering*, vol. 47, no. 4, pp. 1345–1354, 2014.

Research Article

Experimental Study on the Gas Flow Characteristics and Pressure Relief Gas Drainage Effect under Different Unloading Stress Paths

Chaolin Zhang ^{1,2}, Jiang Xu,³ Enyuan Wang,^{1,2} and Shoujian Peng³

¹Key Laboratory of Gas and Fire Control for Coal Mines (China University of Mining and Technology), Ministry of Education, Xuzhou, Jiangsu 221116, China

²School of Safety Engineering, China University of Mining and Technology, Xuzhou, Jiangsu 221116, China

³State Key Laboratory of Coal Mine Disaster Dynamics and Control, Chongqing University, Chongqing 400030, China

Correspondence should be addressed to Chaolin Zhang; chaolinzhang@cumt.edu.cn

Received 12 June 2020; Revised 5 July 2020; Accepted 8 July 2020; Published 12 August 2020

Academic Editor: Jingmin Xu

Copyright © 2020 Chaolin Zhang et al. This is an open access article distributed under the Creative Commons Attribution License, which permits unrestricted use, distribution, and reproduction in any medium, provided the original work is properly cited.

Coal seam gas is a critical substance because it can be a source of a large quantity of clean energy as well as a dangerous source of risk. A pressure relief gas drainage is an effective and widely used method for coal seam gas recovery and gas disaster control in coal mines. A series of pressure relief gas drainage experiments were conducted using large-scale coal samples under different unloading stress paths in this study to explore the unloading stress paths. From the experimental results, the dynamic evolutions of gas pressure, coal temperature, and gas production were analyzed. The trends of gas pressure and coal temperature during pressure relief gas drainage were similar: dropping rapidly first and then slowly with time. Correspondingly, gas production was fast in the early stage of pressure relief gas drainage and became stable thereafter. Meanwhile, gas flow characteristics were significantly affected by the unloading stress paths. Gas pressure and coal temperature had the maximum descent by unloading stress in three directions simultaneously, and the unloading stress of the Z direction had the minimal impact when only unloading in one direction of stress. However, the influence of unloading stress paths on gas production was complex and time dependent. The difference coefficient parameter was proposed to characterize the influence degree of unloading stress paths on the pressure relief gas drainage effect. Eventually, the selection of unloading stress path under different situations was discussed based on time, which is expected to provide the basis for pressure relief gas drainage.

1. Introduction

With the rapid industrialization development, the consumption of the fossil fuel that is a nonrenewable resource is increasing day by day. Coal seam gas is an accessory product of the coalification process, which mainly produces methane and low concentrations of carbon dioxide, nitrogen, hydrogen sulfide, sulfur dioxide, and heavier hydrocarbons [1–5]. The total world reserves of coal seam gas are estimated to be 262 trillion m³, and it has received increasing interest from many countries including USA, Australia, Canada, and China [6, 7]. However, coal seam gas is a double-edged sword, which cannot only be a source of high quality clean energy in large quantities but also is a dangerous source of risk in coal mines [8–10]. Coal seam gas with high pressure and high content can easily induce coal-gas dynamic

disasters, e.g., coal and gas outburst, and coal gas explosion [11–13]. Therefore, high-efficient gas drainage is very important for the safety production of the coal mine.

The reserves of China's coal seam gas with a burial depth of below 2000 m are estimated to be 36.8 trillion m³, which is more than that of shale and tight gas [14, 15]. However, coal seams in China are characterized by low gas saturation, low permeability, low reservoir pressure, and a relatively high metamorphic grade [16, 17]. For example, the permeability of most coal seams in China ranges from 10⁻⁴ to 10⁻¹ mD, which is three to four orders of magnitude lower than that of most countries around the world [18, 19]. To improve coal seam gas recovery and control gas disasters, the technology of pressure relief gas drainage is proposed, which is widely used for the low permeability coal seam in China. Yuan expounded the theory and technology of pressure relief gas

drainage systematically and demonstrated the successful application of pressure relief gas drainage in Huainan coal-field in 1998 resulting to an increase in gas production from 10 million m^3 to 2500 million m^3 in ten years [20]. Subsequently, increased in-depth research has been carried out on pressure relief gas drainage technology.

Zhang et al. explored the effect of gas pressure on gas permeability during pressure relief gas drainage and found that permeability and its sensitivity to gas pressure decreased with increasing effective stress or external stress [21, 22]. Yin et al. carried out a series of experiments to study the mining-induced mechanical behavior, gas permeability, and acoustic emission evolution of coal under triaxial loading and unloading conditions [23, 24]. Chen et al. studied the stress-strain relationship and its influence on permeability during the confining pressure stress unloaded by X-ray computerized tomography (CT) scanning [25]. Wang et al. concluded that the permeability and gas production can be improved by imposing effective loads on original coal seams through mining speed control during pressure relief gas drainage [26]. Shang et al. compared the pressure relief gas drainage effect by surface well drilling and the use of net-like penetrating boreholes (NPB) in Panyi Coal Mine, and their findings indicated that the average gas extraction concentration and average extraction purity of surface wells were higher than those of NPB by approximately 124.4% and 64.7%, respectively [27].

Most of the aforementioned studies are focused on the permeability evolution of coal under different unloading stress paths, and the coal samples used are small-scale making it difficult to study the parameter variation inside the coal and the drainage effect. Therefore, a series of pressure relief gas drainage experiments using large-scale coal samples under different unloading stress paths were conducted to explore the selection of unloading stress paths in this study considering the long term, high cost, and poor repeatability of pressure relief gas drainage tests in coal mine site.

2. Experimental Methods

2.1. Laboratory Device. The experiments of pressure relief gas drainage under different unloading stress paths are carried out using a large-scale multifunctional (LSMF) device. The LSMF device can simulate gas flow experiments (e.g., coal bed methane (CBM) drainage, carbon dioxide sequestration, carbon dioxide-enhanced CBM recovery (CO_2 -ECBM)), and gas outburst disasters in laboratory that is described amply in Zhang et al. [28]. The LSMF device is comprised of a coal specimen box, a true triaxial loading system, a fast coal uncovering system, a gas flow system, a data acquisition system, and a specimen shaping system. The effective space of the coal specimen box is 1050 mm \times 400 mm \times 400 mm. The true triaxial loading system has nine sets of loading plates at three directions of the coal specimen box, which can be servocontrolled independently to realize different loading and unloading paths.

2.2. Sample Preparation. The experimental coal is taken from Jinjia Coal mine, which is located at the border of Guizhou

and Yunnan provinces of China. Western Guizhou and Eastern Yunnan are the largest coal-producing region in South China and has a potential for high CBM yield [29]. The reconstructed coal sample is used in this study considering the difficulty to gain a large-scale raw coal, and the preparation of coal sample includes sampling, pressing, screening, and shaping [30]. The coal sample is divided into four layers and every layer is pressed for 1 h under a shaping stress of 7.5 MPa [15]. During the shaping stage, the gas drainage boreholes numbered I and II, the gas pressure sensors numbered P1-P40, and the temperature sensors numbered T1-T7 are fixed inside the coal sample as shown in Figure 1. The length of the boreholes is 330 mm and consists of the drainage section (the red part, 160 mm in length) and the sealing section (the blue part, 170 mm in length).

2.3. Experimental Design. The variables considered in the experiments are the unloading stress paths as shown in Figure 2. The initial stress in three directions (i.e., X direction, Y direction, and Z direction) is all 4.0 MPa. The stress is produced by unloading through different paths after the coal sample is saturated with a pore pressure of 1 MPa and the unloading stress rate is 2 MPa/min. The gas drainage experiment with the unloading stress path of OA is carried out first to study the drainage effect when the stress in the three directions is unloaded at the same time. The valves in the gas outlet are opened to start the gas drainage process while σ_x , σ_y , and σ_z decline to 0.1 MPa. The experimental parameters of gas pressure, temperature, and gas flow rate are recorded automatically until the end. To compare the gas drainage effect under the different unloading stress paths, the gas drainage experiments with the unloading stress paths of OB, OC, and OD are conducted in turn. During the unloading stress path of OB, σ_x drops to 0.1 MPa with AN unloading rate of 2 MPa/min while σ_y and σ_z remain unchanged at 4.0 MPa. In addition, σ_y drops to 0.1 MPa during the unloading stress path of OC and σ_z drops to 0.1 MPa during the unloading stress path of OD.

3. Results and Discussion

3.1. Gas Drainage Effect with Stress Unloaded in Three Directions. Figure 3 shows the dynamic evolution of gas pressure with the unloading stress path of OA. The linear distance between the four gas pressure sensors (P3, P4, P5, and P6) and the borehole is 280 mm. As shown in Figure 3(a), the gas pressure curves of four sensors are almost coincident, which decline quickly at first and then drop slowly. The gas pressure drops from 1.0 MPa to 0.03 MPa after 8 h of gas drainage. The gas pressure sensors of P13, P14, P15, and P16 are fixed near the outer wall of borehole. However, the pressure evolution trend of four sensors shows significant differences. The sensor of P15 is located near the middle of the drainage section of borehole, and P15 gas pressure drops faster than that of the other three sensors. The sensors of P13 and P14 were located near the sealing part of THE borehole, and the gas pressure decreases at the slowest rate. The sensor of P16 is located at the front of the drainage section of borehole, and the gas pressure descent rate is

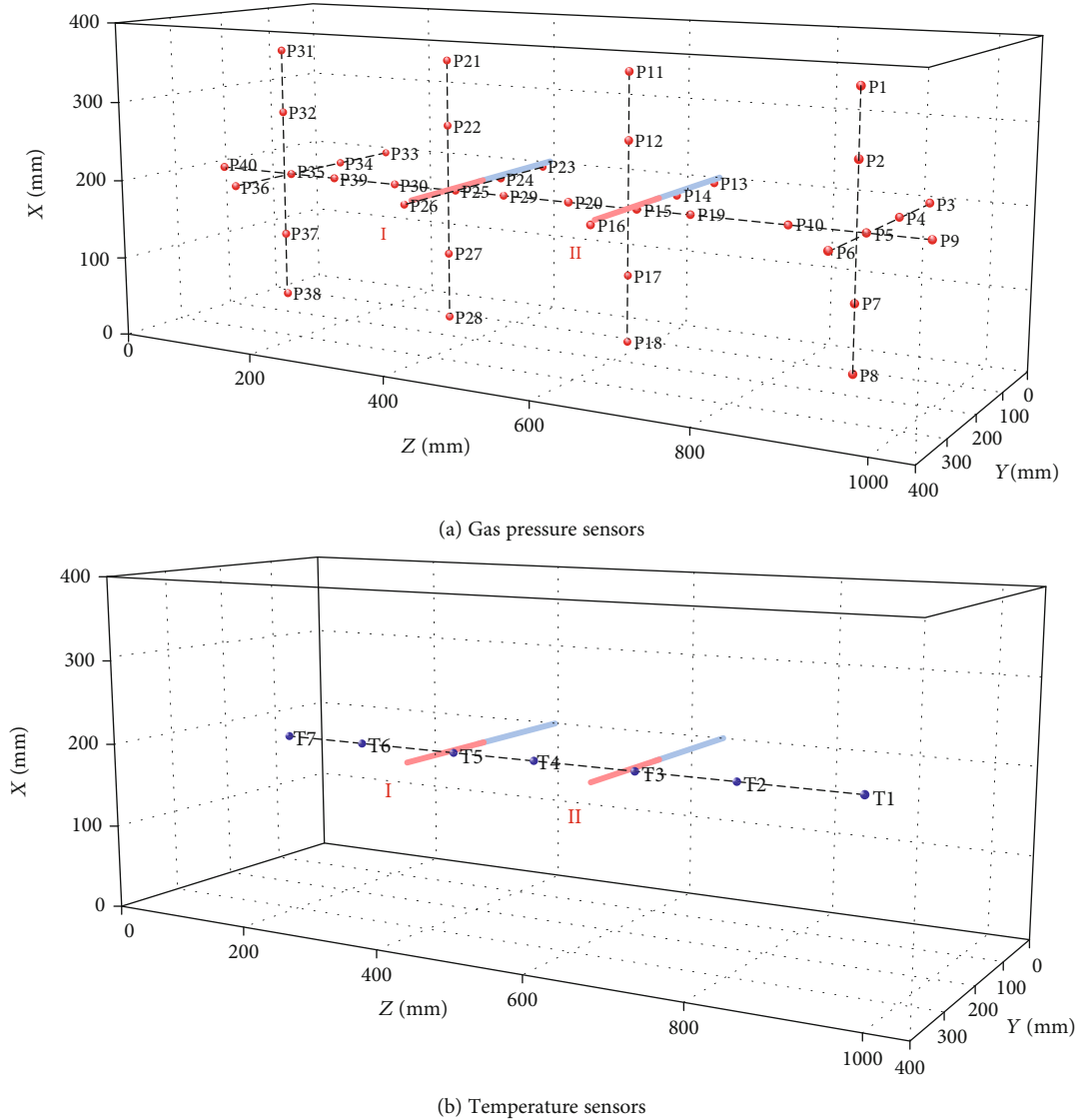


FIGURE 1: Positions of gas pressure sensors and temperature sensors.

average which is a little larger than that of $P13$ and $P14$, as shown in Figure 3(b).

The gas pressure of 12 gas pressure sensors along the line $x = 200$ mm, $y = 250$ mm, and $z = 40-1010$ mm at different times are shown in Figure 3(c). It is apparent that the gas pressure at the drainage section of the borehole is always minimum at any time. The gas pressure at borehole I and borehole II is 0.57 MPa and 0.33 MPa after drainage of 1 min, respectively. However the gas pressure at other positions is still almost equal to the initial gas pressure. After gas drainage time of 8 h, the gas pressure at borehole I and borehole II is about 0.1 MPa and the gas pressure at other positions is approximately 0.03 MPa. That is, the decreasing rate of gas pressure reduces with the increase of distance from borehole and the difference between gas pressures at different positions decreases as the gas drainage progresses.

Gas desorption is an endothermic process that contributes to the drop in the coal temperature during gas drainage. Therefore, the variations of temperature at different positions

are calculated and the curves of $\Delta T1$, $\Delta T2$, $\Delta T3$, and $\Delta T4$ are shown in Figure 4(a). We observe an overall trend of temperature drop similar to that of gas pressure during gas drainage: the fast and then slow drop rate in temperature and gas pressure. At the same time, the temperature sensor of $T3$, located near the middle of the drainage section of borehole, drops at the fastest rate during the whole drainage process with the final maximum drop of 12.5°C at last. The temperature sensor of $T1$, located farthest from borehole, drops at the slowest rate during the whole drainage process with a final minimum drop of 9.7°C. The temperature sensors of $T2$ and $T4$ are located at the same distance from borehole. However, the drop rate of $T4$ is faster than that of $T2$, especially after 90 mins of gas drainage. At last, the temperature drop of $T2$ is 11.8°C but the temperature drop of $T4$ is 12.4°C which is almost equal to that of $T3$.

The temperature drop curves of 7 temperature sensors along the line $x = 200$ mm, $y = 250$ mm, and $z = 152-936$ mm at different times are shown in Figure 4(b) showing

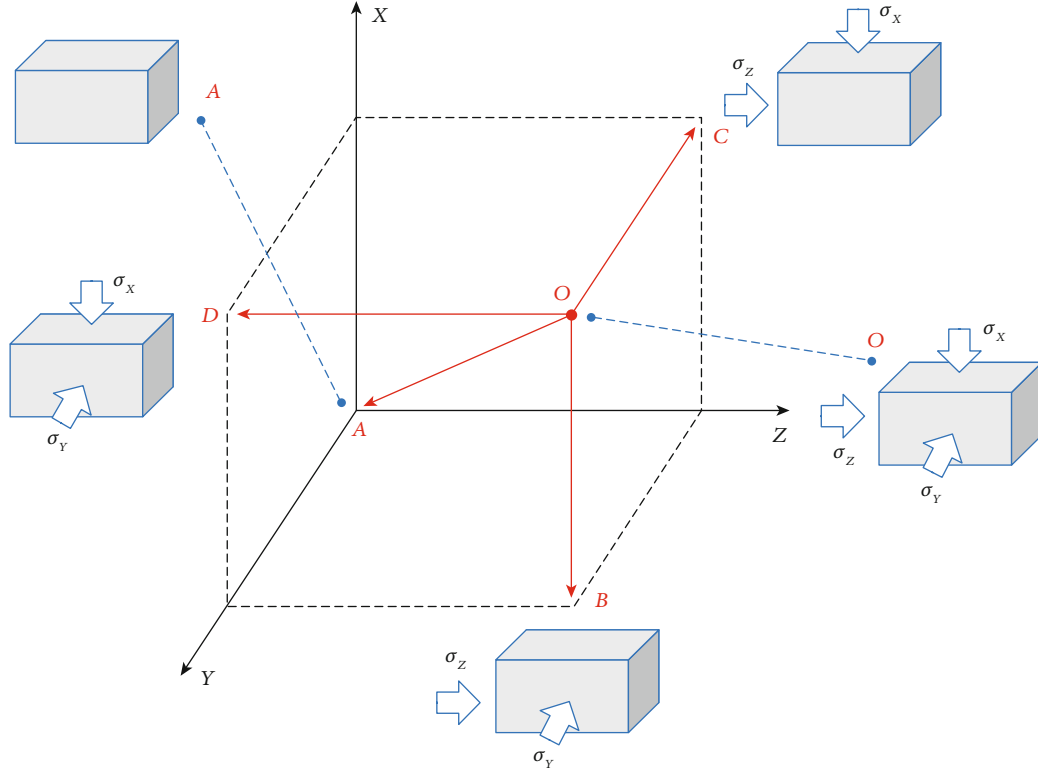


FIGURE 2: Unloading stress paths of pressure relief gas drainage experiments.

that the temperature of coal near boreholes drops fastest, followed by that between boreholes and far away from boreholes. As the gas drainage progresses, the temperature of coal between two boreholes (i.e., $T4$) is close to that near the boreholes, which indicates that two adjacent boreholes make the temperature of coal between borehole drop faster. This is mainly because that borehole interaction can accelerate the gas desorption of coal between boreholes and lead to the temperature of coal between boreholes declining faster [3].

Figure 5(a) shows the gas flow rate and gas production of different branch boreholes during gas drainage. The gas flow rate of borehole I (i.e., qI) has a maximum of 39.86 L/min at the beginning, then decreases with the gas drainage and finally drops to 0.45 L/min. Similarly, the gas flow rate of borehole II (i.e., qII) has a maximum of 40.78 L/min at the beginning, then decreases with gas drainage and finally drops to 0.35 L/min. However, the difference between gas production of borehole I (i.e., QI) and gas production of borehole II (i.e., QII) increases gradually with the process of gas drainage, then QI and QII reach 1285.34 L and 1219.43 L, respectively. The different drainage effects between two branch boreholes are mainly because of the incompletely homogeneous coal [31]. Therefore, the total gas flow rate and gas production of boreholes are critical, as shown in Figure 5(b). It can be seen that q (i.e., $qI + qII$) has the same evolution trend of qI and qII and Q (i.e., $QI + QII$) has the same evolution trend of QI and QII . The difference is that the peaks of q and Q are significant reaching 80.64 L/min and 2054.77 L, respectively.

3.2. Gas Flow Characteristics under Different Unloading Stress Paths. In order to study the influence of unloading stress paths on gas flow characteristics, gas pressure, or temperature at the same position during different experiments were compared together. Three types of sensor positions were chosen, namely, the position near boreholes, the position between boreholes, and the position far away from boreholes. The curves of $P25$, $P29$, and $P40$ during different experiments are shown in Figure 6. As can be seen from Figure 6(a), four curves have a sharp drop in the initial stage due to four gas pressure sensors that are close to borehole I. The curves of $P25$ - XYZ and $P29$ - Z almost coincide, and they are lower than the curve of $P25$ - Y while the curve of $P25$ - X remains the highest during the whole drainage process demonstrating that the unloading stress in the Z direction, and three directions has the most significant effect on gas pressure decline near the boreholes. The curves of $P29$ and $P40$ during different experiments have a similar evolution trend. $P29$ and $P40$ drop the fastest when unloading stress is in the three directions and drop the slowest when unloading stress in the Z direction. The impact of unloading stress in the X direction and Y direction on $P29$ and $P40$ is almost the same, as shown in Figures 6(b) and 6(c).

The curves of $\Delta T3$, $\Delta T4$, and $\Delta T6$ during different experiments are shown in Figure 7. As shown, coal temperature has the maximum descent when unloading stress is in the three directions and has the minimum descent when unloading stress is in the Z direction. $\Delta T3$ of unloading stress in X direction is bigger than that in Y direction when temperature sensors are near the borehole and are similar when temperature sensors are between boreholes and far away from

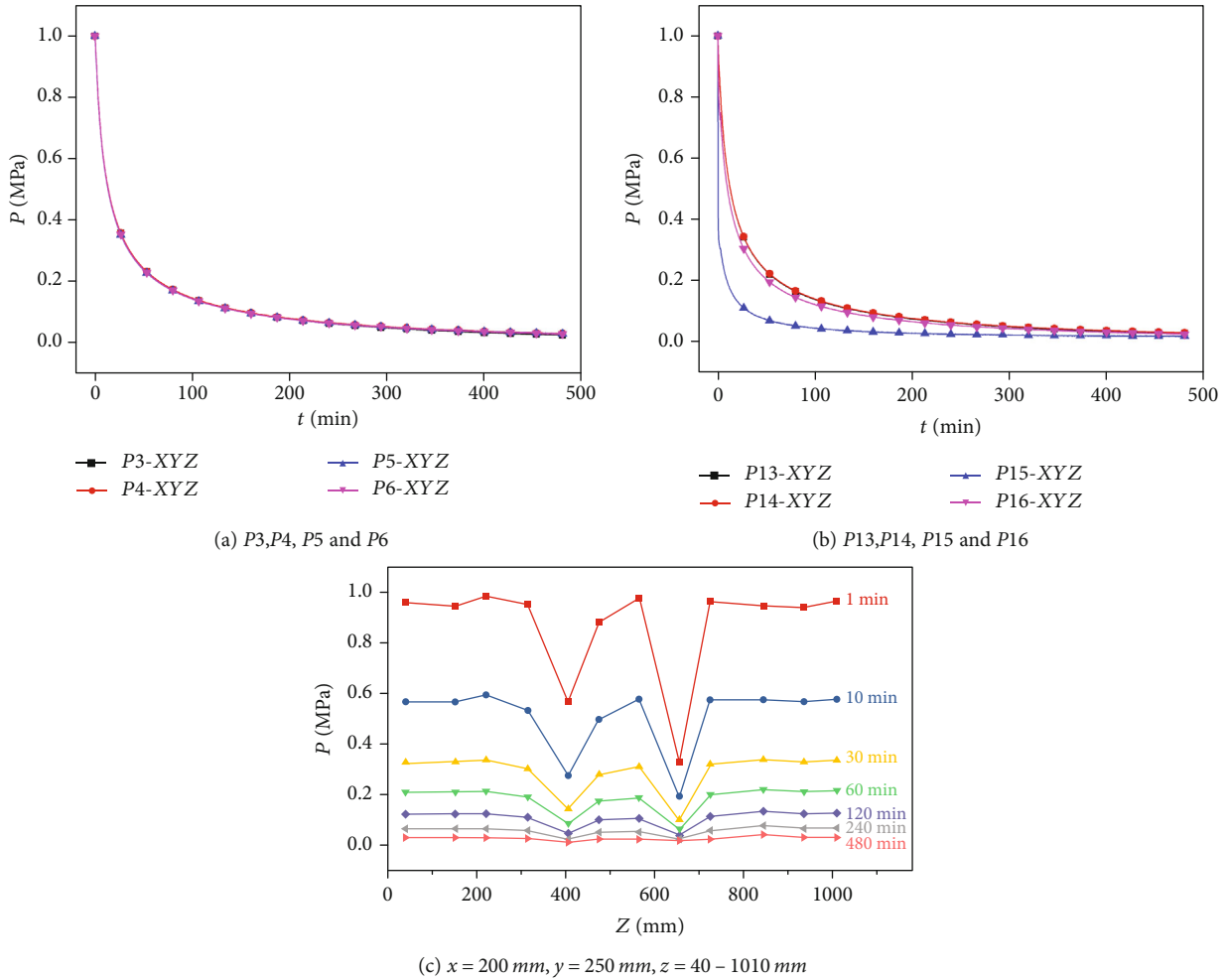


FIGURE 3: Evolution of gas pressure during gas drainage.

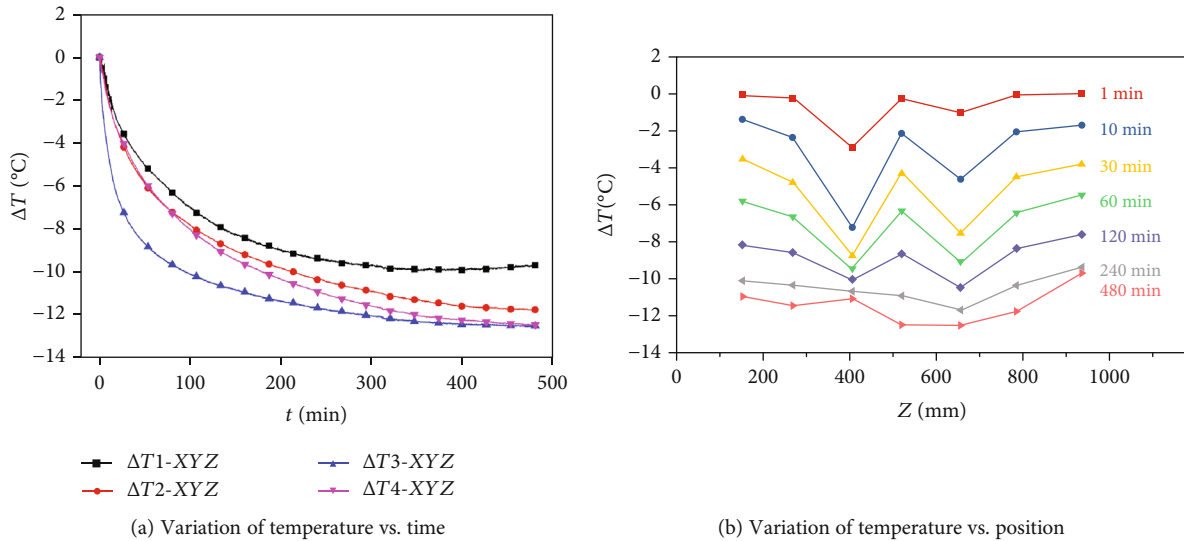
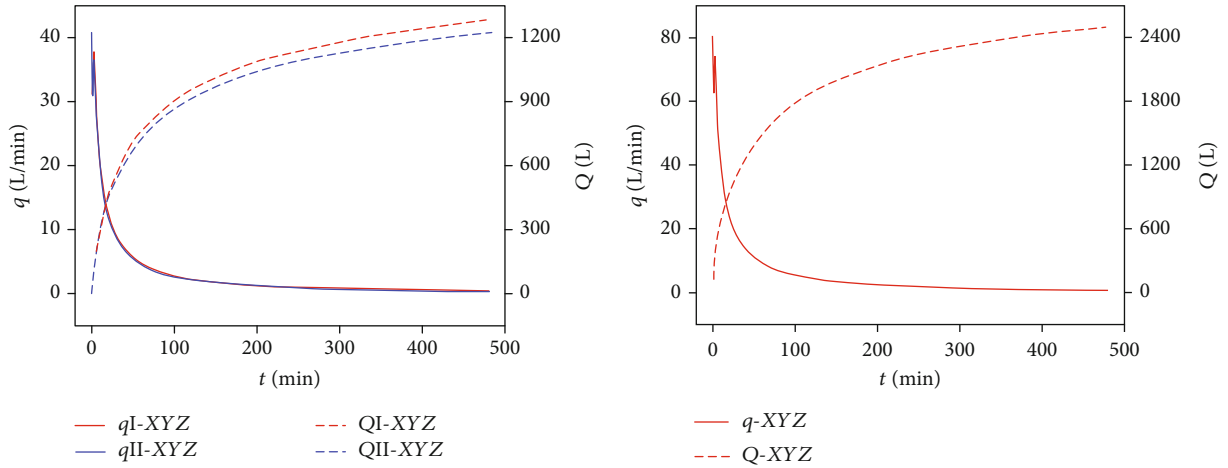


FIGURE 4: Evolution of coal temperature during gas drainage.

boreholes. In summary, gas flow characteristics are significantly affected by the unloading stress paths. Gas pressure and temperature have the maximum descent by unloading

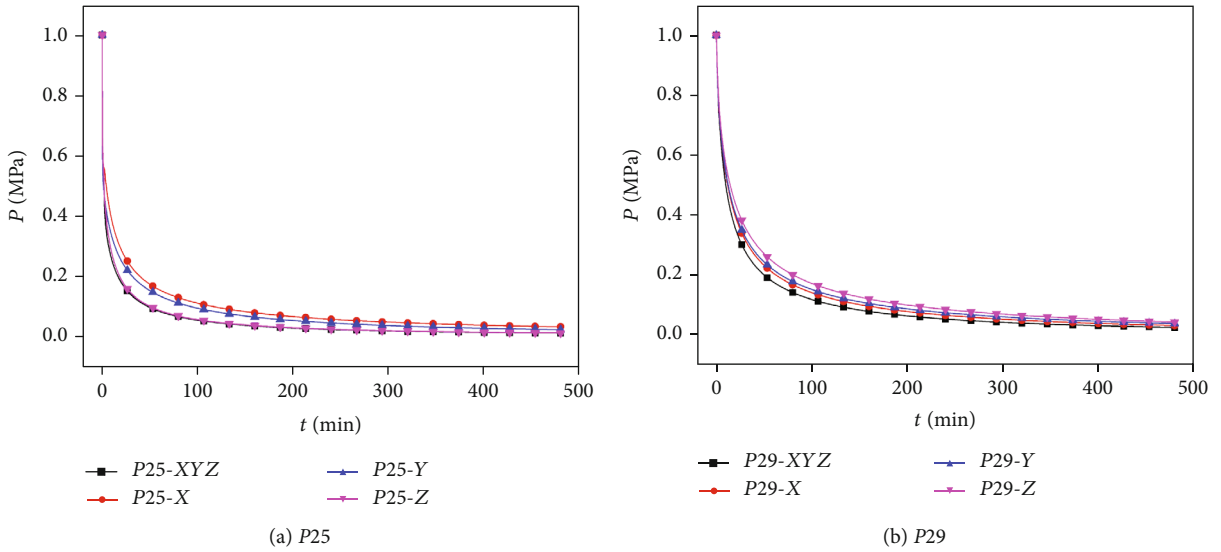
stress in the three directions and unloading stress of Z direction has the minimal impact only if the unloading stress is in one direction.



(a) Gas flow rate and gas production of different branch boreholes

(b) Total gas flow rate and gas production of two boreholes

FIGURE 5: Drainage effect of pressure relief gas drainage.



(a) P25

(b) P29

(c) P40

FIGURE 6: Evolution of gas pressure under different unloading stress paths.

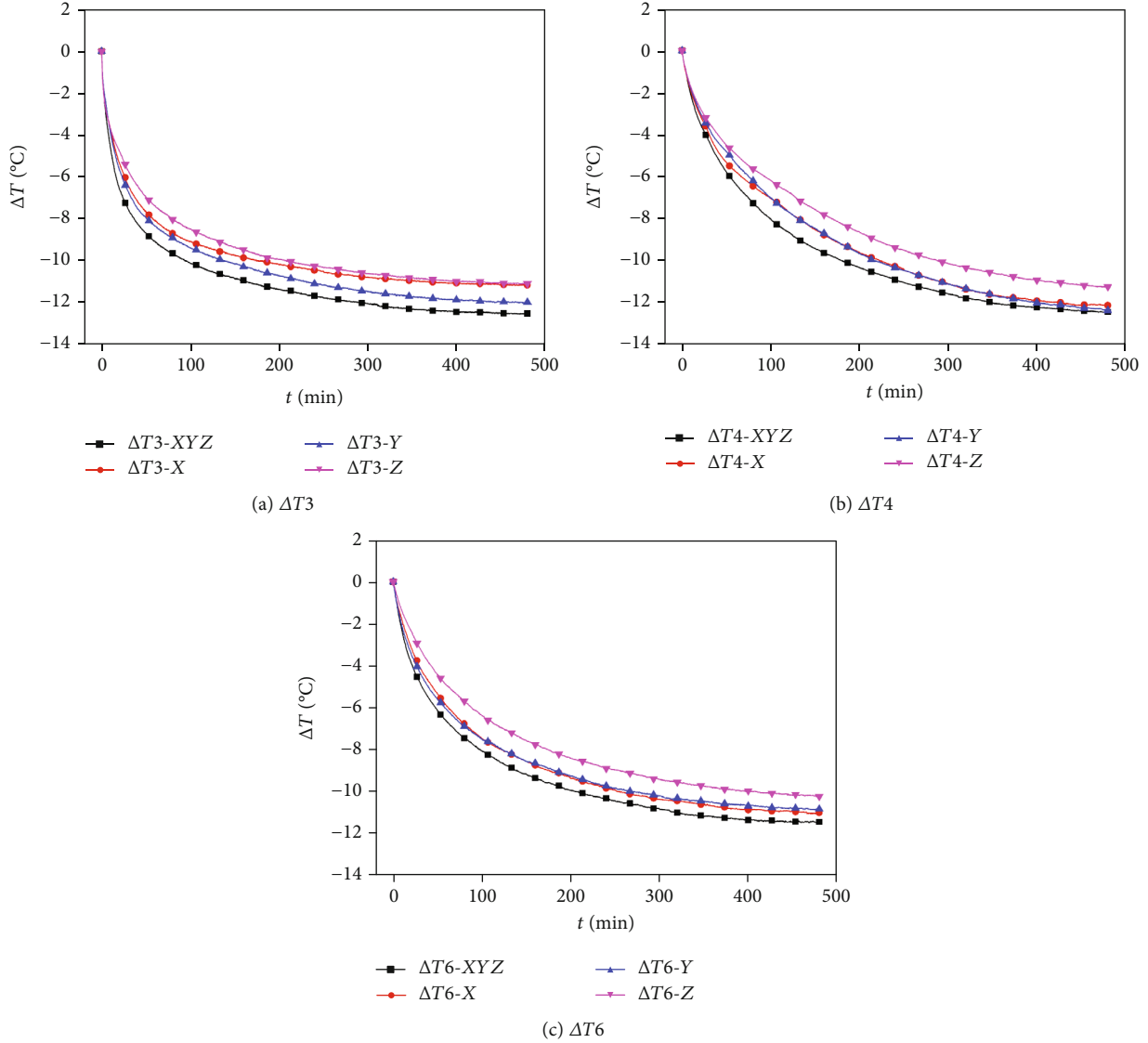


FIGURE 7: Variation of temperature under different unloading stress paths.

3.3. Gas Drainage Effect under Different Unloading Stress Paths. Total gas flow rate and gas production of two boreholes during different experiments are shown in Figure 8(a) demonstrating the impact of unloading stress paths on the gas drainage. Total gas flow rate peaks at the beginning of gas drainage and is 80.64 L/min, 80.54 L/min, 81.14 L/min, and 76.27 L/min with stress unloaded in three directions, namely, X direction, Y direction, and Z direction, respectively. The difference in the gas flow rates decreases gradually, which all have a minimum of 0.83 L/min after drainage of 8 h. Correspondingly, total gas production of four experiments are 2504.77 L, 2380.66 L, 2375.11 L, and 2287.00 L at last. It is apparent that the total gas production with stress unloaded in three directions is the highest and that with stress unloaded in Z direction is the lowest.

Total gas production is one of the key parameters indicating the gas drainage effect and the total gas production outputs at different drainage times with different unloading stress paths are compared further as shown in Figure 8(b).

The total gas production outputs of the three different unloading stress paths are 1108.23 L, 992.18 L, 977.00 L, and 883.93 L after drainage of 30 mins. The total gas production with stress unloaded in three directions is the highest and serves as the control group and therefore the difference coefficient of gas production is defined below.

$$k = \frac{Q-i - Q-XYZ}{Q-XYZ} \times 100\% \quad i = X, Y, Z, \quad (1)$$

Here, k is the difference coefficient of gas production.

The difference coefficients of the three experiments are -10.5%, -11.8%, and -20.2% after drainage of 30 mins indicating that the gas production declines when unloading stress in the Z direction is the largest. However, the difference coefficients of three experiments change to -7.3%, -8.2%, and -13.9% after drainage of 120 mins and finally change to -5.0%, -5.2%, and -8.7%. It is clear that the difference

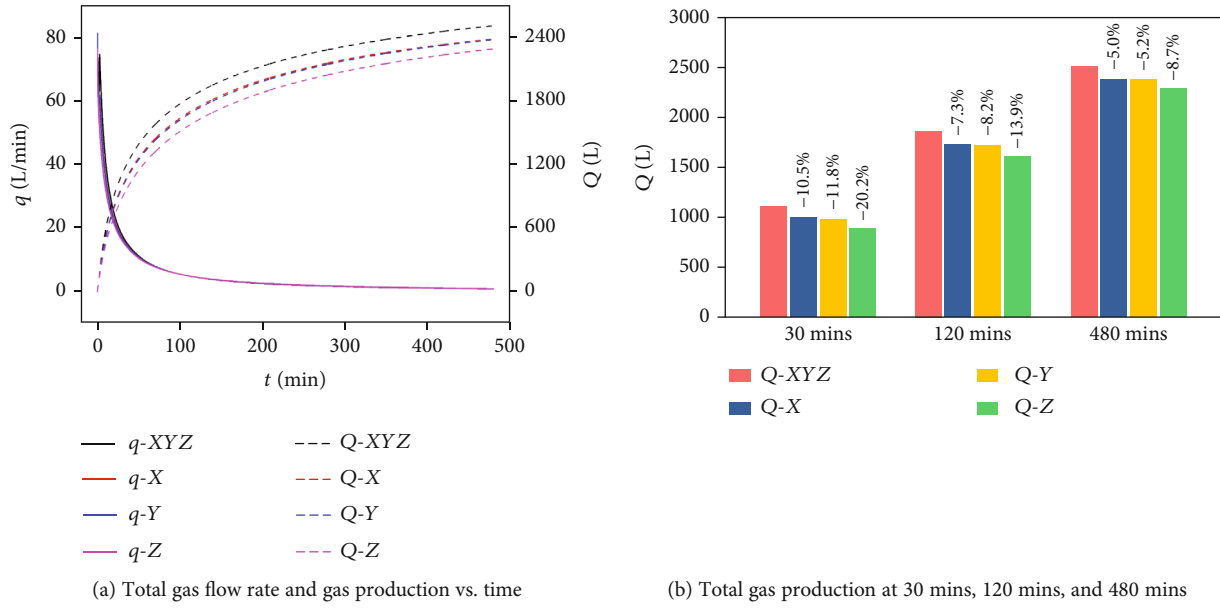


FIGURE 8: Total gas flow rate and gas production under different unloading stress paths.

coefficient of gas production is not only affected by unloading stress paths but also the drainage time.

3.4. Implication for Unloading Stress Path Selection. From the experimental results, the selection of unloading stress path is very important before pressure relief gas drainage, especially when only one direction of stress can be unloaded. Moreover, the effect of pressure relief gas drainage is controlled by unloading stress path and drainage time at the same time, as shown in Figure 9. From the evolution of three curves, we conclude that the gas production when unloading stress is in the Z direction has the largest drop followed by that when unloading stress is in the Y direction and then that when the unloading stress is in the X direction. That is to say, unloading stress in the three directions is the best unloading stress path, while unloading stress in the X direction is the best unloading stress path if only one direction of stress is chosen. Therefore, three directions of stress should be unloaded before pressure relief gas drainage to achieve the desired site conditions. Notably, it is possible that only one direction of stress can be unloaded considering the complex conditions, the difficulty, and long period of unloading stress.

Figure 9 shows that the evolution trends of the three curves are time dependent. The distribution area of the difference coefficient of gas production can be divided into three parts taking -5% and -10% as the demarcation points, namely, light green area, light yellow area, and light red area. The gas drainage effect can be considered to be approximately equal to that with three directions of stress unloaded in the light green area but they have a small gap in the light yellow area and a large gap in the light red area. As a result, the gas drainage effect in a single direction of stress unloaded is poor when conducting a short-term gas drainage (i.e., drainage period before line A) and the gas drainage effect in the X direction or Y direction of stress unloaded is feasible when

conducting a medium-term gas drainage (i.e., drainage period between lines A and B) and the gas drainage effect in the Z direction of stress unloaded is satisfied only when conducting a long-term gas drainage (i.e., drainage period after line B).

In conclusion, the selection of unloading stress path before pressure relief gas drainage can be implemented as follows: Three directions of stress unloaded at the same time is the best selection of unloading stress path if conditions are favorable. The X direction of stress unloaded is the most suitable selection of unloading stress path if only one direction of stress is unloaded, followed by the Y direction of stress unloaded. The Z direction of stress unloaded is a viable selection of unloading stress path only for the long-term gas drainage.

4. Conclusions

Physical experiments of pressure relief gas drainage under different unloading stress paths were conducted using an LSMF device. Gas pressure, coal temperature, and gas flow rate were monitored during the whole drainage period. Gas pressure declines accompanied by a decrease in the coal temperature during drainage showed a similar evolution trend: dropping fast in the early stage and then declining slowly. At the same time, gas flow characteristics were significantly affected by unloading stress paths. Gas pressure and coal temperature had the maximum descent by simultaneously unloading stress in three directions and unloading stress of the Z direction had the minimal impact since only unloading was in one direction of stress. The influence of unloading stress paths on pressure relief gas drainage effect was time dependent, and the following conclusions are drawn: Three directions of stress unloaded is the best selection of unloading stress path if conditions permit. The X direction of stress unloaded is the best selection of unloading stress path if only one direction of stress can be unloaded, followed by the Y

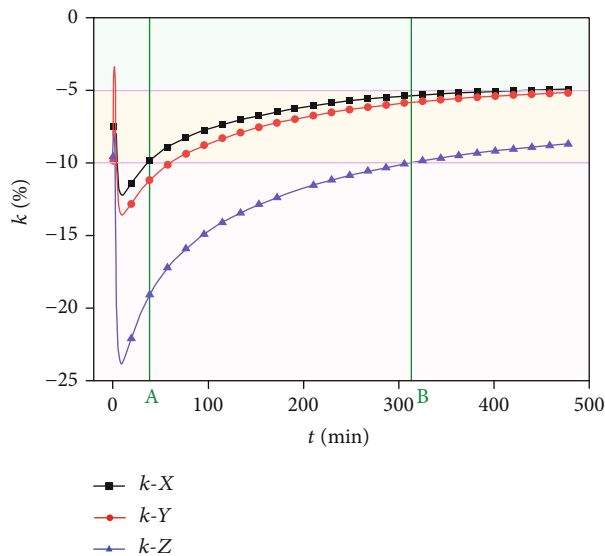


FIGURE 9: Difference coefficient of gas production under different unloading stress paths.

direction of stress unloaded. The Z direction of stress unloaded is a viable selection of unloading stress path only for the long-term gas drainage.

Data Availability

The data used to support the findings of this study are available from the corresponding author upon request.

Conflicts of Interest

The authors declare that there are no conflicts of interest regarding the publication of this study.

Acknowledgments

This work was supported by the National Natural Science Foundation of China (No. 51904293), the National Science and Technology Major Project of China (No. 2016ZX05044-002), the National Science Foundation of Jiangsu Province (No. BK20190627), and the China Postdoctoral Science Foundation (No. 2019M661998).


References

- [1] M. Pillalamarri, S. Harpalani, and S. Liu, "Gas diffusion behavior of coal and its impact on production from coalbed methane reservoirs," *International Journal of Coal Geology*, vol. 86, no. 4, pp. 342–348, 2011.
- [2] Y. Du, X. Chen, L. Li, and P. Wang, "Characteristics of methane desorption and diffusion in coal within a negative pressure environment," *Fuel*, vol. 217, pp. 111–121, 2018.
- [3] C. Zhang, J. Xu, S. Peng, Q. Li, and F. Yan, "Experimental study of drainage radius considering borehole interaction based on 3D monitoring of gas pressure in coal," *Fuel*, vol. 239, pp. 955–963, 2019.
- [4] L. Zhang, T. Ren, N. Aziz, and C. Zhang, "Evaluation of Coal Seam Gas Drainability for Outburst-Prone and High-CO₂-Containing Coal Seam," *Geofluids*, vol. 2019, Article ID 3481834, 14 pages, 2019.
- [5] G. Wang, Y. Liu, and J. Xu, "Short-term failure mechanism triggered by hydraulic fracturing," *Energy Science & Engineering*, vol. 8, no. 3, pp. 592–601, 2020.
- [6] T. A. Moore, "Coalbed methane: A review," *International Journal of Coal Geology*, vol. 101, pp. 36–81, 2012.
- [7] Q. Niu, L. Cao, S. Sang et al., "Study on the anisotropic permeability in different rank coals under influences of supercritical CO₂ adsorption and effective stress and its enlightenment for CO₂ enhance coalbed methane recovery," *Fuel*, vol. 262, article 116515, 2020.
- [8] C. Ö. Karacan, F. A. Ruiz, M. Cotè, and S. Phipps, "Coal mine methane: A review of capture and utilization practices with benefits to mining safety and to greenhouse gas reduction," *International Journal of Coal Geology*, vol. 86, no. 2-3, pp. 121–156, 2011.
- [9] S. A. Keim, K. D. Luxbacher, and M. Karmis, "A numerical study on optimization of multilateral horizontal wellbore patterns for coalbed methane production in Southern Shanxi Province, China," *International Journal of Coal Geology*, vol. 86, no. 4, pp. 306–317, 2011.
- [10] Q. Li, J. Xu, F. Yan, S. Peng, C. Zhang, and X. Zhang, "Evolution characteristics of reservoir parameters during coalbed methane drainage via in-seam horizontal boreholes," *Powder Technology*, vol. 362, pp. 591–603, 2020.
- [11] K. Jin, Y. Cheng, T. Ren et al., "Experimental investigation on the formation and transport mechanism of outburst coal-gas flow: Implications for the role of gas desorption in the development stage of outburst," *International Journal of Coal Geology*, vol. 194, pp. 45–58, 2018.
- [12] G. Wang, P. Wang, Y. Guo, and W. Li, "A Novel True Triaxial Apparatus for Testing Shear Seepage in Gas-Solid Coupling Coal," *Geofluids*, vol. 2018, Article ID 2608435, 9 pages, 2018.
- [13] Y. Gao, F. Gui, and A. Nieto, "A comparative study of gas explosion occurrences and causes in China and the United States," *International Journal of Mining, Reclamation and Environment*, vol. 30, no. 4, pp. 269–278, 2015.
- [14] H. C. Lau, H. Li, and S. Huang, "Challenges and opportunities of coalbed methane development in China," *Energy & Fuels*, vol. 31, no. 5, pp. 4588–4602, 2017.
- [15] C. Zhang, J. Xu, S. Peng, X. Zhang, X. Liu, and Y. Chen, "Dynamic Evolution of Coal Reservoir Parameters in CBM Extraction by Parallel Boreholes Along Coal Seam," *Transport in Porous Media*, vol. 124, no. 2, pp. 325–343, 2018.
- [16] Y. Cheng, Y. Lu, Z. Ge, L. Cheng, J. Zheng, and W. Zhang, "Experimental study on crack propagation control and mechanism analysis of directional hydraulic fracturing," *Fuel*, vol. 218, pp. 316–324, 2018.
- [17] C. Zhang, J. Xu, S. Peng, Q. Li, F. Yan, and Y. Chen, "Dynamic behavior of gas pressure and optimization of borehole length in stress relaxation zone during coalbed methane production," *Fuel*, vol. 233, pp. 816–824, 2018.
- [18] T. Xia, F. Zhou, J. Liu, S. Hu, and Y. Liu, "A fully coupled coal deformation and compositional flow model for the control of the pre-mining coal seam gas extraction," *International Journal of Rock Mechanics and Mining Sciences*, vol. 72, pp. 138–148, 2014.

- [19] L. Zhang, C. Zhang, S. Tu, H. Tu, and C. Wang, "A Study of Directional Permeability and Gas Injection to Flush Coal Seam Gas Testing Apparatus and Method," *Transport in Porous Media*, vol. 111, pp. 573–589, 2016.
- [20] L. Yuan, "Theory of pressure relieved gas extraction and technique system of integrated coal production and gas extraction," *Journal of China Coal Society*, vol. 34, no. 1, pp. 1–8, 2009.
- [21] C. Zhang, L. Zhang, S. H. Tu, D. Y. Hao, and T. Teng, "Experimental and numerical study of the influence of gas pressure on gas permeability in pressure relief gas drainage," *Transport in Porous Media*, vol. 124, no. 3, pp. 995–1015, 2018.
- [22] C. Zhang, S. H. Tu, and L. Zhang, "Pressure-relief and methane production performance of pressure relief gas extraction technology in the longwall mining," *Journal of Geophysics and Engineering*, vol. 14, no. 1, pp. 77–89, 2017.
- [23] G. Z. Yin, M. H. Li, C. B. Jiang, J. Xu, and W. P. Li, "Mechanical behavior and permeability evolution of gas infiltrated coals during protective layer mining," *International Journal of Rock Mechanics and Mining Sciences*, vol. 80, pp. 292–301, 2015.
- [24] G. Z. Yin, H. Qin, and G. Huang, "Experimental study of characteristics of seepage and acoustic emission of gas-filled coal under different stress paths," *Chinese Journal of Rock Mechanics and Engineering*, vol. 32, no. 7, pp. 1315–1320, 2013.
- [25] H. D. Chen, Y. P. Cheng, H. X. Zhou, and W. Li, "Damage and permeability development in coal during unloading," *Rock Mechanics and Rock Engineering*, vol. 46, no. 6, pp. 1377–1390, 2013.
- [26] F. K. Wang, J. F. He, Y. P. Liang, Y. J. Luo, Z. W. Liao, and L. Li, "Study on the permeability characteristics of coal containing coalbed methane under different loading paths," *Energy Science & Engineering*, vol. 6, no. 5, pp. 475–483, 2018.
- [27] Z. Shang, H. F. Wang, Y. P. Wang, B. Li, J. Dong, and Q. Q. Liu, "Optimal selection of coal seam pressure-relief gas extraction technologies: a typical case of the Panyi Coal Mine, Huainan coalfield, China," *Energy Sources, Part A: Recovery, Utilization, and Environmental Effects*, pp. 1–21, 2019.
- [28] C. L. Zhang, J. Xu, G. Z. Yin, S. J. Peng, Q. X. Li, and Y. X. Chen, "A novel large-scale multifunctional apparatus to study the disaster dynamics and gas flow mechanism in coal Mines," *Rock Mechanics and Rock Engineering*, vol. 52, no. 8, pp. 2889–2898, 2019.
- [29] L. Li, D. Z. Tang, Z. J. Pan, H. Xu, and L. L. Guo, "Evaluation of coalbed methane potential of different reservoirs in western Guizhou and eastern Yunnan, China," *Fuel*, vol. 139, pp. 257–267, 2015.
- [30] G. Z. Yin, C. B. Jiang, J. G. Wang, J. Xu, D. M. Zhang, and G. Huang, "A New Experimental Apparatus for Coal and Gas Outburst Simulation," *Rock Mechanics and Rock Engineering*, vol. 49, no. 5, pp. 2005–2013, 2016.
- [31] D. S. Yang, X. Y. Qi, W. Z. Chen, S. G. Wang, and F. Dai, "Numerical investigation on the coupled gas-solid behavior of coal using an improved anisotropic permeability model," *Journal of Natural Gas Science and Engineering*, vol. 34, pp. 226–235, 2016.

Research Article

Numerical Simulation of the Influence of Natural Fractures on Hydraulic Fracture Propagation

Song Yaobin,^{1,2} Lu Weiyong ,^{1,2} He Changchun,³ and Bai Erhu⁴

¹Department of Mining Engineering, Luliang University, Lvliang, Shanxi 033000, China

²Key Laboratory of Maintenance and Inspection of Coal Mine Mechanical Equipment of Lvliang City, Shanxi 033000, China

³School of Civil Engineering and Architecture, East China University of Technology, Nanchang, Jiangxi 330013, China

⁴School of Energy Science and Engineering, Henan Polytechnic University, Jiaozuo, Henan 454000, China

Correspondence should be addressed to Lu Weiyong; 489698551@qq.com

Received 12 June 2020; Revised 1 July 2020; Accepted 7 July 2020; Published 24 July 2020

Academic Editor: Jingmin Xu

Copyright © 2020 Song Yaobin et al. This is an open access article distributed under the Creative Commons Attribution License, which permits unrestricted use, distribution, and reproduction in any medium, provided the original work is properly cited.

According to the theory of plane mechanics involving the interaction of hydraulic and natural fractures, the law of hydraulic fracture propagation under the influence of natural fractures is verified using theoretical analysis and RFPA^{2D}-Flow numerical simulation approaches. The shear and tensile failure mechanisms of rock are simultaneously considered. Furthermore, the effects of the approach angle, principal stress difference, tensile strength and length of the natural fracture, and elastic modulus and Poisson's ratio of the reservoir on the propagation law of a hydraulic fracture are investigated. The following results are obtained: (1) The numerical results agree with the experimental data, indicating that the RFPA^{2D}-Flow software can be used to examine the hydraulic fracture propagation process under the action of natural fractures. (2) In the case of a low principal stress difference and low approach angle, the hydraulic fracture likely causes shear failure along the tip of the natural fracture. However, under a high stress difference and high approach angle, the hydraulic fracture spreads directly through the natural fracture along the original direction. (3) When natural fractures with a low tensile strength encounter hydraulic fractures, the hydraulic fractures likely deviate and expand along the natural fractures. However, in the case of natural fractures with a high tensile strength, the natural fracture surface is closed, and the hydraulic fracture directly passes through the natural fracture, propagating along the direction of the maximum principal stress. (4) Under the same principal stress difference, a longer natural fracture corresponds to the easier initiation and expansion of a hydraulic fracture from the tip of the natural fracture. However, when the size of the natural fracture is small, the hydraulic fracture tends to propagate directly through the natural fracture. (5) A smaller elastic modulus and larger Poisson's ratio of the reservoir result in a larger fracture initiation pressure. The presented findings can provide theoretical guidance regarding the hydraulic fracturing of reservoirs with natural fractures.

1. Introduction

In recent years, hydraulic fracturing has been widely used in the engineering practices of petroleum, natural gas, shale gas, and coal mining [1–5]. The propagation of hydraulic fractures plays a key role in the optimisation of hydraulic fracture design and represents a challenging problem corresponding to the theoretical study of hydraulic fractures [6–9]. However, in the case of fractured reservoirs, the presence of natural fractures can change the path of the hydraulic fracture propagation, leading

to the formation of a complicated fracture propagation system with multibranch fractures, which increases the complexity of the hydraulic fracture network [10, 11]. Therefore, the accurate prediction and control of the hydraulic fracture morphology in fractured reservoirs is critical to improve the oil and gas production in fractured reservoirs [12–16].

Results of numerical simulation and experimental testing have indicated that the horizontal principal stress difference and approach angle corresponding to the hydraulic and natural fractures are the main factors affecting the trends of

hydraulic fractures [17–20]. Rahman et al. suggested that under a low approach angle and low stress difference, a hydraulic fracture could be easily captured, and the natural fracture could open to divert part of the fracturing fluid, thereby preventing the further expansion of the hydraulic fracture. For an intermediate approach angle, the natural fracture was open, and the passing of the hydraulic fracture through the natural fracture depended on the stress difference. Under a low stress difference, only the natural fractures opened. However, under a high stress difference, the hydraulic fractures penetrated the natural fractures. In the case of a high approach angle, the hydraulic fractures always penetrated the natural fractures, regardless of the magnitude of the stress difference. Moreover, Rahman and Rahman indicated that the change in the pore water pressure did not directly influence the interaction between hydraulic and natural fractures; this change only accelerated the restering stress when the hydraulic fracture penetrated the natural fracture, and the pore water pressure influenced the distribution of the water stress in the natural fracture [21]. In the existing calculation model, the mechanical properties of natural fractures are not considered. Moreover, the hydraulic fractures passing through or captured by the natural fractures are identified by assuming that the friction coefficient of the natural fractures is constant. In contrast, the mechanical strength of natural fractures considerably influences the extension behaviour of hydraulic fractures [22, 23]. A mutual interference occurs between the hydraulic and natural fractures, and the natural fractures are prone to shear failure. Specifically, natural fractures inflate under the action of water pressure, resulting in a large amount of fluid loss in the natural fractures [24, 25]. Considering the impact of natural fractures on hydraulic fractures, several studies have been undertaken. However, several aspects such as whether the direction of expansion of hydraulic fractures changes under the action of natural fractures and the mechanism of change in the fracture propagation path have not been effectively addressed [26].

The equivalent plane model is one kind of the equivalent models. With the help of the equivalent plane model in this paper, the actual process is transformed and abstracted into an equivalent, simple, and easy mathematical model, which is convenient for theoretical analysis. In this study, an equivalent plane model of hydraulic and natural fractures is established by combining the stress-seepage theory with seepage-damage mechanics. Moreover, the mechanisms of shear fractures and tensile failure are considered. The RFPA^{2D}-Flow software is used to examine the mechanism of hydraulic fracture propagation under the action of natural fractures. Furthermore, the trends of the hydraulic fracture propagation under the action of the approach angle, principal stress difference, tensile strength, and length of the natural fracture are clarified. These findings not only help improve the established theory of hydraulic fracture networks but also provide theoretical support for engineering practices, such as the optimization of the arrangement of field fracturing boreholes, minimization of the interference of natural fractures in the expansion of hydraulic fractures, effective enhancement of the increase in permeability owing to the hydraulic fractures, and the development of hydraulic fractures in a fractured reservoir.

2. Plane Model and Propagation Mechanism of the Intersection of Hydraulic and Natural Fractures

2.1. Plane Model of Intersection of Hydraulic and Natural Fractures. The influence of the natural fractures on hydraulic fracture propagation depends on the position of the natural fractures. When a hydraulic fracture meets a natural fracture located near a borehole, the natural fracture gradually expands as the fluid pressure is higher than the normal stress acting on the surface of the natural fracture. The following 4 situations may occur during the continuous expansion of the hydraulic fracture: (1) When the natural fracture is in the closed state, shear failure occurs at the intersection (Figure 1(a)). Even if the path of the hydraulic fracture propagation is not affected in this case, a considerable loss of the fracturing fluid occurs. (2) The natural fracture is penetrated by the hydraulic fracture in a closed state (Figure 1(b)). (3) After the expansion of the natural fracture, the hydraulic fracture penetrates the natural fracture at their intersection point and continues to expand along the original direction (Figure 1(c)). (4) The hydraulic fracture expands from one end of the natural fracture and deviates. This phenomenon occurs because the hydraulic fracture propagates along the strike of the inflated natural fracture, and the hydraulic fracture later propagates in a direction perpendicular to the minimum principal stress (Figure 1(d)). The plane model of the intersection of hydraulic and natural fractures is shown in Figure 1.

2.2. Propagation Mechanism of the Intersection of Hydraulic and Natural Fractures. According to the relevant theories of hydraulic fracture propagation, the main hydraulic fracture of coal and rock mass expands in the direction perpendicular to the minimum horizontal principal stress after its initiation. When the hydraulic fracture propagates along the direction of the maximum horizontal principal stress, it intersects with a natural fracture. In Figure 2, the approach angle θ is the angle of intersection between the hydraulic and natural fractures. σ_1 and σ_3 denote the maximum and minimum horizontal principal stresses, respectively.

2.2.1. Hydraulic Fractures Penetrate the Natural Fractures Directly. When a hydraulic fracture intersects a natural fracture, the natural fracture does not inflate if the fluid pressure at the tip of the hydraulic fracture is less than the normal stress σ_n acting on the surface of the natural fracture. The hydraulic fracture in this case directly passes through the natural fracture and extends along the direction of the maximum horizontal principal stress. At this time, the fluid pressure in the hydraulic fracture can be expressed as follows [27, 28].

$$\tau + \sigma_t < p, \quad (1)$$

where τ is the component of the shear stress on the natural fracture under the far-field stress, σ_t is the tensile strength of the natural fracture, and p is the water pressure in the hydraulic fracture.

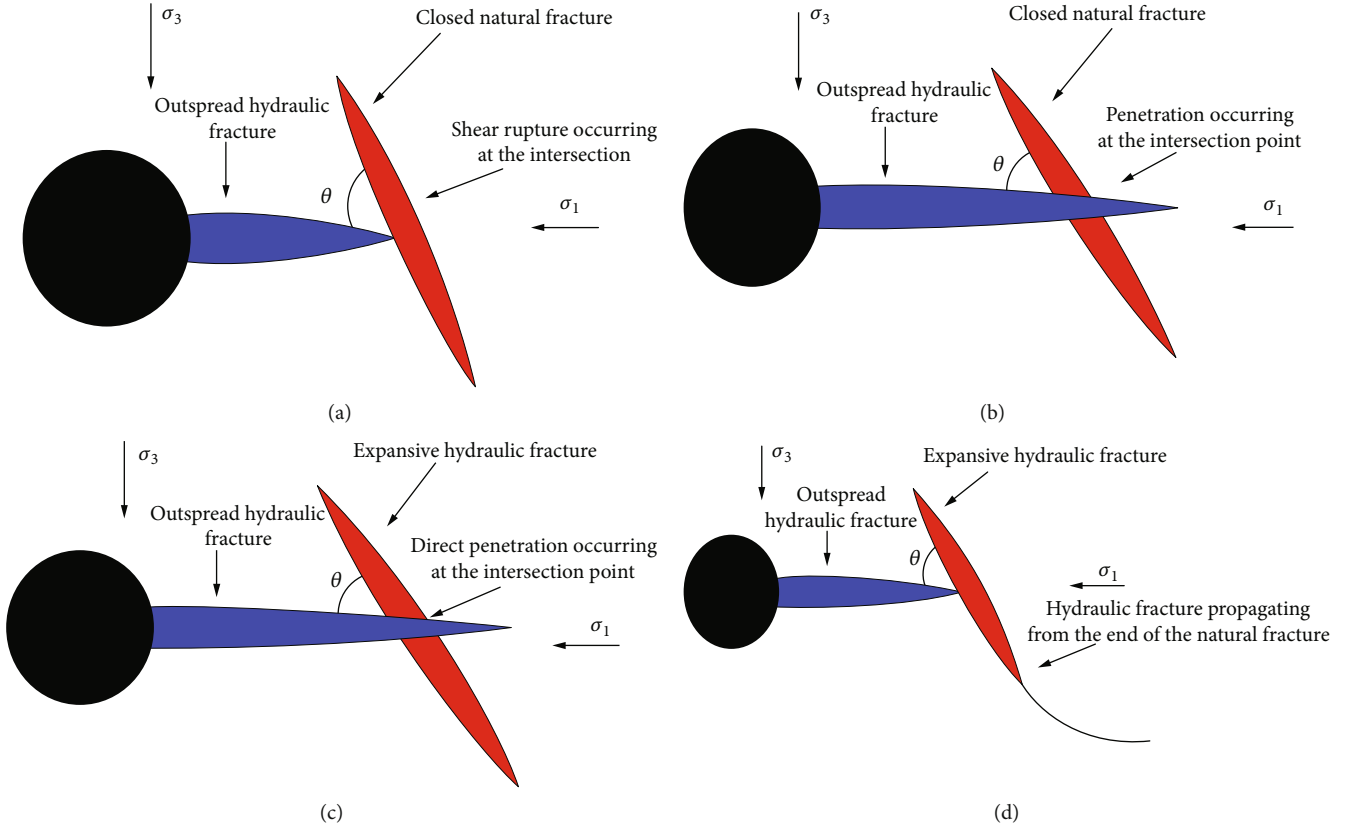


FIGURE 1: Plane models demonstrating the intersection of hydraulic and natural fractures. (a) Hydraulic fracture propagation when shear fracture occurs in the natural fracture. (b) Hydraulic fracture penetrates the natural fracture in the closed state directly. (c) Hydraulic fracture penetrates the natural fracture. (d) Hydraulic fracture expands from one end of the natural fracture.

According to the results of Blanton's research, the shear stress in Equation (1) can be expressed as follows [29, 30]:

$$\tau = p + (\sigma_1 - \sigma_3)(\cos 2\theta - b \sin 2\theta), \quad (2)$$

where

$$\begin{aligned} b &= \frac{1}{2a} \left[v(x_0) - \frac{x_0 - l}{K_f} \right], \\ x_0 &= \left[\frac{(1 + a^2) + e^{\pi/2K_f}}{1 + e^{\pi/2K_f}} \right]^{1/2}, \\ v(x_0) &= \frac{1}{\pi} \left[(x_0 + l) \ln \left(\frac{x_0 + l + a}{x_0 + l} \right)^2 \right. \\ &\quad \left. + (x_0 - l) \ln \left(\frac{x_0 - l - a}{x_0 - l} \right)^2 \right. \\ &\quad \left. + a \ln \left(\frac{x_0 + l + a}{x_0 - l - a} \right)^2 \right], \end{aligned} \quad (3)$$

where a is the relative sliding length of the natural fracture and l is the length of the natural fracture.

By substituting Equation (2) into Equation (1), Equation (4) can be obtained to evaluate whether the hydraulic fracture directly passes through the natural fracture.

$$\frac{\sigma_1 - \sigma_3}{\sigma_{t0}} > \frac{1}{\cos 2\theta - b \sin 2\theta}. \quad (4)$$

When Equation (4) is satisfied, the fracture directly passes through the natural fracture and propagates along the original direction. Moreover, Equation (4) indicates that the passing of the hydraulic fracture through the natural fracture is influenced by the principle stress difference $\Delta\sigma$ ($\Delta\sigma = \sigma_1 - \sigma_3$), approach angle θ , tensile strength σ_t , and length l of the natural fracture, among other factors.

2.2.2. Hydraulic Fracture Propagates along the Natural Fracture. Considering the ground stress field and the orientation of the natural fractures shown in Figure 2, the normal stress σ_n and shear stress τ acting on the natural fracture surface can be obtained using a two-dimensional stress solution, which can be expressed as follows [31].

$$\sigma_n = \frac{\sigma_1 + \sigma_3}{2} + \frac{\sigma_1 - \sigma_3}{2} \cos 2(90 - \theta), \quad (5)$$

$$\tau = \frac{\sigma_1 - \sigma_3}{2} \sin 2(90 - \theta). \quad (6)$$

When the shear stress acting on the natural fracture surface is greater than the shear strength of the natural fracture surface, shear failure occurs in the natural fracture [32]. According to the linear friction theory, the mathematical condition under which this shear failure occurs is as follows [33, 34].

$$|\tau| > C_0 + K_f(\sigma_n - p), \quad (7)$$

where C_0 is the cohesion of the natural fracture and K_f is the friction coefficient of the natural fracture surface.

By substituting Equations (5) and (6) into Equation (7), the following expression can be obtained:

$$(\sigma_1 - \sigma_3)(\sin 2\theta + K_f \cos 2\theta) - K_f(\sigma_1 + \sigma_3 - 2p) > 2C_0. \quad (8)$$

The fluid pressure in the natural fracture surface must be lower than the normal stress acting on the natural fracture surface; otherwise, the fracture is opened, that is, the fluid pressure satisfies the following relation:

$$p < \frac{\sigma_1 + \sigma_3}{2} + \frac{\sigma_1 - \sigma_3}{2} \cos 2(90 - \theta). \quad (9)$$

According to the theory of fracture propagation, the Griffith linear fracture propagation requires the minimum fluid pressure. Assuming that the fracture is a Griffith fracture, the water pressure at the tip of the hydraulic fracture can be expressed as follows:

$$p = \sigma_3 + \sqrt{\frac{2E\gamma}{\pi L(1 - \mu^2)}}, \quad (10)$$

where E is the elastic modulus of the reservoir rock, γ is the surface energy per unit area of the reservoir rock, L is the half length of the Griffith fracture, and μ is the Poisson's ratio of the reservoir rock.

Hence, the following expression can be obtained:

$$\sigma_1 - \sigma_3 > \frac{2c - 2K_f \sqrt{2E\gamma/(\pi L(1 - \mu^2))}}{\sin 2\theta - K_f + K_f \cos 2\theta}. \quad (11)$$

According to Equation (11), when hydraulic fractures encounter natural fractures, the factors that determine whether the hydraulic fractures can extend along the natural fractures include the horizontal principal stress difference $\Delta\sigma$, approach angle θ , length of the natural fracture l , friction coefficient K_f , elastic modulus of the rock mass E , and Poisson's ratio μ .

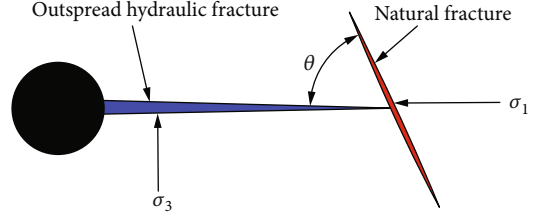


FIGURE 2: Plane model of a hydraulic fracture intersecting a natural fracture.

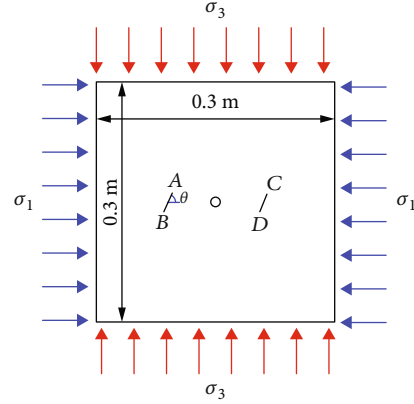


FIGURE 3: Geometric model.

3. Verification of Simulation Results of Hydraulic Fracture Propagation under the Influence of Natural Fractures

3.1. Geometric Model. In this paper, RFPA^{2D}-Flow software, a seepage-stress coupling analysis system for rock fracture instability, is used to analyze the interaction mechanism between natural fractures and hydraulic fractures based on the damage mechanics theory, in which both tensile and shear failure criteria of the rock are chosen [35, 36]. In this numerical simulation, a two-dimensional plane stress model (Figure 3) sized 0.5 m \times 0.5 m is adopted. All the boundaries are impermeable and constrained by the confining pressure. Both the bottom and left boundaries are fixed. The centre of the borehole with a diameter of 0.02 m coincides with the centre of the model. The model is divided into 300 \times 300 cells. Cracks AB and CD are arranged in advance at equal distances on the left and right sides of the borehole, respectively. The lengths and widths of the two preexisting cracks are, respectively, 0.04 m and 0.002 m. The tensile strength of the two preexisting cracks is 6.5 MPa, and the internal friction angle is 30°. The maximum principal stress σ_1 in the horizontal direction is 10 MPa, and the minimum principal stress σ_3 in the vertical direction is 5 MPa. The initial water pressure applied in the borehole is 0 MPa, and the step increment is 0.5 MPa.

3.2. Parameter Selection. To ensure that the numerical calculation can more closely simulate the real physical experiment, the actual physical parameters of the experimental sample are adopted in the numerical simulation as much as possible.

TABLE 1: Parameters used in the numerical simulation.

Parameter	Value and unit	Parameter	Value and unit
Tensile strength σ_t	6.5/10.5 MPa	Internal friction angle	30°
Elastic modulus E	50 GPa	Residual strength	0.1%
Compression tension ratio	10	Pore water pressure coefficient	0.1
Permeability coefficient k	0.000864 m/d	Maximum compression strain coefficient	200
Maximum tension strain coefficient	1.5	Water increment Δp_w for each step	0.5 MPa
Initial water pressure p_{w0}	0 MPa	Vertical principle stress σ_1	5 MPa
Horizontal principle stress σ_1	10 MPa	Approach angle θ	45/90°

The relevant parameters utilized in this numerical simulation are presented in Table 1. Parameters such as compressiveness, tension strength, elastic module, and Poisson's ratio can be determined based on the experimental test. The permeability can be calculated by the laboratory experiment. Before water is poured into the fracturing borehole, there is no water pressure. Therefore, the initial water pressure is 0 MPa.

3.3. Propagation of Hydraulic Fractures under the Influence of Natural Fractures. Figure 4 indicates that (1) the hydraulic fracture penetrates the natural fracture from one end and passes through the natural fracture. Subsequently, the hydraulic fracture continues to extend along the other end of the natural fracture. In other words, the hydraulic fracture completely extends along the natural fracture, as shown in Figure 4(a). (2) When the hydraulic fracture encounters the natural fracture, it does not deviate and expand along the natural fracture but directly penetrates the natural fracture and continues to expand along the direction of the maximum horizontal stress, as shown in Figure 4(b). (3) When the hydraulic fracture encounters the natural fracture, the left hydraulic fracture deviates; after this fracture expands from one end of the natural fracture, it eventually propagates along the direction of the maximum principle stress. However, the right hydraulic fracture directly penetrates the natural fracture, as shown in Figure 4(c).

The numerical results indicate that the hydraulic fracture can propagate via three paths under the action of natural fractures. (1) The hydraulic fracture extends completely along the natural fracture. The fractures are generated around the natural fracture, and their expansion is not evident. (2) The hydraulic fracture penetrates the natural fracture and expands along the original direction. The length of the generated hydraulic fracture is considerably larger than that of the natural fracture; however, few short fractures are present around the natural fracture. (3) The hydraulic fracture propagates through and along the natural fracture simultaneously, including cases (1) and (2), resulting in a larger number of fractures and a wider distribution range. These three cases are consistent with the theoretical plane model of the intersection of the hydraulic and natural fractures. In the exploitation of oil and gas resources, the third case leads to the formation of a hydraulic fracture network and can reduce the engineering quantity, thereby improving the exploitation efficiency of the oil and gas resources.

Renshaw and Pollard et al. examined the critical approach angle of a hydraulic fracture passing through a natural fracture under different stress conditions by conducting a physical experiment and obtained the critical curve of the hydraulic fracture passing through the natural fracture (black solid line in Figure 5)[37]. The Renshaw and Pollard criterion can be used to predict the results of the interaction of the hydraulic and natural fractures. A comparison of the numerical results, indicated by the red stars and blue dots in Figure 5, and the experimental results obtained by Renshaw and Pollard et al. indicate that the numerical results are in agreement with the Renshaw and Pollard criterion. In other words, the numerical results are consistent with the experimental results.

4. Influence of Natural Fractures on the Hydraulic Fracture Propagation

The homogeneity, size, number of cells, borehole aperture, and basic mechanical parameters of the model were kept unchanged, and the single variable method was used to examine the influence of the approach angle, principle stress difference, tension strength and length of the natural fracture, elastic modulus, and Poisson's ratio on the hydraulic fracture propagation.

4.1. Influence of the Approach Angle on the Hydraulic Fracture Propagation. When the approach angle θ is 0°, 30°, 45°, 60°, and 90°, the propagation of the hydraulic fracture is as shown in Figures 6(A)–6(E), respectively. The following observations can be made: (1) When θ is 0°, 30°, and 45°, the hydraulic fracture first propagates along the direction perpendicular to the minimum principal stress σ_3 . After the hydraulic fracture intersects the natural fracture, it extends along the natural fracture and propagates from one end of the natural fracture. Subsequently, the fracture deviates and continues expanding in the direction of the maximum horizontal principal stress σ_1 . For a smaller angle θ , this phenomenon is more notable because a smaller θ corresponds to a smaller normal stress σ_n on the natural fracture. Consequently, a smaller shear stress τ and tensile stress σ_t are required for the sliding of the hydraulic fracture and opening of the natural fracture surface, respectively. The natural fracture opens easily, and the hydraulic fracture continues to expand along one end of the natural fracture surface. In the case of a low stress difference and approach angle, the natural

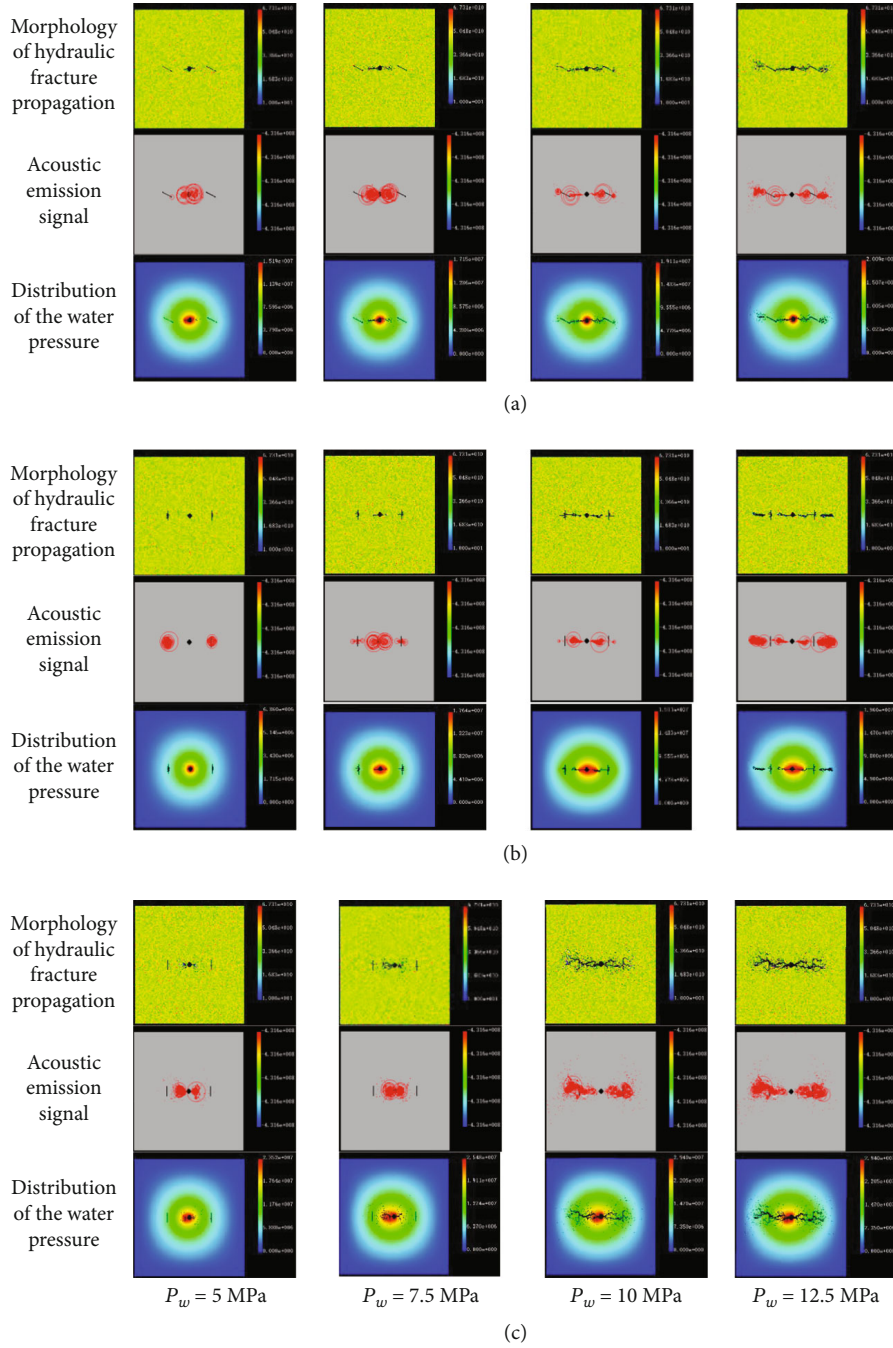


FIGURE 4: Propagation processes of a hydraulic fracture under the action of a natural fracture. (a) Propagation of a hydraulic fracture along a natural fracture. (b) Propagation of a hydraulic fracture penetrating the natural fracture. (c) Propagation of a hydraulic fracture through and along a natural fracture.

fracture is activated by the hydraulic fracture, and part of the pore water pressure is transferred, thus preventing the hydraulic fracture from further passing through the natural fracture. (2) When θ is 60° and 90° , the hydraulic fracture directly passes through the natural fracture, indicating that the hydraulic fracture can easily pass through the existing natural fracture under a high approach angle. This finding can be attributed to the fact that a larger approach angle θ corresponds to a larger normal stress σ_n on the natural fracture. Consequently, a greater shear stress τ tensile stress σ_t

are required for the sliding of the hydraulic fracture and opening of the natural fracture surface, respectively. The natural fracture is difficult to be opened, and the hydraulic fracture penetrates the natural fracture directly.

4.2. Influence of Difference in the Main Stress on the Hydraulic Fracture Propagation. Considering the minimum main stress σ_3 as 5 MPa and the maximum main stress σ_1 as 5 MPa, 10 MPa, 15 MPa, 20 MPa, 25 MPa, and 30 MPa, the corresponding horizontal stress difference $\Delta\sigma$ is 0 MPa,

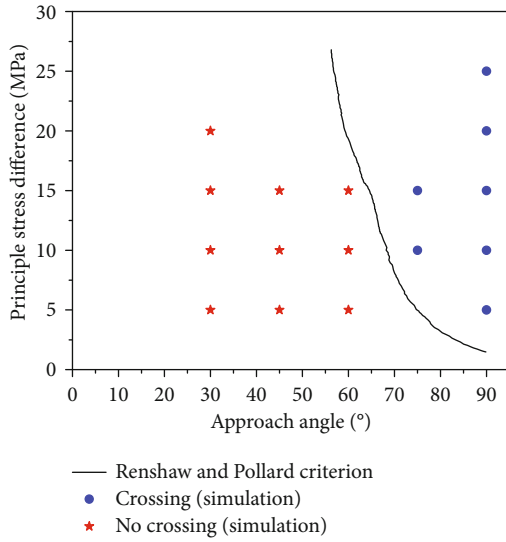


FIGURE 5: Comparison of numerical simulation and experimental results.

5 MPa, 10 MPa, 15 MPa, and 20 MPa, respectively. The process of hydraulic fracture propagation under different horizontal stress differences is shown in Figure 7. The following observations can be made: (1) When the horizontal stress difference $\Delta\sigma$ is 5 MPa, the hydraulic fracture first propagates along the direction perpendicular to the minimum principal stress. After intersecting with the natural fracture, the hydraulic fracture expands from one end of the natural fracture and deviates to expand along the direction of the maximum principal stress again. This finding shows that the natural fracture is activated by the hydraulic fracture, and a part of the pore water pressure is transferred under the condition of a low stress difference, thereby preventing the hydraulic fracture from further passing through the natural fracture. (2) When the horizontal stress difference $\Delta\sigma$ is 10 MPa and 15 MPa, after the hydraulic fracture intersects with the natural fracture, the hydraulic fracture on the left side propagates along the direction perpendicular to the natural fracture. Furthermore, the fluid permeates along the interface of the natural fracture. After the left hydraulic fracture permeates along the interface for a certain distance, it penetrates the interface and expands along the original direction. The hydraulic fracture on the right side penetrates directly through the natural fracture and continues expanding along the direction perpendicular to the minimum principle stress. (3) When the horizontal stress difference $\Delta\sigma$ is 20 MPa and 25 MPa, after the hydraulic fracture intersects the natural fracture, it expands along the direction of the maximum principle stress. This finding shows that the hydraulic fracture easily passes through the existing natural fracture under a high stress difference.

When the principal stress difference $\Delta\sigma$ is small, the random distribution of the crystals and defects in the rock influence the propagation process. The rupturing of the rock far from the natural fracture in the model is more notable, and the shape of the hydraulic fracture is more tortuous. At this

time, the natural fracture is more likely to be opened, and the hydraulic fracture is more likely to expand along the natural fracture. With the increase in the principal stress difference $\Delta\sigma$, the propagation form of the hydraulic fracture is relatively straight and parallel to the direction of the maximum principal stress σ_1 . The branch fractures at the tip of the hydraulic fracture are not significant. At this time, the hydraulic fracture is more likely to expand after penetrating the natural fracture.

4.3. Effect of Tensile Strength of the Natural Fracture on the Hydraulic Fracture Propagation. When the tension strength σ_t of the natural fracture is 6 MPa, 8 MPa, 10 MPa, 12 MPa, and 14 MPa, the process of the hydraulic fracture propagation is as shown in Figure 8. The following observations can be made: (1) When the tensile strength σ_t of the natural fracture is small, the hydraulic fracture is more likely to deviate and expand along the natural fracture. Due to the change in the stress field surrounding the natural fracture, the hydraulic fracture extends at the end of natural fracture when the hydraulic fracture approaches the natural fracture or its tip. The width of the hydraulic fracture in the extension part is considerably smaller than its initial width. (2) However, with the increase in the tensile strength, the hydraulic fracture tends to penetrate the natural fracture and expands along the direction of the maximum principal stress. This aspect can be explained by the fact that the hydraulic fractures tend to extend in the direction of the least resistance. When the tensile strength of the natural fracture surface is large, the hydraulic fracture surface does not undergo shear and tensile failure, which impedes the opening of the natural fracture in the process of hydraulic fracture propagation. However, when the tensile strength of the natural fracture is small, the weak plane characteristics of the natural fracture surface are apparent, which facilitates the propagation of the hydraulic fracture along the natural fracture. This finding shows that the propagation pattern of a hydraulic fracture is closely related to the interface material of the natural fracture. The hydraulic fracture easily expands along the direction of the least resistance instead of along the whole path. Consequently, the branch fractures occur easily.

4.4. Effect of the Natural Fracture Length on the Hydraulic Fracture Propagation. The hydraulic fracture may extend along the natural fracture. After extending for a certain distance, the branches of the hydraulic fractures tend to deviate, which is beneficial for the hydraulic fracture expansion. In some cases, the hydraulic fracture extends through the natural fracture. Under the same principal stress difference, a smaller natural fracture length l corresponds to an easier expansion of the hydraulic fracture from the natural fracture tip, as shown in Figures 9(A) and 9(B). However, in the case of a natural fracture with a larger length, the hydraulic fracture tends to directly propagate through the natural fracture, as shown in Figures 9(C)–9(E). According to Equation (11), when the principle stress difference is fixed, a smaller natural fracture can more easily satisfy the mechanical conditions of the hydraulic fracture propagating along the natural fracture. In contrast, a longer natural fracture makes it more difficult

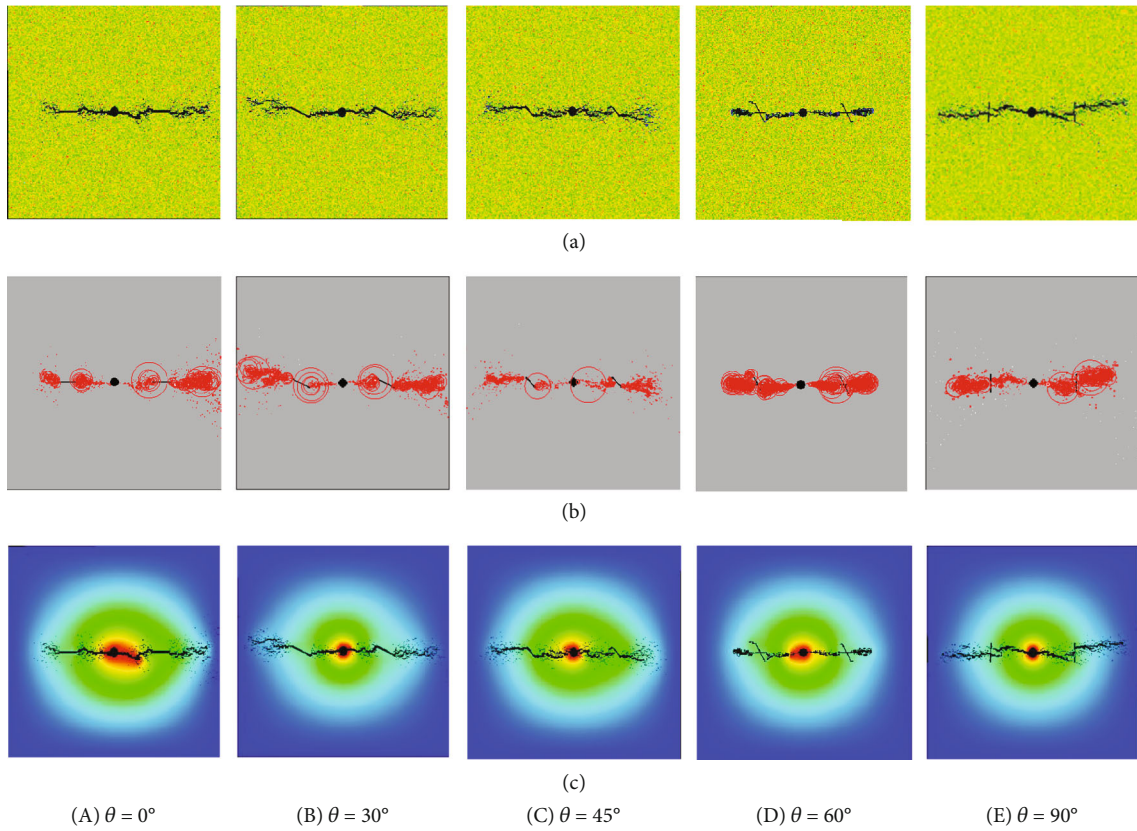


FIGURE 6: Process of hydraulic fracture propagation under different approach angles. (a) Morphology of hydraulic fracture propagation. (b) Acoustic emission signal. (c) Cloud map of pore water pressure.

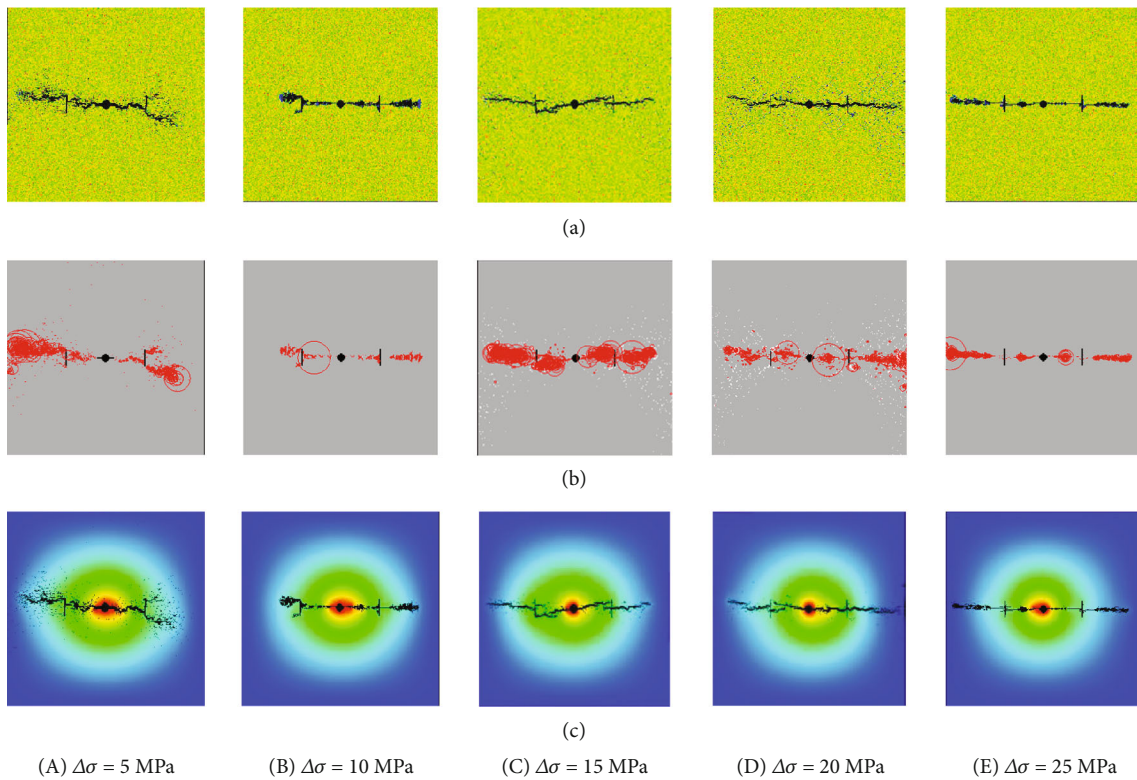


FIGURE 7: Process of hydraulic fracture propagation under different horizontal principle stress differences $\Delta\sigma$. (a) Morphology of the hydraulic fracture propagation. (b) Acoustic emission signal. (c) Cloud map of the pore water pressure.

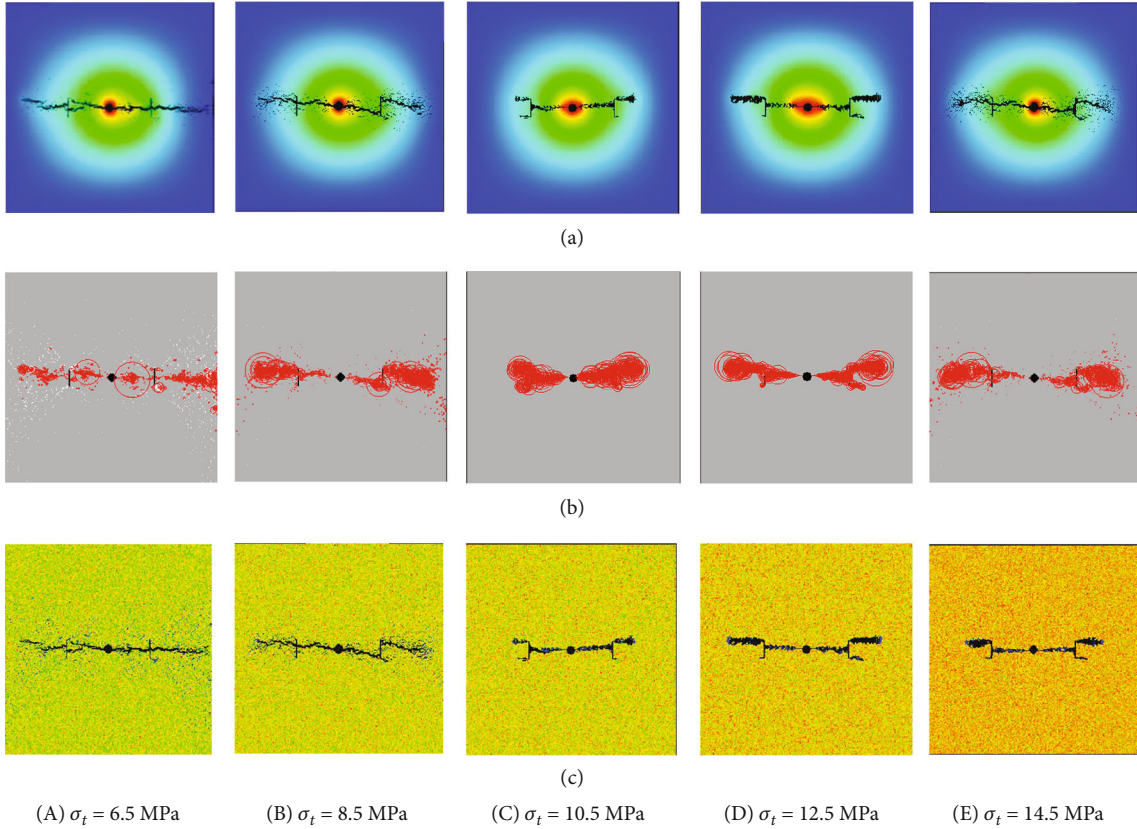


FIGURE 8: Process of hydraulic fracture propagation under different tensile strengths σ_t . (a) Cloud map of the pore water pressure. (b) Acoustic emission signal. (c) Morphology of the hydraulic fracture propagation.

to satisfy the mechanical conditions of the hydraulic fracture propagating along the natural fracture.

4.5. Influence of Elastic Properties of the Reservoir Rock on the Hydraulic Fracture Propagation. The elastic modulus E and Poisson's ratio μ are two important parameters to express the ability of a rock to resist deformation under the action of an external load. These two parameters are strongly related to the strength and brittleness of the rock. In general, a larger elastic modulus of the rock corresponds to a smaller Poisson's ratio. The elastic model of sedimentary rock is characterised by a higher heterogeneity. In the numerical simulation performed using the RFPA^{2D}-Flow software, both the nonuniformity of the rock strength and elastic modulus are considered. Therefore, the initiation and expansion processes of a hydraulic fracture under the action of a natural fracture, simulated using the RFPA^{2D}-Flow software, are sufficiently realistic.

The relationship between the elastic modulus of the reservoir rock and the opening pressure of the natural fracture is shown in Figure 10. The following observations can be made: (1) For a certain approach angle θ , the critical opening pressure required for a natural fracture gradually decreases with the increase in the elastic modulus E . This aspect can quantitatively explain the fact that the effect of perforation fracturing in a reservoir with a high elasticity and brittleness is more notable than that in a reservoir with a low elasticity

and high toughness. (2) For a certain elastic modulus E , with the increase in the approach angle θ , the opening pressure required for the natural fracture increases. When the approach angle θ is 90° , the opening pressure of the natural fracture reaches its maximum value.

The relationship between the Poisson's ratio μ of the reservoir rock and opening pressure of the natural fracture is shown in Figure 11. The following observations can be made: (1) For a certain approach angle θ , when the Poisson's ratio μ is small, the opening pressure of the natural fracture is also small. With the increase in the Poisson's ratio μ , the opening pressure of the natural fracture increases. In particular, a reservoir with a higher elastic modulus usually has a smaller Poisson's ratio. Therefore, the influence of the elastic modulus and Poisson's ratio on the opening pressure of the natural fracture is consistent. (2) For a certain Poisson's ratio, with the increase in the approach angle, the opening pressure of the natural fracture also increases. When the approach angle θ is 90° , the opening pressure of the natural fracture exhibits its maximum value.

5. Discussion

The influence of natural fractures on hydraulic fracture propagation has been always a hot topic. In this paper, only two natural fractures are chosen. In fact, the number of the natural fractures is far more than two natural fractures in

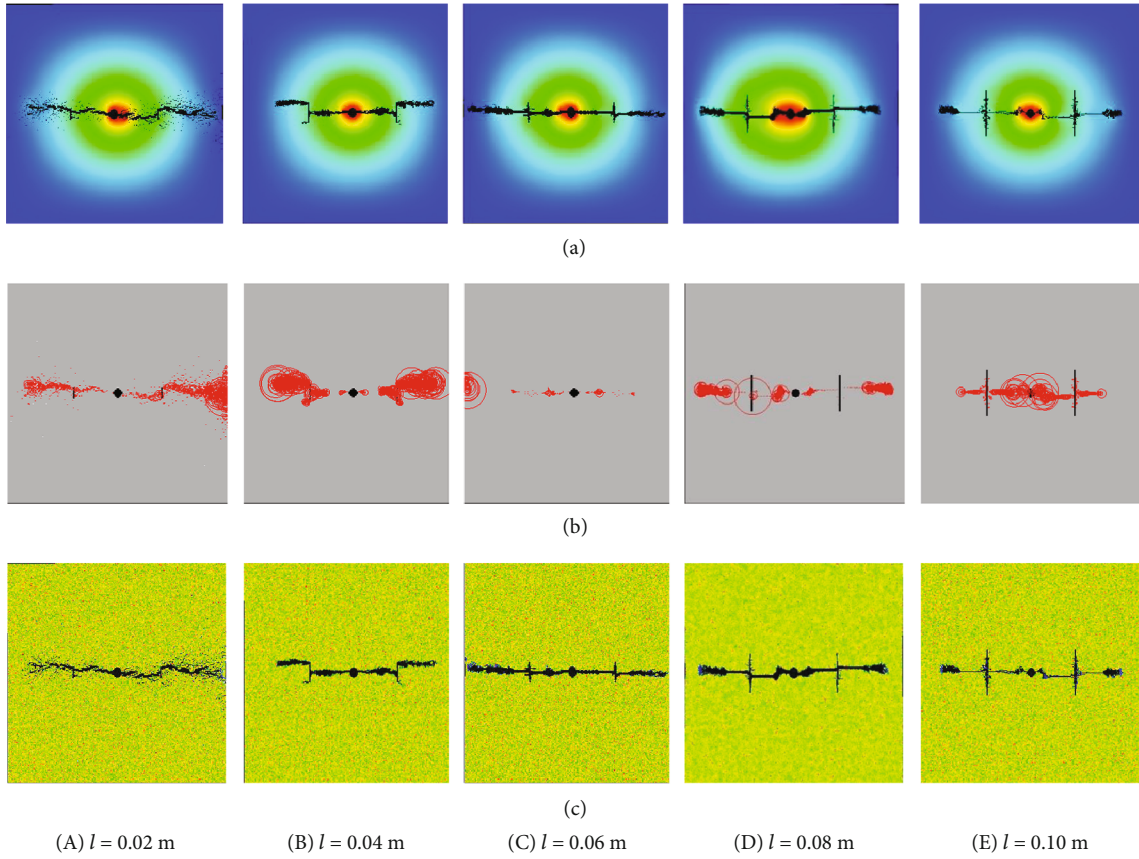


FIGURE 9: Process of hydraulic fracture propagation under different natural fracture lengths l . (a) Cloud map of the pore water pressure. (b) Acoustic emission signal. (c) Morphology of the hydraulic fracture propagation.

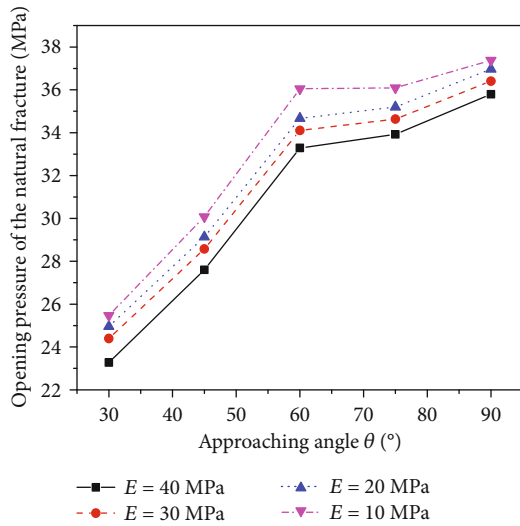


FIGURE 10: Opening pressure of the natural fracture under different elastic moduli.

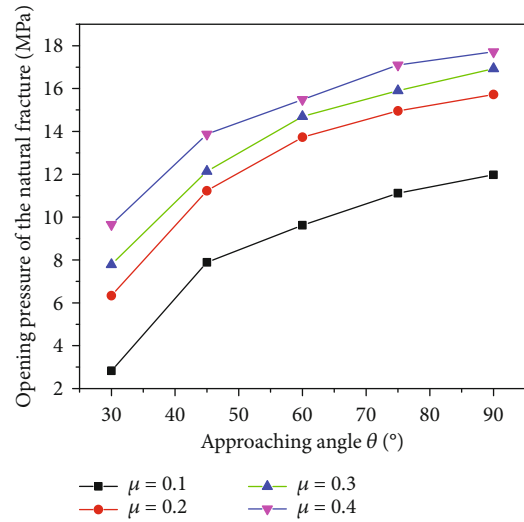


FIGURE 11: Opening pressure of the natural fracture under different Poisson's ratios.

the fractured reservoir. In the next research, more natural fractures should be adopted in the numerical model. Of course, the plane model and propagation mechanism of the intersection of hydraulic and natural fractures will become more complex.

RFPFA^{2D}-Flow is a good numerical computational software, which can realize the visualization of the hydraulic fracture process. However, the process of the numerical simulation depends on the increment step, not the time. Therefore, much more dependent variable, such as water

pressure, length, and width of the hydraulic fracture and the like, which regard time as independent variable, cannot be obtained.

6. Conclusions

- (1) Considering the tensile and shear failure mechanisms of rock rupture, a theoretical model for the hydraulic fracture propagation under the action of a natural fracture is established based on the equivalent plane fracture theory of hydraulic and natural fractures. The morphology of the hydraulic fracture determined using the numerical simulation is in agreement with the existing physical experiment results.
- (2) In the case of a large approach angle, the hydraulic fracture directly passes through the natural fracture, and the initiation pressure of the natural fracture gradually increases. When the approach angle is 90° , the initiation pressure of the natural fracture reaches its maximum value. When the approach angle is small, the hydraulic fracture expands along the natural fracture, propagates from one end, and deviates and continues expanding along the direction of the maximum horizontal principal stress.
- (3) Under a low principle stress difference, the hydraulic fracture tends to expand along the natural fracture, and the development of the hydraulic fracture is relatively complex. However, with the increase in the principal stress difference, the hydraulic fracture tends to penetrate the natural fracture. This aspect shows that under a low principal stress difference, the natural fracture is more likely to be opened, which facilitates the development of the hydraulic fracture.
- (4) When the tensile strength of the natural fracture is large, the hydraulic fracture cannot induce shear and tensile failure, which impedes the opening of the natural fracture and the propagation of the hydraulic fracture. In contrast, when the tensile strength of the natural fracture is small, the weak surface features of the natural fracture are prominent, which facilitates the opening of the natural fracture.
- (5) With the increase in the elastic modulus or decrease in the Poisson's ratio, the critical opening pressure of the natural fracture decreases. Since the reservoir rock with a higher elastic modulus usually has a smaller Poisson's ratio, the influence of the elastic modulus and Poisson's ratio on the opening pressure of the natural fracture is consistent.

Data Availability

The data in the manuscript can be available on request through Weiyong Lu, whose email address is 489698551@qq.com.

Conflicts of Interest

The authors declare that they have no known competing financial interests or personal relationships that could have appeared to influence the work reported in this paper.

Acknowledgments

The authors would like to particularly thank Dalian Mechsoft Co. Ltd for their help in providing the free RFPA^{2D}-Flow software for three months. This work was supported by the Transformation of Scientific and Technological Achievements Programs (TSTAP) of Higher Education Institutions in Shanxi (No. 2020CG050), the Special Project of 2019 Plan for the Introduction of High-Level Scientific and Technological Talents in Development Zone of Lvliang City (development of automatic disassembly platform for hydraulic support pin shaft) (No. 2019L0002), the Science and Technology Project of Lvliang City in 2019 (pressure relief and permeability improvement technology by integrated hydraulic flushing and cutting for low permeability coal seam containing methane) (No. 2019L0008), and the National Natural Science Foundation of China (Nos. 51774111 and 51974105).

References

- [1] W. Lu, B. Huang, and X. Zhao, "A review of recent research and development of the effect of hydraulic fracturing on gas adsorption and desorption in coal seams," *Adsorption Science & Technology*, vol. 37, no. 5-6, pp. 509–529, 2019.
- [2] S. Tripoppoom, J. Xie, R. Yong et al., "Investigation of different production performances in shale gas wells using assisted history matching: hydraulic fractures and reservoir characterization from production data," *Fuel*, vol. 267, article 117097, 2020.
- [3] G. Gunarathna and B. G. Da Silva, "Influence of the effective vertical stresses on hydraulic fracture initiation pressures in shale and engineered geothermal systems explorations," *Rock Mechanics and Rock Engineering*, vol. 52, no. 11, pp. 4835–4853, 2019.
- [4] L. Zhai, H. Zhang, D. Pan et al., "Optimisation of hydraulic fracturing parameters based on cohesive zone method in oil shale reservoir with random distribution of weak planes," *Journal of Natural Gas Science and Engineering*, vol. 75, article 103130, 2020.
- [5] L. Cheng, D. Wang, R. Cao, and R. Xia, "The influence of hydraulic fractures on oil recovery by water flooding processes in tight oil reservoirs: an experimental and numerical approach," *Journal of Petroleum Science and Engineering*, vol. 185, article 106572, 2020.
- [6] P. Behnoudfar, M. B. Asadi, A. Gholilou, and S. Zendehboudi, "A new model to conduct hydraulic fracture design in coalbed methane reservoirs by incorporating stress variations," *Journal of Petroleum Science and Engineering*, vol. 174, pp. 1208–1222, 2019.
- [7] K. Cao, P. Siddhamshetty, Y. Ahn, R. Mukherjee, and J. S. I. Kwon, "Economic model-based controller design framework for hydraulic fracturing to optimize shale gas production and water usage," *Industrial & Engineering Chemistry Research*, vol. 58, no. 27, pp. 12097–12115, 2019.

- [8] J. Wang, Z. Wang, B. Sun, Y. Gao, X. Wang, and W. Fu, "Optimization design of hydraulic parameters for supercritical CO₂ fracturing in unconventional gas reservoir," *Fuel*, vol. 235, pp. 795–809, 2019.
- [9] X. Wang, X. Peng, S. Zhang, Y. Liu, F. Peng, and F. Zeng, "Guidelines for economic design of multistage hydraulic fracturing, Yanchang tight formation, Ordos Basin," *Natural Resources Research*, vol. 29, no. 2, pp. 1413–1426, 2020.
- [10] C. R. Tiedeman and W. Barrash, "Hydraulic tomography: 3D hydraulic conductivity, fracture network, and connectivity in mudstone," *Groundwater*, vol. 58, no. 2, pp. 238–257, 2019.
- [11] X. Zhao, Z. Rui, X. Liao, and R. Zhang, "The qualitative and quantitative fracture evaluation methodology in shale gas reservoir," *Journal of Natural Gas Science & Engineering*, vol. 27, no. P2, pp. 486–495, 2015.
- [12] T. Guo, Z. Rui, Z. Qu, and N. Qi, "Experimental study of directional propagation of hydraulic fracture guided by multi-radial slim holes," *Journal of Petroleum Science and Engineering*, vol. 166, no. 3, pp. 592–601, 2018.
- [13] Z. Rui, T. Guo, Q. Feng, Z. Qu, N. Qi, and F. Gong, "Influence of gravel on the propagation pattern of hydraulic fracture in the glutenite reservoir," *Journal of Petroleum Science & Engineering*, vol. 165, no. 7, pp. 627–639, 2018.
- [14] Y. He, S. Cheng, Z. Sun, Z. Chai, and Z. Rui, "Improving oil recovery through fracture injection and production of multiple fractured horizontal wells," *Journal of Energy Resources Technology*, vol. 142, no. 5, pp. 1–19, 2020.
- [15] S. Liu, L. Zhang, K. Zhang, J. Zhou, H. He, and Z. Hou, "A simplified and efficient method for water flooding production index calculations in low permeable fractured reservoir," *Journal of Energy Resources Technology*, vol. 141, no. 11, article 112905, 2019.
- [16] L. Zhu, Y. Shengchao, Z. Weibing et al., "Dynamic loading induced by the instability of voussoir beam structure during mining below the slope," *International Journal of Rock Mechanics and Mining Sciences*, vol. 132, no. 6, article 104343, 2020.
- [17] H. Zheng, C. Pu, and C. T. II, "Study on the interaction mechanism of hydraulic fracture and natural fracture in shale formation," *Energies*, vol. 12, no. 23, p. 4477, 2019.
- [18] H. Fatahi, M. M. Hossain, and M. Sarmadivaleh, "Numerical and experimental investigation of the interaction of natural and propagated hydraulic fracture," *Journal of Natural Gas Science and Engineering*, vol. 37, pp. 409–424, 2017.
- [19] W. Xu, Y. Li, J. Zhao, X. Chen, and S. S. Rahman, "Simulation of a hydraulic fracture interacting with a cemented natural fracture using displacement discontinuity method and finite volume method," *Rock Mechanics and Rock Engineering*, vol. 53, no. 7, pp. 3373–3382, 2020.
- [20] W. Xu, J. Zhao, S. S. Rahman, Y. Li, and Y. Yuan, "A comprehensive model of a hydraulic fracture interacting with a natural fracture: analytical and numerical solution," *Rock Mechanics and Rock Engineering*, vol. 52, no. 4, pp. 1095–1113, 2019.
- [21] M. M. Rahman and S. S. Rahman, "Studies of hydraulic fracture-propagation behavior in presence of natural fractures: fully coupled fractured-reservoir modeling in poroelastic environments," *International Journal of Geomechanics*, vol. 13, no. 6, pp. 809–826, 2013.
- [22] W. Yao, S. Mostafa, Z. Yang, and G. Xu, "Role of natural fractures characteristics on the performance of hydraulic fracturing for deep energy extraction using discrete fracture network (DFN)," *Engineering Fracture Mechanics*, vol. 230, article 106962, 2020.
- [23] S. Han, Y. Cheng, Q. Gao, C. Yan, Z. Han, and X. Shi, "Analysis of instability mechanisms of natural fractures during the approach of a hydraulic fracture," *Journal of Petroleum Science and Engineering*, vol. 185, article 106631, 2020.
- [24] B. Shen, T. Siren, and M. Rinne, "Modelling fracture propagation in anisotropic rock mass," *Rock Mechanics & Rock Engineering*, vol. 48, no. 3, pp. 1067–1081, 2015.
- [25] P. L. Clarke and R. Abedi, "Modeling the connectivity and intersection of hydraulically loaded cracks with in situ fractures in rock," *International Journal for Numerical & Analytical Methods in Geomechanics*, vol. 42, no. 14, pp. 1592–1623, 2018.
- [26] O. Kolawole and I. Ispas, "Interaction between hydraulic fractures and natural fractures: current status and prospective directions," *Journal of Petroleum Exploration and Production Technology*, vol. 10, no. 4, pp. 1613–1634, 2020.
- [27] C. Song, Y. Lu, B. Xia, and H. Ke, "Effects of natural fractures on hydraulic fractures propagation of coal seams," *Journal of Northeastern University (Natural Science)*, vol. 35, no. 5, pp. 756–760, 2014.
- [28] X. Liu, Y. Ding, P. Luo, and L. Liang, "Influence of natural fracture on hydraulic fracture propagation," *Special Oil and Gas Reservoirs*, vol. 2, no. 25, pp. 148–153, 2018.
- [29] T. L. Blanton, "Propagation of hydraulically and dynamically induced fractures in naturally fractured reservoirs," *Society of Petroleum Engineers*, vol. 5, no. 15261, pp. 1–15, 1986.
- [30] T. L. Blanton, "An experimental study of interaction between hydraulically induced and pre-existing fractures," *Society of Petroleum Engineers*, vol. 8, no. 10847, pp. 559–562, 1982.
- [31] Y. Lu, C. Song, Y. Jia et al., "Analysis and numerical simulation of hydrofracture crack propagation in coal-rock bed," *Cmes-computer Modeling in Engineering & Sciences*, vol. 105, no. 1, pp. 69–86, 2015.
- [32] C. Song, Y. Lu, H. Tang, and Y. Jia, "A method for hydrofracture propagation control based on non-uniform pore pressure field," *Journal of Natural Gas Science and Engineering*, vol. 33, pp. 287–295, 2016.
- [33] W. Song, J. Zhao, and Y. Li, "Hydraulic fracturing simulation of complex fractures growth in naturally fractured shale gas reservoir," *Arabian Journal for Science and Engineering*, vol. 39, no. 10, pp. 7411–7419, 2014.
- [34] W. Cheng, Y. Jin, M. Chen, T. Xu, Y. Zhang, and C. Diao, "A criterion for identifying hydraulic fractures crossing natural fractures in 3D space," *Petroleum Exploration and Development Online*, vol. 41, no. 3, pp. 371–376, 2014.
- [35] W. Lu, Y. Wang, and X. Zhang, "Numerical simulation on the basic rules of multihole linear codirectional hydraulic fracturing," *Geofluids*, vol. 2020, Article ID 6497368, 14 pages, 2020.
- [36] W. Lu and C. He, "Numerical simulation of the fracture propagation of linear collaborative directional hydraulic fracturing controlled by pre-slotted guide and fracturing boreholes," *Engineering Fracture Mechanics*, vol. 235, article 107128, 2020.
- [37] C. E. Renshaw and D. D. Pollard, "An experimentally verified criterion for propagation across unbounded frictional interfaces in brittle, linear elastic materials," *International Journal of Rock Mechanics and Mining Sciences & Geomechanics Abstracts*, vol. 32, no. 3, pp. 237–249, 1995.

Research Article

Development and Application of Fluid-Solid Coupling Similar Materials in Discharge Test of Old Goaf Water

Zhenhua Li,¹ Mingxiao Ma,¹ and Yongsheng Bao² 

¹School of Energy Science and Engineering, Henan Polytechnic University, Jiaozuo, 454000 Henan, China

²Datong Coal Mine Group Co. Ltd., Datong, 037003 Shanxi, China

Correspondence should be addressed to Yongsheng Bao; yongshengbao@126.com

Received 30 April 2020; Revised 11 June 2020; Accepted 24 June 2020; Published 14 July 2020

Academic Editor: Guozhong Hu

Copyright © 2020 Zhenhua Li et al. This is an open access article distributed under the Creative Commons Attribution License, which permits unrestricted use, distribution, and reproduction in any medium, provided the original work is properly cited.

To study the evolution law of the discharge pathway for the old goaf water in the Datong mining area, a new fluid-solid coupling similar material was developed based on the fluid-solid coupling similarity theory. In the developed similar material, sand and barite powder were used as aggregate, polyurethane and white portland cement as binder, and water and silicone oil as regulator. The effects of different proportions on mechanical properties and water physical properties of materials were obtained through the experiments. The results show that the strength of the developed material is mainly controlled by cement and polyurethane, the hydrophilicity is affected by silicone oil, and the permeability coefficient is mainly affected by cement and polyurethane. For grouting agent, cement can realize the overall control function, and polyurethane can realize the local control in a certain range. As an ideal fluid-solid coupling similar simulation material, the developed material can simulate rock mass with different permeability and different strength. Besides, this material has been successfully applied to an experimental study on the mechanism of old goaf water discharge in an extra-thick coal seam in the Datong mining area, and the development and evolution characteristics of the old goaf water discharge pathway is obtained. This new kind of fluid-solid coupling similar material is developed based on the fluid-solid coupling similarity theory, which is suitable for revealing the evolution law of discharge pathway for the old goaf water in the Datong mining area.

1. Introduction

As a large coal mining country, China has rich coal resources with a vast geographical distribution. However, the hydrogeological conditions of coal deposits are complex, and China is also one of the countries with the most serious mine water disasters [1, 2]. With the continuous increase of mining depth, major and critical water inrush hazards occur frequently. The old goaf water inrush hazards account for more than 70% of all kinds of coal mine water disasters [3, 4]. Water inrush in the old goaf has the characteristics of large water volume, short time, and strong destructiveness. As a result, serious accidents of casualties and water inrush hazards are easily caused, which seriously threaten the safe production of the coal mine [5, 6].

Due to complex causes of water inrush from the old goaf, the water inrush problem cannot be comprehensively analyzed by theoretical analysis and numerical simulation. Nev-

ertheless, the fluid-solid coupling model test can intuitively and comprehensively reflect the disaster-causing mechanism under the coupling action of a mining-induced stress field and seepage field [7, 8]. Besides, this test can be mutually verified with the mathematical model. Different from the traditional model test of similar materials, the influence of a water body on a rock mass should be considered in the fluid-solid coupling model test [9, 10].

The scientific and reasonable nature of hydrophilic similar simulation material is the premise and foundation of the fluid-solid coupling model test. Zhang and Hou [11] developed a solid-liquid two-phase mold material, in which sand was used as aggregate and paraffin as binder. Then, a model test on coal mining under water-rich aeolian sand layer was carried out. Huang et al. [12] studied similar solid-liquid coupling materials in which bentonite and quartz sand were taken as the aggregate and silicone oil and Vaseline as the binder for clay aquiclude. Li Shuca et al. [13] and Li Shuzhen

et al. [14] used Vaseline and paraffin as the grouting agent and sand and talc as the aggregate and developed the fluid-solid coupling similar simulation material. This material can be applied in a tunnel water inrush model test to simulate low and medium strength rock materials with different permeability. Sun et al. [15] and Chen et al. [16] used paraffin and Vaseline as the grouting agent, river sand and calcium carbonate as the aggregate, and hydraulic oil as the regulator, then developed a new type of fluid-solid coupling similar material for the deep water-resisting layer. When paraffin and Vaseline are taken as the grouting agent in similar materials, the problems of water disintegration and strength change of rock material are solved [17]. However, these materials need heating treatment in the development process, the preparation process is complex with high difficulty, and the application process is easily affected. Wang et al. [18] employed latex and white cement as a grouting agent and developed a new type of surrounding rock material suitable for the fluid-solid coupling model test. Huang and Hu [19] used soil as the grouting agent and rapeseed oil and water as regulators and obtained the best similar proportion of clay aquiclude. Combined with a large number of data at home and abroad, organic materials are selected as grouting agents for fluid-solid coupling similar materials, which can maintain strength without disintegration. In addition, similar materials must meet two similar conditions of solid deformation and permeability simultaneously [20].

Previous studies mainly focused on the complex cementing agents produced by paraffin. On this basis, a more concise material which satisfies the hydrodynamic and mechanical properties is developed. More precisely, polyurethane is selected as a new type of grouting agent and incorporated with cement and silicone oil in this paper. According to the fluid-solid coupling similarity theory, through the proportioning test, a new type of similar material for the fluid-solid coupling test is successfully developed and applied in the old goaf water discharge experiment in the Datong mining area.

2. Similarity Theory of Fluid-Solid Coupling

On the basis of three similar theorems, the similarity relation between the model and the prototype parameters is derived by using the fluid-solid coupling mathematical model of the continuous medium, and the following similarity relation is derived [21]:

The seepage equation is expressed as

$$K_x \frac{\partial^2 p}{\partial^2 x} + K_y \frac{\partial^2 p}{\partial^2 y} + K_z \frac{\partial^2 p}{\partial^2 z} = S \frac{\partial p}{\partial t} + \frac{\partial e}{\partial t} + W, \quad (1)$$

where K_x , K_y , and K_z are the permeability coefficients (cm/s) in the x , y , and z coordinate directions; p is the water pressure (MPa); S is the water storage coefficient; e is the volume strain; W is the source sink term; and t is the time.

The equilibrium equation is described as

$$\sigma_{ij,i} + X_j = \frac{\rho \cdot \partial^2 u_i}{\partial t^2}, \quad (2)$$

where $\sigma_{ij,i}$ is the total stress tensor, ρ is the density (g/cm^3), and X_j is the volume force.

The effective stress equation is expressed as

$$\sigma_{ij} = \bar{\sigma}_{ij} + \alpha \delta p, \quad (3)$$

where $\bar{\sigma}_{ij}$ is the effective stress tensor, α is the Biot effective stress coefficient, and δ is the Kronecker sign.

According to Equations (1), (2), and (3), the main similarity between the fluid-solid coupling variable model and the prototype is deduced as follows:

The model similarity relation is

$$C_G = C_\lambda. \quad (4)$$

The geometric similarity relation is

$$C_u = C_e C_l. \quad (5)$$

The gravity similarity formula is

$$C_G C_e = C_\gamma C_l. \quad (6)$$

The stress similarity formula is

$$C_\sigma = C_\gamma C_l. \quad (7)$$

The external load similarity formula is

$$C_h = C_\gamma C_l^3. \quad (8)$$

The similarity formula of the water storage coefficient is

$$C_S = \frac{1}{C_\gamma \sqrt{C_l}}. \quad (9)$$

The permeability coefficient similarity formula is

$$C_K = \frac{\sqrt{C_l}}{C_\gamma}, \quad (10)$$

where C_λ refers to the lame constant similarity scale, C_u is the displacement similarity scale, C_e is the volume strain similarity scale, C_γ is the volume weight similarity scale, C_G is the mass similarity scale, and C_l is the geometry similarity scale.

3. Development of Fluid-Solid Coupling Similar Materials

3.1. Selection of Raw Materials. For fluid-solid coupling materials, stability, nonhydrophilicity, and good deformation characteristics are basic requirements. Therefore,

nonhydrophilic organic cementitious material should be selected as the grouting agent. Referring to the domestic and foreign research, proportion tests, and observation studies, transparent polyurethane, cement, and silicone oil are selected as the grouting agent, river sand and barite powder are used as the aggregate, and then appropriate mixing water is added to make the nonhydrophilic similar material, as shown in Figure 1.

- (1) *Grouting Agent*. White portland cement and transparent polyurethane are used as the grouting agent. White portland cement is a hydraulic cementitious material. Its mechanical strength, deformation characteristics, and water can be adjusted. However, the single use of white portland cement cannot fully adjust the material properties and cannot make the material have good water physical property. Therefore, white portland cement is used with another grouting agent. Transparent polyurethane is a polymer liquid material made of VAE and high polymer emulsion as a raw material after process modification. Its characteristics include homogeneous water-based material, high polymer, strong adhesion, non-toxic and pollution-free, short bonding time, stable performance, and nonhydrophilic. With cement, the material properties can be improved stably.
- (2) *Aggregate*. Sand and barite powder are selected as the aggregate. River sand with particle size ≤ 2 mm is selected to ensure uniform distribution of internal components of the material when it is cemented together under the action of the grouting agent. Barite powder with fineness of 625 meshes is selected as the fine aggregate. The grain size of the river sand is relatively coarse, and its nonhydrophilicity cannot be guaranteed. Thus, barite powder is used to fill the gap between the river sand to ensure the nonhydrophilicity.
- (3) *Regulator*. Dimethyl silicone oil and water are selected as the regulators. As the mixing water, water mainly reacts with cement. The silicone oil can make the surface of the material more compact, ensure the adequate reaction of cement and water, and improve the strength of the material, so that the material will not collapse when encountering water.

3.2. Experimental Scheme and Sample Making. A large number of experiments have shown that the properties of materials are mainly determined by cement and polyurethane. Therefore, cement content and polyurethane content are taken as two factors in the experimental design. Each factor is set at five levels. When the content of other components is fixed, the cement mass ratio is kept unchanged and the polyurethane content is changed, or the polyurethane content is kept unchanged and the cement content is changed. The experimental scheme is shown in Table 1. 25 groups of samples were made with a double opening mold with a diameter of 50 mm and a height of 100 mm. 10 samples were made for each group, and 250 samples were made for the

experimental study. The sample making process is shown in Figure 2.

4. Property Tests of Similar Materials

4.1. Hydrophilicity Test. As an important index of water rationality of similar materials, hydrophilicity can be measured by water absorption. The smaller the water absorption, the stronger the nonhydrophilicity. The water absorption rate was obtained by comparing the cured dry sample with the sample soaked for 24 hours, as shown in Figure 3. The test results show that the average water absorption rate of the sample is between 1.012 and 1.060%, which indicates that the material meets the requirements of nonhydrophilicity and is a nonhydrophilic material.

4.2. Test of Uniaxial Compressive Strength and Softening Effect. In this test, a WSM-10KN universal testing machine was used to carry out the uniaxial compression test on samples after maintenance, so as to determine the total stress-strain curve of the sample in the process of uniaxial compression. The slope of the elastic section is the elastic modulus E . The failure mode of the sample on the test machine is similar to that of the rock, as shown in Figure 4. Figure 5 shows the stress-strain curve of 14 groups of samples.

In order to simulate the coupling effect between the water flow and deformation failure of the surrounding rock, it is necessary to consider the softening effect of similar materials under long-term immersion. The water absorption sample was immersed into water for 7 days, and then the compressive strength of the immersed sample was compared with that of samples in the natural state. As shown in Table 2, the effect of immersion on the compressive strength is within 6%~20.3%, and it can be concluded that the softening effect of the material basically meets the experimental requirements.

4.3. Uniaxial Tensile Strength Test. The tensile strength of the sample was indirectly tested by the Brazilian splitting method, and the tensile strength of the sample is calculated from the following formula:

$$\sigma_t = \frac{2P}{\pi Dt}, \quad (11)$$

where D is the diameter of the sample, P is the pressure value when the sample is damaged, and t is the thickness of the sample. The tensile and compressive strength values of some samples are shown in Table 3.

As shown in Table 3, the tension-compression ratio σ_t/σ_c range of similar materials is 0.091-0.11, which is very close to 0.1 (the average tension-compression ratio of rock). It indicates that similar materials can well simulate the tensile properties of rock.

4.4. Brittleness Analysis. To simulate the permeability evolution caused by rock fracture and its influence on the mechanical properties of rock mass, it is necessary to analyze and verify the brittleness characteristics of the developed material, so as to ensure that the material is still



FIGURE 1: Raw similar materials.

TABLE 1: Experimental proportioning scheme.

Level	Factor					
	Cement content (%)	Polyurethane content (%)				
1	2	2	4	6	8	10
2	4	2	4	6	8	10
3	6	2	4	6	8	10
4	8	2	4	6	8	10
5	10	2	4	6	8	10

brittle after coupling with water. In this paper, the method proposed by Pan et al. [22] was used to define brittle rocks. In other words, E/λ of the prepeak and postpeak weakening modulus of the stress-strain curve was analyzed to determine the brittleness of the material. Materials with different E/λ have different brittleness characteristics. It is stipulated that materials with $E/\lambda < 3$ are brittle materials; otherwise, they are not brittle materials. As shown in Table 4, the developed materials are all brittle materials with $E/\lambda < 3$, which meet the fracture and mechanical similarity requirements of rock.

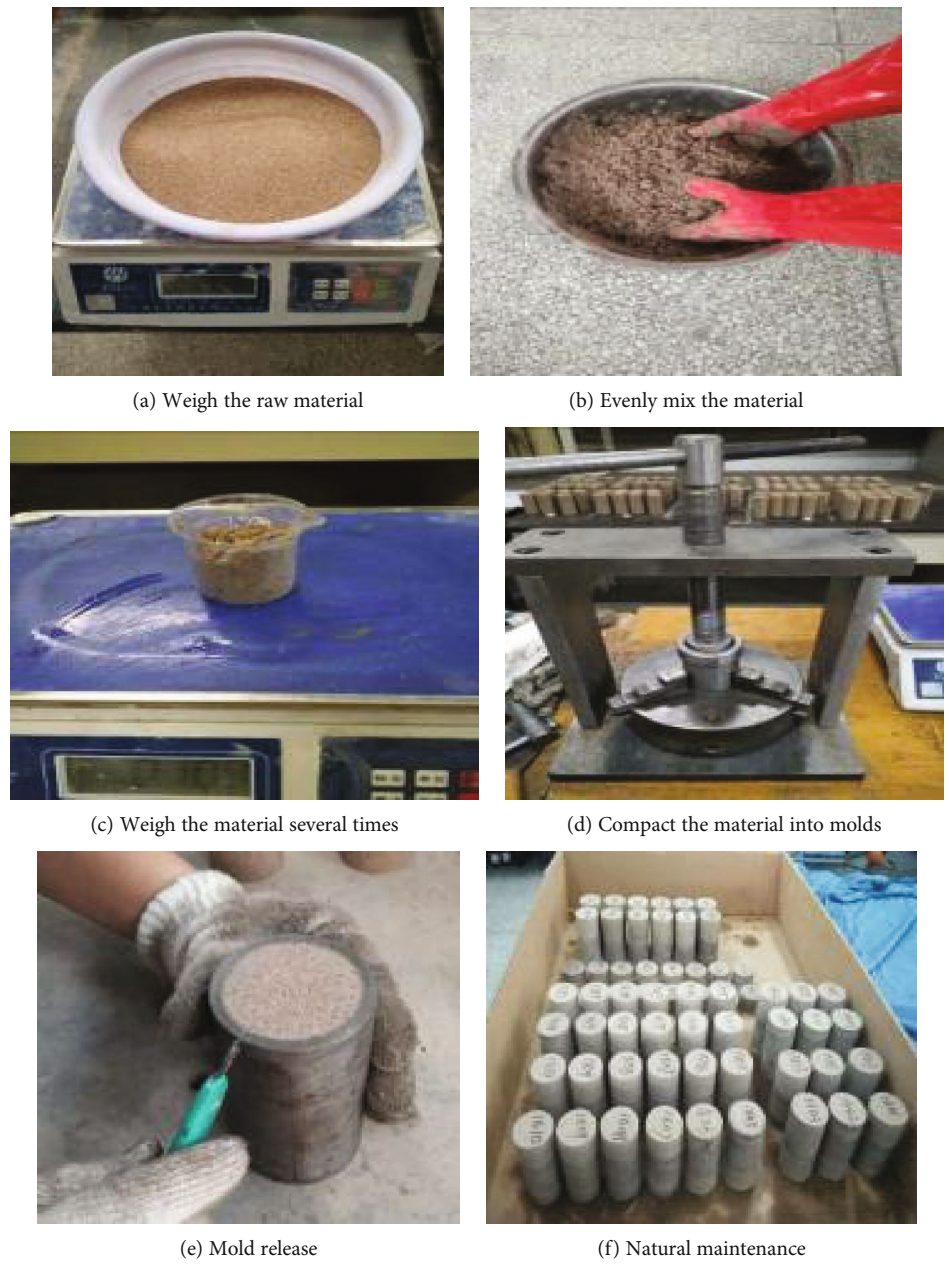


FIGURE 2: Sample preparation process.

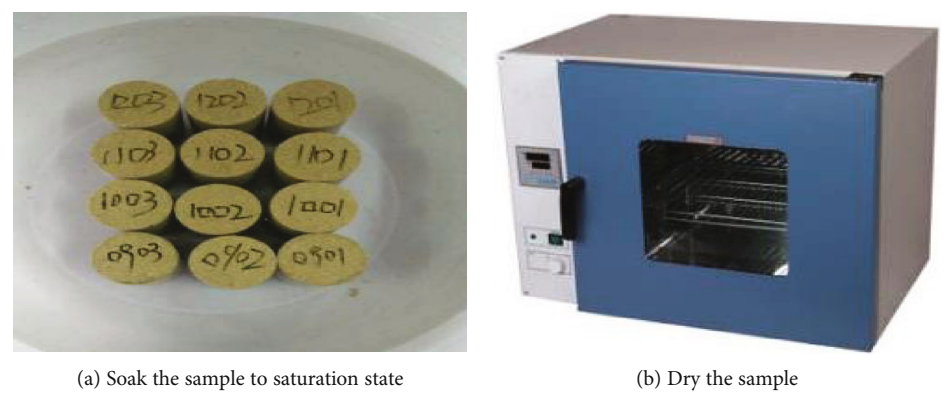
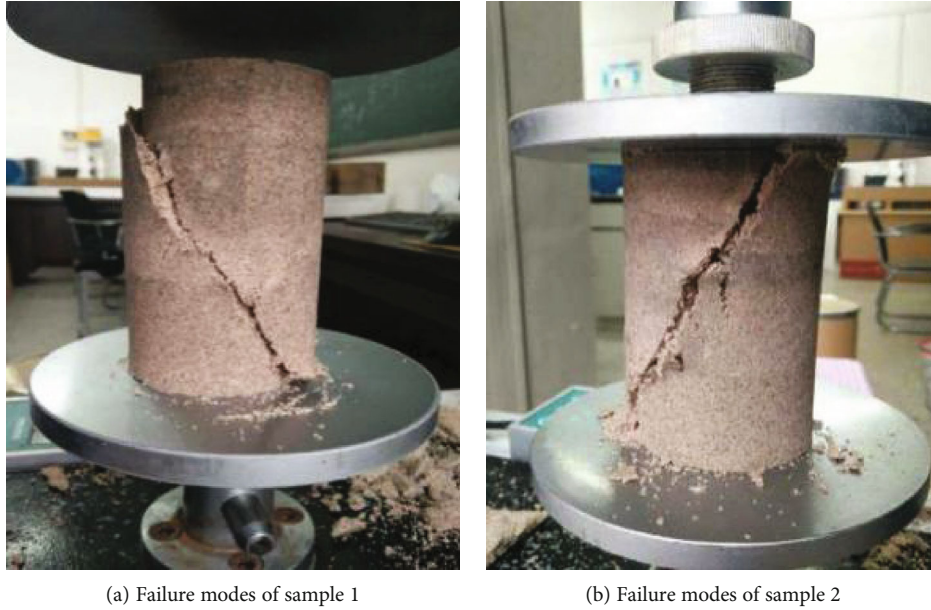


FIGURE 3: Hydrophilicity test.



(a) Failure modes of sample 1

(b) Failure modes of sample 2

FIGURE 4: Typical failure modes of samples.

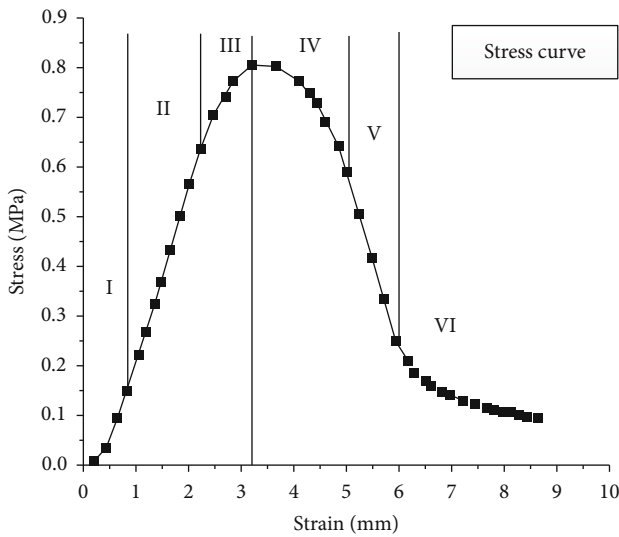


FIGURE 5: Stress-strain curve of 14 groups of similar materials.

TABLE 2: Strength comparison of some samples in natural state and after immersion.

Group number	Compressive strength (MPa)	Compressive strength of material after 7 days of immersion (MPa)	Strength reduction rate (%)
1	0.2	0.167	20%
7	0.73	0.56	13%
14	0.86	0.77	12%
20	1.46	1.36	9%
25	1.99	1.85	6%

TABLE 3: Tensile strength values of some test blocks.

Group number	Compressive strength σ_c (MPa)	Tensile strength σ_t (MPa)	σ_t/σ_c
01	0.20	0.020	0.11
02	0.44	0.045	0.10
03	0.68	0.067	0.098
04	0.92	0.084	0.091
05	1.16	0.126	0.108

TABLE 4: Test results of brittleness characteristics of some similar materials.

Group no.	Elastic modulus Prepeak E (MPa)	Weakening modulus After peak λ (MPa)	E/λ
1	42	20	2.1
2	68	31	2.2
3	94	36	2.6
4	96	34	2.8
5	123	49.2	2.5

4.5. Determination of Permeability Coefficient. The permeability coefficient is another important property index to characterize the water rationality of similar materials. The permeability of the developed material is low. Since the water flow is small and the water level is difficult to control, the variable head method is used. However, the conventional permeameter is only suitable for testing the permeability coefficient of granular materials, and there is a problem of lax sealing between the sample and the sleeve side wall of the sample. To this end, a set of a sealed permeability coefficient testing device was designed and developed by glue injection based on the principle of variable water head test

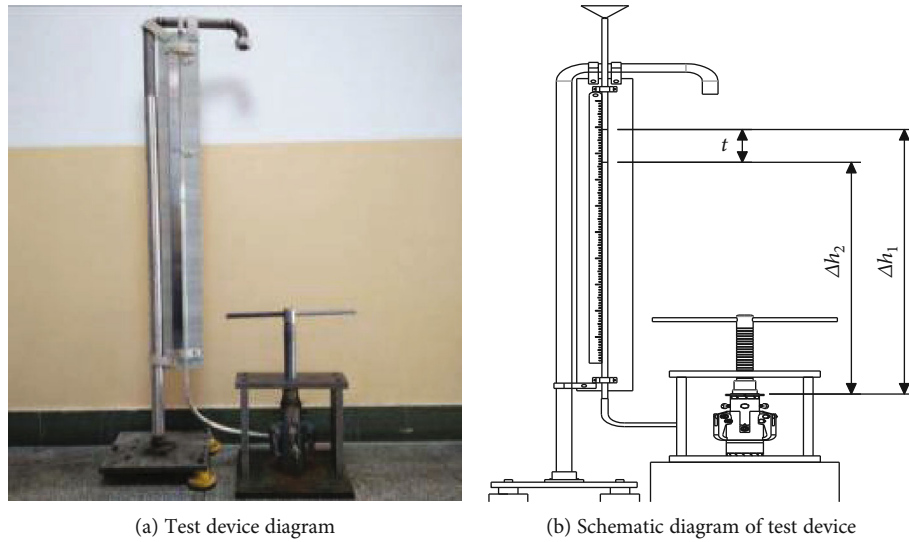


FIGURE 6: Test and test principle of permeability coefficient of similar materials.

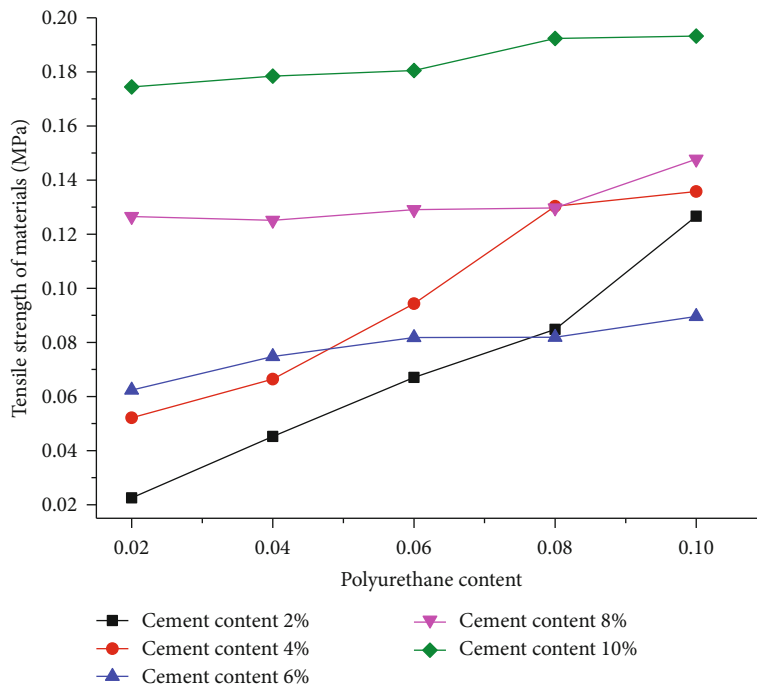


FIGURE 7: Effect of cement and polyurethane content on tensile strength of materials.

and Specification of Soil Test SL237-1999 [23, 24]. Then, the self-developed device was used to test the permeability coefficient of the sample, as shown in Figure 6. The range of the permeability coefficient measured by the device is 7.12×10^{-7} - 5.18×10^{-5} , namely, the simulation has a wide range. After the cement and polyurethane are added, the permeability coefficient of the material decreases integrally. When the proportionality of cement increases, the gap between the materials decreases, which has an important influence on the permeability coefficient of the materials.

5. Analysis of Factors Affecting the Properties of Similar Materials

As shown in Figures 7 and 8, the compressive and tensile strengths increase with the increase of cement or polyurethane content when the content of other components is fixed. When the cement content is less than 6%, the tensile and compressive strengths of the material increase rapidly with the increase of polyurethane. At this time, the strength of the material is mainly determined by the cohesiveness of

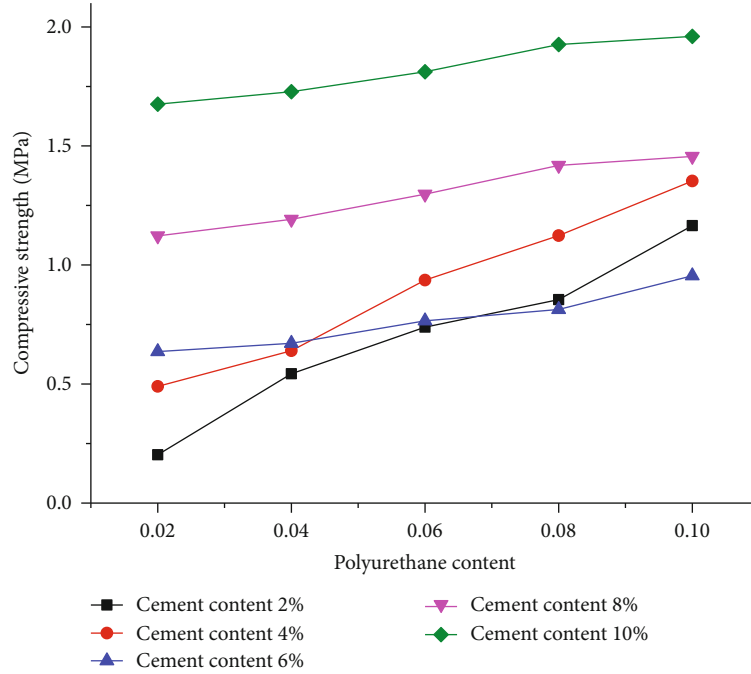


FIGURE 8: Effect of cement and polyurethane content on compressive strength of materials.

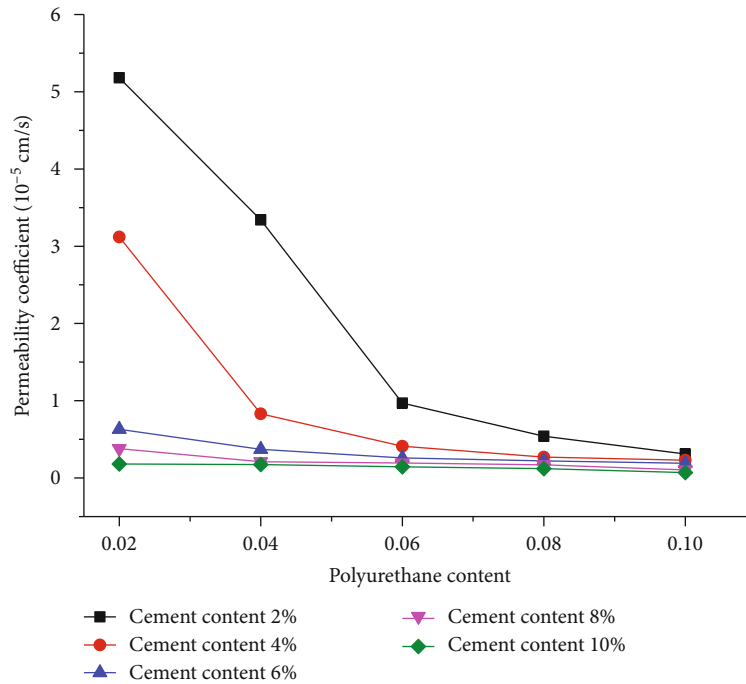


FIGURE 9: Effect of cement and polyurethane content on permeability coefficient of materials.

polyurethane. When the cement content is more than 6%, the tensile and compressive strengths of the material increase rapidly with the increase of cement content. As the cement content increases, the cementitious material produced by the hydration reaction increases, which affects the cementation ability of polyurethane. At this time, the strength of the material is mainly determined by the cement. Comparing the influence of the two substances, it is found that the

cement content determines the strength of the material comprehensively, and the polyurethane content can adjust the strength within a certain range. When the content of cement and polyurethane is at 4%, the permeability coefficient decreases with the increase of silicone oil.

Through a large number of experiments, it is proven that the amount of cement and polyurethane can adjust the permeability coefficient. As shown in Figure 9, with the increase

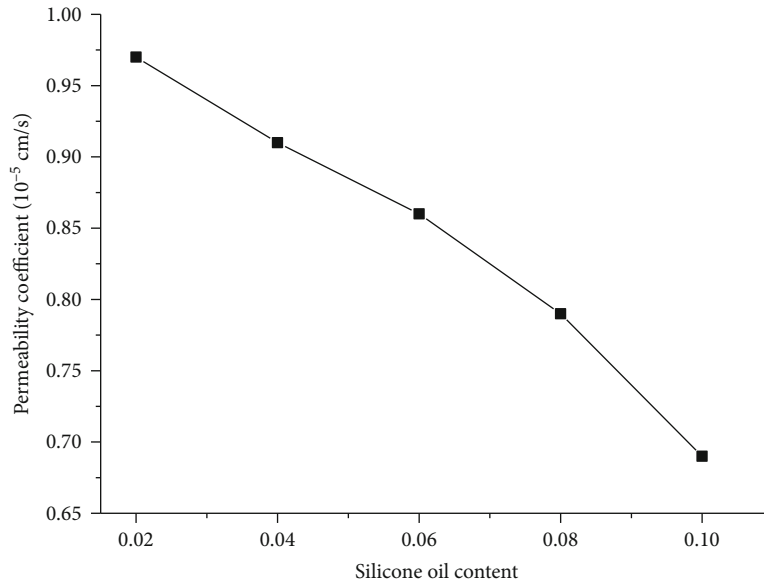


FIGURE 10: Effect of silicone oil on permeability coefficient of materials.

TABLE 5: Proportion of model test.

No.	Lithology	Thickness (m)	Model thickness (cm)	Compressive strength (MPa)		Material ratio (sand : barite powder : cement : polyurethane : silicone oil)
				Actual strength	Simulation strength	
1	Silty mudstone	12	6	42.5	0.14	1 : 0.125 : 0.011 : 0.017 : 0.024
2	Fine sandstone	17.5	8.75	55.2	0.18	1 : 0.125 : 0.014 : 0.017 : 0.011
3	#14 coal	3.4	1.7	16.5	0.06	1 : 0.111 : 0.009 : 0.001 : 0.046
4	Coarse-grained sandstone	11.1	5.55	39.5	0.13	1 : 0.125 : 0.012 : 0.017 : 0.048
5	Medium-grained sandstone	12.2	6.1	40.6	0.13	1 : 0.125 : 0.013 : 0.017 : 0.023
6	Silty mudstone	21.1	10.55	42.5	0.14	1 : 0.125 : 0.011 : 0.017 : 0.024
7	Fine sandstone	14.1	7.05	55.2	0.18	1 : 0.125 : 0.014 : 0.017 : 0.011
8	Sandy conglomerate	15.1	7.55	54.6	0.18	1 : 0.125 : 0.012 : 0.0177 : 0.24
9	Siltstone	10.3	5.15	40.1	0.13	1 : 0.142 : 0.012 : 0.017 : 0.024
10	Silty mudstone	12.1	6.05	42.5	0.14	1 : 0.125 : 0.011 : 0.017 : 0.024
11	Sandy conglomerate	16.2	8.1	54.6	0.18	1 : 0.125 : 0.012 : 0.0177 : 0.24
12	Carbonaceous mudstone	7	3.5	26.4	0.09	1 : 0.142 : 0.01 : 0.014 : 0.024
13	#3-5 coal	21	10.5	16.5	0.06	1 : 0.111 : 0.009 : 0.011 : 0.023
14	Medium sandstone	20.1	10.05	42.5	0.14	1 : 0.125 : 0.013 : 0.017 : 0.024

of cement and polyurethane content, the permeability coefficient of materials decreases. With the increase of cement and polyurethane content, the small gap between the materials becomes smaller and smaller, resulting in greater difficulty for water flow. When the polyurethane content is more than 6%, the permeability coefficient fluctuates from 1.01×10^{-5} to 7×10^{-6} . As shown in Figure 10, when the content of cement

and polyurethane is fixed, silicone oil, as a regulator, has a certain influence on the permeability coefficient. Since silicone oil has water retention and hydrophobicity, it can fully react with the cement, and a hydrophobic surface can be formed, resulting in more difficult water flow. Therefore, the permeability coefficient can be controlled in a certain range by changing the content of cement, polyurethane, and silicone oil.

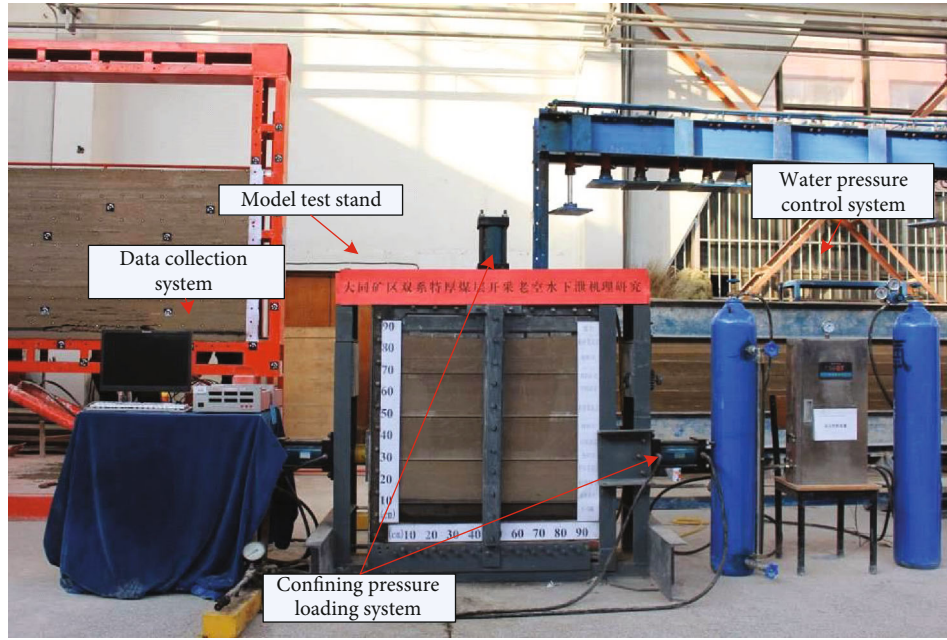


FIGURE 11: Multifield coupling simulation test system of old goaf and water discharge.

6. Application of Similar Materials in Old Goaf Water Discharge Test

The Datong coalfield is a double system coalfield of Jurassic and Permo-Carboniferous. The upper 14# coal seam has been fully mined, and a large amount of old goaf water is stored in the goaf. When mining the 3-5# coal seams, due to the development of a fracture zone, the goaf of the upper coal seam is permeated. As a result, the old goaf water in the goaf of the upper coal seam flows downward, easily resulting in a water inrush accident of the 3-5# coal seams. In this test, water inrush in double series coal seam mining in the Datong mining area is taken as the research object, so as to explore the change of water pressure and the law of pathway formation and evolution when the old goaf is discharged. The geometric similarity ratio of the experiment is 1/200, and the model size is $1000 \times 1000 \times 200$ mm. The model applied a load of 0.03 MPa in the vertical direction and a load of 0.01 MPa in the horizontal direction. Then, water pressure of 0.001 MPa is applied according to the actual calculation. The ratio of rock mechanics parameters is shown in Table 5, and the physical figure of the model is shown in Figure 11.

As shown in Figure 12, as the working face moves forward from the open-off cut, the water pressure in the aquifer does not change significantly because the aquifer is far away from the mining coal seam, and the strength of the sandstone in the key layer has a good water isolation effect. In this process, the fracture formed by the tensile and shear failure of each layer in the open-off cut develops obliquely upward at a certain angle. At the same time, the development height of the crack also extends outwards. When the working face advances to about 140 m, the aquifer begins to fluctuate. At this time, the key layer is gradually damaged, and the water begins to seep out from the small fissures. When the working

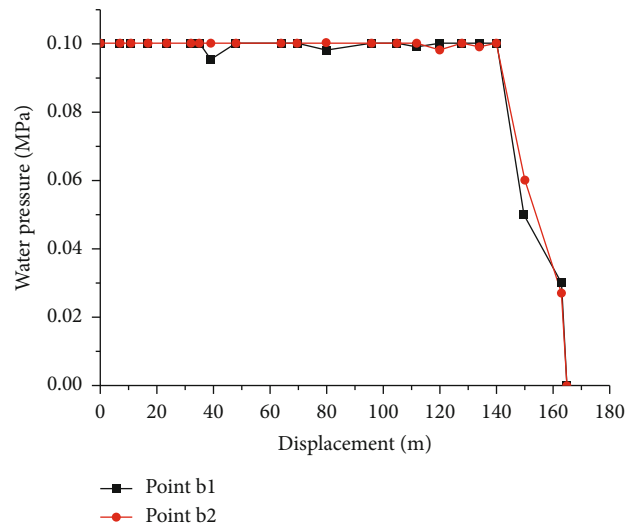


FIGURE 12: Relation curve between displacement and water pressure.

face advances to 145 m, the key layer collapses, the water inrush pathway develops and penetrates, and the water pressure of the aquifer drops sharply and tends to 0 MPa. Therefore, the key layer has the function of water separation, which plays a decisive role in the generation of a water inrush pathway with the water pressure change [25].

A key layer refers to the strata which control the whole or partial overburden movement from the overburden to the surface. The clear location of the water inrush is in the middle of the key layer, and the period of water inrush occurs after the key layer is broken. As shown in Figure 13, under the influence of mining, the fracture of the key layer is a V-shaped structure. The vertical fracture and the fractures

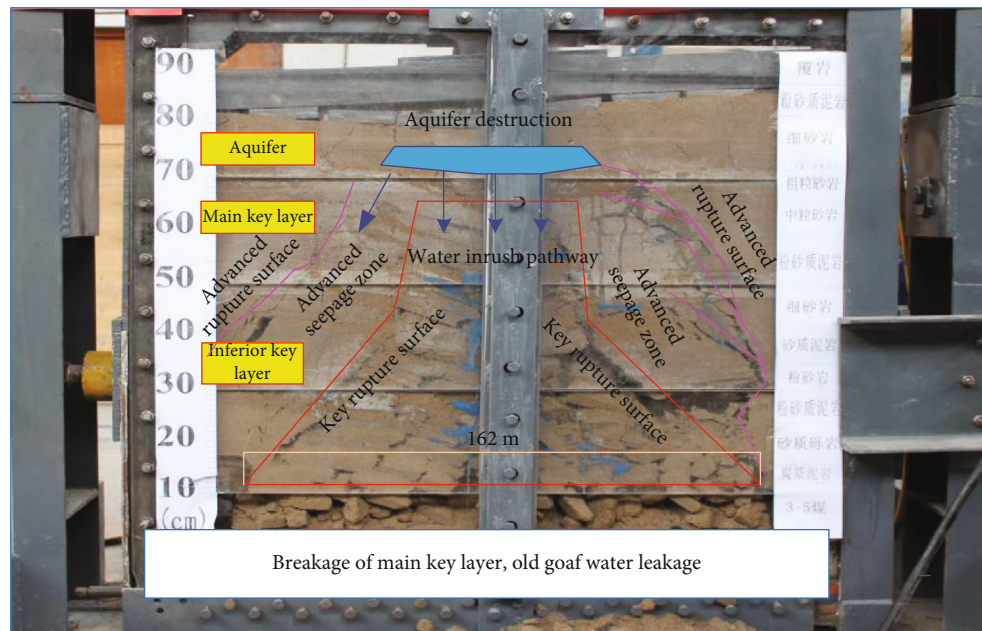


FIGURE 13: Distribution of broken main key layer and water-conducting pathway.

formed at the open-off cut and coal wall of the working face are main water-conducting pathways, while the lead fracture on both sides of the goaf is not an effective water pathway. The application of the similar material reveals the damage characteristics of similar materials and the distribution characteristics of roof water inrush pathways. It is concluded that there is a high probability of water inrush at the open-off cut and the middle of the goaf. This finding has certain guiding significance for solving practical engineering problems.

7. Conclusions

- (1) A new type of fluid-solid coupling simulation material is developed and tested. The compressive strength of similar materials is 0.20-1.99 MPa, the tensile strength is 0.02-0.19 MPa, and the permeability coefficient is 7×10^{-7} - 5.18×10^{-5} . This material is suitable for the large-scale simulation test of most rock masses
- (2) The control effect of the new fluid-solid coupling similar material on the mechanical properties in different proportions is obtained. The tensile and compressive strengths are mainly controlled by cement, and polyurethane is adjusted within a certain range. The permeability coefficient is controlled by the cement and polyurethane. Silicone oil has the function of water retention. The deformation and water physical properties can be controlled by the proportionality of cement and polyurethane
- (3) The change of water pressure stress and the formation and evolution of the water-conducting pathway in the old goaf water discharge are preliminarily revealed. Mechanical properties and water physical

properties of the material are verified. This study provides a reference for solving the water inrush problems in the actual project.

Data Availability

The data used to support the findings of this study are included within the article.

Conflicts of Interest

The authors declare that they have no conflicts of interest.

Acknowledgments

This work was supported by the National Natural Science Foundation of China (51774110, 51704095, and U1904128) and Program for Science & Technology Innovation Talents in Universities of Henan Province (19HASTIT047).

References

- [1] W. Y. Hu, *Theory and method of mine water disaster control*, Coal Industry Press, Beijing, 2005.
- [2] D. Ma, H. Duan, X. Li, Z. Li, Z. Zhou, and T. Li, "Effects of seepage-induced erosion on nonlinear hydraulic properties of broken red sandstones," *Tunnelling and Underground Space Technology*, vol. 91, p. 102993, 2019.
- [3] F. H. Wu, "Forecast and control of goaf water," *Coal technology*, vol. 23, pp. 59-60, 2004.
- [4] C. H. Bu, "Application and outlook of detection, prevention and control technique of coal mine water disaster," *China Coal*, vol. 40, pp. 100-107, 2014.
- [5] D. Ma, J. Wang, X. Cai et al., "Effects of height/diameter ratio on failure and damage properties of granite under coupled

- bending and splitting deformation,” *Engineering Fracture Mechanics*, vol. 220, p. 106640, 2019.
- [6] D. W. Jin, Y. F. Liu, Z. B. Liu, and J. Y. Cheng, “New progress of study on major water inrush disaster prevention and control technology in coal mine,” *Coal science and technology*, vol. 41, pp. 25–29, 2013.
- [7] D. Ma, H. Duan, W. Liu, X. Ma, and M. Tao, “Water–sediment two-phase flow inrush hazard in rock fractures of overburden strata during coal mining,” *Mine Water and the Environment*, vol. 39, no. 2, pp. 308–319, 2020.
- [8] W. L. Shen, J. B. Bai, W. F. Li, and X. Y. Wang, “Prediction of relative displacement for entry roof with weak plane under the effect of mining abutment stress,” *Tunnelling and Underground Space Technology*, vol. 71, pp. 309–317, 2018.
- [9] D. Ma, J. Wang, and Z. Li, “Effect of particle erosion on mining-induced water inrush hazard of karst collapse pillar,” *Environmental Science and Pollution Research*, vol. 26, no. 19, pp. 19719–19728, 2019.
- [10] Y. Xue, P. G. Ranjith, F. Dang et al., “Analysis of deformation, permeability and energy evolution characteristics of coal mass around borehole after excavation,” *Natural Resources Research*, pp. 1–19, 2020.
- [11] J. Zhang and Z. J. Hou, “Study on solid-liquid coupling test materials,” *Chinese Journal of Rock Mechanics and Engineering*, vol. 23, pp. 3157–3161, 2004.
- [12] Q. X. Huang, W. Z. Zhang, and Z. C. Hou, “Study on similar materials of aquiclude in solid-liquid coupling test,” *Chinese Journal of Rock Mechanics and Engineering*, vol. 29, pp. 2813–2818, 2010.
- [13] S. C. Li, Y. Zhou, L. P. Li et al., “Development and application of a new similar material for underground engineering fluid-solid coupling model test,” *Chinese Journal of Rock Mechanics and Engineering*, vol. 31, pp. 1128–1137, 2012.
- [14] S. Li, X. Feng, S. Li, L. Li, and G. Li, “Research and development of a new similar material for solid-fluid coupling and its application,” *Chinese Journal of Rock Mechanics and Engineering*, vol. 29, pp. 281–288, 2010.
- [15] W. B. Sun, S. C. Zhang, Y. Y. Li, and C. Lu, “Development of similar material for the solid fluid coupling simulation and deep water inrush simulation test,” *Chinese Journal of Rock Mechanics and Engineering*, vol. 34, pp. 2665–2670, 2015.
- [16] J. T. Chen, L. M. Yi, W. B. Sun, C. Lu, S. C. Zhang, and X. Z. Sun, “Development and application for new solid-fluid coupling similar materials of deep floor aquifuge,” *Chinese Journal of Rock Mechanics and Engineering*, vol. 34, pp. 3956–3964, 2015.
- [17] D. Ma, M. Rezaia, H. S. Yu, and H. B. Bai, “Variations of hydraulic properties of granular sandstones during water inrush: effect of small particle migration,” *Engineering Geology*, vol. 217, pp. 61–70, 2017.
- [18] K. Wang, S. C. Li, Q. S. Zhang et al., “Development and application of new similar materials of surrounding rock for a fluid-solid coupling model test,” *Rock and Soil Mechanics*, vol. 37, pp. 2521–2533, 2016.
- [19] Q. X. Huang and H. M. Hu, “Experimental study on the whole process similar simulation material and proportion of stress and strain of clay aquiclude,” *Journal of Mining and Safety Engineering*, vol. 34, pp. 1174–1178, 2017.
- [20] Y. Xue, T. Teng, F. Dang, Z. Ma, S. Wang, and H. Xue, “Productivity analysis of fractured wells in reservoir of hydrogen and carbon based on dual-porosity medium model,” *International Journal of Hydrogen Energy*, pp. 1–10, 2019.
- [21] Y. Q. Hu, Y. S. Zhao, and D. Yang, “Simulation theory & method of 3D solid-liquid coupling,” *Journal of Liaoning Technical University*, vol. 2, pp. 204–206, 2007.
- [22] Y. S. Pan, M. T. Zhang, L. G. Wang, and G. Z. Li, “Simulation test of similar materials for underground chamber rock burst,” *Chinese Journal of Geotechnical Engineering*, vol. 19, pp. 49–56, 1997.
- [23] Ministry of construction of the people’s Republic of China, *GB/T 50123-1999 Standard for Soil Test Methods*, China Planning Press, Beijing, 1999.
- [24] Z. Z. Cao, P. Xu, Z. H. Li, M. X. Zhang, Y. Zhao, and W. L. Shen, “Joint bearing mechanism of coal pillar and backfilling body in roadway backfilling mining technology,” *CMC-Computers Materials & Continua*, vol. 54, no. 2, pp. 137–159, 2018.
- [25] X. X. Miao, H. Pu, and H. B. Bai, “Principle of water-resisting key strata and its application in water-preserved mining,” *Journal of China University of Mining and Technology*, vol. 1, pp. 1–4, 2008.

Research Article

The Influence of Hydrogeology to Generation of Hydrogen Sulfide of Low-Rank Coal in the Southeast Margin of Junggar Basin, China

Qigen Deng^{1,2,3}, Tao Zhang,² Fajun Zhao,^{1,2} Hao Wang,² and Jingping Yin²

¹State Key Laboratory Cultivation Base for Gas Geology and Gas Control, Henan Polytechnic University, Jiaozuo 454003, China

²School of Safety Science and Engineering, Henan Polytechnic University, Jiaozuo 454003, China

³State Collaborative Innovation Center of Coal Work Safety and Clean-Efficiency Utilization, Jiaozuo 454003, China

Correspondence should be addressed to Qigen Deng; dengqigen@hpu.edu.cn

Received 1 May 2020; Revised 28 May 2020; Accepted 4 June 2020; Published 30 June 2020

Academic Editor: Guozhong Hu

Copyright © 2020 Qigen Deng et al. This is an open access article distributed under the Creative Commons Attribution License, which permits unrestricted use, distribution, and reproduction in any medium, provided the original work is properly cited.

The salinity, chemical properties, and migration characteristics of groundwater in coal measures are the key factors that affect the generation, migration, and reservoir of hydrogen sulfide (H₂S) in low-rank coal seams. Taking the Jurassic coal and rock strata in the southeastern margin of the Junggar basin as the research object, according to the hydrogeological characteristics of the coal measures, the region is divided into 4 hydrogeological units. The coalbed methane contains a large number of secondary biogas. Along the direction of groundwater runoff, the salinity and the pH value increase gradually. The salinity in the hydrogeological units is low; it is not conducive to the propagation of sulfate-reducing bacteria and the formation of hydrogen sulfide of the Houxia, the south of Manasi River, and Hutubi and Liuhuangu area, the western region of the Miquan. The high salinity center and depressions of low water level (hydrodynamic stagnation zone) in the hydrogeological unit of the Liuhuangu and the Miquan are the main areas for the production and enrichment of H₂S in the low-rank coal. The high salinity in water is formed by infiltration, runoff, and drought evaporation. At the same time, the deep confined water environment closed well; in conditions of hydrocarbon-rich, under the action of sulfate-reducing bacteria, bacterial sulfate reduction will occur and hydrogen sulfide formed. According to the circulation characteristics of water bearing H₂S in the region, imbricate and single bevel two kind generation and enrichment mode of hydrogen sulfide under the action of hydrodynamic control. The solubility of hydrogen sulfide in pure water and solutions of NaCl and Na₂SO₄ with different molar concentrations was calculated. The H₂S solubility of groundwater in coal measures of 4 hydrogeological units was estimated.

1. Introduction

The Xinjiang Uygur Autonomous region is a domestic coal-producing province with predicted reserves accounting for about 40% in China. The southeastern margin of Junggar basin is a typical development basin of coalbed methane of inland low-rank coal. Hydrogen sulfide (H₂S) in coal-bearing strata in many mining areas is abnormally enriched, particularly serious in the southeastern margin of Junggar basin, such as Urumqi, Changji, and Fukang, and there are many accidents involving death and injury [1]. It is generally believed that H₂S can be formed by biochemical degradation in the early peat accumulation, the bacterial sulfate reduction

(BSR) in the peat accumulation period and at the stage of coal formation, thermochemical sulfate reduction (TSR) during coal evolution, and thermal decomposition sulfides (TDS) and magma (volcanic eruption) activity, and it is widely believed that the BSR and TSR are the main origins of H₂S in coal and rock seams [1–5]. Bacterial sulfate reduction (BSR) is a metabolic process in which sulfate-reducing bacteria absorb sulfate under the condition of no oxygen reduction, oxidize organic compounds to obtain energy, and reduce sulfate to form hydrogen sulfide. The chemical properties of underground fluids and the characteristics of microbial activity in the groundwater have an important influence on the generation of biogas-bearing hydrogen sulfide in the

low-rank coal seams; it is the main controlling factors affecting the formation, migration, and reservoir of hydrogen sulfide in low-rank coal seams [6, 7]. Based on the anomalous enrichment of coal and rock strata in the southeastern margin of Junggar basin, this paper analyzes the geological overview of the study area and discusses the effects of salinity of groundwater in coal measures on the formation, migration, and accumulation of H_2S in low-rank coal seams. The H_2S solubility of water bodies in coal measures was calculated. The research has a certain supporting role in supplementing and improving the causes, distribution characteristics, occurrence rules, and disaster prevention of existing coal mine (coal methane) H_2S . At the same time, it provides theoretical support for atmospheric environmental pollution control. Furthermore, it provides reference for the exploration and development of low-rank coal seam coalbed methane containing H_2S in the southeastern margin of Junggar basin, China.

2. Regional Geological Survey

The area is in the binding site of the southern margin of Junggar basin, northern Tianshan Mountain, and Bogda Mountain, China. The coal and rock strata form a series of northwest, northeast east and southeast east linear fault-fracture zones [8, 9]. The structural division belongs to the southeastern margin of the Junggar basin front fold belt, and most of the surface is covered by the Quaternary strata, and the Jurassic strata are widely exposed. The regional coalfield geological map is shown in Figure 1.

The regional coal-bearing strata are mainly the Badaowan formation of lower Jurassic and the Xishanyao formation of middle Jurassic [10, 11]. In the early Jurassic, the coal-sedimentary deposits were mainly concentrated in the area of the Fukang-Shuixigou area east of Urumqi, forming the Badaowan formation (J_1b) coal seam. The coal seams are thicker in the east of Urumqi, thinner in the west, and thinner from the bottom up. The coal seam can be collected in a total of 3~15 layers and available in thickness from 45 m to 66 m, the coal content is 9%~11%, and the vitrinite reflectance of coal is generally 0.7%~1.0%.

In the middle Jurassic, the coal-riching effect was enhanced, and the rich coal belt migrated westward, appearing in the areas of Fukang, Urumqi, and Manasi, forming the Xishanyao formation (J_2x) coal seam. Coal seams become thinner towards the west to east strata, and the best development is in the Urumqi area. The coal seam can be collected in a total of 11~35 layers and available in thickness from 34.1 m to 151.9 m, and the coal content is 11.7%~25%. There are 3~11 layers of coal seams that can be collected in total in Toutunhe, with a thickness of 25.6 m~52.5 m which are available and a coal-containing coefficient of 12.8%~17.6%. The vitrinite reflectance of coal in the east of Urumqi is generally less than 0.5%, most of which is in the lignite stage. The vitrinite reflectance of coal in the west of Urumqi is generally 0.5%~0.7%, mainly in long flame coal and gas coal.

The burial depth of coal seams in the east of Urumqi is shallow, generally less than 800 m, and the coal seams are relatively flat. The buried depth of the coal seam in the west of Urumqi is between 400 m and 1200 m, which is deeper

and deeper from the southern margin to the basin. The formation is steeper; the dip angle is $15^\circ\sim 25^\circ$ in the west of Urumqi and over 45° in the Miqan-Fukang area.

3. Hydrogeology

The study area has a typical arid and midtemperate continental climate. The evaporation is much larger than the rainfall, and the melting of snow and ice is the main source of coal measure formation water [6, 12]. According to regional structural characteristics, hydrodynamic parameters of coal measure aquifers, salinity, chemical characteristics of groundwater, etc., and the area can be classified into 4 hydrogeological units: Manasi River-Hutubi River (Ma-Hu), Liuhuanguo area, Miqan area, and Houxia area. This study focuses on two units of hydrogeology: Liuhuanguo area and Miqan area.

The main flow direction of regional groundwater is a centripetal movement from south to north and westward, and it migrates to the deep. In the hydrogeology unit of Ma-Hu, there are many surface rivers with strong runoff and the alternation between groundwater and surface water is frequent. In the hydrogeological unit of Liuhuanguo, the groundwater is controlled by the south-north small channel anticline, the Kalaza anticline, and the Xishan anticline in the Changji tectonic belt, and the groundwater flows from south to north. In the Miqan hydrogeological unit, the structural extrusion causes the regional groundwater flow to run from Badaowan to the oblique south wing to the core and to the southwest direction along the core. Hydrogeological unit division and groundwater migration characteristics are shown in Figure 2.

3.1. Effect of Salinity on the Formation of Hydrogen Sulfide

3.1.1. Composition Characteristics of Regional Coalbed Methane $\delta^{13}C$. The methane $\delta^{13}C$ value in the regional coalbed methane mostly falls to $-41.8\text{‰}\sim -64.7\text{‰}$, generally less than -50.0‰ , which is generally light. Among them, the $\delta^{13}C$ value of methane in the west of Urumqi is more than $-53.3\text{‰}\sim -62.5\text{‰}$, and the $\delta^{13}C$ value of methane in the east of Urumqi is more than $-62.1\text{‰}\sim -50.7\text{‰}$ [10, 13, 14]. According to the classification of coalbed methane genesis [12], it can be seen that the genetic type of regional coal seam gas has diverse characteristics, both biogenetic features and thermogenic features, but most of them belong to the mixed genetic characteristics.

3.1.2. Characteristics of $\delta^{34}S$ in the Region. The range of various sulfur isotope values ranges from -14.5‰ to 11.6‰ , which is generally low. Among them, the sulfur isotope value of pyrite in coal is between 8.7‰ and 11.6‰ , with an average of 10.2‰ ; the $\delta^{34}S$ of H_2S in the coal seam is negative, and the range of values is $-14.5\text{‰}\sim -9.4\text{‰}$, with an average of -12.3‰ ; the value of $\delta^{34}S$ in the coal mine groundwater is -0.6‰ ; the value of $\delta^{34}S$ measured in crude oil in the Houxia area of the regional boundary is 14.17‰ . The formation of H_2S generally exhibits the characteristics of BSR [2, 4, 5]. It can be seen that the regional coalbed methane contains a large amount of secondary biogas, among which methanogens and sulfate-reducing bacteria (SRB) are the main microorganisms of secondary organisms [2, 15].

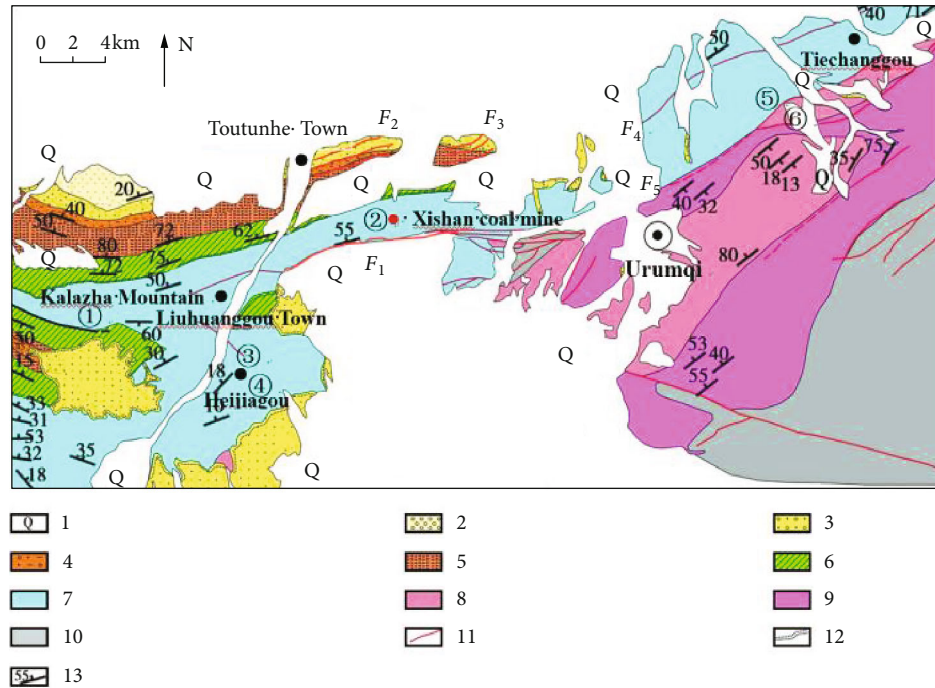


FIGURE 1: Map of coal geology in the region: 1: Quaternary, 2: upper section of Changji River Group, 3: lower middle section of Changji River Group, 4: front mountain group, 5: Upper Cretaceous and Lower Tertiary, 6: Lower Cretaceous Tugulu Group, 7: Jurassic, 8: Triassic, 9: Permian, 10: Pre-Permian, 11: fault, 12: unconformity, and 13: rock formation. ①: Kalaza anticline, ②: Xishan anticline, ③: north small channel anticline, ④: south small channel anticline, ⑤: Qidaowan anticline, and ⑥: Badaowan anticline. F_1 : Xishan fault, F_2 : Wangjiagou fault, F_3 : Jiujiawan fault, F_4 : Wanyaogou fault, and F_5 : Hongshanzui-Baiyanggou fault.

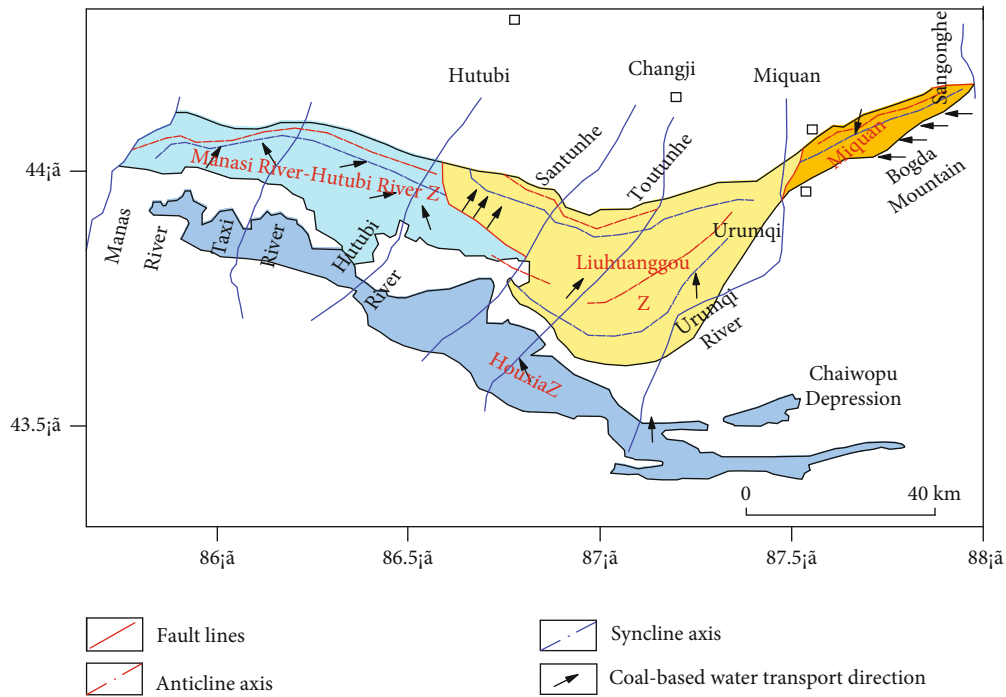


FIGURE 2: Division of hydrogeological units and characteristics of groundwater migration in the region.

3.1.3. *Effect of Salinity on the Formation of Hydrogen Sulfide.* Total dissolved solid (TDS) is the main controlling factor for microbial reproduction and gas production. When the local

layer water TDS is less than 4000 mg/L, the SRB activity is low and the gas production is very small. When the TDS is less than 10^3 mg/L, the SRB is not easy to survive. As the

concentration of TDS increases, the SRB will be significantly enhanced and the gas production efficiency will increase. When the TDS exceeds 10000 mg/L, especially in the range of 2×10^4 mg/L \sim 8×10^4 mg/L, it is very suitable for SRB reproduction. After that, with the increase of salinity, the amount of SRB bacteria decreases greatly. When the TDS reaches 3.5×10^5 mg/L, SRB is difficult to survive. Under reducing conditions when the temperature is 37°C and 50°C, respectively, the effects of different salinity on SRB growth are shown in Figure 3 [16].

The TDS of the groundwater is less than 4000 mg/L (low salinity) as a region that is not conducive to SRB reproduction and hydrogen sulfide production. The TDS ranged from 4000 mg/L to 10000 mg/L (medium salinity), as the area where SRB can reproduce and produce hydrogen sulfide. And the TDS greater than 10000 mg/L (high salinity) is the most favorable region for SRB reproduction and gas production. The statistical results of coal seam water salinity of the groundwater in coal measures in the four hydrogeological units in the region are shown in Table 1 [17].

The TDS of the four units of the groundwater in coal measures in the area varies greatly. The distribution of salinity has the characteristics of north-south zoning and east-west section. The salinity gradually increases along the direction of groundwater runoff. The low salinity zone is mainly distributed in the southern end of Houxia, Manasi River-Hutubi River, and Liuhuanguo units. This area has frequent alternating hydraulic power, and the reduction and sealing environment is poor. The SRB is not fertile, and the amount of hydrogen sulfide is small. The medium salinity area is distributed in most areas of Manasi River-Hutubi River, Liuhuanguo, and Miqan units. This area is mostly a weak groundwater flow area, and the efficiency of SRB production and hydrogen sulfide production is increased. The high salinity is distributed in the north of the Liuhuanguo unit and the northwest of the Miqan unit. This area has good sealing conditions and is a low water catchment area (hydrodynamic retention area). The SRB is highly proliferated and is the main area for the formation and enrichment of low-rank coal hydrogen sulfide. According to the degree of mineralization and the effect of salinity on SRB reproduction and hydrogen sulfide production, the distribution of salinity and the relationship between SRB reproduction and hydrogen sulfide production can be obtained as shown in Figure 4.

3.2. Influence to Hydrogen Sulfide Formation of Groundwater Chemical Characteristics. The mountains and rivers in the southeast of the region stand, the snow and ice melt, and the groundwater flows from the south to the west and north and gradually flows to the deep. In the direction of runoff, due to the large hydraulic gradient, the alternating action is strong; during the process of infiltration and runoff, dissolution and leaching of calcium feldspar and albite will occur. The possible chemical reactions are shown in Equations (1)–(3) [5, 17]:

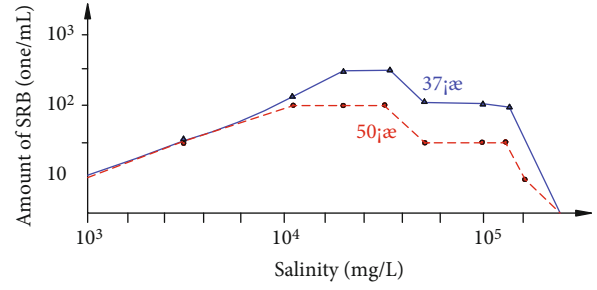
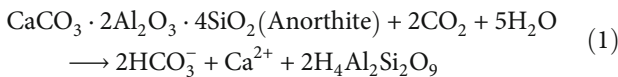
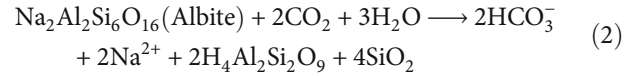
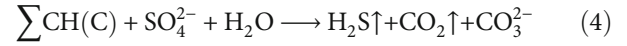


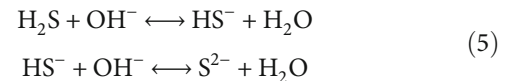
FIGURE 3: The effect of different salinity on the growth of SRB.



High salinity water may form under severe drought evaporation. And the deep water environment is well sealed. In the hydrocarbon-rich conditions, under the action of SRB, BSR action will occur and H_2S will be formed. The possible reaction formula is shown in Equation (4) [3, 17]:



A series of BSR promote the formation of calcium carbonate crystals in the water by CO_2 and soluble calcium ions, which facilitates the reaction in a positive direction and leads to a decrease in Ca^{2+} content. From the south to the north of the basin, the cation Ca^{2+} in the deep pressure water of each coal mine was reduced from 57.8% to 21.2% [9], and the chemical characteristics such as Ca^{2+} and H_2S content in the water body met the above rules. H_2S is a dibasic acid that is easily soluble in water, and there are two ionization balances in H_2S in aqueous solution [5]:



The groundwater is weakly alkaline, and the pH value is mostly between 7.5 and 9.0. It can be seen that the sulfide in the groundwater in coal measures mainly exists in the form of H_2S and HS^- .

3.3. Influence of Groundwater Control on Hydrogen Sulfide Formation. The high salinity formation water formed by the melting of snow in the southeastern mountains, and the rainfall during the runoff flows into the depression or fault zone in the front of the mountain, and its Quaternary sediments are about 400 m~1300 m thick; a thick layer of loose sand and gravel is piled up. The geological structure of the depression or the basal uplift provides a huge space for the occurrence and migration of groundwater (H_2S). Regional hydrocarbon sources are widely developed. In deep closed environments, groundwater migration is slow or stagnant, SRB is highly proliferated, BSR will occur, and hydrogen sulfide is formed. The regional underground hydrogen

TABLE 1: TDS distribution of groundwater in coal measures.

Hydrogeological unit	Layer	Salinity of groundwater (mg/L)
Manasi River-Hutubi River	Xishanyao formation (J ₂ x)	1256-4856 2342
	Xishanyao formation (J ₂ x)	3489-17527 12925
Liuhuanggou area	Badaowan formation (J ₁ b)	4875-18509 13261
	Xishanyao formation (J ₂ x)	4588-15855 11029
Miquan area	Badaowan formation (J ₁ b)	5893-18783 12418
	Badaowan formation (J ₁ b)	487-2047 1405

sulfide-containing water cycle characteristics can be described as shown in Figure 5.

The regional hydrodynamic gas control is mainly characterized by hydrodynamic closed gas control and hydrodynamic plugging gas control. The east of Urumqi is affected by geological structures, and its groundwater in coal measure monoslanting south wing is recharged by rivers and glacial meltwater, mostly weak runoff areas, and stagnant areas. The sealing conditions are good, and the generated H₂S dissolves into the water body or escapes to gas and with the flow of water to the deep part of the coal seam. Meanwhile, the poor continuity of the surrounding rock sand body causes the slowness or the stagnation of the groundwater of the coal-bearing areas. Therefore, the H₂S diffusing upward in coal rock will be blocked. At the same time, the slowness of groundwater carries H₂S to the deep part and H₂S will be blocked, resulting in anomalous enrichment of H₂S in coal rock and water. The H₂S accumulation model of northward monoclinic is shown in Figure 6 [17].

The west of Urumqi is affected by the Urumqi-Miquan strike-slip fault, and the thrust nappe tectonic belt is developed. It is a kind of fracture with a slip motion moving perpendicular to the fracture surface, and an anticline distribution with a geese shape and imbricate is formed. In the coal outcrops in the southwestern part of the west of Urumqi, water is alternately connected, which is the infiltration area of the formation water. The local zone forms a discharge zone where the hydraulic power alternates strongly. The reduction environment is poor, and SRB reproduction and formation of H₂S are not used, and the groundwater body will continuously dissolve and take away the generated H₂S during the migration process, eventually leading to H₂S dissipation. It is not conducive to the enrichment of H₂S. In the area of the Xishan coal mine in the northwestern part of the west of Urumqi, the deep hydraulic performance is the retention zone. For H₂S generated by the BSR action, some of gas is integrated into the water body and slowly migrated to the deep part; some of it is mixed into the gas of the coal seam and migrates vertically or longitudinally along the gas source

at the depression. The distribution of hydrogen sulfide in the regional coal and rock layers is extremely uneven. In the southern part of the west of Urumqi, the hydrodynamic alternating of the shallow strata is relatively strong, and H₂S is rarely enriched. However, in the hydrological detention area (Xishan mining area) in the northern part of the west of Urumqi, hydrogen sulfide enrichment is extremely serious. The area of the imbricate H₂S formation and aggregation mode is shown in Figure 7.

4. Hydrogen Sulfide Solubility of Groundwater in Coal Measures

The solubility of H₂S in water is usually affected by temperature, pressure, salinity, water chemistry, and mixed gases [18, 19]. Duan et al. [20, 21] and others believe that the solubility of H₂S is essentially a gas-liquid equilibrium problem, and the gas-liquid equilibrium problem can be calculated by the equilibrium of H₂S in the chemical position $\mu_{\text{H}_2\text{S}}^l$ of the gas phase and the chemical position $\mu_{\text{H}_2\text{S}}^l$ of the liquid phase. As shown in

$$\begin{aligned} \mu_{\text{H}_2\text{S}}^l(T, P, m) &= \mu_{\text{H}_2\text{S}}^{l(0)}(T, P) + RT \ln \alpha_{\text{H}_2\text{S}}(T, P, m) = \mu_{\text{H}_2\text{S}}^{l(0)}(T, P) \\ &\quad + RT \ln m_{\text{H}_2\text{S}} + RT \ln \gamma_{\text{H}_2\text{S}}(T, P, m), \end{aligned} \quad (6)$$

$$\begin{aligned} \mu_{\text{H}_2\text{S}}^v(T, P, y) &= \mu_{\text{H}_2\text{S}}^{v(0)}(T) + RT \ln f_{\text{H}_2\text{S}}(T, P, y) \\ &= \mu_{\text{H}_2\text{S}}^{v(0)}(T) + RT \ln y_{\text{H}_2\text{S}}(P) + RT \ln \varphi_{\text{H}_2\text{S}}(T, P, y), \end{aligned} \quad (7)$$

where $\mu_{\text{H}_2\text{S}}^{v(0)}$ is the standardization degree of H₂S in the gas phase, which is the ideal gas chemical position at a pressure of 1 bar; $\mu_{\text{H}_2\text{S}}^{l(0)}$ is the standardization degree of hydrogen sulfide in the liquid phase, which is the chemical position of the ideal solution per unit weight molar concentration; m is gas solubility; $y_{\text{H}_2\text{S}}$ is hydrogen sulfide component; $\gamma_{\text{H}_2\text{S}}$ is hydrogen sulfide activity coefficient; T is temperature; and P is pressure. When the phase balance $\mu_{\text{H}_2\text{S}}^v = \mu_{\text{H}_2\text{S}}^l$, it can get

$$\begin{aligned} \ln \frac{y_{\text{H}_2\text{S}} P}{m_{\text{H}_2\text{S}}} &= \frac{\mu_{\text{H}_2\text{S}}^{l(0)}(T, P) - \mu_{\text{H}_2\text{S}}^{v(0)}(T)}{RT} - \ln \varphi_{\text{H}_2\text{S}}(T, P, y) \\ &\quad + \ln \gamma_{\text{H}_2\text{S}}(T, P, m), \end{aligned} \quad (8)$$

where H₂S solubility ($m_{\text{H}_2\text{S}}$) is a function of the difference in T , P , $y_{\text{H}_2\text{S}}$, H₂S fugacity coefficient ($\varphi_{\text{H}_2\text{S}}$), $\gamma_{\text{H}_2\text{S}}$, $\mu_{\text{H}_2\text{S}}^{v(0)}$, and $\mu_{\text{H}_2\text{S}}^{l(0)}$. Let $\mu_{\text{H}_2\text{S}}^{v(0)}$ be zero; because only a small amount of water vapor is contained in the gas phase, the difference in the fugacity coefficient of the pure gas is very small, and the fugacity coefficient $\ln \varphi_{\text{H}_2\text{S}}$ determined by the pure gas state equation can be approximated. Therefore, the molar fraction of $y_{\text{H}_2\text{S}}$ in the

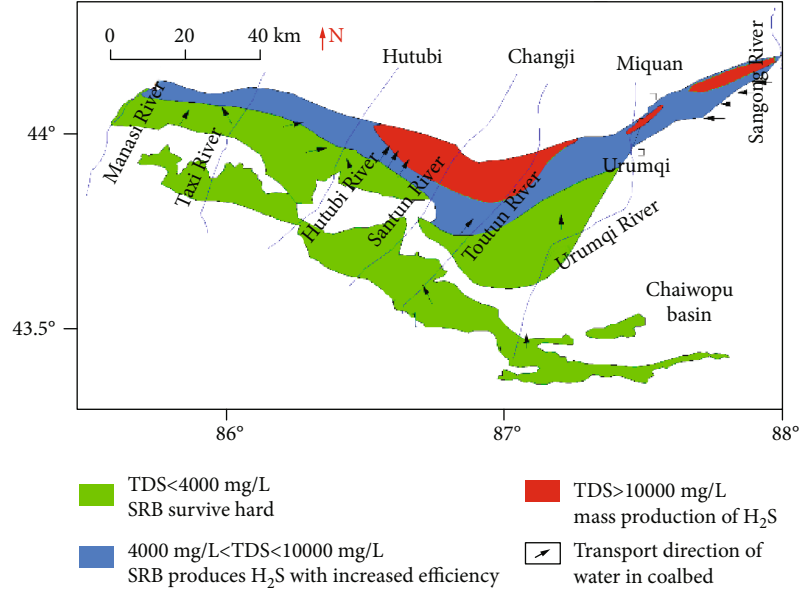


FIGURE 4: TDS distribution of groundwater and characteristics of SRB propagation and H₂S generation.

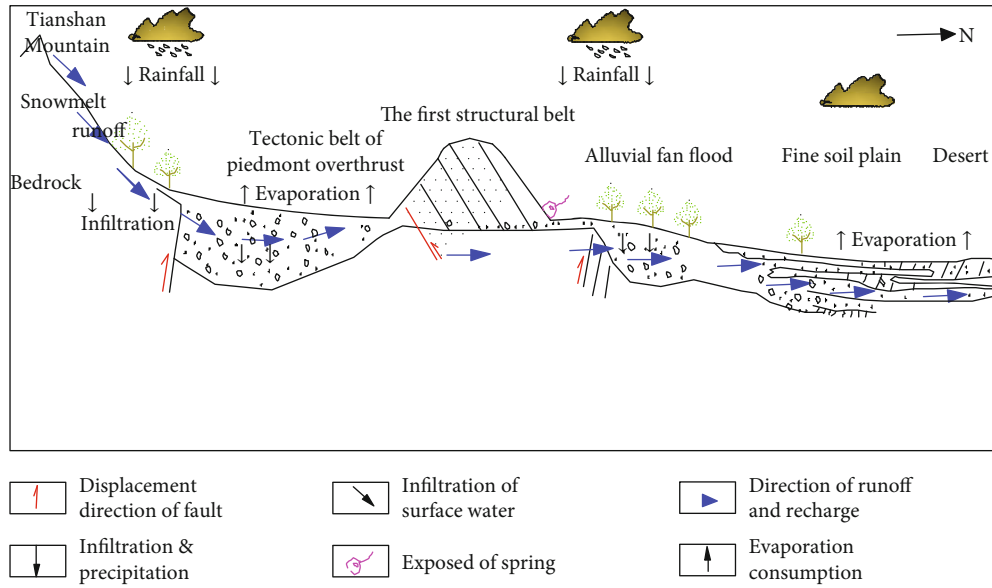


FIGURE 5: Cycle characteristics of water bearing H₂S.

gas phase can be approximated by

$$y_{\text{H}_2\text{S}} = \frac{P - P_{\text{H}_2\text{O}}}{P}. \quad (9)$$

In the formula, $P_{\text{H}_2\text{O}}$ can be approximated as the saturation pressure of pure water. The activity coefficient of H₂S in the liquid phase can be derived from the Pitzer model [22]:

$$\ln \gamma_{\text{H}_2\text{S}} = \sum_C 2\lambda_{\text{H}_2\text{S}-\text{C}} m_C + \sum_a 2\lambda_{\text{H}_2\text{S}-\text{a}} m_a + \sum_C \sum_a \xi_{\text{H}_2\text{S}-\text{a}-\text{C}} m_C m_a, \quad (10)$$

where λ and ζ are binary and ternary interaction parameters,

respectively, and c and a represent cations and anions, respectively. Substituting Equation (10) into Equation (8) yields

$$\ln \frac{y_{\text{H}_2\text{S}} P}{m_{\text{H}_2\text{S}}} = \frac{\mu_{\text{H}_2\text{S}}^{l(0)}}{RT} - \ln \varphi_{\text{H}_2\text{S}} + \sum_C 2\lambda_{\text{H}_2\text{S}-\text{C}} m_C + \sum_a 2\lambda_{\text{H}_2\text{S}-\text{a}} m_a + \sum_C \sum_a \xi_{\text{H}_2\text{S}-\text{a}-\text{C}} m_C m_a, \quad (11)$$

where λ , ζ , and the dimensionless standardized degree $\mu_{\text{H}_2\text{S}}^{l(0)}/RT$ are all functions of temperature and pressure; these parameters can be determined by regression of

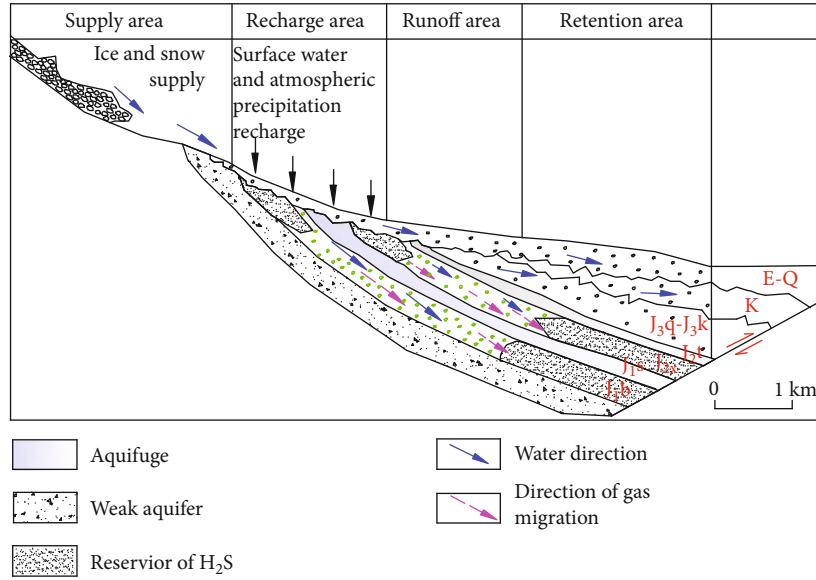


FIGURE 6: Single level of H₂S formation and accumulation model in the east of Urumqi.

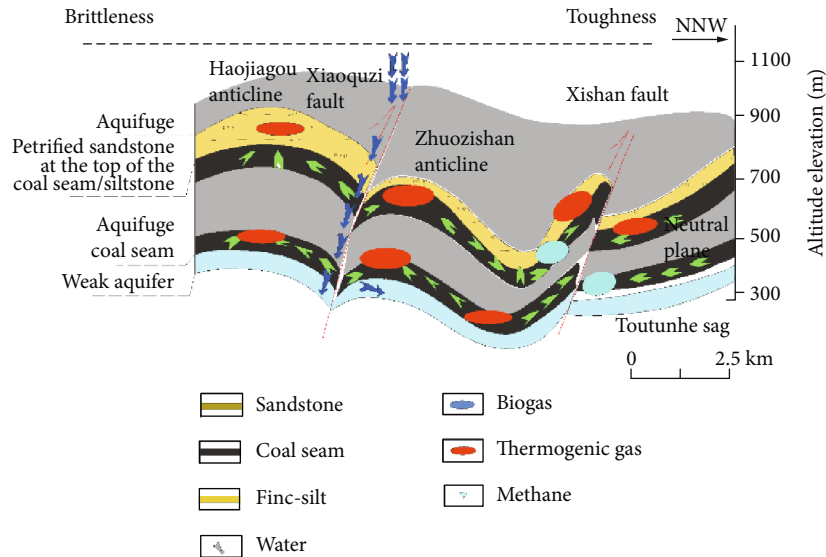


FIGURE 7: Imbricate of H₂S formation and accumulation model in the west of Urumqi.

solubility experimental data of pure gas. According to the Pitzer model [22], the H₂S solubility calculation model can be expressed as follows:

$$\begin{aligned}
 Par(T, P) = & C_1 + C_2 + \frac{C_3}{T} + C_4 T^2 + \frac{C_5}{680 - T} + C_6 P \\
 & + \frac{C_7 P}{680 - T} + \frac{C_8 P^2}{T}. \quad (12)
 \end{aligned}$$

Equations (11) and (12) form the basic equation for the calculation of the solubility of H₂S.

The interaction parameters for calculating the solubility of H₂S were shown in Table 2 [20, 21].

According to the gas interaction parameters in Table 3, the solubility of H₂S in pure water and different molar NaCl

and Na₂SO₄ solutions was obtained by the above formula, as shown in Figures 8–10 [20, 21, 23–25].

It can be seen that under the same conditions, the solubility of H₂S in pure water is greater than that of aqueous solution containing salinity, and its solubility decreases as the temperature of the solution rises. The higher the degree of mineralization, the lower the solubility of hydrogen sulfide. With the increase of pressure, the solubility of hydrogen sulfide can be significantly improved, especially in the initial stage of 0.1 MPa~6.0 MPa.

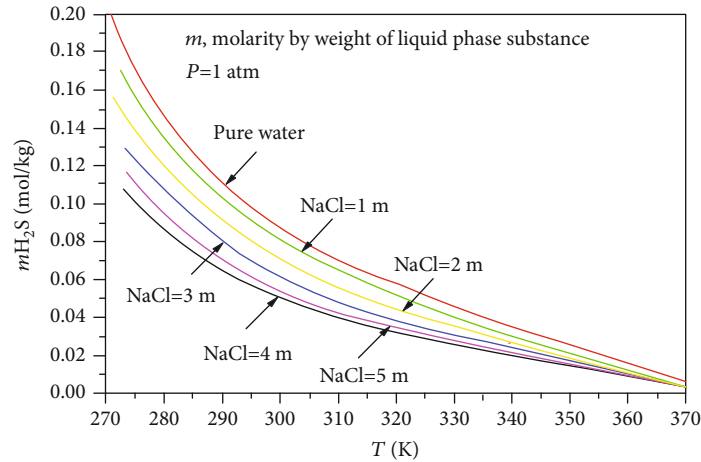
Studies have shown that the variation law of the regional geothermal gradient is the following [16]: when the buried depth is less than 1000 m, it is between 24°C and 41°C, with an average of 33°C; the buried depth is 1000 m~2000 m, which is between 34°C and 73°C; the average is 53.8°C. According to the reservoir parameters of the 1000 m

TABLE 2: Interaction parameters of H₂S solubility.

T - P coefficient	$\frac{\mu_{\text{H}_2\text{S}}^{(0)}}{RT}$	$\lambda_{\text{H}_2\text{S}-\text{Na}}$	$\zeta_{\text{H}_2\text{S}-\text{Na}-\text{Cl}}$
C_1	42.564957	8.5004999×10^{-2}	$-1.0832589 \times 10^{-2}$
C_2	$-8.6260377 \times 10^{-2}$	$3.5330.78 \times 10^{-5}$	
C_3	-6084.3775	-1.5882605	
C_4	6.8714437×10^{-5}		
C_5	-102.76849		
C_6	8.4482895×10^{-4}	1.1894926×10^{-5}	
C_7	-1.0590768		
C_8	3.5665902×10^{-3}		

TABLE 3: Reservoir parameters of 1000 m depth of coal measures and solubility of H₂S in the region.

Hydrogeological unit	Formation temperature (°C)	Reservoir pressure (MPa)	Salinity (mg/L)	Solubility of H ₂ S (mg/L)
Manasi River-Hutubi River	32.3	8.9	2100	54200
Liuhuangou area	35.2	9.1	11500	49680
Miquan area	32.6	8.8	10800	50320
Houxia area	28.3	9.8	1210	59840

FIGURE 8: Solubility of H₂S in pure water and NaCl solution.

reservoir depth of the four hydrogeological units, the solubility of H₂S in the groundwater in coal measures can be estimated, as shown in Table 3. And the characteristics of SRB propagation and hydrogen sulfide production in the region are shown in Figure 4.

5. Conclusions

(1) Four hydrogeological units are divided. The salinity in the hydrogeological units is low, where hydraulic power alternates strongly; it is not conducive to the survival of SRB and the formation of hydrogen sulfide. The high salinity center and depressions of low water level (hydrodynamic stagnation zone) are the main areas for the proliferation of SRB and pro-

duction and enrichment of H₂S in the low-rank coal. The increase in salinity is conducive to the proliferation of SRB and the formation of hydrogen sulfide

- (2) The deep confined water environment closed well; under the action of SRB, BSR will occur and H₂S can form. Imbricate and single bevel two kind generation and enrichment mode of hydrogen sulfide under the hydrodynamic control was obtained
- (3) In calculating the solubility of hydrogen sulfide gas in the groundwater in coal measures, in addition to the factors mentioned in the paper, it should be considered in combination with the chemical type of formation water and the characteristics of mixed gas components

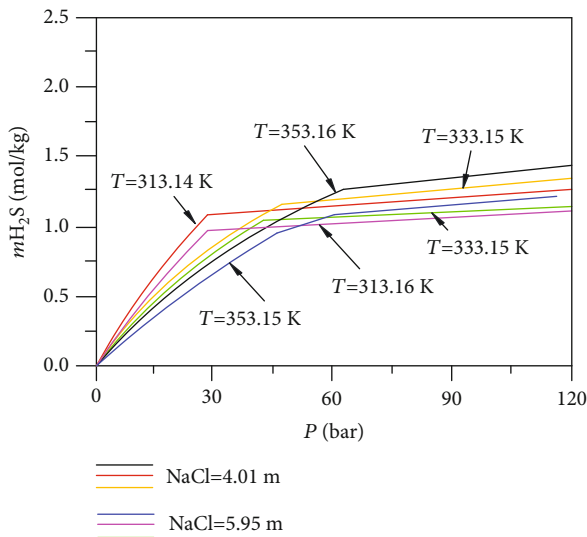


FIGURE 9: Solubility of H_2S in NaCl solution.

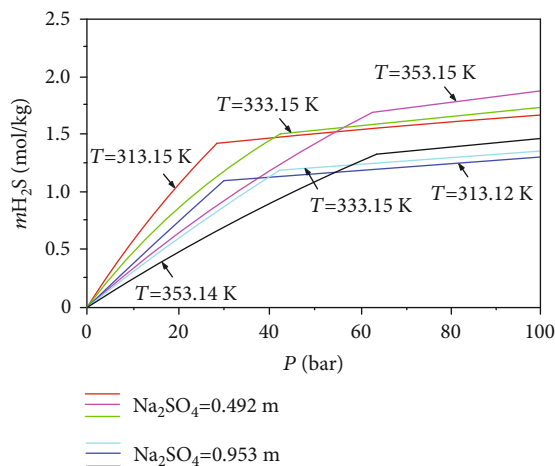


FIGURE 10: Solubility of H_2S in Na_2SO_4 solution.

Data Availability

The data used to support the findings of this study are available from the corresponding author upon request.

Conflicts of Interest

The authors declare that they have no conflicts of interest.

Acknowledgments

The authors are grateful to Professor Mingju Liu of Henan Polytechnic University for his ardent guidance and help. This work was supported by the National Natural Science Foundation of China under grant No. 51774116, the Key Scientific Research Project of Colleges and Universities in Henan Province under grant No. 14B440006, and the Training Plan of Young Backbone Teachers in Colleges and Universities of Henan Province under grant No. 2019GGJS052.

References

- [1] Q. Deng, J. Yin, X. Wu, T. Zhang, H. Wang, and M. Liu, "Research advances of prevention and control of hydrogen sulfide in coal mines," *The Scientific World Journal*, vol. 2019, Article ID 8719260, 15 pages, 2019.
- [2] Q. Deng, X. Wu, Y. Wang, and M. Liu, "Activity characteristics of sulfate reducing bacteria and formation mechanism of hydrogen sulphide," *Applied Ecology and Environmental Research*, vol. 16, no. 5, pp. 6369–6383, 2018.
- [3] H. G. Machel, "Bacterial and thermochemical sulfate reduction in diagenetic settings – old and new insights," *Sedimentary Geology*, vol. 140, no. 1-2, pp. 143–175, 2001.
- [4] M. Liu, Q. Deng, F. Zhao, and Y. Liu, "Origin of hydrogen sulfide in coal seams in China," *Safety Science*, vol. 50, no. 4, pp. 668–673, 2012.
- [5] Q. Deng, M. Liu, X. Cui, and J. Wen, "A study of hydrogen sulfide genesis in coal mine of southeastern margin of Junggar basin," *Journal of Earth Science Frontiers*, vol. 24, no. 5, pp. 395–401, 2017.
- [6] Y. Li, C. Zhang, D. Tang et al., "Coal pore size distributions controlled by the coalification process: An experimental study of coals from the Junggar, Ordos and Qinshui basins in China," *Fuel*, vol. 206, pp. 352–363, 2017.
- [7] S. Tao, Z. Pan, S. Chen, and S. Tang, "Coal seam porosity and fracture heterogeneity of marcolithotypes in the Fanzhuang block, southern Qinshui Basin, China," *Journal of Natural Gas Science and Engineering*, vol. 66, pp. 148–158, 2019.
- [8] J. J. Tian and S. G. Yang, "Sequence strata and coal accumulation of lower and middle Jurassic formation from southern margin of Junggar Basin, Sinkiang, China," *Journal of China Coal Society*, vol. 36, no. 1, pp. 58–64, 2011.
- [9] Y. Li, J. Yang, Z. Pan, S. Meng, K. Wang, and X. Niu, "Unconventional natural gas accumulations in stacked deposits: a discussion of Upper Paleozoic coal-bearing strata in the eastern margin of the Ordos Basin, China," *Acta Geologica Sinica*, vol. 93, no. 1, pp. 111–129, 2019.
- [10] L. Yong, C. Daiyong, W. Yingchun, W. Anmin, Z. Qiang, and W. Peng, "Middle to low rank coalbed methane accumulation and reservoiring in the southern margin of Junggar Basin," *Acta Petrolei Sinica*, vol. 37, no. 12, pp. 1472–1482, 2016.
- [11] Z. H. Chen, Z. P. Meng, and L. J. Zeng, "Formation mechanism and enrichment patterns of middle-low rank coalbed methane in southern Junggar Basin, China," *Journal of China Coal Society*, vol. 42, no. 12, pp. 3203–3211, 2017.
- [12] L. Duan, W. K. Wang, Y. Q. Cao, L. J. Wang, and B. Liu, "Hydrochemical characteristics and formation mechanics of groundwater in the middle of northern slope of Tianshan Mountains," *Journal of Arid Land Resources and Environment*, vol. 21, no. 9, pp. 29–34, 2007.
- [13] J. Guo, X. Wang, and X. Pang, "Evaluation and hydrocarbon expulsion characteristics of the middle-lower Jurassic source rock in the southern margin of Junggar basin," *Journal of China University of Mining & Technology*, vol. 42, no. 4, pp. 595–605, 2013.
- [14] S. Tao, S. Chen, and Z. Pan, "Current status, challenges, and policy suggestions for coalbed methane industry development in China: a review," *Energy Science & Engineering*, vol. 9, no. 7, pp. 1–16, 2019.
- [15] C. Z. Jia, "Foreland thrust-fold belt features and gas accumulation in Midwest China," *Petroleum Exploration & Development*, vol. 32, no. 4, pp. 9–15, 2005.

- [16] D. Y. Yu, F. M. Peng, X. W. Liu, and J. L. Zheng, "Effect of environment on the growth of sulfate reducing bacteria," *Materials Protection*, vol. 29, no. 2, pp. 1-2, 1996.
- [17] Q. Deng, J. Wei, H. Li, Y. Wang, X. Wu, and M. Liu, "Hydrogen sulfide accumulation factors in coal mine of southeastern margin of Junggar basin in China," *Applied Ecology and Environmental Research*, vol. 17, no. 1, pp. 683-697, 2019.
- [18] L. Zhang and R. Sun, "An improved thermodynamic model for calculating solubility of the CO₂-CH₄-N₂-C₂H₆- H₂S gas mixture in water," *Geological Journal of China Universities*, vol. 22, no. 4, pp. 589-597, 2016.
- [19] S. Mao, L. Shi, Q. Peng, and M. Lü, "Thermodynamic modeling of binary CH₄-CO₂ fluid inclusions," *Applied Geochemistry*, vol. 66, no. 20, pp. 65-72, 2016.
- [20] Z. Duan, R. Sun, R. Liu, and C. Zhu, "Accurate thermodynamic model for the calculation of H₂S solubility in pure water and brines," *Energy & Fuels*, vol. 21, no. 4, pp. 2056-2065, 2007.
- [21] Z. H. Duan and Q. Wei, "Model for the calculation of the solubility of CH₄: H₂S and CO₂ in aqueous solutions," *Acta Geologica Sinica*, vol. 85, no. 7, pp. 1079-1093, 2011.
- [22] K. S. Pitzer, J. C. Peiper, and R. H. Busey, "Thermodynamic properties of aqueous sodium chloride solutions," *Journal of Physical and Chemical Reference Data*, vol. 13, no. 1, pp. 1-102, 1984.
- [23] J. I. Lee and A. E. Mather, "Solubility of hydrogen sulfide in water," *Berichte der Bunsengesellschaft für physikalische Chemie*, vol. 81, no. 10, pp. 1020-1023, 1977.
- [24] S. Ingolf and C. H. Whitson, "Peng-Robinson predictions for hydrocarbons, CO₂, N₂, and H₂S with pure water and NaCl brine," *Fluid Phase Equilibria*, vol. 77, no. 92, pp. 217-240, 1992.
- [25] B. Rumpf, Á. Pérez-Salado Kamps, R. Sing, and G. Maurer, "Simultaneous solubility of ammonia and hydrogen sulfide in water at temperatures from 313 K to 393 K," *Fluid Phase Equilibria*, vol. 158-160, no. 9, pp. 923-932, 1999.